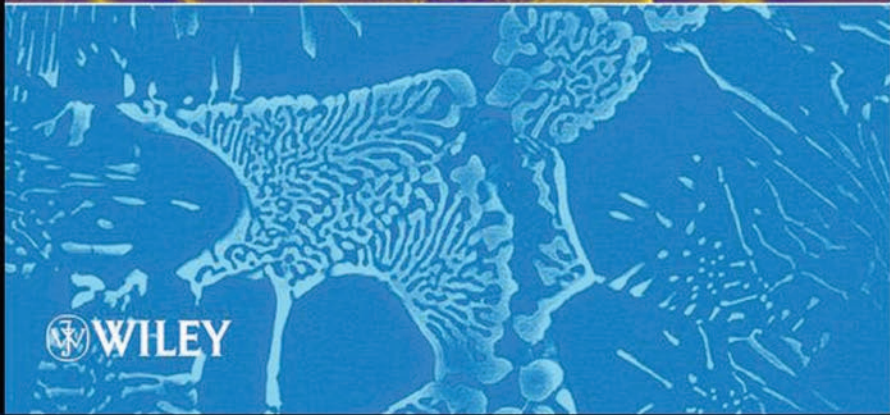
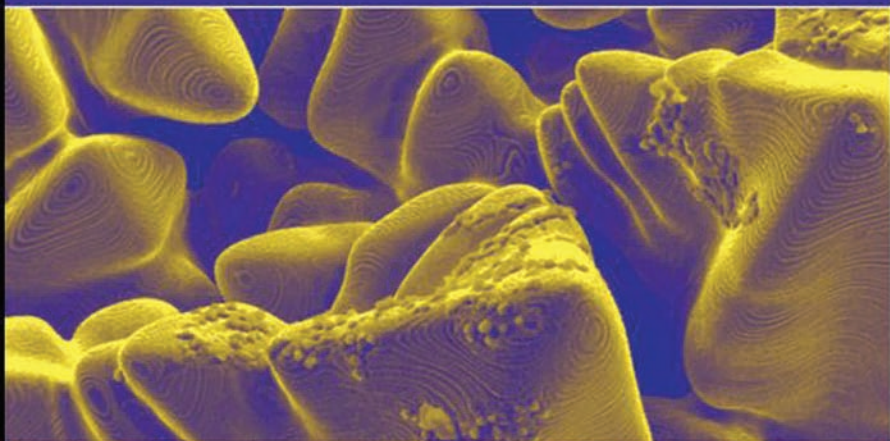


# WELDING METALLURGY AND WELDABILITY OF NICKEL-BASE ALLOYS

JOHN N. DUPONT • JOHN C. LIPPOLD  
SAMUEL D. KISER



 WILEY



# **WELDING METALLURGY AND WELDABILITY OF NICKEL-BASE ALLOYS**



---

# **WELDING METALLURGY AND WELDABILITY OF NICKEL-BASE ALLOYS**

---

John N. DuPont  
John C. Lippold  
Samuel D. Kiser

 **WILEY**

A JOHN WILEY & SONS, INC., PUBLICATION

Copyright © 2009 by John Wiley & Sons, Inc. All rights reserved.

Published by John Wiley & Sons, Inc., Hoboken, New Jersey.  
Published simultaneously in Canada.

No part of this publication may be reproduced, stored in a retrieval system, or transmitted in any form or by any means, electronic, mechanical, photocopying, recording, scanning, or otherwise, except as permitted under Section 107 or 108 of the 1976 United States Copyright Act, without either the prior written permission of the Publisher, or authorization through payment of the appropriate per-copy fee to the Copyright Clearance Center, Inc., 222 Rosewood Drive, Danvers, MA 01923, (978) 750-8400, fax (978) 750-4470, or on the web at [www.copyright.com](http://www.copyright.com). Requests to the Publisher for permission should be addressed to the Permissions Department, John Wiley & Sons, Inc., 111 River Street, Hoboken, NJ 07030, (201) 748-6011, fax (201) 748-6008, or online at <http://www.wiley.com/go/permission>.

**Limit of Liability/Disclaimer of Warranty:** While the publisher and author have used their best efforts in preparing this book, they make no representations or warranties with respect to the accuracy or completeness of the contents of this book and specifically disclaim any implied warranties of merchantability or fitness for a particular purpose. No warranty may be created or extended by sales representatives or written sales materials. The advice and strategies contained herein may not be suitable for your situation. You should consult with a professional where appropriate. Neither the publisher nor author shall be liable for any loss of profit or any other commercial damages, including but not limited to special, incidental, consequential, or other damages.

For general information on our other products and services or for technical support, please contact our Customer Care Department within the United States at (800) 762-2974, outside the United States at (317) 572-3993 or fax (317) 572-4002.

Wiley also publishes its books in a variety of electronic formats. Some content that appears in print may not be available in electronic formats. For more information about Wiley products, visit our web site at [www.wiley.com](http://www.wiley.com).

***Library of Congress Cataloging-in-Publication Data:***

DuPont, John N.

Welding metallurgy and weldability of nickel-base alloys / John N. DuPont,  
John C. Lippold, and Samuel D. Kiser.

p. cm.

ISBN 978-0-470-08714-5 (cloth)

1. Nickel-Welding. 2. Nickel-Metallurgy. 3. Nickel alloys-Welding. 4. Nickel alloys-Metallurgy. I. DuPont, John N., 1964- II. Kiser, Samuel D. 1945- III. Title.

TS227.L657 2009

673'.733252-dc22

2009017253

Printed in the United States of America.

10 9 8 7 6 5 4 3 2 1

*This book is dedicated to Alden and Pauline DuPont, who inspired me when I was young, and Ryan and Caitlin, who have been inspiring me ever since.*

*John N. DuPont  
Lehigh University, 2009*

*This book is dedicated to my wife, Mary Catherine Juhas, who has supported me throughout my career and remains a constant source of strength, inspiration, and good humor.*

*John C. Lippold  
The Ohio State University, 2009*

*This book is dedicated to Jackie Kiser, my friend, my spiritual partner, and my co-worker in all that I set out to do.*

*Samuel D. Kiser  
Special Metals Welding Products Company, 2009*



# CONTENTS

---

<b>Preface</b>	<b>xiii</b>
<b>1. Introduction</b>	<b>1</b>
1.1 Ni-base Alloy Classification	2
1.1.1 Commercially Pure Nickel Alloys	2
1.1.2 Solid-Solution Strengthened Alloys	3
1.1.3 Precipitation-Strengthened Alloys	4
1.1.4 Other Specialty Alloys	5
1.2 History of Nickel and Ni-base Alloys	5
1.3 Corrosion Resistance	11
1.4 Nickel Alloy Production	12
References	14
<b>2. Alloying Additions, Phase Diagrams, and Phase Stability</b>	<b>15</b>
2.1 Introduction	15
2.2 General Influence of Alloying Additions	16
2.3 Phase Diagrams for Solid-Solution Alloys	20
2.3.1 The Ni-Cu System	20
2.3.2 The Ni-Cr System	21
2.3.3 Ni-Mo System	22
2.3.4 The Ni-Fe-Cr System	22
2.3.5 Ni-Cr-Mo System	24
2.4 Phase Diagrams for Precipitation Hardened Alloys— $\gamma'$ Formers	26
2.5 Phase Diagrams for Precipitation-Hardened Alloys— $\gamma''$ Formers	30
2.6 Calculated Phase Stability Diagrams	33
2.7 PHACOMP Phase Stability Calculations	40
References	43
<b>3. Solid-Solution Strengthened Ni-base Alloys</b>	<b>47</b>
3.1 Standard Alloys and Consumables	47
3.2 Physical Metallurgy and Mechanical Properties	51

3.3	Welding Metallurgy	57
3.3.1	Microstructural Evolution in the Fusion Zone	57
3.3.1.1	<i>Interfaces in Single Phase Austenitic Weld Metal</i>	57
3.3.1.1.1	<i>Solidification Subgrain Boundaries (SSGBs)</i>	57
3.3.1.1.2	<i>Solidification Grain Boundaries (SGBs)</i>	58
3.3.1.1.3	<i>Migrated Grain Boundaries (MGBs)</i>	59
3.3.1.2	<i>Elemental Segregation during Solidification</i>	59
3.3.1.3	<i>Phase Transformation Sequence</i>	70
3.3.2	Heat Affected Zone	81
3.3.3	Postweld Heat Treatment	82
3.3.3.1	<i>Stress Relief Heat Treatments</i>	83
3.3.3.2	<i>Homogenization of Weld Metal Microstructure</i>	87
3.4	Mechanical Properties of Weldments	91
3.4.1	Hydrogen Effects	91
3.4.2	Postweld Heat Treatment	93
3.5	Weldability	100
3.5.1	Fusion Zone Solidification Cracking	100
3.5.2	HAZ Liquefaction Cracking	118
3.5.3	Avoiding Solidification and Liquefaction Cracking	123
3.5.4	Ductility-Dip Cracking	128
3.5.4.1	<i>Description of Ductility-Dip Cracking</i>	128
3.5.4.2	<i>Proposed Mechanisms for Ductility-Dip Cracking</i>	130
3.5.4.3	<i>Ductility-Dip Cracking in Ni-base Weld Metals</i>	131
3.5.4.4	<i>Avoiding Ductility-Dip Cracking</i>	143
3.6	Corrosion Resistance	143
3.7	Case Studies	149
3.7.1	Pitting Corrosion in MONEL <sup>®</sup> Welds	149
	References	150
<b>4.</b>	<b>Precipitation-Strengthened Ni-base Alloys</b>	<b>157</b>
4.1	Standard Alloys and Consumables	158
4.2	Physical Metallurgy and Mechanical Properties	161
4.3	Welding Metallurgy	173
4.3.1	Microstructural Evolution in the Fusion Zone	173
4.3.1.1	<i>Elemental Segregation during Solidification</i>	173
4.3.1.2	<i>Phase Transformations—<math>\gamma'</math> Formation</i>	175

4.3.1.3	<i>Phase Transformations—Carbide Formation</i>	182
4.3.1.4	<i>Phase Transformations—<math>\gamma''</math> Formation</i>	184
4.3.1.5	<i>Effect of Nb and C</i>	187
4.3.1.6	<i>Fusion Zone Microstructure Predictions using New PHACOMP</i>	196
4.3.2	Heat-Affected Zone	201
4.3.3	Postweld Heat Treatment	204
4.4	Mechanical Properties of Weldments	206
4.5	Weldability	207
4.5.1	Solidification Cracking	208
4.5.1.1	<i>Effect of Minor Element Additions—B and Zr</i>	208
4.5.1.2	<i>Effect of Nb Additions</i>	210
4.5.1.3	<i>Cast Pin Tear Test Results</i>	220
4.5.1.4	<i>Summary of Solidification Cracking</i>	222
4.5.2	HAZ Liquation Cracking	223
4.5.2.1	<i>Composition Effects</i>	224
4.5.2.2	<i>Effect of Grain Size</i>	226
4.5.2.3	<i>Effect of Heat Treatment</i>	228
4.5.2.4	<i>Effect of Thermal Stress/Strain</i>	234
4.5.2.5	<i>Summary of HAZ Liquation Cracking</i>	235
4.5.3	Strain-Age Cracking	235
4.5.3.1	<i>Mechanism for Strain-Age Cracking</i>	237
4.5.3.2	<i>Effect of Residual, Thermal and Aging Stresses, and Joint Restraint</i>	242
4.5.3.3	<i>Composition Effects</i>	244
4.5.3.4	<i>Grain Size</i>	245
4.5.3.5	<i>Preweld Condition of the Base Metal</i>	245
4.5.3.6	<i>Effect of Welding Procedure</i>	246
4.5.3.7	<i>Effect of Postweld Heat Treatment</i>	246
4.5.3.8	<i>Summary of Strain-Age Cracking</i>	248
References		248

## **5. Oxide Dispersion Strengthened Alloys and Nickel Aluminides 255**

5.1	Oxide Dispersion Strengthened Alloys	255
5.1.1	Physical and Mechanical Metallurgy	255
5.1.2	Welding Metallurgy	259
5.1.3	Summary of the Weldability of ODS Alloys	268
5.2	Nickel Aluminide Alloys	268
5.2.1	Physical and Mechanical Metallurgy	268
5.2.2	Weldability of the Ni-Aluminides	272
5.2.2.1	<i>Elevated Temperature Cracking</i>	272
5.2.2.2	<i>Hot Ductility Behavior</i>	274
5.2.2.3	<i>Brazing</i>	276

5.2.3	Summary of the Weldability of Nickel Aluminide Alloys	276
	References	278
<b>6.</b>	<b>Repair Welding of Ni-base Alloys</b>	<b>281</b>
6.1	Solid-Solution Strengthened Alloys	281
6.2	Precipitation-Strengthened Alloys	283
6.2.1	Alloy 718	284
6.2.1.1	<i>Effect of <math>\delta</math>-phase Formation</i>	284
6.2.1.2	<i>Rejuvenation Heat Treatments</i>	292
6.2.1.3	<i>Summary of Repair Weldability of Alloy 718</i>	294
6.2.2	Waspaloy	295
6.3	Single Crystal Superalloys	298
6.3.1	Control of Single Crystal Weld Repairs	302
6.3.2	Solidification Cracking	314
6.3.3	Optimizing Processing Parameters	317
	References	324
<b>7.</b>	<b>Dissimilar Welding</b>	<b>327</b>
7.1	Application of Dissimilar Welds	327
7.2	Influence of Process Parameters on Fusion Zone Composition	328
7.3	Carbon, Low Alloy and Stainless Steels	331
7.3.1	Determining Weld Metal Constitution	332
7.3.2	Fusion Boundary Transition Region	334
7.3.3	Weldability	342
7.3.3.1	<i>Solidification Cracking</i>	342
7.3.3.2	<i>Clad Disbonding</i>	345
7.3.3.3	<i>Creep Failure in the HAZ of Carbon Steel or Low Alloy Steel</i>	345
7.3.3.4	<i>Postweld Heat Treatment Cracking</i>	346
7.4	Postweld Heat Treatment Cracking in Stainless Steels Welded with Ni-base Filler Metals	347
7.5	Super Austenitic Stainless Steels	349
7.6	Dissimilar Welds in Ni-base Alloys—Effect on Corrosion Resistance	357
7.7	9%Ni Steels	357
7.7.1	Physical Metallurgy of 9%Ni Steels	357
7.7.2	Hot Cracking of Ni-base Deposits	361
7.8	Super Duplex Stainless Steels	363
7.9	Case Studies	364

7.9.1	Postweld Heat Treatment Cracking of Thick Section Welds in Alloy 800H Made with ENiCrFe-2 Filler Metal	364
7.9.2	Alloy 925 Welded with ERNiCrMo-15 (INCO-WELD 725NDUR) for Manufacturing Vacuum Insulated Oil Patch Tubing	367
7.9.3	Corrosion-Fatigue of Alloy 625 Weld Overlays	369
7.9.4	Overlay of “Safe-End” Welds using High-Cr, Ni-base Filler Metals	373
	References	376
<b>8.</b>	<b>Weldability Testing</b>	<b>379</b>
8.1	Introduction	379
8.1.1	Weldability Testing Approaches	380
8.1.2	Types of Weldability Test Techniques	380
8.2	The Varestreint Test	381
8.2.1	Technique for Quantifying Weld Solidification Cracking	383
8.2.2	Technique for Quantifying HAZ Liquation Cracking	386
8.3	Modified Cast Pin Tear Test	388
8.4	The Sigmajig Test	392
8.5	The Hot Ductility Test	394
8.6	The Strain-to-Fracture Test	399
8.7	Other Weldability Tests	401
	References	402
<b>Appendix A</b>	<b>Composition of Wrought and Cast Nickel-Base Alloys</b>	<b>403</b>
<b>Appendix B</b>	<b>Composition of Nickel and Nickel Alloy Consumables</b>	<b>409</b>
<b>Appendix C</b>	<b>Corrosion Acceptance Testing Methods</b>	<b>415</b>
<b>Appendix D</b>	<b>Etching Techniques for Ni-base Alloys and Welds</b>	<b>419</b>
	<b>Author Index</b>	<b>423</b>
	<b>Subject Index</b>	<b>431</b>



## **PREFACE**

---

The motivation for this textbook arose from our desire to develop a reference for engineers, scientists and students that would represent an up-to-date perspective on the welding metallurgy aspects and weldability issues associated with Ni-base alloys. Although this subject has been treated in handbooks and other reference texts associated with welding/joining and engineering materials, this represents the first stand-alone textbook dedicated to the topics of welding metallurgy and weldability of nickel and nickel alloys.

This book focuses on the metallurgical behavior of Ni-base alloys with particular emphasis on weldability issues. It does not specifically address welding process or procedure issues, nor does it provide guidance as to process/procedure selection. The book begins with a chapter introducing the history of nickel and nickel alloy development. The second chapter discusses the role of alloying elements and presents phase diagrams that describe phase stability in these alloys, including the use of thermodynamic computational techniques to develop phase diagrams for complex systems. Two chapters are then dedicated to the two largest groups of Ni-base alloys, the solid-solution strengthened alloys and the precipitation-strengthened alloys (or “superalloys”). Another chapter describes the weldability issues associated with specialty alloys—nickel aluminides and oxide dispersion strengthened alloys. Finally, there are chapters that address the topics of repair welding, dissimilar welding, and weldability testing. Some of these chapters contain case studies that will allow the reader to see how the concepts described can be applied in “real world” situations.

In the preparation of this textbook, the authors have brought together a collective 80 years of experience with Ni-base alloys. For many years, Professors DuPont and Lippold have conducted research and taught courses on these topics at Lehigh University and Ohio State University, respectively. Mr. Kiser has been involved with Ni-base consumable development and applications at Special Metals Welding Products Company (formerly INCO) for over 40 years. This combined effort has resulted in a textbook that has both technical breadth and depth, providing a resource for university students, and practicing engineers and scientists.

Special thanks go to Dr. S. Suresh Babu (Ohio State University), Dr. Steve Matthews (Haynes International), Dr. Charles Robino (Sandia National Laboratories), and Mr. J. Patrick Hunt, Mr. Brian A. Baker and Dr. Rengang Zhang (all from Special Metals Corp.), who carefully reviewed individual

chapters and made many helpful suggestions that have been incorporated into the manuscript. We would also like to acknowledge the following former students from Lehigh and Ohio State whose theses and dissertations contributed to this text: Dr. Qiang Lu, Dr. Ming Qian, Dr. Nathan Nissley, Mr. Matt Collins, Dr. Steve Banovic, Dr. Weiping Liu, Dr. Timothy Anderson, Mr. Michael Minicozzi, Dr. Matthew Perricone, Dr. Brian Newbury, Mr. Jeff Farren, and Dr. Ryan Deacon. The authors also acknowledge the hard work and diligence of Lehigh students Andrew Stockdale and Gregory Brentrup for their help with obtaining permissions for use of figures and other reference material in this book.

Finally, the authors are grateful to Lehigh University, Ohio State University, and Special Metals Company, A Division of Precision Cast Parts Corp., for making available the time and providing the environment for the many hours of writing and editing that allowed this book to become a reality.

# Introduction

Ni-base alloys are one of the most important classes of engineering materials, since they can be used in a wide range of environments and applications. These alloys are selected for both aqueous and high temperature corrosion resistance, high strength at both ambient and high temperatures, ductility and toughness at low temperatures, specific electrical properties, and many other physical property-dependent applications. The Ni-base alloy welding consumables offer some properties in the as-welded condition that no other family of welding products can offer, such as the ability to be diluted by a number of diverse alloying elements while maintaining strength and ductility from cryogenic temperatures to temperatures approaching the solidus. They are also quite versatile. For example, the family of Ni-Cr-Mo welding products is used to weld 9% Ni steel to produce excellent as-welded strength and impact toughness at liquid nitrogen temperatures. Nickel and nickel-iron alloys are used to weld cast irons because they can be diluted by iron and carbon while remaining ductile and providing good machining characteristics. They are also widely used in the power generation industry for dissimilar welds between carbon steels and austenitic stainless steels in order to provide a transition in coefficient of thermal expansion for elevated temperature service.

Relative to steels, Ni-base alloys can be used both at cryogenic temperatures and temperatures approaching 1200°C (2190°F) because the matrix of the solid solution alloys remains austenitic<sup>1</sup> from solidification to absolute zero. With appropriate alloying additions, these alloys provide useful corrosion resistance and have applications in a wide range of industries, including Power Generation, Petrochemical, Chemical Processing, Aerospace, and Pollution Control. Welding is a critical fabrication technique for Ni-base alloys. Considerable research and development has been conducted over the last 50 years in an effort to better understand and control the weldability of these alloys, and to develop welding consumables that meet the ever

<sup>1</sup>Note that here and elsewhere in the text, the terms “austenite” and “austenitic” are used to refer to the face-centered cubic structure that is the predominant phase in Ni-base alloys.

increasing demands on corrosion resistance and mechanical properties of welded joints.

This book is designed to provide basic information regarding the welding metallurgy and weldability of Ni-base alloys. The text includes comprehensive coverage of the two most important classes of Ni-base alloys, namely solid-solution strengthened alloys and precipitation-strengthened alloys. One chapter is dedicated to oxide dispersion strengthened (ODS) alloys and nickel-aluminide alloys. In addition to providing basic information regarding the welding metallurgy of these alloy systems, concepts regarding weld repair, and selection and application of Ni-base alloys in dissimilar welds are addressed. Many important concepts are demonstrated through the use of “case studies” that relate these concepts to actual applications.

## 1.1 Ni-BASE ALLOY CLASSIFICATION

There is no systematic classification system for Ni-base alloys as there is for steels and aluminum alloys. For this reason, most Ni-base alloys are known by their trade names or by the alloy number that was originally assigned by the alloy producer. For example, INCONEL<sup>®</sup> alloy 600<sup>ii</sup> and HASTELLOY<sup>®</sup> alloy C-22<sup>iii</sup> are also referred to as Alloy 600 and Alloy C-22. Ni-base alloys are generally classified by composition, as shown in Figure 1.1. The following provides a brief summary of these classifications.

### 1.1.1 Commercially Pure Nickel Alloys

Commercially pure nickel alloys are those that contain primarily nickel (>99wt%). There is an entire family of commercially pure nickel alloys anchored by Alloys 200 and 201. These materials have low strength and hardness, and are used principally for their corrosion resistance in caustic environments. Alloy 201 has a limit of 0.02 wt% carbon so that it can be used above 315 °C (600 °F) without the danger of being “graphitized.” Because carbon is relatively mobile in the nickel matrix above 315 °C, carbon additions beyond the solubility limit (~0.02 wt%) will result in precipitation of graphite particles that render the material brittle and weak.

There are a number of additional commercially pure nickel alloys that exist for electrical or magnetostrictive limited applications. These alloys have good weldability but are susceptible to porosity when welded. If these alloys are kept clean before and during welding, they will exhibit good resistance to cracking, but gas shielding or fluxing must be sufficient to prevent the formation of porosity. The commercially pure nickel welding consumables have additions of up to 1.5% aluminum and 2.0-to-3.5% titanium to counter the

<sup>ii</sup> INCONEL is a registered trademark of Special Metals, a PCC Company.

<sup>iii</sup> HASTELLOY is a registered trademark of Haynes International, Inc.

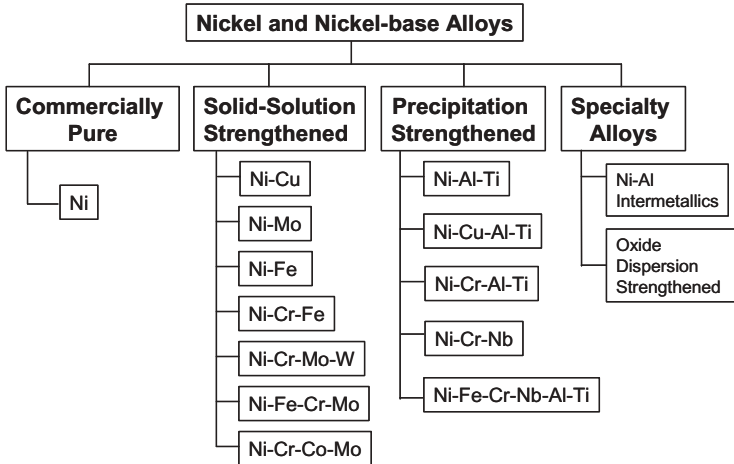


**Figure 1.1** Classification of Nickel and Nickel-Base Alloys.

effects of even small amounts of atmospheric contamination. Both Ti and Al combine with oxygen to form oxides and nitrogen to form nitrides, thereby controlling porosity in the weld deposits.

### 1.1.2 Solid-Solution Strengthened Alloys

Nickel and copper are isomorphous (complete solid solubility), which allows production of single phase alloys over the entire composition range. This family of materials generally exhibits good corrosion resistance to seawater and other general corrosion environments. The Ni-Cu alloys are usually quite weldable, but may be susceptible to porosity if proper shielding or well-deoxidized consumables are not used. Other solid-solution strengthened Ni-base alloys may contain only iron and most of these alloys are used for their particular coefficient of expansion or electrical properties. The Ni -36 wt% Fe alloy commonly known as INVAR<sup>iv</sup> exhibits the lowest coefficient of expansion of any of the Ni-base alloys and expands and contracts at a rate of less than  $1.0 \times 10^{-6}$  in/in/F. when heated and cooled over a range of several hundred degrees up to about 300°F. The Ni-Fe alloys have reasonable weldability, but the development of consumables with good solidification cracking resistance with near-matching expansion properties has presented a challenge to consumable manufacturers. The Ni-Fe alloys and their consumables may also be susceptible to ductility-dip cracking. This cracking mechanism is described in detail in Chapter 3.

Other solid-solution alloys contain a variety of substitutional elements including chromium, molybdenum, and tungsten. Each element imparts

<sup>iv</sup>INVAR is a registered trademark of Imphy SA, France.

particular characteristics and has the ability to alter the welding response of each alloy. Maximum ultimate tensile strength values of the solid-solution strengthened Ni-base alloys approach 120 ksi (830 MPa) with yield strengths in the range of 50 to 70 ksi (345 to 480 MPa). These alloys are used in a broad range of applications requiring good corrosion resistance. If higher strength levels are required, it is necessary to select precipitation-strengthened alloys.

### 1.1.3 Precipitation-Strengthened Alloys

The precipitation-strengthened Ni-base alloys contain additions of titanium, aluminum and/or niobium that form a strengthening precipitate with nickel after an appropriate heat treatment. Under most conditions, these precipitates are coherent with the austenite matrix, and thus strain the matrix such that the strength of the alloy increases substantially. The most common of these precipitates are called gamma prime [ $\gamma'$ -Ni<sub>3</sub>Al, Ni<sub>3</sub>Ti, and Ni<sub>3</sub>(Ti,Al)] and gamma double prime ( $\gamma''$ -Ni<sub>3</sub>Nb). By optimizing alloying additions and heat treatment, these alloys can be strengthened to reach ultimate tensile strength values exceeding 200 ksi (1380 MPa) with 0.2% offset yield strengths over 150 ksi (1035 MPa).

The first precipitation-hardened Ni-Cr alloy (X-750) is strengthened by gamma prime and exhibits the combination of good oxidation resistance and high temperature strength to near the gamma prime solvus temperature. Unfortunately, it is subject to postweld strain age cracking (SAC) when welded and direct-aged without an intervening annealing treatment. This cracking mechanism is described in detail in Chapter 4. In an effort to improve weldability and avoid SAC, a second generation of precipitation-hardening Ni-Cr alloys was developed that are strengthened by gamma double prime. The most popular of these alloys is Alloy 718. Because the gamma double prime precipitate forms more slowly than gamma prime, Alloy 718 is generally immune to SAC during postweld heat treatment. One of the major applications for Alloy 718 is for aerospace gas turbine shafting and pressure containment. When melted properly to produce low levels of impurities, this alloy provides tremendous design opportunities with excellent fatigue life at service temperatures up to 760°C (1400°F) when properly designed.

The precipitation-strengthened alloys are often referred to as “superalloys” based on their retention of unusually high strength and corrosion resistance at elevated temperatures. The term has been loosely applied to many other high strength complex alloys, but generally the term “superalloys” is used to describe Ni-base alloys with their superior strength properties provided by the gamma prime and gamma double prime phases.

The use of “superalloys” for rotating gas turbine blades or “buckets” began with alloys such as IN713C. This alloy was similar to Alloy X-750, but was only produced as a casting and contained such high additions of aluminum and titanium that it age-hardened upon cooling from casting temperatures. Structural repairs were limited due to its extreme susceptibility to SAC, but

blade tip build-up was performed without cracking. After decades of technological development, other members of the “superalloy” family were added to include the very high strength, corrosion-resistant single crystal turbine blade alloys. Welded blade tip buildup due to erosion during service is possible if the welding process is well controlled and the residual stresses are kept low. The primary challenges to weld repair of these materials include the avoidance of stray grains in the melt pool and elimination of cracking. Important processing considerations for repair of single crystal alloys are described in Chapter 6.

#### 1.1.4 Other Specialty Alloys

There are other alloys that could fit into the “super” category by nature of impressive high temperature creep strength, such as the oxide dispersion strengthened alloys MA6000 and MA754<sup>v</sup>. These alloys exhibit superior creep strength by employing both precipitation hardening and dispersion hardening created by a fine dispersion of particles that are stable at high temperatures. Ytria ( $Y_2O_3$ ) is one example of the dispersoid used for strengthening. These materials also have excellent high temperature oxidation resistance, but they suffer from the inability to maintain their high strength across the weld joint when joined by conventional fusion welding techniques. When melted by fusion welding, the dispersoid tends to agglomerate and the local stiffening caused by the dispersoid is lost within the fusion zone and the heat-affected zone. Welding of ODS alloys is discussed in more detail in Chapter 5.

Nickel-aluminides are alloys designed around either the NiAl or Ni<sub>3</sub>Al compound. They exhibit very high strength and corrosion resistance, but are very difficult to weld because of their low ductility over a wide temperature range. Ni-Cr-B and Ni-Mo-Si alloys have been developed for wear resistance in a variety of environments, but these alloys are also difficult to weld due to high hardness, low ductility and the formation of low-melting range phases within their compositions.

## 1.2 HISTORY OF NICKEL AND NI-BASE ALLOYS

Commercially useful Ni-base alloys were first introduced in the late nineteenth century and were developed to a high level of sophistication during the twentieth century. The element nickel was initially named by the Swedish scientist and government-sponsored mineralogist, Axel Frederik Cronstedt, in 1754 when he published “Continuation of Results and Experiments on the Los Cobalt Ore.”(1). Earlier, it was known to exist as a reddish mineral, nickel arsenate-octahydrate ( $Ni_3As_2O_8 \cdot 8H_2O$ ) ore that became known as Annabergite after the town of Annaberg in Saxony where it was mined. It contained 29.5% Ni and is also known as nickel bloom or nickel ochre. Miners in the area of

<sup>v</sup>The mechanically alloyed (MA) alloys were developed by the International Nickel Company.

Erzgebirge retrieved a related red-colored ore called “nicolite” or nickel arsenide (NiAs). Because of its reddish color, the ore was initially thought to contain copper (kupfer), but when smelted, the arsenic-bearing fumes generated were extremely noxious to the smelters and the primary metal was difficult to isolate. Thus, they thought that “Old Nick,” (an early reference to satan or the devil) was involved in making their work difficult and dangerous.(2) Therefore the term “kupfer nicell” came to be applied to the ore, which literally meant “devil’s copper.” The term Kupfer-nicell was first used in 1654 near what is present day Dresden, Germany.

It wasn’t until about 100 years later that Cronstedt officially named the element nickel after much scientific inquiry. In his words, “*Kupfernickel is the ore which contains the largest amount of the semi-metal previously described, and of which an account has been published. For this reason, I have given its regulus the same name, or, for the sake of convenience, I have called it NICKEL, until it can be proved to be only a composition of metals or semi-metals previously known.*”(3) Obviously, Cronstedt had only rudimentary tools for defining or analyzing the new discovery, but his pronouncement was apocryphal and the name was adopted! Over one hundred years later, a significant ore body was discovered in the Sudbury basin in Ontario, Canada and primitive mining began in the late nineteenth century. This deposit, made up principally of sulfide compounds, also contained significant amounts of copper and became an item of great interest to the Orford Copper Company in New Jersey. About the same time, nickel was being smelted and refined in Clyddich, Wales.

The International Nickel Company (INCO) was formed from the Orford Copper Company and the Canadian Copper Company on March 29, 1902.(4) In the same year, Ambrose Monell (photo in Figure 1.2) filed a patent for one of the first nickel alloys to become commercially significant. It contained approximately 2/3 nickel and 1/3 copper and is the precursor of MONEL<sup>®vi</sup> alloy 400 (70Ni-30Cu) that is still in use today. It is not accidental that this is the ratio of nickel-to-copper found in most of the ores in the Sudbury basin. This useful alloy was produced by simply refining the ore and producing the alloy from the metallic elements found naturally.

A decade later in December 1912, another nickel producer, the Haynes Stellite company, was founded by Elwood Haynes (photo in Figure 1.3) in Kokomo, Indiana.(5) Haynes had been working on nickel and cobalt alloys with additions of chromium and was eventually granted patents on Ni-Cr and Co-Cr alloys. The Ni-Cr patent was initially rejected because of competing patents by A.L. Marsh of INCO. Haynes Stellite, after 50 years of ownership by Union Carbide Corporation and another 30 years by Cabot Corporation, is now known as Haynes International with their headquarters still located in Kokomo, Indiana. Their history is well-marked by numerous popular

<sup>vi</sup>MONEL is a registered trademark of Special Metals, a PCC Company.



**Figure 1.2** Photo of Ambrose Monell. (From INCO archives with caption—“U.S. Patent 811,239 issued to Ambrose Monell on January 30, 1906 for a new and useful improvement in the manufacture of nickel-copper alloys”.)

HASTELLOY® alloys of the Ni-Mo, Ni-Cr-Mo and Ni-Cr-Mo-W types. Table 1.1 provides a timeline of major alloy developments over the last century.(5–7)

As exploration and mining technology improved, the supply of nickel and copper largely exceeded the demand. The onset of World War I brought about the need for ballistic steels for defense against high energy projectiles. Demand for nickel increased during the war because it was the key element that induced the hardness and toughness in these special military-oriented steels. Following World War I, the demand for nickel again languished and INCO, in a visionary moment in 1922, created the Huntington Works in Huntington, West Virginia, whose charter included the development of useful new nickel alloys and their introduction to the marketplace. The locale of Huntington, West Virginia was chosen because of three important characteristics:

- 1) there was an abundance of low-sulfur natural gas that would be needed for melting, annealing, and heat treating;



**Figure 1.3** Photo of Elwood Haynes.

- 2) Huntington is situated near the confluence of the Guyandotte and Ohio rivers both of which were navigable; and
- 3) the Huntington area was populated with a ready supply of low-wage inhabitants who tilled the land and could readily be trained as mill workers.

Additionally, a rail system already served the city of Huntington, which was named for the railroad magnate Collis P. Huntington.

In 1922, INCO authorized the expenditure of \$3,000,000 (approximately \$40,000,000 in 2008 dollars) to build a research and development facility, and rolling mill on the east bank of the Guyandotte River in West Virginia, and the Huntington Works of INCO came into being.(8) Initially, inconsequential markets such as laundry services, and domestic and commercial kitchen sinks were fabricated using MONELL metal, as it was called initially. Later, the name was changed to MONEL<sup>®</sup> because the U.S. Patent office would not issue a patent that contained a personal name. The alloy was chosen because of its stainless, non-rusting nature before the commercial use of stainless steels began. The facility at Huntington became the primary production facility for

**TABLE 1.1** Timeline showing the development of many Ni-base alloys.

Time Period	Alloys
1900–1909	MONEL <sup>1</sup> alloy 400, Ni-Cr alloys.
1910–1919	HAYNES <sup>2</sup> alloy 6B.
1920–1929	MONEL alloy K-500, HASTELLOY A, HASTELLOY B.
1930–1939	INCONEL alloy 600, MONEL alloy R-405, PERMANICKEL alloy 300, HASTELLOY C, and HASTELLOY D.
1940–1949	INCONEL alloy X-750, INCOLOY alloy 800, INCOLOY alloy 801, DURANICKEL alloy 301, HAYNES STELLITE alloy 21, HAYNES STELLITE alloy 31, NI-SPAN-C alloy 902, NIMONIC alloy 75, NIMONIC alloy 80, NIMONIC alloy 80A, NIMONIC alloy 90, and HAYNES alloy 25.
1950–1959	INCONEL alloy 751, INCOLOY alloy 825, HASTELLOY X, NIMONIC alloy 105, NIMONIC alloy 108, PE 11, and PE 16.
1960–1969	INCONEL alloy 718, INCONEL alloy 690, INCONEL alloy 625, INCOLOY alloy 840, NIMONIC alloy 81, HASTELLOY C-276, and HAYNES 188.
1970–1979	INCONEL alloy 601, INCONEL alloy 617, INCONEL alloy MA 754, INCONEL alloy 706, INCOLOY alloy 800H, INCOLOY alloy 903, INCOLOY alloy MA 956, UDIMET alloy 720, NIMONIC alloy 101, NIMONIC alloy 86, HASTELLOY B-2, and HASTELLOY C-4.
1980–1989	INCONEL alloy 601GC, INCONEL alloy 625LCF, INCONEL alloy 725, INCOLOY alloy 925, INCOLOY alloy 800HT, INCOLOY alloy 907, INCOLOY alloy 908, INCOLOY alloy 909, ALLCOR <sup>3</sup> , HASTELLOY C-22, HASTELLOY G-30, and HASTELLOY C-2000.
1990–1999	INCONEL alloy 622, INCONEL alloy 686, INCONEL alloy 783, INCONEL alloy 718SPF, INCOLOY alloy 890, NILO alloy 365, NILO Filler Metal CF36, INCOLOY alloy 864, INCOLOY alloy 832, NI-ROD Filler Metal 44HT, VDM <sup>4</sup> 59, VDM B-4, and HASTELLOY B3.
2000+	HASTELLOY G-35, HAYNES 282, INCONEL alloy 693, HASTELLOY C-2000, INCONEL Filler Metal 52M, INCONEL alloy 740, INCONEL alloy TD, and INCOLOY alloy 27-7Mo.

<sup>1</sup>The following are registered trademarks of Special Metals, a PCC Company: MONEL, INCONEL, PERMANICKEL, INCOLOY, DURANICKEL, NI-SPAN-C, NIMONIC, UDIMET, NILO, AND NI-ROD.

<sup>2</sup>The following are registered trademarks of Hayes International: HAYNES, HASTELLOY, HAYNES STELLITE.

<sup>3</sup>ALLCOR is a registered trademark of Allegheny Ludlum-ATI.

<sup>4</sup>VDM is a registered trademark of VDM Alloys of Germany.

wrought nickel alloys and the primary location for INCO's nickel alloy research.

Shortly after the establishment of the Huntington Works, a foundry and the early beginnings of a welding research facility were established in Bayonne, N.J. From the 1930s to the 1950s, the atomic hydrogen and the oxy-fuel welding

processes were used extensively, and the nickel alloy base metals were used as welding consumables when drawn to welding wire. With the advent of “Heliarc” welding (now known as the gas-tungsten arc welding, GTAW) and the gas-metal arc welding (GMAW) processes, improved welding consumable alloy compositions were required in order to avoid the tendency for porosity and cracking imposed by the faster heating and cooling cycles of the new processes. Typically, aluminum and titanium were added to control oxygen and nitrogen contamination from the atmosphere and niobium and titanium were useful initially for cracking resistance.

During the first half of the twentieth century, companies including Sherritt-Gordon and Falconbridge established nickel mining and refining operations, and Henry Wiggin and Co. Ltd. in the United Kingdom (UK) and Haynes Alloys in Kokomo, Indiana started nickel alloy research and production facilities. The Henry Wiggin Co. first initiated and then worked closely with the Rolls Royce Co. to develop the NIMONIC<sup>®</sup> family of nickel-chromium alloys. Haynes Alloys also began to develop commercial alloys under the HASTELLOY<sup>®</sup> trademark. Other nickel alloy producers were formed in Europe and the Asia Pacific, but alloy development generally lagged that of the USA and UK.

In the 1920s and 1930s, market demands for higher strength Ni-base alloys drove the research of INCO physicist, Paul D. Merica to conceive of and then to develop precipitation-hardening nickel alloys.(6,9) From the early days of Monell, the metallurgy of nickel alloys was relatively unknown except that the basic structure was austenitic, and therefore the matrix arranged itself in the face-centered-cubic structure as it solidified. In fact, it became known that nickel was the most effective and useful austenite stabilizer in most of the early alloys being developed. The demands of early marine, naval, and oil and gas applications for higher strength combined with corrosion resistance prompted the research that resulted in the addition of aluminum and titanium to Ni-Cu alloys to produce a much stronger version of the 70Ni-30Cu alloy that would form a second phase when properly heat treated.(10) The second phase became known as gamma prime ( $\gamma'$ ). This precipitation strengthened Ni-Cu alloy became known as K-MONEL<sup>®</sup> and later MONEL<sup>®</sup> alloy K-500. When precipitation-hardened by heat treatment, the alloy nearly doubles in tensile and yield strength relative to standard Alloy 400 due to the formation of  $\gamma'$ .

The ability to significantly increase the strength of Ni-base alloys by precipitation-hardening became one of the most transformational technical discoveries of the nickel alloy industry in the twentieth century. Due to the remarkable increase in strength-to-weight ratio made possible by the precipitation-hardening alloys, the aerospace industry was literally thrust into the age of jet propulsion since the weight of turbine engines could be reduced significantly. The later development of INCONEL<sup>®</sup> alloy 718 further advanced the development of gas-turbine jet propelled aircraft. The precipitation-hardening effect made possible by the formation of gamma prime will be

discussed in detail in Chapters 2 and 4. With the introduction of precipitation-hardened MONEL<sup>®</sup> K-500, many new applications for Ni-base alloys evolved such as non-magnetic drill collars that were used for directional control during oil well drilling, and large Navy marine propeller shafts with excellent torsional strength and salt-water corrosion resistance. Other high-strength nickel alloys of the times included INCONEL<sup>®</sup> alloy X-750.

While not strictly associated with nickel alloy development, other transformational discoveries for the use of nickel were realized in the iron foundry industry. These included the development of the NI-HARD<sup>®</sup> family<sup>vii</sup> of Fe-based grinding and crushing alloys and ductile iron that used the master alloy Ni-Mg to inoculate the bath of iron with magnesium to precipitate spheroidal graphite particles instead of flakes. These developments span the 1930s through the late 1940s.

The next dramatic application of Ni-base alloy technology was the development of nuclear power plants for electricity generation. At the forefront of the construction of commercial nuclear power plants was INCONEL<sup>®</sup> alloy 600. It was selected due to its record of excellent corrosion resistance in aqueous environments and it was used extensively from the late 1950s through the late 1970s, during the worldwide construction boom of nuclear power plants. It was later learned that the alloy was susceptible to stress-corrosion cracking in the nuclear primary water environment. This discovery spawned the development of alloys and welding consumables containing 30% chromium for resistance to stress-corrosion cracking.

The role of nickel and Ni-base alloys in technological developments over the past 100 years are well-documented. From the time it was named by Cronstedt in the late eighteenth century to the present, milestone uses and alloy developments have allowed tremendous progress in many industries that would not have been possible with other alloy systems. Although initially found to be difficult to refine and separate, nickel has become the unique and nearly universal acceptor as the solvent element in many modern alloys and welding products. Because of its near total immunity for forming compounds with carbon, (it is only known to form nickel carbonyl, a highly toxic gas) its metallurgy and weldability issues are considerably simpler than those of iron-based materials. As the reader of this text will find, the mysteries of the metallurgy of nickel and the difficult problems associated with weldability have been addressed successfully on most fronts.

### 1.3 CORROSION RESISTANCE

The range of Ni-base alloys available today is expansive and one can be chosen for nearly any type of corrosion-resisting application. The commercially-pure nickel alloys 200 and 201 find application in the production and processing of

<sup>vii</sup>NI-HARD is a registered trademark of Special Metals, a PCC Company.

caustics such as NaOH and KOH. These alloys are chosen in the production and processing of caustics because nickel is the key alloying element that imparts resistance to stress-corrosion-cracking in pure caustic. Additionally, alloys that contain at least 42% nickel are virtually immune to chloride ion stress-corrosion-cracking, the bane of the austenitic stainless steels. The precipitation-hardening pure nickel alloys 300 and 301 find use for their high strength and high thermal conductivity in glass molds and as thermal spray alloys. The nickel-copper alloys are often used in seawater and for salt production, as well as in general acid-resisting applications. As increasing amounts of copper are added to nickel, the resistance of the alloy to reducing acids is enhanced, but neither nickel nor copper provide resistance to oxidation nor to oxidizing acids.

The precipitation-hardening Ni-Cu alloys K-500 and K-501 find use in high torsional stiffness shafting, and general and marine corrosion resisting service. The Ni-Cr alloys containing iron, cobalt, and aluminum find use at temperatures up to 1150°C (2100°F) due to excellent oxidation-resistance and creep strength. Some specially formulated nickel alloys provide useful oxidation and sulfidation resistance to 1260°C (2300°F) but cannot contain the solid-solution-strengtheners, molybdenum. There is a family of Ni-Cr-Co-Mo alloys that are limited in application to 1177°C (2150°F) because of the tendency for molybdenum to ablate or sublime catastrophically above this temperature. The precipitation hardening versions of these alloys are relied upon heavily for both land-based and aerospace gas turbine uses up to about 760°C (1400°F). Other Ni-Cr alloys containing Mo and W are extremely resistant to pitting and crevice corrosion. These alloys make use of the protection against reducing acids of molybdenum and tungsten while relying on chromium to impart resistance to oxidizing species. These alloys are quite useful when a variety of acidic conditions exist or may be encountered such as in flue gas desulfurization service. The simple Ni-Mo alloys are used for a wide range of concentrations of hydrochloric acid.

The solid-solution strengthened Ni-Fe-Cr alloys are mainly used for medium to high temperature thermal processing and hydrocarbon processing in creep-resisting temperature regimes. There are also a number of precipitation-hardening Ni-Fe and Ni-Fe-Cr alloys used for high strength, controlled expansion applications.

## 1.4 NICKEL ALLOY PRODUCTION

Currently, there are numerous nickel alloy production facilities throughout the world. There are at least five major mills in the USA along with multiple mills in South America, Germany, France, the United Kingdom, Japan, China, Italy and Spain. Melting methods used for nickel alloys range from simple air induction melting (AIM) to complex triple melt processes called for by some gas turbine rotating parts specifications. Triple melting normally involves a combination of vacuum induction melting (VIM), electroslag remelting (ESR) and

vacuum arc remelting (VAR). The triple melt process is often used to produce “superalloys” that require exceptionally low impurity levels for combined high-strength and high-temperature fatigue properties.

Other melting methods used are electric arc furnace (EAF) melting followed by argon-oxygen-decarburization (AOD), pressurized ESR, and combined VIM/VAR. The AOD process allows the careful control of carbon while protecting against chromium loss due to the presence of argon in the decarburizing gas injected into the molten bath. The pressurized ESR process allows the introduction of nitrogen into the melt of iron-containing stainless steels for the production of alloys resistant to pitting and crevice corrosion. The vacuum-augmented melting methods (such as VIM/VAR) are employed to eliminate gases such as oxygen and nitrogen, thereby reducing oxides and nitrides to very low levels. ESR is capable of reducing sulfur and other elements that can be removed by fluxing reaction of the slag.

Once melting has been completed, processing to various mill forms such as plate, sheet, bar, and wire are accomplished by a series of conventional hot-working and cold working operations with annealing operations applied as necessary. Continuous casting has found little use for production of nickel alloys primarily because of the specialty nature of most nickel alloys which limits the use of large melts and continuous runs of the same alloy. Thus conventionally cast ingots are produced from the above melting processes. Flux casting and bottom-pouring are improvements that have been introduced as quality demands continue to increase. From the ingot stage, there may be an overhaul step or in some cases the final melt process may provide a suitable surface for hot break-down of the ingot.

Some alloys require a high-temperature homogenization before break-down, while others can be directly rolled or forged from the preheating furnace. The breakdown is usually applied to multiple pieces of smaller cross-section called billets or blooms. These are, in turn, reduced to either finished or semi-finished product forms. Most finished product forms are produced using a combination of hot and cold rolling with annealing, blasting, and pickling, but seamless tubing and some shapes are produced by hot extrusion and further cold working. As product section thickness is reduced, bright annealing with hydrogen is sometimes used to produce clean, smooth surfaces of final products without the use of chemical pickling.

During the various cold working processes such as rolling or drawing, the nickel alloys exhibit a work hardening rate characteristic of each alloy. The work hardening rate is typically higher for the more complex alloys (high alloy content) and with increasing carbon content. The simple alloys such as commercially pure nickel can sometimes be rolled or drawn without an intermediate annealing step, but in contrast, most of the nickel alloys require intermediate annealing to induce recrystallization and softening for further reductions in section.

Nickel alloy welding products are principally produced by the cold-drawing process and it is not unusual for multiple draws and anneals to be used to

produce the desired diameter and properties. Surface conditioning during working and for final production is critical for making welding consumables that are easy to use and that produce clean, strong ductile welds. More information on welding consumables utilized for the various types of Ni-base alloys can be found in subsequent chapters.

## REFERENCES

1. Howard-White, F. B. 1963. *Nickel, An Historical Review*, D. Van Nostrand Co. Inc., pp. 31–33.
2. Ibid, pp. 24 and footnote 2, pp. 266.
3. Ibid. pp. 31.
4. Thompson, J. and Beasley, N. 1960. *For the Years to Come*, G.P Putnam and Sons, New York and Longman, Green and Co., Toronto, p. 143.
5. Sponaugle, C. 2005. History of Haynes International, Inc. *Pittsburgh ENGINEER*, pp. 7–9 Winter 2005.
6. Patel, S. J., 2006. A Century of Discoveries, Inventors, and New Nickel Alloys, *JOM* September, 2006 pp. 18–19.
7. Hodge, F. G. 2006. The History of Solid-Solution-Strengthened Ni Alloys for Aqueous Corrosion Service, *JOM*, September, 2006 pp. 28–31.
8. Thompson and Beasley, 4, op.cit., pp. 176–180.
9. Decker, R. F. 2006. The evolution of wrought, age-hardenable superalloys, *JOM*, September 2006, pp. 32–36.
10. Merica, P. U.S. Patent 1,572,744 (filed June 26, 1923).

# Alloying Additions, Phase Diagrams, and Phase Stability

## 2.1 INTRODUCTION

A very wide range of Ni-base alloy compositions have been developed for an equally impressive range of applications. For example, Ni alloys are widely used in the aircraft, power generation, petrochemical, defense, and transportation industries. The extensive development and use of Ni-base alloys can, at least in part, be attributed to two unique characteristics of Ni. First, Ni is capable of dissolving high concentrations of alloying elements compared to other metals. The explanation for this dates back to some of the early work on the electron configuration of metals conducted by Pauling and has been attributed to the relatively full shell of d-band electrons in the Ni atom. (1) Second, the addition of Cr (and/or Al) to Ni provides excellent corrosion resistance resulting from the formation of a protective  $\text{Cr}_2\text{O}_3$  (or  $\text{Al}_2\text{O}_3$ ) surface oxide layer. This permits use of Ni-base alloys in a wide variety of applications that require protection due to various forms of degradation, such as aqueous corrosion, oxidation, and sulfidation. The subsequent discovery of improvements in creep strength provided by the addition of Ti and Al to promote precipitation of the ordered  $\gamma'$ - $\text{Ni}_3(\text{Ti},\text{Al})$  phase extended the use of these alloys to applications requiring a combination of high temperature strength and corrosion resistance.

While these attributes are certainly beneficial, the wide range and high concentration of alloying elements used in Ni-base alloys can sometimes present a challenge for microstructure control. For example, many alloys designed to be single phase actually exhibit compositions that are beyond the solubility limit and, given enough time and exposure to elevated temperatures, can form a wide range of brittle secondary phases. Examples of alloys in this category include the Mo-bearing materials such as Alloys 622 and 625. A similar phenomenon occurs in two phase ( $\gamma + \gamma'$ ) superalloys, where brittle

phases (such as  $\sigma$ , P,  $\mu$ , Laves) with complex crystal structures can form during long term, elevated temperature exposure. Such phases can also form during solidification. As shown in more detail in later chapters, the closed-packed, face centered cubic (fcc) crystal structure of Ni-base alloys leads to very low diffusion rates of substitutional alloying elements. This, in turn, leads to extensive microsegregation during solidification. This factor is particularly important when coupled with the high cooling rates (typically in the range of tens to several hundred °C/sec) and short solidification times (on the order of 0.01 to 10sec.) experienced in the fusion zone during welding. As a result, many unexpected (and often undesirable) phases form during the terminal stages of solidification in the fusion zone due to microsegregation.

Phase stability diagrams provide one of the most effective tools for understanding phase transformations and the resultant microstructures of engineering alloys. The primary objective of this chapter is to provide a brief overview of pertinent phase stability diagrams for Ni-base alloy systems that form the basis for commercial alloys. The general influence of alloying elements on phase stability of Ni-base alloys will be reviewed first, followed by a description of pertinent phase diagrams for solid-solution and precipitation-strengthened alloys. The discussion of phase diagrams will include a description of general transformations that can occur during solidification, which are pertinent to the fusion zone, and transformations that are possible in the solid state, which are pertinent to microstructure evolution in the heat affected zone or in the weld metal during multipass welding. The recent emergence of computational thermodynamics for calculation of multi-component phase diagrams will also be described. The use of PHACOMP and New PHACOMP calculation procedures developed specifically for phase stability prediction in Ni-base alloys will also be reviewed. This information will provide a useful background for more detailed discussions of specific alloy systems discussed in subsequent chapters.

## 2.2 GENERAL INFLUENCE OF ALLOYING ADDITIONS

The general effect of various alloying elements on the phase stability in Ni base alloys is summarized in Table 2.1.(2) The elements Co, Cr, Fe, Mo, and Ta are generally used as solid solution strengtheners. Elements that exhibit similar atomic radii, electronic structure, and crystal structure relative to Ni are most likely to remain in solid solution. On the other hand, the ability of a dissolved element to increase strength by solid-solution hardening can be assessed by its atomic size difference compared to that of Ni. Table 2.2 summarizes approximate atomic diameters and solubility data for various elements in Ni at 1000 °C (1830 °F).(3) These data show that Al, Ti, Mn, Nb, Mo, and W provide the best combination of atomic radii mismatch and appreciable solubility needed for solid-solution strengthening. The elements Cr, Mo, Mn, and W are used in many single phase commercial alloys for solid-solution

**TABLE 2.1 Summary of the general effect of various alloying elements on phase stability in Ni-base alloys. (Courtesy ASM International from [2])**

Effect	Element
Solid Solution Strengtheners	Co, Cr, Fe, Mo, W, Ta
$\gamma'$ -Ni <sub>3</sub> (Al,Ti) Former	Al, Ti
Solid Solution Strengthening of $\gamma'$	Cr, Mo, Ti, Si, Nb
$\gamma''$ -Ni <sub>3</sub> Nb Former	Nb
Carbide Formers:	
MC and M(C,N)	W, Ta, Ti, Mo, Nb
M <sub>7</sub> C <sub>3</sub>	Cr
M <sub>23</sub> C <sub>6</sub>	Cr, Mo, W
M <sub>6</sub> C	Mo, W
TCP Phase ( $\sigma$ , P, $\mu$ , Laves)	Ti, V, Zr, Nb, Ta, Al, Si
Surface Oxide (Cr <sub>2</sub> O <sub>3</sub> /Al <sub>2</sub> O <sub>3</sub> ) Former	Cr, Al

**TABLE 2.2 Summary of approximate atomic diameters and solubility data for various elements in Ni at 1000 °C (1830 °F). (Courtesy ASM International from [3])**

Solute	Approximate atomic size difference compared to nickel, %	Approximate solubility in nickel at 1000 °C, wt%
C	+43	0.2
Al	-15	7
Si	+6	8
Ti	-17	10
V	-6	20
Cr	-0.3	40
Mn	+10	20
Fe	+0.3	100
Co	-0.2	100
Cu	-3	100
Nb	-15	6
Mo	-9	34
Ta	-15	14
W	-10	38

strengthening. As discussed in more detail in later chapters, some of these elements (e.g., Cr and Mo) can participate in solid-state precipitation reactions during long time, high temperature operation as well as eutectic-like reactions at the end of solidification. Additions of Mo and W are also useful for increasing creep strength due to their low diffusivity in Ni. Although Ti and Al can be effective solid-solution strengtheners, they typically improve strength by precipitation of the  $\gamma'$ -Ni<sub>3</sub>(Ti,Al) phase in Ni base superalloys. Niobium is also an effective strengthener and is used for both solid-solution strengthening and for its ability to strengthen by promoting precipitation of the  $\gamma''$ - Ni<sub>3</sub>Nb phase.

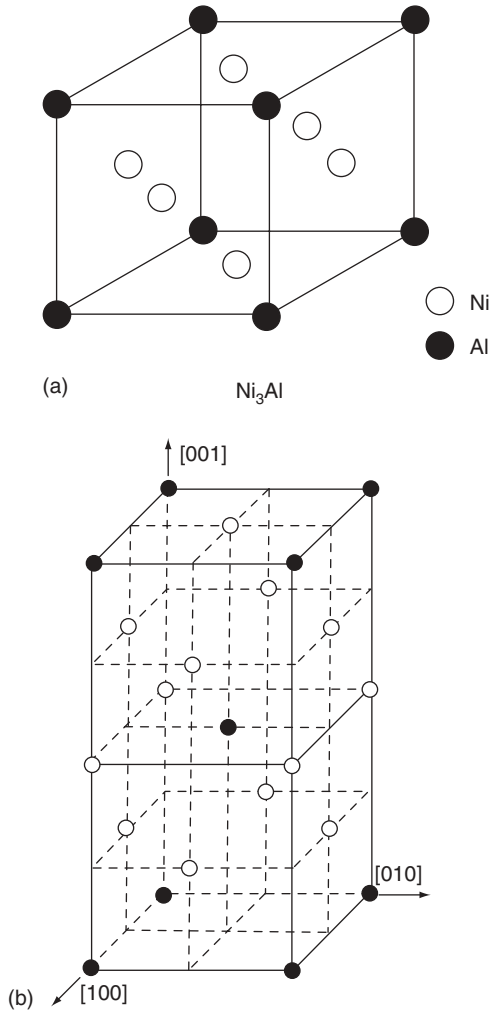


**Figure 2.1** a) Crystal structure of the  $\gamma'$ - $\text{Ni}_3(\text{Ti},\text{Al})$  ordered FCC phase (Courtesy ASM International from [4]), b) Crystal structure of the  $\gamma''$ - $\text{Ni}_3\text{Nb}$  phase. (From Sundaraman and Mukhopadhyay [8])

As shown in Figure 2.1a,  $\gamma'$ - $\text{Ni}_3(\text{Ti},\text{Al})$  is an ordered L12 structure phase that has very good crystallographic matching with the Ni-fcc matrix.(4) The Al atoms reside on the cube corners while Ni resides on the face centers. In commercial alloys, elements such as Cr, Co and Fe can substitute for Ni, and Nb can substitute for Ti and Al in the  $\text{Ni}_3(\text{Al},\text{Ti})$  phase. The mismatch between the  $\gamma$  matrix and  $\gamma'$  precipitate is generally less than one percent. The coarsening rate of precipitates is directly proportional to the surface energy of the

matrix/precipitate interface.(5) The good crystallographic matching between the  $\gamma$  matrix and  $\gamma'$  precipitate in superalloys leads to a very low surface energy that, in turn, leads to very low coarsening rates of the precipitates. The  $\gamma'$  phase shows the remarkable effect of increasing yield strength with increasing temperature up to  $\sim 800^\circ\text{C}$  ( $1470^\circ\text{F}$ ). (6) This effect is thought to occur due to ordering effects and the relatively low mobility of super lattice dislocations that occurs with increasing temperature. Additional increases in the strength of  $\gamma'$  can be accomplished by solid-solution strengthening. In this case, the additional strengthening is obtained by dissolution of elements such as Cr and Nb directly within the  $\gamma'$  phase, with Nb being the most effective. (6) The  $\gamma''$ - $\text{Ni}_3\text{Nb}$  phase can form in alloys with sufficient Nb additions. (7) The crystal structure of this phase is shown in Figure 2.1b, where the Nb atoms are shown as the dark spheres, but Ti and Al can substitute for Nb in this phase. (8) This is a body centered tetragonal (bct) phase that imparts strength to many commercial alloys by the development of high coherency strains in the matrix. However, the  $\gamma''$  phase is metastable and will generally be replaced with the orthorhombic  $\delta$  phase with the same  $\text{Ni}_3\text{Nb}$  stoichiometric composition with long exposure times at elevated temperature. The  $\delta$  phase is generally undesirable because it is incoherent with the Ni matrix and therefore not an effective strengthener. In addition, it can lead to embrittlement associated with a loss in ductility. The effect of  $\delta$  phase formation on the repair weldability of  $\gamma''$ -strengthened alloys will be reviewed in Chapter 6.

Many Ni-base alloys with appreciable carbon levels can form various types of carbides, depending on the alloy composition, processing route, and service history. The MC-type carbide exhibits an fcc crystal structure and typically forms at the end of solidification by eutectic-type reactions with the  $\gamma$  matrix. (9) The M(CN) carbonitrides are similar, except that appreciable levels of C are replaced by N. These eutectic-type reactions and the concomitant carbides and carbonitrides are promoted by the strong tendency of C, N, and some metallic elements (most notably Ti and Nb) to segregate to the liquid during solidification. As a result, MC carbides are typically distributed along the interdendritic and solidification grain boundary regions. The MC carbides can often be replaced by  $\text{M}_{23}\text{C}_6$  and  $\text{M}_6\text{C}$  carbides during thermal processing and/or high temperature service. (10) The  $\text{M}_{23}\text{C}_6$  carbides are generally Cr rich and form in the  $760\text{--}980^\circ\text{C}$  ( $1400\text{--}1800^\circ\text{F}$ ) range with a complex cubic crystal structure. These carbides tend to form on grain boundaries and, when present as discrete particles, can improve creep strength by restricting grain boundary sliding. The  $\text{M}_6\text{C}$  carbides form in the range from  $815$  to  $980^\circ\text{C}$  ( $1500$  to  $1800^\circ\text{F}$ ) and also exhibit a complex cubic crystal structure. These carbides tend to form when the Mo and/or W content is greater than 6–8 atomic percent.

The Topologically Closed Packed (TCP) phases such as  $\sigma$ , P, and  $\mu$  can form in highly alloyed materials during thermal processing and/or during long term service. (11) Some of these phases can also form at the end of solidification. For example,  $\sigma$  can form due to segregation of Mo (12), while Laves can form due to segregation of Nb. (9) These phases exhibit complex crystal structures

and, when formed in the solid state, their closed packed planes are parallel to the {111} planes of the austenite matrix. These phases are generally to be avoided because they typically produce a loss in strength and can promote premature failure. Loss in strength is promoted by depletion of solid-solution strengthening elements from the matrix, such as Cr, Mo, and W. Depletion of Cr from the matrix can also reduce corrosion resistance. Early failure can occur due to the high hardness and plate like morphology of these phases that cause premature cracking and brittle failure. Lastly, Cr and Al are important elements for providing high temperature corrosion resistance. Most commercial alloys contain 10–30 wt% Cr, which leads to corrosion protection by forming a passive  $\text{Cr}_2\text{O}_3$  surface film.(13) This surface oxide provides protection by limiting inward diffusion of oxygen and sulfur-bearing species as well as outward diffusion of alloying elements.

## 2.3 PHASE DIAGRAMS FOR SOLID-SOLUTION ALLOYS

### 2.3.1 The Ni-Cu System

The Ni-Cu system forms the basis for the MONEL<sup>®</sup> family of alloys. These two elements exhibit very similar atomic characteristics. They are each face centered cubic, have less than three percent difference in atomic radii, and exhibit similar electronegativity and valence state. As a result, the Ni-Cu phase diagram (Figure 2.2) is an isomorphous system in which there is complete solid

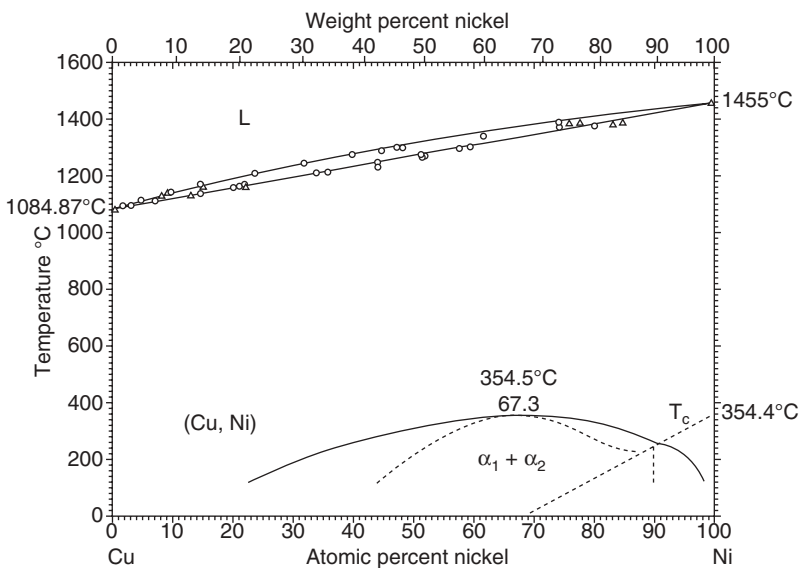


**Figure 2.2** Ni-Cu binary phase diagram. (Courtesy ASM International from [14])

solubility across the entire composition range.(14) Phase separation associated with the spinodal decomposition shown below 350°C (660°F) is based only on thermodynamic calculations, and the spinodal decomposition has not been observed experimentally due to the slow diffusion rates of copper in nickel at this temperature. Minor alloy additions are often made to MONEL-type alloys that provide solid-solution strengthening. The strength of MONEL alloys cannot be increased by heat treatment and must be accomplished through work hardening and solid solution-strengthening. There are some Ni-Cu alloys that have Al and Ti additions for purposes of precipitation strengthening by  $\gamma'$ , but their phase stability cannot be represented by the simple Ni-Cu system shown in Figure 2.2. Although the Ni-Cu system exhibits complete solid solubility, the large differences in melting point between Ni (1455°C/2650°F) and Cu (1085°C/1985°F), coupled with the low diffusivity of Cu in Ni, can result in microsegregation of Cu in fusion welds of Ni-Cu alloys.(15) This is discussed in more detail in Chapter 3.

### 2.3.2 The Ni-Cr System

As mentioned above, Cr is a key alloying element in many Ni-base alloys for providing corrosion protection through the formation of a passive  $\text{Cr}_2\text{O}_3$  surface oxide. The differences in crystal structure between Cr (bcc) and Ni (fcc) results in a binary phase diagram (Figure 2.3) with terminal solid-solution phase fields.(16) The system exhibits a eutectic reaction at 53 wt% Cr and can

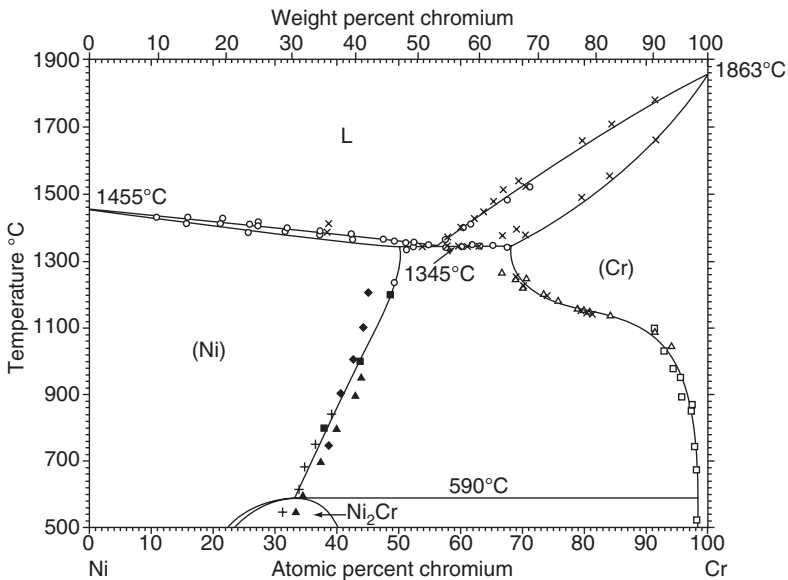


**Figure 2.3** Ni-Cr binary phase diagram. (Courtesy ASM International from [16])

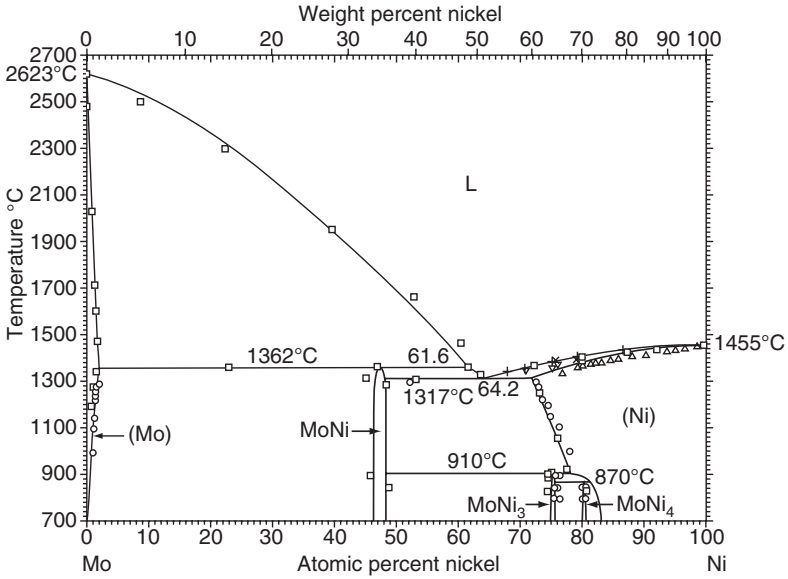
show ordering at the Ni-rich end at temperatures below 590°C (1095°F). Nickel has a maximum solid solubility of 47wt% Cr at the eutectic temperature. The high solubility of Cr in Ni makes this system ideal as the basis for most of the corrosion resistant, solid-solution and precipitation-strengthened alloys that are described in Chapters 3 and 4, respectively.

### 2.3.3 Ni-Mo System

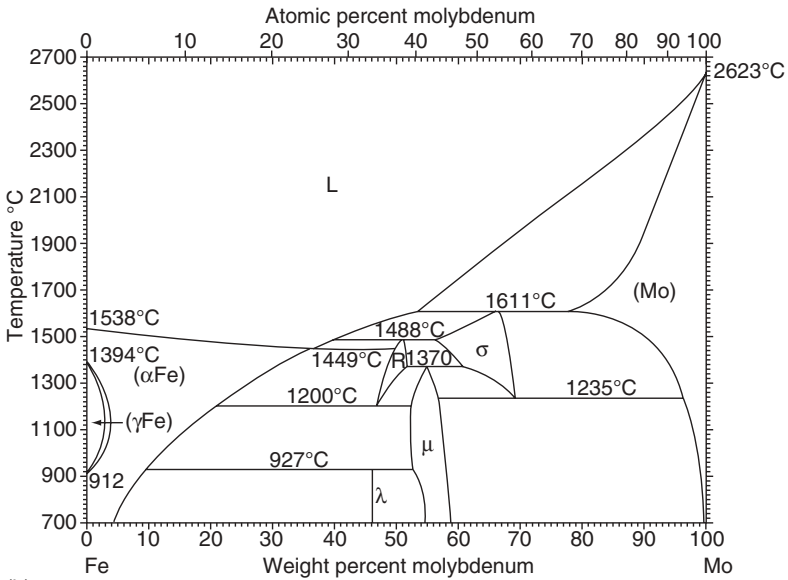
The Ni-Mo system forms the basis for the Hastelloy B family of alloys with Mo contents up to approximately 30wt%. As shown by the Ni-Mo phase diagram in Figure 2.4a (17), Ni can dissolve a maximum of 28wt% Mo at the eutectic temperature. Ordered phases such as Ni<sub>4</sub>Mo and Ni<sub>3</sub>Mo can form at lower temperatures and cause embrittlement. Figure 2.4b provides an interesting comparison between the solubility of Mo in Fe and Ni.(18) As mentioned previously, the wide use of Ni-base alloys is largely derived from their ability to dissolve large amounts of alloying elements. A quick comparison between Figure 2.4a and 2.4b shows that fcc Fe (austenite) can only dissolve a maximum of approximately 3 wt% Mo, which is significantly less than the 28wt% possible with Ni. Such large differences in solubility can also be observed with other key alloying elements as well, such as Cr (maximum 11 wt% in fcc Fe versus 47 wt% in Ni) and Nb (maximum 1.5wt% fcc Fe versus 18wt% in Ni).(18)

### 2.3.4 The Ni-Fe-Cr System

The Ni-Fe-Cr ternary system forms the basis for many commercial Ni alloys as well as stainless steels. Thus, the system has been extensively evaluated and phase stability in this system is well known. The liquidus projection for this system is shown in Figure 2.5, while a series of isothermal sections from 1000 to 650°C (1830 to 1200°F) is shown in Figure 2.6.(18) For reference, the box superimposed in each phase diagram represents the combined range of Fe contents (0–40wt% Fe) and Cr contents (10–30wt% Cr) that can be present in commercial Ni-base alloys. Depending on composition, the Ni-Fe-Cr alloys can exhibit two possible primary solidification phases, namely austenite ( $\gamma$ ) or delta ferrite ( $\delta$ ). In general, alloys high in Cr and low in Ni will exhibit a primary ferrite solidification mode, while alloys that are Ni rich will solidify as primary austenite. The phase boundary line separating these two solidification modes occurs at an approximate Cr:Ni ratio of 3:2. As shown in Figure 2.5, essentially all commercial alloys exhibit compositions that are located in the primary  $\gamma$  austenite phase field of the liquidus projection, indicating that austenite will be the primary solidification phase. This is certainly observed in practice. Solidification mode changes can occur under high cooling rate conditions for some stainless steel alloys that are close to the phase boundary line. These effects do not occur in Ni-base alloys because the nominal composition is far removed from the phase boundary line.



(a)



(b)

**Figure 2.4** a) Ni-Mo binary phase diagram (Courtesy ASM International from [17]), b) Fe-Mo phase diagram. (Courtesy ASM International from [18])

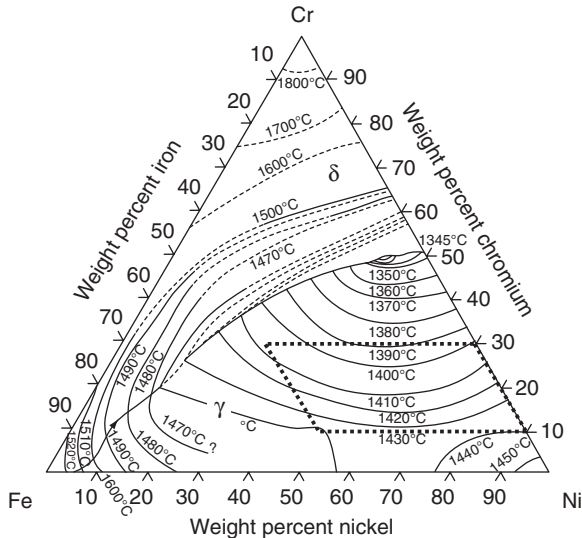


**Figure 2.5** Ni-Fe-Cr liquidus projection. (Courtesy ASM International from [18])

The brittle  $\sigma$  sigma phase becomes stable with increasing Fe and Cr contents and decreasing temperature. The increased stability of this phase with decreasing temperature can be attributed to the decrease in Fe and Cr solubility in Ni that occurs with decreasing temperature. Note that sigma phase is not stable at temperatures above 1000 °C (1830 °F). Indeed, the sigma phase is known to form as a product of solid-state precipitation during exposure at lower temperatures for times long enough to permit nucleation and growth. As mentioned above, this phase is detrimental to both corrosion resistance and mechanical properties and efforts to avoid this phase are usually made by exercising careful control over composition and processing history.

### 2.3.5 The Ni-Cr-Mo System

The Ni-Cr-Mo system forms the basis for solid-solution strengthened alloys and also serves as the matrix for some precipitation-hardened alloys. The liquidus projection for the Ni-Cr-Mo system is shown in Figure 2.7, and a series of isothermal sections from 1250 to 600 °C (2280 to 1110 °F) are shown in Figure 2.8.(18) The boxed composition space in each figure represents typical Cr contents (10–30 wt%) and Mo contents (0–15 wt%) that can be found in commercial alloys. These diagrams reveal several important phase stability features of this system. First, the presence of Mo stabilizes a rather wide range

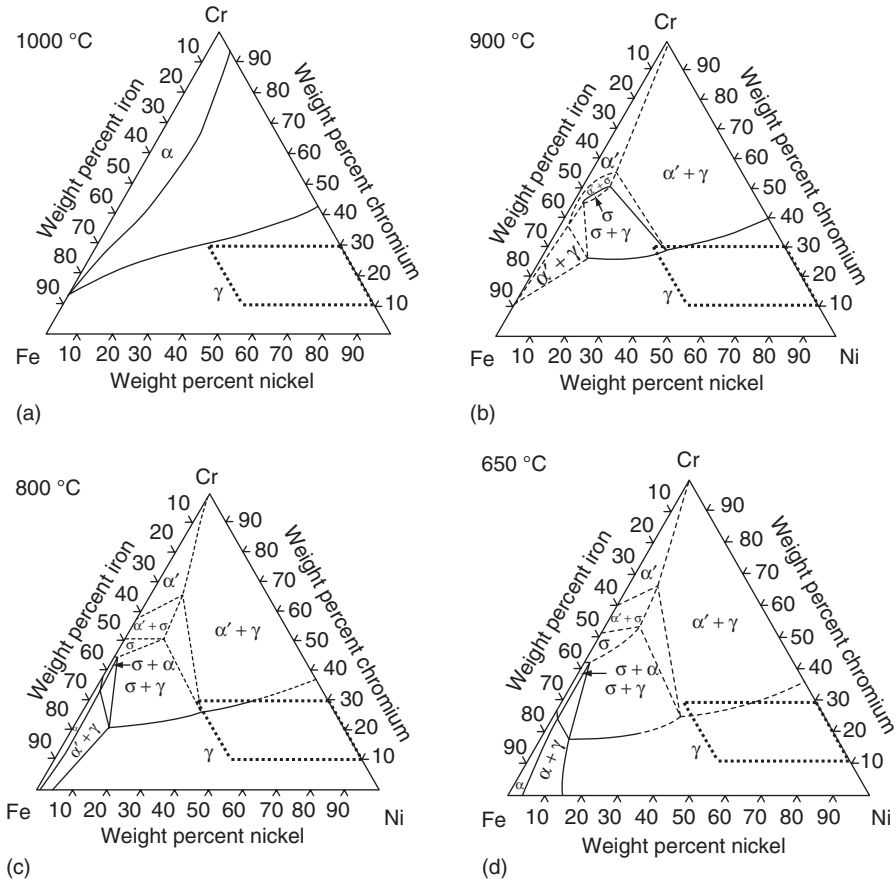


**Figure 2.6** Ni-Fe-Cr isothermal sections at a) 1000 °C, b) 900 °C, c) 800 °C, d) 650 °C. (Courtesy ASM International from [18])

of intermetallic compounds. Many of these phases, such as  $\sigma$  and P, are often observed in welds of commercial alloys.(19) Second, solidification of these alloys always initiates with austenite. However, as described in more detail in Chapter 3, Mo segregates aggressively to the liquid during solidification causing significant enrichment of Mo in the liquid.(12,19,20) The liquidus projection indicates that this will promote the formation of intermetallic compounds in the interdendritic regions at the end of solidification. The formation of these terminal solidification phases has important implications with respect to fusion zone solidification cracking susceptibility. Lastly, these intermetallic phases can also form in the solid state by precipitation reactions due to the decreasing solubility of Mo and Cr in Ni that occurs with decreasing temperature.

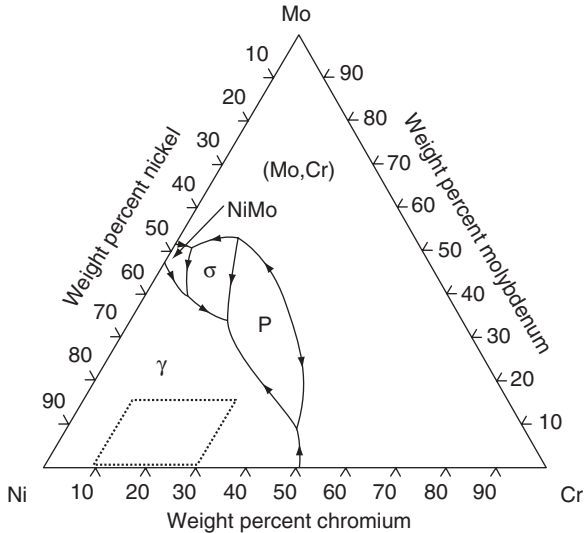


**Figure 2.7** Ni-Cr-Mo liquidus projection. (Courtesy ASM International from [18])

## 2.4 PHASE DIAGRAMS FOR PRECIPITATION HARDENED ALLOYS— $\gamma'$ FORMERS

The Ni-Al and Ni-Ti systems (Figure 2.9) form the basis for the  $\gamma$ - $\gamma'$  precipitation hardened microstructures of Ni-base superalloys.(18) Ni can dissolve a maximum of approximately 11 wt% of both Al and Ti. The solubility decreases appreciably with temperature, thus providing the driving force for precipitation-strengthening reactions. Most superalloys have a combined Al + Ti content below 10 wt%, and even small additions of Al or Ti will result in precipitation of the  $\text{Ni}_3\text{Al}$  or  $\text{Ni}_3\text{Ti}$  phases. As shown previously in Figure 2.1a, the  $\text{Ni}_3\text{Al}$  phase has an ordered fcc crystal structure and excellent crystallographic matching with the  $\gamma$  matrix. Reference to Figure 2.9a indicates this phase can form over a range of compositions. The stable form of the  $\text{Ni}_3\text{Ti}$  phase, often designated eta ( $\eta$ ), exhibits a hexagonal closed packed crystal structure and forms at the specific stoichiometric composition of 75Ni-25Ti (atomic percent). The  $\text{Ni}_3\text{Ti}$  phase can form the ordered fcc structure in metastable form at lower temperatures.

Figure 2.10a shows the Ni-Al-Ti liquidus projection (18), while Figure 2.10b and 2.10c show Ni-Al-Ti isothermal sections at 1150 and 750 °C (2100 and 1380 °F).(21) Within the simple ternary system, no new phases form in the Ni-rich corner that are not revealed by the binary diagrams, i.e.,  $\gamma$ -austenite,  $\gamma'$ - $\text{Ni}_3\text{Al}$ , and  $\eta$ - $\text{Ni}_3\text{Ti}$ . The liquidus projection shows that, for the Al and Ti concentrations of interest to commercial alloys, solidification will initiate as  $\gamma$ -austenite. Both Al and Ti will segregate to the liquid during solidification,

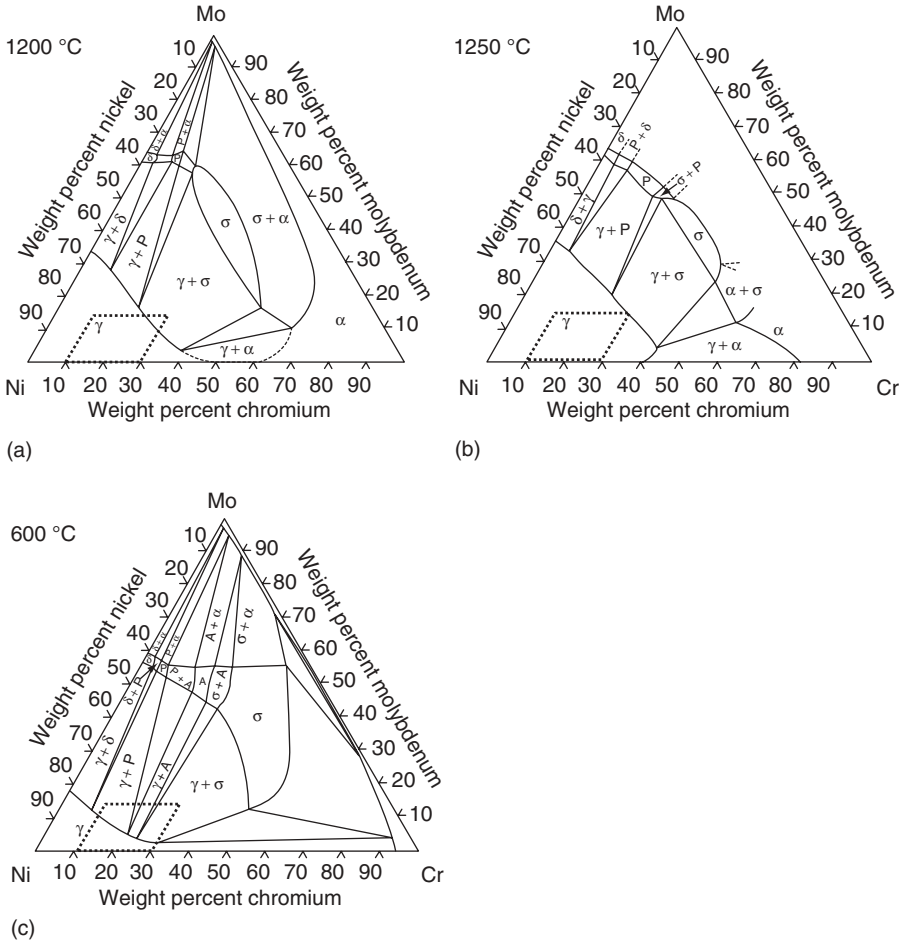


**Figure 2.8** Ni-Cr-Mo isothermal sections at a) 1250°C, b) 1200°C, and c) 600°C. (Courtesy ASM International from [18])

causing a progressive increase in the Al and Ti concentrations in the liquid as solidification proceeds. Thus, at sufficiently high Al and/or Ti concentrations, solidification will terminate by eutectic reactions involving either the  $\gamma'$ -Ni<sub>3</sub>Al or  $\eta$ -Ni<sub>3</sub>Ti phase. The exact phase that forms will depend primarily on the actual alloy composition. Various examples of this solidification sequence will be described in more detail in Chapter 4.

Reference to the isothermal sections indicate phase stability tendencies in the ternary Ni-Al-Ti system that are expected based on the behavior of the binary alloys—namely that Ti additions promote formation of the  $\eta$ -Ni<sub>3</sub>Ti phase, while Al additions promote formation of the  $\gamma'$ -Ni<sub>3</sub>Al phase. The hexagonal  $\eta$ -Ni<sub>3</sub>Ti phase typically appears as coarse platelets and does not provide

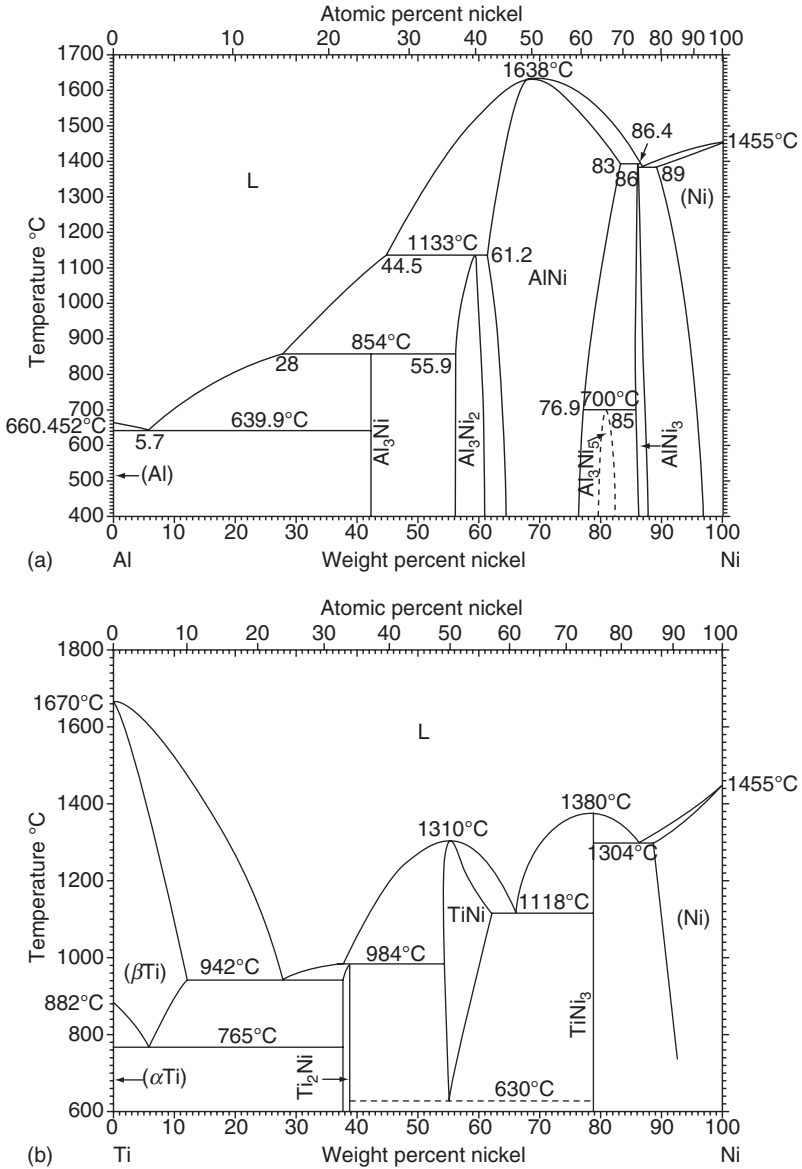


**Figure 2.9** a) Binary Ni-Al phase diagram, b) Binary Ni-Ti phase diagram. (Courtesy ASM International from [18])

significant strengthening. There are also important differences in solubility between these two phases. As shown in Figure 2.10b and c, the  $\eta$ -Ni<sub>3</sub>Ti phase cannot dissolve appreciable quantities of Al, whereas the  $\gamma'$ -Ni<sub>3</sub>Al phase can dissolve up to approximately 13 wt% (16 at%) Ti at 750 °C (1380 °F), as shown in Figure 2.10c. This is important because the strength of  $\gamma'$  can be increased

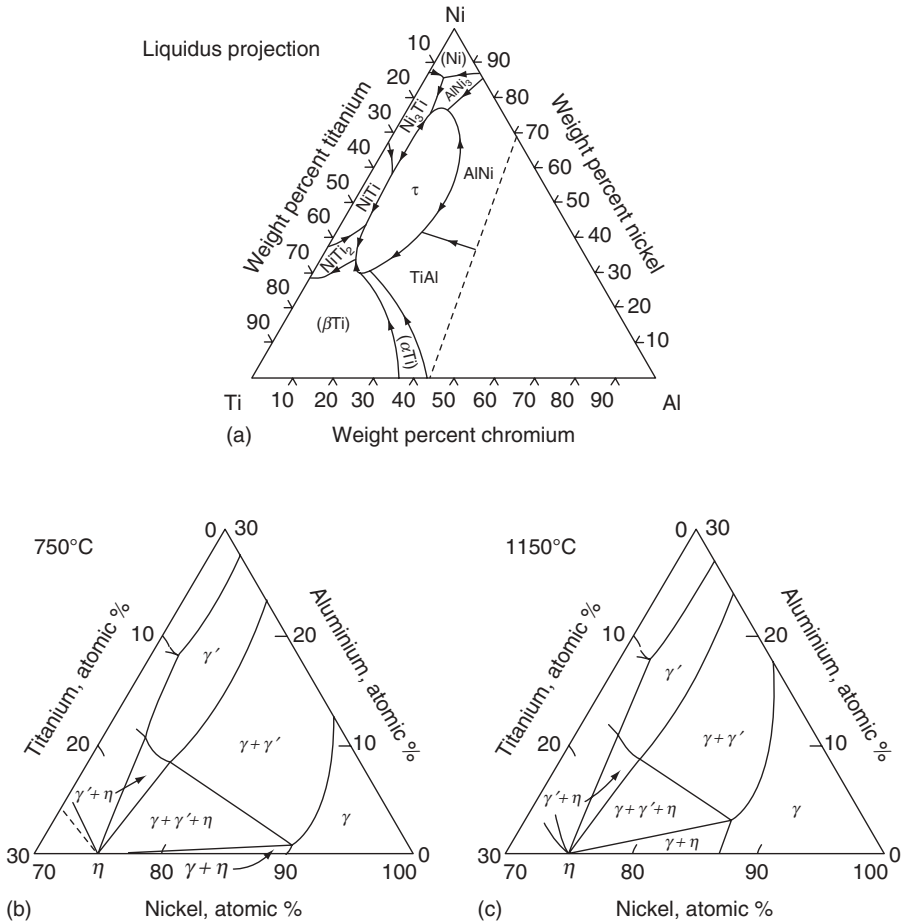


**Figure 2.10** a) Ni-Al-Ti liquidus projection, and Ni-Al-Ti isothermal sections at b) 1150°C and c) 750°C. (Courtesy ASM International from [18])

by solid-solution strengthening with Ti additions.(6) Thus, the  $\gamma'$ -Ni<sub>3</sub>Al phase is preferred in this system.

Since most Ni-base alloys contain Cr, it is useful to consider the influence of Cr on phase stability in  $\gamma$ - $\gamma'$  alloys. Figure 2.11 shows sections through the Ni<sub>3</sub>Ti-Ni<sub>3</sub>Al-Ni<sub>3</sub>Cr composition space at 750 and 1000°C (1380 and 1830°F).(22) The addition of Cr produces no new phases within this temperature range, and the  $\gamma'$  phase exhibits appreciable solubility for both Ti and Cr. Figure 2.12 summarizes the location of the  $\gamma'$ -Ni<sub>3</sub>Al phase field for a variety of Ni-Al-X systems.(23) Of these elements, Cr, Ti, and Si are particularly attractive because they exhibit both appreciable solubility and solid-solution strengthening in the  $\gamma'$  phase.

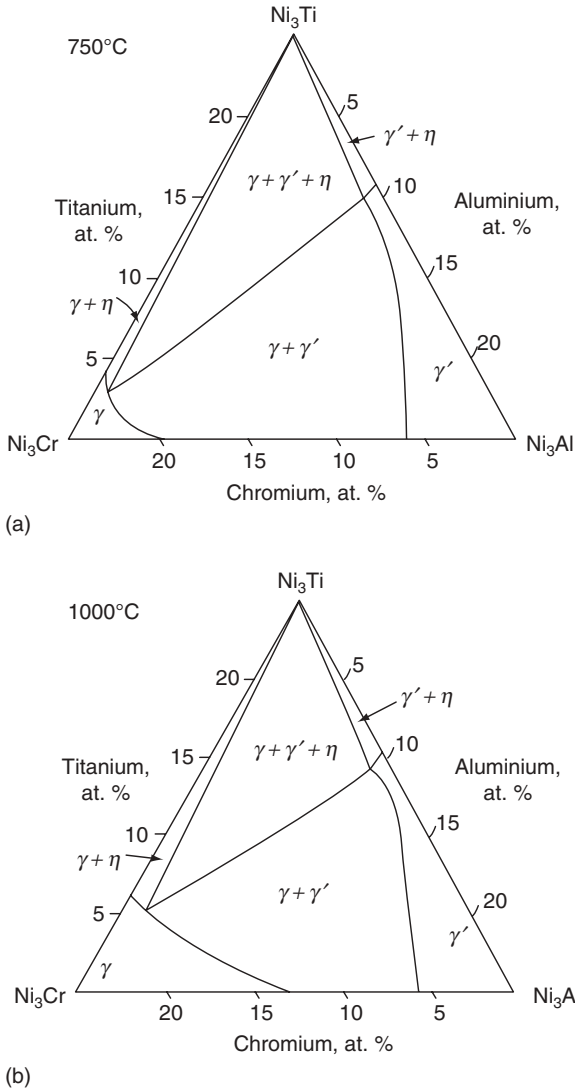


**Figure 2.11** Quaternary N-Cr-Al-Ti system taken through the Ni<sub>3</sub>Ti-Ni<sub>3</sub>Al-Ni<sub>3</sub>Cr composition space at 750°C and 1000°C. (From Betteridge and Heslop [22])

### 2.5 PHASE DIAGRAMS FOR PRECIPITATION-HARDENED ALLOYS— $\gamma''$ FORMERS

As mentioned above, many Ni-base superalloys contain Nb additions that are designed to provide strength by formation of the  $\gamma''$ -Ni<sub>3</sub>Nb phase. The Ni-Nb binary phase diagram is shown in Figure 2.13.(18) This system exhibits a simple

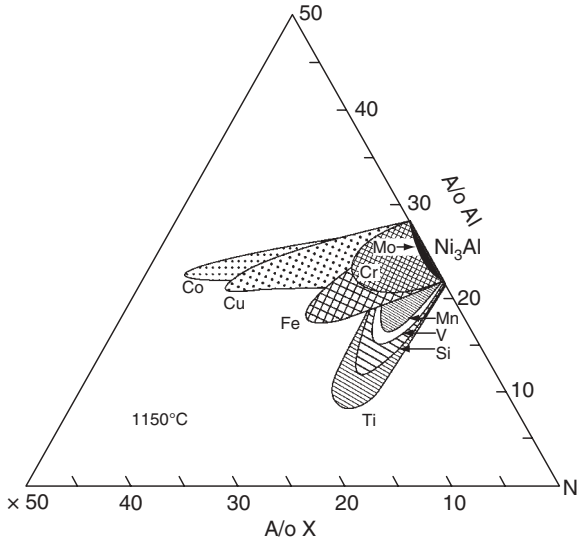


**Figure 2.12** Ternary phase diagram of the Ni-Al-X systems at 1150°C. (From Guard and Westbrook [23])

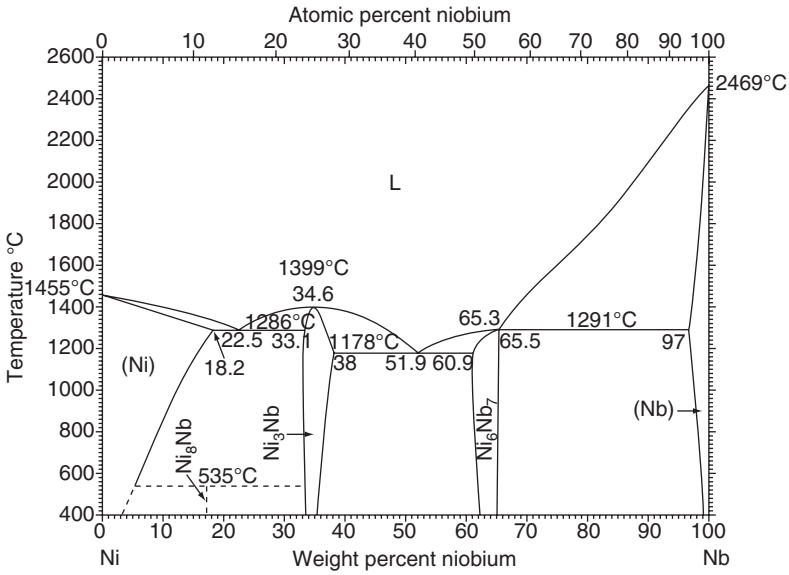


**Figure 2.13** Ni-Nb binary phase diagram. (Courtesy ASM International from [18])

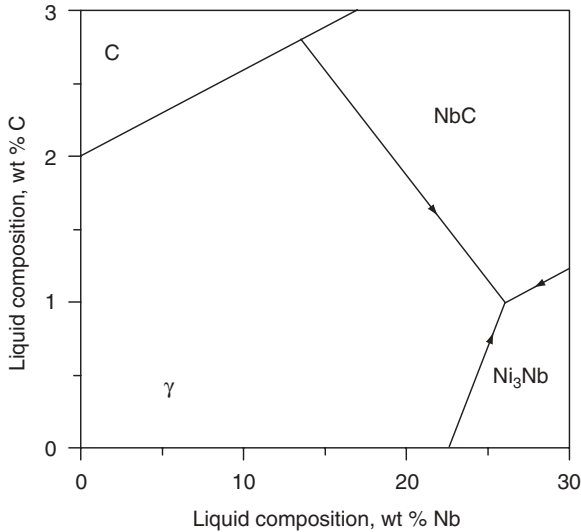


**Figure 2.14** Ni-Nb-C ternary liquidus projection. (From Stadelmaier and Fiedler [26])

eutectic reaction involving  $\gamma$  and  $\text{Ni}_3\text{Nb}$  at 22.5 wt% Nb, with the  $\gamma$  phase exhibiting a maximum Nb solid solubility of 18.2 wt%. In commercial alloys, the presence of other elements such as Cr and Fe have been shown to decrease the maximum Nb solid solubility by nearly 50% (approximately 9 wt% Nb).<sup>(24)</sup>

The C content of most commercial Nb-bearing superalloys is sufficiently high to promote the formation of both carbides and intermetallics at the end of solidification.<sup>(24,25)</sup> Thus, the Ni-Nb-C system provides a basis for initial understanding of solidification reactions and microstructural evolution in the fusion zone of these alloys. This is reproduced in Figure 2.14 from the data of Stadelmaier and Fiedler.<sup>(26)</sup> Austenite is the primary solidification phase for both ternary and multi-component commercial alloys with minor additions of Nb and C. Carbon and Nb are known to segregate aggressively to the liquid in both the simple ternary system as well as commercial alloys.<sup>(24,25)</sup> Thus, according to the ternary Ni-Nb-C liquidus projection, solidification will terminate with the formation of eutectic type reactions involving NbC and/or  $\text{Ni}_3\text{Nb}$ . These reaction sequences are generally observed in commercial alloys as well (see Chapter 4 for more details), except that the  $\text{Ni}_3\text{Nb}$  phase is replaced by the Laves phase due to the presence of Fe, Cr, Si, and Mo. The Laves phase is an intermetallic compound with the  $\text{A}_2\text{B}$  type structure, where A = Fe, Ni, Cr and B = Nb, Mo, and Si. In commercial alloys,  $\text{Ni}_3\text{Nb}$  will form in the solid state, generally during long term aging.

## 2.6 CALCULATED PHASE STABILITY DIAGRAMS

Although the simple binary and ternary phase diagrams described above are useful for assessing qualitative effects of major alloying additions on phase stability, they are often limited for use in commercial alloys. Commercial alloys can contain up to ten or more alloying elements. The presence of additional alloying elements, often in minor quantities, can often have a profound effect on the location of the phase boundary lines. In these cases, the simple binary or ternary phase diagrams described above can only be used for a qualitative assessment of phase stability because the presence of quaternary and higher alloy additions moves the locations of the phase boundaries. In addition, even binary and ternary diagrams are not always available over the required temperature ranges of interest. Experimental determination of multi-component phase diagrams is seldom conducted due to the large number of iterations required to identify the role of temperature and individual alloying elements.

However, there are now several thermodynamic databases (27) and calculation routines (28) available for predicting phase stability in multi-component commercial alloys. These routines determine phase stability through free energy minimization calculations that are based on published thermodynamic data that have been assembled into a database. It should be recognized that the phase stability relationships generated represent equilibrium conditions and that the data generated must be used carefully when considering non-equilibrium conditions, such as those encountered during welding.

Kinetic models for predicting the time/temperature behavior of diffusion-controlled phase transformations are also available.(29) These calculation routines have become invaluable for understanding and controlling the microstructure and properties of advanced engineering alloys, and have found many applications for assessing microstructure formation in fusion zones and heat affected zones of Ni-base alloys. The generation and use of such results are introduced here using Ni-Cr-Mo solid solution alloys and a  $\gamma''$  precipitation hardened alloy as examples. The objective here is to simply introduce the capability of this approach for surmounting the limitations of binary and ternary phase diagrams. More detailed discussions for specific alloys will be provided in later chapters.

Turchi *et al.* recently conducted detailed calculations of phase stability for the Ni-Cr-Mo system over a broad range of temperatures.(30) This work was conducted to assess the types of undesirable phases that may occur at low temperatures during very long term aging of welds produced with Ni-Cr-Mo solid solution alloys that are currently be considered for use in spent nuclear fuel storage applications. Figure 2.15a shows an example of the ternary isothermal diagram for this system calculated at 1250 °C (2280 °F). The experimentally determined diagram at the same temperature is shown in Figure 2.15b. The calculated diagram correctly predicts the presence of the P,  $\sigma$ , and

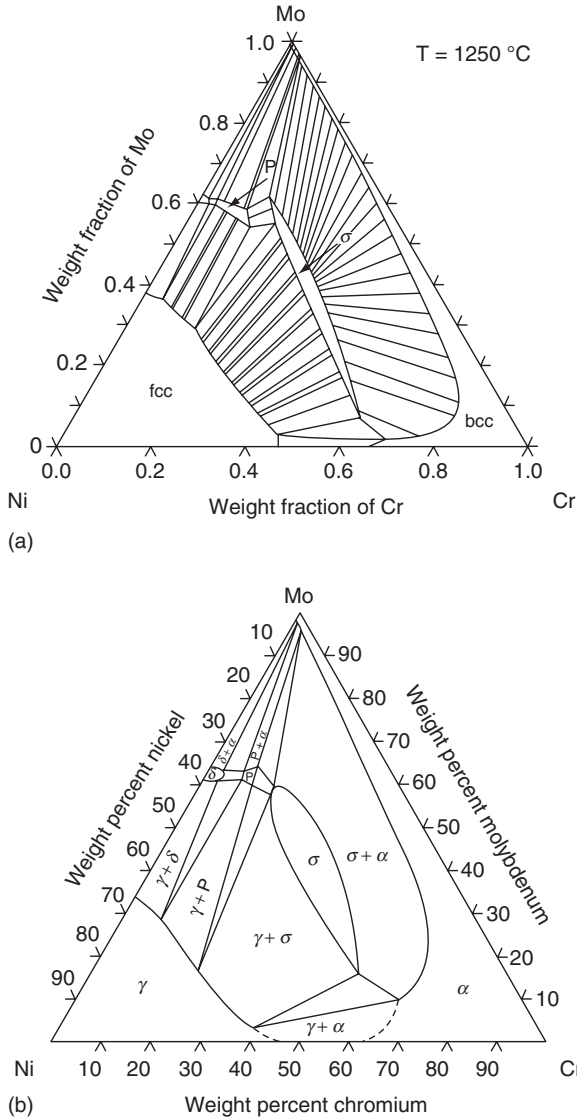


**Figure 2.15** Ni-Cr-Mo ternary isothermal diagram calculated at 1250°C (a) compared to the experimentally determined diagram (b) at the same temperature. (From Turchi *et al.* [30])

$\mu$  intermetallic phases, and there is generally good agreement on the position of the phase boundary lines. In this particular application, calculations were used to determine phases that may be stable during very long times at lower temperatures. Such lower temperature results cannot be obtained experimentally in reasonable time frames due to the low diffusion rates of Cr and Mo

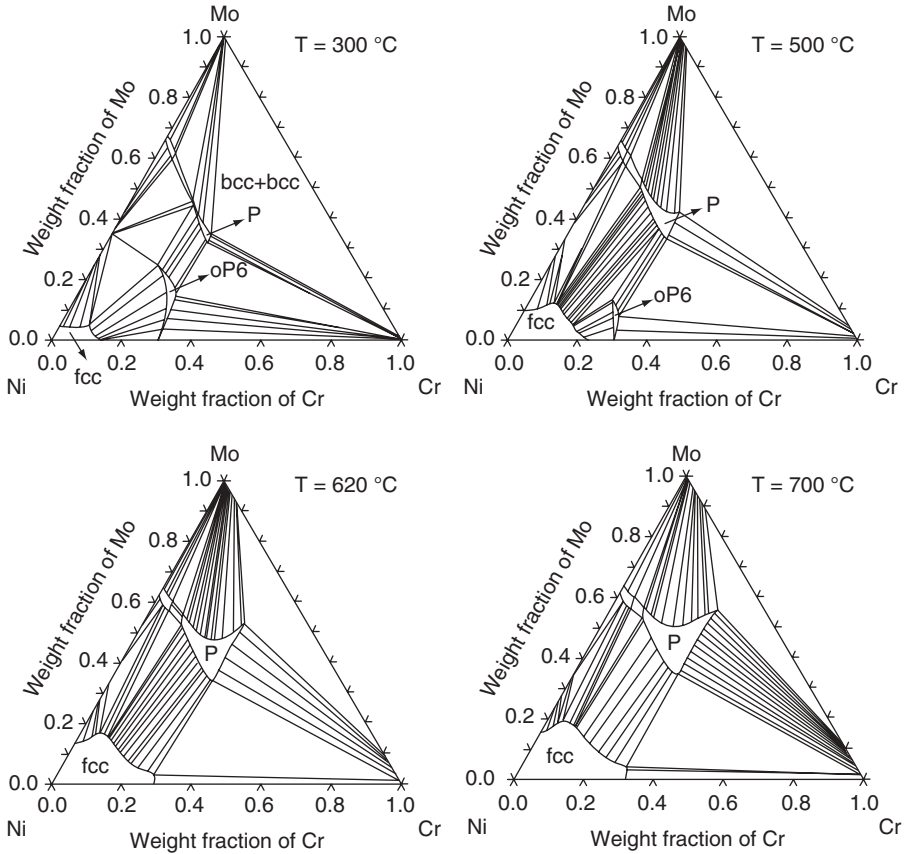


**Figure 2.16** Series of Ni-Cr-Mo ternary isothermal diagrams that calculated at lower temperatures. (From Turchi *et al.* [30])

in Ni and concomitantly long transformation times. Figure 2.16 shows a series of ternary isothermal diagrams that were calculated at lower temperatures. Calculations can then be performed to display the region of single phase austenite stability as a function of Cr and Mo content over a wide range of temperatures, as shown in Figure 2.17. Of interest for this application is the continuously shrinking austenite phase field with decreasing temperature. Because of the decreasing solubility of Cr and Mo with decreasing temperature, there is the potential for formation of brittle intermetallic phases at lower temperatures and very long aging times.

The diagrams described in the preceding sections are useful for assessing solid-state transformations, but cannot be used to assess phase formation that may take place in the fusion zone during solidification. In this case, liquidus projections can be calculated. An example of a calculated liquidus projection for interpreting phase formation in the fusion zone of Ni-Cr-Mo HASTELLOY®

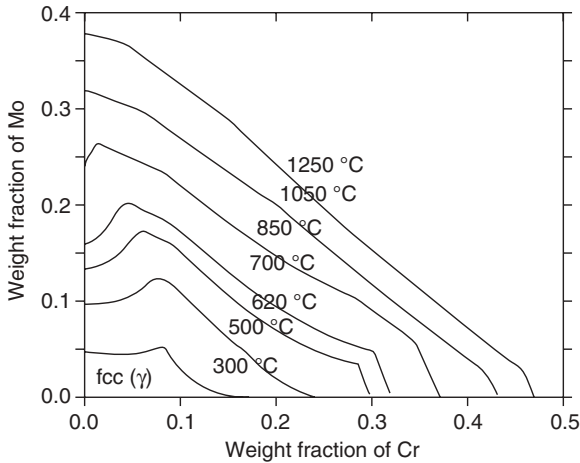


**Figure 2.17** Results of thermodynamic calculations showing the region of single phase austenite stability as a function of Cr and Mo content over a wide range of temperatures. (From Turchi *et al.* [30])

alloys is shown in Figure 2.18a (31), and Figure 2.18b shows the experimentally determined Ni-Cr-Mo liquidus projection that was used to validate the thermodynamic database.(32) There is generally good agreement between the two diagrams. Once validated, the database can be used to assess the influence of all alloying elements present in the alloy. An example of a multi-component liquidus projection for Alloy C-22 is shown in Figure 2.19. The arrow in the diagram represents a calculated solidification path that was superimposed on the diagram for quantitative predictions of solidification behavior, and will be discussed in more detail in Chapter 3. In this case, inclusion of all alloying elements in the calculations is found to widen the region for P-phase stability, thus causing this phase to form at the end of solidification. Successive calculations made with iterative alloying additions showed that W had the biggest effect of stabilizing the P phase, and this behavior would not be revealed by use of the simple Ni-Cr-Mo liquidus projection.

Many of these thermodynamic routines also have the ability to conduct multi-component solidification simulations. It is generally necessary to consider the solid-state diffusion of substitutional alloying elements to be negligible (i.e., Scheil conditions) and that of interstitial elements to be infinite. DuPont *et al.* have shown this accurately represents most cooling rate conditions associated with fusion welding in Ni-base alloys.(25) These calculations then permit predictions of phase formation as a function of temperature during solidification, the solidification temperature range, and the final distribution of alloying elements. Example calculations from HASTELLOY® type alloys are shown in Figure 2.20 and Figure 2.21.(33) Figure 2.20 shows Scheil solidification simulations for alloys C-22 and C-276 that reveal the phases that

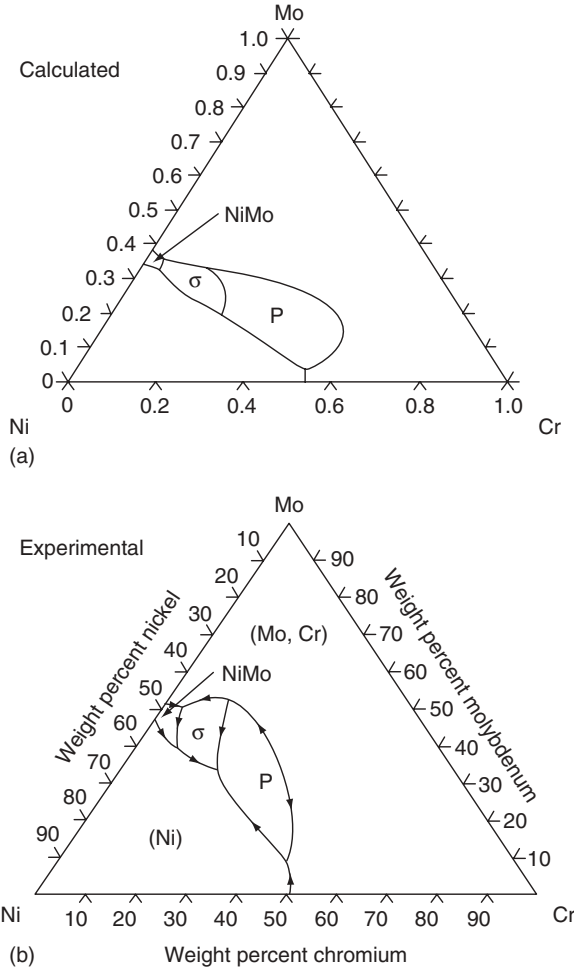


**Figure 2.18** Liquidus projections for the ternary Ni-Cr-Mo system, a) calculated projection, b) experimentally determined projection. (From Perricone *et al.* [31])

will form during the terminal stages of solidification ( $\sigma$  in C-22, P in C-276), their formation temperature, and the solidification temperature range. Figure 2.21a shows the calculated distribution of alloying elements expected to exist across the cellular/dendritic substructure of the weld for Ni, Cr, and Mo for Alloy C-22. Experimental measurements on the same alloy made by Cieslak *et al.* are provided in Figure 2.21b and show very good agreement between the measured and calculated results.(19)

The thermodynamic databases can also be coupled with kinetic calculation routines for determining time-temperature-transformation (TTT) and continuous cooling transformation (CCT) diagrams to describe the rate of diffusion-controlled reactions such as precipitation. These results are very

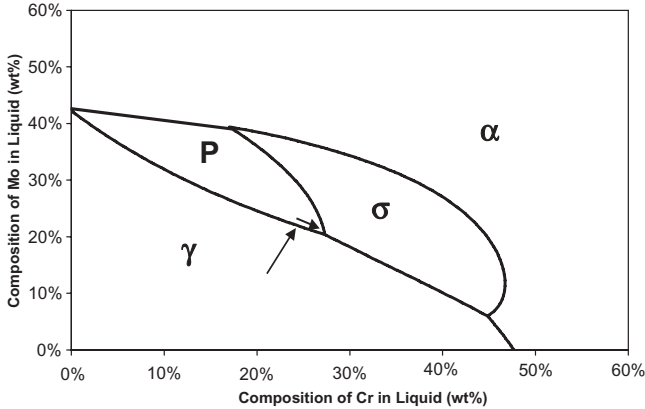


**Figure 2.19** Calculated multi-component liquidus projection for Alloy C-22. (From Perricone *et al.* [31])

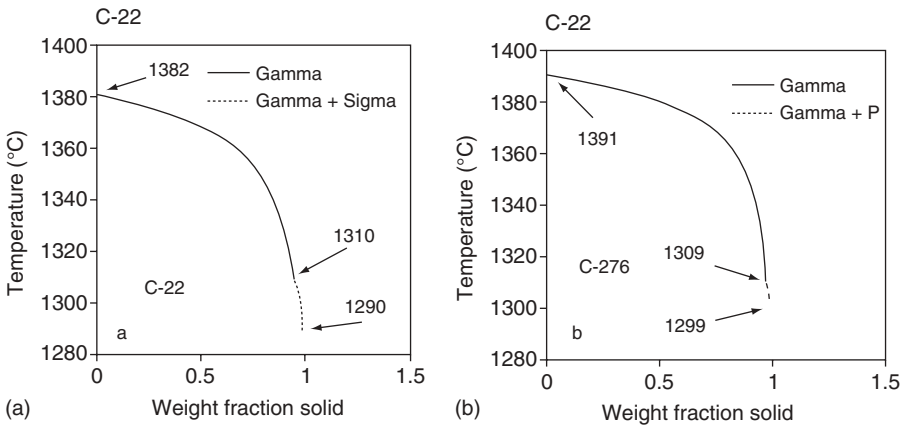
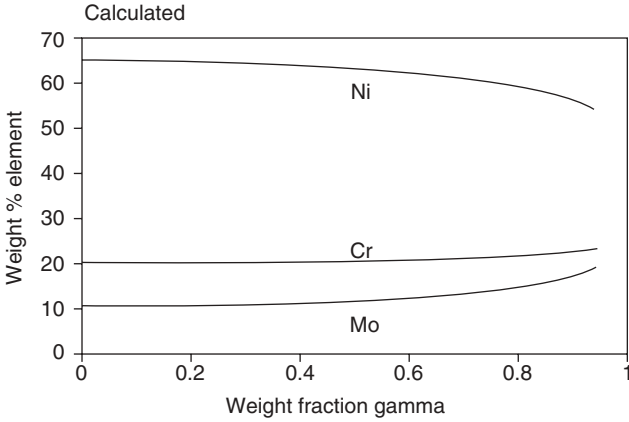
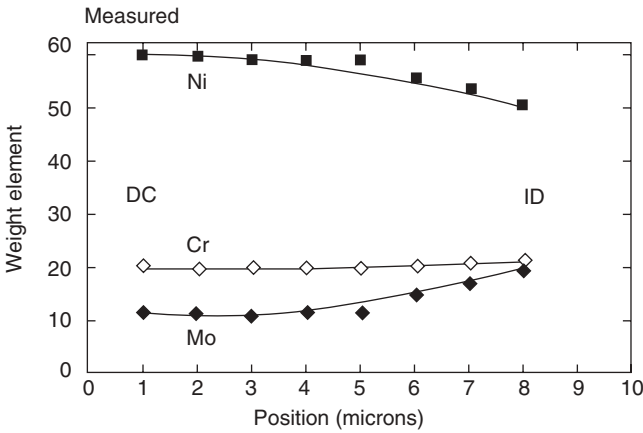


**Figure 2.20** Scheil solidification simulations for alloys C-22 and C-276. (From DuPont *et al.* [33])

useful for optimizing heat treatment schedules and assessing phase formation in the heat affected zone during welding of precipitation strengthened alloys. An example of a recent calculation of a TTT diagram for Alloy 718 is shown in Figure 2.22a, and the experimentally determined TTT diagram is shown in Figure 2.22b.(34) The calculated diagram was determined by a modified Johnson-Mehl-Avrami model, and input parameters for the model such as driving forces and precipitate compositions were obtained from the thermodynamic database. Alloy 718 is strengthened primarily by the  $\gamma''$  phase, but small amounts of  $\gamma'$  can also form. Although these phases are both advantageous in terms of strength, the brittle  $\delta$  and  $\sigma$  phases can also form at longer

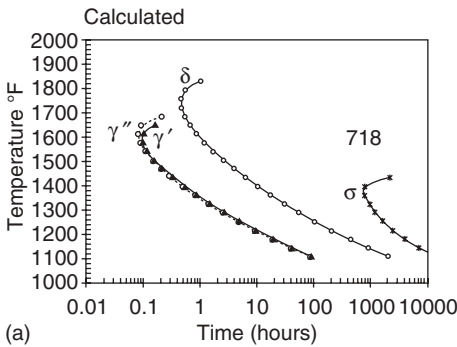


(a)

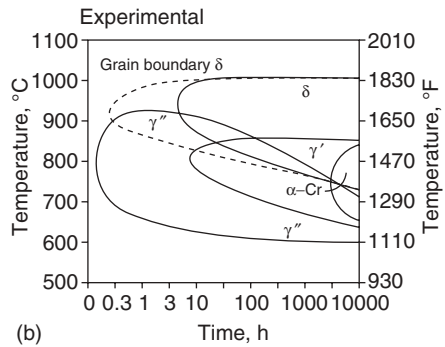


(b)

**Figure 2.21** Calculated (a) and measured (b) distribution of alloying elements expected to exist across the dendritic substructure of the weld for Ni, Cr, and Mo for Alloy C-22. (From DuPont *et al.* [33])



(a)



(b)

**Figure 2.22** TTT diagrams for Alloy 718, a) calculated, and b) experimentally determined. (Courtesy ASM International from [34])

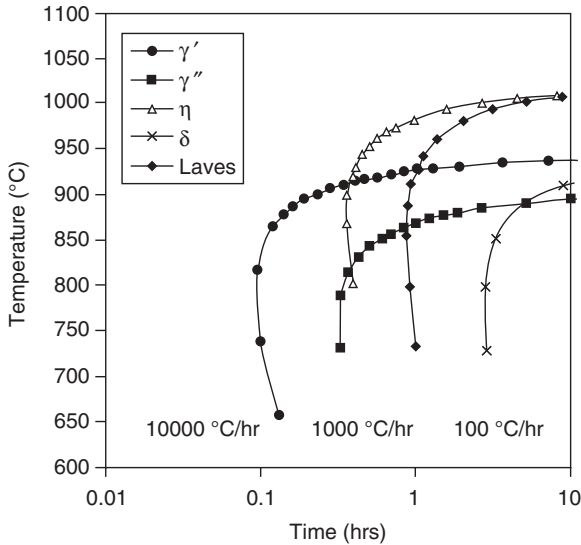


**Figure 2.23** Calculated CCT diagrams for Alloy 706. (Courtesy ASM International from [34])

times during thermo-mechanical processing or during service, and typically need to be avoided. The assessment of phase formation in the HAZ of welds is more accurately accomplished with the aid of CCT diagrams, and these can also be calculated. An example of this for Alloy 706 is shown in Figure 2.23. Alloy 706 is similar to Alloy 718 in that it contains Nb and is strengthened primarily by  $\gamma''$ .

The development of these multi-component phase stability diagrams have been invaluable for interpreting microstructural evolution in the fusion zone and HAZ of commercial Ni-base alloys, and have also found extensive use for efficient alloy design. The use of such diagrams is expected to become more common as Ni-base alloys grow in complexity to meet more demanding applications. More detailed descriptions on the use of calculated phase stability diagrams are provide for specific alloys in the following chapters.

## 2.7 PHACOMP PHASE STABILITY CALCULATIONS

Early developers of Ni-base superalloys relied predominately on available binary and ternary phase diagrams, since the multi-component thermodynamic routines described in the previous section were not available. As such, the prediction of detrimental TCP phases such as  $\sigma$ , P, and  $\mu$  was difficult. Efforts to avoid these phases without the availability of multi-component phase diagrams led to a phase stability calculation routine known as PHACOMP (for PHase COMPUTation).(11) In fact, many early alloys were

developed, at least in part, through the application of this technique. More recently, the PHACOMP routine has been replaced by a more refined approach known as New PHACOMP.(35) Although each of these techniques is slowly being replaced by multi-component thermodynamic and kinetic calculations, they can still be used to understand important phase stability effects in nickel alloys. In fact, recent work has shown that the New PHACOMP procedure can be used for both qualitative (36) and quantitative (37) phase predictions in superalloy weld metals. Thus, the general development and use of these procedures warrants a brief introduction here, and their use for predicting phase formation in Ni-base alloy welds will be discussed in more detail in Chapter 4.

The primary objective of the PHACOMP routine is to predict the solid solubility of the  $\gamma$ -austenite matrix, i.e., the position of the phase boundary between the  $\gamma$  and  $\gamma + \sigma$  (or  $P, \mu$ , or Laves) phase fields. This approach began with the observation that the undesirable TCP phases are electronic compounds in which one or more of the elements in the phase exhibits an electropositive character. Thus, attempts were made to apply electron vacancy concepts for predicting the solubility of the austenite matrix. With this approach, the average electron hole number ( $N_v$ ) is calculated for the austenite matrix via:

$$N_v = \sum (x_i)(n_v) \quad (\text{Eqn. 2.1})$$

Where  $x_i$  is the atomic fraction of element  $i$  in the austenite matrix and  $n_v$  is the electron hole number of element  $i$ . It is important to note that the value of  $x_i$  represents the concentration of element  $i$  dissolved in the austenite matrix after accounting for the formation of other phase such as carbides,  $\gamma'$ , and  $\gamma''$ , and does not represent the nominal concentration. The appropriate  $n_v$  values for important elements are shown in Table 2.3. Critical  $N_v$  values for various alloys were then established by comparison to validated phase diagrams that were available at the time. An example is shown in Figure 2.24, where the dotted line represents a constant  $N_v$  value of 2.49 that corresponds approximately to the position of the  $\gamma/(\gamma + \sigma)$  phase boundary line for Alloy U-700 in the Ni-Co-Cr system at 1200 °C (2190 °F). (11) Thus,  $N_v = 2.49$  is the critical value for  $\sigma$  formation in U-700, and the composition of the austenite matrix in this alloy should be controlled such that  $N_v$  values below 2.49 are maintained. Slightly different critical  $N_v$  values have been established for other alloys, such as 2.32 for René 80 and 2.38 for IN-738. Examination of the elements listed in Table 2.3 indicates that additions such as Ti, V, Zr, Nb, Ta, Al and Si exhibit particularly strong tendencies to form TCP phases. The very low  $n_v$  value for nickel is a reflection of its ability to dissolve a large amount of alloying elements due to its electronic configuration in which the d-band shell is relatively full of electrons.(1)

Although non-conservative results were obtained with some alloys, the PHACOMP routine was used for over 30 years as an aid to alloy development.

**TABLE 2.3** List of  $n_v$  and  $m_d$  values for alloying elements typically present in Ni-base alloys. (From Sims [11] and Morinaga *et al.* [35])

Element	$n_v$	$m_d$
Ti	6.66	2.271
V	5.66	1.543
Cr	4.66	1.142
Mn	3.66	0.957
Fe	2.66	0.858
Co	1.71	0.777
Ni	0.66	0.717
Zr	6.66	2.944
Nb	5.66	2.117
Mo	4.66	1.550
Ta	5.66	2.224
W	4.66	1.655
Al	7.66	1.900
Si	6.66	1.900

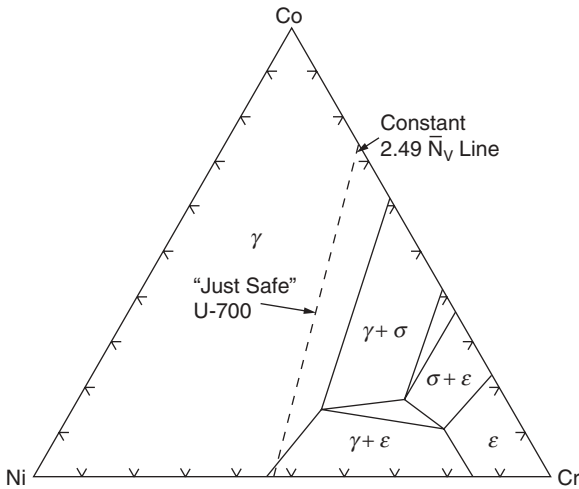


**Figure 2.24** Constant  $N_v = 2.49$  line corresponding approximately to the position of the  $\gamma/(\gamma + \sigma)$  phase boundary line for Alloy U-700 in the Ni-Co-Cr system. (From Sims [11])

One limitation of the approach is the lack of a temperature dependent  $N_v$  term to account for changes in solubility with temperature. With the more sophisticated New PHACOMP, the average  $d$ -electron energy above the Fermi level,  $M_d$ , is calculated from knowledge of the austenite composition and compared with a temperature dependent critical value,  $M_{d,crit}$ , needed to satisfy conditions

for exceeding the solid solubility. When such conditions are met, a TCP phase is expected to form. The temperature dependence of  $M_{d,crit}$  was determined from the  $\gamma/(\gamma + \text{TCP})$  solvus of a wide range of binary and ternary alloys. The value of  $M_d$  in the austenite is calculated by:

$$M_d = \sum (x_i)(m_d) \quad (\text{Eqn. 2.2})$$

where  $x_i$  is atomic fraction of element  $i$  in the austenite and  $m_d$  is the metal  $d$ -level of element  $i$ . Values of  $m_d$  for various elements are summarized in Table 2.3. The temperature dependent value of  $M_{d,crit}$  is expressed as:

$$M_{d,crit} = 6.25 \times 10^{-5} (T) + 0.834 \quad (\text{Eqn. 2.3})$$

where  $T$  is in K.

Zhang *et al.* used this technique as an aid to developing new corrosion resistant single crystal superalloys with a reduced amount of  $\gamma/\gamma'$  eutectic and a narrow solidification temperature ranges for improving casting characteristics and weldability.(38) Direct use of this approach for predicting the solidification behavior of fusion welds in superalloys is described in Chapter 4.

## REFERENCES

1. Pauling, L. 1938. The nature of the interatomic forces in metals, *Physical Review*, 54: 899–904.
2. Stoloff, N. S. 1990, Wrought and P/M superalloys, in *ASM Handbook, Volume 1*, ASM International, Materials Park, OH, pp. 950–980.
3. Brooks, R.B. 1982, *Heat treatment, structure and properties of nonferrous alloys*, ASM International, Materials Park, OH, p. 145.
4. Liu, C. T., Stiegler, J. O., and Froes, F. H. 1990, Ordered intermetallics, *ASM Handbook, Vol. 2, Properties and selection: nonferrous alloys and special-purpose materials*, ASM International, Materials Park, OH, pp. 913–942.
5. Lifshitz, I. M. and Sloyozov, V.V. 1961. The kinetics of precipitation from supersaturated solid solutions, *Journal of Physical Chemistry of Solids*, 19(1–2): 35–50.
6. Thornton, P. H., Davies, P. H., and Johnston, T. L. 1970. Temperature dependence of the flow stress of the gamma prime phase based upon  $\text{Ni}_3\text{Al}$ , *Metallurgical Transactions A*, 1(1): 207–218.
7. Brooks, J. W. and Bridges, P. J. 1988, Metallurgical Stability of INCONEL Alloy 718, *Superalloys 1988*, ASM International, Materials Park, OH, pp. 33–42.
8. Sundaraman, M. and Mukhopadhyay, P. 1993, Overlapping of  $\gamma''$  precipitate variants in inconel 718: *Materials Characterization*, v. 31, pp. 191–196.
9. DuPont, J. N., Robino, C. V., Marder, A. R., Notis, M. R., and Michael, J. R. 1988. Solidification of Nb-Bearing Superalloys: Part I. Reaction Sequences, *Metallurgical and Material Transactions A*, 29A: 2785–2796.

10. Ross, E. W. and Sims, C. T. 1987, Nickel-Base Alloys, *Superalloys II—High Temperature Materials for Aerospace and Industrial Power*, ASM International, Materials Park, OH, pp. 97–133
11. Sims, C. T. 1987, Prediction of Phase Composition, *Superalloys II—High Temperature Materials for Aerospace and Industrial Power*, John Wiley & Sons, New York, NY, pp. 218–240.
12. Perricone, M. J. and DuPont, J. N. 2006. Effect of Composition on the Solidification Behavior of Several Ni-Cr-Mo and Fe-Ni-Cr-Mo Alloys, *Metallurgical and Materials Transactions A*, 37A: 1267–1280.
13. Giggins, C. S. and Pettit, F. S. 1969. Oxidation of Ni-Cr alloys between 800 and 1200 °C, *Transactions of the Metallurgical Society of AIME*, 245: 2495–2507.
14. Chakrabarti, D. J., Laughlin, D. E., Chen, S. W., and Chang, Y. A. 1991. Ni-Cu System, in *Phase diagrams of binary nickel alloys*, P. Nash, ed., ASM International, Materials Park, OH, pp. 85–96.
15. Heckel, R. W., Ricketts, J. H., and Buchwald, J. 1965. Measurement of the degree of segregation in Monel 400 weld metal by X-ray line broadening, *Welding Journal*, 34(7): 332s–336s.
16. Nash, P. 1991. Ni-Cr System, *Phase diagrams of binary nickel alloys*, P. Nash, ed., ASM International, Materials Park, OH, pp. 75–84.
17. Singleton, M. F. and Nash, P. 1991. Ni-Mo System, *Phase diagrams of binary nickel alloys*, P. Nash, ed., ASM International, Materials Park, OH, pp. 207–212.
18. Baker, H. Ed. 1992, *Alloy phase diagrams*, ASM International, Materials Park, OH.
19. Cieslak, M. J., Headley, T. J., and Romig, A. D. 1986. The welding metallurgy of Hastelloy alloys C-4, C-22, and C-276, *Metallurgical Transactions A*, 17A: 2035–2047.
20. Banovic, S. W., DuPont, J. N., and Marder, A. R. 2003. Dilution and microsegregation in dissimilar welds between super austenitic stainless steel and nickel base alloys, *Science and Technology of Welding and Joining*, 6(6): 374–383.
21. Taylor, A. and Floyd, R. W. 1952. Phase stability in the Ni-Al-Ti system, *Journal of the Institute of Metals*, 81: 455–460.
22. Betteridge, W. and Heslop, J. 1974, *The nimonic alloys*, Crane, Russak, and Company, New York, NY.
23. Gaurd, R. W. and Westbrook, J. H. 1959. Phase stability in superalloys, *Transactions of the Metallurgical Society of AIME*, 215: 807–816.
24. Knorovsky, G. A., Cieslak, M. J., Headley, T. J., Romig, A. D., and Hammeter, W. F. 1989. Inconel 718: A solidification diagram, *Metallurgical Transactions A*, 20A: 2149–2158.
25. DuPont, J. N., Robino, C. V., and Marder, A. R. 1998. Solidification of Nb-Bearing Superalloys: Part II. Pseudo Ternary Solidification Surfaces, *Metallurgical and Material Transactions A*, 29A: 2797–2806.
26. Stadelmaier, H. H. and Fiedler, M. 1975. The ternary system nickel-niobium-carbon, *Z. Metallkde*, 9: 224–225.
27. Saunders, N. 2001, *Fe-Data Thermodynamic Database 3.0*, Thermotech, Ltd., The Surrey Research Park, Guildford, UK, Thermotech, Ltd.

28. Sundman, B. 2001, *Thermo-Calc. S-100 44[N]*. Thermotech, Ltd., The Surrey Research Park, Stockholm, Sweden.
29. Saunders, N., Guo, Z., Miodownik, A. P., and Schille, J. P. 2006. Modeling the material properties and behavior of Ni- and Ni-based superalloys, *Superalloys 718, 625, 706 and Derivatives*, ASM International, Materials Park, OH, pp. 571–580.
30. Turchi, P. A., Kaufman, L., and Liu, Z. 2006. Modeling of Ni-Cr-Mo based alloys: Part I: phase stability, *Computer Coupling of Phase Diagrams and Thermochemistry*, 30: 70–87.
31. Perricone, M. J., DuPont, J. N., and Cieslak, M. J. 2003. Solidification of Hastelloy Alloys: An Alternative Interpretation, *Metallurgical and Materials Transactions A*, 34A: 1127–1132.
32. Jena, A. K., Rajendraprasad, S. B., and Gupta, K. P. 1989. The Cr-Mo-Ni System, *Journal of Alloy Phase Diagrams*, 5: 164–177.
33. DuPont, J. N., Newbury, B. D., Robino, C. V., and Knorovsky, G. A. 1999. The Use of Computerized Thermodynamic Databases for Solidification Modeling of Fusion Welds in Multi-Component Alloys, *Ninth International Conference on Computer Technology in Welding*, National Institute of Standards and Technology, Detroit, MI, pp. 133–142.
34. Saunders, N., Guo, Z., Miodownik, A. P., and Schille, J. P. 2006. Modeling the material properties and behavior of Ni- and Ni-based superalloys, *Superalloys 718, 625, 706 and Derivatives*, ASM International, Materials Park, OH, pp. 571–580.
35. Morinaga, N., Yukawa, N., Adachi, H., and Ezaki, H. 1984, *New PHACOMP and Its Applications to Alloy Design*, ASM International, Champion, Pa, pp. 523–532.
36. Cieslak, M. J., Knorovsky, G. A., Headley, T. J., and Romig, A. D. 1986. The use of New PHACOMP in understanding the solidification microstructure of nickel base alloy weld metal, *Metallurgical Transactions A*, 17A: 2107–2116.
37. DuPont, J. N. 1998. A Combined Solubility Product/New PHACOMP Approach for Estimating Temperatures of Secondary Solidification Reactions in Superalloy Weld Metals, *Metallurgical and Material Transactions*, 29A: 1449–1456.
38. Zhang, J. S., Hu, Z. Q., Murata, Y., Morinaga, N., and Yukawa, N. 1993. Design and development of hot corrosion resistant nickel base single crystal superalloys by the d-electrons alloy design theory; Part II: effects of refractory metals Ti, Ta, and Nb on microstructures and properties, *Metallurgical Transactions A*, 24A: 2451–2464.



# Solid-Solution Strengthened Ni-base Alloys

Solid-solution strengthened Ni-base alloys are widely used in applications that require a combination of moderate strength and excellent corrosion resistance at temperatures up to 800 °C (1470 °F), and in some cases to temperatures as high as 1200 °C (2190 °F). These alloys are widely used in the power generation, chemical processing, and petrochemical industries, and a number of other specialty industries such as pulp and paper, composite tooling, and cryogenic liquid handling. They are strengthened primarily by the addition of substitutional alloying elements such as Cr, Fe, and Mo which provide solid-solution strengthening of the austenite<sup>1</sup> microstructure. This chapter describes the standard alloys in this class, along with the welding consumables that are generally recommended for use with these alloys. The physical metallurgy and mechanical properties of the solid-solution strengthened alloys are also reviewed. The welding metallurgy and weldability of this alloy class are reviewed in detail and corrosion issues associated with welded structures are discussed.

## 3.1 STANDARD ALLOYS AND CONSUMABLES

Solid-solution strengthened Ni-base alloys can be categorized by alloying additions as shown in Tables 3.1–3.3. Both the alloy designation and UNS number are provided to allow identification of the alloy by common “trade” names and to facilitate cross-referencing to other standards.

Table 3.1 lists a number of both commercially pure and low-alloy nickel materials, and the nickel-copper alloys. The compositions of a number of popular nickel-chromium, nickel-chromium-iron, and nickel-chromium-molybdenum alloys are listed in Table 3.2. Alloys with additions of molybde-

<sup>1</sup>Note that the terms “austenite” and “austenitic” are used to refer to the Ni-rich face centered cubic phase that is predominant in Ni-base alloys.

**TABLE 3.1 Composition of Ni and Ni-Cu Alloys.<sup>A</sup>**

Alloy	UNS No.	C	Cu	Fe	Mn	Ni	Si	Al
<i>Nickel and Low-Alloy Nickel Alloys</i>								
200	N02200	0.15	0.25	0.40	0.35	99.0 min	0.35	—
201	N02201	0.02	0.25	0.40	0.35	99.0 min	0.35	—
CZ100	N02100	1.00	1.25	3.00	1.50	Bal.	2.00	—
205	N02205	0.15	0.15	0.20	0.35	99.0 min	0.15	—
211	N02211	0.20	0.25	0.75	4.25–5.25	93.7 min	0.15	—
233	N02233	0.15	0.10	0.10	0.30	99.0 min	0.10	—
253	N02253	0.02	0.10	0.05	0.003	99.9 min	0.005	—
270	N02270	0.02	0.001	0.005	0.001	99.97 min	0.001	—
<i>Nickel-Copper Alloys</i>								
M25S	N04019	0.25	27.0–31.0	2.50	1.50	60.0 min	3.50–4.50	—
M35–2	N04020	0.35	26.0–33.0	2.50	1.50	Bal.	2.00	0.50
400	N04400	0.30	Bal.	2.50	2.00	63.0–70.0	0.50	—
401	N04401	0.10	Bal.	0.75	2.25	40.0–45.0	0.25	—
404	N04404	0.15	Bal.	0.50	0.10	52.0–57.0	0.10	0.05
405	N04405	0.30	Bal.	2.50	2.00	63.0–70.0	0.50	—

<sup>A</sup>Single value is a maximum.

num are widely used for improved aqueous corrosion resistance. In some cases, molybdenum also provides strength at elevated temperatures, but limits the upper range of application due to its tendency for severe oxidation above about 1150 °C (2100 °F).

There are also a number of iron-nickel alloys that are technically iron-based, but contain very high levels of nickel (30–45 wt%) and are often listed in handbooks along with true Ni-base alloys. Compositions of some of these alloys are also listed in Table 3.2. These include iron-nickel-chromium alloys that are used for elevated temperature applications and exhibit corrosion properties intermediate between the austenitic stainless steels and Ni-Cr-Fe alloys, including the popular grades 800, 800H and 825. These intermediate Ni-containing alloys and other specialty steels are often welded using Ni-base filler metals in order to achieve weld metal properties that match or exceed those of the base metal in the as-welded condition. Examples include:

- 1) the use of Ni-Cr consumables for welding 9% nickel steel for excellent as-welded impact strength at cryogenic temperatures,
- 2) welding Alloy 800H with Ni-Cr-Co-Mo consumables to provide overmatching creep strength above 870 °C (1600 °F), and
- 3) welding superduplex and superaustenitic stainless steels with Ni-Cr-Mo alloys for overmatching pitting resistance in the as-welded condition.

A number of nickel-iron, nickel-molybdenum, and iron-nickel alloys are listed in Table 3.3. The nickel-molybdenum “B” alloys contain virtually no

**TABLE 3.2 Composition of Ni-Cr, Ni-Cr-Fe, and Ni-Cr-Mo Alloys.<sup>A</sup>**

Alloy	UNS	C	Cr	Fe	Mn	Ni	Mo	Si	Al	Other
<i>Nickel-Chromium, Nickel-Chromium-Iron, and Nickel-Chromium-Molybdenum Alloys</i>										
600	N06600	0.15	14-17	6-10	1.0	72.0 min	—	0.5	—	—
601	N06601	0.1	21-25	Bal.	1.0	58-63	—	0.5	1.0-1.7	—
617	N06617	0.15	20-24	3.0	1.0	Bal.	8-10	1.0	0.8-1.5	Co 10-15
625	N06625	0.10	20-23	5.0	0.5	Bal.	8-10	0.5	0.40	Nb 3.15-4.15
690	N06690	0.05	27-31	7-11	0.5	58.0 min	—	0.5	—	—
693	N06693	0.15	27-31	2.5-6.0	1.0	Bal.	—	0.5	2.5-4.0	Ti 1.0, Nb 0.5-2.5
C-4	N06455	0.015	14-18	3.0	1.0	Bal.	14-17	0.08	—	—
C-22	N06022	0.01	20-24	3.0	0.5	Bal.	12-14	0.08	—	Co 2.5, 3 W
C-276	N10276	0.02	14.5-16.5	4-7	1.0	Bal.	15-17	0.08	—	Co 2.5
C-2000	N06200	0.1	22-24	3.0	0.5	Bal.	15-17	0.08	0.5	—
59	N06059	0.10	22-24	1.5	0.50	Bal.	15-16.5	0.1	0.4	—
230	N06230	0.05-0.15	20-24	3.0	0.30-1.0	Bal.	1-3.	0.25-0.75	0.2-0.5	—
RA333	N06333	0.08	24-27	Bal.	2.0	44-47	2.5-4	0.75-1.5	—	—
G3	N06985	0.015	21.0-23.5	18-21	1.0	Bal.	6-8	—	—	Cu 1.5-2.5
HX	N06006	0.05-0.15	20.5-23.0	17-20	1.0	Bal.	8-10	—	—	W 0.2-1.0
S	N06635	0.02	14.5-17	3.0	0.30-1.0	Bal.	14-16.5	0.2-0.75	0.1-0.5	—
W	N10004	0.12	5.0	6.0	1.0	63.0	24.0	—	—	—
X	N06002	0.05-0.15	20.5-23.0	17-20	1.0	Bal.	8-10	—	0.5	Co 0.5-2.5, W 0.2-1.0
686	N06686	0.01	19-23	2.0	0.75	Bal.	15-17	0.08	—	W 3.0-4.4
<i>Iron-Nickel-Chromium Alloys</i>										
HP	N08705	0.35-0.75	19-23	Bal.	2.00	35-37	—	2.5	0.15-0.6	—
800	N08800	0.10	19-23	Bal.	1.5	30-35	—	1.0	0.15-0.6	Ti 0.15-0.60
801	N08801	0.10	19-22	Bal.	1.5	30-34	—	1.0	—	Ti 1.0
802	N08802	0.2-0.5	19-23	Bal.	1.50	30-35	—	0.75	0.15-1.0	—
800H	N08810	0.05-0.1	19-23	Bal.	1.50	30-35	—	1.0	0.15-0.6	Ti 0.15-0.60
800HT	N08811	0.06-0.1	19-23	39.5 min	1.50	30-35	—	1.0	0.15-0.6	Ti 0.25-0.60
825	N08825	0.05	19.5-23.5	Bal.	1.00	38-46	2.5-3.5	0.5	0.2	Ti 0.6-1.2

<sup>A</sup> Single value is a maximum.

TABLE 3.3 Composition of Other Ni-base Alloys and Fe-Ni Alloys.<sup>A</sup>

Alloy	UNS No.	C	Cr	Mo	Fe	Mn	Ni	Si	Al	Ti	Nb	Co
<i>Nickel-Iron Alloys</i>												
52	N14052	0.05	0.25	—	Bal.	0.6	50.5 nom	0.3	0.1	—	—	—
Ni-Fe	N14076	0.05	2-3	0.5	Bal.	1.5	75-78	0.5	—	—	—	—
Ni-Fe	N14080	0.05	0.3	3.5-6	Bal.	0.8	79-82	0.5	—	—	—	—
<i>Nickel-Molybdenum Alloys</i>												
B	N10001	0.12	1.0	26-33	6	1.0	Bal.	1.0	—	—	—	—
B-2	N10665	0.01	1.0	26-30	2.0	1.0	69	0.1	0.5	—	—	—
B-3	N10675	0.01	1-3	27-32	1-3	3.0	65 min	0.1	0.5	—	—	—
B-10	N10624	0.01	6-10	21-25	5.0-8.0	1.0	Bal.	0.1	0.5	—	—	—
NiMo	N30007	0.07	1.0	30-33	3.0	1.0	Bal.	1.0	0.2	—	—	—
NiMo	N30012	0.12	1.0	26-30	4-6	1.0	Bal.	1.0	0.15	—	—	—
<i>Iron-Nickel Low Expansion Alloys</i>												
36(INVAR)	K93601	0.10	0.5	0.5	Bal.	0.6	34-38	0.35	0.1	—	—	—
42	K94100	0.05	0.5	0.5	Bal.	0.8	42.0 nom	0.3	0.15	—	—	—
48	K94800	0.05	0.25	—	Bal.	0.8	48.0 nom	0.05	0.1	—	—	—
902	N09902	0.06	4.9-5.75	—	Bal.	0.8	41-43.5	1.0	0.3-0.8	2.2-2.75	—	—
903	N19903	—	—	—	42.0	—	38.0	—	0.9	1.4	3.0	15.0
907	N19907	—	—	—	42.0	—	38.0	0.15	0.03	1.5	4.7	13.0
909	N19909	0.06	—	—	Bal.	—	38.0	0.4	0.03	1.5	4.7	13.0
KOVAR	K94610	0.04	0.2	0.2	53 nom	0.5	29.0	0.2	0.1	—	—	17.0

<sup>A</sup> Single value means maximum.

chromium and were developed to resist various acids, including hydrochloric, sulfuric, acetic, and phosphoric. Also listed in this table are several iron-nickel alloys specifically designed for low thermal expansion. A number of these alloys contain cobalt in the range from 13–17 wt%, and many have additions of Nb and Ti.

A number of commonly used Ni-base filler metals used for joining the solid-solution strengthened alloys are listed in Table 3.4 and are cross-referenced to the AWS classification for wire electrodes (ER, electrode rod) used for gas tungsten arc and gas metal arc welding. A selection guide for use of these filler metals with various base metals is also included.

### 3.2 PHYSICAL METALLURGY AND MECHANICAL PROPERTIES

Solid-solution strengthened Ni-base alloys are primarily strengthened by the addition of substitutional alloying elements including Cr, Fe, Mo, W and Cu. The addition of Co, Ta, and Re in some alloys also contributes to solid-solution strengthening. Nb may also provide some solid-solution strengthening, but it is primarily added as a carbide former or to form a strengthening precipitate ( $\text{Ni}_3\text{Nb}$ ). These elements are only effective strengtheners if they do not exceed the solubility limit of the Ni-rich austenite phase. The solubility limits for common solid-solution strengthening elements can be found in Table 2.2.

The addition of the substitutional alloying elements results in expansion of the Ni-rich, fcc lattice, resulting in a net strengthening (or hardening) of the austenite phase. These alloys normally contain carbides, the nature of which is determined by a combination of composition and heat treatment. The alloying additions of Nb, Ti, W, Mo, and Ta will all form MC-type carbides.  $\text{M}_{23}\text{C}_6$  carbides are promoted by Cr, Mo, and W. The addition of Cr may also stabilize the  $\text{M}_7\text{C}_3$  carbide, while Mo and W will promote the formation of  $\text{M}_6\text{C}$  carbide. Under most processing conditions, the MC and  $\text{M}_{23}\text{C}_6$  carbides are most commonly found in these alloys.

Most solid-solution strengthened Ni-base alloys are supplied in the solution-annealed condition. Solution annealing assures that alloying additions are dissolved in the austenite matrix and that the material is free of embrittling phases. Most alloys are solution annealed in the temperature range from 1000 to 1200 °C (1830 to 2190 °F). The time and temperature of the solution annealing heat treatment is used to control the base metal grain size. Rapid cooling (water quenching) from the solution annealing temperature is sometimes required to prevent the formation of carbides and/or embrittling species during cooling. When the alloy will be used in elevated temperature service, it is usually not necessary to water quench the alloy since it will be heated through the formation temperature range when it is put in service. The sensitivity of individual alloys to carbide formation during cooling may vary, however, and it is best to consult with the alloy manufacturer when considering these alloys for elevated temperature service.

**TABLE 3.4 Composition of Ni-base Filler Metals.<sup>A</sup>**

AWS Class	UNS		C	Cr	Fe	Mn	Ni	Mo	Si	Other
	Alloy	No.								
<i>Coated Electrodes</i>										
ENi-1	WE141	W82141	0.10	—	0.75	0.75	92.0min	—	1.25	Ti 1.0-4.0
ENi-CI	WE99	W82001	2.00	—	8.00	2.50	85.0min	—	4.00	Cu 2.5
ENiCu-7	WE190	W84190	0.15	—	2.50	4.00	62.0-69.0	—	1.50	Cu Bal., Al 1.75, Ti 1.0
ENiCrFe-1	WE132	W86132	0.08	13-17	11.0	3.50	62.0min	—	0.75	Nb 1.5-4.0
ENiCrFe-2	Weld A	W86133	0.10	13-17	12.0	1.00-3.5	62.0min	0.5-2.5	0.75	Nb 0.5-3.0
ENiCrFe-3	WE182	W86182	0.10	13-17	10.0	5.00-9.5	59.0min	—	1.0	Nb 1-2.5, Ti 1.0
ENiCrFe-7	WE152	W86152	0.05	28.0-31.5	7-12	5.00	Bal.	—	0.75	Nb 1-2.5
ENiMo-7	B-2	W80665	0.02	1.0	2.25	1.75	Bal.	26-30	0.2	W 1.0
ENiCrMo-3	WE112	W86112	0.10	20-23	7.0	1.0	55.0min	8-10	0.75	Nb 3.15-4.15
ENiCrMo-4	WE C-276	W80276	0.02	14.5-16.5	4.0-7.0	1.0	Bal.	15-17	0.2	W 3.0-4.5
ENiCrMo-10	WE C-22	W86022	0.02	20-22.5	2.0-6.0	1.0	Bal.	12.4-14.5	0.2	W 2.5-3.5, Co 2.5
ENiCrMo-14	WE 686	W86686	0.02	19-23	5.0	1.0	Bal.	15-17	0.25	W 3.0-4.4
ENiCrCoMo-1	WE 117	W86117	0.05-0.15	21-26	5.0	0.3-2.5	Bal.	8-10	0.75	Co 9.0-15.0, Nb 1.0
<i>Bare Welding Electrodes and Rods</i>										
ERNi-1	FM61	N02061	0.15	—	1.00	1.00	93.0min	—	0.75	Cu, 25, Ti 2.5-3.5, Al 1.5
ERNi-CI	FM99	N02215	1.00	—	4.00	2.50	90.0min	—	0.75	Cu 4.0
ERNiFeMn-CI	FM44	N02216	0.50	—	Bal.	10.0-14.0	35.0-45.0	—	1.0	Cu 2.5
ERNiCu-7	FM60	N04060	0.15	—	2.50	4.00	62.0-69.0	—	1.25	Cu Bal., Ti 1.5-3.0, Al 1.25
ERNiCu-8	FM64	N05504	0.25	—	2.0	1.5	63.0-70.0	—	—	Cu Bal., Ti 0.35-0.85, Al 2.3-3.15

ERNiCr-3	FM82	N06082	0.10	18.0-22.0	3.0	2.50-3.50	67.0 min.	—	Nb 2.0-3.0
ERNiCr-4	FM72	N06072	0.01-0.10	42.0-46.0	0.50	0.20	Bal.	—	Ti 0.3-1.0
ERNiCrFe-5	FM62	N06062	0.08	14.0-17.0	6.00-10.0	1.00	70.0 min.	—	Nb 1.5-3.0
ERNiCrFe-6	FM92	N07092	0.08	14.0-17.0	8.00	2.00-2.70	67.0 min	—	Ti 2.5-3.5
ERNiCrFe-7	FM52	N06052	0.04	28.0-31.5	7.00-11.0	1.00	Bal.	—	Al 1.10, Ti 1.0
ERNiCrFe-7A	FM52M	N06054	0.04	28.0-31.5	7.00-11.0	1.00	Bal.	—	Al 1.10, Ti 1.0, Nb 0.5-1.0
ERNiFeCr-1	FM65	N08065	0.05	19.5-23.5	22.0 min	1.00	38.0-46.0	2.5-3.5	Cu 1.50-3.0, Al 0.20, Ti 0.6-1.2
ERNiMo-3	W	N10004	0.12	4.0-6.0	4.0-7.0	1.0	Bal.	23-26	W 1.0, Co 2.5
ERNiCrMo-3	625	N06625	0.10	20-23	5.0	0.50	58.0 min.	8-10	Nb 3.15-4.15, Al 0.40, Ti 0.4
ERNiCrMo-7	C-4	N06455	0.015	14-18	3.0	1.0	Bal.	14-18	W 0.50, Ti 0.70
ERNiCrMo-10	C-22	N06022	0.015	20-22.5	2-6	0.50	Bal.	12.5-14.5	W 2.5-3.5, Co 2.5
ERNiCrMo-13	59	N06059	0.01	22-24	1.5	0.5	Bal.	15-16.5	Al 0.1-0.4
ERNiCrMo-14	FM686	N06686	0.01	19-23	5.0	1.0	Bal.	15-17	W 3.0-4.4, Al 0.5, Ti 0.25
ERNiCrMo-17	C-2000	N06200	0.01	22-24	3.0	0.5	Bal.	15-17	Al 0.5, Cu 1.3-1.9, Co 2.0
ERNiCrWMo-1	230-W	N06231	0.05-0.15	20-24	3.0	0.3-1.0	Bal.	1-3	0.25-0.75 Al 0.2-0.5, Co 5.0, W 13-15
ERNiCrCoMo-1	617	N06617	0.05-0.15	20-24	3.0	1.0	Bal.	8-10	1.0 Co 10-15, Al 0.8-1.5

<sup>A</sup> Single value is a maximum.

TABLE 3.4 *Continued*

AWS Classification	Major Uses
E/ERNi-1	Joining Alloys 200 and 201
E/ERNiCu-7	Dissimilar combinations of steels and Ni alloys
ERNiCr-3	Joining Alloys 400, 405, and K-500
	Joining of Alloys 600 and 601
	Alloys 800, 800H and 800HT for service temperatures to 850°C (1560°F)
E/ERNiCrFe-7/7A	Dissimilar combinations of steels and Ni alloys
E/ERNiCrMo-2	Joining high-Cr alloys, such as Alloy 690
E/ERNiCrMo-3	Joining Alloy HX
	Joining Alloys 625
	Joining of 9% Ni steels for cryogenic service
E/ERNiCrMo-4	Dissimilar combinations of steels and Ni alloys
E/ERNiCrCoMo-1	Joining Alloy C-276 and other pitting resistant alloys
	Joining Alloy 617
ERNiFeCr-1	Joining Alloy 800HT for service temperatures above 760°C (1400°F) to 1150°C (2100°F)
E/ERNi-CI	Joining Alloy 825
ENiFe-CI	Joining/repair of cast irons, especially in thin sections
	Joining/repair of cast irons, especially thick sections and high phosphorus

Water quenching from the solution annealing temperature is effective in preventing the formation of  $M_{23}C_6$  carbides during cooling in order to help avoid intergranular attack in certain environments. However, it should be noted that when water-quenched, the HAZ may be subject to carbide formation if repair welding becomes necessary. Cold work can be applied to these alloys to increase base metal strength, but this is not normal, especially in applications that require welding. The HAZ in alloys strengthened by cold work will undergo recrystallization resulting in local softening of the structure.

In applications where intergranular stress corrosion is a concern, the material may be subjected to heat treatment in the carbide precipitation range, 600 to 800°C (1110 to 1470°F). By holding the material in this range stable  $M_{23}C_6$  carbides having a discrete, globular morphology will form at the grain boundaries and prevent “sensitization” during fabrication. For example, Alloy 690, which is a Ni-30Cr alloy used in intermediate temperature nuclear power applications, is heat treated in this manner to prevent intergranular stress corrosion cracking in service. By using an extended heat treatment in the  $M_{23}C_6$  precipitation range, the chromium-depleted region originally surrounding the carbide can be eliminated. This occurs since extended exposure in the carbide precipitation range allows the Cr-depleted region at the carbide/matrix interface to “heal” by the diffusion of matrix Cr into the initially depleted region.

A similar treatment at 1040°C (1900°F) for one hour is used in mill annealed Alloy 825 to prevent intergranular attack. As described above, this treatment precipitates the carbides and then allows matrix chromium to diffuse to the area adjacent to the grain boundary to eliminate the depletion. For Alloy 800H, a postweld heat treatment at a minimum of 885°C (1625°F) is prescribed when service temperatures are above 540°C (1000°F). This treatment again precipitates  $M_{23}C_6$  carbides that coalesce into blocky, discrete particles instead of films that can cause stress relaxation cracking in service. The importance of these treatments will be described in more detail in Section 3.6.

Representative microstructures of solid-solution strengthened Ni-base alloys are shown in Figure 3.1. In most cases, these alloys are supplied in the solution annealed condition, as represented by the Alloy 625 microstructure in Figure 3.1A. In some cases, the base metal may be subjected to an aging treatment in the carbide precipitation range in order to protect against intergranular stress corrosion cracking (IGSCC). This microstructure is represented by the Alloy 690 microstructure shown in Figure 3.1B.

The mechanical properties of a number of solid-solution strengthened Ni-base alloys are listed in Table 3.5. The yield strengths of these alloys range from 40 to 65ksi (275 to 450MPa) with tensile strengths in the range from 70 to 120ksi (485 to 830MPa). These alloys have good room temperature ductility based on their austenitic (fcc) structure. The toughness of these

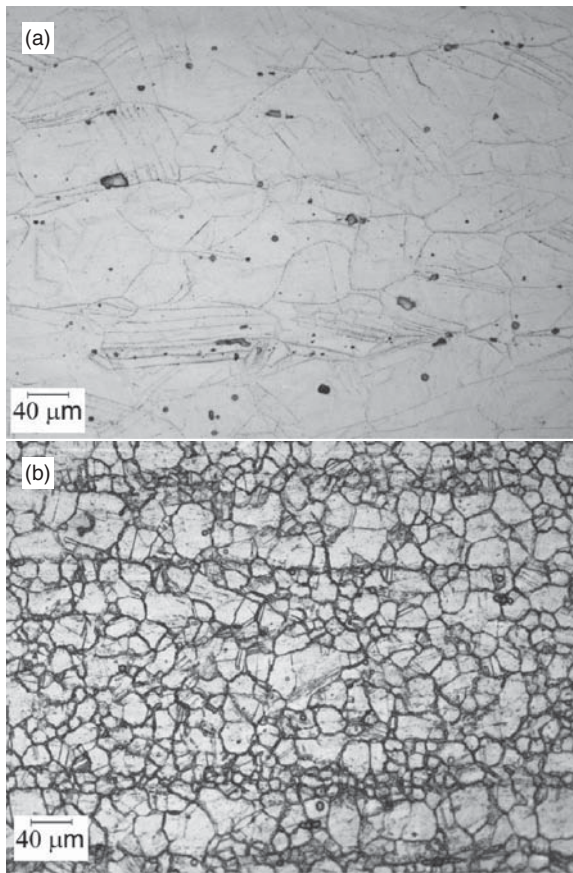


**Figure 3.1** Representative base metal microstructures of solid-solution strengthened Ni-base alloys, a) Alloy 625 in solution annealed condition, b) Alloy 690 in solution annealed and aged condition to precipitate grain boundary carbides.

**TABLE 3.5 Mechanical Properties of Base Metals.**

Alloy	UNS	Tensile Strength, ksi(MPa)	0.2% Offset, Yield Strength, ksi(MPa)	Elongation, %	RA, %	Hardness, R <sub>B</sub>
Alloy 200	N02200	70 (485)	40 (275)	40	50	70
Alloy 400	N04400	85 (585)	50 (345)	35	45	75
Alloy 600	N06600	80 (550)	50 (345)	40	40	90
Alloy 601	N06601	90 (620)	55 (380)	40	35	95
Alloy 617	N06617	115 (795)	65 (450)	40	40	98
Alloy C-22	N06622	100 (690)	55 (380)	35	40	97
Alloy 625	N06625	120 (830)	60 (415)	30	35	95
Alloy 690	N06690	90 (620)	55 (380)	40	35	95
Alloy 800	N08800	85 (585)	45 (310)	40	40	85
Alloy 800H	N08810	85 (585)	40 (275)	45	40	80
Alloy 800HT	N08811	85 (585)	40 (275)	40	40	80
Alloy 825	N08825	95 (655)	50 (345)	35	40	90

alloys is also good over a wide range of temperatures, including cryogenic temperatures.

### 3.3 WELDING METALLURGY

#### 3.3.1 Microstructural Evolution in the Fusion Zone

The solid-solution strengthened Ni-base alloys solidify as austenite and are essentially fully austenitic at the end of solidification. This austenite is stable during cooling from the solidification temperature range and the room temperature microstructure is fully austenitic. Segregation during solidification of these alloys results in local variation in composition at the solidification subgrain level. In many alloys, the segregation of alloy and impurity elements can lead to the formation of a second phase (or phases) at the end of solidification. In this section, microstructure evolution in these alloys is described and the effect of segregation during solidification is reviewed in detail.

**3.3.1.1 Interfaces in Single Phase Austenitic Weld Metal** It is important to understand the nature of the various boundaries, or interfaces, that are present in Ni-base weld metal, since many of the defects associated with the fusion zone both during fabrication and service are associated with these boundaries. Boundaries are especially evident in Ni-base alloy weld metals, since the austenite solidification structure is clearly apparent after polishing and etching. At least three different boundary types can be observed metallographically.<sup>(1)</sup> These are shown schematically in Figure 3.2 and described in the following sections.

**3.3.1.1.1 Solidification Subgrain Boundaries (SSGBs)** The solidification subgrains represent the finest structure that can be resolved in the light optical microscope. These subgrains are normally present as cells or dendrites and the boundary separating adjacent subgrains is known as a solidification subgrain boundary (SSGB). These boundaries are evident in the microstructure because their composition is different from that of the bulk microstructure. Solute redistribution that creates this compositional gradient at the SSGB is dictated by Case 2 (microscopic) solute redistribution, also referred to as Scheil partitioning. The degree of segregation along SSGBs in Ni-base alloys is described in detail in Section 3.3.1.2.

There is virtually no crystallographic misorientation across the SSGB and these boundaries are characterized crystallographically as “low angle” boundaries. The low misorientation (typically less than five degrees) results from the fact that subgrain growth during solidification occurs along preferred crystallographic directions (or easy growth directions). In fcc and bcc metals, these are  $\langle 100 \rangle$  directions. Because of this, the dislocation density along the SSGB

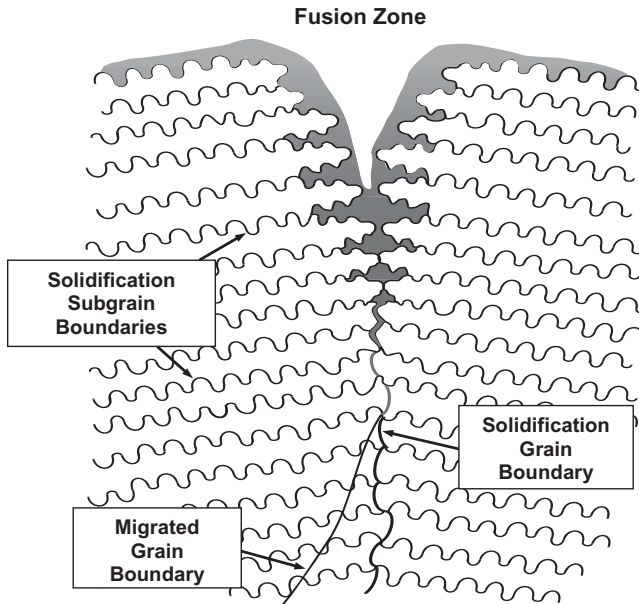


**Figure 3.2** Schematic of boundaries observed in weld metals that solidify as austenite. (From Lippold *et al.* [1].)

is generally low since there is not a large structural misorientation to accommodate.

**3.3.1.1.2 Solidification Grain Boundaries (SGBs)** The solidification grain boundary (SGB) results from the intersection of packets, or groups, of subgrains. Thus, SGBs are the direct result of competitive growth that occurs along the trailing edge of the weld pool. Because each of these packets of subgrains has a different growth direction and orientation, their intersection results in a boundary with high angular misorientation. These are often called “high angle” grain boundaries. This misorientation results in the development of a dislocation network along the SGB.

The SGB also exhibits a compositional component resulting from solute redistribution during solidification. This redistribution can be modeled using Case 3 (macroscopic) solidification boundary conditions and often results in high concentrations of solute and impurity elements at the SGBs. These compositions may lead to the formation of low melting liquid films along the SGBs at the conclusion of solidification that promote weld solidification cracking. When weld solidification cracking occurs in Ni-base alloy weld metals, it is almost always along SGBs.

**3.3.1.1.3 Migrated Grain Boundaries (MGBs)** The SGB that forms at the end of solidification has both a compositional and crystallographic component. In some situations, it is possible for the crystallographic component of the SGB to migrate away from the compositional component. This new boundary carries with it the high angle misorientation of the “parent” SGB and is called a migrated grain boundary (MGB).

The driving force for migration is the same as for simple grain growth in base metals, a lowering of boundary energy. The original SGB is quite tortuous since it forms from the intersection of opposing cells and dendrites. The crystallographic boundary can lower its energy by straightening and, in the process, it pulls away from the original SGB. Further migration of the boundary is possible during reheating, such as during multipass welding.

Because it carries the crystallographic misorientation of the SGB with it, the MGB represents a high angle boundary, normally with misorientations greater than 30 degrees. The composition of the boundary varies locally, depending on the composition of the microstructure where it has migrated. It is also possible that some segregation can occur along MGBs in the solid state, possibly by a “sweeping” mechanism. Grain boundary “sweeping” describes the effect of mobile grain boundaries assimilating, or “sweeping up” solute or impurity elements as they migrate. Since these elements must then move with the boundary, it is generally thought that fast diffusing interstitial elements (S, P, B, O, etc.) are most likely to be swept into the boundary.

MGBs are most prevalent in fully austenitic weld metals. When a second phase forms at the end of solidification along the SGBs and SGBs, this phase may be effective in “pinning” the crystallographic component of the SGB, thus preventing it from migrating away from the parent SGB. In this case, a MGB does not form because the high angle crystallographic boundary cannot migrate away. The formation of MGBs and the pinning effect from second phase particles is an important part of the mechanism for ductility-dip cracking and is discussed in more detail in Section 3.5.2.

An example of the three interface types in Filler Metal 52 weld metal is shown in Figure 3.3. Note that the actual migration distance of the MGB is only a few microns away from the SGB and that it cuts through the center of the solidification subgrains.

**3.3.1.2 Elemental Segregation during Solidification** The weldability, mechanical properties, and corrosion resistance of Ni-base alloys are largely controlled by the solidification behavior and resultant microstructure of the fusion zone. The primary microstructural features of interest include the distribution of alloying elements across the cellular/dendritic substructure and the phases that form in the fusion zone during solidification. The fusion zone solidification behavior is, in turn, controlled by solute redistribution behavior. Solute redistribution of alloying elements in Ni-base alloys can most effec-

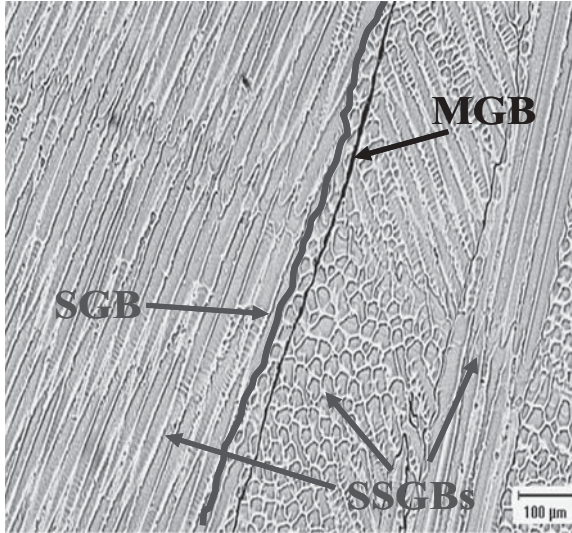


**Figure 3.3** Microstructure of Filler Metal 52 weld metal showing the three boundary types typical of austenite solidification.

tively be assessed with the aid of the Brody-Flemings equation (2), which is given by:

$$C_s = kC_o \left[ 1 - \frac{f_s}{1 + \alpha k} \right]^{k-1} \quad (3.1)$$

Where  $C_s$  is the solid composition at the solid/liquid interface,  $C_o$  is the nominal alloy composition,  $f_s$  is the fraction solid, and  $k$  is the equilibrium distribution coefficient. The  $\alpha$  parameter in equation (3.1) is a dimensionless diffusion parameter defined as:

$$\alpha = \frac{D_s t_f}{L^2} \quad (3.2)$$

Where  $D_s$  is the diffusivity of solute in the solid,  $t_f$  is the solidification time (cooling time between the liquidus and terminal solidus), and  $L$  is half the dendrite arm spacing. The  $D_s t_f$  term in the numerator essentially represents the distance a solute atom can diffuse in the solid during solidification, while the half dendrite arm spacing,  $L$ , represents the length of the concentration gradient. Thus, when  $D_s t_f \ll L^2$ , the solute is able to diffuse only a small fraction of the total gradient length and solid state diffusion will be insignificant. This represents the case in which  $\alpha \approx 0$  and equation (3.1) reduces to the well-known Scheil equation.(3)

$$C_s = kC_o[1 - f_s]^{k-1} \quad (3.3)$$

The Scheil equation describes solute redistribution when diffusion in the solid is insignificant. It assumes equilibrium at the solid/liquid interface, complete diffusion in the liquid, negligible diffusion in the solid, and negligible dendrite tip undercooling. Many studies have used these simple concepts to explore the solidification behavior in Ni-base alloy weld metals.(4–19). These studies have demonstrated that the solute redistribution behavior and resultant weld metal microstructure are primarily controlled by the pertinent values of  $k$  and  $D_s$  for the alloying elements of interest. The value of  $D_s$  will control the potential for back-diffusion in the solid during solidification. The value of  $k$ , which is defined by  $k = C_s/C_l$  ( $C_s$  is the solid composition,  $C_l$  is the liquid composition at a particular temperature), describes how strongly an alloying element partitions to the liquid and solid phases during solidification. Elements that exhibit values of  $k < 1$  segregate to the liquid during solidification. Elements with very low  $k$  values can produce steep concentration gradients across the cellular or dendritic substructure of the weld. However, the elemental gradient can be eliminated if solid-state diffusion of that particular element in the solid is high enough. Thus, with these concepts in mind, it is useful to summarize the behavior of alloying elements in Ni-base alloys based on their known values of  $k$  and  $D_s$  in order to understand microstructural development in the fusion zone.

The back-diffusion potential of alloying elements in nickel can be assessed by direct estimation of the  $\alpha$  parameter in Equation 3.2. The  $t_f$  and  $L$  terms will each depend on the cooling rate of the weld ( $\epsilon$ ) via

$$t_f = \frac{\Delta T}{\epsilon} \quad (3.4)$$

$$L = \frac{\lambda}{2} = \frac{A\epsilon^{-n}}{2} \quad (3.5)$$

Where  $\Delta T$  is the solidification temperature range,  $\lambda$  is the dendrite spacing, and  $A$  and  $n$  are material constants. (Equation 3.4 assumes a linear cooling rate through the solidification temperature range.) Thus, by knowing the solidification temperature range, cooling rate, and dendrite spacing-cooling rate relationship, the  $\alpha$  parameter can be directly estimated as a function of cooling rate and the potential influence of solid-state diffusion can be determined.

Table 3.6 summarizes diffusivity data for many alloying elements in nickel. Upper bound values of  $\alpha$  for each element can be calculated by determining  $D_s$  at the liquidus temperature, approximately 1350°C for many nickel alloys (6,12), using a large, but representative, value of  $\Delta T$  of 200°C, and reported values of  $A = 32$  and  $n = 0.31$ .(20) Using these values,  $\alpha$  can be calculated as a function of cooling rate and is shown in Figure 3.4 for the substitutional

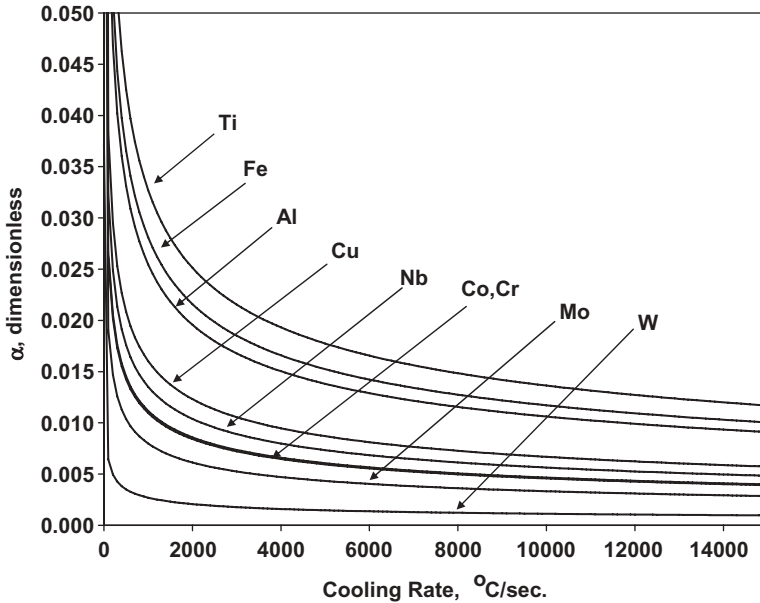


**Figure 3.4** Dimensionless  $\alpha$  parameter as a function of cooling rate for a wide range of alloying elements typically present in Ni base alloys. (From Joo and Takeuchi [20].)

alloying elements listed in Table 3.6. The values of  $A$  and  $n$  used here were for Alloy 713. However, the values do not vary significantly among many Ni-base alloys.(21) The  $\alpha$  value decreases with increasing cooling rate due to the decrease in solidification time ( $t_f$ ) with increasing cooling rate. More importantly, note that  $\alpha \ll 1$  for all the elements considered under all cooling rate conditions. Use of various values of  $\Delta T$ ,  $A$ , and  $n$  representative of other nickel base alloys does not change this result significantly. It is also important to note that an upper bound value of  $D_s$  was calculated at a typical liquidus temperature of  $1350^\circ\text{C}$  ( $2460^\circ\text{F}$ ). The value of  $\alpha$  can only decrease with the use of  $D_s$  values calculated at lower solidification temperatures.

These results clearly demonstrate that solid-state diffusion of substitutional alloying elements in nickel alloys is insignificant during solidification of fusion welds. Experimental evidence has been published that supports these calculations for a variety of elements, including Fe, Cr, Nb, Mo, and Si.(11,22) In that work, dendrite core compositions were experimentally measured in samples that were solidified under a very wide range of cooling rates, including samples quenched during solidification and samples cooled at  $0.2^\circ\text{C}/\text{sec}$  and  $650^\circ\text{C}/\text{s}$ . The dendrite core compositions were identical in all cases, indicating that solid-state diffusion is indeed negligible.

Calculation of the  $\alpha$  parameter for C in Ni will yield values that are significantly greater than unity. This is to be expected, since C diffuses by an interstitial mechanism and therefore exhibits diffusion rates that are orders of

**TABLE 3.6 Diffusion Data for Various Alloying Elements in Nickel.**

Element	Diffusion Coefficient, $D_0$ (m <sup>2</sup> /sec)	Activation Energy, Q (kJ/mol)	Reference
Fe	$8.0 \times 10^{-5}$	255	1
Cr	$1.1 \times 10^{-4}$	272	2
Co	$1.4 \times 10^{-4}$	275	3
Nb	$7.5 \times 10^{-5}$	264	4
Mo	$1.0 \times 10^{-4}$	275	5
W	$2.0 \times 10^{-4}$	299	6
Al	$1.9 \times 10^{-4}$	268	3
Ti	$4.1 \times 10^{-4}$	275	6
Cu	$5.7 \times 10^{-5}$	258	2
C	$8.0 \times 10^{-6}$	135	7

## References:

1. Lacombe, P., 1961, *Colloque sur les Joints de Grains, Saclay*, Presses Universitaires de France, Paris: 56–67.
2. Hirano, K., Agarwala, R. P., 1962, Averbach, B. L., and Cohen, M., Diffusion in cobalt-nickel alloys, *Journal of Applied Physics*, 33: 3049–3054.
3. Swalin, R. A., Martin, A., 1956, Solute diffusion in nickel-base substitutional solid solutions, *Journal of Metals*, 8(206): 567–572.
4. Kurokawa, S., Ruzzante, J. E., Hey, A. M., Dymont, F., 1983, Diffusion of Niobium in Iron and Iron Alloys, *Metal Science*, 17(9): 433–438.
5. Heijwegen, C. P. and Rieck, G. D., 1974, Diffusion in the Mo-Ni, Mo-Fe, and Mo-Co Systems, *Acta Metallurgica*, 22(10): 1269–1281.
6. Jung, S. B., Yamane, T., Minamino, Y., Hirao, K., Araki, H., Saji, S., 1992, Interdiffusion and its size effect in nickel solid solutions of nickel-cobalt, nickel-chromium and nickel-titanium, *Journal of Materials Science Letters*, 11(20): 1333–1337.
7. Bose, S. K. and Grabke, H. J., 1978, Diffusion Coefficient of C in Fe-Ni Austenite in the Temperature Range 950–1100 C, *Zeitschrift fur Metallkunde*. 69(1): 8–15.

magnitude higher than the substitutional alloying elements. Evidence for this is reflected in the activation energy term (Q) for diffusion of C in Ni shown in Table 3.6. Note that Q for the substitutional alloying elements varies over a fairly narrow range of 255 to 299kJ/mol, while the value for C is approximately half this at 135kJ/mol. In this case, the potential for back diffusion cannot be determined directly with the simple B-F model of Equation 3.1.

More detailed back-diffusion model calculations for back-diffusion of C in welds of nickel alloys have been conducted and the result is shown in Figure 3.5.(11) In this figure, the solute redistribution behavior of C in Ni was calculated with the Clyne-Kurz model that takes the temperature dependent diffusion rate of C into account.(23) Comparison is made between the Scheil equation that assumes negligible solid-state diffusion and the lever law that assumes infinite solid-state diffusion. Note that the detailed results from the Clyne-Kurz model are essentially identical to that of the lever law, indicating that complete solid-state diffusion of C is expected in Ni-base alloys during solidification. A similar effect can be expected for N in Ni. This calculation

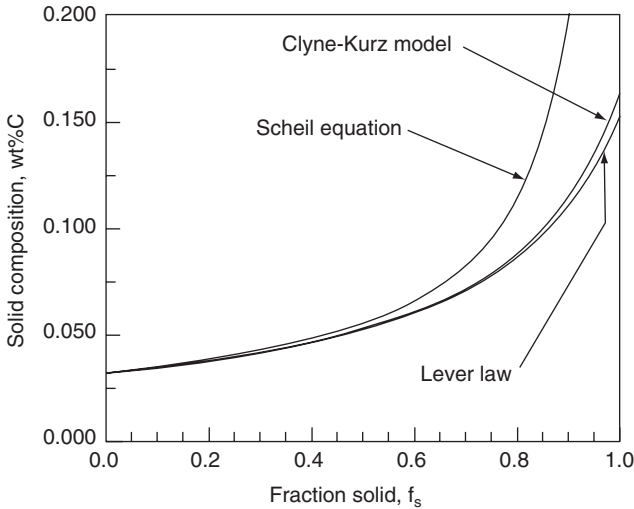


**Figure 3.5** Comparison of solute redistribution behavior of carbon in a Ni-base superalloy calculated using the lever law, Scheil equation, and Clyne-Kurz models. (From DuPont *et al.* [11].)

was conducted for a cooling rate of  $650^{\circ}\text{C}/\text{sec}$  through the solidification temperature range that is achievable during arc welding. Higher cooling rates typical of high energy density welding (such as electron beam or laser welding) may alter this result and begin to limit C diffusion in the solid. Aside from this possibility, these results demonstrate that solid-state diffusion of substitutional alloying elements during solidification of fusion welds in nickel alloys is insignificant while C (and N) can be expected to exhibit complete diffusion in the solid.

The result presented above for substitutional alloying elements carries important implications. First, it indicates that solute redistribution and the final concentration gradients across the cellular/dendritic substructure in fusion welds of Ni-base alloys produced under cooling rate conditions typical of arc welding can be calculated with reasonable accuracy using the simple Scheil equation. (Welds produced with high energy density processes may experience dendrite tip undercooling that would reduce the extent of microsegregation.) Second, it demonstrates that, except for the case where  $k = 1$ , some level of microsegregation can always be expected in the as-solidified weld. Examples of this are shown in Figure 3.6 and 3.7 for fusion welds in a Ni-Cr-Mo type alloy and a Nb-bearing superalloy.(11,24) Last, the final degree of microsegregation can be assessed by direct determination of the  $k$  value for the element of interest, where the degree of microsegregation will increase with decreasing  $k$  value (for  $k$  values  $< 1$ ).

For example, the lowest concentration will occur at the dendrite core where solidification initiates, and the concentration at this location is given by  $kC_0$ .

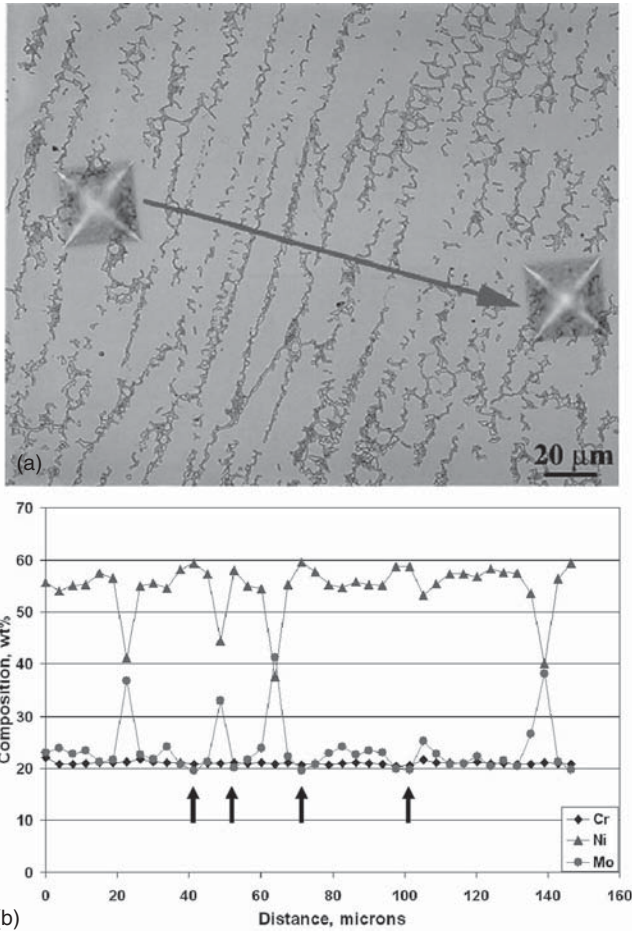


**Figure 3.6** Example of interdendritic P phase and microsegregation of Ni, Cr, and Mo observed in the fusion zone of a Ni-Cr-Mo alloy. a) Photomicrograph showing microprobe line scan, b) microprobe results for Cr, Ni, and Mo. (From DuPont *et al.* [11].)

With this last point in mind, Table 3.7 summarizes experimentally measured  $k$  values determined in welds for a wide range of alloying elements in Ni-base alloys. The table includes both solid-solution and precipitation-strengthened alloys, since the segregation behavior of an element during solidification is independent of its intended purpose. Values for pertinent binary Ni alloys are also provided for reference. It should be noted that nearly all these values represent electron probe microanalysis (EPMA) measurements in which the core composition is measured and  $k$  is then determined by the ratio of the core to nominal composition,  $k = C_{\text{core}}/C_o$ . Thus, these values represent  $k$  at the start of solidification and do not account for variations in  $k$  that may occur during solidification as the temperature decreases.

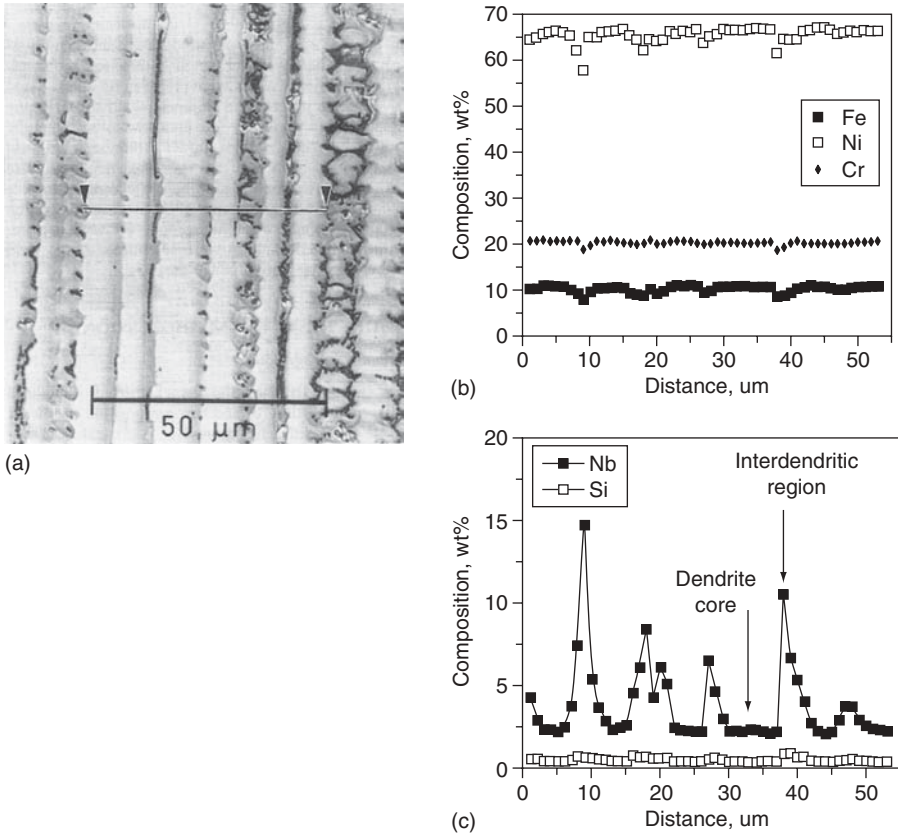


**Figure 3.7** Example of interdendritic NbC and Laves phases and microsegregation observed in the fusion zone of a Ni-base superalloy. a) Photomicrograph showing microprobe line trace, b) Fe, Ni, and Cr composition profiles, and c) Nb and Si composition profiles. (From Perricone and DuPont [24].)

Many important observations can be made from the data shown in Table 3.7. Note that, except for Nb and perhaps Si and Ti, there are not large differences between the segregation behavior exhibited by complex multi-component alloys and the Ni-X binary systems. The segregation potential of Nb has been shown to be very important (4,6,11,12) for controlling microstructural evolution in superalloys that rely on the  $\gamma''$ -Ni<sub>3</sub>Nb phase for strengthening (details of this are covered in Chapter 4). The value for Nb is lower in the multi-component alloys than the simple binary Ni-Nb system. This indicates that the presence of other alloying elements decreases the solubility of Nb in Ni. Note that the  $k$  value for Nb is also more variable than other elements shown in Table 3.7.

As shown in Figure 3.8, recent research has shown that the value of  $k$  for Nb depends on the Fe content of the alloy.(11) This can be interpreted

**TABLE 3.7 Summary of Equilibrium Distribution Coefficients for Various Elements in Ni-base Alloys.**

Alloy	Ni	Fe	Cr	Co	Nb	Mo	W	Al	Ti	Si	Cu	C	Ref.
Monel 400	1.07	—	—	—	—	—	—	—	—	—	0.78	—	26
B-2	1.06	1.00	—	—	—	0.86	—	—	—	—	—	—	14
B-3	1.03	—	—	—	—	0.89	—	—	—	—	—	—	14
W	1.06	1.03	0.99	—	—	0.85	—	—	—	0.51	—	—	14
C4	1.04	0.90	0.96	—	—	0.88	—	0.74	—	—	—	—	7
C-22	1.05	0.98	0.94	—	—	0.85	0.91	—	—	—	—	—	7
C-276	1.08	1.01	0.95	—	—	0.82	1.01	—	—	—	—	—	7
C-2000	1.02	1.06	0.96	—	—	0.91	—	—	—	—	0.89	—	18
242	1.04	—	1.00	—	—	0.89	—	—	—	—	—	—	48
Ni-20Cr-12Mo	1.05	1.07	1.00	—	—	0.71	—	—	—	—	—	—	24
Ni-20Cr-24Mo	1.08	—	1.02	—	—	0.81	—	—	—	—	—	—	24
Ni-44Fe-20Cr-12Mo	1.05	1.07	1.00	—	—	0.71	—	—	—	—	—	—	24
IN718	1.00	1.04	1.03	—	0.48	0.82	—	1.00	0.69	0.67	—	—	13
IN725	—	1.1	0.99	—	0.55	0.79	—	—	0.66	—	—	—	14
IN738	1.03	—	0.98	1.09	0.52	0.87	1.13	0.92	0.69	—	—	—	76
IN625	—	—	—	—	0.54	—	—	—	—	0.57	—	0.21	6
IN625/C Steel	1.04	1.02	1.05	—	0.46	—	—	—	—	—	—	—	12
IN909	0.97	1.10	—	1.02	0.49	—	—	—	0.65	0.67	—	—	5
IN903	0.97	1.06	—	1.05	0.58	—	—	0.95	0.76	—	—	—	RN (1)
Thermo-Span	0.97	1.10	1.10	1.02	0.42	—	—	0.79	0.58	0.69	—	—	17
RR2000	—	—	1.10	1.08	—	0.97	—	0.97	0.60	—	—	—	VAM (2)
RR2060	—	—	1.06	1.10	—	0.91	0.81	0.95	0.65	—	—	—	VAM (2)
SRR99	—	—	0.95	1.09	—	—	1.06	1.00	0.68	—	—	—	VAM (2)

TABLE 3.7 Continued

Alloy	Ni	Fe	Cr	Co	Nb	Mo	W	Al	Ti	Si	Cu	C	Ref.
MAR-M002	—	—	0.95	1.16	—	—	1.12	0.99	0.60	—	—	—	VAM (2)
Ni-10Fe-19Cr-Nb-Si-C	1.02	1.00	1.06	—	0.45	—	—	—	—	0.71	—	0.27	12
Ni-45Fe-19Cr-Nb-Si-C	1.00	1.06	1.02	—	0.25	—	—	—	—	0.58	—	—	12
20Cb-3	0.97	1.08	0.93	—	0.33	—	—	—	—	0.89	—	—	12
HR-160	0.96	—	1.01	1.08	—	—	—	—	0.44	0.71	—	—	10
Ni-Fe	—	~1	—	—	—	—	—	—	—	—	—	—	25
Ni-Cr	—	—	0.90	—	—	—	—	—	—	—	—	—	25
Ni-Co	—	—	—	~1	—	—	—	—	—	—	—	—	25
Ni-Nb	—	—	—	—	0.75	—	—	—	—	—	—	—	25
Ni-Mo	—	—	—	—	—	0.82	—	—	—	—	—	—	25
Ni-W	—	—	—	—	—	—	~1.2*	—	—	—	—	—	25
Ni-Al	—	—	—	—	—	—	—	0.80	—	—	—	—	25
Ni-Ti	—	—	—	—	—	—	—	—	0.87	—	—	—	25
Ni-Si	—	—	—	—	—	—	—	—	—	0.70	—	—	25
Ni-Cu	—	—	—	—	—	—	—	—	—	—	0.7**	—	25
Ni-C	—	—	—	—	—	—	—	—	—	—	—	0.28	25

\* Estimated at Ni-15wt% W.

\*\* Estimated at Ni-30wt% Cu.

(1) RN—Nakkali, R. Richard, N. L., Chaturvedi, M. C., 1993, Microstructural characterization of Incoloy 903 weldments, *Metallurgical and Materials Transactions A*, 24A: 1169–2047.(2) VAM—Wills, V. A. and McCartney, D. G., 1991, A comparative study of solidification features in nickel-base superalloys: microstructural evolution and microsegregation, *Materials Science and Engineering A*, 145: 223–232.

based on differences in solubility exhibited by the simple Ni-Nb and Fe-Nb systems.(25) For example, the maximum solid solubility of Nb in  $\gamma$ -nickel is 18wt%. By comparison,  $\gamma$ -iron has a maximum solid solubility of only 1.5wt% Nb. Thus, based on these differences, Fe additions decrease the solubility of Nb in  $\gamma$ , thus leading to the decreased k values shown in Figure 3.8. A similar trend has been observed for Mo in nickel alloys when used in dissimilar weld applications involving alloys high in Fe.(22) Details of this can be found in Chapter 7.

The data in Table 3.7 also shows that elements with similar atomic radii to Ni, namely Fe, Cr, and Co, have k values that are close to unity. This trend is expected based on the influence of atomic size difference on solubility, where elements of similar atomic radii generally exhibit appreciable solubility. The atomic radii differences of Fe, Cr, Co compared to Ni are less than one percent for all these elements. Thus, although these elements cannot back diffuse during solidification, their concentration gradients are not large to begin with because their k values are all close to unity. This behavior is particularly beneficial for Cr, which is used for corrosion protection by formation of a passive  $\text{Cr}_2\text{O}_3$  scale. The presence of significant concentration gradients would lead to preferential attack in the dendrite cores for alloys that rely exclusively on Cr as a passive film former. In fact, preferential corrosion often occurs at the dendrite cores in welds of Mo-bearing alloys due to microsegregation of Mo.

Reference to Table 3.7 indicates this can be directly attributed to the somewhat low value of k for Mo. The behavior of tungsten (W) is surprising and not well understood. Tungsten is appreciably larger than Ni (10% larger

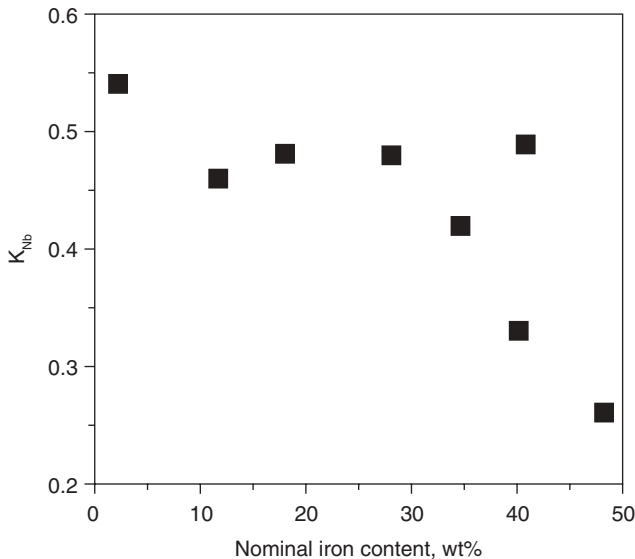


**Figure 3.8** Variation in the Nb distribution coefficient,  $k_{\text{Nb}}$ , as a function of Fe content for several Ni-base alloys. (From DuPont *et al.* [11].)

atomic radius) and exhibits a different crystal structure (bcc), yet shows very little tendency for segregation in Ni alloys. This makes W attractive for solid solution strengthening. Carbon exhibits the greatest partitioning behavior of the elements listed in Table 3.7, and this accounts for the formation of various carbide phases (most notably the MC type) at the end of solidification in many Ni-base alloys. Although there is strong partitioning to the liquid phase during solidification, the final carbon distribution in the solid can be expected to be uniform due to the high solid-state diffusivity of C in fcc Ni.

**3.3.1.3 Phase Transformation Sequence** The phase transformation sequences observed in fusion welds of a number of solid-solution strengthened Ni-base alloys are summarized in Table 3.8. The table is not meant to represent an all-inclusive list of microstructure evolution in commercially available

**TABLE 3.8 Summary of Transformation Sequences Observed in Fusion Welds of Solid-solution Strengthened Ni-base Alloys.**

Alloy	Transformation Sequence	Reference
Monel 400	$L \rightarrow L + \gamma \rightarrow \gamma$	26
IN52	$L \rightarrow L + \gamma \rightarrow L + \gamma + \text{TiC} \rightarrow \gamma + \text{TiC} \rightarrow \gamma + \text{TiC} + \text{M}_{23}\text{C}$	29
800	$L \rightarrow L + \gamma \rightarrow L + \gamma + \text{TiC} \rightarrow \gamma + \text{TiC}$	28
B-2	$L \rightarrow L + \gamma \rightarrow L + \gamma + \text{M}_6\text{C} \rightarrow \gamma + \text{M}_6\text{C}^1$	14
W	$L \rightarrow L + \gamma \rightarrow L + \gamma + \text{P} \rightarrow L + \gamma + \text{P} + \text{M}_6\text{C} \rightarrow \gamma + \text{P} + \text{M}_6\text{C} \rightarrow \gamma + \mu + \text{M}_6\text{C}^2$	14
C-4	$L \rightarrow L + \gamma \rightarrow L + \gamma + \text{TiC} \rightarrow \gamma + \text{TiC}$	7,16
C-22	$L \rightarrow L + \gamma \rightarrow L + \gamma + \text{P} \rightarrow L + \gamma + \text{P} + \sigma \rightarrow \gamma + \text{P} + \sigma \rightarrow \gamma + \text{P} + \sigma + \mu$	7,16
C-276	$L \rightarrow L + \gamma \rightarrow L + \gamma + \text{P} \rightarrow \gamma + \text{P} \rightarrow \gamma + \text{P} + \mu$	7,16
242	$L \rightarrow L + \gamma \rightarrow L + \gamma + \text{M}_6\text{C} \rightarrow \gamma + \text{M}_6\text{C}^3$	48
Ni-20Cr-12Mo	$L \rightarrow L + \gamma \rightarrow \gamma$	24
Ni-20Cr-24Mo	$L \rightarrow L + \gamma \rightarrow L + \gamma + \text{P} \rightarrow \gamma + \text{P}$	24
Ni-44Fe-20Cr12Mo	$L \rightarrow L + \gamma \rightarrow L + \gamma + \sigma \rightarrow \gamma + \sigma$	24
625 (0.03 Si, 0.009 C)	$L \rightarrow L + \gamma \rightarrow L + \gamma + \text{NbC} \rightarrow L + \gamma + \text{NbC} + \text{Laves} \rightarrow \gamma + \text{NbC} + \text{Laves}$	4
625 (0.03 Si, 0.038 C)	$L \rightarrow L + \gamma \rightarrow L + \gamma + \text{NbC} \rightarrow \gamma + \text{NbC}$	4
625 (0.38 Si, 0.008 C)	$L \rightarrow L + \gamma \rightarrow L + \gamma + \text{NbC} \rightarrow L + \gamma + \text{NbC} + \text{M}_6\text{C} \rightarrow L + \gamma + \text{NbC} + \text{M}_6\text{C} + \text{Laves} \rightarrow \gamma + \text{NbC} + \text{M}_6\text{C} + \text{Laves}$	4
625 (0.46 Si, 0.035 C)	$L \rightarrow L + \gamma \rightarrow L + \gamma + \text{NbC} \rightarrow L + \gamma + \text{NbC} + \text{Laves} \rightarrow \gamma + \text{NbC} + \text{Laves}$	4
HR-160	$L \rightarrow L + \gamma \rightarrow L + \gamma + (\text{Ni,Co})_{16}(\text{Ti,Cr})_6\text{Si}_7 \rightarrow \gamma + (\text{Ni,Co})_{16}(\text{Ti,Cr})_6\text{Si}_7$	10
C-4 Gd	$L \rightarrow L + \gamma \rightarrow L + \gamma + \text{Ni}_5\text{Gd} \rightarrow \gamma + \text{Ni}_5\text{Gd}$	19

1. Tentative phase identification.

2. Actual reaction sequence not determined.

3. Minor amount of additional  $\text{M}_6\text{C}$ -type phase also observed.

alloys, but provides examples from the available classes of alloys that can be used to identify general trends between alloy composition and fusion zone microstructure. The Ni-Cu type alloys, such as MONEL 400, generally solidify as single phase austenite with no secondary constituents. This is to be expected based on the simple Ni-Cu isomorphous phase diagram (see Figure 2.2) that exhibits complete solid solubility across the entire composition range. Based on the discussion above on elemental partitioning, the austenite dendrites in these alloys will exhibit microsegregation of Cu. For example, Choi *et al.* measured dendrite core Cu concentrations of  $\sim 25$  wt% in a weld of MONEL 400 that had a nominal Cu concentration of 32 wt%.(26)

Fusion welds in Fe-Ni-Cr type alloys with only minor alloy additions also solidify predominately in the fully austenitic mode. This is expected based on the simple Fe-Ni-Cr liquidus projection (Figure 2.5), which indicates that austenite is the only stable phase associated with solidification temperatures at the Ni-rich end of the Fe-Ni-Cr system. Additions of carbon to these alloys often leads to precipitation of  $M_{23}C_6$  type carbides in the solid state during the cooling portion of the weld thermal cycle. This can be understood with reference to Figure 3.9, which shows the solubility of Ni and C in austenite in an 18 wt% Cr alloy.(27) The solubility decreases appreciably with decreasing temperature and precipitation of the  $M_{23}C_6$  carbide is expected near 950 °C (1740 °F) for carbon contents over  $\sim 0.02$  wt% when the Ni concentration is greater than  $\sim 35$  wt%. The simultaneous presence of C and strong carbide forming elements such as Ti and Nb can lead to the formation of MC type carbides in the interdendritic regions at the terminal stages of solidification by eutectic type reactions involving  $\gamma$  and MC phases. This has been observed in

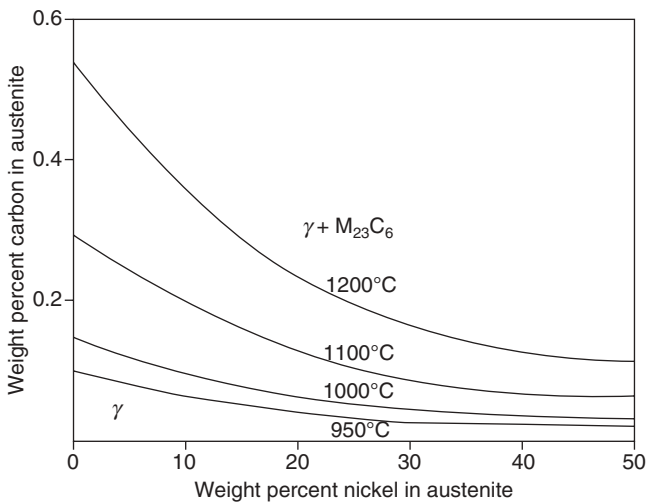


**Figure 3.9** Solubility of Ni and C in austenite at various temperatures for a constant Cr content of 18 wt%. Above the solubility limit a Cr-rich,  $M_{23}C_6$  carbide forms. (From Tuma *et al.* [27].)

**TABLE 3.9 Crystal Structures and Compositions of  $\mu$ ,  $\sigma$ , and P Phases Observed in Fusion Welds of Several Solid-solution Strengthened Ni-base Alloys.**

Alloy	Composition (wt%)				
	Ni	Mo	Cr	W	Fe
<i><math>\mu</math> Phase—Hexagonal</i>					
C-22 (3Fe-21Cr-13Mo)	33	39	19	6	2
C-276 (5Fe-16Cr-16Mo)	33	41	15	6	4
<i><math>\sigma</math> Phase—Tetragonal</i>					
AL6XN (48Fe-21Cr-6Mo)	13	17	29	—	38
Ni-44Fe-20Cr-12Mo	15	21	26	—	38
C-22 (3Fe-21Cr-13Mo)	35	35	23	4	2
<i>P Phase—Orthorhombic</i>					
C-22 (3Fe-21Cr-13Mo)	33	37	22	5	2
C-276 (5Fe-16Cr-16Mo)	34	40	16	7	4
Ni-20Cr-24Mo	31	47	21	—	—

a number of Ni-Fe-Cr type alloys, such as Alloy 800 and Filler Metals 52 and 82.(28,29)

Microstructure evolution in fusion welds of Ni-Mo and Ni-Cr-Mo type alloys is more complicated due to the potential formation of intermetallic topologically closed packed (TCP) phases such as  $\sigma$ ,  $\mu$ , and P that are stabilized by the presence of Mo. Tungsten additions also stabilize these TCP phases. They are generally undesirable from both a weldability and properties point of view. Their formation has been shown to extend the solidification temperature range and increase solidification cracking susceptibility. Their complex crystal structure leads to limited slip systems, which makes these phases brittle and can lead to reduced toughness and ductility if they are present in high proportions. Their high Cr and Mo contents will reduce the Cr and Mo concentrations in the austenite matrix, thereby reducing corrosion resistance. The crystal structure and typical compositions of these phases determined from fusion zones in several Ni alloys are shown in Table 3.9.(7,24) The nominal Fe, Cr, and Mo contents of these alloys are indicated for reference. Typical examples of the P and  $\sigma$  phases in fusion welds are shown in Figure 3.10. Note that these phases are located in the interdendritic region, indicating they are associated with eutectic-like reactions that occur in the solute enriched liquid that is present at the end of solidification due to segregation. All these phases are high in Cr and Mo. The  $\mu$  and P phases are particularly high in Mo, while the  $\sigma$  phase is high in Cr. The Ni and Fe concentrations of these phases generally scale with the nominal alloy composition.

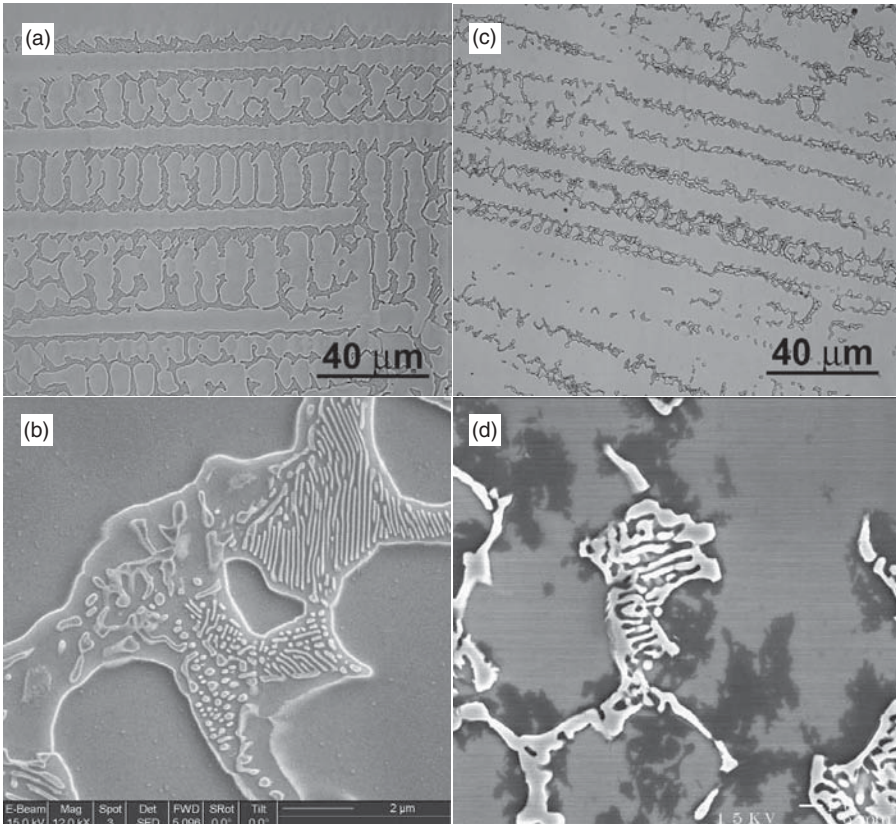


**Figure 3.10** Examples of  $\sigma$  phase (a and b) and P phase (c and d) observed in the fusion zone of Ni-Cr-Mo type alloys. (From Perricone and DuPont [24].)

Simple Ni-Mo alloys such as B-2 generally solidify as single phase austenite with small amounts of the  $M_6C$  carbide.(14) Ni-Cr-Mo alloys with Mo contents below  $\sim 15$ wt% and very low Fe and W can also solidify as single phase austenite without the formation of the brittle TCP phases.(7,24) Evidence for this is shown in Table 3.9 by Hastelloy C-4 and the experimental Ni-20Cr-Mo alloy. Alloy C-4 has small Ti additions that promote formation of the TiC phase at the end of solidification in a manner similar to that described above for Ni-Fe-Cr alloys. With higher Mo additions, combined with the presence of Fe and W, TCP phases typically cannot be avoided in the fusion zone during solidification. The type and number of phases that form and their corresponding reaction sequence will depend on alloy composition.

Cieslak *et al.* investigated the solidification behavior of fusion welds in alloys C-22 and C-276.(7) Alloy C-22 is a nominal Ni-21Cr-13Mo-3Fe-2W alloy, while Alloy C-276 is nominally Ni-16Cr-16Mo-5Fe-4W. Since multi-component liquidus projections were not available at the time, microstructural

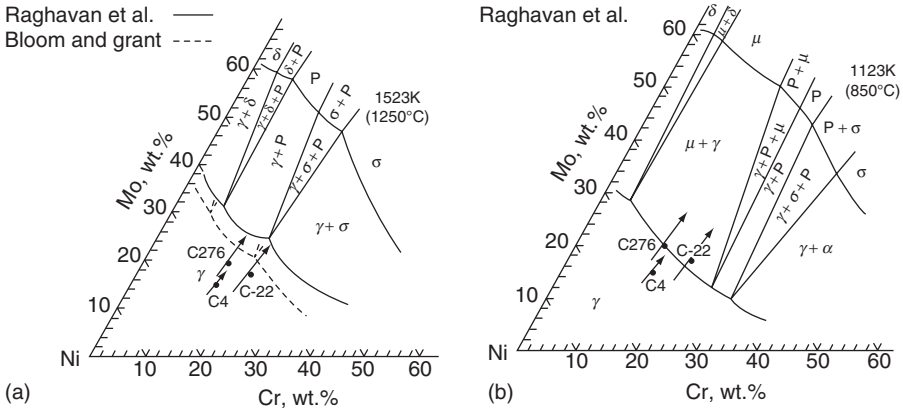


**Figure 3.11** Equivalent Ni-Cr-Mo compositions for Alloys C-4, C-22, and C-276 plotted on Ni-Cr-Mo isothermal sections at a) 1250°C and b) 850°C. (From Cieslak *et al.* [7].)

evolution was assessed with the aid of Ni-Cr-Mo isothermal projections and the use of an equivalent composition model given by:

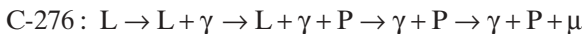
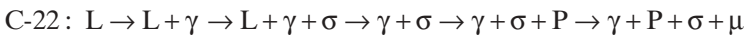
$$Mo_{eq} = wt\%Mo + wt\%W \tag{3.6a}$$

$$Ni_{eq} = wt\%Ni + wt\%Fe + \sum wt\%X_i \tag{3.6b}$$

$$Cr_{eq} = wt\%Cr \tag{3.6c}$$

where  $\sum X_i$  represents the sum of all other minor elements. This model was based on the observed similarity in partitioning behavior between the Mo and W and between Ni and Fe. Mo and W each partition to the TCP phases, while Ni and Fe were each observed to partition to the austenite. This equivalent composition model is shown on the Ni-Cr-Mo isothermal sections at 1250 and 850°C (2280 and 1560°F) in Figure 3.11.

Here, the dot associated with each arrow represents the equivalent nominal alloy composition. The start of the tail of the arrow represents the dendrite core equivalent composition, and the arrowhead represents the interdendritic equivalent composition (as measured by microprobe data). Thus, the arrow represents the variation in equivalent composition across the cellular/dendritic substructure. Based on this analysis, the following transformation sequences were proposed for fusion welds in Alloys C-22 and C-276.



For each alloy, the  $\mu$  phase forms as a product of a solid-state transformation associated with decomposition of the P phase. The major difference between

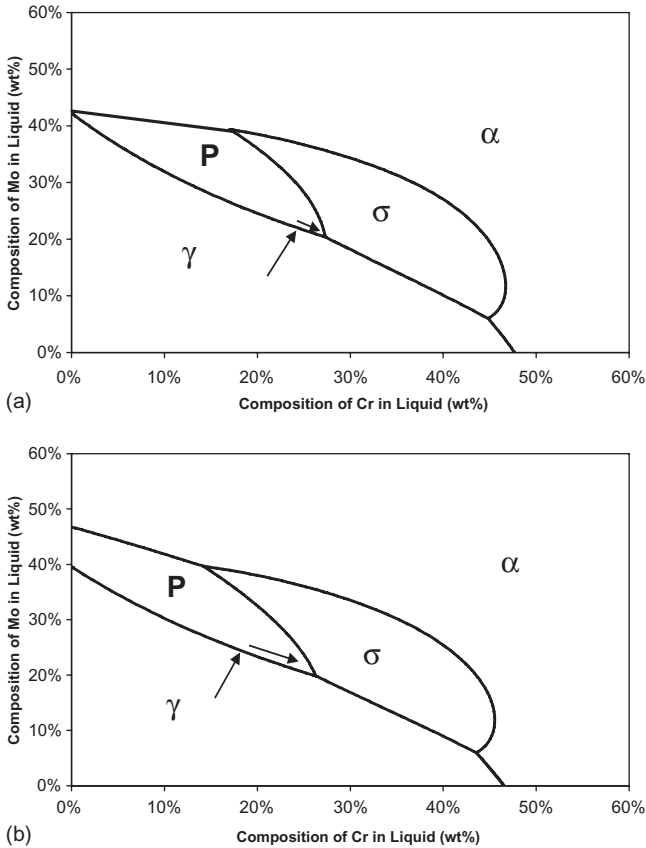


**Figure 3.12** Calculated liquidus projections and solidification paths for a) Alloy C-22 and b) Alloy C-276. (From Perricone and DuPont [16].)

the alloys lies within the solidification sequence, in which  $\sigma$  is expected as a terminal solidification product in C-22, while P is expected as a terminal solidification product in C-276. Formation of the P phase in Alloy C-22 was thought to occur by a solid-state transformation from the decomposition of  $\sigma$ . Results of the analysis for Alloy C-4 are also shown to demonstrate that this alloy will not form TCP phases because its range of equivalent composition does not enter into any of the TCP phase fields.

This data was recently analyzed in more detail using calculated multi-component liquidus projections and solidification modeling.(16) The results are shown in Figure 3.12. These multi-component liquidus projections provide a more accurate interpretation of the solidification behavior of these alloys because they account for phase stability at the solidification temperatures.

In addition, the influence of all alloying elements on position of the phase boundary lines is taken into account. The arrows in the diagrams represent the

solidification path as calculated using the ternary analog of the Scheil equation. Here, the start of the arrow represents the nominal alloy composition and the arrow represents the variation Cr and Mo concentration in the interdendritic liquid as solidification proceeds. These results show that the P phase is actually a product of solidification for both alloys. For C-22, both P and  $\sigma$  form during solidification, while only the P phase forms during solidification of Alloy C-276. This difference is caused by variations in Cr contents between the two alloys and its associated effect on the solidification path. Alloy C-22 is higher in Cr than C-276 (21 wt% vs. 16 wt%). As a result, the end of the primary L  $\rightarrow$   $\gamma$  solidification path for C-22 is located very close to the three phase  $\gamma$ -P- $\sigma$  ternary eutectic point. Thus, the liquid composition only has to “travel” a small distance after initial formation of P phase before the  $\sigma$  phase will form. The lower Cr content of Alloy C-276 causes the end of the primary L  $\rightarrow$   $\gamma$  solidification path to intersect the  $\gamma$ /P phase boundary farther away from the three phase  $\gamma$ -P- $\sigma$  ternary eutectic point. Thus, the remaining interdendritic liquid is consumed along this line by the L  $\rightarrow$   $\gamma$  + P reaction before the ternary type eutectic point is reached, avoiding formation of the  $\sigma$  phase. For each alloy,  $\mu$  forms in the solid state by decomposition of the P phase. The revised transformation sequence for these alloys is summarized in Table 3.8.

Iterative calculations of liquidus projections made with minor additions of Fe and W showed that Fe additions expand the  $\sigma$  phase field, while W additions expand the P phase field. The influence of Cr and Mo in phase stability can be assessed directly from the liquidus projections shown in Figure 3.12, where Cr additions stabilize  $\sigma$  and Mo additions stabilize P. Thus, Fe and Cr stabilize  $\sigma$  while W and Mo stabilize P. Note that these trends are also consistent with the phase compositions provided in Table 3.9, where  $\sigma$  is high in Fe and Cr and P is high in W and Mo. These observed trends are useful for future alloy development strategies where the alloy composition needs to be properly balanced for weldability and mechanical properties.

Microstructural evolution in fusion welds of Nb-bearing alloys, whether designed as solid-solution strengtheners or precipitation hardeners, has been shown to be very sensitive to the Nb and C contents and, to a lesser degree, the Si content.(4,6,11–13,30,31) Available results for Alloy 625 are summarized in Table 3.8 since this is a solid-solution alloy. Fusion zone microstructures in Nb-bearing precipitation hardened alloys will be discussed in Chapter 4. The results in Table 3.8 were obtained by systematic variations in Nb (~0 to ~3.6 wt%), Si (~0.03 to ~0.40), and C (~0.009 to ~0.036 wt%) to Alloy 625. The NbC and Laves constituents are the usual secondary phases observed in welds of Nb-bearing alloys. Each of these phases is high in Nb. In fact, removal of Nb from Alloy 625 results in single phase austenite solidification and complete elimination of the NbC and Laves phases.(4) As shown in Table 3.8, the Laves phase can be prevented when the Si content is low and the C content is high. Alloys high in Si and low in C can form an additional carbide ( $M_6C$ ) during solidification. These effects are described in more quantitative detail

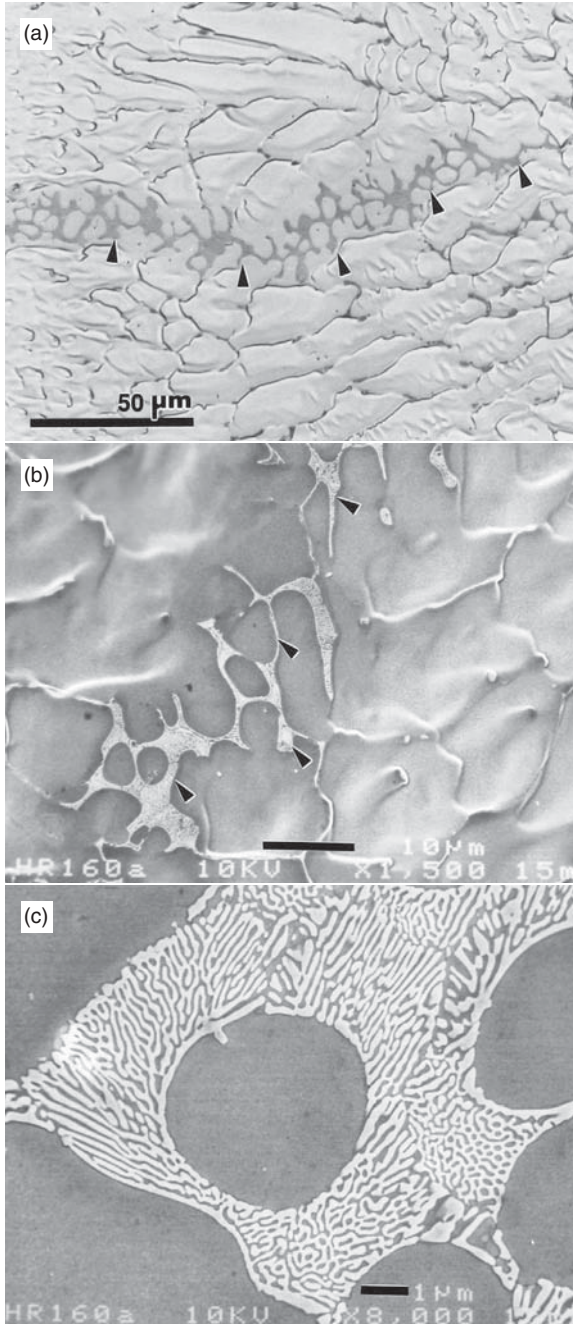
in Chapter 4 which discusses microstructure evolution of weld metals of Nb-containing precipitation hardened alloys.

Table 3.8 also contains the transformation sequences observed in two specialty Ni-base alloys. These provide interesting examples because they demonstrate how the solidification behavior of multi-component alloys can often be understood by reference to the appropriate Ni-X binary systems. Alloy HR-160 is a high temperature Ni-Co-Cr alloy with the addition of  $\approx 2.7$  wt% Si (nominal composition: 37Ni, 29Co, 28Cr, 2.75Si, 0.5Mn, 0.5Ti, 0.05C) that was designed for good corrosion resistance in gaseous sulfidizing atmospheres. Si, as with Cr and Al, promotes the formation of a protective oxide scale for corrosion protection. The seemingly small additions of Si and Ti ( $\sim 0.5$  wt%) have a strong influence on microstructure development in fusion welds of this alloy.(10) As shown by the data in Table 3.7, Ti and Si have rather low  $k$  values in this alloy and therefore each segregate strongly to the liquid during solidification. Thus, solidification of this alloy initiates by formation of primary austenite dendrites which reject Si and Ti to the liquid. As solidification proceeds, the austenite and liquid each gradually become enriched in these elements until the maximum solid solubility in austenite is reached. At this point, the remaining liquid transforms to austenite and the  $(\text{Ni},\text{Co})_{16}(\text{Ti},\text{Cr})_6\text{Si}_7$  phase forms by a eutectic-type reaction. The microstructure associated with this solidification sequence is shown in Figure 3.13.

Although the secondary phase within the eutectic-type constituent is rather complex, the microstructure morphology of Alloy HR-160 is similar to that expected in a simple eutectic system where single phase cored dendrites form prior to a two phase, interdendritic eutectic constituent. The similarities in solidification characteristics between the Ni-Si and Ni-Ti binary systems and Alloy HR-160 are summarized in Table 3.10. The Ni-Si and Ni-Ti systems each exhibit a terminal eutectic reaction consisting of  $L \rightarrow (\gamma + \text{Ni}_3\text{X})$ , where X is Ti or Si. In Alloy HR-160, both Si and Ti react with the solute-rich eutectic liquid to form a ternary-type compound— $(\text{Ni},\text{Co})_{16}(\text{Ti},\text{Cr})_6\text{Si}_7$ .

This phase is very similar to the G phase that forms in both the Ni-Ti-Si (32) and Co-Ti-Si systems.(33) In those ternary systems, the G phase has the stoichiometric composition of  $\text{A}_{16}\text{Ti}_6\text{Si}_7$ , where A = Ni or Co. Thus, in Alloy HR-160, Co and Ni behave similarly as do Cr and Ti to form the  $(\text{Ni},\text{Co})_{16}(\text{Ti},\text{Cr})_6\text{Si}_7$  phase. The temperature of the  $L \rightarrow (\gamma + \text{Ni}_3\text{Si})$  reaction (1143 °C) in the Ni-Si binary system is very similar to that observed in Alloy HR-160 (1162 °C).

Of course, in the simple Ni-Si system, the reaction occurs at a single temperature and composition. By contrast, the  $L \rightarrow [\gamma + (\text{Ni},\text{Co})_{16}(\text{Ti},\text{Cr})_6\text{Si}_7]$  reaction in the multi-component HR-160 alloy may occur over a range of temperature and composition. The combined (Ti + Si) “eutectic” composition of 12.4 wt% is intermediate to the Ni-Si (11 wt% Si) and Ni-Ti systems (14 wt% Ti). As described later in this chapter, Si and Ti additions to this alloy also have a strong effect on weldability.



**Figure 3.13** Solidification microstructure in the fusion zone of Alloy HR-160 showing dendritic substructure and interdendritic  $\gamma/(\text{Ni,Co})_{16}(\text{Ti,Cr})_6\text{Si}_7$  eutectic constituent. (From DuPont *et al.* [10].)

**TABLE 3.10 Comparison Among Eutectic Reaction Temperatures and Compositions, Maximum Solid Solubility, and Partition Coefficients for HR-160, Ni-Ti, and Ni-Si Systems.**

System	Eutectic Reaction	Eutectic Temperature, °C (°F)	Eutectic Composition, wt%	C <sub>Smax</sub> , wt%	k
Ni-Si	$L \rightarrow \gamma + \text{Ni}_3\text{Si}$	1143 (2090)	11 Si	8.2 Si	0.75
Ni-Ti	$L \rightarrow \gamma + \text{Ni}_3\text{Ti}$	1304 (2380)	14 Ti	11.6 Ti	0.83
HR-160	$L \rightarrow \gamma + (\text{Ni,Co})_{16}(\text{Ti,Cr})_6\text{Si}_7$	1162 (2125)	12.4 (Si+Ti)	7.8 (Si+Ti)	0.71 (Si) 0.44 (Ti)

The C-4 Gd alloy listed in Table 3.8 is an Alloy C-4 base alloy with Gd additions that are provided for neutron absorption purposes. This alloy was recently developed for applications involving transportation and storage of spent nuclear fuel.(19,34) Gd is added because it has the highest neutron cross section available among the elements, thus making this alloy ideal for safe handling of radioactive fuel. The solidification behavior and corresponding fusion zone microstructure of this alloy have many similarities to the simple Ni-Gd binary system. Recent microprobe measurements have shown that essentially no Gd is dissolved in the austenite matrix, indicating that the  $k_{\text{Gd}} \approx 0$ . Solidification begins with a primary  $L \rightarrow \gamma$  stage in which the liquid becomes enriched in Gd. This process continues until the Gd concentration in the liquid is enriched to the  $L \rightarrow \gamma + \text{Ni}_5\text{Gd}$  eutectic composition, at which point solidification terminates by the formation of the interdendritic  $\gamma/\text{GdNi}_5$  constituent. Additional similarities between this multi-component alloy and the Ni-Gd system have also recently been revealed.(19) For example, the amount of eutectic type constituent increases with increasing Gd content, the proportional amount of each phase within the eutectic is relatively insensitive to nominal Gd content, and the eutectic temperature is not strongly dependent on the nominal Gd concentration.

With these similarities in mind, detailed microstructural characterization and thermal analysis results have recently been combined to develop a binary  $\gamma$ -Gd solidification diagram to represent the solidification behavior of this system.(19) The term “solidification” diagram is used in preference to “phase” diagram since the information used to construct the diagram was acquired from thermal analysis solidification scans and characterization of as-solidified weld microstructures. As such, the diagram cannot be considered a phase diagram, but rather pertains mainly to understanding solidification behavior of fusion welds. The  $\gamma$ -Gd phase diagram is shown in Figure 3.14a, and the Ni-Gd phase diagram is provided in Figure 3.14b for comparison.(25) There are several similarities between these two diagrams. Each shows formation of the  $\text{Ni}_5\text{Gd}$  phase, exhibits a eutectic reaction at similar

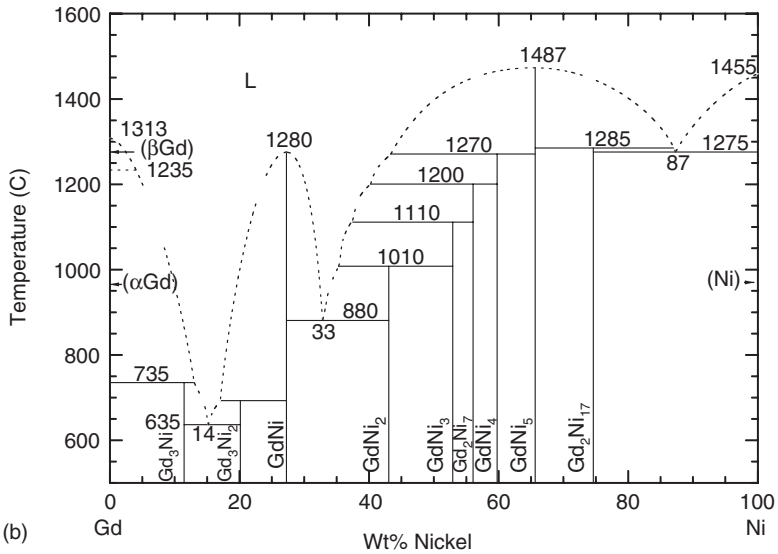
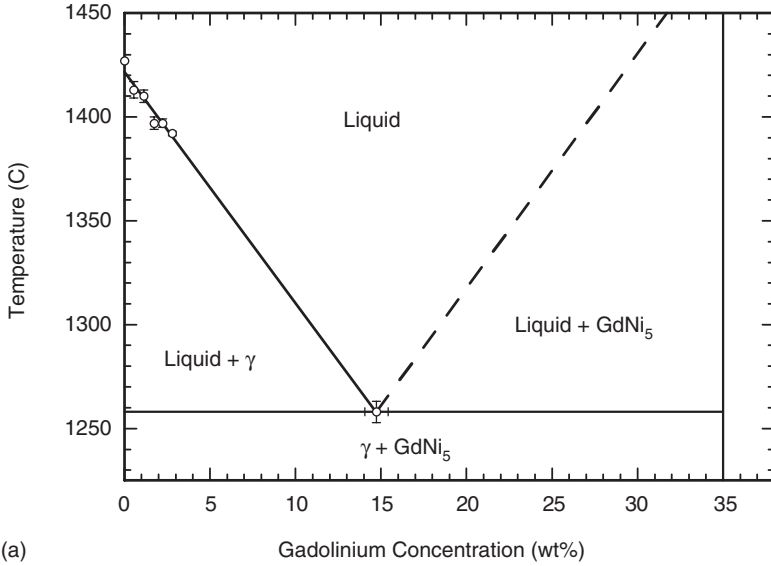


**Figure 3.14** Comparison of a) solidification diagram for C-4 Gd alloy and b) Ni-Gd binary phase diagram. (From Baker [25]. Courtesy ASM International.)

temperature and composition (1270 °C and 13wt% Gd in the Ni-Gd binary, 1258 °C and 14.7wt% Gd in the C-4 Gd alloy), and exhibits no solubility for Gd in austenite. The only major difference is formation of the Ni<sub>17</sub>Gd<sub>2</sub> phase that forms in the Ni-Gd binary, but not in the multi-component C-4 Gd alloy.

### 3.3.2 Heat Affected Zone

A number of metallurgical reactions occur in the HAZ of solid-solution strengthened Ni-base alloys that can influence the properties and weldability of these materials. These reactions include recrystallization, grain growth, particle dissolution, precipitate formation, grain boundary segregation, and grain boundary liquation. Since most alloys are supplied in the solution annealed condition, recrystallization does generally not occur. In materials that have been strengthened by cold work or that contain some residual “warm work” from forging, extrusion, or other hot working processes, recrystallization in the HAZ may be possible. Recrystallization may also occur in annealed materials that are cold formed prior to welding. If the amount of cold work exceeds approximately 10%, it may be necessary to re-anneal the material prior to welding.

When these alloys are in the solution annealed condition, fusion welding will generally result in some grain growth in the HAZ. The degree of grain growth is dependent on the starting base metal microstructure and the weld heat input. If the base metal grain size is small and weld heat input and amount of initial plastic deformation is high, substantial grain growth can be expected. If the initial base metal grain size is large and the amount of plastic deformation is low, grain growth may be minimal even under high weld heat input conditions. When the weld heat input is low and temperature gradients in the HAZ are steep, little grain growth in the HAZ is expected. Typical HAZ microstructures for two solid-solution strengthened alloys (Alloys 625 and 690) are shown in Figure 3.15. These can be compared to the corresponding base metal microstructures in Figure 3.1. Note that the Alloy 625 HAZ exhibits some grain growth, but essentially no other changes. The Alloy 690 base metal microstructure was heat treated to produce stable  $M_{23}C_6$  carbides along grain boundaries. These carbides dissolve in a narrow region along the fusion boundary in the Alloy 690 HAZ. This dissolution can potentially compromise the corrosion resistance of the HAZ, if re-precipitation of Cr-rich carbides leads to “sensitization” of the grain boundary.

Some alloys may also undergo grain boundary liquation in the region of the HAZ just adjacent to the fusion boundary. Such liquation is the result of impurity and/or solute segregation along the grain boundary, or due a phenomenon known as “constitutional liquation.” The segregation mechanism for grain boundary liquation in the HAZ of these alloys is shown schematically in Figure 3.16. The segregation of S, P, Pb and B has the most profound effect on grain boundary liquation, but in most Ni-base alloys these elements are controlled to very low levels. B is added to some alloys to improve creep properties and, thus, segregation of this element to the grain boundary may lead to liquation. Generally, the tendency for HAZ grain boundary liquation is greater with solution annealed materials which exhibit coarse grains and, thus, less grain boundary area. For this reason, high heat input welding processes are usually not recommended for solution annealed materials. The

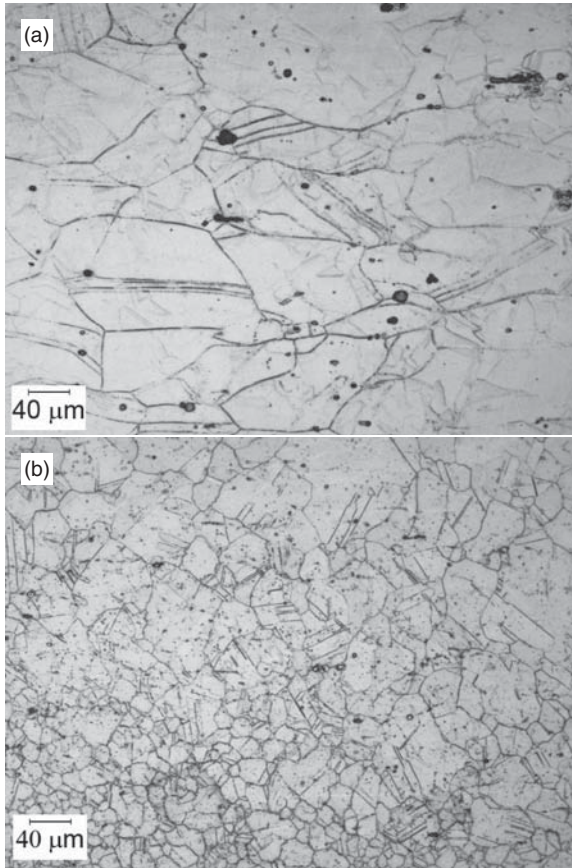


**Figure 3.15** HAZ microstructure in a) Alloy 625 and b) Alloy 690. See Figure 3.1 for base metal microstructure.

presence of both TiC and NbC in the base metal may lead to constitutional liquation at the interface between these particles and the austenitic matrix. This liquid can subsequently penetrate the grain boundaries. Both of these liquation mechanisms can promote cracking in the HAZ, as is discussed in more detail in Section 3.5.2.

### 3.3.3 Postweld Heat Treatment

Postweld heat treatment (PWHT) is conducted on weldments in solid-solution strengthened alloys for several reasons, including relief of residual stress, homogenization, dissolution of undesirable secondary phases that may have formed in the fusion zone or HAZ, dimensional stability, and improvement of corrosion properties. In some cases, recrystallization can occur during PWHT (35), but this is unusual. As described previously, alloys such as 625,

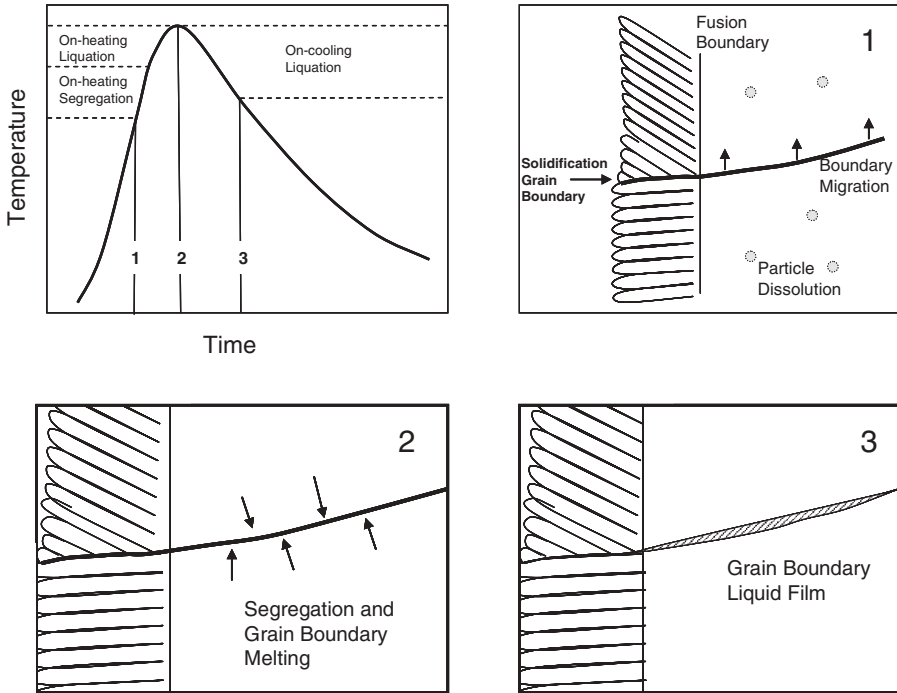


**Figure 3.16** Schematic showing HAZ solute segregation and localized melting along grain boundaries.

600, 690 and 825 employ a PWHT to form stable grain boundary carbides that improve resistance to stress corrosion cracking and prevent intergranular attack (IGA) in certain environments. IGA can be prevented by reversing grain boundary sensitization by allowing chromium to diffuse to the areas that were sensitized during welding.(36) The importance of this is discussed in Section 3.6, Corrosion Resistance.

**3.3.3.1 Stress Relief Heat Treatments** Significant residual stress can develop in welds in Ni-base alloys, particularly in thick-section, multipass welds. This may be undesirable since these alloys are often used at elevated temperatures where the relief of residual stress in service can lead to dimensional instability. High levels of residual stress can also accelerate the formation of undesirable phases when the structure is heated to elevated temperature.

Reduction of residual stress during PWHT occurs via a stress relaxation process.(37) This occurs when the yield strength of the material drops below the residual stress level, promoting local plastic deformation. As the material deforms plastically (relaxes) the residual stresses are reduced or eliminated. Subsequent reductions in the residual stress will occur during PWHT due to

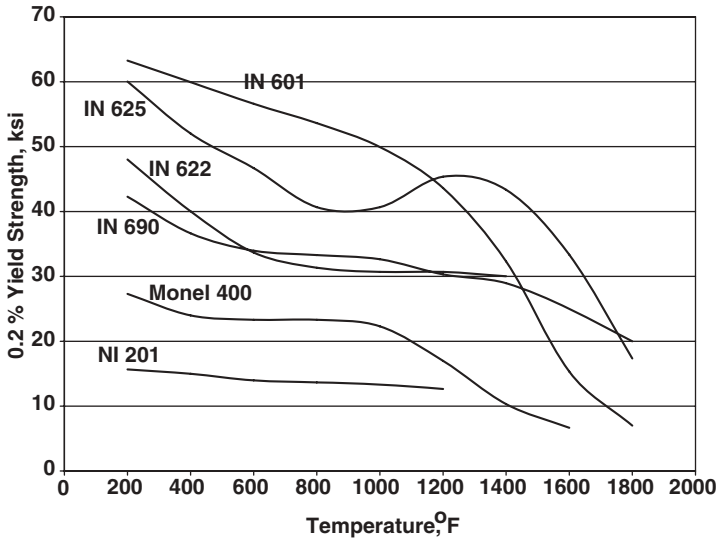


**Figure 3.17** Variation in yield strength with temperature for various solid solution strengthened alloys. (Courtesy Special Metals, Publication No. SMC-035.)

creep. Thus, the yield strength at the PWHT temperature sets an upper bound limit on the level of remaining residual stress and provides a useful initial estimate for identifying effective PWHT temperatures. Figure 3.17 shows the variation in yield strength with temperature for several commonly used solid-solution strengthened Ni-base alloys. These data demonstrate that higher PWHT temperatures are required for residual stress relief of the more highly alloyed materials that retain strength at higher temperatures.

Recommended stress relief heat treatments are provided for several base metals in Table 3.11. Generally, stress relief PWHT for nickel and nickel-copper alloys, such as Alloys 200 and 400, is conducted in the temperature range from 700-to-900 °C (1300-to-1650 °F). Note that the time at the stress relief temperature must be carefully controlled to avoid excessive grain growth in the base metal. For alloys such as 600, 625, and 690, stress relief in the 700–900 °C range can lead to the formation of  $M_{23}C_6$  carbides and there is the potential for delta phase formation in segregated regions of the weld. The potential for carbide precipitation and embrittlement by  $\delta$  phase formation can complicate the aim of stress-relief for these alloys. Stress relief should be carried out in the narrow temperature range of 955–980 °C (1750–1800 °F) with the time of exposure carefully controlled. In particular, exposure in this temperature range should be limited for alloys containing Nb (such as Alloy 625), since embrittlement due to  $\delta$ -phase formation can potentially reduce ductility and toughness (see Figure 3.22). For alloys 800, 800H and 800HT, a stress relief minimum of 900 °C (1650 °F) is used to coarsen  $M_{23}C_6$  carbides to prevent deleterious grain boundary carbide films from forming during service.

**TABLE 3.11 Recommended Stress Relief Temperatures for Several Solid-Solution Strengthened Ni-base Alloys.**

Alloy	UNS #	Heat Treatment	Comment
Alloy 200	N02200	1075 °F(580 °C)/3 hr 1300 °F(705 °C)/20 min 1600 °F(870 °C)/5 min	Control grain size to ASTM 3.5 max (0.1 mm max)
Alloy 400	N04400	1400 °F(760 °C)/20 min 1600 °F(870 °C)/8 min 1700 °F(925 °C)/5 min	Control grain size to ASTM 3.5 max (0.1 mm max)
Alloy 600	N06600	1650–1800 °F (900–980 °C) for 30–60 min	Provide dimensional stability
Alloy 625	N06625	1750–1800 °F (955–980 °C) for 30–60 min	Note careful temperature control to avoid embrittlement
Alloy 800	N08800	1650 °F(900 °C)/1hr	Per ASME Section VIII
Alloy 800H	N08810	+1 hr/in of thickness	Part 3 Paragraph 56.6e
Alloy 800HT	N08811		

It should be noted that the data in Figure 3.17 is for base metals, and that the temperature dependence of yield strength for the weld metal may be different due to the difference in microstructure. Although yield strength data for the fusion zone is often difficult to obtain, data for each location in the weldment should be used for developing PWHT temperatures whenever available. Some high temperature tensile properties for selected nickel-chromium weld metals are provided in Table 3.12.

Diehl and Messler have shown that the stress relaxation technique is a useful method for identifying PWHT temperatures required for effective stress relief.(38) With this procedure (described in ASTM Test Procedure E328), an initial load is applied to a sample at a fixed temperature to produce a given strain level. The initial strain is typically set so that the applied stress is equal to the yield strength at the temperature of interest. The decrease in load and resultant stress that occur are then monitored as a function of time. The stress typically is reduced very quickly at the early stages by plastic flow, and additional reductions occur at later times due to creep. This procedure is useful because it permits direct estimation of the remaining residual stress expected for a given PWHT temperature and time.

Figure 3.18 shows stress relaxation results for Alloy 625.(38) Figure 3.18a shows the yield strength as a function of temperature for the base metal and weld metal, and Figure 3.18b and 3.18c show stress relaxation results for the base metal and weld metal, respectively. The starting weld metal strength is higher than that of the base metal, probably due to the refined solidification structure and the presence of second phases that form during solidification and subsequent precipitation in the solute rich interdendritic regions of the fusion zone. The increased yield strength of the weld results in higher levels

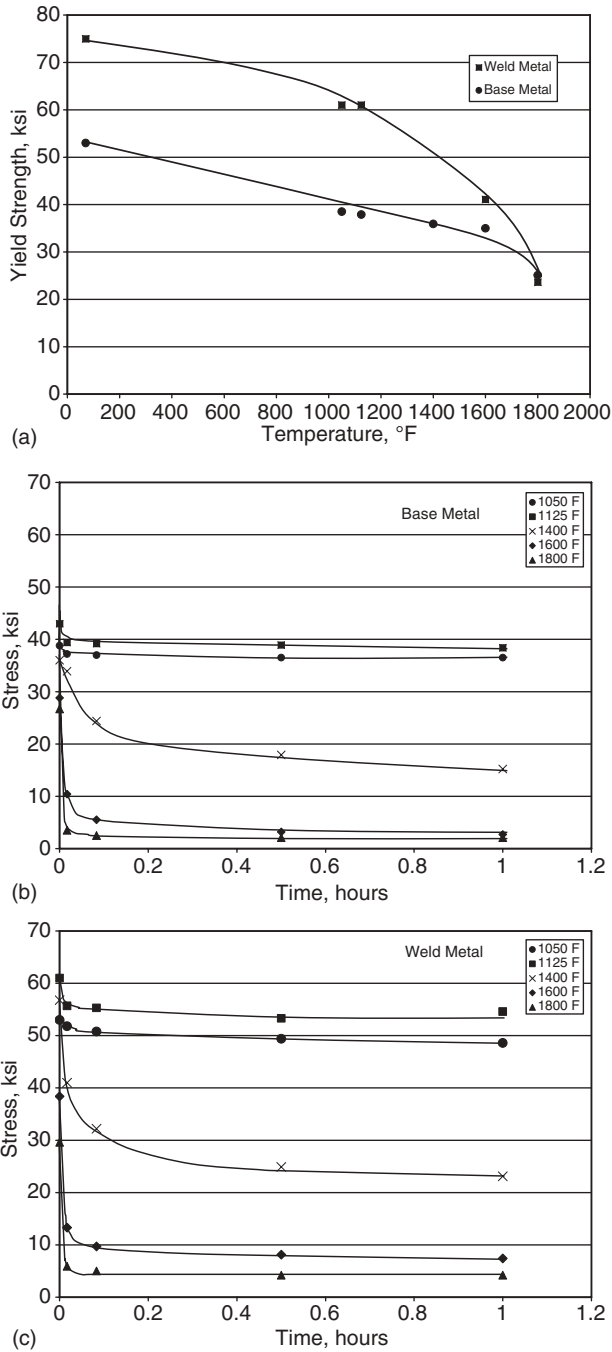


**Figure 3.18** Stress relaxation results for Alloy 625. a) yield strength as a function of temperature for the base metal and weld metal, b) stress relaxation results for the base metal, c) stress relaxation results for the weld metal. (From Diehl and Messler [38]. Courtesy American Welding Society.)

of residual stress in the surrounding HAZ as compared to the base metal. These results also show the additional level of stress reduction that occurs due to creep at the higher PWHT temperatures. For example, note that the level of residual stress is similar to the yield strength at the lower temperatures of 565 and 605 °C (1050 and 1125 °F). However, the residual stress level is significantly reduced below the yield strength at the higher temperatures due to creep that occurs after initial plastic deformation. Comparison of these data to the more sophisticated hole drilling technique that uses strain gages showed that the stress relaxation technique provided comparable results. These results highlight the importance of stress relaxation results for determining effective PWHT times and temperatures.

It should be noted that the stress relief of Alloys 800, 800H, and 800HT in thick sections can lead to stress relief cracking during postweld heat treatment. If postweld stress relief is not applied, the weldment may be susceptible to “relaxation cracking” during elevated temperature service exposure. Thus, heavy section weldments must be stress relieved according to the recommendations in Table 3.11 in order to avoid the potential for service failure.

**3.3.3.2 Homogenization of Weld Metal Microstructure** PWHT is often required to eliminate fusion zone concentration gradients in order to restore corrosion resistance in welds of solid-solution strengthened alloys. The PWHT times and temperatures required for effective homogenization can be estimated with available diffusion equations. By assuming that the as-solidified microsegregation pattern exhibits a sinusoidal type variation across the dendritic substructure, Kattamis and Flemings developed an expression for castings that describes how the concentration changes with time ( $t$ ) and position ( $x$ ) during homogenization.(39) Their expression is given by:

$$C_{(x,t)} = \bar{C} + (C_{\max} - \bar{C}) \sin\left(\frac{\pi x}{l}\right) \exp\left[-\frac{4\pi^2 Dt}{\lambda^2}\right] \quad (3.7)$$

Where  $C_{(x,t)}$  is the concentration of the element of interest at any position and time,  $\bar{C}$  is the mean concentration within the gradient,  $l$  is half the dendrite spacing (i.e., length of concentration gradient),  $C_{\max}$  is the maximum initial concentration that exists in the interdendritic region,  $D$  is the diffusivity of the element of interest, and  $\lambda$  is the dendrite spacing. For most conditions,  $C_{\max}$  can be taken as the maximum solid solubility. It is useful to define an index of residual segregation ( $\delta$ ) as:

$$\delta = \frac{C_M - C_m}{C_M^0 - C_m^0} \quad (3.8)$$

Where  $C_M^0$  and  $C_m^0$  are initial maximum and minimum concentrations that exist at the interdendritic region and dendrite core, respectively.  $C_M$  and  $C_m$  are the concentrations at those same locations after some time at the PWHT

temperature. The value of  $\delta$  is initially unity before homogenization begins and tends towards zero as the concentration gradient is relaxed and homogenization nears completion. Thus, the value of  $\delta$  provides a convenient parameter for following the extent of homogenization for a particular PWHT time and temperature. The values of  $C_M$  and  $C_m$  can be determined as a function of time and temperature through Equation 3.7. Inserting the appropriate values of position ( $x$ ) for the interdendritic region for  $C_M$  (where  $x = 3l/2$ ) and dendrite core for  $C_m$  ( $x = l/2$ ) into Equation 3.7 and combining with Equation 3.8 leads to the following expression for the index of residual segregation.

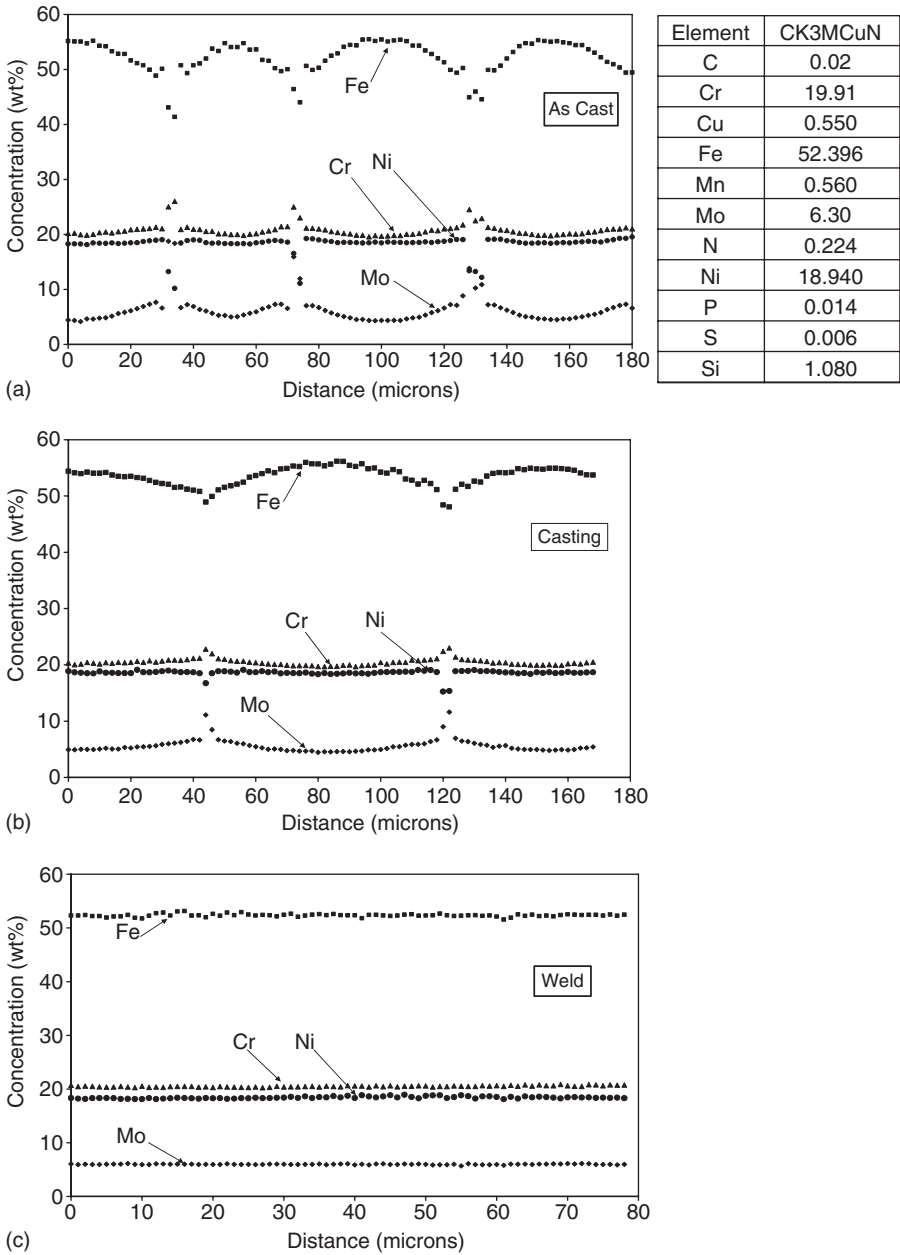
$$\delta = \exp\left[-\frac{4\pi^2 Dt}{\lambda^2}\right] \quad (3.9)$$

Although more detailed models are available (39), Equation 3.9 is useful for making estimates of the PWHT times and temperatures required for effective homogenization.

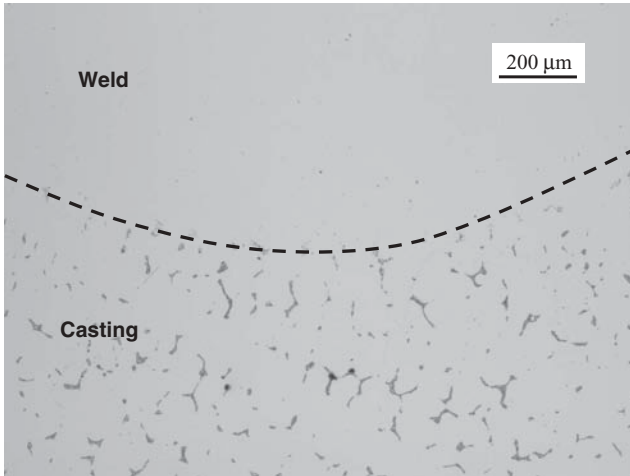
Figures 3.19 and 3.20 show examples of heat treatments conducted on castings and welds of Alloy CK3MCuN.(40) The composition of this alloy is 52Fe-19Ni-20Cr-6.3Mo-1.1Si-0.55Cu-0.56Mn-0.22N-0.02C. Although this alloy is actually a super-austenitic stainless steel, it exhibits a microstructure that is essentially identical to that of the Mo bearing, Ni-base alloys, exhibiting substantial as-solidified concentration gradients and interdendritic  $\sigma$  phase. Heat treatments at various times and temperatures were explored to identify procedures that could eliminate the concentration gradients and restore corrosion resistance. The concentration gradients that exist in the as-cast condition are shown in Figure 3.19a. The weld showed the identical extent of segregation in terms of minimum and maximum concentrations, the only difference being the smaller primary dendrite arm spacing (PDAS) due to the higher cooling rates. The cast alloy had a PDAS of  $\sim 60\mu\text{m}$ , whereas the weld was  $\sim 10\mu\text{m}$  due to the higher solidification rates. Figures 3.19b and 3.19c show the extent of residual segregation that persists after heat treating at  $1150^\circ\text{C}$  ( $2100^\circ\text{F}$ ) for one hour in the casting and weld, respectively. The concentration gradients in the casting are only moderately reduced, while those in the weld under the same heat treatment conditions are essentially eliminated due to the finer solidification structure (shorter diffusion distances).

Figure 3.20 shows the difference in the weld and cast base metal microstructure after the same heat treatment. Note that the secondary phase is completely dissolved in the weld. The second phase content in the cast base metal was not reduced significantly from the as-cast condition.

Figure 3.21 shows the calculated variation in the index of residual segregation for Mo as a function of time for temperatures of  $1150$  and  $1205^\circ\text{C}$  ( $2100$  to  $2200^\circ\text{F}$ ). The diffusivity of Mo was used in these calculations because this represents the slowest diffusing element in the alloy. Results for primary dendrite arm spacing (PDAS) of  $60\mu\text{m}$  and  $10\mu\text{m}$  are shown. The calculations for  $\delta$  were found to be in reasonable agreement with the experimental



**Figure 3.19** Concentration gradients in Alloy CK3MCuN. a) As-cast condition, b) As-cast + 1150°C/1 hr, c) As-welded + 1150°C/1 hr. (From DuPont [40].)



**Figure 3.20** Photomicrograph of weld on Alloy CK3MCuN casting after 1150°C/1 hr. (From DuPont [40].)

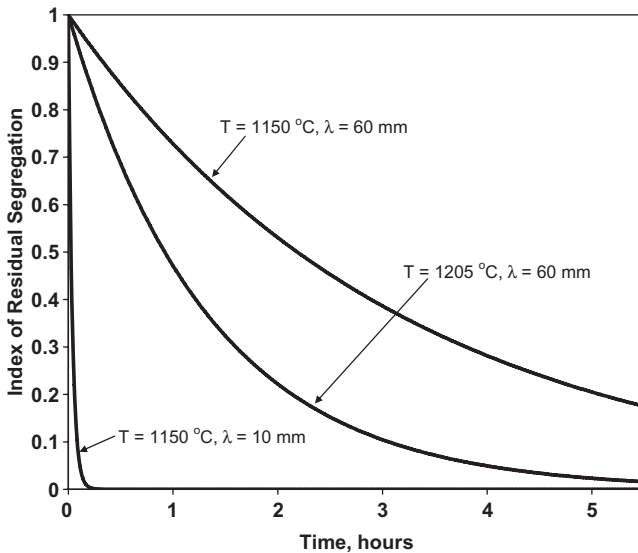


**Figure 3.21** Calculated values of the index of residual segregation for Alloy CK3MCuN as a function of PWHT time and temperature. (From DuPont [40].)

observations in which a 1250°C/4 hour heat treatment was found to be required for nearly complete homogenization in the casting (with  $\lambda = 60\mu\text{m}$ ), while the weld was fully homogenized at 1150°C/1 hour (for  $\lambda = 10\mu\text{m}$ ). These results show that, in applications where welds are made on a wrought material, lower heat inputs are beneficial for reducing the PDAS and associated PWHT times. More information that describes the effect of PWHT on mechanical properties in welds of solid solution alloys can be found in the next section.

### 3.4 MECHANICAL PROPERTIES OF WELDMENTS

In general, the solid-solution strengthened alloys can retain near base metal properties in the as-welded condition. Unlike the precipitation-strengthened alloys (see Chapter 4) that must be heat treated following welding to develop strength, the solid-solution strengthened alloys can be put into service following welding without significant degradation in mechanical properties. Segregation during solidification may reduce the solid-solution strengthening effect in the fusion zone, but this may be compensated by the formation of second phases that form interdendritically to provide second phase strengthening. The mechanical properties of the HAZ do not usually deviate significantly from those of the base metal, since grain growth is the only metallurgical phenomenon that influences properties in this region. In alloys that are additionally strengthened by cold work, recrystallization and grain growth in the HAZ can lead to local softening. This is unusual, however, since most of the solid-solution strengthened alloys are welded in the solution annealed condition. As a result, little degradation in the strength and ductility of these alloys is expected due to welding.

Reference to Tables 3.1 through 3.6 shows the difference in chemical composition between weld metals and base metals. Most of the weld metals for solid-solution strengthened Ni-base alloys contain additions of Al, Ti, Mn, Nb, and sometimes Mo and other deoxidizers and malleabilizers. All of these elements can act as strengthening agents and, as a result, most of the solid-solution-strengthened Ni-base welding products provide strength above that of the nominally matching base metals. A notable exception to this is Alloy 625. The base metal exhibits a minimum tensile strength of 120 ksi (830 MPa), while the weld metals for this alloy (the ERNiCrMo-3 types) often only provide about 90% of that strength level. In these cases, the weld metal strength rather than the base metal strength must be used for design purposes.

The typical weld metal mechanical properties of consumables used to join the solid-solution strengthened alloys are provided in Table 3.12. Table 3.12A lists the room temperature mechanical properties of a wide range of consumables. Weld metal strength is generally comparable to the wrought alloy strength listed in Table 3.5. Table 3.12B lists the short term elevated temperature strength and ductility of ERNiCrFe-2 (INCO A) and ERNiCr-3 (FM 82) weld metal. Note that these filler metals retain reasonably good strength at temperatures up to 650 °C (1200 °F).

#### 3.4.1 Hydrogen Effects

It has been observed that a loss in weld metal ductility may occur when welding is conducted with shielding gases containing > 1% hydrogen (41) or when welding with flux-based welding processes when the flux has absorbed moisture. Argon-hydrogen mixtures are often used for the gas-tungsten arc welding of Ni-base alloys for improving the wetting and flow characteristics

**TABLE 3.12 Mechanical Properties of Weld Metals, a) Typical Weld Metal Properties in the As-Welded Condition, b) Typical Short Time Elevated Temperature Tensile Data for All Weld Metal Specimens.**

a)

AWS Classif.	Type	Tensile Strength, ksi (MPa)	Yield Strength, ksi (MPa)	Elongation %	RA %	Hardness, Rockwell B
ERNi-1	FM 61	55 (380)	30 (209)	25	30	75
ERNiCu-7	FM 60	75 (517)	40 (276)	40	50	80
ERNiCr-3	FM 82	85 (586)	45 (310)	35	40	85
ERNiCr-4	FM 72	100 (690)	60 (414)	35	40	90
ERNiCrFe-7	FM 52	90 (620)	45 (310)	35	40	85
ERNiCrFe-7A	FM 52M	90 (620)	45 (310)	35	40	85
ERNiFeCr-1	FM 65	85 (586)	40 (276)	30	35	80
ERNiMo-3	FM W	100 (690)	60 (414)	30	35	90
ERNiMo-7	FM B2	110 (760)	65 (450)	30	35	90
ERNiCrMo-1	Hast G	85 (586)	45 (310)	30	35	85
ERNiCrMo-3	FM 625	110 (760)	65 (450)	35	40	95
ERNiCrMo-4	C-276	100 (690)	60 (414)	35	40	95
ERNiCrMo-10	C-22	110 (760)	60 (414)	40	40	95
ERNiCrMo-13	FM 59	110 (760)	60 (414)	40	40	95
ERNiCrMo-14	FM 686	110 (760)	60 (414)	40	45	90
ERNiCrMo-17	C-2000	100 (690)	60 (414)	35	40	90
ERNiCrCoMo-1	FM 617	110 (760)	65 (450)	35	35	95
ERNiCrWMo-1	230-W	110 (760)	65 (450)	35	35	95

b)

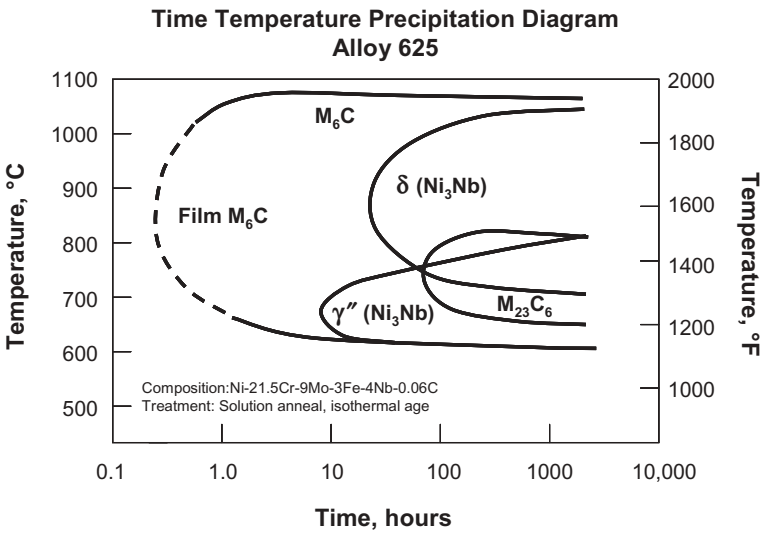
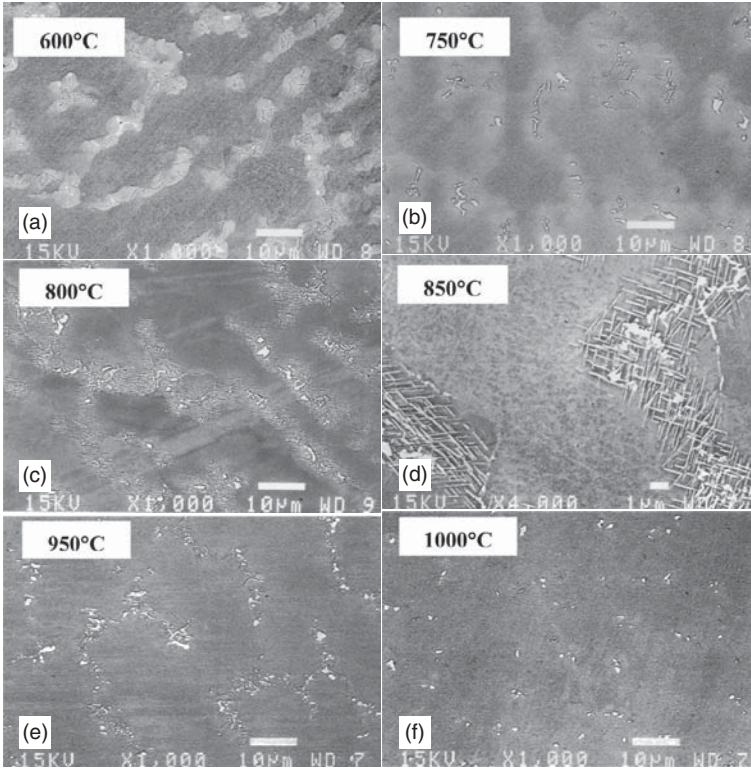
	Temperature °C (°F)	Tensile Strength ksi (MPa)	Yield Strength ksi (MPa)	Elongation %
Inco Weld A	27 (80)	95 (655)	57 (395)	39
ENiCrFe-2	150 (300)	87 (600)	50 (345)	41
	315 (600)	81 (560)	44 (305)	42
	425 (800)	79 (545)	43 (295)	42
	540 (1000)	76 (525)	42 (290)	41
	650 (1200)	66 (455)	40 (275)	30
	760 (1400)	50 (345)	35 (240)	22
	870 (1600)	30 (205)	29 (200)	36
FM 82	27 (80)	99 (680)	54.1 (375)	46
ERNiCr-3	150 (300)	91 (630)	50 (345)	45
	315 (600)	85 (585)	45.5 (315)	44
	425 (800)	84.3 (580)	47.5 (330)	50
	540 (1000)	85 (585)	45.5 (315)	44
	650 (1200)	67.5 (465)	42.7 (295)	31
	760 (1400)	51.2 (355)	39.2 (270)	29
	870 (1600)	26.9 (185)	24.3 (170)	34
	980 (1800)	14.8 (100)	11.9 (80)	22

of the weld metal. This loss in ductility is associated with the pick up of hydrogen in the weld metal which results in hydrogen embrittlement. The study by Young *et al.* shows that hydrogen levels as low as 5 ppm were sufficient to reduce the strength and ductility of Filler Metal 82 multipass weld deposits.(41) As hydrogen levels in the weld deposit increased from 3 ppm-to-12 ppm, ultimate tensile strength dropped from 110-to-90 ksi (620 MPa) and ductility (reduction in area) from 50-to-20%. Changing shielding gas to 100% He or Ar-He mixtures restored the mechanical properties of the Filler Metal 82 deposits.

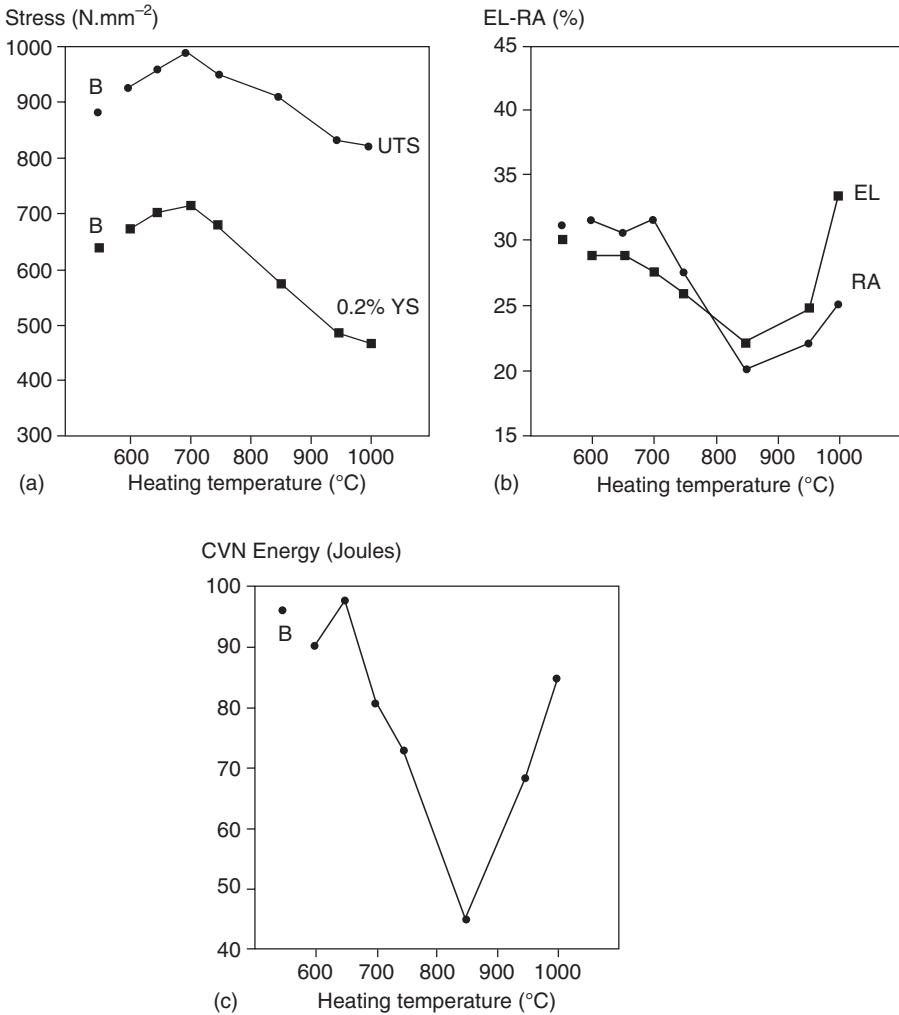
### 3.4.2 Postweld Heat Treatment

Although the mechanical properties of solid-solution strengthened Ni-base alloys are often sufficient in the as-welded condition, PWHT is sometimes recommended to relieve residual stresses, reduce hydrogen content, or homogenize the microstructure. Cortial *et al.* investigated the influence of postweld heat treatment on the mechanical properties of Alloy 625 welds.(42) This alloy derives its strength from solid-solution hardening from Mo and Nb. However, the presence of Nb can also lead to precipitation of various phases during both heat treatment and high temperature exposure. Heat treatment temperatures typical of those used in industrial practice were evaluated and consisted of an eight hour hold at temperatures from 600-to-1000°C (1110-to-1830°F).

Figure 3.22 shows the Alloy 625 weld metal microstructures after these heat treatments and the time-temperature precipitation behavior for this alloy in the solution annealed condition. No major microstructural change was observed between 600° and 700°C (1110° and 1290°F). At temperatures above 700°C, transmission electron microscopy (TEM) showed that  $\gamma''$  (Ni<sub>3</sub>Nb) forms in the interdendritic regions. Preferential formation of  $\gamma''$  in the interdendritic regions can be attributed to microsegregation of Nb during weld solidification. The  $\gamma''$  will only form during heat treatment where the solid solubility of Nb is exceeded at the particular heat treatment temperature. The reduced Nb concentration in the cell cores place this region within the single phase field, while the solubility limit is exceeded in the interdendritic regions where the Nb content is higher. In the range from 850-to-950°C (1560-to-1740°F), the  $\gamma''$  phase dissolves and the orthorhombic intermetallic  $\delta$  phase forms. This phase is also of the stoichiometry Ni<sub>3</sub>Nb and exhibits the needle type morphology shown in Figures 3.22c and 3.22d. As mentioned earlier, this phase is generally undesirable due to its adverse effect on mechanical properties. Above 850°C, M<sub>6</sub>C carbides form on the grain boundaries. At 1000°C (1830°F), the  $\delta$  phase dissolves and the amount of M<sub>6</sub>C grain boundary carbide increases slightly. It was also observed that the extent of microsegregation is not significantly altered from the as-welded condition for heat treatment temperatures up to 850°C, but decreased appreciably at 950°C and above. At 1000°C, the welds were essentially fully homogenized.



**Figure 3.22** Weld metal microstructures of Alloy 625 after heat treatment at the indicated temperatures for eight hours and a time-temperature-precipitation diagram for this alloy. (From Cortial *et al.* [42].)



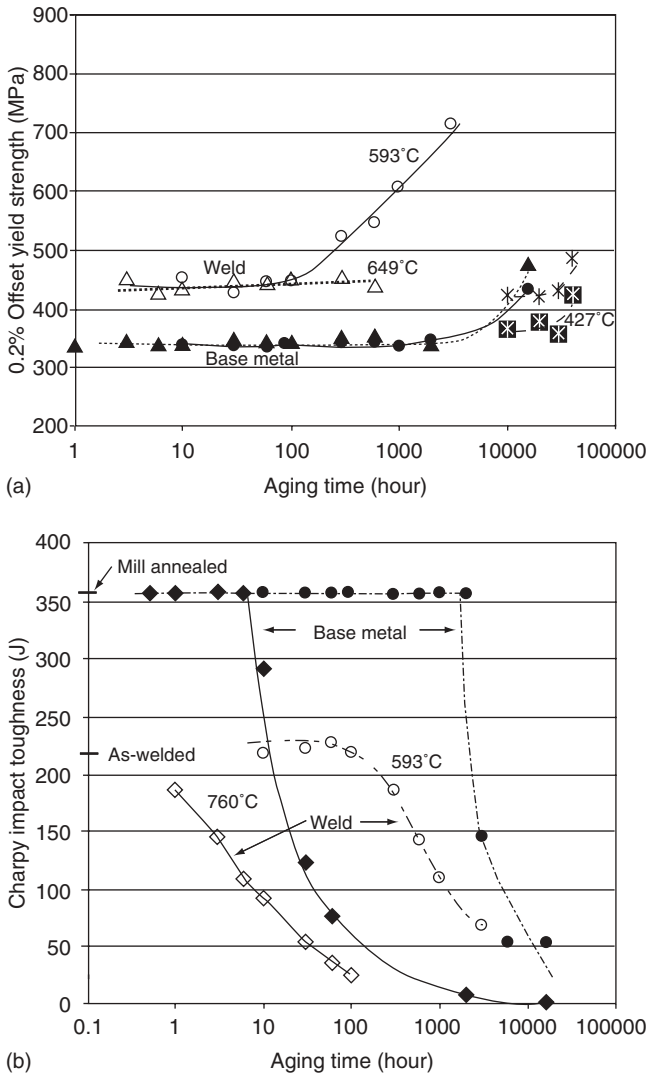
**Figure 3.23** Variation in room temperature mechanical properties of Alloy 625 welds as a function of heat treatment for 8 hours, a) strength, b) ductility, and c) impact energy. The “B” data points indicate the property in the as-welded condition. (From Cortial *et al.* [42].)

Figure 3.23 shows the variation in room temperature strength, ductility, and impact toughness of Alloy 625 welds as a function of heat treatment temperature for eight hours. The data point labeled “B” indicates properties in the as-welded condition. A strength peak at 700°C is associated with formation of  $\gamma'$ . The loss in strength and ductility, and sharp drop in toughness in the 750–950°C range is associated with formation of the brittle  $\delta$  intermetallic phase. At 1000°C, the ductility is restored due to dissolution of  $\delta$  phase, but

the strength decreases due to grain growth. Grain growth occurs at this temperature because the  $\delta$  phase dissolves and can therefore no longer pin the grain boundaries during the heat treatment exposure. Similar effects have been observed for the base metal of Alloy 625 (43), where mechanical properties are adversely affected in the range from 600 to 800°C (1110 to 1470°F) due to formation of  $\delta$  phase. Thus, from a mechanical property standpoint, there is little benefit to heat treating welds of Alloy 625, since the as-welded properties are generally better than those in the heat treated condition and detrimental effects would be expected for both the base metal and weld. However, as discussed in Section 3.6, heat treatment can be used to provide improved corrosion resistance in some environments and is often needed to reduce residual stresses. In these cases, the heat treatment should be carefully controlled to prevent embrittlement. For heat treating weld metals containing Nb (such as Alloy 625), the temperature range from 750 to 950°C (1355 to 1740°F) should be avoided to avoid losses in ductility and toughness.

Edgecumbe-Summers *et al.* evaluated the mechanical properties of gas tungsten arc (GTA) welds in Alloy C-22.(44) The welds were observed to be approximately 25% stronger than the base metal, but 30–40% less ductile. This difference was attributed to the presence of TCP phases in the weld. Although the hard TCP phases provide a slight increase in strength, they also serve as nucleation sites for microvoids during plastic deformation, thus initiating failure earlier during straining compared to the wrought base metal that contains little or no TCP phases. The influence of aging at temperatures from 425-to-760°C (800-to-1400°F) for up to 40,000 hours was also investigated.

Figure 3.24 shows the variation in base metal and weld metal yield strength and Charpy impact energy with aging time for various temperatures. The yield strength was measured on cross-welded (transverse) specimens. In Alloy C-22, an ordered  $\text{Ni}_2(\text{Cr},\text{Mo})$  phase forms below approximately 600°C (1110°F) and promotes strengthening. There is some evidence of this ordering and associated strengthening at the very long times at the temperature of 427°C (800°F). The base metal does not show any strengthening at 593°C (1100°F) for the times investigated, but the weld metal exhibits significant strengthening at the same temperature. Although the reasons for this were not investigated in this work, it is likely that the segregation present in the weld accelerates the ordering kinetics of the  $\text{Ni}_2(\text{Cr},\text{Mo})$  phase. The loss in base metal toughness occurs due to formation of TCP phases along the grain boundaries. The accelerated loss in toughness of the welds is attributed to enhanced TCP formation. The need for nucleation of TCP phases in the welds is avoided since these phases already exist in the interdendritic regions after solidification and, thus, the growth of the TCP phases is accelerated relative to the base metal, where nucleation requires thousands of hours. The growth rate of the TCP phases is also probably enhanced in the interdendritic regions of the welds due to the higher Mo concentration in these regions resulting from solidification segregation.



**Figure 3.24** Variation in the mechanical properties of Alloy C-22 base metal and weld metal as a function of aging time and temperature, a) yield strength and b) Charpy impact toughness. (From Edgecumbe *et al.* [44].)

The relatively low weld metal mechanical properties of Alloy C-22 can be restored with the use of proper solution heat treatments. El-Dasher *et al.* evaluated TCP phase dissolution and recrystallization in multipass welds in Alloy C-22. (35) Solution times of 20 minutes, 24 hours, 72 hours, and 168 hours were investigated at temperatures of 1075°, 1121°, 1200°, and 1300°C (1970°, 2050°, 2190°, and 2370°F). Complete TCP dissolution was observed at 1075° and 1121°C for 24 hours and at 1200° and 1300°C for 20 minutes. Full recryst-

tallization (>95%) was also observed in the fusion zone at the following temperature-time combinations: 1075°C/168 hours, 1121°C/24 hours, and 1200°C and 1300°C after 20 minutes. Grain growth also occurred in the 1300°C sample. Recrystallization was observed to occur first near the weld root and was attributed to this being the region of highest plastic strain due to residual stresses.

The fracture toughness and tensile properties of Alloys 600 and 690 and their respective filler metals (Filler Metals 82 and 52) have been evaluated by Brown and Mills.(45) These alloys are used extensively in nuclear reactor applications. Alloy 600 was used initially, but was found to be susceptible to stress corrosion cracking in high temperature deaerated water. These failures have been found to be associated with low hot working and annealing temperatures that result in relatively high yield strengths and limited grain boundary carbides.(46) Higher temperature annealing produces microstructures with grain boundary carbides and increased resistance to SCC.(47) Alloy 690 has higher Cr content and improved SCC resistance that is less dependent on the heat treatment conditions.

Tensile properties were measured on all-weld-metal samples along the welding direction, while fracture toughness ( $J_{IC}$ ) tests were conducted both longitudinally and transverse to the welding direction. Tests were conducted at 54° and 338°C (130° and 640°F) in air and water with an elevated hydrogen content. The tensile properties of the base metals and welds were generally not affected by the test conditions. The welds exhibited slightly higher yield strengths, 345–490 MPa (50–71 ksi), compared to the base metals, 275–407 MPa (40–59 ksi), and the elongations of the welds and base metals were similar (27–60%). The only environmental effect observed on the tensile properties was a slight reduction in the tensile elongation of the Filler Metal 82 welds, which was reduced to 10–27% when tested in 54°C water.

Figure 3.25 summarizes the fracture toughness results for the base metals and welds. There are significant differences between the base metal and weld metal toughness values as well as differences due to test condition. The test orientation also has an effect on the fracture toughness of the welds. In the absence of environmental effects that occur in water at 54°C, the welds generally exhibit higher  $J_{IC}$  values than the base metals. The slightly lower  $J_{IC}$  values of the base metals were attributed to the presence of large primary MC type carbides that fracture under the influence of stress, effectively causing premature void nucleation. By comparison, the finer carbides present in the weld metals resisted premature void nucleation caused by particle fracture. In the welds, nucleation of finer voids required particle/matrix decohesion. The base metal and weld metal fracture toughness values are each considered very high when environmental factors are not significant. The significant reduction in fracture toughness observed in water at 54°C for the base metals and welds was accompanied by a change in fracture mechanism from ductile microvoid coalescence to brittle intergranular fracture, and this ductile-to-brittle transition was attributed to a hydrogen induced cracking mechanism.

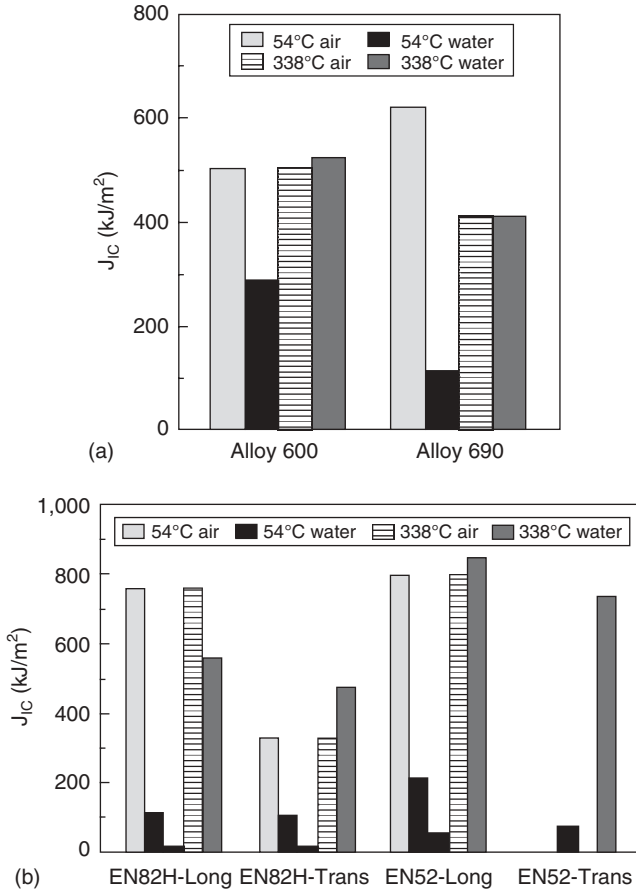


**Figure 3.25** J<sub>IC</sub> fracture toughness behavior at 54°C (130°F) and 338°C (640°F) in air and water for a) Alloy 600 and 690 base metals and b) 52 and 82H weld metals. (From Brown and Mills [45].)

This effect was very pronounced in the welds and Alloy 690 base metal. The Alloy 600 base metal was somewhat less susceptible to hydrogen induced cracking. The Filler Metal 82 weld exhibited an effect of orientation, where toughness values associated with crack propagation longitudinally oriented to the weld were higher than those orientated transverse to the weld. This difference was attributed to the anisotropic nature of the columnar grains and interdendritic secondary phases (Nb-rich MC carbides) in the weld metal. In the transverse direction, the crack propagated along the columnar grain boundaries and interdendritic phases, which reduced toughness. The limited data available for the Filler Metal 52 weld metal indicated that the orientation effect was not as severe. This was attributed to the crack tip location differences for each weld metal. For the Filler Metal 82 welds, the crack tip was

placed at the weld root where extensive alignment between the crack propagation direction and columnar grain boundaries/interdendritic phases occurred. The crack tip for the Filler Metal 52 weld was placed near the mid-section of the weld where the grain morphology and interdendritic phase distribution was slightly more isotropic.

### 3.5 WELDABILITY

In this section, the weldability of solid-solution strengthened Ni-base alloys is discussed. The term weldability is used here to describe susceptibility to cracking during fabrication. As reviewed in Section 3.3, these alloys solidify as austenite (Ni-rich fcc phase) resulting in strong segregation of alloying and impurity elements. Such segregation influences susceptibility to weld solidification cracking and may promote embrittlement during PWHT. These alloys are also susceptible to HAZ and weld metal liquation cracking, again resulting from segregation to grain boundaries in the HAZ and residual solidification segregation in reheated weld metal. Finally, these alloys have been shown to be susceptible to an intergranular, high-temperature embrittlement phenomenon known as ductility-dip cracking (DDC).

#### 3.5.1 Fusion Zone Solidification Cracking

Weld solidification cracking in the fusion zone of Ni-base alloys has been the subject of considerable investigation and the mechanism is generally well understood. As is characteristic of weld solidification cracking in other systems, cracks form during the terminal stages of solidification when liquid films are distributed along solidification grain boundaries and, in some cases, interdendritic sites. At this stage, shrinkage strains across the partially solidified boundaries can become appreciable. If the terminal liquid is distributed along the boundaries as a continuous film, the strains cannot be accommodated and the boundaries separate to form a crack.

Figures 3.26 and 3.27 show examples of solidification cracks in the fusion zone of Ni-base alloys. Note that the solidification cracks reside along solidification grain boundaries and interdendritic regions that are the last regions to solidify. The dark constituent in the crack region, indicated by the arrows in Figure 3.26, is a eutectic-type constituent that was the terminal liquid phase at the end of solidification. Such a continuous liquid film along the solidification grain boundary can promote cracking by interfering with the formation of solid/solid boundaries.

Figure 3.27 shows how the fraction of the terminal solidification liquid films can vary among different alloys. In the case of Alloy 625, there is considerable liquid along the solidification grain boundary as indicated by the light-colored phase in Figure 3.27a. This film can lead to cracking, but if it is present in a high fraction, it can also lead to the “healing” of cracks that form. In contrast,

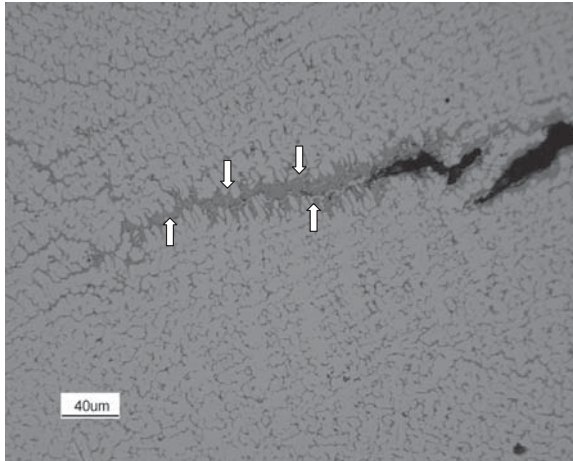


**Figure 3.26** Example of a solidification crack in a Ni-base alloy. The dark constituent (arrows) along the crack path is a eutectic constituent that formed as from the terminal solute rich liquid at the end of solidification. This is an example of crack “healing”.

liquid films are not apparent along the solidification grain boundaries in Alloy 230W (Figure 3.27b). In fact, liquid films were present along the boundary, but are so thin that they are almost imperceptible, even under high magnification in the SEM.

Susceptibility to weld solidification cracking is a function of both metallurgical factors and the level of local strain present at the end of solidification. In terms of metallurgical factors, it is well established that the solidification temperature range as well as the amount and distribution of the interfacial terminal liquid are the primary factors that control solidification cracking susceptibility of Ni-base alloys.(4,7,10,13,22,31,34,48) Solute redistribution plays an important role in solidification cracking as it affects the solidification temperature range and amount of terminal liquid.

The effect of the solidification temperature range can be understood in simplified terms by considering its influence on the size of the solid + liquid (mushy) zone. During welding, the mushy region trails behind the liquid weld pool. It is this mushy region that is susceptible to cracking under the influence of shrinkage strain and external restraint. The interface between the liquid weld pool and mushy zone (i.e., start of the mushy zone) is located where the actual temperature intersects the liquidus temperature of the alloy (assuming dendrite tip undercooling is negligible). Similarly, the interface between the mushy zone and completely solidified weld (i.e., end of the mushy zone) is positioned where the actual temperature intersects the terminal solidus temperature of the alloy. For a fixed temperature gradient in the mushy zone (constant processing parameters), composition variations that promote low temperature reactions at the terminal stages of solidification will widen the

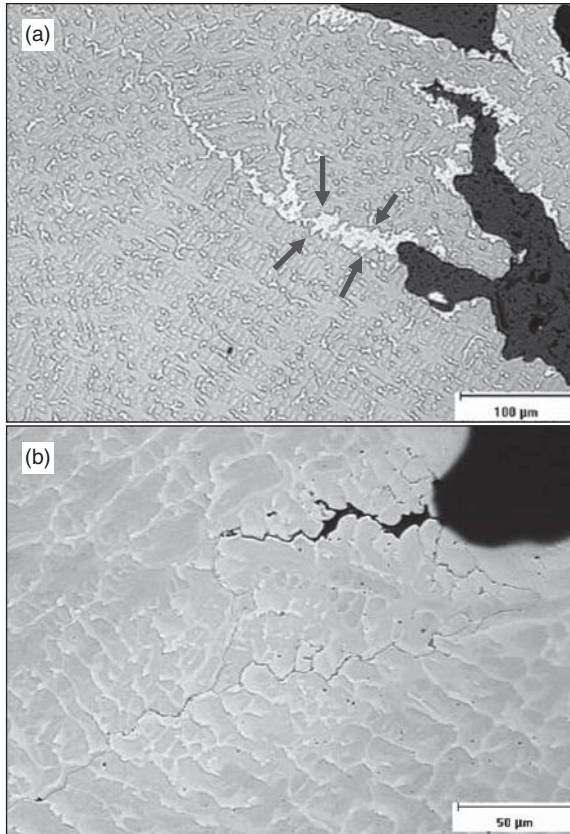


**Figure 3.27** Microstructure near the crack tip of a solidification crack in a) Alloy 625, and b) Alloy 230W. Light-etching phase in (a) is Nb-rich eutectic liquid along the solidification grain boundaries at the crack tip. Arrows indicate crack healing. Note difference in magnification. (From Lippold *et al.* [55].)

solidification temperature range and generally aggravate the cracking tendency by expanding the crack-susceptible mushy zone.

The actual distance a solidification crack propagates through the mushy zone depends on the distribution of terminal liquid that exists near the end of the solid + liquid region and the level of local strain present.(31) The distribution of liquid near the end of the mushy zone is, in turn, controlled by the amount of terminal liquid and solid/liquid surface tension. When the amount of terminal liquid is moderate, between approximately one-to-ten volume percent (31,49) and/or the surface tension is low, the liquid tends to wet the boundary and forms a continuous film. This type of morphology is most detrimental as it interferes with the formation of solid/solid boundaries, thus reducing the ability of the material to accommodate strain. In contrast, a small amount of terminal liquid, generally less than approximately one

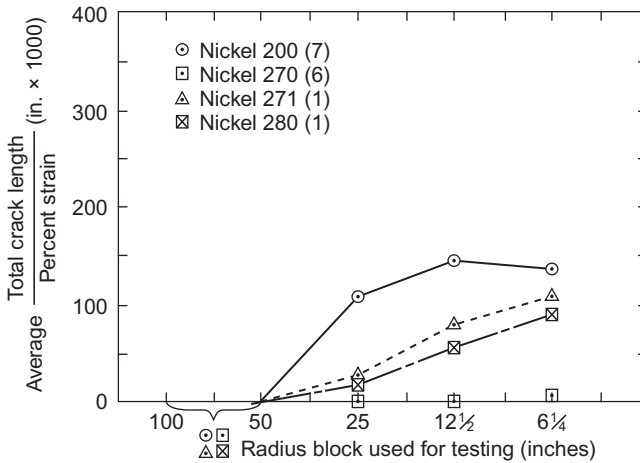
volume percent, that exhibits a high surface tension with the solid will often exist as isolated globules and promote solid/solid bridging, thereby reducing cracking tendency. When the amount of terminal liquid is high, (greater than approximately ten volume percent), it can often flow into the cracks and provide a “crack healing” effect.(31,50) For a given alloy system, the solidification temperature range and amount of terminal liquid are controlled primarily by composition. (Processing parameters become important under high cooling rate conditions where dendrite tip undercooling can be significant). Thus, many studies have attempted to establish the relationship between solidification cracking susceptibility and composition in Ni-base alloys.

For alloys that generally solidify as single phase austenite with no appreciable intermetallic and/or carbide formation at the end of solidification, the cracking susceptibility is controlled largely by the degree of impurity and/or trace elements. The most important impurity elements in Ni-base alloys are sulfur, phosphorus, and sometimes lead and silver. Boron can also increase cracking susceptibility, but it is not present in most of the solid-solution strengthened alloys. In Chapter 4, it will be shown that B can be an issue with respect solidification cracking in “superalloys,” since this element is often intentionally added to improve creep, or stress-rupture, properties.

For the commercially pure Ni alloys as well as many of the Ni-Cu, Ni-Cr, and Ni-Fe-Cr type alloys, the influence of elements such as S, P, and B on weldability is well known. The solidification parameters important relative to weld solidification cracking susceptibility are summarized in Table 3.13. Note that P, S, and B all have very low solubility in austenite and segregate aggressively (low  $k$  values) to the liquid during solidification. This segregation promotes the formation of low melting point liquid films in the interdendritic and solidification grain boundary regions and significantly increases cracking susceptibility. Although the behavior of these impurity elements in complex, multi-component alloys cannot be accurately represented by the simple solidification parameters shown in Table 3.13, the data illustrates their general effect. This has been verified experimentally in commercial Ni-base alloys.(51–54) The elements B and S are particularly harmful because they lower the solid/liquid surface energy and promote extensive wetting of boundaries by the low melting point films. Although Si can exert a similar effect by the for-

**TABLE 3.13 Summary of Partition Coefficients, Maximum Solid Solubility, and Terminal Eutectic Temperature in the Ni-P, Ni-S, Ni-B, and Ni-Si Systems.**

System	$k$	Maximum Solubility (wt%)	Terminal Eutectic Temperature, °C (°F)
Ni-P	0.02	0.32 P	870 (1600)
Ni-S	~ 0	~ 0 S	637 (1180)
Ni-B	0.04	0.7 B	1093 (2000)
Ni-Si	0.70	8.2 Si	1143 (2090)



Alloy	C	Mn	Fe	S	Si	Cu	Ni
200	0.08	0.18	0.200	0.005	0.18	0.13	Bal.
270	0.01	<0.001	0.003	<0.001	<0.001	<0.001	Bal.
271	0.11	---	0.001	<0.001	0.023	---	Bal.
280	0.12	---	0.002	<0.001	---	<0.001	Bal.

**Figure 3.28** Vareststraint weldability results showing the influence of S and Si on the weldability of several commercially pure Ni alloys. (From Lingenfelter [54]. Courtesy American Welding Society.)

mation of low melting point Ni-Si compounds (silicides), it is not as deleterious as the other elements except when present in relatively large amounts.

An example of the effects of S and Si are provided in Figure 3.28 which shows Vareststraint test results for several commercially-pure Ni alloys.(54) Note that the cracking susceptibility increases (as measured by total crack length/percent strain) as the amount of S and Si increases. The P and S levels are held to low levels in Ni-base alloys where resistance to solidification cracking is important, with S levels typically < 0.003 wt% and P levels < 0.01 wt%. The addition of Mn is often beneficial because it can combine with S to form MnS that exhibits a globular morphology, thus reducing the tendency to wet the grain boundaries. In general, alloys that solidify as single phase austenite can be readily welded as long as their impurity element content is held to low values.

It is interesting to note in Figure 3.28 that no cracking could be induced in Ni-270, even at the highest level of applied strain. Ni-270 is an extremely high purity Ni alloy and thus the solidification temperature range should be extremely small. As a result, the transition from 100% liquid to 100% solid is very abrupt, effectively eliminating the mushy zone in which cracking occurs. This resistance to cracking at any applied strain for an essentially pure alloy demonstrates the important effect of the solidification temperature range and resultant mushy zone size on cracking susceptibility.

**TABLE 3.14 Summary of Terminal Solidification Reactions and Associated Temperatures for Several Commercial Nickel Alloys.**

Alloy	Terminal Solidification Reaction	Temperature, °C (°F)
B-2	$L \rightarrow L + \gamma + M_6C$	1277 (2330)
W	$L \rightarrow L + \gamma + P$	1250 (2280)
C-22	$L \rightarrow L + \gamma + \sigma$	1285 (2345)
C-276	$L \rightarrow L + \gamma + P$	1285 (2345)
242	$L \rightarrow L + \gamma + M_6C$	1260 (2300)
625 (0.03 Si, 0.009 C)	$L \rightarrow L + \gamma + \text{Laves}$	1150 (2100)
625 (0.03 Si, 0.038 C)	$L \rightarrow L + \gamma + NbC$	1246 (2275)
625 (0.38 Si, 0.008 C)	$L \rightarrow L + \gamma + \text{Laves}$	1148 (2100)
625 (0.46 Si, 0.035 C)	$L \rightarrow L + \gamma + \text{Laves}$	1158 (2115)
HR-160	$L \rightarrow L + \gamma + (Ni,Co)_{16}(Ti,Cr)_6Si_7$	1162 (2125)
C-4 Gd	$L \rightarrow L + \gamma + Ni_5Gd$	1258 (2295)

In more highly alloyed solid-solution strengthened alloys, the formation of carbide and/or intermetallic phases at the terminal stages of solidification generally control solidification cracking susceptibility. In general, these phases are the product of a eutectic reaction that occurs at the end of solidification. This eutectic reaction occurs at a lower temperature than the alloy solidus and expands the solidification temperature range, making the alloy more susceptible to cracking. Table 3.14 summarizes the terminal reactions and associated reaction temperatures observed in several commercial alloys. This data, taken in combination with available Varestraint weldability results, are useful for identifying general trends between alloy composition and weldability. A description of the Varestraint test can be found in Chapter 8.

Cieslak investigated the weldability of the Ni-Cr-Mo type alloys C-4, C-22, and C-276.(6) Varestraint weldability results from that study are shown in Figure 3.29, where the cracking susceptibility falls in the order of C-276 > C-22 > C-4. As discussed in Section 3.3, C-4 does not form any of the TCP phases at lower temperature. This alloy only forms a very minor amount of TiC at the end of solidification. Although the exact formation temperature of this phase in C-4 could not be measured, carbides typically form at higher temperatures than TCP phases in Ni-base alloys.(4,31) Cieslak suggested that C-4 is expected to display very good weldability characteristics, similar to that of Type 304 stainless steel. The higher cracking susceptibility of Alloys C-22 and C-276 was attributed to the formation of TCP phases at lower temperatures,  $\sigma$  in C-22 and P in C-276, each at approximately 1285 °C (2345 °F). The slightly higher cracking susceptibility of Alloy C-276 was attributed to the larger amount of terminal liquid that existed at the end of solidification. However, all of these alloys should show good resistance to weld solidification cracking under most practical fabrication conditions.

Rowe *et al.* recently conducted Varestraint testing on a wide range of Ni-Cr-Mo type alloys, and their results are shown in Figure 3.30.(18) These results

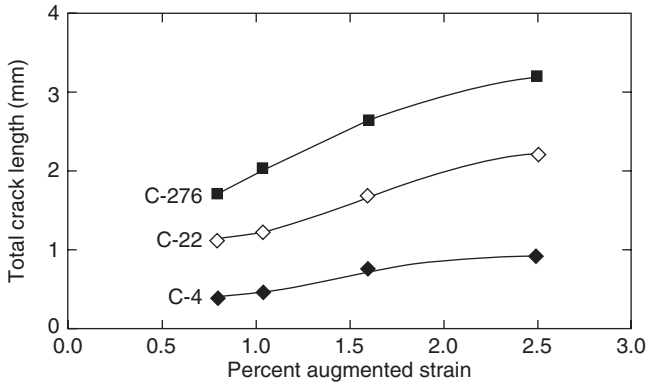


**Figure 3.29** Varestraint weldability results for Alloys C-4, C-22, and C-276. (From Cieslak *et al.* [6].)

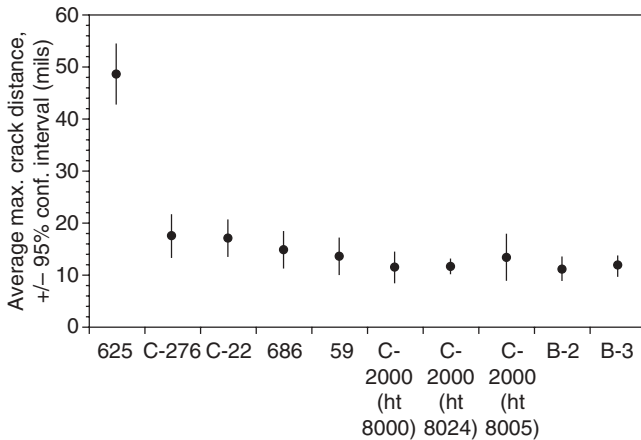


**Figure 3.30** Varestraint weldability results for a number of commercial alloys. (From Rowe *et al.* [18]. Courtesy American Welding Society.)

are generally in agreement with data from similar alloys obtained by Lienert *et al.* (14) and Maguire and Headley. (48) Lienert showed that the cracking resistance of Alloy B-2 is essentially equivalent to that of C-4, while Maguire and Headley showed that the cracking resistance of Alloys 242 and W are similar to that of Alloy 625. Thus, in Figure 3.30, results for Alloy C-4 would be expected to be similar to that of B-2, and Alloys 242 and W similar to that of Alloy 625. These trends can be rationalized from the data presented in Table 3.15. In general, the “B” and “C” type alloys investigated here form TCP and/or carbide phases at relatively high temperatures (1277-to-1285 °C). Thus, their cracking resistance is generally quite good. Although detailed characterization results are not available for Alloys 686, 59, C-2000, and B-3,

**TABLE 3.15 Ranking of Solidification Cracking Susceptibility based on Varestraint Data.**

Alloy	Varestraint MCL or MCD (mm)	Reference
B-3	0.3–0.5	1,2
B-2	0.5	2
59	0.5	2
C-276	0.5–0.7	1,2
686	0.6	2
C-22	0.7–1.0	2,3
617	1.0	4
230W	1.1	4
214	1.1	1
625	1.2–2.2	1,2,4
W	1.5	4
Waspaloy (1)	1.5	1
718 (1)	1.75	5
X	2.0	4
HR-160	2.5–3.0	1,5

(1) precipitation hardenable alloy.

#### References

1. Rowe, M. D., Ishwar, V. R., and Klarstrom, D. L. 2006. Properties, weldability, and applications of modern wrought heat resistant alloys for aerospace and power generation industries, *Transactions of ASME*, 128: 354–361.
2. Rowe, M. D., Crook, P., and Hoback, G. L. 2003. Weldability of a corrosion resistant Ni-Cr-Mo-Cu alloy, *Welding Journal*, 82(11): 313s–320s.
3. Gallagher, M. 2007. *Unpublished research performed at The Ohio State University*.
4. Lippold, J. C., Sowards, J., Alexandrov, B. T., Murray, G., and Ramirez, A. J. 2007. Weld solidification cracking in Ni-base alloys, *2<sup>nd</sup> International Workshop on Hot Cracking*, Berlin, March 2007, Springer-Verlag.
5. DuPont, J. N., Michael, J. R., and Newbury, B. D. 1999. Welding metallurgy of alloy HR-160, *Welding Journal*, 78(12): 408s–414s.

it is expected these alloys display similar solidification characteristics based on their similar level of cracking resistance. The terminal solidification temperatures of Alloys 625, W, and 242 are lower than the more weldable alloys and similar to each other (1246, 1250, and 1260 °C, respectively), thus resulting in higher cracking susceptibility. For Alloy 625, the solidification temperature range can be extended even further if the Laves phase forms (down to ~1150 °C).

Lippold *et al.* used the Varestraint test to study the solidification cracking susceptibility of filler metals 617, 625, X, W, and 230W.(55) Maximum crack distance (MCD) over a range of applied strain for these alloys is shown in Figure 3.31. Based on these results, Alloys 625 and X are judged the most susceptible, while Alloys 617 and 230W are the most resistant. In this study, the solidification temperature range of the filler metal deposit was measured using the Single Sensor Differential Thermal Analysis (SS-DTA) technique

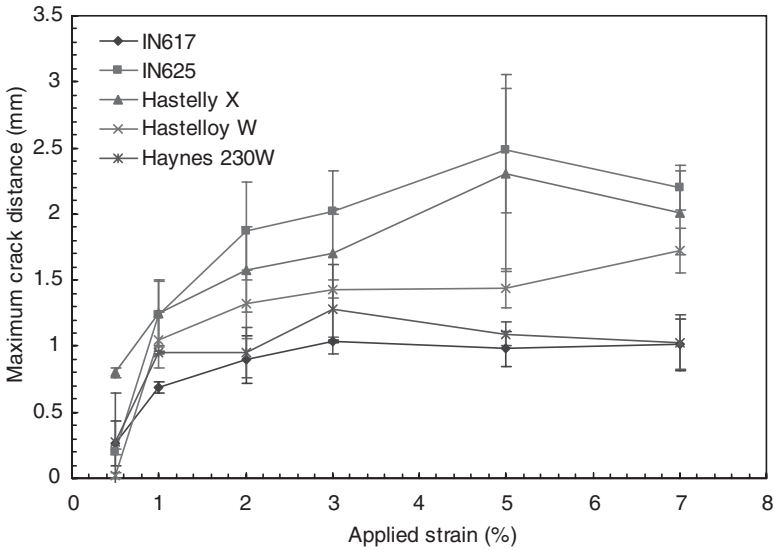


**Figure 3.31** Summary of maximum crack distance (MCD) versus strain for several solid-solution strengthened filler metals. (From Lippold *et al.* [55].)

**TABLE 3.16 Solidification Temperature Range and SCTR Values for Several Solid-solution Strengthened Ni-base Filler Metals.**

Weld Metal	Solidification Range (°C)		Varestraint SCTR, °C
	Scheil-Gulliver	SS-DTA	
617	160	93	85
625	243	97 (306)*	205
Hastelloy W	325	162	145
Hastelloy X	160	108	190
Haynes 230W	125	139	95

\*Value in parentheses includes end of eutectic solidification.

(56,57) and compared to the solidification temperature range calculated using the Scheil-Gulliver approximation (58), as shown in Table 3.16. Note that, except for Alloy 230W, the measured solidification temperature range is less than the Scheil-Gulliver simulations. This study also determined the actual solidification cracking temperature range (SCTR) using the technique described in Chapter 8. The values of SCTR are also reported in Table 3.16 and are plotted in Figure 3.32.

Based on solidification cracking theory, the SCTR should be less than or equal to the solidification temperature range (or mushy region), since cracking will occur only when a substantial solid has formed. Thus, the SCTR values

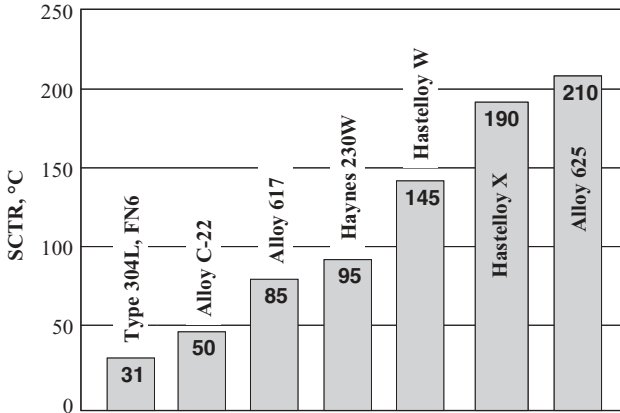


**Figure 3.32** Solidification cracking temperature range for the filler metals in Figure 3.31. Type 304L with Ferrite Number (FN) 6 and Alloy C-22 are listed for comparison.

for Alloy 625, and 230W seem most appropriate when compared to both SS-DTA and Scheil-Gulliver values. For Alloys 617 and W, the SCTR and SS-DTA values are nearly equivalent, while the SCTR for Alloy X is greater than both the simulated and measured solidification temperature range. Since these materials are also susceptible to ductility dip cracking (DDC), it is possible that some portion of the crack length measured in the Varestraint test is actually DDC extension off the solidification crack. This would result in an artificially high value of the SCTR.

The cracking susceptibility of the Ni-base alloys shown in Figure 3.31 and listed in Table 3.16 is considered moderate based on the SCTR values. Type 304L weld metal (with Ferrite Number 6) is known to be extremely resistant to weld solidification cracking and exhibits an SCTR value of 31 °C. Alloys with SCTR values of less than 100 °C are known to be resistant to weld solidification cracking, while alloys with SCTR values in the range from 100-to-200 °C have moderate susceptibility. Based on these ranges, filler metals 617, 230W, and W would be expected to be moderately resistant to weld solidification cracking, while filler metal X would have moderate-to-high susceptibility.

The solidification cracking susceptibility of Alloy 625 has been investigated with factorial variations in Nb, Si, and C.<sup>(4)</sup> It is interesting to note that the Nb-free alloys in this investigation all solidified as single phase austenite without formation of any terminal solidification phases and exhibited good weldability. This clearly shows the deleterious influence of low melting point phases on weldability. With the addition of Nb, the NbC and Laves phases formed and cracking susceptibility, as determined using the Varestraint test, increased significantly. The Laves phase is known to be particularly effective in expanding the solidification temperature range of Alloy 625 and other

Nb-bearing alloys because it forms at such a low temperature.(13,21) The terminal solidification phase and associated solidification temperature range were strongly affected by the relative amount of Nb and C and, to a lesser degree, the Si content.

No simple relation was observed between the maximum crack length obtained from Varestraint results and the measured solidification temperature range. It should be noted that, although Nb is added to Alloy 625 as a solid-solution strengthener, its strong segregation tendency ( $k_{Nb} = 0.54$  in Alloy 625) and associated formation of the Nb-rich NbC and Laves phases indicates that much of the Nb will be tied up as secondary phases in the weld metal. For example, the NbC phase is ~85–90 wt% Nb and the Laves phase is ~22–36 wt% Nb.(4,13,16,31) Thus, the solidification behavior of Nb-bearing alloys is very sensitive to the relative amounts of Nb and C and the corresponding type of terminal phase that forms, i.e., NbC or Laves. These trends hold whether Nb is added for solid-solution strengthening or precipitation hardening by formation of the  $\gamma'$ -Ni<sub>3</sub>Nb phase. Since most commercial alloys have Nb additions for precipitate strengthening, the solidification behavior and associated weldability of these alloys are discussed in more detail in Chapter 4.

It should be pointed out that in actual practice, Alloy 625 shows good resistance to weld solidification cracking and is often selected for use in moderate restraint applications to avoid problems with cracking, particularly when welding dissimilar materials. The apparent disagreement between the Varestraint results in Figures 3.30–3.32 and actual practice can be explained by the crack backfilling phenomenon. As shown in Figure 3.27A, Alloy 625 weld metal exhibits a high fraction of Nb-rich, terminal solidification liquid. When restraint is low, this liquid is available to heal any cracks that form by a backfilling mechanism. However, in the Varestraint test, the applied (or augmented) strains are high enough to overcome the backfilling effect. This suggests that for weld metals that achieve resistance to solidification cracking through a crack backfilling mechanism, the Varestraint test may not accurately reflect their susceptibility to cracking, particularly when testing is performed at high strains. The high applied strains used during this test force cracking to occur even in cases where considerable terminal liquid is present. The use of a threshold strain for cracking rather than maximum crack distance (MCD) at saturated strain may be a more appropriate measure of susceptibility for these weld metals.

Despite its wide solidification range, sound welds in Alloy 625 can usually be made by insuring the deposition of slightly convex weld bead shapes. By the same logic, the slightly convex back-filled crater rarely exhibits cracking. Although when present in high concentration (such as Alloy 625), Nb promotes the formation of the low-melting Laves phase, the judicious use of Nb and the careful control of weld bead shape allows crack-free welds to be deposited using many of the Nb-bearing Ni-Cr-Fe-Mo consumables.

Figure 3.33 shows Varestraint results for Alloy HR-160 compared to Types 304 and 310 stainless steels and Alloy 718.(10) Type 304 solidifies as primary

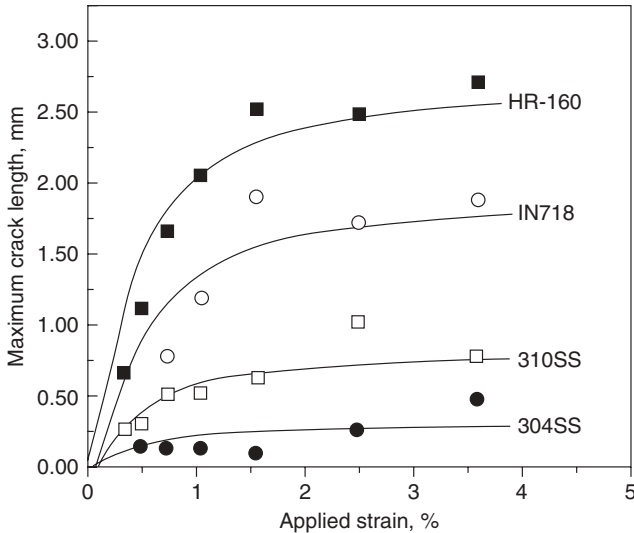


**Figure 3.33** Varcstraint weldability results for Alloys HR-160, IN718, and Types 304 and 310 stainless steel. (From DuPont *et al.* [10]. Courtesy American Welding Society.)

delta ferrite and, as a result, exhibits excellent weldability. The cracking susceptibility of Type 310 is slightly higher because it solidifies in the fully austenitic mode. Alloy 718 is known to be susceptible to cracking due to a eutectic reaction resulting in the formation of the Laves phase at  $\sim 1200^\circ\text{C}$  ( $2190^\circ\text{F}$ ).<sup>(13)</sup> The results in Figure 3.33 show that the addition 2.6 wt% Si has a very strong, deleterious result on the cracking resistance of Alloy HR-160 and is attributed to formation of  $(\text{Ni},\text{Co})_{16}(\text{Ti},\text{Cr})_6\text{Si}_7$  phase that occurs at  $\sim 1160^\circ\text{C}$  ( $2120^\circ\text{F}$ ). Microstructural characterization showed that the terminal liquid associated with this phase aggressively wets the solidification grain boundaries and interdendritic regions and contributes to the high cracking susceptibility of this alloy. In fact, cracks were found to form outside of the strained region of the sample, indicating the shrinkage strain from welding is sufficient to promote cracking in this alloy without the addition of any externally applied strain.

Figure 3.34 summarizes recent weldability and microstructural characterization results obtained on Alloy C-4 with various additions of Gd.<sup>(59)</sup> The figures show the cracking susceptibility, amount of terminal  $\gamma/\text{Ni}_5\text{Gd}$  eutectic type constituent, and solidification temperature range as a function of Gd concentration. These results are useful because they provide a more quantitative view of the relations between alloy composition, solidification behavior, and resultant cracking susceptibility. As described previously in this chapter and summarized in Table 3.8 and Table 3.14, these alloys solidify in a manner analogous to a simple binary alloy in which solidification begins with primary  $L \rightarrow \gamma$  and terminates with a  $L \rightarrow \gamma + \text{Ni}_5\text{Gd}$  eutectic-type reaction at  $\sim 1258^\circ\text{C}$  ( $2296^\circ\text{F}$ ).

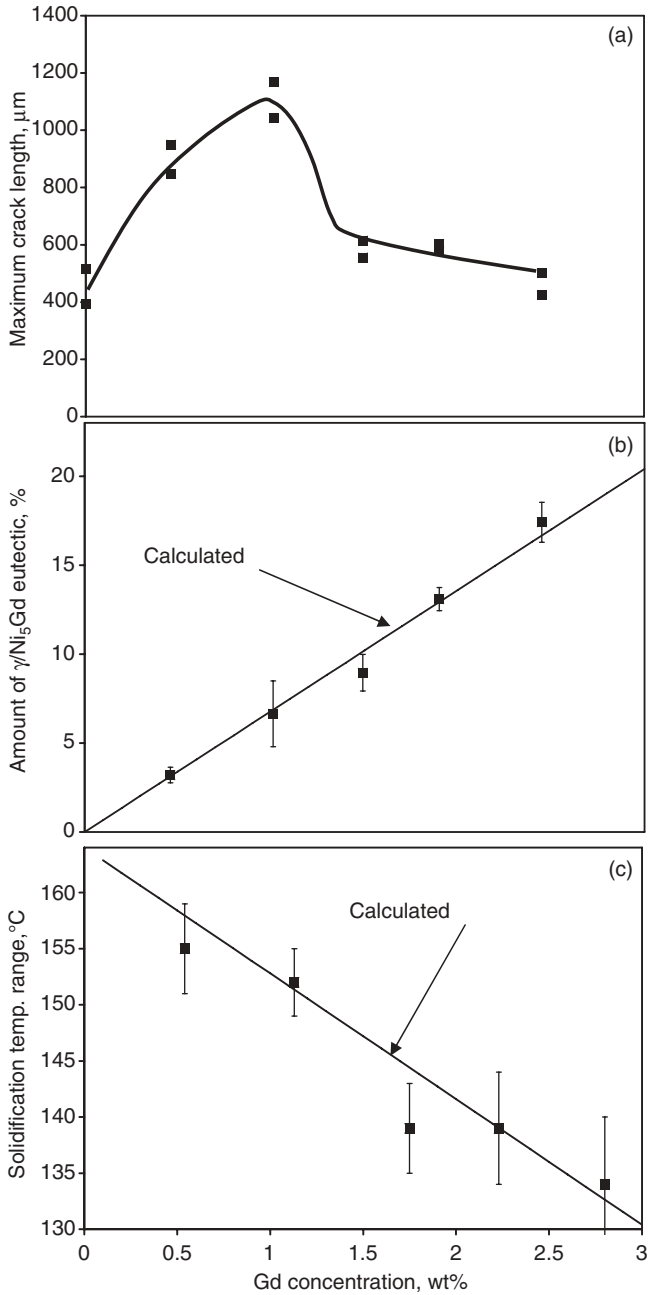


**Figure 3.34** Influence of gadolinium (Gd) concentration in Alloy C-4 on the a) Varestraint maximum crack length, b) amount of terminal  $\gamma/\text{Ni}_5\text{Gd}$  constituent, and c) solidification temperature range. (From DuPont and Robino [59].)

The lines in Figure 3.34B and 3.34C represent the fraction of terminal eutectic-type constituent and solidification temperature range, respectively, calculated with the aid of the pseudo-binary diagram (Figure 3.14) and the Scheil equation. Experimental measurements are also provided, and there is good agreement between the calculated and measured values. At low Gd concentrations, the solidification temperature range is high, but the fraction of terminal eutectic liquid is very low. Thus, the cracking susceptibility is low. As the Gd concentration increases, there is only a slight decrease in the solidification temperature range, but a rather significant increase in the fraction of terminal eutectic liquid (as reflected by the amount of  $\gamma/\text{Ni}_5\text{Gd}$ ). This leads to the increase in cracking susceptibility shown in Figure 3.34A that reaches a maximum at ~1 wt% Gd. With increasing amounts of Gd, the amount of terminal liquid increases to the point where cracking susceptibility decreases due to healing, or backfilling, of solidification cracks. The reduction in the solidification temperature range with increasing Gd concentration also assists in decreasing the cracking susceptibility. The amount of terminal liquid required to promote backfilling is consistent with other results, where the critical value of 7–10 volume percent has been indicated.(49,50) For the C-4 Gd system, this occurs when the Gd concentration reaches ~1.5 wt%. An example of crack healing at this Gd level is shown in Figure 3.35.

The deleterious influence of B on cracking susceptibility of Ni-base alloys has also been observed in this system. Figure 3.36 shows the maximum crack length as a function of B concentration for a C-4 alloy with a constant Gd concentration of 2 wt%. Note the five fold increase in cracking susceptibility with an increase of only 500 ppm B. Figure 3.37 shows a microstructure of the alloy with 230 ppm B, where the arrows indicate the presence of an additional phase that forms after the  $\text{Ni}_5\text{Gd}$  phase, and this additional phase covers most of the grain boundaries. Preliminary results have identified this phase as  $\text{M}_3\text{B}_2$ , which has also been identified in other Ni base alloys containing B.(60) Differential thermal analysis indicated this phase solidifies at a low temperature of ~1200 °C (2190 °F). Thus, the adverse effect of B can be attributed to both a widening of the solidification temperature range and extensive wetting of the solidification grain boundaries. Strong, deleterious effects on solidification cracking resistance have been observed in others materials as well, such as Alloys 214 and 230.

Based on the numerous solidification cracking studies that have been conducted using the Vareststraint test, it is possible to develop an approximate ranking of cracking susceptibility for Ni-base alloys, as previously shown in Table 3.15. This ranking is limited to studies where cracking susceptibility is reported as either maximum crack length (10,18,61) or maximum crack distance.(55,62) (See Figures 3.31 and 3.38) Both these metrics provide an estimate of the extent of the mushy zone over which cracks propagate. Assuming that the temperature gradients and cooling rates through the solidification temperature range are approximately the same, data from these various studies can be used to provide a rough order ranking of cracking susceptibility.

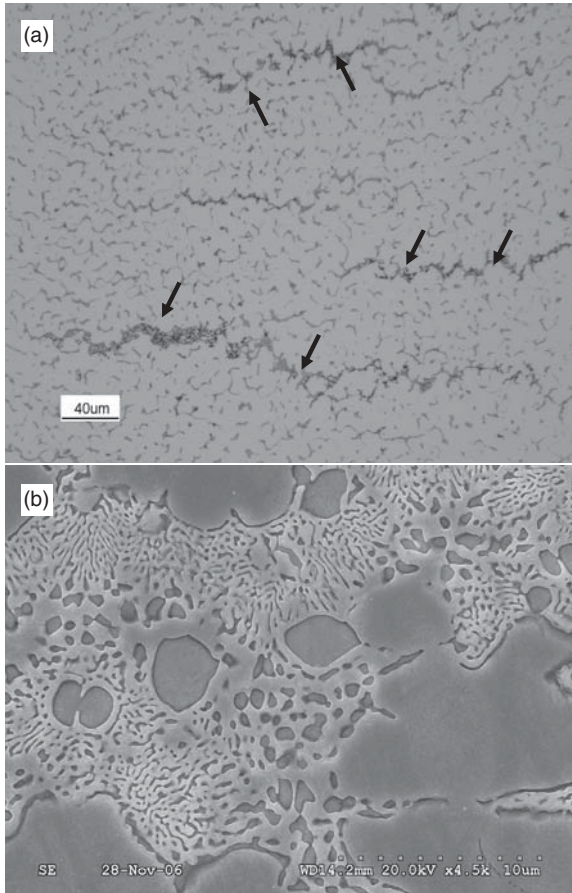


**Figure 3.35** Backfilling of solidification cracks observed in the fusion zone of Alloy C-4 with 1.5 wt% Gd addition. a) low magnification showing backfilled cracks (arrows), and b) higher magnification SEM photo showing the eutectic  $\gamma$ / $\text{Ni}_5\text{Gd}$  constituent in the backfilled region.

Based on this analysis, Alloys B-2, B-3, C-276, and C-22 are the most resistant to solidification cracking. Alloys 617, 214, and W exhibit intermediate resistance, while Alloys X and HR-160 are the most crack susceptible. The cracking susceptibility of Alloy 625 ranges from intermediate to high, based on data from three studies.

By combining the data in Table 3.15 with weldability data from other studies, a general classification scheme for cracking susceptibility can be developed for Ni-base alloys as shown in Table 3.17. Several precipitation-hardened alloys are included in these results as a basis for comparison. These alloys will be discussed in more detail in Chapter 4.

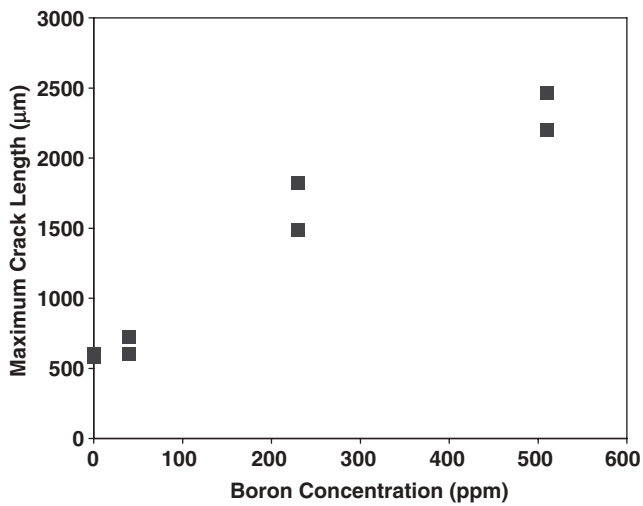


**Figure 3.36** Influence of B concentration on the cracking susceptibility of Alloy C-4 with 2wt% Gd.

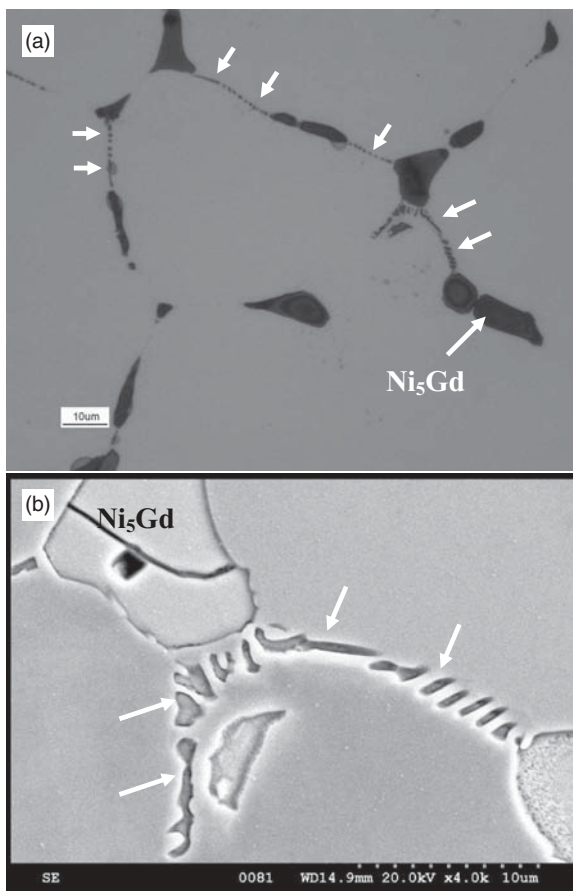


**Figure 3.37** Photomicrograph showing extensive wetting of Alloy C-4, 2wt% Gd fusion zone grain boundaries by a B-rich phase, a) optical micrograph, b) SEM/BSE of grain boundary.

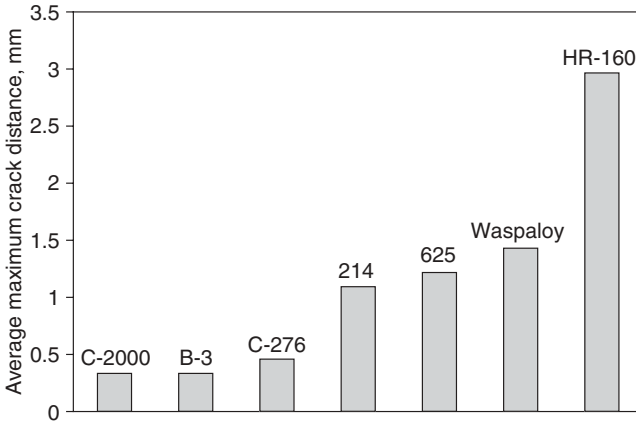


**Figure 3.38** Varestraint weldability results for a number of commercial alloys. (From Rowe *et al.* [61].)

**TABLE 3.17 Qualitative Classification of Solidification Cracking Behaviors of Various Commercial Alloys.**

Alloy Type	Cracking Susceptibility		
	Low	Moderate	High
Ni Alloys	200,270,271,280		
Ni-Cu	400		
Ni-Mo	B2,B3		
Ni-Cr		600, 601, 230	
Ni-Cr-Mo	C-4, C-22, C-276 C-2000, 59, 686	Hast W, 242, Hast X, 617	
Ni-Cr-Mo-Nb		625	
Ni-Co-Cr-Si			HR-160

The commercially pure Ni materials are resistant to cracking because their solidification temperature range is relatively narrow. This was confirmed by Lingenfelter in his study on a very wide range of Ni alloys.(54) In that work, the commercially pure Ni materials were tested under heat inputs nearly 30% higher than the remaining alloys and still exhibited the lowest crack lengths among all the alloys considered. (As explained in more detail below, higher heat inputs typically increase cracking severity.) Monel 400 exhibited only slightly higher cracking susceptibility than the commercially pure Ni alloys. The single phase solidification of the Ni and Ni-Cu alloys also contributes to their good cracking resistance. Although terminal solidification phases form in the B- and C-type alloys, these terminal reactions occur at relatively high temperatures and do not significantly expand the solidification temperature range, thus maintaining solidification cracking resistance. The slightly reduced

resistance to alloys in the Moderately Crack Susceptible regime can be attributed to the lower temperature terminal reactions that occur in these alloys. The alloys in the Crack Susceptible category are all Nb-bearing alloys and, as explained in more detail in Chapter 4, these alloys form Laves phase at a low temperature (1150–1200°C). The poor cracking resistance of HR-160 is attributed primarily to its high Si content.

It should also be pointed out that the solidification cracking susceptibility rankings provided in Tables 3.15 and 3.17 are from Varestraint test results. This test is described in some detail in Chapter 8. The Varestraint test has been used to determine weld solidification cracking susceptibility since the 1960s and has been widely accepted as a laboratory method for assessing cracking behavior. However, this test is not standardized and considerable variation exists among laboratories in terms of how the test is conducted and how cracking is quantified. This is an “augmented strain” test in which strains well above those expected in actual welds are applied in order to force the material to crack.

In the authors’ opinion, the Varestraint test provides a good measure of solidification cracking susceptibility in most alloy systems, and has been shown to be quite reliable for stainless steels.<sup>(63)</sup> Because much of the reported Varestraint data is from samples tested at high applied strains, the behavior of the liquid films along the solidification grain boundaries may be altered relative to the behavior at lower strains. An example of this is Alloy 625, which forms considerable low melting eutectic liquid at the end of solidification (see Figure 3.27A). Under low strain conditions, this liquid can be effective in “healing” cracks, but at high strains the “healing” effect is overwhelmed and cracks will form. Thus, field experience with Alloy 625 is that it is quite resistant to weld solidification, despite what the data in Figures 3.30–3.32 suggest. At low to medium restraint, Alloy 625 exhibits good weldability with respect to weld solidification cracking. At high restraint levels, weld solidification cracking would be expected, especially with concave weld bead shape.

It also should be noted that the behavior of some alloys in Table 3.17 can be highly dependent on slight variations in composition that are often permitted within the specification (heat-to-heat variability). This has been observed, for example, in Alloys 625 and 800.<sup>(4,28)</sup> Such variations could allow an alloy to behave differently than that summarized in Table 3.17. In addition, nearly any engineering alloy can exhibit cracking under unfavorable conditions, which include fabrication conditions involving high restraint, high heat input, and unfavorable weld shape.

Thus, the classification provided in Table 3.17 should be used as a general guideline based on Varestraint testing performed at relatively high strains. Nearly all the alloys listed would be resistant if the strains applied during solidification were low. Therefore, the guideline is best applied to welds made under high restraint conditions, such as multipass welds in thick sections. This classification is most useful for making comparisons among alloys when solidification cracking is a concern during fabrication or repair.

### 3.5.2 HAZ Liquation Cracking

All engineering alloys melt and solidify over a range of temperatures. In general, the higher the alloy content, the larger the melting/solidification temperature range. Thus, solid-solution strengthened Ni-base alloys can exhibit particularly wide melting and solidification temperature ranges due to their high alloy content. During welding, the base metal just adjacent to the fusion zone will experience a range of peak temperatures that is between the liquidus and effective (non-equilibrium) solidus temperature of the alloy. The microstructure within this region will therefore undergo partial melting and is described as the partially melted zone (PMZ) region of the HAZ. Liquation cracking can occur in the PMZ in Ni-base alloys when the liquid within the locally melted region cannot sustain the applied strain and forms a crack, usually along a grain boundary. This tendency for HAZ grain boundary liquation is increased with welding processes that are made at high heat input, such as gas metal arc welding (GMAW) in the spray transfer mode.

Grain boundary melting and HAZ liquation cracking can occur by two basic mechanisms—a segregation mechanism and a penetration mechanism. For the segregation mechanism, solute and/or impurity elements segregate to the grain boundaries by a diffusion mechanism and act to suppress the local melting temperature of the grain boundary. For the penetration mechanism, local melting occurs in the microstructure at elevated temperature and is intersected by a mobile grain boundary. The liquid then penetrates and wets the grain boundary.

For alloys that are single phase, the segregation of alloy and impurity elements (S, P, and B) to the grain boundaries can cause a local depression of the melting temperature and promote the formation of continuous liquid films along these boundaries.(64–66) Thus, the grain boundaries typically undergo some degree of liquation within the PMZ of single phase materials. It has been suggested that grain boundary segregation can be increased during grain growth within the HAZ as solute and impurity elements are swept into and accumulate in the migrating boundary.(64) Subsequent solidification of the solute-rich grain boundaries can often be observed in the PMZ as thick boundaries when the microstructure is appropriately polished and etched. An example of this segregation and associated cracking is shown for Alloy 617 in Figure 3.39.

Liquation by the penetration mechanism can also occur in Ni-base alloys that contain secondary constituents such intermetallics, carbides, or TCP phases by a process known as constitutional liquation.(67–68) In this case, the rapid heating associated with the weld thermal cycle does not permit sufficient time for dissolution of the secondary phase within the matrix. Upon heating above the eutectic temperature, the secondary phase reacts with the matrix to form an interfacial liquid film that is at the eutectic composition. This type of liquation has been observed at carbides and intermetallic phases in a number of Ni-base alloys, including the precipitation-strengthened alloys Udiment

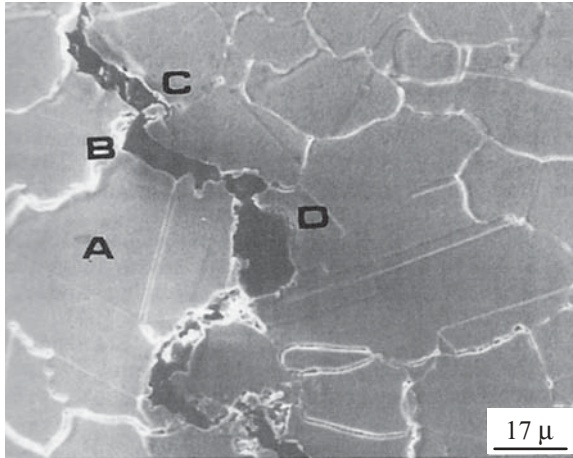


**Figure 3.39** Photomicrograph showing evidence of grain boundary liquation (arrows) in the HAZ of Alloy 617. (From Lundin *et al.* [75].)

700, Waspaloy, and Alloy 718, and the solid-solution strengthened alloys Hastelloy X and Alloy 625.(69–73) This mechanism is more common in precipitation-strengthened alloys and is discussed in more detail in Chapter 4.

Another manifestation of the penetration mechanism is the localized melting of residual eutectic constituents. In this case, the rapid heating cycle does not permit sufficient time for dissolution of the eutectic constituent, and constituent simply melts when it exceeds the eutectic temperature. If the alloy is above its maximum solid solubility, the eutectic constituent cannot dissolve regardless of the heating rate, and localized melting will always occur. An example of liquation in a Ni-base alloy containing the NbC carbide and Laves phase is shown in Figure 3.40.(74) The liquation can be identified by partial dissolution near the edges of the secondary constituents.

For the penetration mechanism, localized melting is generally not sufficient in itself to promote cracking, as the locally melted regions are initially isolated. However, intersection of the moving grain boundaries with the liquid (due to grain growth) causes the liquid to penetrate and wet the boundaries, often leading to complete grain boundary coverage by the liquid film. It is difficult for the boundaries to support localized strain in this condition, and cracks can form. In general, the two forms of the penetration mechanism (constitutional liquation and eutectic melting) are more detrimental from a cracking perspective than the segregation mechanism. This is true for two main reasons. First, constitutional liquation and eutectic melting generally produce more residual liquid and, second, the temperature at which these liquid films solidify can be substantially below the alloy solidus. Since the grain boundary liquid films can persist to temperatures well below the alloy solidus (depending on the eutectic temperature), the distance to which liquid films will be present along base metal grain boundaries can be significant and sufficient strain can

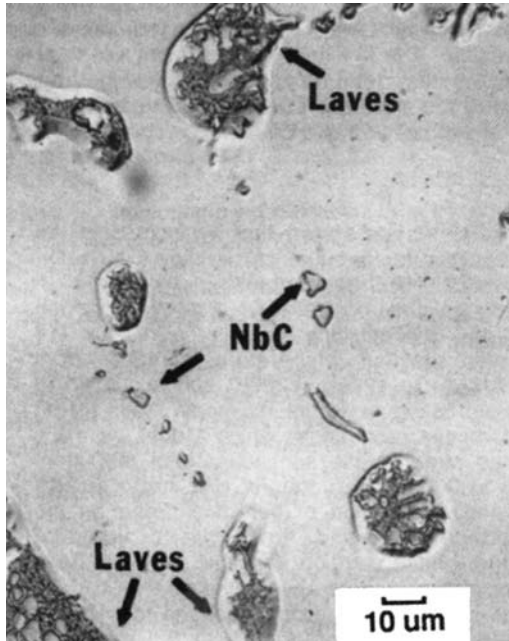


**Figure 3.40** Example of HAZ liquation in a Ni-base alloy containing NbC carbide and Laves phase. (From Kelly [74].)

promote cracking. This distance is also a function of the temperature gradient in the HAZ and can be influenced by welding process and process conditions, particularly heat input.

Based on the discussion above, there are apparent differences between the types of liquation and associated degree of cracking susceptibility expected between solid solution and precipitation strengthened Ni-base alloys. Most solid solution alloys are designed to be single phase with all alloying elements in solution. Thus, the segregation mechanism is most typical for solid-solution strengthened alloys, and cracking susceptibility is generally lower than that of precipitation-strengthened alloys. An example of this is shown in Figure 3.41, which compares Gleeble hot ductility results for a solid-solution strengthened alloy (Alloy 617) with the precipitation strengthened alloy Thermo-Span.(17,75) The zero ductility range (ZDR) is typically used as an indicator of HAZ cracking susceptibility in these tests. This parameter is given by the difference between the nil strength temperature (NST) and the temperature at which the alloy begins to recover ductility upon cooling from the NST. Alloys with wider ZDR values exhibit more extensive liquation and associated cracking susceptibility. Alloy 617 exhibits a ZDR of  $\sim 100^{\circ}\text{C}$ , while the Thermo-Span alloy has a ZDR nearly twice that value at  $\sim 190^{\circ}\text{C}$ . Also, note that the solid-solution strengthened alloy regains essentially all its ductility during cooling, while

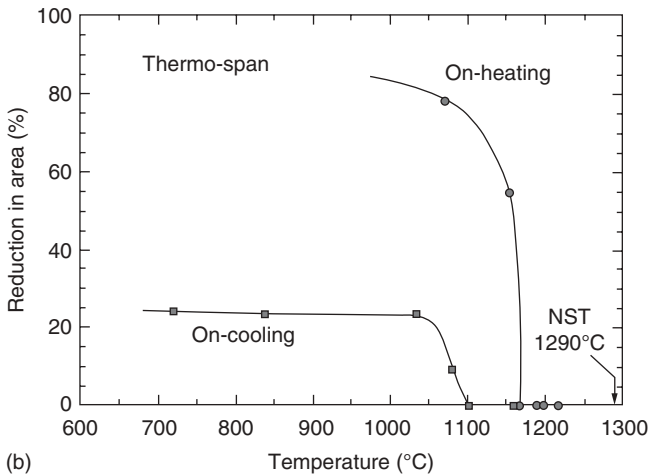
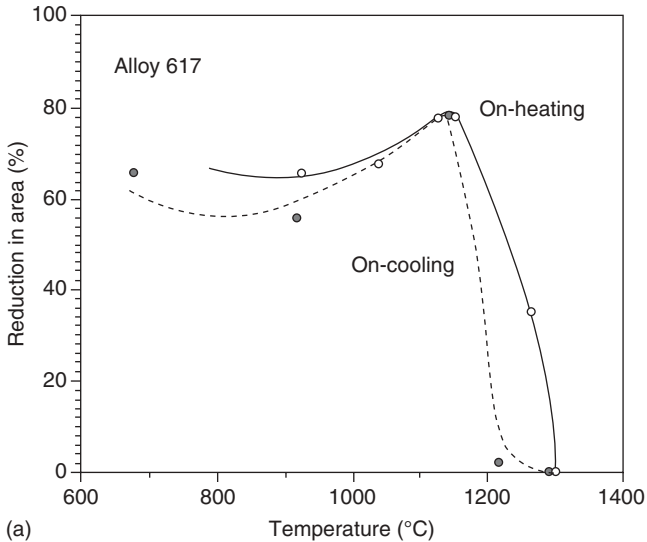


**Figure 3.41** Gleeble hot ductility results for a) solid-solution strengthened Alloy 617 [74] and b) precipitation-hardened Thermo-Span alloy. (From Kelly [74] and Robino *et al.* [17].)

ductility for the cooling portion of the precipitation-hardened alloy is significantly less than the ductility exhibited during heating.

Eutectic melting and constitutional liquation can occur in alloys that are classified as solid-solution strengthened materials, particularly those with Nb and Ti additions. It is well known that NbC and TiC are subject to constitutional liquation in the austenite matrix. (64,71,73) For example, the base metal of Alloy 625 contains NbC that can result in constitutional liquation and

subsequent HAZ liquation cracking. In some alloys, residual eutectic and secondary constituents can be remnant from the original casting process when the post-casting and/or thermo-mechanical working treatments are not sufficient for complete dissolution of the secondary constituent. In these alloys, it is the condition of the starting base metal microstructure, rather than the general alloy classification that dictates the susceptibility to HAZ liquation cracking.

The influence P, S, and B on liquation cracking is similar to that of fusion zone solidification cracking, where these elements are known to be particularly harmful. Phosphorous is generally the least deleterious and B the most detrimental, with the role of S mainly being intermediate.(76) These elements all aggravate cracking by segregating to the grain boundary, resulting in liquid films that persist to low temperatures. Thus, a good rule of thumb is to maintain impurities as low as possible as a means to avoid cracking. In many alloys in which special double-melting techniques are used, total S + P contents may be as low as 100 ppm (0.01 wt%). At this level, S and P do not promote liquation cracking.

On the other hand, boron is added to some Ni-base alloys to improve creep properties and it may be necessary to balance the benefit of improved creep resistance with a potential degradation in weldability. The effect of boron on liquation cracking can be significant, and an example of this is shown in Figure 3.42.(52) This figure shows Gleeble hot ductility results for two heats of Alloy 214 with essentially identical compositions except for a variation in B (0.0002 versus 0.003 wt%). Each alloy has a NST value of  $\sim 1355^{\circ}\text{C}$  ( $2470^{\circ}\text{F}$ ). The low B heat exhibits a small ZDR value of  $\sim 50^{\circ}\text{C}$ , while the small increase in B to 0.003 wt% expands the ZDR by a factor of five to  $\sim 250^{\circ}\text{C}$ . Recent results have shown that the behavior of B-containing alloys is dependent on the grain boundary character, where segregation and associated cracking tendency is higher for high angle boundaries compared to low angle boundaries, such as twin boundaries.(77) It should be noted that the effect of B on the weldability of Ni-base alloys is generally more of an issue with the precipitation-strengthened alloys, and this topic is discussed in more detail in Chapter 4.

Finally, liquation cracking can also occur in multipass welds where initial weld passes become the HAZ of subsequent passes. This phenomenon is called *weld metal liquation cracking* and represents a special form of HAZ liquation cracking where the HAZ is previously deposited weld metal. In this case, liquation results due to local melting along grain boundaries in the underlying weld metal. Because segregation occurs along both solidification grain boundaries and migrated grain boundaries in the initial weld, these boundaries are susceptible to melting when they are reheated. An example of weld metal liquation cracking in a multipass weld made with Alloy 625 weld metal is shown in Figure 3.43. It should be noted that weld metal liquation cracks in Ni-base weld metals may occur in the same vicinity as solid-state, ductility dip cracks. In practice, it may be very difficult to differentiate these two forms of cracking. The difference between these forms of cracking will be described in more detail in Section 3.5.4.

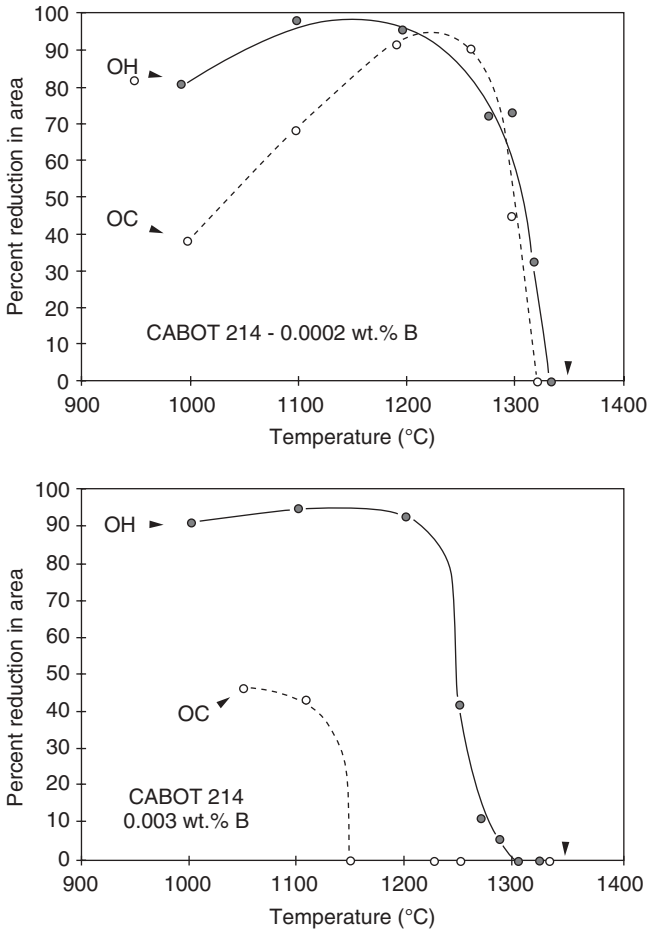


**Figure 3.42** Gleeble hot ductility results for two heats of Alloy 214 with different B levels. (From Cieslak *et al.* [52].)

### 3.5.3 Avoiding Solidification and Liquefaction Cracking

Fundamentally, there are three factors that contribute to solidification and liquation cracking: alloy composition, welding parameters, and restraint. Selection of welding process and process conditions can influence cracking susceptibility, but these only serve to modify the composition and restraint conditions that promote cracking. Weld metal solidification cracking can often be avoided by proper selection of a welding consumable. As discussed previously, if weld metals solidify over a narrow temperature range and avoid the formation of low-melting eutectic constituents, cracking susceptibility is generally low. Liquation cracking susceptibility is affected both by the alloy composition and the condition of the base metal microstructure with fine-grained

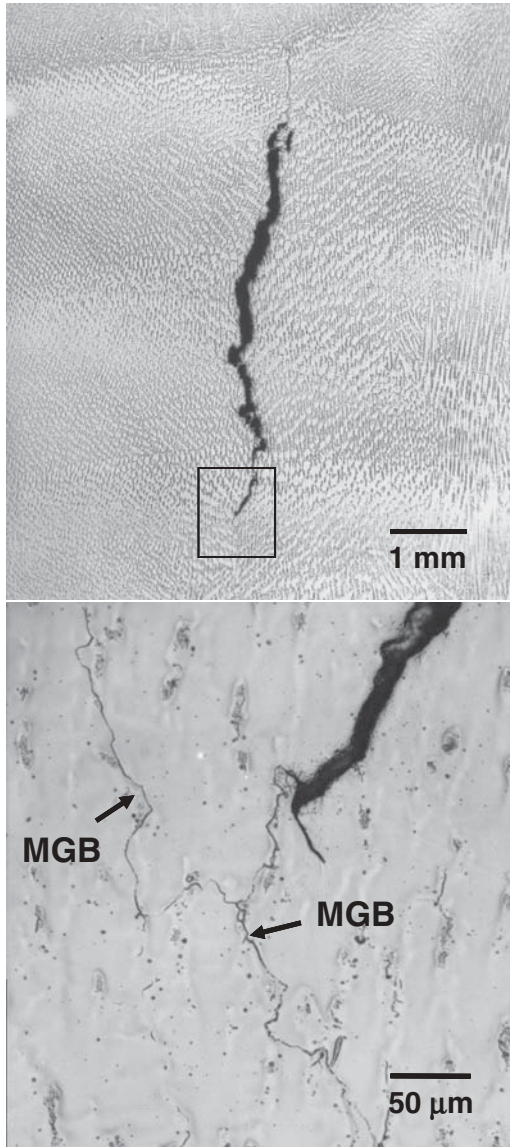


**Figure 3.43** Weld metal liquation crack in an Alloy 625 multipass weld.

base materials providing better resistance to HAZ liquation cracking than coarse-grained materials.

The control of impurities to low levels is always advisable, since the elements P, S, and B (and when present Pb and Ag) are known to increase cracking susceptibility. It is also advisable to limit elements that form low melting eutectic constituents, such as Nb, Ti, and Si. This approach is often

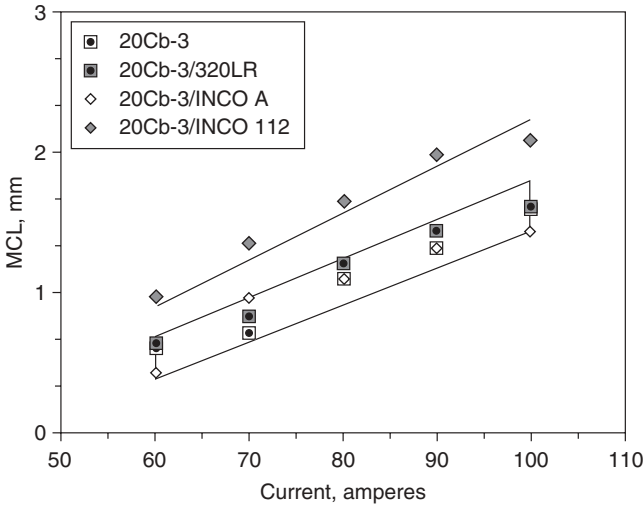


**Figure 3.44** Varestraint results showing maximum crack length as a function of welding current (heat input) for Alloy 20Cb-3 autogenous gas tungsten arc welds and three different filler metals. (From DuPont [78].)

not possible, however, since these elements are usually intentional additions to the base metal or filler metal. In such cases, some balance between desired properties and weldability must be achieved.

In general, the use of low heat input welding processes and conditions is favorable for avoiding both types of cracking. From a solidification cracking standpoint, lower heat input leads to smaller weld sizes that, in turn, reduce solidification shrinkage strains. Lower heat inputs also lead to steep temperature gradients at the trailing edge of the weld pool and in the base metal HAZ, reducing the width of crack susceptible region in both locations. An example of the heat input effect is demonstrated by the Varestraint results in Figure 3.44 (78) which shows the maximum crack length as a function of welding current for autogenous gas tungsten arc welds in Alloy 20Cb-3 and welds made with three different filler metals. In each case, there is a linear increase in maximum crack length with increasing welding current, indicating that the size of the crack susceptible mushy zone is increasing with higher currents.

This can be understood from simple heat flow considerations. The temperature gradient ( $G$ ) at the weld centerline, where the maximum crack length typically occurs, is given by the Rosenthal equation as:

$$G = \frac{2\pi k(T_L - T_o)^2}{\eta VI} \quad (3.10)$$

Where  $k$  is the thermal conductivity,  $T_L$  is the liquidus temperature,  $T_o$  is the initial temperature,  $\eta$  is the heat source transfer efficiency,  $V$  is the voltage,

and  $I$  is the current. The length of the mushy zone ( $L$ ) is given simply by the ratio of solidification temperature range ( $\Delta T$ ) to temperature gradient (assuming a linear temperature gradient over the solidification temperature range). Thus, the mushy zone length is related to the welding current and solidification temperature range by:

$$L \approx \frac{\Delta T \eta V I}{2\pi k (T_L - T_o)^2} \quad (3.11)$$

Although the Rosenthal heat flow solutions do not provide highly accurate results, Equation 3.11 reveals the linear dependence of the mushy zone size and corresponding maximum crack length on welding current that is manifested by the experimental results shown in Figure 3.44. These results indicate that lower heat inputs are beneficial for minimizing fusion zone solidification cracking. It should be noted that the temperature range over which cracking occurs does not change, but that the spatial regime over which cracking can occur becomes narrower due to the steeper temperature gradient resulting from the low heat input weld. The combination of steep temperature gradient and lower restraint associated with low heat input welding is often used to avoid/minimize weld solidification cracking in these alloys.

The weld pool shape can also influence solidification cracking susceptibility. The macroscopic shape of the weld pool affects both the grain structure within the weld and the restraint that is imposed during solidification. Examples of weld bead shape control are provided in Figure 3.45. By adjusting the depth-to-width ( $D/W$ ) ratio of the weld, the grain structure of the weld metal can be altered. Since grains tend to grow perpendicular to the solid/liquid interface, welds with a low  $D/W$  ratio and elliptical weld pool shape will exhibit the radial grain structure shown in Figure 3.45A. When the  $D/W$  ratio increases and the weld pool becomes more teardrop shaped, a more distinct weld centerline will form as the grains will tend to grow towards and converge at the weld centerline, as shown in Figure 3.45B. In this case, the maximum shrinkage strain is perpendicular to a distinct centerline along which liquid films may be present. Such a situation tends to promote cracking. Even if the  $D/W$  ratio is minimized, the surface contour of the weld can also influence cracking. Welds that exhibit a concave contour will generally place the weld surface in tension, which promotes cracking. In contrast, welds that exhibit a flat or convex contour typically induce compressive strains at the surface and distribute the strain across the weld (or at the weld toe). The example shown in Figures 3.45C and 3.45D demonstrates how altering the welding procedure in order to replace a concave weld bead with a convex bead is effective in eliminating solidification cracking. In general, excessive travel speed increases the tendency for tear-drop shaped solidification patterns that produce the distinct centerline shown in Figure 3.34B. Reduced travel speed provides for more competitive grain growth and eliminates the distinct centerline feature, as shown in Figure 3.34A.

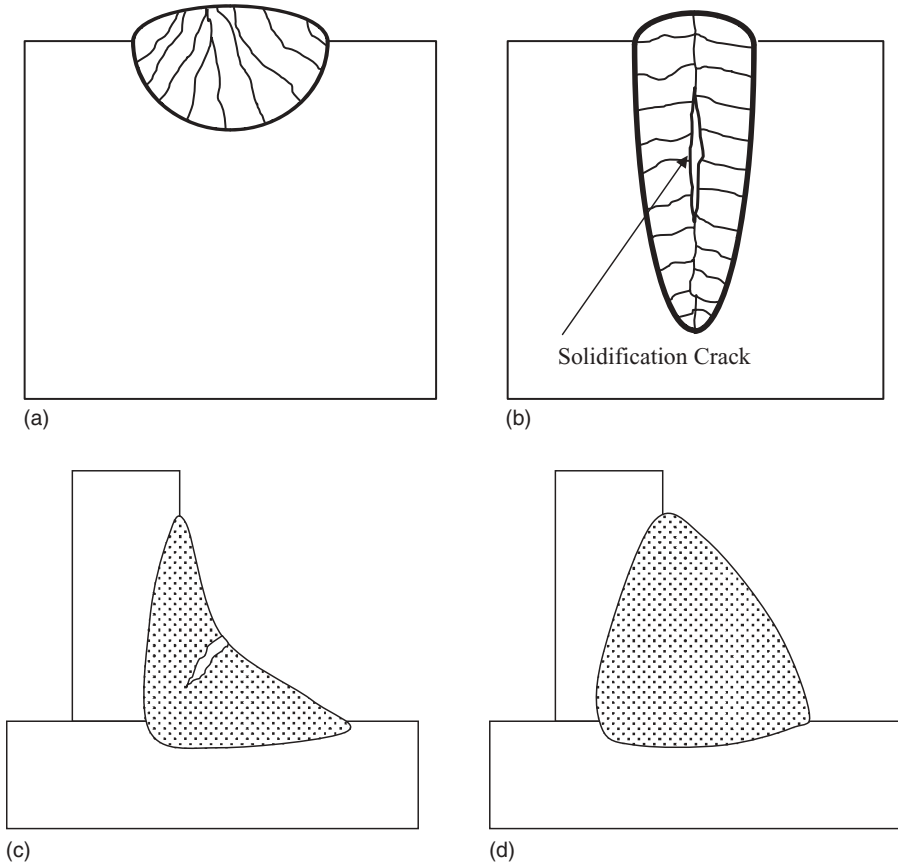


**Figure 3.45** Schematic illustration showing influence of pool shape on grain morphology and resultant solidification cracking susceptibility.

Lower heat inputs are also favorable for minimizing HAZ liquation cracking because they decrease the size of the PMZ. Cracking of any form cannot occur without some level of tensile strain. Tensile strains in the weld region will develop due to residual stresses from mechanical restraint and solidification shrinkage. Low heat input combined with reduced levels of restraint each help to reduce the level of tensile strain experienced by the weld. In multipass welding, filling of the joint with a larger number of smaller passes is beneficial because it reduces heat input, residual stress, and shrinkage strains. Liquation cracking susceptibility can be minimized to some degree by control of the starting microstructure of the base metal. For example, heat treatments that dissolve intermetallic phases and eutectic-type constituents will eliminate the possibility of liquation at lower temperature and improve cracking resistance. With this approach, an effective temperature for dissolution needs to be identified, and this can initially be assessed with the aid of multi-component ther-

modynamic calculations (as discussed in Chapter 2) prior to experimental verification.

Lastly, it has been shown that fine grained materials are more resistant to HAZ liquation cracking than coarse grained materials.(79) It has been suggested that larger grain sizes increase cracking susceptibility by promoting more extensive grain boundary wetting by the liquid films and inducing higher stress concentrations. Unfortunately, many nickel alloys are used at high temperature where large grain size is favored for better creep resistance. Thus, as with alloy composition, grain size must be balanced for both weldability and performance. In some cases, when coarse grained material is desired for creep resistance, welding can be performed on fine-grained material followed by a grain-coarsening solution annealing treatment.

It is often tempting for welding engineers to try to resolve weld solidification cracking and liquation cracking problems by a “knob turning” exercise. In this scenario, the perfect combination of welding conditions (current, voltage, travel speed, wire feed speed, etc.) is sought in an effort to make the cracking disappear. Occasionally, this approach is successful, particularly if cracking is the result of poor weld bead shape control. In most cases, however, these efforts can be quite futile since the underlying cause for cracking is most often associated with the composition of the base metal and filler metal and concomitant solidification behavior. It is important to know the weldability characteristics of the materials at the outset, prior to developing a welding procedure. In many cases, it is possible to optimally choose consumables based on the expected dilution from the base to avoid weld solidification cracking. If data is not available, this can often be accomplished by weldability testing, as described in Chapter 8.

### 3.5.4 Ductility-Dip Cracking

Until recently, ductility-dip cracking (DDC) in welded structures was considered more of a curiosity than a serious weldability issue. With the introduction of high-Cr (25–30wt%) filler metals designed to combat stress corrosion cracking in the power generation industry, DDC has evolved into a weldability problem that has challenged both the manufacturers and users of these consumables. Considerable research conducted since the early 1990s has done much to elucidate the mechanism of DDC in welded structures, and it is now possible to predict DDC susceptibility through testing and metallurgical characterization.

**3.5.4.1 Description of Ductility-Dip Cracking** Ductility dip cracking (DDC) is a solid-state phenomenon that has been observed in a number of structural materials, including austenitic stainless steels, copper alloys, titanium alloys, and Ni-base alloys. In materials susceptible to DDC, a precipitous drop in ductility occurs in the temperature range between the solidus ( $T_s$ ) and approximately  $0.5T_s$ . Often this drop in ductility occurs over a very narrow

temperature range, as shown schematically in Figure 3.46. Since contraction stresses during welding can be large in this temperature range, this dip in ductility can result in local exhaustion of ductility and subsequent DDC.

Haddrill and Baker (80) defined DDC as the loss in ductility, over a temperature range below the solidus that is sufficient to produce cracking under the influence of thermal strain caused by welding. Most literature concerning DDC uses terminology that is both confusing and inconsistent. DDC has been referred to as hot cracking, hot tearing, hot fissuring, reheat cracking, microfissuring, and “polygonization” cracking in the welding literature.(81) Since many of these terms refer to different types of “hot” cracking and elevated temperature solid-state cracking, there has been much confusion over the true meaning of “ductility-dip cracking.” It is likely that the literature contains many references to liquation cracking and microfissuring in weld metals that are in fact DDC.

In an effort to clarify the terms used to describe weld cracking, Hemsworth *et al.*(81) divided and defined high temperature cracking as two separate types, segregation cracking and ductility-dip cracking. The term “segregation cracking” refers to the type of cracking where intergranular liquid films are present. These forms of cracking, namely weld solidification cracking, HAZ liquation cracking, and weld metal liquation cracking, are now generally referred to as the three forms of “hot” cracking. Thus, by definition, hot cracking is characterized by the presence of a liquid film and occurs at higher temperatures, as shown in Figure 3.46. The hot cracking susceptibility of solid-solution strengthened Ni-base alloys was described in Sections 3.5.1 and 3.5.2.

According to Hemsworth *et al.*(80), ductility-dip cracking can also take three forms, occurring in the weld metal, HAZ, or reheated weld metal. This is consistent with observations of ductility-dip cracking in welded structures,

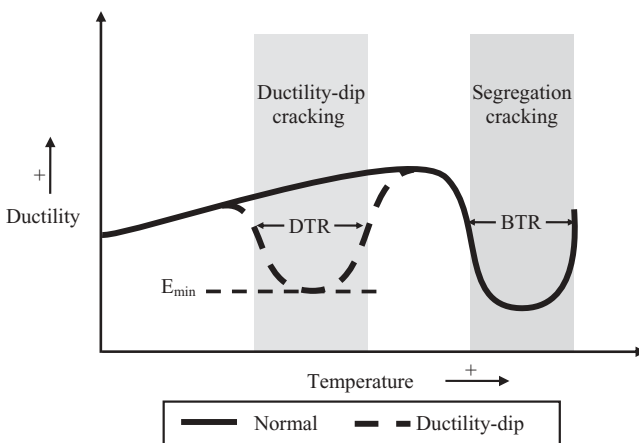


**Figure 3.46** Schematic illustration of ductility as a function of temperature. The dotted line represents a solid-state ductility dip. (From Nissley [100].)

although in practice DDC is most often observed in the weld metal. Unfortunately, the term ductility-dip cracking, as defined by Hemsworth *et al.* is not specific enough to define a single cracking mechanism, since their broad definition would still include such forms of cracking as reheat cracking, stress-relief cracking, and strain-age cracking. These latter cracking mechanisms all require that a precipitation strengthening mechanism acts in concert with stress relaxation to promote cracking—normally in the base metal HAZ. Grain boundary impurity segregation also contributes to these forms of cracking.

DDC requires neither the formation of strengthening precipitates nor grain boundary impurity segregation. High purity, solid-solution strengthened alloys are often more susceptible to DDC than those that undergo precipitation reactions or have moderate impurity levels. Thus, the DDC that is described here represents a distinct form of HAZ and weld metal cracking resulting from grain boundary sliding, or separation, and elevated temperature ductility exhaustion. Theories that have been proposed to describe this mechanism are summarized in the following section.

**3.5.4.2 Proposed Mechanisms for Ductility-Dip Cracking** The presence of a ductility dip in austenitic alloys was reported as early as 1912 by Bengough.(82) Since that time, a number of theories have been proposed to describe DDC, as listed in Table 3.18. In 1961, Rhines and Wray (83) reported that a ductility-dip occurs in copper alloys, nickel alloys, austenitic stainless steels, titanium, and aluminum. They believed that the ductility dip was caused by grain boundary shearing, similar to creep-rupture failures. At temperatures below the recrystallization temperature, the voids have time to join by grain boundary shearing and cause a fracture. Above the recrystallization temperature, the formation of new grain boundaries makes difficult the joining of the voids. This mechanism is in general agreement with that recently proposed by Ramirez and Lippold (84), and Noecker and DuPont.(85,86)

**TABLE 3.18 Summary of Ductility-dip Cracking Theories.**

Name [REF]	Description	Year
Rhines & Wray [83]	Grain boundary shearing up to recrystallization temperature.	1961
Yamaguchi <i>et al.</i> [87]	Sulfur segregation and embrittlement.	1979
Zhang <i>et al.</i> [92,93]	Combination of effects up to recrystallization temperature.	1985
Ramirez and Lippold [84]	Grain boundary sliding and microvoid formation, effect of boundary tortuosity.	2005
Noecker and DuPont [85,86]	Grain boundary sliding, carbide distribution and morphology.	2008
Young <i>et al.</i> [101]	Precipitation-induced cracking	2008

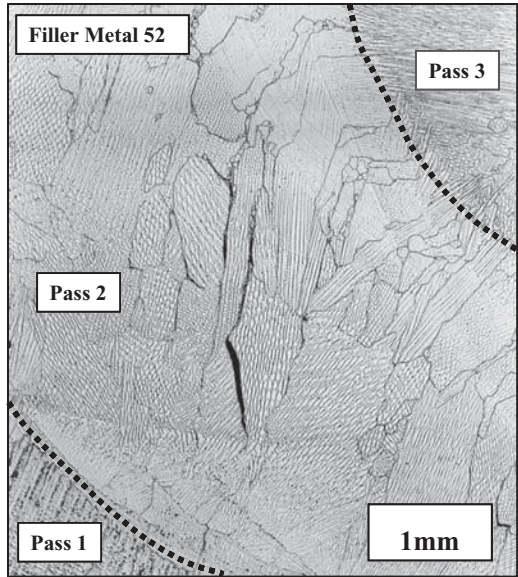
Yamaguchi *et al.*(87) proposed that increases in sulfur content increased the tendency for a ductility dip between 950 and 1150°C (1740 and 2100°F), where sulfur segregated to and embrittled the grain boundaries which cracked under an applied stress. Similar sulfur segregation mechanisms have also been proposed by Matsuda (88) and more recently by Nishimoto *et al.*(89,90) Recent work by Collins *et al.*(91) with Filler Metal 82 also showed that sulfur additions increase susceptibility to DDC.

While sulfur and other impurities may contribute to DDC, the work by Ramirez and Lippold concluded that differences in susceptibility could not be simply explained by impurity (S and P) content since many materials with very low impurity content were also susceptible.(84) For example, autogenous welds on Alloy 690 were found to be highly susceptible to DDC in the strain-to-fracture test even though the total impurity (P + S) content of the alloy was less than 0.010wt% (100ppm). Zhang *et al.*(92) reported that the combined effects of grain-boundary precipitation, grain-boundary sliding, grain boundary migration, and grain boundary serration affect the DDC performance of the low expansion alloy INVAR (Fe-36Ni). They also suggested that recrystallization and decreased flow stress were factors in the recovery of ductility at elevated temperatures.(93)

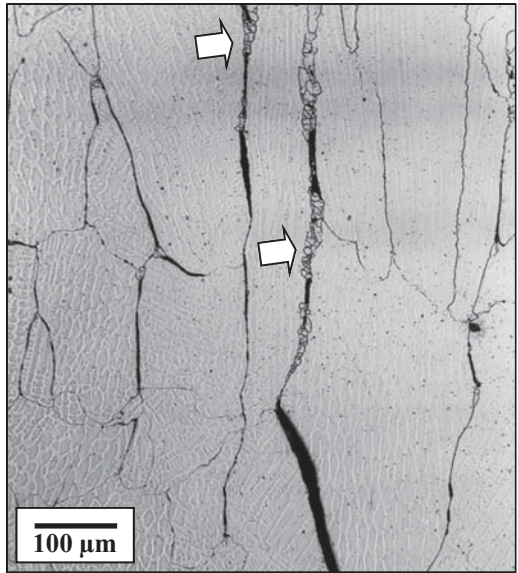
Ramirez and Lippold (84) have conducted a comprehensive study of DDC in Ni-base alloys and concluded that DDC is essentially an elevated temperature, grain boundary creep phenomenon. They found that impurity (P,S,O, and H) segregation, grain boundary precipitation, and boundary “tortuosity” affect DDC susceptibility and that controlling the nature of grain boundaries is the key to avoiding DDC in Ni-base weld metals. Details of their proposed mechanism are provided in Section 3.5.4.3.

At the time of this writing, there is still not general agreement on the mechanism for DDC in Ni-base alloys (or other materials), and it is possible that DDC manifests itself differently in different materials. Remarkably, virtually all austenitic (fcc matrix) alloys exhibit a ductility dip. Even austenitic stainless steel weld metals that contain ferrite show a perceptible dip in ductility above  $0.5T_s$ .(94) Standardized methods for assessing susceptibility to DDC and continued detailed metallurgical characterization work will be required in order to develop a better understanding of DDC.

**3.5.4.3 Ductility-Dip Cracking in Ni-base Weld Metals** Ductility-dip cracking (DDC) can be a serious weldability issue in many Ni-base weld metals, particularly in thick-section multipass welds where restraint levels are high. An example of DDC in a thick-section weld made with Filler Metal 52 is shown in Figure 3.47. Three weld passes from this multipass weld are shown, with severe cracking occurring in the second pass. The inset photomicrograph shows a higher magnification of the cracked region and reveals that cracking has occurred along the weld metal migrated grain boundaries. Note that the grain size is quite large and that in some cases, very fine grains are present along the large grain boundaries. This is presumably due to recrystallization



(a)



(b)

**Figure 3.47** Ductility-dip cracking in a thick-section, multipass weld made with Filler Metal 52, a) photomicrograph showing 3 passes from the multipass weld, b) higher magnification of pass 2 showing severe DDC and recrystallization along the migrated grain boundaries (arrows).

resulting from high strain concentration along these boundaries at elevated temperature. This local recrystallization phenomenon is not normally observed in weld metals susceptible to DDC, but is indicative of the high local strains at grain boundaries that promotes DDC in these weld metals.

As noted in the previous section, ductility-dip cracking is a grain boundary phenomenon and in Ni-base weld metals cracking is always observed along migrated grain boundaries (see Figures 3.2 and 3.3). As described in Section 3.3.1.1, weld metal migrated grain boundaries are high angle, crystallographic boundaries that form from parent solidification grain boundaries in the solid state. In single phase austenitic materials, these boundaries are readily detected in the microstructure following metallographic polishing and etching. Examples of weld metal migrated grain boundaries in Filler Metals 82 and 52 are shown in Figure 3.48. Note that the appearance of these boundaries is quite different due to grain boundary “pinning” that occurs at elevated temperature. In the Filler Metal 82 weld metal, formation of NbC at the end of solidification via

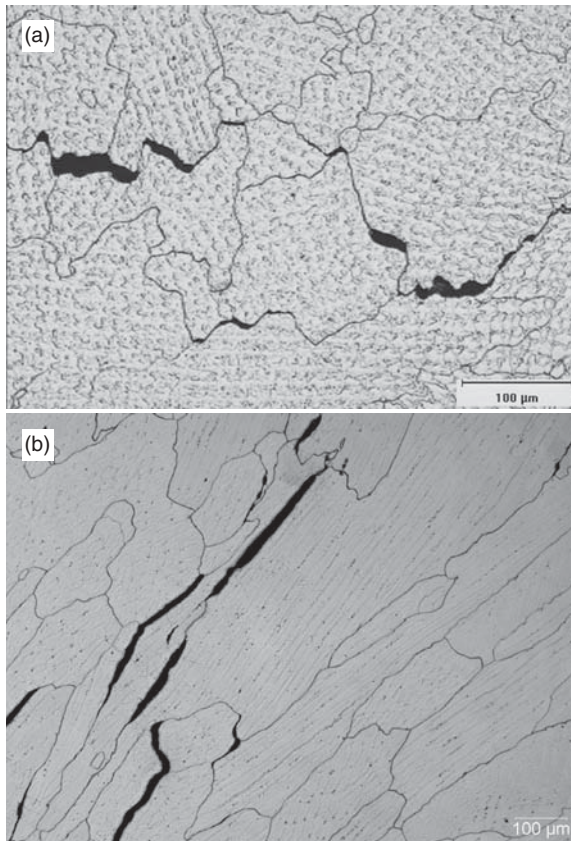


**Figure 3.48** Ductility-dip cracks in Ni-base weld metals, a) Filler Metal 82, and b) Filler Metal 52.

a eutectic reaction (see Section 3.3.1.2) provides the pinning agent that results in the development of “tortuous” grain boundaries. In contrast, Filler Metal 52 weld metal boundaries are quite straight since this weld metal forms no elevated temperature precipitate capable of pinning the migrated grain boundaries. The importance of grain boundary pinning through proper filler metal design will be discussed in more detail in Section 3.5.4.4, Avoiding Ductility-dip Cracking.

A number of tests have been used to determine susceptibility to DDC. Most prevalent are the hot ductility test, the double-spot Varestraint test, and the strain-to-fracture test. The hot ductility and strain-to-fracture tests are described in some detail in Chapter 8. The double-spot Varestraint test was originally developed by Lippold *et al.* (95) in order to isolate DDC from solidification cracking during standard transverse Varestraint testing. With this test, an initial gas tungsten arc spot weld was applied to a sample and then a second spot weld applied within this initial weld upon performing a standard spot Varestraint test (see Chapter 8). Weld metal DDC could then be generated in the initial spot weld upon the application of sufficient strain. While this was an improvement over the standard Varestraint test, there were still three major complicating issues:

- 1) weld metal liquation cracking and DDC could not be separated,
- 2) it was difficult to determine the temperature range over which cracking occurred, and
- 3) some materials only exhibited DDC at the highest achievable strain (~10%).

Despite these issues, the double-spot Varestraint test did provide some useful DDC susceptibility data for a number of Ni-base filler metals. For example, Kikel and Parker (96) were able to compare the DDC susceptibility of Filler Metal 52 and Alloy 690 with that of Filler Metals 82 and 625.

The strain-to-fracture test was developed by Nissley and Lippold (97) to avoid the shortcomings of the Varestraint and hot ductility tests for determining susceptibility to DDC. The details of the test are provided in Chapter 8. This is a Gleeble-based test that allows weld or base metals to be evaluated using microstructure, strain, and temperature as the principal variables. Using this test, strain-temperature envelopes can be developed that show the regime over which DDC occurs for a given material. Examples of such data for weld metals of Filler Metals 52, 52M, and 82 are shown in Figure 3.49. As is typical of DDC in Ni-base alloys and stainless steels, a steep drop in ductility occurs between 650° and 800°C (1200° and 1470°F). A ductility minimum occurs between 850° and 1050°C (1560° and 1920°F) and then there is a gradual increase in ductility above 1050°C.

Relative susceptibility to DDC can be determined by the minimum threshold strain for cracking across the entire temperature range and the severity of cracking above the threshold strain. For example, in Figure 3.49 the minimum

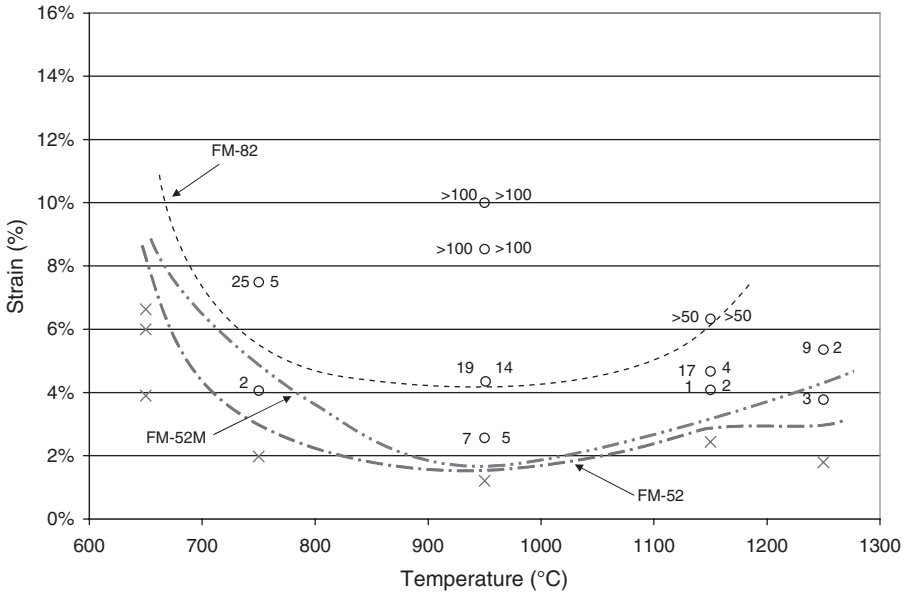


**Figure 3.49** Strain-to-fracture tests results for Filler Metals 82, 52 and 52M. The “X” symbols represent no cracks and the “O” symbols represent cracking at a given temperature-strain combination. The lines indicate the threshold strain for fracture for each weld metal and the numbers represent the number of cracks observed. (From Lippold and Nissley [98].)

threshold strain for Filler Metals 52 and 52M is slightly less than 2%, while that of Filler Metal 82 is over 4%. Although this difference in minimum threshold strain may seem small, actual practice has shown that weld metals with threshold strains between 4% and 6% are moderately susceptible to DDC, while those that exceed 6% tend to be quite resistant.

In essentially all of the Ni-base filler metals that have been tested using the strain-to-fracture test, the minimum threshold strain tends to fall very close to 950°C (1740°F). For this reason, simple screening of a number of weld metals can be conducted by testing at multiple strains at this single temperature. In this manner, the threshold strain and the severity of cracking as a function of increasing strain can be determined with just a few samples. In Figure 3.50, a number of commercial Ni-base filler metals are compared using this approach. For the 30 wt% chromium filler metals (52, 52M, Sanicro 68HP, and Sanicro 69HP), the threshold strains are all in the range from about 1% to 2.5%, while the threshold strain for Filler Metal 82 is approximately 4%. This predicts a higher DDC resistance for Filler Metal 82 which is consistent with fabrication experience in multipass, heavy section welding.

The data in Figure 3.50 also reveals considerable heat-to-heat variation for Filler Metal 52M. Note that the “C” heat of this filler metal exhibits a lower

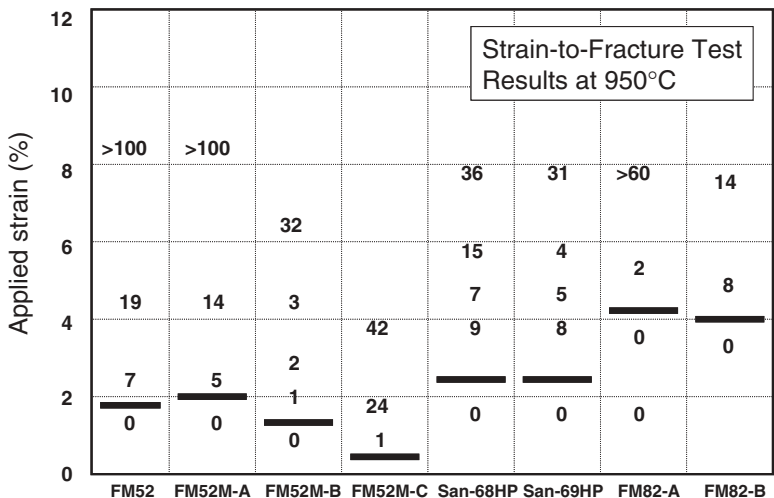


**Figure 3.50** Strain-to-fracture test results at 950°C for a number of Ni-base filler metals. The heavy horizontal line represents the threshold strain for cracking, while the numbers represent the number of cracks observed at a given strain. (From Lippold and Nissley [98].)

threshold strain for cracking and considerably higher cracking severity at 4% strain compared to heats A and B. This suggests that the strain-to-fracture test is sensitive enough to determine heat-to-heat variations in DDC susceptibility and can serve as a useful screening tool for assessing weldability.

At the time of this writing, two experimental high chromium filler metals have been tested that show remarkable improvement in DDC resistance relative to Filler Metals 52 and 52M. These filler metals contain 4wt% Mo and additions of Nb up to 2.5 wt%. Strain-to-fracture test results for these experimental filler metals at 950°C are shown in Figure 3.51 and compared to standard grades of Filler Metals 52, 52M, and 82.(98) Note the significant improvement in both threshold strain for cracking and crack severity for the experimental filler metals 52X-D and 52MSS (originally designated as 52X-H). The 52X-D filler metal (4Mo-1Nb) shows only a slight improvement in threshold strain for cracking relative to the 52 and 52M filler metals, but is remarkably resistant to severe cracking at strains above the threshold. The 52MSS filler metal (4Mo-2.5Nb) exhibits an extremely high threshold strain (~10%) and is resistant to severe cracking at strains exceeding 12%.

To further investigate the DDC resistance of the 52MSS filler metal, a full strain-to-fracture curve was developed and compared to those of Type 304L and Filler Metal 82, as shown in Figure 3.52. This data shows a lower threshold strain than that presented in Figure 3.51, but still predicts a high resistance to DDC. Filler Metal 82 is known to be resistant to DDC, except in cases where extremely high restraint is present. Austenitic stainless steel filler metals that

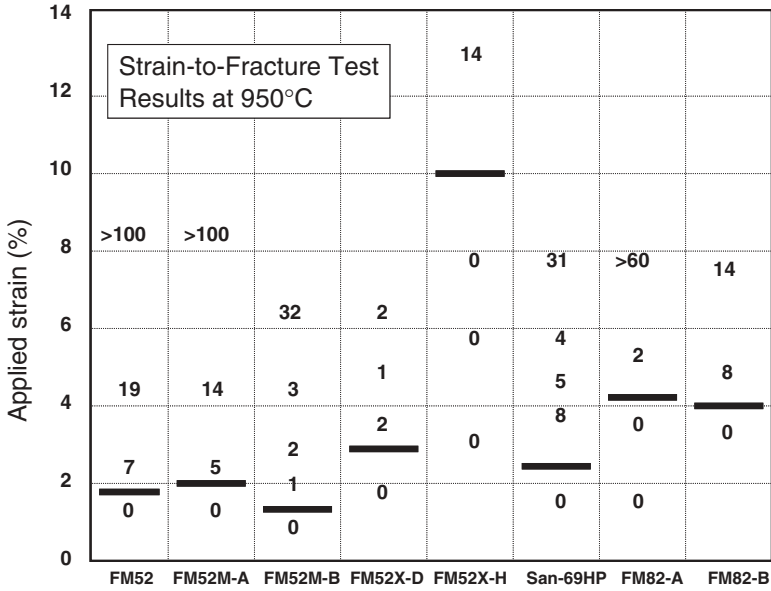


Figure 3.51 Strain-to-fracture test results at 950°C for two experimental high chromium filler metals as compared to Filler Metals 52, 52M, 82, and Sanicro 69HP. [98]

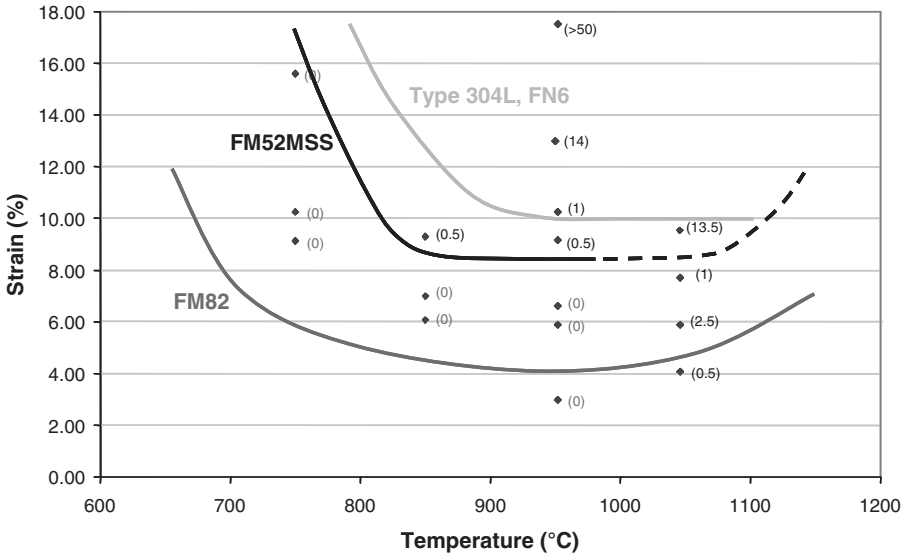


Figure 3.52 Comparison of strain-to-fracture results for Filler Metal 52XMSS with those of Type 304L (Ferrite Number 6) and Filler Metal 82 weld metal. (From Lippold and Nissley [98].)

contain ferrite at the level of Type 304L in Figure 3.52 are immune to DDC under all cases. Thus, the STF results for the 52MSS filler metal suggest a high resistance to DDC, even under high restraint conditions. The reasons for such high resistance are discussed in the following paragraphs.

DDC in Ni-base weld metals has been clearly shown to be associated with migrated grain boundaries (see Figures 3.47 and 3.48). Thus, it is essential to understand the nature of these grain boundaries in order to determine the mechanism of DDC. In high chromium weld metals, such as Filler Metals 52 and 52M, the weld metal grains are quite large and the boundaries relatively straight. When examined at high magnification in the scanning and transmission electron microscopes (SEM and TEM), these boundaries are generally found to be decorated with small carbides that are of the  $M_{23}C_6$  type. Examples of SEM and TEM images of migrated weld metal grain boundaries from Filler Metal 52 are shown in Figure 3.53. In contrast, filler metals that contain sufficient Nb will form NbC precipitates at the end of solidification. Since these precipitates are present at the end of solidification, they are able to pin the migrated grain boundaries and impede their motion away from the parent solidification grain boundary. The net effect of this “pinning” is to produce a boundary that is not straight, and referred to as “tortuous.” Examples of a tortuous migrated grain boundary in Filler Metal 82 as compared to a straight boundary characteristic of Filler Metal 52 are shown in Figure 3.54.(99)

To a first approximation, resistance to DDC in Ni-base weld metals can be significantly influenced by controlling the nature of grain boundary carbide precipitation. This is best illustrated by the schematic from Ramirez and Lippold shown in Figure 3.55.(84) In the case where no grain boundary carbides form, or when the carbides form at temperatures outside the DDC susceptibility range, the grain boundaries are quite straight and strain will accumulate at grain boundary triple points due to grain boundary sliding, as shown in Figure 3.55A. This has been verified in strain-to-fracture tests, where at strains just above the threshold strain for cracking, cracks first initiate at the triple points. In weld metals where carbides are present along the migrated grain boundaries upon the application of strain, strain will accumulate at the triple points and at the carbide/matrix interface, as shown in Figure 3.55B. In this case, the boundaries are still quite straight and susceptibility to DDC is expected to still be high.

When carbides form at the end of solidification and are present to pin the migrated grain boundaries, the strain distribution is altered dramatically as shown in Figure 3.55C. The tortuous grain boundaries that result from boundary pinning provide a mechanical locking of the boundaries that effectively oppose grain boundary sliding. Although DDC may still be possible, the strain required for crack initiation is much higher and the cracks tend to be much shorter. The DDC resistance of Filler Metal 82 and the 52MSS filler metal (Figures 3.51 and 3.52) can be directly attributed to the mechanical locking of grain boundaries to oppose elevated temperature grain boundary sliding. Thus, the addition of alloying elements, such as Nb, that promote the forma-

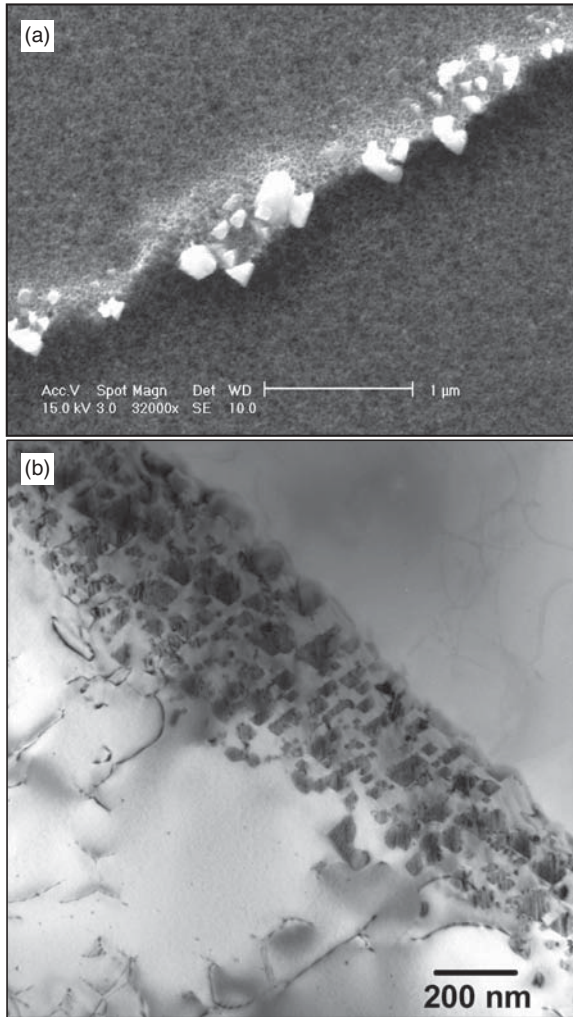


**Figure 3.53** Grain boundary carbides of the  $M_{23}C_6$  type in Filler Metal 52, a) SEM image, b) TEM image. (From Lippold and Nissley [98].) TEM image courtesy Dr. Antonio Ramirez.

tion of carbides at the end of solidification appear to be an effective method of improving DDC resistance in Ni-base filler metals.

The effect of Nb additions on grain boundary tortuosity in high-Cr, Ni-base filler metals was studied using electron backscattered diffraction (EBSD) in the SEM. (98,100) Using this technique, the high angle, migrated grains boundary can be mapped and their degree of tortuosity readily assessed. Figure 3.56 shows EBSD patterns for the 52MSS experimental filler metal and a standard Filler Metal 52M (FM52M-C) whose DDC susceptibility was shown in Figures 3.50 and 3.51. The extreme grain boundary tortuosity of the 2.5 wt% Nb con-



**Figure 3.54** SEM photomicrographs of weld metal migrated grain boundaries, a) Filler Metal 82 showing pinning by MC carbides, b) Filler Metal 52. (From Collins *et al.* [99]. Courtesy American Welding Society.)

taining filler metal is readily apparent when contrasted to the Filler Metal 52M grain boundary structure. Although Filler Metal 52M does contain some Nb (~1 wt%), this level is not sufficient to generate sufficient NbC precipitation at the end of solidification to promote grain boundary pinning. The relatively straight migrated grain boundaries that exist in weld deposits made using this filler metal make it inherently susceptible to DDC.

The effect of  $M_{23}C_6$  carbide precipitation on DDC susceptibility has been studied in some detail by Noecker and DuPont. (85,86) Their studies used Gleeble hot ductility testing to show that by controlling precipitation of  $M_{23}C_6$  along migrated weld metal grain boundaries in Filler Metal 52, improvement in DDC resistance could be achieved. This presumably occurs due to a microscopic grain boundary locking mechanism, whereby carbides of appropriate size and distribution can oppose grain boundary sliding. This may explain the beneficial effect of Mo additions to the experimental 52MSS filler metal. The

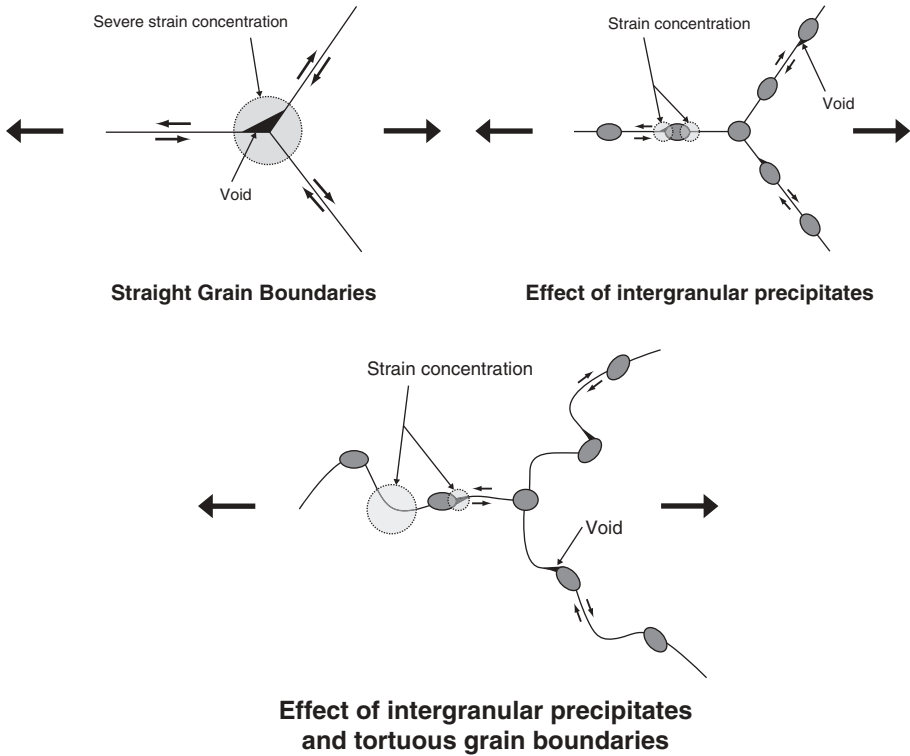


**Figure 3.55** Schematic showing grain boundary strain accumulation as a function of boundary geometry and precipitation behavior. (From Ramirez and Lippold [84].)

Mo may alter the nature of the  $M_{23}C_6$  precipitation such that it forms in a temperature range that is more beneficial to the locking of grain boundaries or that Mo acts as grain boundary strengthener to resist sliding and decohesion at elevated temperatures.

Young *et al.* (101) studied the DDC susceptibility of a wide range of Ni-Cr weld metals with Cr content in the range from 16–33 wt%. They propose that DDC in these weld metals results from the combination of macroscopic thermal and solidification stresses and local grain boundary stresses generated by precipitation of partially coherent  $(Cr,Fe)_{23}C_6$  carbides. This represents a form of precipitation-induced cracking via grain boundary misfit stresses that is compared to other sub-solidus cracking phenomena, such as strain-age cracking in Ni-base superalloys. They argue that the beneficial effects of Nb (or Ti) additions are to minimize grain boundary  $(Cr,Fe)_{23}C_6$  precipitation, rather than influence boundary tortuosity and grain boundary sliding.

It should be noted that other factors influence DDC susceptibility in Ni-base weld metals and have been summarized by Ramirez and Lippold. (84) Although impurity segregation to grain boundaries is not necessary to promote

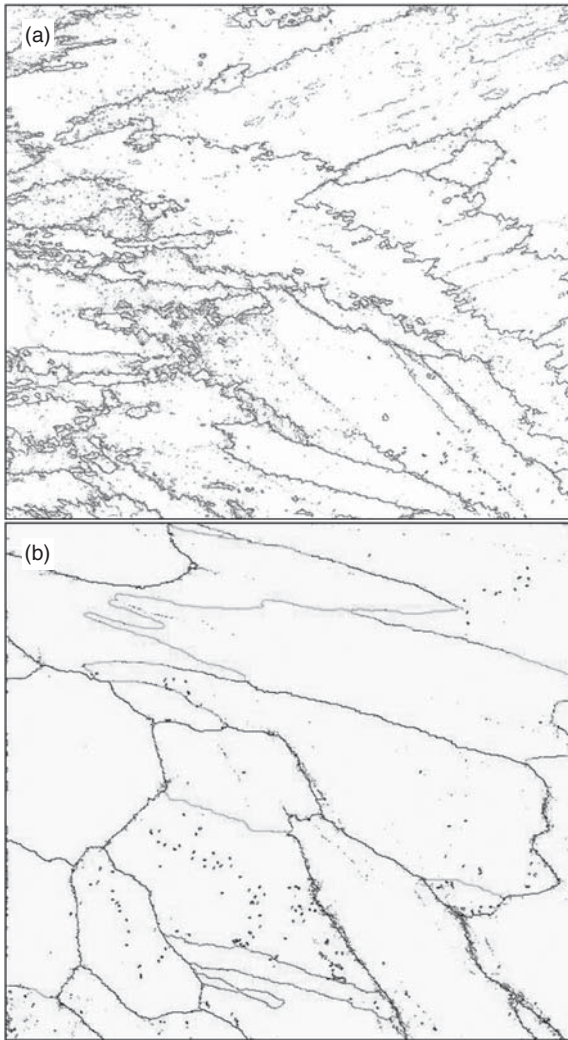


**Figure 3.56** Electron backscattered diffraction (EBSD) patterns showing the nature of the weld metal migrated grain boundaries in a) FM52X-H and b) FM52M-C from Figure 3.51. (From Lippold and Nissley [98].)

DDC, it has been shown to exacerbate DDC in some cases. Collins *et al.* (91,99) showed the deleterious effect of sulfur on DDC in Filler Metals 52 and 82, as did Nishimoto *et al.* (89) in their studies of Invar. Collins *et al.* (91) also showed that the use of hydrogen in argon shielding gas tends to increase susceptibility to DDC. This observation has been supported by industry experience, where changing from 98Ar-2H<sub>2</sub> shielding gas to 100% helium has resulted in a dramatic improvement in DDC resistance with Filler Metal 82. There is also some

evidence that oxygen may contribute to DDC (100), although the effect of this element has not been clearly identified.

**3.5.4.4 Avoiding Ductility-Dip Cracking** DDC has become a particularly difficult problem in applications where high-Cr (~30 wt%), Ni-base consumables are required to provide corrosion compatibility with high-Cr base metals, such as Alloy 690. In applications, that do not require this level of corrosion resistance, consumables such as Filler Metals 82 and 625 will usually be effective in avoiding DDC. (Note that this may not be true in heavy section, multipass welds.) Both these consumables contain sufficient Nb to ensure that NbC forms at the end of solidification, thus promoting weld metal microstructures with tortuous grain boundaries that are resistant to DDC.

When use of resistant filler metals is not an option, precautions should be taken to minimize weld restraint through either joint design or process variables. While not particularly attractive from a productivity standpoint, the use of small stringer beads that minimize the overall heat input in large weldments can help reduce susceptibility to DDC. As noted in the previous section, the use of argon-hydrogen shielding gases tends to increase susceptibility to DDC. These shielding gas mixtures have been recommended because they improve the wetting characteristics of many Ni-base filler metals and help prevent lack-of-fusion defects. The use of pure argon or helium shielding gases will generally improve resistance to DDC, but may not be effective in totally eliminating it.

Ultimately, filler metals must be designed that are resistant to DDC by the formation of weld metal microstructures that resist elevated temperature grain boundary sliding. The 52MSS (Ni-30Cr-4Mo-2.5Nb) filler metal discussed in the previous section shows considerable promise in terms of generating such a microstructure, but research must continue to better understand the underlying mechanism. It should be noted that while the addition of Nb appears promising with regards to the improvement in DDC resistance, the formation of low melting Nb-rich eutectic constituents potentially increases susceptibility to weld solidification cracking (see Section 3.5.1) It is likely that a careful balance will have to be maintained so as not to solve one weldability problem while creating another.

## 3.6 CORROSION RESISTANCE

The compositions of many commercial solid-solution strengthened Ni-base alloys are provided in Tables 3.1–3.3. The corrosion rates of several nickel-base alloys in the corrosion environments in which they are commonly used are presented in Table 3.19. The galvanic series for several base and weld metals in both seawater at 25 °C (77 °F) and brine at 67 °C (152 °F) are shown in Tables 3.20 and 3.21, respectively.

**TABLE 3.19 Corrosion Resistance of Several Nickel Alloys.**

Alloy/Consumable	Environment	Performance
Ni200/FM 61/FM99 <sup>a</sup>	23% NaOH at 220 °F (104 °C)	0.16 mpy (0.004 μm/y)
	75% NaOH at 400 °F (204 °C)	0.8 mpy (0.020 μm/y)
Ni-Cu400/FM60/WE190	60–65% HF <sup>b</sup> at 60–80 °F (15–27 °C)	22 mpy (0.56 μm/y)
Alloy 600 <sup>c</sup> /FM82	80% NaOH at 572 °F (300 °C)	<1 mpy (<0.025 μm/y)
Alloy 625/FM625	25% P <sub>2</sub> O <sub>5</sub> + 2% HF (boiling)	2 mpy (0.05 μm/y)
Alloy C-276	40% NH <sub>4</sub> H <sub>2</sub> PO <sub>4</sub> at 200 °F (93 °C)	<2 mpy (<0.05 μm/y)
Alloy C-22	Green Death <sup>d</sup> at 125 °C	0.87 mm. max. depth
Alloy C-2000	Green Death at 125 °C	0.70 mm. max. depth
Alloy 686/686CPT	Green Death at 125 °C	no attack

a) FM99 is needed for highest concentration of NaOH.

b) Acid contains 1.5–2.5% fluosilicic acid, 0.3–1.25% sulfuric acid, and 0.01–0.03% iron.

c) Alloy 600 stress-relieved to avoid SCC.

d) 11.9% H<sub>2</sub>SO<sub>4</sub> + 1.3% HCl + 1% FeCl<sub>3</sub> + 1% CuCl<sub>2</sub>.

**From:** High-Performance Alloys for Resistance to Aqueous Corrosion, Special Metals, SMC026/9M/2000 and Corrosion Data Survey-Metals Section Sixth Edition, 1985 NACE publication.

**TABLE 3.20 Galvanic Series for Several Ni-base Alloys in Synthetic Seawater at 25 °C.**

Voltage (a)	Material
	Cathode (protected)
+0.25	FM 625 (ERNiCrMo-3)
0	
-1.25	Cast 400 (b)
-1.50	Wrought 400
	WE 190 (ENiCu-7)
-1.60	FM 60 (ERNiCu-7)
	Anode (Corroded)

(a) Voltage vs. SCE (Saturated Calomel Electrode).

(b) Cast 400 was produced by induction melting a small piece of wrought Alloy 400.

**TABLE 3.21 Galvanic Series for Several Ni-base Alloys in Brine at 67 °C.**

Voltage (a)	Material
	Cathode (protected)
-1.25	FM 625 (ERNiCrMo-3)
-1.40	Wrought 400
-1.50	ENiCrFe-2
-1.70	WE 190 (ENiCu-7)
-1.80	Cast 400 (b)
-3.25	FM 60 (ERNiCu-7)
	Anode (Corroded)

(a) Voltage vs. SCE (Saturated Calomel Electrode).

(b) Cast 400 was produced by induction melting a small piece of wrought Alloy 400.

Commercially pure nickel, including Alloy 200 (previously known as “A nickel”) is used primarily in the production and storage of caustics such as sodium hydroxide. Since the nominal carbon content of Alloy 200 (0.07 wt%) exceeds the solubility limit, this alloy cannot be used at temperatures above about 315 °C (600 °F) due to the formation of graphite in the matrix. For this reason, Alloy 201 was created which has a maximum 0.02 wt% carbon making it suitable for higher temperatures in similar environments. Alloy CZ100 is the cast equivalent of Alloy 200 with similar, but not equivalent, properties. In order to produce sound castings, the silicon content is elevated to enhance fluidity during casting. Additionally, much higher carbon and manganese are added for deoxidation and cracking resistance. Nickel 205, 211, and 233 are slight modifications of 200 and 201, developed to provide specific characteristics for electrical and electronic applications. Nickel 253 and 270 are ultra-pure variations made from carbonyl nickel pellets with the latter being produced by powder techniques. Weldability of these ultra pure nickel alloys is compromised by their extreme susceptibility to hot cracking when contaminated with even minute amounts of sulfur or other commonly encountered minor elements. They are also quite susceptible to DDC.

The 400-series of nickel alloys are used for general corrosion resistance in marine environments, pickling equipment, salt production equipment including evaporators and piping, and architectural applications. In addition to these applications, the nickel-copper family of materials is used extensively in applications that require resistance to sulfuric, hydrofluoric, phosphoric, and organic acids. Alloy 401 has reduced nickel for cost savings along with lower carbon and iron. Alloy 404 has all elements other than nickel and copper held to low levels for improved brazeability and Alloy 405 has a significant addition of sulfur (0.025–0.060%) for improved machinability. Note that M25S and M35–2 are the cast equivalents of the nickel-copper alloys and both have substantial additions of silicon to enhance fluidity during casting.

A number of the nickel-chromium and nickel-chromium-iron alloys are listed in Table 3.2. These alloys are primarily used for high temperature applications requiring high temperature corrosion resistance and strength. Alloy 600 is the original oxidation and carburization resistant nickel alloy which has been used for decades for thermal processing fixtures and equipment. With a 72% minimum nickel content, it resists carburization and with 15% chromium, it has suitable oxidation resistance for many thermal processing tasks. Alloy 600 is also used for high temperature handling of caustics. Alloy 601 was developed with increased chromium and an Al addition to enhance higher temperature oxidation resistance with some nickel being replaced with iron in order to make the alloy more affordable. Alloy 601 has useful oxidation resistance to 1260 °C (2300 °F). Alloy 693 has higher Cr with other additions for improved high temperature oxidation and chloridation resistance along with intermediate temperature metal dusting resistance in environments with high carbon activities.

The iron-nickel-chromium alloys including Alloys HP, 800 and 800H are all high temperature alloys, except for Alloy 825 which is an aqueous corrosion resisting alloy noted for its sulfuric acid resistance and resistance to chloride ion stress corrosion cracking. Alloy HP is one of a series of cast high carbon nickel chromium alloys that offers good creep strength for elevated temperature applications such as hydrogen reformers and ethylene pyrolysis furnaces.

The nickel-chromium-molybdenum alloys listed in Table 3.2 are all designed for aqueous corrosion resistance except for Alloy 617. Alloy 617 and associated consumables shown in Table 3.4 are designed for high temperature strength and corrosion resistance and rely on cobalt, molybdenum and chromium for very high creep strength. The other alloys which contain higher levels of molybdenum and sometimes tungsten are designed specifically for localized (pitting and crevice) corrosion resistance. Alloys such as C-276, C-22, C-2000, Alloy 59 and Alloy 686 exhibit excellent pitting and crevice corrosion resistance which makes them suitable for service in demanding applications such as wet limestone scrubbers that are used to remove  $\text{SO}_2$  from flue gas in fossil-fired power boilers. These applications represent corrosion environments of greater than 100,000ppm  $\text{Cl}^-$  along with oxidizing species such as ferric and cupric chloride in very low pH conditions including a wide variety of concentrations of sulfuric acid.

The corrosion resistance of welds in solid-solution strengthened alloys is generally lower than that of their wrought counterparts. This can be attributed to several factors. The fusion zone will contain concentration gradients and interdendritic secondary phases that form due to solute redistribution during solidification. These gradients and secondary phases can lead to accelerated localized corrosion. The exact location of attack within the microstructure depends largely on the alloy and environmental conditions. For example, alloy-depleted dendrite core regions are often selectively attacked under HCl reducing environments, oxidizing environments containing nitric acid, and high temperature sulfur bearing gases associated with coal combustion conditions.(102,103) Other environments, such as those containing  $\text{HNO}_3$  and HF, have been observed to selectively attack the interdendritic phases.(104) In either case, the relative reduction in corrosion resistance compared to the base metal is associated with the presence of concentration gradients and interdendritic phases.

The fusion zone corrosion resistance can often be improved by postweld heat treatment (PWHT). With this approach, proper time and temperatures must be selected for adequate diffusion in order to eliminate the gradients. Techniques for making estimates of proper PWHT schedules based on knowledge of diffusivity data and dendrite arm spacing were described in Section 3.3.3. When second phase dissolution is also required, the PWHT has the added requirement of being conducted above the solvus temperature of the precipitate. Under conditions where stress corrosion cracking is a concern, the presence of residual stress can often accelerate cracking in the weld

relative to that of the base metal. In this case, PWHT can be conducted to relieve the residual stress. As described in Section 3.3.3, stress relaxation techniques are a fairly simple means for identifying adequate time and temperatures for effective stress relief.

Cortial *et al.*(42) investigated the influence of PWHT on the corrosion resistance of welds in Alloy 625. Heat treatment temperatures from 600-to-1000°C (1110-to-1830°F) were evaluated with an eight-hour hold time. The microstructural changes and mechanical property variations associated with these treatments were described in Section 3.4. Resistance to intergranular corrosion was found to be adversely affected by the presence of the  $\gamma''$  and  $\delta$  interdendritic phases. The  $\gamma''$  phase was observed to form in the range from 700-to-750°C (1290-to-1380°F), while the  $\delta$  phase formed between 850° and 950°C (1560-to-1740°F). As a result, resistance to intergranular corrosion after PWHT in the 700-to-950°C range was reduced relative to the as-welded condition due to increased amounts of  $\gamma''$  and  $\delta$ . At a PWHT of 1000°C (1830°F), the intergranular corrosion resistance returned to a level similar to that of the as-welded condition due to dissolution of the  $\gamma''$  and  $\delta$  phases.

Pitting corrosion was not observed in any condition up to a test temperature of 90°C (195°F). At 95°C (205°F), pitting was observed in samples in the as-welded condition as well as samples heat treated in the range of 600-to-850°C (1110-to-1560°F). At PWHT temperatures above 950°C (1740°F), the pitting resistance improves, which is attributed to homogenization. PWHT temperatures at 850°C and below did not have a significant effect on homogenization, while temperatures above 950°C resulted in nearly complete homogenization. Calculation of the residual index of segregation for the slowest diffusing element (Mo) using Equation 3.9 for the observed dendrite arm spacing of ~10 $\mu$ m yields values of  $\delta \approx 0.1$  for 950°C/8 hour and  $\delta \approx 0.8$  for an 850°C/8 hour treatment. Thus, results from Equation 3.9 are in line with the experimental observations of homogenization.

It is interesting to compare the effect of PWHT on residual stress relief, mechanical properties, and corrosion resistance for welds in Alloy 625 in view of identifying the optimum PWHT schedule. PWHT temperatures above ~870°C (1600°F) for times longer than ~0.5 hour are required for significant stress relief (see Section 3.3.3). However, the impact energy and intergranular corrosion resistance are adversely affected in this range due to the formation of the  $\delta$ -phase (Section 3.4). A PWHT temperature of 1000°C (1800°F) restores toughness and intergranular corrosion resistance, but the restoration is still slightly below or similar to that of the as-welded condition, and the yield strength is reduced relative to the as-welded condition.

In terms of pitting corrosion resistance, a PWHT at ~950°C (1740°F) and above is beneficial due to homogenization. These results highlight the importance of selecting the appropriate PWHT schedule based on the particular application. In conditions in which resistance to pitting corrosion or SCC is the primary concern, the reduction of residual stress, lower yield strength, and homogenized microstructure are important and require the use of a PWHT

above  $\sim 950^{\circ}\text{C}$ . On the other hand, if corrosion and localized cracking issues are not a concern and the ambient temperature mechanical properties control performance, the use of a PWHT appears to have little benefit.

In many cases, particularly for field fabrication, PWHT is not an option. An alternative approach to PWHT for homogenization is to use consumable selection to choose a weld metal that can accept dilution from the base metal being welded while providing greater corrosion resistance to the proposed environment than that of the base metal in the as-welded condition. There are numerous examples beginning with the use of Alloy 625 for welding 904L, 317L, or Alloy 825. In each case, the Alloy 625 weld provides greater pitting and crevice corrosion resistance in the as-welded condition than do the base metals. When the “superaustenitics” such as AL6XN were introduced, Alloys 625 and 112 (for SMAW) were used extensively, until the base metal manufacturers found that higher amounts of nitrogen boosted the pitting resistance. It was discovered later that the Nb in 625 and 112 could lead to niobium nitrides aligned at the fusion boundary if the nitrogen were high enough, and meeting bend test requirements could be compromised. It was a relatively simple matter to substitute welding materials with higher corrosion resistance that contained W instead of Nb such as Alloy 622 and WE 122(NiCrMo-10) or even 686CPT products (NiCrMo-14).

Figure 3.57 compares the corrosion rates of Alloy 22 base metal and welds in the ASTM G28A test. This test consists of a 24 hour immersion in a boiling

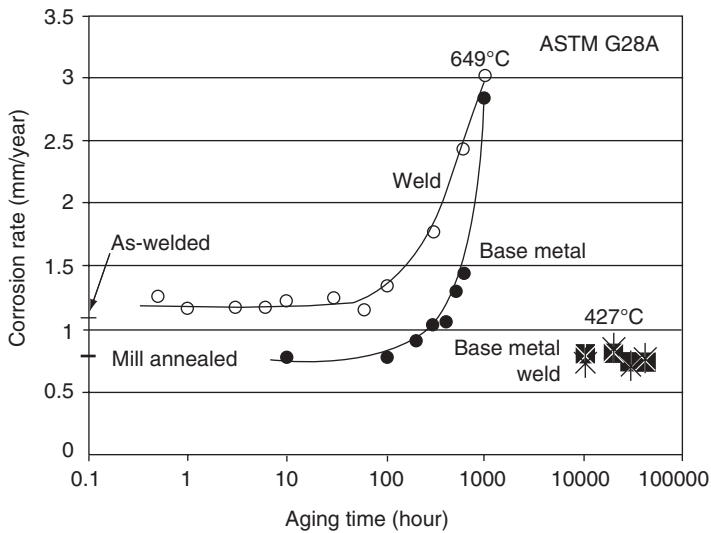


**Figure 3.57** Corrosion rates of Alloy 22 base metal and welds from ASTM G28 tests. (From Edgecumbe-Summers *et al.* [44].)

solution of 50% sulfuric acid ( $\text{H}_2\text{SO}_4$ ) and 42 g/l of ferric sulfate ( $\text{Fe}_2(\text{SO}_4)_3$ ). The results are shown as a function of aging time and temperature. The weld metal corrosion rate is initially higher than the base metal, and this reduced corrosion resistance is attributed to the presence of TCP phases in the weld. The base metal and weld corrosion rates increase with increasing aging time when heat treated at 649°C (1200°F) due to TCP formation. The corrosion behavior of the base and weld metal becomes comparable at the longest aging times and higher temperatures, presumably because the amount of TCP phase in each specimen is similar at the longer times. Very little difference between the weld and base metal is observed at the lower temperature of 427°C (800°F), and aging has little effect at the times investigated. This probably occurs because TCP formation kinetics are extremely slow at this lower temperature. As previously explained, the TCP phases can be dissolved in Alloy 22 with proper selection of heat treatment schedules. Complete TCP dissolution in welds of Alloy 22 has been shown to occur in the range from 1075-to-1121°C (1965-to-2050°F) for 24 hours and in the range from 1200-to-1300°C (2190-to-2370°F) for 20 minutes.

### 3.7 CASE STUDIES

#### 3.7.1 Pitting Corrosion in MONEL® Welds

The possibility of galvanic corrosion sometimes calls for careful selection of higher alloy consumables relative to the base metal. Examples of Ni-Cu alloys in seawater when welded with “matching composition” Ni-Cu consumables are shown in Figure 3.58.(105) This shows a corner weld from a shipboard desalination unit fabricated using Alloy 400 made with GTAW using ERNiCu-7 that has suffered severe pitting of the weld metal with little attack in the Alloy 400 base metal. Figure 3.58B shows a cross-section of the weld with severe pitting, and Figure 3.58C shows the pitting of the weld at the fusion boundary and only general corrosion of the Alloy 400. A brief corrosion study produced the galvanic series in synthetic seawater at 25°C (77°F) that is shown in Table 3.20. Further corrosion studies prompted by galvanic corrosion in salt producing equipment produced the galvanic series for saturated brine at 67°C (152°F) shown in Table 3.21. The result of each study of galvanic effects was the selection of NiCrMo-3 consumables for welding Alloy 400 in order to deposit a weld metal that was cathodic to the base metal. A salt plant constructed in Coatzacoalcos, Mexico used 160,000 pounds of Alloy 400 welded exclusively with NiCrMo-3 welding consumables in order to avoid galvanic attack associated with “matching composition” consumables. The NiCrMo-3 consumables have become standard choices for most types of salt plant equipment fabricated using Alloy 400 including evaporators, pumps, valves and classifiers.

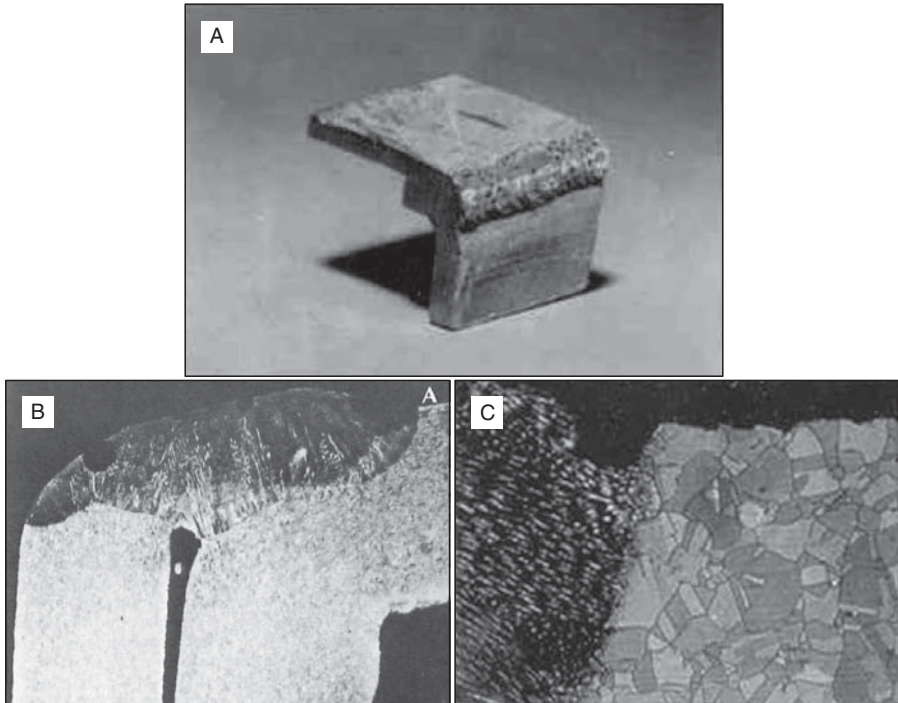


**Figure 3.58** Corrosion of an Alloy 400/ERNiCu-7 weld in seawater. a) Corner joint from seawater distillation unit, b) cross section showing pitting attack, and c) local attack at the fusion boundary.

## REFERENCES

1. Lippold, J. C., Clark, W. A. T., and Tumuluru, M. 1992. An investigation of weld metal interfaces. *The Metal Science of Joining*, published by The Metals, Minerals and Materials Society, Warrendale, PA, pp. 141–146.
2. Brody, H. D. and Flemings, M. C. 1966. Solute redistribution in dendritic solidification, *Transactions of AIME*, 236(5): 615–624.
3. Scheil, E. 1942. *Z. Metallkde*, 34: 70–77.
4. Cieslak, M. J. 1991. The welding and solidification metallurgy of Alloy 625, *Welding Journal*, 70(2): 49s–56s.
5. Cieslak, M. J., Headley, T. J., Knorovsky, G. A., Romig, A. D., and Kollie, T. 1990. A comparison of the solidification behavior of incoloy 909 and inconel 718, *Metallurgical Transactions A*, 21A: 479–488.
6. Cieslak, M. J., Headley, T. J., Kollie, T., and Romig, A. D. 1988. A melting and solidification study of Alloy 625, *Metallurgical Transactions A*, 19A: 2319–2331.
7. Cieslak, M. J., Headley, T. J., and Romig, A. D. 1986. The welding metallurgy of Hastelloy alloys C-4, C-22, and C-276, *Metallurgical Transactions A*, 17A: 2035–2047.

8. Cieslak, M. J., Knorovsky, G. A., Headley, T. J., and Romig, A. D. 1986. The use of New PHACOMP in understanding the solidification microstructure of nickel base alloy weld metal, *Metallurgical Transactions A*, 17A: 2107–2116.
9. DuPont, J. N. 1998. A combined solubility product/New PHACOMP approach for estimating temperatures of secondary solidification reactions in superalloy weld metals, *Metallurgical and Material Transactions*, 29A: 1449–1456.
10. DuPont, J. N., Michael, J. R., and Newbury, B. D. 1999. Welding metallurgy of alloy HR-160, *Welding Journal*, 78(12): 408s–414s.
11. DuPont, J. N., Robino, C. V., and Marder, A. R. 1998. Solidification of Nb-bearing superalloys: Part II. pseudo ternary solidification surfaces, *Metallurgical and Material Transactions A*, 29A: 2797–2806.
12. DuPont, J. N., Robino, C. V., Marder, A. R., Notis, M. R., and Michael, J. R. 1988. Solidification of Nb-bearing superalloys: Part I. reaction sequences, *Metallurgical and Material Transactions A*, 29A: 2785–2796.
13. Knorovsky, G. A., Cieslak, M. J., Headley, T. J., Romig, A. D., and Hammeter, W. F. 1989. Inconel 718: A solidification diagram, *Metallurgical Transactions A*, 20A: 2149–2158.
14. Lienert, T. J., Robino, C. V., Hills, C. R., and Cieslak, M. J. 1990. A welding metallurgy study of Hastelloy alloys B-2 and W, *Trends in Welding Research I*, ASM International, Materials Park, OH, pp. 159–165.
15. Perricone, M. J., DuPont, J. N., and Cieslak, M. J. 2003. Solidification of Hastelloy Alloys: An alternative interpretation, *Metallurgical and Materials Transactions A*, 34A: 1127–1132.
16. Perricone, M. J. 2003. *Microstructural development of superaustenitic stainless steel and Ni base alloys in castings and conventional arc welds*, PhD Thesis, Lehigh University, Bethlehem, PA.
17. Robino, C. V., Michael, J. R., and Cieslak, M. J. 1997. Solidification and welding metallurgy of thermo-span alloy, *Science and Technology of Welding and Joining*, 2(5): 220–230.
18. Rowe, M. D., Crook, P., and Hoback, G. L. 2003. Weldability of a corrosion resistant Ni-Cr-Mo-Cu alloy, *Welding Journal*, 82(11): 313s–320s.
19. Susan, D. F., Robino, C. V., Minicozzi, M. J., and DuPont, J. N. 2006. A solidification diagram for Ni-Cr-Mo-Gd alloys estimated by quantitative microstructural characterization and thermal analysis, *Metallurgical and Material Transactions A*, 37A: 2817–2825.
20. Joo, H. and Takeuchi, H. 1994. Cast structure of Inconel 713C alloy, *Tokai Daigaku Kiyō*, 34(1): 203–209.
21. Heubner, U., Kohler, M., and Prinz, B. 1988. Determination of the solidification behavior of some selected superalloys, *Superalloys 1988*, TMS, Warrendale, PA, 18–22 Sept. pp. 437–447.
22. Banovic, S. W. and DuPont, J. N. 2003. Dilution and microsegregation in dissimilar metal welds between super austenitic stainless steels and Ni base alloys, *Science and Technology of Welding and Joining*, 6(6): 274–383.
23. Clyne, T. W. and Kurz, W. 1981. Solute redistribution during solidification with rapid solid-state diffusion, *Metallurgical Transactions A*, 12A: 965–971.

24. Perricone, M. J. and DuPont, J. N. 2005. Effect of composition on the solidification behavior of several Ni-Cr-Mo and Fe-Ni-Cr-Mo alloys, *Metallurgical and Material Transactions A*, 37A: 1267–1289.
25. Baker, H. Ed. 1992. *Alloy phase diagrams*, ASM Handbook, ASM International, Materials Park, OH.
26. Choi, I. D., Matlock, D. K., and Olson, D. L. 1988. The influence of composition gradients on tensile properties of weld metal, *Acta Metallurgica*, 22: 1563–1568.
27. Tuma, H., Vyklicky, M., and Loebel, K. 1970. Activity and solubility in austenitic chromium-nickel steels with about 18wt% Cr, *Arch Eisenhüttenwes*, 40(9): 727–731.
28. Lippold, J. C. 1984. An investigation of weld cracking in Alloy 800, *Welding Journal*, 63(3): 91s–103s.
29. Ramirez, A. J. and Lippold, J. C. 2004. High temperature behavior of Ni-base weld metal Part I. Ductility and microstructural characterization, *Materials Science and Engineering A*, 380: 259–271.
30. DuPont, J. N., Robino, C. V., and Marder, A. R. 1988. Modeling solute redistribution and microstructural development in fusion welds of Nb bearing superalloys, *Acta Metallurgica*, 46(13): 4781–4790.
31. DuPont, J. N., Robino, C. V., and Marder, A. R. 1988. Solidification and weldability of Nb-bearing superalloys, *Welding Journal*, 77: 417s–431s.
32. Williams, K. J. 1971. The 1000°C isotherm of the Ni-Si-Ti system from 0 to 16% Si and 0 to 16% Ti, *Journal of the Institute of Metals*, 99: 310–315.
33. Markiv, V. Y. and Gladyshevskiy, E. I. 1966. Phase equilibria in the Ti-Co-Si system, *Russian Metallurgy*, 3: 118–121.
34. DuPont, J. N., Robino, C. V., Mizia, R. E., and Williams, D. B. 2004. Physical and welding metallurgy of Gd-enriched austenitic alloys for spent nuclear fuel applications—part II: nickel base alloys, *Welding Journal*, 83(11): 289s–300s.
35. El-Dasher, B. S., Edgecumbe, T. S., and Torres, S. G. 2006. The effect of solution annealing on the microstructural behavior of Alloy 22 welds, *Metallurgical and Material Transactions A*, 37A: 1027–1038.
36. Was, G. S. 1990. Grain boundary chemistry and intergranular fracture in austenitic nickel-base alloys; a review, *Corrosion*, 46(4): 319–330.
37. Ernst, S. C. 1993. Postweld heat treatment of nonferrous high temperature materials, *ASM Handbook*, Vol. 6, ASM International, Materials Park, OH, 572–574.
38. Diehl, M. J. and Messler, R. W. 1995. Using stress relaxation tests for evaluating and optimizing postweld heat treatments of alloy 625 welds, *Welding Journal*, 74(5): 109s–114s.
39. Kattamis, T. Z. and Flemings, M. C. 1965. Segregation in Castings, *Transactions of AIME*, 233: 992–999.
40. DuPont, J. N. 2007. *Unpublished research on homogenization treatments of high alloy castings and welds, unpublished research*, Lehigh University.
41. Young, G. A., Battige, C. K., Lewis, N., Penik, M. A., Kikel, J., Silvia, A. J., and McDonald, C. K. 2003. Factors affecting the hydrogen embrittlement resistance of Ni-Cr-Mn-Nb welds, *6th Int. Trends in Welding Research*, ASM International, pp. 666–671.

42. Cortial, F., Corrieu, J. M., and Vernot-Loier, C. 1995. Influence of heat treatment on microstructure, mechanical properties, and corrosion resistance of weld alloy 625, *Metallurgical and Material Transactions A*, 26A: 1273–1286.
43. Kohler, M. 1991. Effect of the elevated temperature precipitation in alloy 625 on properties and microstructure, *Superalloys 718, 625, and Various Derivatives*, (E. A. Loria, Editor), TMS, Warrendale, PA, pp. 363–373.
44. Edgecumbe-Summers, T. S., Rebak, R. B., and Seeley, R. R. 2000. *Influence of thermal aging on the mechanical and corrosion properties of C-22 alloy welds*, Lawrence Livermore National Laboratory UCRL-JC-137727.
45. Brown, C. M. and Mills, W. J. 1999. Effect of water on mechanical properties and stress corrosion behavior of Alloy 600, Alloy 690, FM 82H, and FM 52 welds, *Corrosion*, 55(2): 173–186.
46. Garud, Y. S. and Gerber, T. L. 1983. Intergranular stress corrosion cracking of Ni-Cr-Fe alloy 600 tubes in PWR primary water—review and assessment for model development. Palo Alto, CA. EPRI Report NP-3057.
47. Webb, G. L. and Burke, M. G. 1995. *Stress corrosion cracking behavior of alloy 600 in high temperature water, Seventh International Symposium on Environmental Degradation of Materials in Nuclear Power Systems—Water Reactors*. Vol. I; Breckenridge, CO; USA; 7–10 Aug. 1995. 1–56.
48. Maguire, M. C. and Headley, T. J. 1990. A weldability study of Haynes alloy 242, *Weldability of Materials*, ASM International, Materials Park, OH, pp. 167–173.
49. Clyne, T. W. and Kurz, W. 1982. The effect of melt composition on the solidification cracking of steel, with particular reference to continuous casting, *Metallurgical Transactions B*, 13A: 259–266.
50. Matsuda, F., Nakagawa, H., Katayama, S., and Arata, Y. 1982. Weld metal cracking and improvement of 25% Cr-20% Ni (AISI 310S) fully austenitic stainless steel, *Transactions of the Japan Welding Society*, 13: 41–58.
51. Kelly, T. J. 1990. Rene 220C—the new, weldable, investment cast superalloy, *Welding Journal*, 69(11), 422s–430s.
52. Cieslak, M. J., Stephens, J. J., and Carr, M. J. 1988. A study of the weldability and weld related microstructure of Cabot Alloy 214, *Metallurgical Transactions A*, 19A: 657–667.
53. Savage, W. F., Nippes, E. F., and Goodwin, G. M. 1977. Effect of minor elements on hot-cracking tendencies of Inconel 600, *Welding Journal*, 56(8): 245s–253s.
54. Lingenfelter, A. C. 1972. Vareststraint testing of nickel alloys, *Welding Journal*, 51(9): 430s–436s.
55. Lippold, J. C., Sowards, J., Alexandrov, B. T., Murray, G. and Ramirez, A. J. 2008. *Weld solidification cracking in Ni-base alloys, Hot Cracking Phenomena in Welds II*, Springer, ISBN 978-3-540-78627-6, pp. 147–170.
56. Alexandrov, B. T. and Lippold, J. C., 2006. In-situ weld metal continuous cooling transformation diagrams, *Welding in the World*, 50(9/10): 65–74.
57. Alexandrov, B. T. and Lippold, J. C. 2006. A new methodology for studying phase transformations in high strength steel weld metal, Trends in Welding Research VII, Proc. of the 7<sup>th</sup> International Conference, ASM International, pp. 975–980.
58. Scheil, E. 1942. *Zeitschrift fur Metallkunde*, 34: 70–74.

59. DuPont, J. N. and Robino, C. V. 2007. *Unpublished research on solidification and weldability of Alloy C-4 with Gd additions*, Lehigh University.
60. Vincent, R. 1985. Precipitation around welds in the nickel base superalloy inconel 718, *Acta Metallurgica*, 35(7): 1205–1216.
61. Rowe, M.D, Ishwar, V. R., and Klarstrom, D. L. 2006. Properties, weldability, and applications of modern wrought heat-resistant alloys for aerospace and power generation industries, *Trans. ASME*, 128: 354–361.
62. Gallagher, M. 2007. *Unpublished research performed at The Ohio State University*.
63. Lippold, J. C. and Kotecki, D. J. 2005. *Welding Metallurgy and Weldability of Stainless Steels*, pub. by Wiley and Sons, Inc. Hoboken, NJ, ISBN 0-47147379-0.
64. Lippold, J. C. 1983. An investigation of heat-affected zone hot cracking in alloy 800, *Welding Journal*, 62(1): 1s–11s.
65. Hondors, E. and Seah, M. P. 1984. *Physical Metallurgy* 3rd Ed., Amsterdam, New Hollan, pp. 855–933.
66. Lippold, J. C., Baeslack, W. A., and Varol, I. 1992. Heat-affected zone liquation cracking in austenitic and duplex stainless steels, *Welding Journal*, 71(1): 1–14.
67. Pepe, J. J. and Savage, W. F. 1970. The weld heat-affected zone of the 18Ni maraging steel, *Welding Journal*, 49(12): 545s–553s.
68. Pepe, J. J. and Savage, W. F. 1967. Effects of constitutional liquation in 18-ni maraging steel weldments, *Welding Journal*, 46(9): 411s–422s.
69. Duvall, D. S. and Owczarski, W. A. 1967. Further heat affected zone studies in heat resistant nickel alloys, *Welding Journal*, 46(9): 423s–432s.
70. Lin, W., Nelson, T. W., Lippold, J. C., and Baeslack, W. A. 1993. A study of the HAZ crack-susceptible region in Alloy 625. *International Trends in Welding Science and Technology*, Eds. S. A. David and J. M. Vitek, ASM International, Materials Park, OH, pp. 695–702.
71. Owczarski, W. A., Duvall, D. S., and Sullivan, C. P. 1966. A model for heat affected zone cracking in nickel base superalloys, *Welding Journal*, 45(4): 145s–155s.
72. Savage, W. F. and Krantz, B. M. 1966. An investigation of hot-cracking in Hastelloy X, *Welding Journal*, 45(1): 13s–25s.
73. Thompson, R. G. and Genculu, S. 1983. Microstructural evolution in the HAZ of Inconel 718 and correlation with the hot ductility test, *Welding Journal*, 62(12): 337s–345s.
74. Kelly, T. J. 1990. Welding metallurgy of investment cast nickel based superalloys, *Trends in Welding Research I*, ASM International, Materials Park, OH, pp. 151–157.
75. Lundin, C. D., Qiao, C. Y. P., and Swindeman, R. W. 1993. HAZ hot cracking behavior of HD 556 and Inconel 617, *International Trends in Welding Science and Technology*, Eds. S. A. David and J. M. Vitek, ASM International, Material Park, OH, pp. 801–806.
76. Richards, N. L. and Chaturvedi, M. C. 2000. Effect of minor elements on weldability of nickel base superalloys, *International Materials Reviews*, 45(3): 109–129.

77. Guo, Z., Chaturvedi, M. C., and Richards, N. L. 1998. Effect of nature of grain boundaries on intergranular liquation during weld thermal cycling of nickel base alloy, *Science and Technology of Welding and Joining*, 3(5): 257–259.
78. DuPont, J. N. 2000. *Unpublished research on solidification cracking susceptibility of stainless steels and nickel alloys*, Lehigh University.
79. Thompson, R. G., Cassimus, J. J., Mayo, D. E., and Dobbs, J. R. 1985. The relationship between grain size and microfissuring in Alloy 718, *Welding Journal*, 64(4): 91s–96s.
80. Haddrill, D. M. and Baker, R. G. 1965. Microcracking in Austenitic Weld Metal, *British Welding Journal*, 12(9).
81. Hemsworth, B., Boniszewski, T., and Eaton, N. F. 1969. Classification and definition of high temperature welding cracks in alloys. *Metal Construction & British Welding Journal*, pp. 5–16.
82. Bengough, G. D. 1912. A study of the properties of alloys at high temperatures, *Journal of the Institute of Metals*, VII: pp. 123–174.
83. Rhines, F. N. and Wray, P. J. 1961. Investigation of the intermediate temperature ductility minimum in metals, *Transactions of the ASM*, 54: 117–128.
84. Ramirez, A. J. and Lippold, J. C. 2004. High temperature cracking in nickel-base weld metal, Part 2—Insight into the mechanism, *Materials Science and Engineering A*, 380: 245–258.
85. Noecker, F. F. and DuPont, J. N. 2009. Metallurgical investigation into ductility dip cracking in Ni-based alloys, Part I, *Welding Journal*, 88(1): 7s–20s.
86. Noecker, F. F. and DuPont, J. N. 2009. Metallurgical investigation into ductility dip cracking in Ni-based alloys, Part II, *Welding Journal*, 88(3): 62s–77s.
87. Yamaguchi, S. 1979. Effect of Minor Elements on Hot Workability of Nickel-Base Superalloys, *Met. Technol.*, 6(5): 170–175.
88. Matsuda, F. 1984. Weldability of Fe-36% Ni alloy, II.-effect of chemical composition on reheated hot cracking in weld metal, *Trans. JWRI*, 13(2): 241–247.
89. Nishimoto, K., Mori, H., and Hongoh, S. 1999. *Effect of sulfur and thermal cycles on reheat cracking susceptibility in multipass weld metal of Fe-36% Ni alloy*, International Institute of Welding, IIW Doc. IX-1934-99.
90. Hirata, H. 2001. Mechanism of hot cracking in multipass weld metal of Fe-36%Ni Invar alloy, welding of Fe-36%Ni Invar alloy (I), *Quarterly Journal of the Japan Welding Society*, 19(4): 664–672.
91. Collins, M. G. and Lippold, J. C. 2003. An investigation of ductility-dip cracking in nickel-based filler metals—Part I, *Welding Journal*, 82(10): 288s–295s.
92. Zhang, Y. C., Nakagawa, H., and Matsuda, F. 1985. Weldability of Fe-36%Ni Alloy (Report VI), *Transactions of JWRI*, 14(5): 125–134.
93. Zhang, Y. C., Nakagawa, H., and Matsuda, F. 1985. Weldability of Fe-36%Ni Alloy (Report V), *Transactions of JWRI*, 14(2): 119–124.
94. Nissley, N. E., Collins, M. G., Guaytima, G., and Lippold, J. C. 2002. Development of the Strain-to-Fracture Test for Evaluating Ductility-Dip Cracking in Austenitic Stainless Steels and Ni-base Alloys, *Welding the World*, 46(7–8): 32–40.
95. Lippold, J. C. and Lin, W. 1994. *Unpublished research performed at Edison Welding Institute*.

96. Kikel, J. M. and Parker, D. M. 1998. Ductility dip cracking susceptibility of filler metal 52 and Alloy 690, Trends in Welding Research, Proceedings, 5th International Conference, Pine Mountain, GA, 757–762.
97. Nissley, N. E. and Lippold, J. C. 2003. Development of the strain-to-fracture test for evaluating ductility-dip cracking in austenitic alloys, *Welding Journal*, 82(12): 355s–364s.
98. Lippold, J. C. and Nissley, N. E. 2008. *Ductility dip cracking in high-Cr Ni-base filler metals, Hot Cracking Phenomena in Welds II*, Springer, ISBN 978-3-540-78627-6, pp. 409–426.
99. Collins, M. G., Ramirez, A., and Lippold, J. C. 2004. An investigation of ductility-dip cracking in Ni-base filler metals-Part 3, *Welding Journal*, 83(2): 39s–49s.
100. Nissley, N. 2006. *Intermediate temperature grain boundary embrittlement in Ni-base weld metal*. PhD Dissertation, The Ohio State University.
101. Young, G.A, Capobianco, T.E, Penik, M.A, Morris, B. W., and McGee, J. J. 2008. The mechanism for ductility dip cracking in nickel-chromium alloys, *Welding Journal*, 87(2): 31s–43s.
102. Kain, V., Sengupta, P., De, P. K., and Banerjee, S. 2005. Case reviews on the effect of microstructure on the corrosion behavior of austenitic alloys for processing and storage of nuclear waste, *Metallurgical and Materials Transactions A*, 36A: 1075–1084.
103. Luer, K. R., DuPont, J. N., Marder, A. R., and Skelonis, C. K. 2001. Corrosion fatigue of alloy 625 weld claddings exposed to combustion environments, *Materials at High Temperatures*, 18: 11–19.
104. Lee, H. T. and Kuo, T. Y. 1999. Effects of niobium on microstructure, mechanical properties, and corrosion behavior in weldments of alloy 690, *Science and Technology of Welding and Joining*, 4(4): 246–255.
105. Kiser, S. 1990. Nickel alloy consumable selection for severe service conditions, *Welding Journal*, 69(11): 30–35.

## **Precipitation-Strengthened Ni-base Alloys**

The combination of high strength and excellent corrosion resistance make the precipitation-strengthened Ni-base alloys unique among metal-based alloy systems. Without the development of these “superalloys” in the 1950s, the “jet age” as we now know it would not have been possible. While the ability to strengthen Ni-base alloys to very high levels via precipitation reactions is not unique to these alloys, maintaining a high fraction of this strength at over half their melting temperature is truly a remarkable characteristic and the key to their widespread use for elevated temperature applications.

The physical metallurgy of the precipitation-strengthened alloys is quite complex since these alloys contain a mixture of intentional additions for solid solution strengthening (Cr, Co, Fe, Mo, W, and Ta), precipitate formation (Ti, Al, and Nb), oxidation resistance (Cr, Al, and Ta), hot corrosion resistance (Cr, La, and Th), creep and stress-rupture properties (B and Zr), and intermediate temperature ductility (Hf). Not surprisingly, the welding metallurgy of these alloys is equally complex, since partitioning of these elements during solidification of the fusion zone can lead to the formation of eutectic-type constituents and secondary phases that are not normally observed in the base metal.

In the HAZ, segregation of alloying elements to the grain boundaries can promote liquation or precipitate formation that negatively influences weldability and mechanical properties of welded structures. Thus, it is not surprising that postweld heat treatment is often required to restore the properties of the weldment. Unfortunately, this can lead to further degradation in the weldability of some alloys through a phenomenon known as strain-age cracking, in which a combination of stress relief and precipitation promotes grain boundary cracking.

This chapter reviews the physical and mechanical metallurgy of the precipitation-strengthened “superalloys,” describes the welding metallurgy of

the fusion zone and HAZ, and provides an in depth discussion of the weldability issues associated with these alloys.

#### 4.1 STANDARD ALLOYS AND CONSUMABLES

Table 4.1 summarizes the compositions of a wide range of precipitation-strengthened Ni-base alloys. The compositions of several common filler metals are provided in Table 4.2. The welding consumables are generally similar in composition to the base metals. Initial development of these alloys dates back to 1926 when the Ni-Cu alloy K-500 was developed with Ti and Al additions to form the  $\gamma'$  precipitate. The same composition was used for a bare filler metal, which became known as FM 64. A coated electrode (WE 134) was also subsequently formulated for alloy K-500. The composition of these materials was simple compared to many modern alloys, but formed the basis for further development of many precipitation-strengthened alloys. Alloy K-500 became a popular propeller shaft alloy for sea-going vessels and was chosen by naval architects for its good torsional stiffness, toughness, and corrosion resistance in marine environments. Later, it was widely used for non-magnetic drill collars.

Permanickel 300 and Duranickel 301 were developed for good hardness and wear resistance coupled with high thermal conductivity. Initially, Alloy 301 was used for glass molds with particular cooling requirements such as cathode ray tube molds. Later, Duranickel 301 was discovered to be an excellent arc spray wire. This alloy was used with the thermal spray process as an arc metalizing wire, which took advantage of the exothermic reaction of aluminum (at 5 wt%) being rapidly oxidized in air. This resulted in a significant increase in bond strength over previously used Ni-bearing spray wires. Permanickel was invented in the late 1930s followed closely by Nimonic 80A in 1941 and Alloy X-750 in 1944. The companion welding products for X-750 were Filler Metal 69 and Welding Electrode 139.

Numerous NIMONIC alloys and other Ni-Cr alloys were developed soon after X-750, including the early casting alloys. Many of these casting alloys were considered virtually unweldable due to large additions of Al + Ti that caused hardening during cooling from the casting temperature. Alloy 713 was created in 1956 and used extensively as a turbine blade alloy. In 1962 one of the most widely used alloys, Alloy 718, was invented by H. L. Eiselstein and US patent # 3,046,108 was granted in 1963. This alloy was hardened primarily by the use of Nb that promoted  $\gamma''$  ( $\text{Ni}_3\text{Nb}$ ) formation. The relatively slow precipitation kinetics of  $\gamma''$  formation (compared to  $\gamma'$  formation) contributed to improved weldability and better resistance to strain-age-cracking during postweld heat treatment. More than 50% of commercial superalloy production was devoted to Alloy 718 by 2006.(1)

Beginning with Nimonic 80A, Ni-Cr alloys began to be developed with additions of cobalt as a high temperature matrix stiffener. René 41, Nimonic

**TABLE 4.1 Compositions (wt%) of Typical Precipitation-Strengthened Nickel-base Alloys.**

Type	UNS	C	Cr	Fe	Mn	Ni	Mo	Ti	Al	Other
K500	N05500	0.25	—	2.00	1.50	63.0–70.0	—	0.35–0.85	2.3–3.15	Cu Bal.
300	N03300	0.40	—	0.60	0.50	97.0Min	—	0.20–0.60	—	Mg 0.2–0.5
301	N03301	0.30	—	0.60	0.50	93.0Min	—	0.25–1.0	4.0–4.75	Si 1.0
80A	N07080	0.10	18.0–21.0	3.0	1.0	Bal.	—	1.8–2.7	1.0–1.8	Co 2.0
X-750	N07750	0.08	14.0–17.0	5.0–9.0	1.0	70.0Min	—	2.25–2.75	0.4–1.0	Nb 0.7–1.2
90	N07090	0.13	18.0–21.0	3.0	1.0	Bal.	—	1.8–3.0	0.8–2.0	Co 15.0–21.0
263	N07263	0.04–0.08	19.0–21.0	0.7	0.60	Bal.	5.6–6.1	1.9–2.4	0.3–0.6	Co 19.0–21.0
713	N07713	0.08–0.20	12.0–14.0	2.50	0.25	Bal.	3.8–5.2	0.5–1.0	5.5–6.5	Nb 1.8–2.8
718	N07718	0.08	17.0–21.0	Bal.	0.35	50.0–55.0	2.8–3.3	0.65–1.15	0.2–0.8	Nb 4.75–5.50
Waspaloy	N07001	0.03–0.10	18.0–21.0	2.00	1.00	Bal.	3.5–5.0	2.75–3.25	1.2–1.6	Co 12–15
Rene 41	N07041	0.12	18.0–22.0	5.00	0.10	Bal.	9.0–10.5	3.0–3.3	1.4–1.8	Co 10.0–12.0
214	N07214	0.05	15.0–17.0	2.0–4.0	0.5	Bal.	0.5	0.5	4.0–5.0	Co 2.0
U520	N07520	0.06	18.0–20.0	—	—	Bal.	5.0–7.0	2.8–3.2	1.8–2.2	Co 12.0–14.0
702	N07702	0.10	14.0–17.0	2.0	1.0	Bal.	—	0.25–1.0	2.75–3.75	W 0.8–1.2
U720	N07720	0.03	15.0–17.0	—	—	Bal.	2.5–3.5	4.5–5.5	2.0–3.0	Cu 0.5
725	N07725	0.03	19.0–22.5	Bal.	0.35	55.0–59.0	7.0–9.5	1.0–1.7	0.35	Co 14.0–16.0
751	N07751	0.10	14.0–17.0	5.0–9.0	1.0	70.0Min	—	2.0–2.6	0.9–1.5	W 1.0–2.0
706	N09706	0.06	14.5–17.5	Bal.	0.35	39.0–44.0	—	1.5–2.0	0.40	Nb 2.75–4.0
925	N09925	0.03	19.5–23.5	22.0Min	1.00	38.0–46.0	2.5–3.5	1.9–2.4	0.1–0.5	Nb 0.7–1.2
945	N09945	0.04	19.5–23.0	Bal.	1.0	45.0–55.0	3.0–4.0	0.5–2.5	0.01–0.7	Nb 2.5–3.3
909	N19909	0.06	—	Bal.	—	35.0–40.0	—	1.3–1.8	0.15	Cu 1.5–3.0
										Co 12.0–16.0
										Nb 4.3–5.2
										Si 0.25–0.50

Single value is a maximum.

**TABLE 4.2 Compositions (wt%) of Typical Filler Metals Used for Welding Precipitation-Strengthened Ni-base Alloys.**

Type	UNS	C	Cr	Fe	Mn	Ni	Mo	Ti	Al	Other
FM64	N05500	0.25	—	2.00	1.50	63.0–70.0	—	0.35–0.85	2.3–3.15	Cu Bal.
FM69	N07750	0.08	14.0–17.0	5.0–9.0	1.0	70.0min	—	2.25–2.75	0.4–1.0	Nb 0.70–1.2
FM718	N07718	0.08	17.0–21.0	Bal.	0.35	50.0–55.0	2.8–3.3	0.65–1.15	0.2–0.8	Nb 4.75–5.50
FM725	N07725	0.03	19.0–22.5	Bal.	0.35	55.0–59.0	7.0–9.5	1.0–1.7	0.35	Nb 2.75–4.0
FM80A	N07080	0.10	18.0–21.0	3.0	1.0	Bal.	—	1.8–2.7	1.0–1.8	Co 2.0
FM90	N07090	0.13	18.0–21.0	3.0	1.0	Bal.	—	1.8–3.0	0.8–2.0	Co 15.0–21.0
FM263	N07263	0.04–0.08	19.0–21.0	0.7	0.60	Bal.	5.6–6.1	1.9–2.4	0.3–0.6	Co 19.0–21.0
FM909	N19909	0.06	—	Bal.	—	35.0–40.0	—	1.3–1.8	0.15	Co 12.0–16.0 Nb 4.3–5.2
625PLUS	N07716	0.03	19.0–22.0	Bal.	0.20	59.0–63.0	7.0–9.5	1.0–1.6	0.35	Si 0.25–0.50 Nb 2.75–4.00
Thermo-Span		0.05	5.0–6.0	30.3–36.7	0.50	23.5–25.5	—	0.7–1.0	0.3–0.6	Co 28.0–30. Nb 4.5–5.2 Si 0.2–0.3

Single value is a maximum.

90, Udimet 520 and 720 and Nimonic 263 are all examples of high temperature precipitation strengthened alloys with increasing amounts of cobalt. Alloys 725, 925 and 945 are alloys with good stress-corrosion-cracking resistance coupled with very high strength for use in sour gas and oil environments. They are very resistant to cracking in hydrogen sulfide and exhibit very slow crack growth rates in slow strain rate autoclave testing. Alloy 751 is a further development based on the X-750 composition that became a common choice for automotive exhaust valves due to good carburization resistance and stiffness.

Alloy 706 was a development based on alloy 718, and is used extensively for land-based gas turbine rotors. Alloys 706 and 718 are sometimes triple melted (vacuum induction melted, followed by electroslag remelting, followed by vacuum arc remelting) in order to produce very clean microstructures that provide good high cycle fatigue strength. Alloy 909 is the culmination of a family of low expansion, precipitation strengthened alloys used for gas turbine rings that require close tolerance sealing with rotating blade tips. In order to maintain the low thermal expansion characteristics, chromium is minimized and the alloy therefore requires oxidation protection before being placed into service. The weldability of the alloy family is good, and wire drawn from Alloy 909 became the choice for welding all of the low expansion turbine sealing alloys.

As discussed in more detail later in this chapter, the weld metals typically exhibit lower strength levels due to microsegregation. The weld metal mechanical properties can be improved by use of postweld solution annealing followed by a precipitation hardening treatment, in which the solution annealing treatment is effective at reducing the microsegregation effects. The creep strength and rupture lives of some alloys and consumables used for gas turbine applications were significantly improved by the additions of B and Zr. The mechanism of strengthening has been explained in terms of improved grain boundary strength and ductility. However, as discussed later in this chapter, it was discovered that the presence of even small amounts of B are extremely detrimental to the weldability and hot cracking resistance of Ni-base alloys.

## 4.2 PHYSICAL METALLURGY AND MECHANICAL PROPERTIES

The physical metallurgy of the precipitation-strengthened Ni-base alloys is somewhat similar to the solid-solution strengthened alloys discussed in Chapter 3 in that they consist of an austenite (fcc) matrix and contain many of the same secondary and intermetallic phases. The major differentiating factor between these systems is the addition of alloying elements that allow strengthening precipitates under appropriate heat treatment conditions. The primary strengthening precipitate is gamma-prime ( $\gamma'$ ), which forms due to the addition of Al and Ti and is of stoichiometry  $\text{Ni}_3(\text{Ti},\text{Al})$ . These alloys can also be strengthened by the formation of gamma-double prime ( $\gamma''$ ), which is usually

**TABLE 4.3 Summary of Strengthening Mechanisms in Ni-base Alloys and Elemental Effects. (From Decker and Mihalisin [2]).**

Strengthening Component	Elemental Effects
Solid Solution Strengthening of $\gamma$	W, Mo, Ti, Al, and Cr most effective
Solid solution strengthening of $\gamma'$	Mo, W, Si, Ti, Cr most effective
Amount of $\gamma'$	Cr, Ti, Al, Nb, Mo, Co, Ta, V, Fe increase amount
$\gamma/\gamma'$ Antiphase Boundary Energy	Ti, Co, Mo, Fe increase; Al and Cr decrease
$\gamma/\gamma'$ Lattice Mismatch	Ta, Nb, C, Ti increase; Cr, Mo, W, Cu, Mn, Si, V decrease
Coarsening Rate of $\gamma'$	Ti, Mo, Nb, Co, Fe, decrease; Cr increases

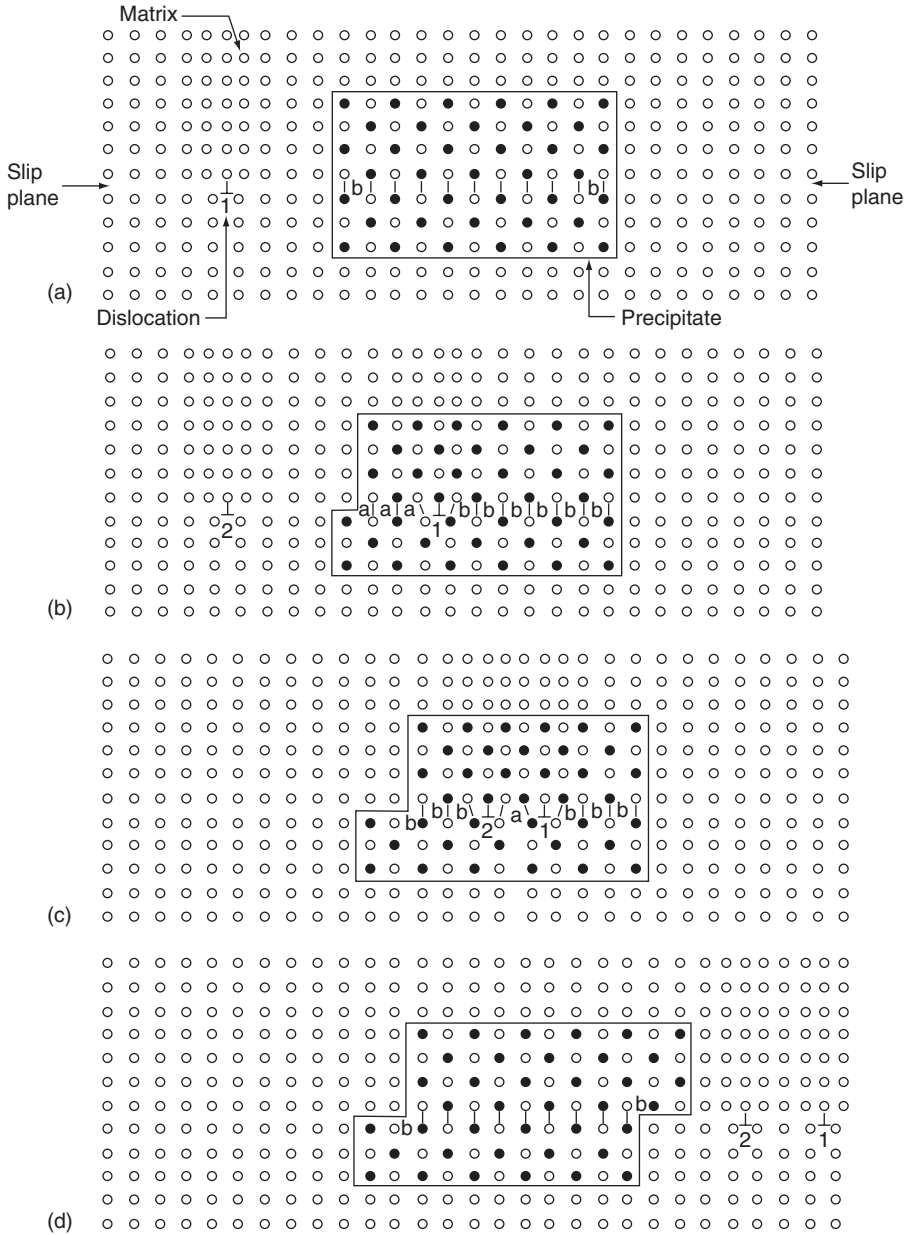
of the form  $\text{Ni}_3\text{Nb}$ . Because of the importance of these precipitates to the mechanical properties and weldability of these alloys, the following section provides a description of the precipitation behavior.

Ni-base alloys with  $\gamma'$ - $\text{Ni}_3(\text{Al},\text{Ti})$  precipitates are strengthened by a variety of mechanisms, as summarized in Table 4.3. This table also includes a description of the influence of various alloying elements.(2) The most important characteristic of these alloys is their ability to retain a high fraction of their room temperature strength at elevated temperatures by the formation of the ordered  $\gamma'$  precipitate. The ordered phase has the unusual characteristic of exhibiting an increase in yield strength with increasing temperature up to approximately  $800^\circ\text{C}$  ( $1470^\circ\text{F}$ ). (3) Although this phenomenon is not completely understood, the process is related, at least in part, to the interaction between dislocations and the  $\gamma'$  precipitates.

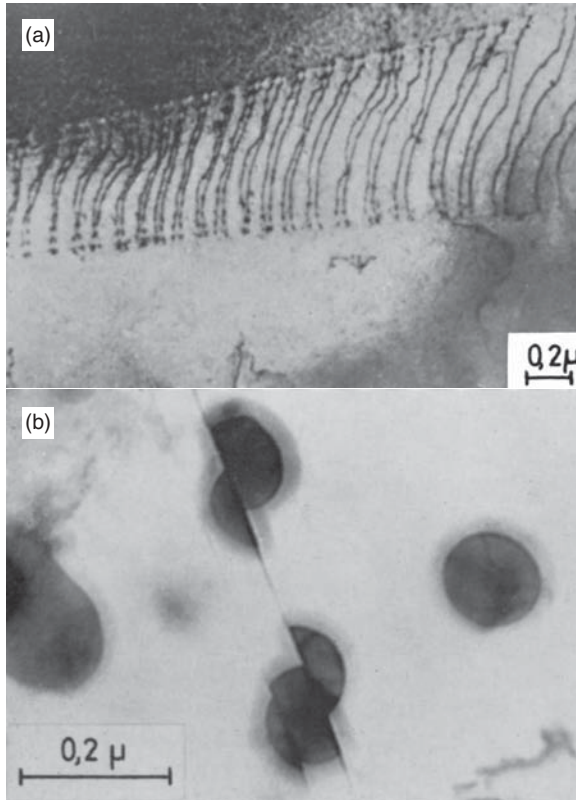
As shown schematically in Figure 4.1, the initial cutting of an ordered  $\gamma'$  precipitate by a single dislocation creates an antiphase boundary (APB) across the slip plane that represents an atomic layer of incorrect bonding. Subsequent movement of a second dislocation through the ordered phase restores the order (Figure 4.1b and c). Thus, dislocations are forced to travel in pairs (often referred to as superlattice dislocations) to maintain the ordered structure after precipitate cutting.

Figure 4.2 shows examples of these paired super lattice dislocations and  $\gamma'$  particle cutting in a Ni-base superalloy. This deformation involves cross-slip of segments of the superlattice dislocations from the  $\{111\}$  slip plane to  $\{001\}$  cross-slip plane. These cross-slipped segments resist deformation since they cannot move without forming an APB. The strengthening from this cross-slip becomes more important with increasing temperature because a component of the cross-slip is thermally activated.

The overall strength of the  $\gamma$ - $\gamma'$  alloy depends on a number of factors, including the ability to solid-solution strengthen both the  $\gamma$  and  $\gamma'$  phases, the amount of  $\gamma'$ , the  $\gamma/\gamma'$  antiphase boundary energy, and the  $\gamma/\gamma'$  lattice mismatch strain. The coarsening rate of the  $\gamma'$  is also important for components used for extended periods at high temperatures. These factors are described below.



**Figure 4.1** Schematic illustration of dislocations interacting with an ordered Ni<sub>3</sub>Al structure. (From Decker and Mihalisin [2])



**Figure 4.2** a) TEM photomicrograph showing paired super lattice dislocations in a nickel superalloys. b) TEM photomicrograph showing  $\gamma'$  precipitate cutting due to dislocations in a nickel superalloy. (From Decker and Mihalisin [2])

Figure 4.3 shows an example of the change in  $\gamma'$  precipitate morphology as a function of  $\gamma/\gamma'$  lattice mismatch in a Ni-base alloy.(4) The degree of lattice mismatch is noted in each figure. The shape of the precipitate will evolve in a manner that minimizes strain and surface energies. At small degrees of lattice mismatch, the strain energy is low and the most favorable shape that minimizes the surface energy is a sphere. At higher degrees of lattice mismatch, the strain energy becomes important and is orientation dependent. In this case, the orientation relationship between the  $\gamma$  and  $\gamma'$  promotes a cuboidal morphology, where the  $\gamma'$  precipitates typically align themselves along the  $\langle 100 \rangle$  directions of the matrix which have the lowest elastic stiffness. The precipitate morphology will also change as the precipitates coarsen. In this case, the starting morphology is typically spherical, but often gradually changes to cubes, arrays of cubes, and dendritic as coarsening proceeds. As discussed in more detail below, the lattice mismatch has important effects on long-term mechanical properties.

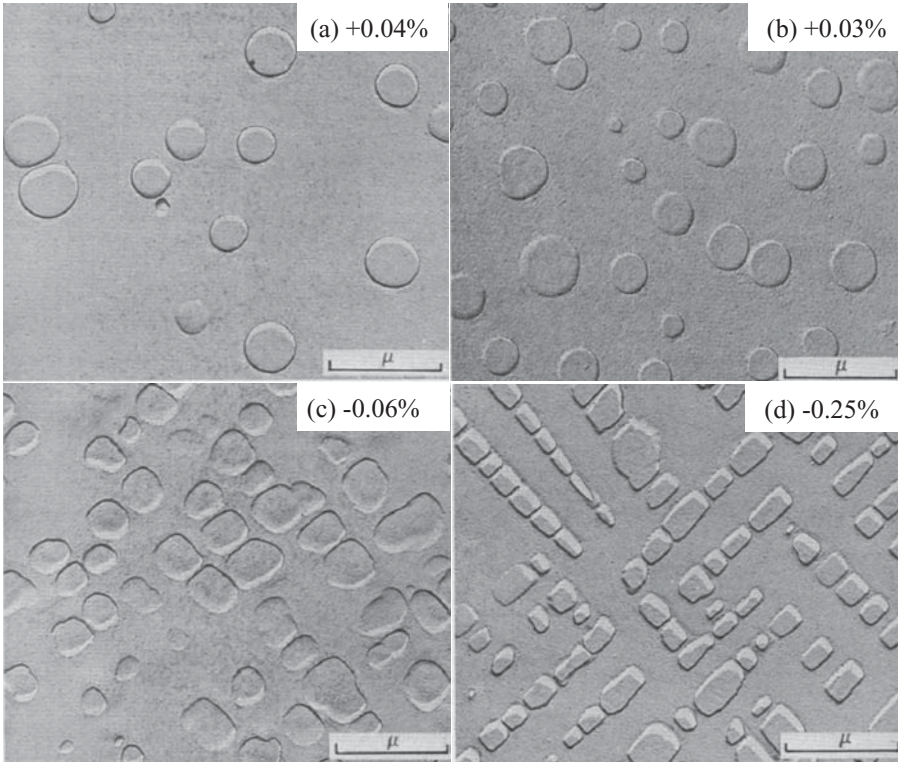


**Figure 4.3** Photomicrograph of  $\gamma'$  in a Ni-Al-Mo alloy at different lattice mismatches. (From Biss and Sponseller [4])

As described in Chapters 2 and 3, alloying elements that exhibit appreciable solubility in Ni combined with the ability to impart lattice mismatch strain are most effective for solid-solution strengthening of the austenite matrix. The elements W, Mo, Ti, Al, and Cr are most effective from this point of view. Although it is not often recognized, the  $\gamma'$  precipitate can also be hardened by solid solution strengthening. Figure 4.4a shows the solubility of various elements in  $\gamma'$  at 1150 °C (2100 °F), while Figure 4.4b shows the effect of several alloying additions on the hardness of  $\gamma'$  at 25 °C (75 °F).<sup>(5)</sup> Note that Mo imparts significant solid solution strengthening to  $\gamma'$ , but only small amounts of Mo will actually contribute to solid-solution strengthening due to its low solubility. The elements Cu, V, and Co exhibit appreciable solubility, but do not impart much strength to  $\gamma'$ . The elements Si, Ti, and Cr are most effective because they exhibit significant solubility and also provide a large increase in strength.

The effect of Al content on the volume fraction of  $\gamma'$  and 0.2% flow stress of a Ni-Cr-Al alloy at 25°, 500°, and 900 °C (75, 930 and 1650 °F) is shown in Figure 4.5.<sup>(6)</sup> These results were obtained at a constant Ni content of 75 wt%,

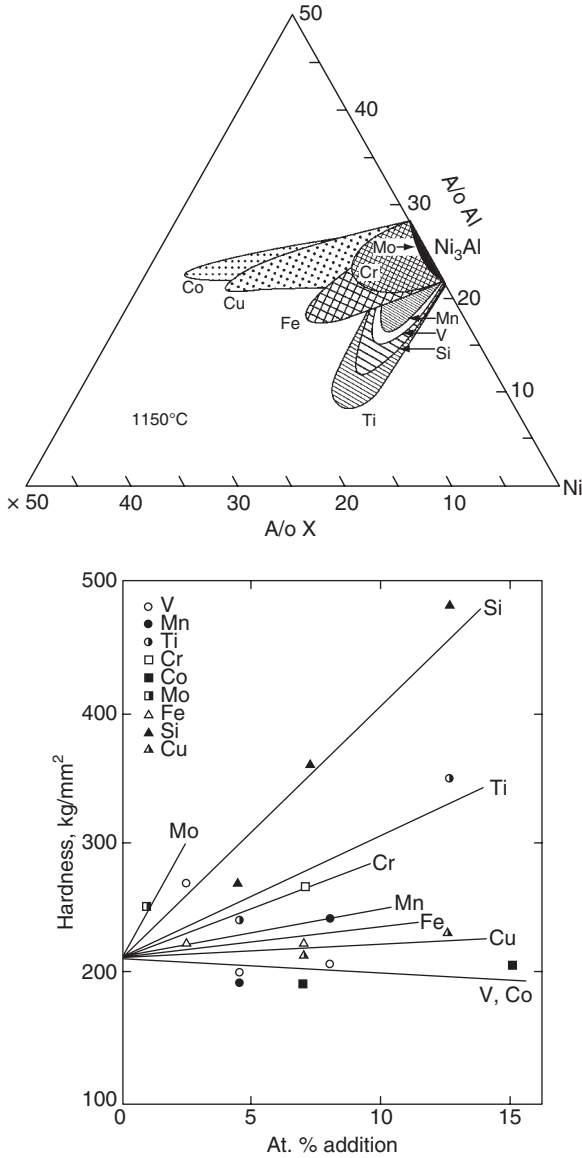


**Figure 4.4** a) Ni-Al-X systems at 1150°C showing solubility of various elements in  $\gamma'$ , b) Effect of various elements on the hardness of  $\gamma'$  at 25°C. (From Gaurd and Westbrook [5])

and the amount of  $\gamma'$  was varied by exchanging Cr for Al. Thus, there is also some effect of  $\gamma$  and  $\gamma'$  solid-solution strengthening from Cr in these results. At room temperature and 500°C (930°F), the strength peaks at approximately 25 volume percent  $\gamma'$ , while the strength continues to increase with increasing  $\gamma'$  content at 900°C (1650°F). This suggests that the direct use of  $\gamma'$  as an

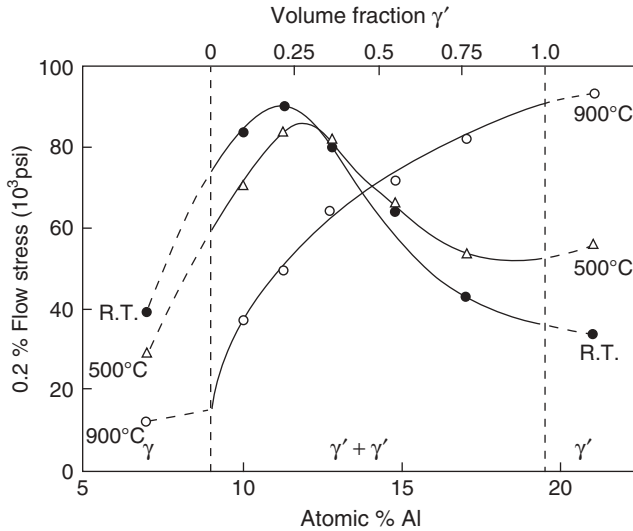


**Figure 4.5** Strength of a Ni-Cr-Al alloy at 25°C, 500°C, and 900°C as a function of  $\gamma'$  content. (From Beardmore *et al.* [6])

engineering alloy may be most effective at higher temperatures. However, the  $\gamma'$  phase is generally brittle and must be embedded in a ductile austenite matrix for adequate toughness and ductility. Although, as described in Chapter 5, work is in progress to develop more ductile ordered intermetallics for high temperature applications.

Many alloys have an upper limit of ~60 volume percent  $\gamma'$  (and a few even higher), but the amount of  $\gamma'$  required is typically application dependent. As shown in Figure 4.6, the creep strength increases with increasing  $\gamma'$  content (7), and thus higher  $\gamma'$  levels are often specified where creep strength is required. The actual amount of  $\gamma'$  will be dependent on the presence of other alloying elements and their associated effect on position of the  $\gamma/(\gamma + \gamma')$  phase boundary. In general, any element that reduces the size of the  $\gamma$  single phase field will lead to higher amounts of the  $\gamma'$  phase. Figure 4.7 shows the influence of total hardening addition on the volume fraction of  $\gamma'$  for several alloy compositions and indicates that Ti, Al, and Nb are each quite effective at increasing the amount of  $\gamma'$ . (8)

The initial cutting of an ordered  $\gamma'$  precipitate by a single dislocation requires an increase in force that is associated with formation of the antiphase boundary. Thus, as the antiphase boundary energy increases more force is required to cut the precipitate, resulting in an increase in strength. The antiphase boundary energy is a significant contribution to the overall strength, but measurements to determine the effect of individual alloying elements are difficult. The data available all suggest that Ti, Co, Mo, and Fe are effective at increasing antiphase boundary energy.

The lattice parameter of both the  $\gamma$  and  $\gamma'$  phases will depend on the amount and type of alloying elements in solution. As elemental additions are made to

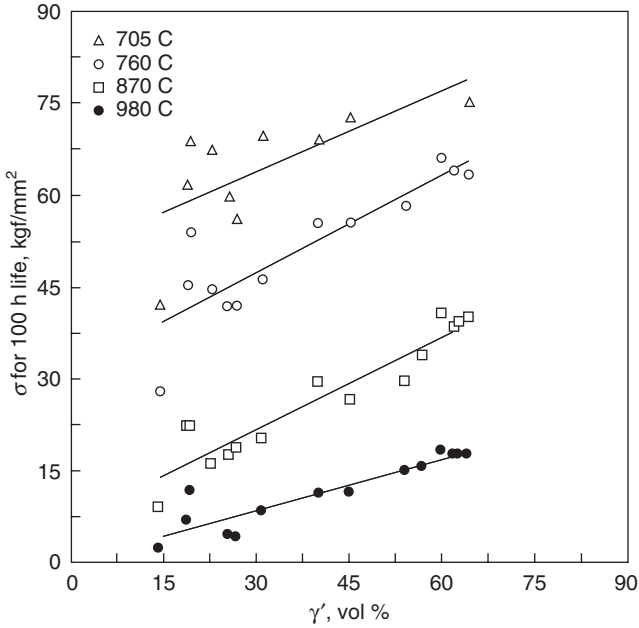


**Figure 4.6** The stress required for 100hr creep life as a function of volume percent  $\gamma'$  for several commercial alloys. (From Decker [7])

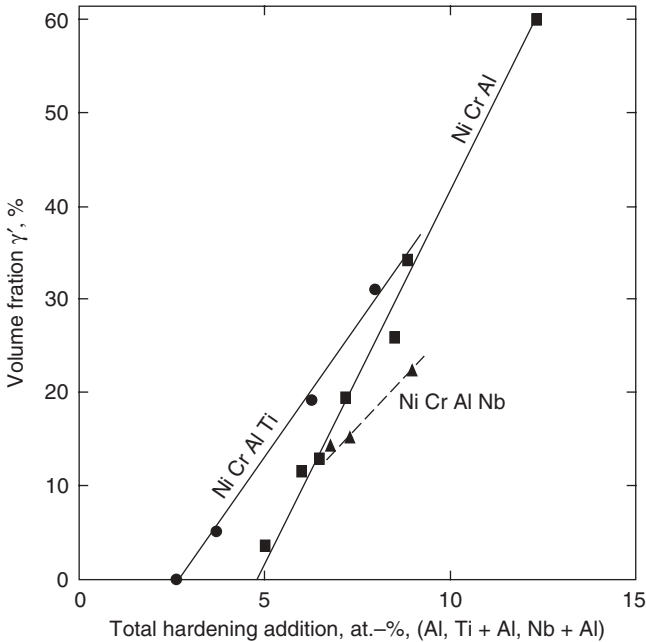


**Figure 4.7** Effect of Al, Ti, and Nb on the amount of  $\gamma'$  formed at 750°C in Ni-Cr-Al-Ti and Ni-Cr-Al-Nb alloys with constant Cr content of 20wt%. (From Gibbons and Hopkins [8])

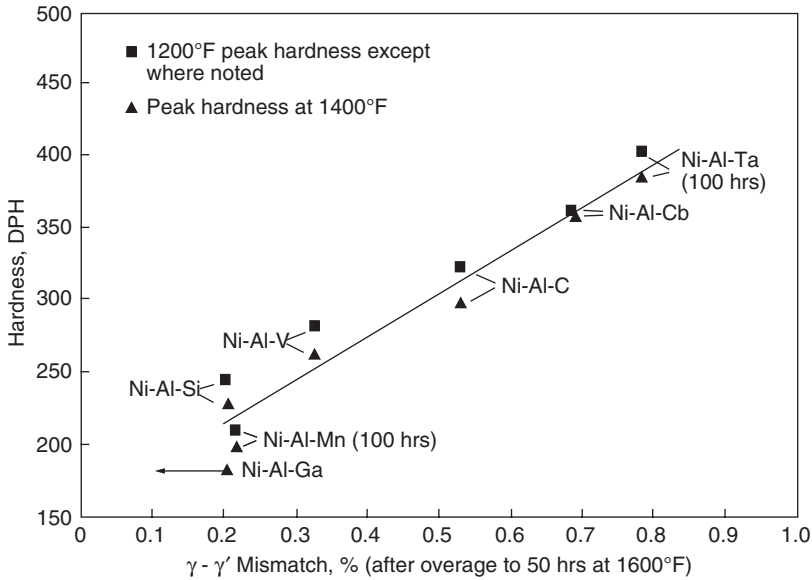


**Figure 4.8** Effect of  $\gamma/\gamma'$  mismatch on the peak hardness of several Ni-Al-X ternary alloys. (From Decker and Mihalisin [2])

an alloy, each element may partition differently to each phase and change the lattice parameter of each phase in a different way. The extent of  $\gamma/\gamma'$  lattice mismatch thus depends on the relative partitioning and lattice parameter changes induced by each alloying element. A useful summary of effects for various elements in Ni-Al-X ternary alloys is shown in Figure 4.8.(2)

This figure shows the peak hardness obtained at 1200°F (650°C) and 1400°F (760°C) as a function of the  $\gamma/\gamma'$  mismatch induced by the presence of various elements. Note that Ta, Cb (Nb), and C provide the most benefit. Ti is also known to have a strong effect on the mismatch as shown in Figure 4.9, which illustrates the effect of the Ti/Al ratio on the  $\gamma/\gamma'$  mismatch for Ni-20Cr-Al-Ti and Ni-20Cr-5Mo-Al-Ti alloys with a constant (Al + Ti) content of 3.5 wt%.(9) The mismatch increases considerably as Ti is substituted for Al in these alloys. The exact behavior of Ti and Al can sometimes be difficult to predict in more complex alloys. It should be noted that the degree of mismatch desired depends on the application. Higher mismatch is certainly desirable for improved strength for short term/high temperature applications or low temperature applications. However, as discussed below, a larger degree of mismatch also accelerates the coarsening rate of the  $\gamma'$  phase over time at elevated temperature, which will decrease strength and lead to decreased rupture life.

The nucleation and growth rate of each  $\gamma'$  particle precipitating in the  $\gamma$  matrix will not be identical during the heat treatment time. As a result, the  $\gamma'$  precipitates will exhibit a range of particle sizes and morphologies (see Figure 4.3). Once precipitation from the matrix by nucleation and growth is complete,

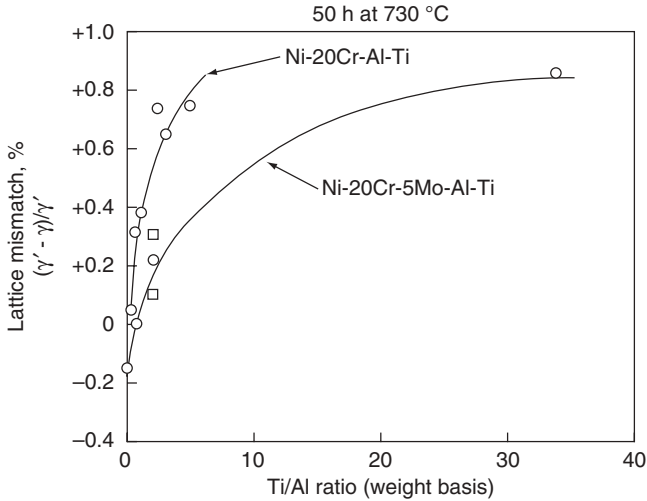


**Figure 4.9** Effect of Ti/Al ratio on the  $\gamma/\gamma'$  mismatch for Ni-20Cr-Al-Ti and Ni-20Cr-5Mo-Al-Ti alloys with a constant (Al + Ti) content of 3.5 wt%. (From Brooks [9])

this variation in particle size can cause precipitate coarsening. (Precipitate growth and coarsening processes can actually overlap in time, but most of the coarsening that occurs in service typically occurs after the nucleation and growth stages).

The process of precipitate coarsening is driven by the variations in particle size and concomitant variations in the matrix composition. The composition of the matrix in equilibrium with the precipitate is dependent on the precipitate size. The matrix in equilibrium with smaller particles has a higher solute concentration than the matrix in equilibrium with larger particles. This situation sets up a concentration gradient in the matrix, and solute will diffuse from the direction of the smaller  $\gamma'$  particles through the matrix toward the larger particles. This causes the smaller particles to shrink (and eventually dissolve) while the larger particles coarsen, resulting in less  $\gamma/\gamma'$  surface area and an associated reduction in overall free energy. This coarsening process has been shown to be dependent on volume diffusion through the  $\gamma$  matrix and follows the classic coarsening theory of Lifshitz and Sloyozov(10) given by:

$$d = \left[ \frac{64\Gamma DC_o V_m^2}{9RT} \right]^{1/3} t^{1/3} \quad (\text{Eqn. 4.1})$$

Where  $d$  is the particle diameter,  $\Gamma$  is the  $\gamma/\gamma'$  surface energy,  $D$  is diffusivity,  $C_o$  is the solubility in the matrix,  $V_m$  is the molar volume,  $R$  is the gas constant,  $T$  is absolute temperature, and  $t$  is time.

Figure 4.10 shows the  $\gamma'$  particle size as a function of  $t^{1/3}$  for a Ni-Al alloy at 700 °C (1290 °F), where the linear relationship between  $d$  and  $t^{1/3}$  confirms

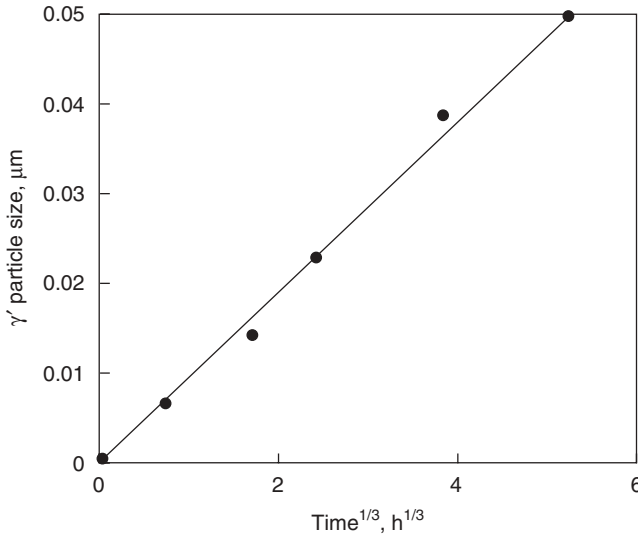


**Figure 4.10** The  $\gamma'$  particle size as a function of  $t^{1/3}$  at 700°C for a Ni-12.7 at% alloy. (From Brooks [9])

the behavior expected from Eqn. 4.1.(9) This relation is important because it demonstrates that the coarsening rate can be reduced by decreasing the  $\gamma/\gamma'$  surface energy. The surface energy is, in turn, affected by the  $\gamma/\gamma'$  lattice mismatch, where larger mismatch produces higher surface energies and correspondingly higher coarsening rates. Thus, lower mismatch between  $\gamma$  and  $\gamma'$  is preferred for creep applications where the coarsening rate needs to be low. An example of this is shown in Figure 4.11, which shows the creep rupture life as a function of  $\gamma/\gamma'$  mismatch for Ni-Cr-Al alloys.(9) The creep life is optimized when the mismatch is minimized due to a reduction in the particle coarsening rate.

As mentioned in Chapter 2, many Ni-base alloys contain Nb additions that promote formation of the  $\gamma''$ -Ni<sub>3</sub>Nb phase. This phase has a body centered tetragonal crystal structure (Figure 2.2b) that is coherent with the austenite matrix. Although many Nb-bearing commercial alloys also contain small amounts of Al and/or Ti and will therefore form small amounts of  $\gamma'$ , strengthening is primarily achieved by the presence of  $\gamma''$  in the Nb-bearing alloys. Strengthening from  $\gamma''$  is caused by large mismatch strains on the order of ~3%. The large mismatch strains provide very high strength at low temperatures. However, as shown by the time-temperature-transformation (TTT) diagram for Alloy 718 in Figure 4.12,  $\gamma''$  is only metastable and will be replaced by the incoherent  $\delta$  phase with the same Ni<sub>3</sub>Nb composition at higher temperatures and longer times.(11) This phase transition is generally associated with a reduction in creep strength and ductility and limits  $\gamma''$ -strengthened alloys to service temperatures of ~650°C (1200°F).(12) An example of the  $\gamma''$

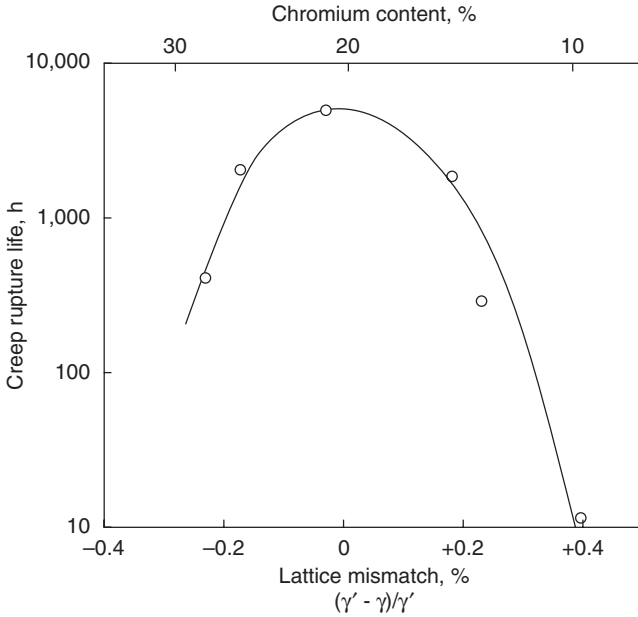


**Figure 4.11** Creep rupture life as a function of  $\gamma/\gamma'$  mismatch at 21,000 psi for Ni-Cr-Al alloys. (From Brooks [9])

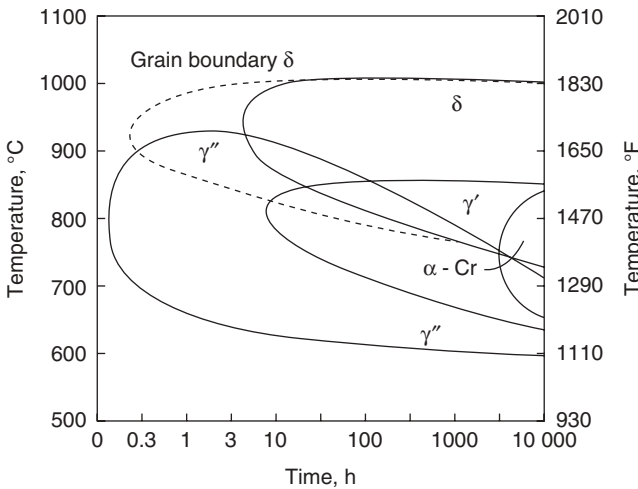


**Figure 4.12** TTT diagram for Alloy 718. (From Brooks and Bridges [11])

and  $\delta$  phases is shown in Figure 4.13 for Alloy 718 that was aged at 815°C(1500°F) for 100 hours. (13) The  $\gamma''$  phase is the smaller equiaxed phase, while the  $\delta$  phase is distinguished by its characteristic needle-shaped morphology. As will be discussed later in this chapter and in Chapter 6, the formation of  $\delta$  phase in service or during postweld heat treatment can result in severe degradation in weldability.

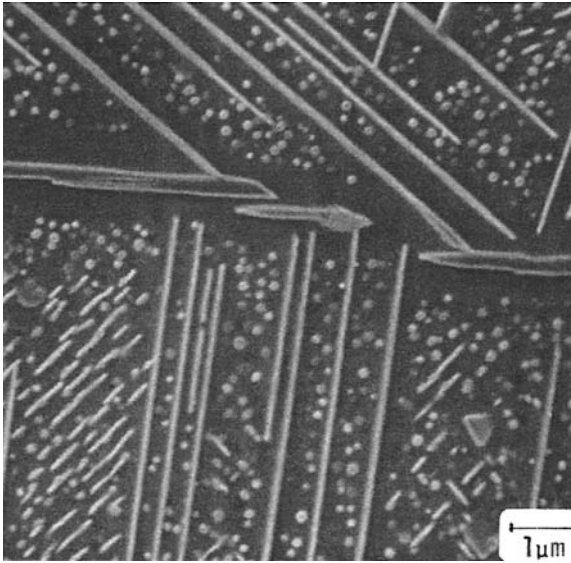


**Figure 4.13** Scanning electron microscope photomicrograph showing presence of fine  $\gamma'$  precipitates and coarse, needle-shaped  $\delta$  precipitates. (From Radavich [13])

The mechanical properties of a number of precipitation-strengthened Ni-base alloys are listed in Table 4.4. This table also includes data on the 1000 hour rupture strength of these alloys at 650, 760, and 870 °C (1200, 1400, and 1600 °F), since this information is often critical for selection of these alloys for elevated temperature service.

### 4.3 WELDING METALLURGY

The welding metallurgy of the precipitation-strengthened Ni-base alloys is similar to the solid-solution strengthened alloys in that many of the alloying elements used in these systems are similar. Thus, the partitioning that occurs during weld solidification and many of the issues associated with second phase formation are analogous. This section describes features that are unique to the precipitation-strengthened alloys.

#### 4.3.1 Microstructural Evolution in the Fusion Zone

**4.3.1.1 Elemental Segregation during Solidification** The elemental segregation behavior of alloying elements during solidification of Ni-base alloys was considered in detail in Chapter 3. That review included both solid-solution and precipitation-strengthened alloys. It is important to note that the segregation behavior of an element during solidification is independent of its intended purpose, i.e., whether the alloy addition is intended to promote strengthening by solid solution or precipitation hardening. In addition, a

TABLE 4.4 Mechanical Properties of Precipitation-Strengthened Ni-base Alloys.

Alloy	UNS	Tensile		0.2% Offset		Elongation, %	Hardness, R <sub>c</sub>	Rupture Stress for 1000-hr Exposure, ksi (MPa)		
		Strength, ksi (MPa)	Yield Strength ksi (MPa)	650 °C(1200 °F)	760 °C(1400 °F)			870 °C(1600 °F)		
K500	N0550	160 (1100)	115 (790)	—	—	20	—	—	—	—
X-750	N07750	160-200 (1100-1380)	100-150 (690-1035)	30-40	30-40	15-30	78 (540)	40 (275)	8 (55)	—
Alloy 80A	N07080	140-180 (970-1240)	85-120 (585-830)	—	—	25-36	73 (520)	32 (220)	—	—
Alloy 90	N07090	160-190 (1100-1310)	110-125 (760-860)	—	—	17-30	—	35 (240)	11 (75)	—
Alloy 263	N07263	140-160 (970-1100)	85-100 (585-690)	—	—	35-45	58 (400)	25 (170)	6 (40)	—
Alloy 282	N07282	170 (1165)	105 (720)	32	32	32	80 (550)	35 (240)	10 (70)	—
Alloy 713	N07713	120 (830)	—	35-40	35-40	5	—	—	—	—
Alloy 718	N07718	150-230 (1035-1590)	130-180 (900-1240)	30-40	30-40	14-30	85 (580)	28 (195)	—	—
Waspaloy	N07001	195 (1345)	130 (900)	34-45	34-45	26	67 (460)	28 (195)	7 (50)	—
René 41	N07041	195 (1345)	155 (1070)	33-40	33-40	15	85 (580)	35 (235)	9 (60)	—
Alloy 725	N07725	170-190 (1165-1310)	120-140 (830-970)	30-40	30-40	25-35	—	—	—	—
Alloy 706	N09706	180-200 (1240-1380)	140-160 (970-1100)	30-40	30-40	15-25	80 (550)	25 (170)	—	—
Alloy 909	N19909	185 (1275)	150 (1035)	—	—	15	47 (325)	—	—	—
Alloy 925	N09925	140 (970)	110 (760)	26-38	26-38	18	—	—	—	—
Alloy 945	N09945	160-180 (1100-1240)	130-150 (900-1035)	40-45	40-45	20-30	—	—	—	—

\* Single value is the typical value in the age-hardened condition.

review of the available data provided in Chapter 3 showed that the segregation tendency of most alloying elements in Ni-base alloys is not significantly affected by the nominal alloy composition. Thus, the information provided in Section 3.3.1 can be used to directly assess the segregation tendency of alloying elements in both solid-solution and precipitation-strengthened alloys.

To briefly summarize, the solute redistribution behavior and final distribution of alloying elements across the dendritic substructure in Ni-base alloys is controlled primarily by the pertinent values of  $k$  (equilibrium distribution coefficient) and  $D_s$  (diffusivity in the solid) for the alloying element of interest. Elements with very low  $k$  values can produce steep concentration gradients across the dendritic substructure of the weld. However, the elemental gradient can be eliminated if solid-state diffusion of that particular element is sufficiently high to promote back diffusion in the solid. A review of available data shows that solid state diffusion of substitutional alloying elements in nickel alloys is insignificant during solidification of fusion welds, while diffusion of interstitial elements such as C and N is expected to be almost infinitely fast under most fusion welding conditions. For the substitutional alloying elements, the final segregation pattern is then reflected directly by the pertinent  $k$  value, where elements with lower  $k$  values produce steeper concentration gradients in the as-solidified weld.

In general, elements with similar atomic radii to Ni, namely Fe, Cr, and Co, have  $k$  values that are close to unity. This trend is expected based on the influence of atomic size differences on solubility, in which elements of similar atomic radii generally exhibit appreciable solubility. Thus, although these elements can not back diffuse during solidification, their concentration gradients are not large to begin with because their  $k$  values are all close to unity. Carbon partitions strongly during solidification of Ni-base alloys ( $k \sim 0.21\text{--}0.27$ ), and this accounts for the formation of various carbide phases at the end of solidification in these alloys. Although there is strong partitioning to the liquid phase during solidification, the final carbon distribution in the solid can be expected to be uniform due to the high solid-state diffusivity of C in Ni. A detailed treatment of elemental segregation behavior is provided in Section 3.3.1.2.

**4.3.1.2 Phase Transformations— $\gamma'$  Formation** Microstructural evolution in the fusion zone of  $\gamma'$  forming alloys can be understood with the aid of the diagrams shown in Figure 4.14, which represent schematic illustrations of the Ni-Al-Ti liquidus projection and a vertical section through the Ni-Al-Ti system. For alloys with low C contents (typically less than  $\sim 0.01$  wt%), the  $\gamma$  and  $\gamma'$ -Ni<sub>3</sub>Al phases are the main constituents that form in these alloys. As described in Chapter 2, the Ni<sub>3</sub>Ti phase can also form during solidification, but this phase is less desirable from a mechanical property standpoint. For an alloy of composition  $C_0$ , solidification begins with primary  $\gamma$  solidification. As solidification proceeds, Al and Ti segregate to the liquid since their  $k$  values are less than one. Thus, the liquid composition moves away from the Ni-rich

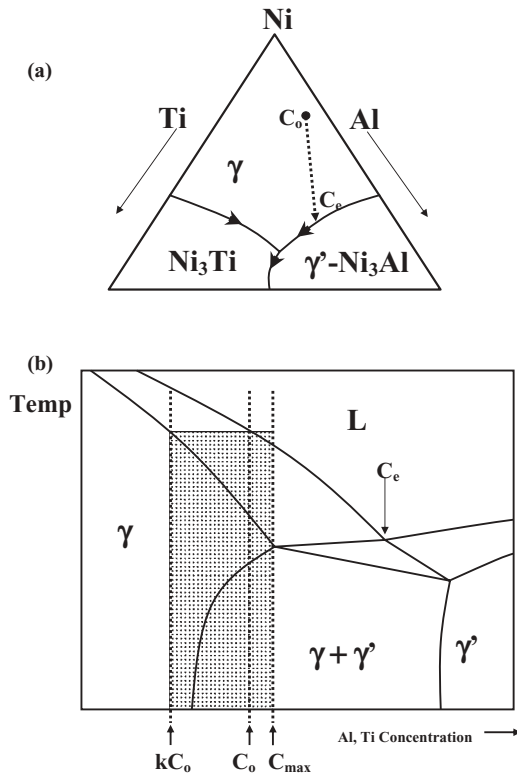


**Figure 4.14** Schematic illustration of a) the Ni-Al-Ti liquidus surface and b) vertical section through the Ni-Al-Ti system.

corner and traces out a solidification path (dotted line in Figure 4.14a) that is directed towards the  $\gamma/\gamma'$  monovariant eutectic line. Since  $\gamma'$  (and not  $\text{Ni}_3\text{Ti}$ ) is the preferred phase, and Ti segregates to the liquid more aggressively than Al (Ti has a lower  $k$  value than Al, see Chapter 3), more Al than Ti is generally required to promote intersection of the primary solidification path with the  $\gamma/\gamma'$  eutectic line instead of the  $\gamma/\text{Ni}_3\text{Ti}$  eutectic line. Many alloys do indeed have more Al than Ti, and this is reflected in the position of the nominal composition  $C_0$  shown in Figure 4.14a.

The primary solidification path intersects the  $\gamma/\gamma'$  monovariant eutectic line at  $C_e$  (the eutectic composition), and the liquid composition then moves down this eutectic line as  $\gamma$  and  $\gamma'$  form simultaneously from the liquid by a eutectic type reaction. Since this system is not a simple binary, the eutectic composition at the intersection point ( $C_e$ ) depends on the nominal composition and pertinent  $k$  values of Al and Ti, and the eutectic type reaction occurs over a range of composition and temperature.<sup>(14)</sup> Strictly speaking, the  $\text{Ni}_3\text{Ti}$  phase would also be expected to form near the end of solidification as the liquid composition would eventually intersect the three phase  $\gamma\text{-Ni}_3\text{Al-Ni}_3\text{Ti}$  equilibrium

point, but this is generally not observed in practice. The general solidification sequence shown in Figure 4.14a accounts for the formation of  $\gamma$  dendrites and the interdendritic  $\gamma/\gamma'$  eutectic that has been observed in many commercial Ni-base superalloys.(14–16)

Microstructural evolution is generally not complete after solidification of  $\gamma'$  forming alloys. The primary  $\gamma$  phase will exhibit a range of Al and Ti concentrations due to microsegregation that is associated with the low diffusivity of Al and Ti in the primary  $\gamma$ . Thus, as shown schematically in Figure 4.14b, the primary  $\gamma$  phase will contain compositions ranging from  $kC_0$  at the cell core to  $C_{\max}$  at the cell boundaries, where  $C_{\max}$  is the maximum solid solubility of Al and Ti in  $\gamma$ . (The  $\gamma$  substructure is referred to here as cellular for simplicity, but can also be dendritic depending on alloy content, welding parameters, and resultant temperature gradient in the liquid. It should also be noted that phase compositions can generally not be determined directly from a vertical section as shown in Figure 4.14b since the tie lines may not lie in the plane of the diagram. The compositions are shown here for reference only.) The composition range is represented by the shaded region in Figure 4.14b. Note that, depending on location within the  $\gamma$  cellular substructure, the cells may enter into the two phase  $\gamma + \gamma'$  region upon further cooling, and precipitation of the  $\gamma'$  phase becomes thermodynamically possible.

For many engineering alloys strengthened by precipitation, the kinetics of nucleation and growth are too slow to permit precipitation during the relatively high cooling rates associated with most weld thermal cycles. However, precipitation of the  $\gamma'$  phase within the  $\gamma$  cells is routinely observed in the fusion zones of these alloys. This can be attributed to the excellent crystallographic matching across the  $\gamma/\gamma'$  interface that leads to very low surface energy and strain energy. The nucleation rate increases exponentially with decreasing activation energy required for nucleation. The activation energy, in turn, decreases with decreasing surface and strain energy. Thus, the good crystallographic matching leads to high nucleation rates that permit formation of  $\gamma'$  even under high cooling rate conditions typical of welding. The final weld microstructure will therefore consist of cored  $\gamma$  dendrites that contain  $\gamma'$  precipitates with  $\gamma/\gamma'$  eutectic at the solidification subgrain (cell and dendrite) boundaries. A representative example of this for alloy PWA-1480 is shown in the TEM photomicrograph in Figure 4.15.(17)

These results suggest that the size and number density of the  $\gamma'$  precipitates should be strongly affected by the weld cooling rate. Figure 4.16 shows examples of the size and number density of  $\gamma'$  precipitates as a function of cooling rate for the directionally solidified Alloy CM247DS.(17) The cooling rates were controlled using a Gleeble thermal simulator and represent a fairly wide range of cooling rates. Note that the size of the  $\gamma'$  precipitates decreases and their number density increases appreciably with increasing cooling rate. These changes are attributed to the increased undercooling below the  $\gamma/(\gamma + \gamma')$  solvus temperature that occurs with increased cooling rate. At low cooling rates, the undercooling is small, leading to low nucleation rates and high growth rates.

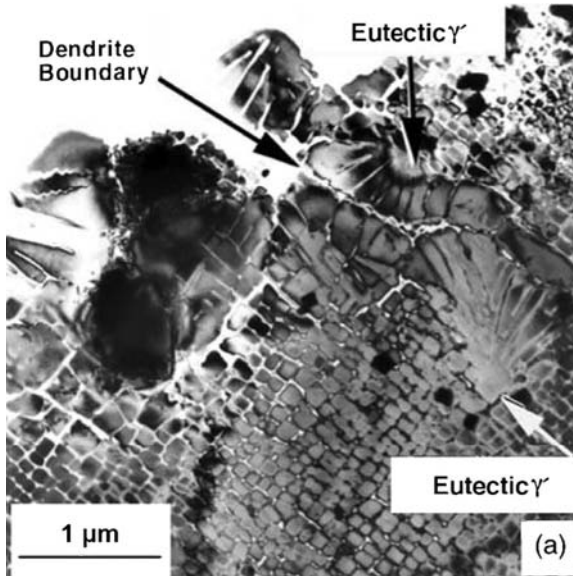


**Figure 4.15** TEM photomicrographs of  $\gamma/\gamma'$  interdendritic eutectic and finely precipitated  $\gamma'$  within the  $\gamma$  dendrites of Alloy PWA-1480. (From Babu *et al.* [17])

Coarsening can also occur at the lowest cooling rates. This leads to large, coarse precipitates. With increased cooling rate, the undercooling becomes high, which causes high nucleation rates and low growth rates, thus promoting a fine distribution of  $\gamma'$  precipitates with a high number density.

The microsegregation of alloying elements that results from solidification also influences the size and number density of  $\gamma'$  precipitates that form in the solid state upon cooling from the solidification temperature range and during any subsequent postweld heat treatment. This is shown schematically in Figure 4.17, where Figure 4.17a represents the composition range that exists across the solidification subgrain (cell or dendrite) after solidification as related to the solvus line separating the  $\gamma$  and  $\gamma + \gamma'$  phase fields. Figure 4.17b, c, and d show the microstructure that will evolve after solidification, during solution treatment at a temperature  $T_{sol}$ , and after quenching and aging, respectively. Note that the solvus temperature will vary from cell center to cell boundary due to the concentration gradient. Thus, during cooling after solidification, the higher solute content that exists near the cell boundary allows this location to enter the  $\gamma + \gamma'$  phase field at higher temperatures, where the nucleation rate is low and the growth rate is high. Coupled with the increased time for growth and coarsening, this leads to the formation of relatively coarse  $\gamma'$  precipitates with a reduced number density in the intercellular regions relative to the cell core regions (Figure 4.17b).

If a postweld heat treatment is applied, the treatment must be performed so that the solution temperature is below the temperature where the maximum

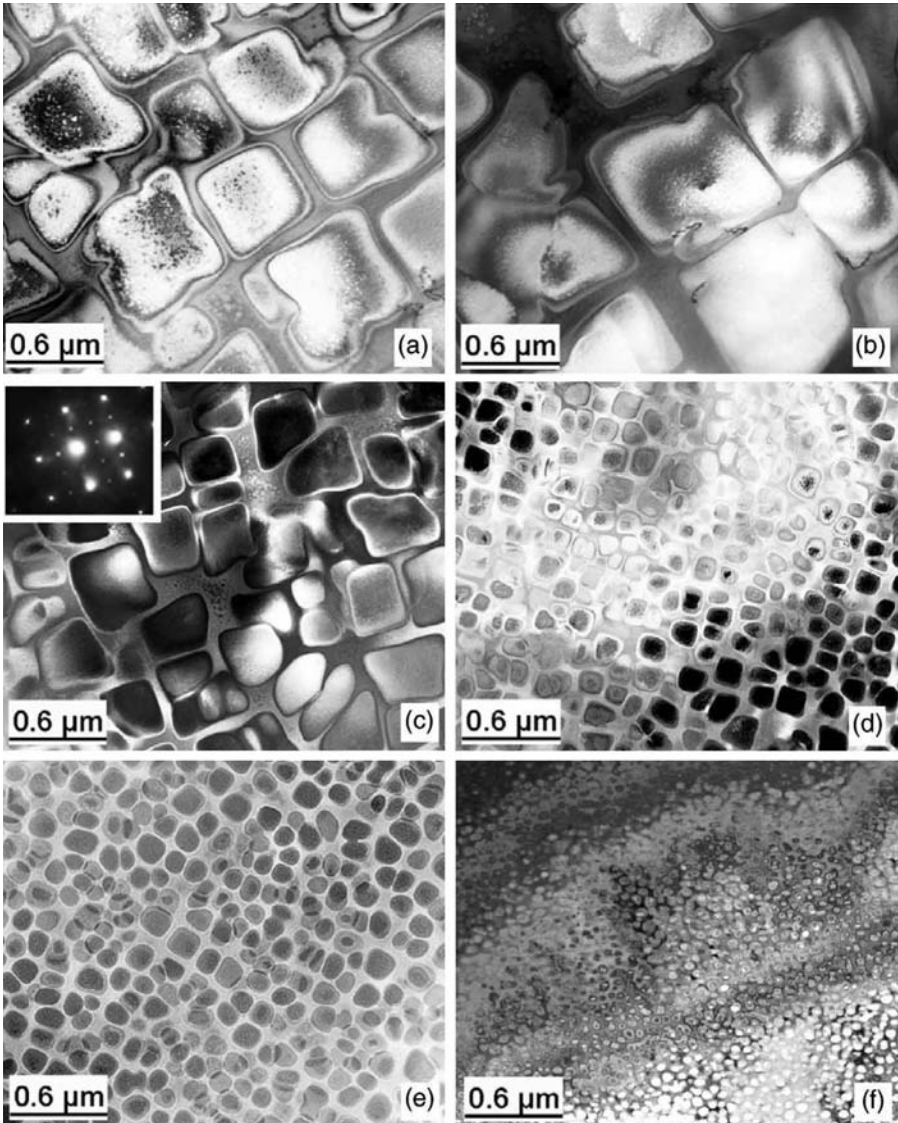


**Figure 4.16** Example of variations in  $\gamma'$  precipitate size and number density with variations in cooling rate for directionally solidified Alloy CM247DS. a) air cooled, b) 0.17 K/s, c) 1 K/s, c) 10 K/s, d) 75 K/s, e) water quenched. (From Babu *et al.* [17])

solid solubility occurs in order to prevent liquation. As a result, the cell boundary region that has a solute concentration beyond the solvus at the solution temperature of  $T_{\text{sol}}$  will not be able to dissolve the  $\gamma'$  precipitates and, in fact, the precipitates in this region can actually coarsen during the solution treatment (Figure 4.17c). The final distribution of  $\gamma'$  within the cell interiors will

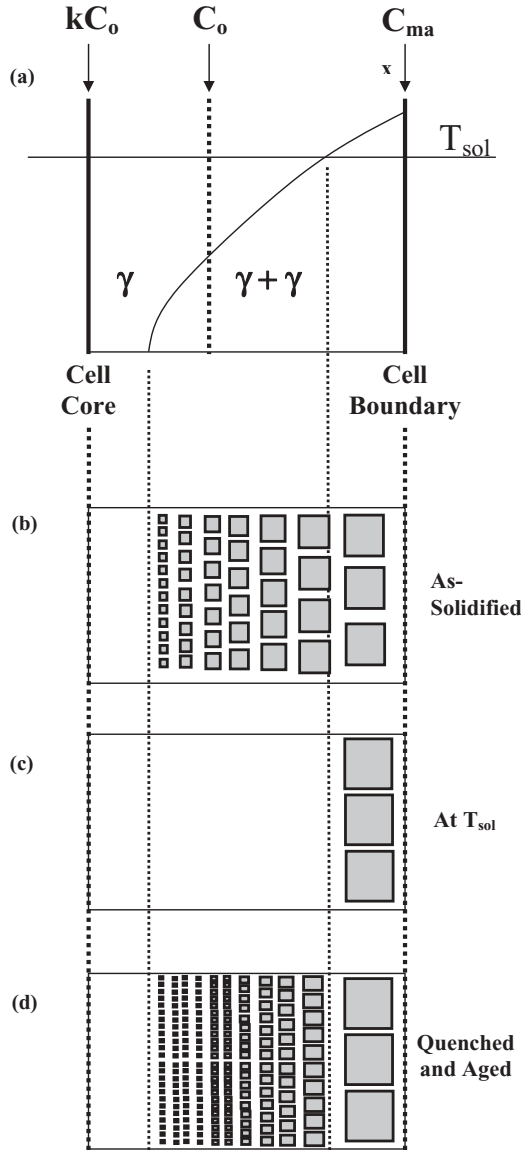


**Figure 4.17** Schematic illustration of evolution of  $\gamma'$  precipitate size and number density a) after solidification, b) during solution treatment, and c) after quenching and d) aging.

depend on the extent of homogenization that occurs during the solution treatment. If the homogenization is complete and the concentration gradient is eliminated, then the solvus temperature within the cell interior region is uniform, and the corresponding  $\gamma'$  precipitate size and number density should also be uniform in this region. However, if homogenization is not complete,

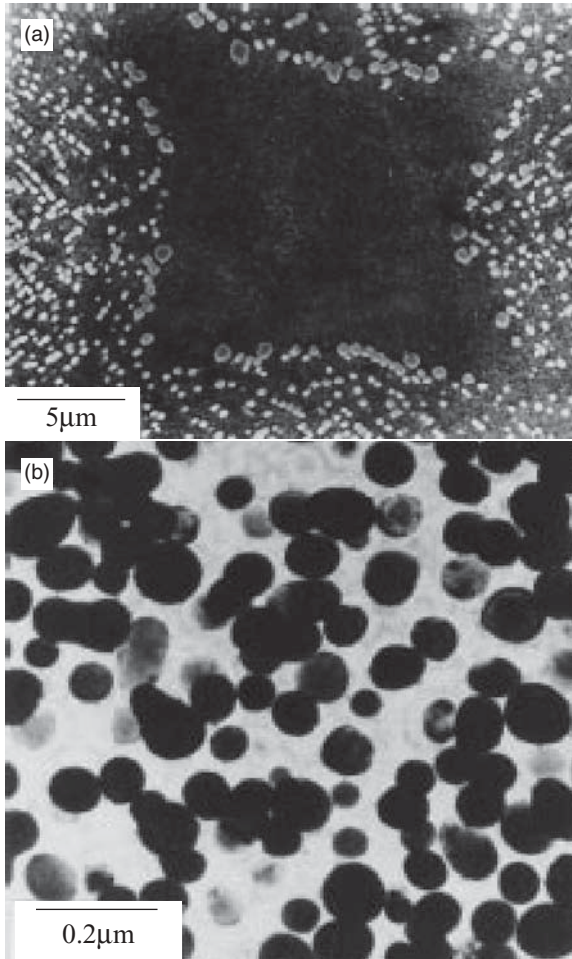


**Figure 4.18** Example of uneven  $\gamma'$  precipitate morphology in Alloy 738 due to microsegregation. a) SEM photomicrograph showing precipitate coarsening in the intercellular region and precipitate dissolution in the cell interior. b) TEM photomicrograph showing smaller  $\gamma'$  particles that formed after solution heat treatment and aging. (From Rosenthal and West [18])

then a variation in the solvus temperature will persist across the cells and lead to another (although smaller) variation in the  $\gamma'$  precipitate size and number density. This condition is shown schematically in Figure 4.17d.

An example of the uneven  $\gamma'$  precipitate morphology due to microsegregation is shown in Figure 4.18 for Alloy IN738.(18) This particular alloy was given a standard heat treatment designed to harden the base metal consisting of solution treatment at 1120°C (2050°F) for two hours, followed by air cooling and aging at 845°C (1550°F) for 16 hours. The SEM photomicrograph

shows precipitate coarsening in the intercellular region which is evidence of the incomplete dissolution of the  $\gamma'$  that occurred during the solution treatment. The TEM photomicrograph (Figure 4.18B) shows smaller  $\gamma'$  particles that formed in the cell core region after solution heat treatment and aging due to either the absence of  $\gamma'$  precipitates after solidification or the effective solutionizing of the solidification  $\gamma'$  during the solution heat treatment.

The variation in  $\gamma'$  precipitate size across the cells also has important consequences in terms of controlling precipitate coarsening in high temperature applications. As mentioned in Section 4.2, coarsening rates need to be minimized for optimum creep performance. In view of this, it is informative to note that the coarsening rate is given by the following relationship (10):

$$\frac{dr}{dt} = \frac{2D\Gamma V_m C_o}{RT} \left( \frac{1}{\bar{r}} - \frac{1}{r} \right) \quad (\text{Eqn. 4.2})$$

Where  $r$  is the radius of any given precipitate,  $\bar{r}$  is the average precipitate radius, and  $(dr/dt)$  is the coarsening rate of a precipitate with radius  $r$ . Other terms were previously defined for Eqn. 4.1.

Note that the coarsening rate increases as the difference in the particle radii increases. In an ideal case, all particles would have the same radii and, according to Eqn. 4.2, the particle coarsening rate would be zero. In the practical condition, the variation in  $\gamma'$  precipitate radii that is induced by microsegregation will lead to accelerated coarsening rates and have a detrimental influence on creep properties. In view of these factors, careful consideration is required when designing postweld heat treatments for these alloys.

**4.3.1.3 Phase Transformations—Carbide Formation** The solidification sequences described above adequately reflect microstructural evolution in low-carbon superalloys. However, alloys with sufficiently high C contents are known to form MC type carbides near the end of solidification prior to the  $L \rightarrow \gamma + \gamma'$  eutectic type reaction.(19) In these cases, microstructural evolution can be qualitatively understood by examination of the Ni-Ti-C liquidus projection shown in Figure 4.19a. This system exhibits three primary phase fields— $\gamma$ , TiC carbide, and  $\text{Ni}_3\text{Ti}$ . As mentioned above, the presence of other alloying elements in superalloys, most notably Al, will favor formation of the  $\gamma'$ - $\text{Ni}_3\text{Al}$  phase over the  $\text{Ni}_3\text{Ti}$  phase. In addition, other carbide forming elements such as Cr, Ta, Nb, and Mo can substitute for Ti in the TiC carbide. Thus, by replacing the  $\text{Ni}_3\text{Ti}$  phase field with  $\gamma'$  ( $\text{Ni}_3\text{Al}$ ), TiC with MC, and Ti with the sum of the  $\gamma'$  forming elements, the resultant pseudo ternary liquidus projection provides a qualitative understanding of phase formation in higher C alloys. This diagram is shown in Figure 4.19b, and this approach is essentially identical to that proposed in earlier work by DuPont *et al.*(20) for understanding microstructural evolution in Nb-bearing superalloys using a pseudo-ternary  $\gamma$ -NbC-Laves liquidus diagram (as described in Section 4.3.1.4).

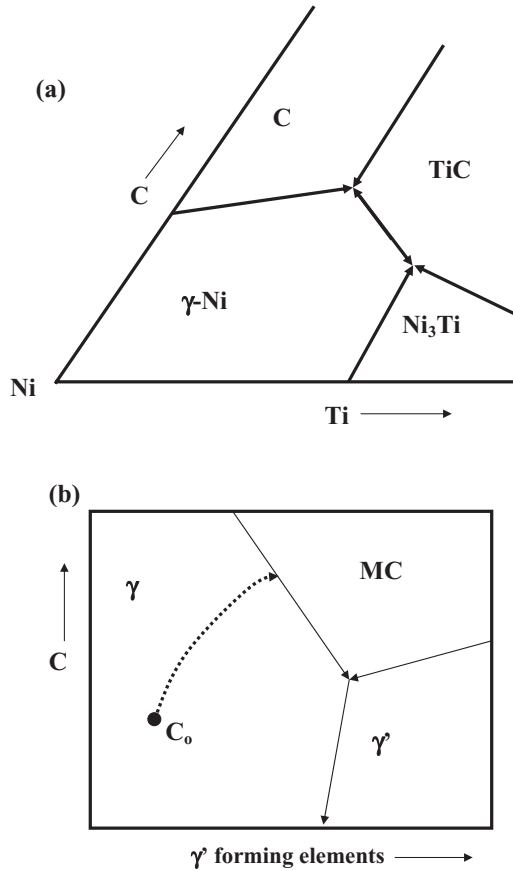


**Figure 4.19** a) Ni-Ti-C liquidus projection b) pseudo-ternary  $\gamma$ -MC- $\text{Ni}_3\text{Al}$  liquidus projection.

The distribution coefficient ( $k$ ) for C in these alloys is on the order of 0.21–0.27 and, thus, C will segregate strongly to the liquid during solidification along with the  $\gamma'$  forming alloying elements such as Ti and Al. As a result, the primary solidification path (dotted line Figure 4.19b) will trace out a curve that represents increasing amounts of C, Ti, and Al in the interdendritic liquid. The primary solidification path will then intersect the  $\gamma$ /MC monovariant eutectic line and cause the  $\gamma$ /MC eutectic to form as the liquid composition follows this line. The Ni-Ti-C system exhibits a ternary eutectic point in which  $\gamma$ , MC, and  $\text{Ni}_3\text{Ti}$  are all expected to form isothermally at the ternary eutectic point by the invariant  $L \rightarrow \gamma + \text{MC} + \text{Ni}_3\text{Ti}$  reaction. This would leave the three solid phases intermixed in the final microstructure. However, the  $\gamma/\gamma'$  eutectic type constituent forms separately from the  $\gamma$ /MC eutectic in commercial alloys, and the  $L \rightarrow \gamma + \gamma'$  reaction is known to occur over a finite solidification temperature range.(19) This indicates that, in multi-component

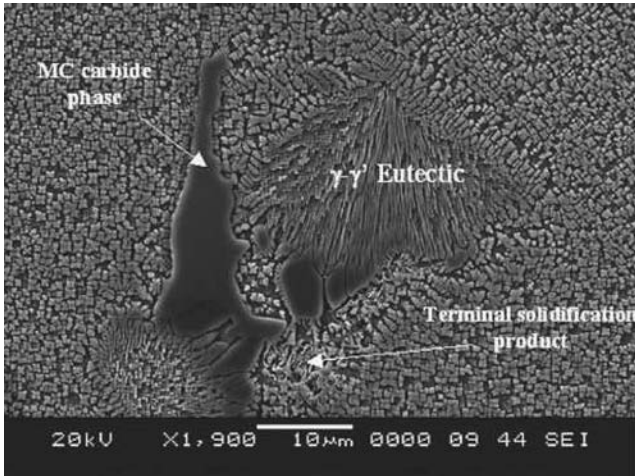


**Figure 4.20** SEM photomicrograph of  $\gamma$ , MC, and  $\gamma'$  phases that form in the fusion zone of Alloy 738.

superalloys, a ternary eutectic point does not exist, but the liquidus projection instead exhibits a so-called class II reaction.(21) In this particular case, the class II reaction refers to termination of solidification at the C-free, pseudo-binary side of the diagram (instead of solidification terminating within the diagram). This detail is reflected by the direction of decreasing temperature as indicated by the arrow on the  $\gamma/\gamma'$  monovariant eutectic line. A typical example of the microstructure that forms from this solidification sequence is shown in Figure 4.20 for Alloy 738.

It should also be mentioned that the presence of small amounts of other elements can lead to additional constituents that form after the  $L \rightarrow \gamma + \gamma'$  reaction. Examples include the formation of various borides, sulfides, and intermetallics. These phases generally have a detrimental effect on weldability because they form at lower temperatures and expand the solidification temperature range. The formation of these phases will be discussed in more detail in Section 4.5.

**4.3.1.4 Phase Transformations— $\gamma''$  Formation** As previously mentioned, many superalloys have been developed that contain significant amounts of Nb as a strengthening element that is added to form the gamma-double prime ( $\gamma''$ ) phase. Microstructural evolution in the fusion zone of these alloys is described in this section. Most of the commercial Nb bearing alloys exhibit a three step solidification process that consist of a primary  $L \rightarrow \gamma$  stage followed by  $L \rightarrow \gamma + \text{NbC}$  and  $L \rightarrow \gamma + \text{Laves}$  reactions at the terminal stages of solidification.(14,20,22–26) Figure 4.21 shows an example of the  $\gamma/\text{NbC}$  and  $\gamma/\text{Laves}$  eutectic type constituents that form in the fusion zone of a Nb-bearing

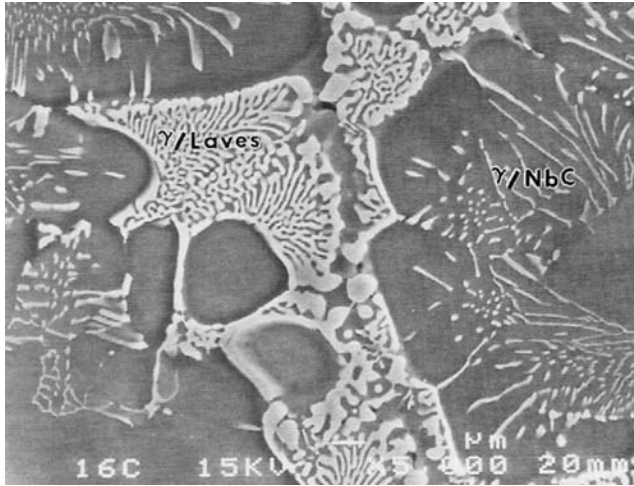


**Figure 4.21** SEM photomicrograph showing NbC and Laves phases in the fusion zone of a Nb-bearing superalloy. (From DuPont *et al.* [20])

superalloy.(20) The Laves phase is an intermetallic compound with a hexagonal crystal structure and  $A_2B$  stoichiometry where “A” represents elements such as Ni, Fe, Cr, and Co, and “B” represents elements such as Nb, Ti, Si, and Mo.

Figure 4.22a summarizes the composition of the Laves phase observed in several commercial alloys, and the enrichment ratios of the same elements are shown in Figure 4.22b.(27)

The enrichment ratio is defined as the concentration of an element in the Laves phase over that in the bulk alloy. The elements Ni, Cr, Fe, and Ti do not strongly partition to the Laves phase, while the refractory type elements Nb, and to a slightly less degree Mo, partition rather strongly. In fact, it is now well known that Laves phase formation in these alloys requires the presence of Nb.(14,20) Table 4.5 summarizes the occurrence and transformation temperatures of the  $L \rightarrow \gamma + NbC$  and  $L \rightarrow \gamma + Laves$  reactions observed in a number of Nb-bearing alloys. The  $L \rightarrow \gamma + NbC$  reaction invariably occurs before the  $L \rightarrow \gamma + Laves$  reaction during solidification. It is generally recognized that C additions can sometimes completely suppress formation of the lower temperature  $L \rightarrow \gamma + Laves$  reaction (e.g., note the absence of the Laves reaction for the high C heat of Alloy 625 in Table 4.5) and that lower carbon alloys (e.g., 909 and Thermo-span) generally do not exhibit the  $L \rightarrow \gamma + NbC$  reaction. It should be noted that, strictly speaking, these alloys are generally not referred to as “ $\gamma$ ” strengthened alloys because the Nb is added as a solid solution strengthener. However, NbC and/or Laves phases form in the fusion zone of these alloys due to extensive segregation of Nb and C during solidification.

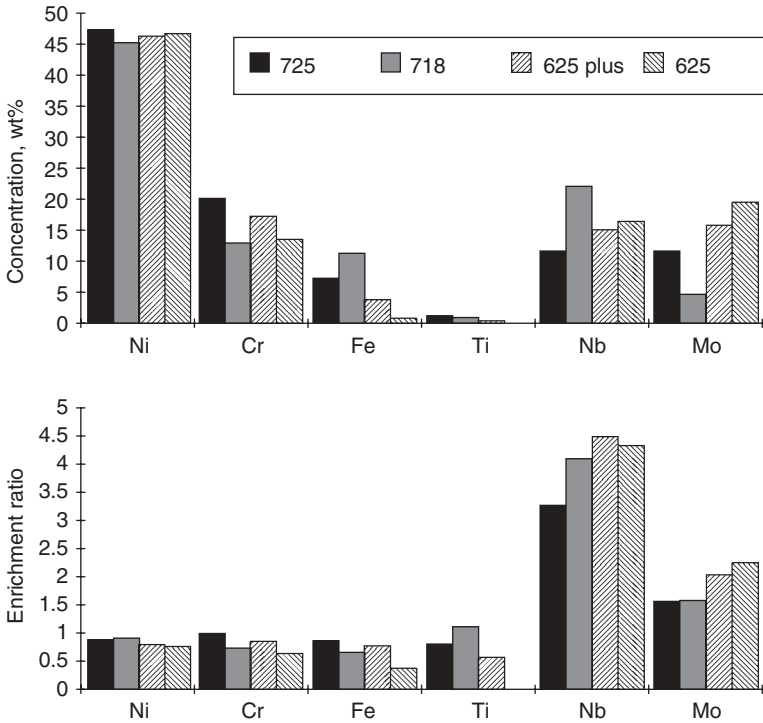


**Figure 4.22** Summary of Laves composition and enrichment ratios for several commercial alloys. (From Maguire and Michael [27])

**TABLE 4.5** Summary of Solidification Reaction Temperatures of Commercial Nb Bearing Superalloys.

Alloy	Solidification Reactions and Temperatures (°C)	
	L → γ + NbC	L → γ + Laves
625 (0.03 Si, 0.009 C)	Not Detected	1150
625 (0.03 Si, 0.038 C)	1246	Does not occur
625 (0.38 Si, 0.008 C)	1206	1148
625 (0.46 Si, 0.035 C)	1231	1158
718	1250	1200
725	1143	1118
903	Not Measured	Not Measured
909	Does not occur	1187°C
Thermo-Span	Does not occur	1226°C

NOTES:

Not Detected—Indicates the reaction occurs, but the amount of constituent is too small to be detected.

Not Measured—The γ/NbC and γ/Laves constituents form, but reaction temperatures have not been measured.

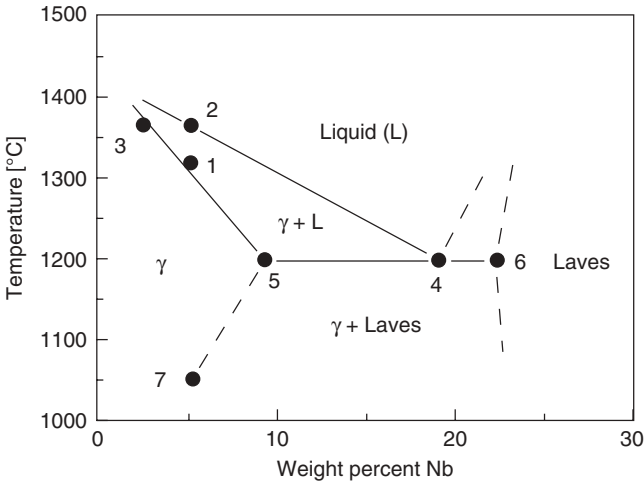


**Figure 4.23** Pseudo binary solidification diagram for Alloy 718.

**4.3.1.5 Effect of Nb and C** Knorovsky *et al.* conducted a detailed investigation of microstructural evolution in fusion welds on Alloy 718.(26) In this alloy, the  $\gamma$ /Laves eutectic type constituent is the major microconstituent that forms, and  $\gamma$ /NbC forms in only small quantities. Thus, ignoring the small amount of  $\gamma$ /NbC, Knorovsky recognized that the alloy solidifies in a manner very similar to that of a binary system in which the solid-solution primary  $\gamma$  phase can be treated as the “solvent” and Nb as the “solute” element. A pseudo-binary solidification diagram was assembled from a combination of micro-chemical measurements and differential thermal analysis and is shown in Figure 4.23. Points 1 and 2 were obtained from the nominal alloy composition, and solidus and liquidus temperatures. Point 3 represents the liquidus temperature and cell core composition. Points 5 and 6 represent the composition of the  $\gamma$  and Laves, respectively, in the  $\gamma$ /Laves eutectic type constituent. Note that Point 5 represents the maximum solid solubility of Nb in  $\gamma$  for Alloy 718 (9.3 wt%). Point 7 is the solubility limit of Nb in the Alloy 718 matrix as reported by Eiselstein.(28) Since Nb diffusion in  $\gamma$  is negligible during solidification, the Scheil equation can be used with this diagram to directly calculate how variations in Nb content will affect the final microstructure of Alloy 718. It was demonstrated that the predictive capabilities of this diagram are quite accurate.

Table 4.6 summarizes solidification reactions and associated temperatures for a set of experimental Nb bearing alloys that have systematic variations in Fe, Nb, Si, and C.(14–16,20) These elements were studied in detail because previous work (23,25) had shown they have a strong influence on fusion zone microstructural evolution and resultant weldability of Nb-bearing superalloys. These alloys permit a more in-depth analysis of elemental effects that is difficult to discern by comparison among the commercial alloys in which the key

**TABLE 4.6 Summary of Solidification Reaction Temperatures of Experimental Nb Bearing Superalloys.**

Alloy		Solidification Reactions and Temperatures (°C)	
		L → $\gamma$ + NbC	L → $\gamma$ + Laves
<i>Ni Base Alloys</i>			
Alloy	Composition		
1.5	Ni-10Fe-19Cr-2.00Nb-0.13Si-0.052C	Not Detected	Does not occur
2	Ni-10Fe-19Cr-1.95Nb-0.06Si-0.132C	Not Detected	Does not occur
3	Ni-10Fe-19Cr-1.82Nb-0.38Si-0.010C	Not Detected	~1190
3.5	Ni-10Fe-19Cr-1.94Nb-0.41Si-0.075C	1322	Does not occur
4	Ni-10Fe-19Cr-1.91Nb-0.40Si-0.155C	1330	Does not occur
5	Ni-10Fe-19Cr-5.17Nb-0.05Si-0.013C	Not Detected	~1190
6	Ni-10Fe-19Cr-4.87Nb-0.08Si-0.161C	1332	~1190
7	Ni-10Fe-19Cr-4.86Nb-0.52Si-0.010C	Not Detected	~1990
7.5	Ni-10Fe-19Cr-4.92Nb-0.46Si-0.081C	1306	~1190
8	Ni-10Fe-19Cr-4.72Nb-0.52Si-0.170C	1328	~1190
<i>Fe Base Alloys</i>			
Alloy	Composition		
9	Fe-31Ni-19Cr-1.66Nb-0.10Si-0.003C	Not Detected	~1250
10	Fe-31Ni-19Cr-1.66Nb-0.01Si-0.108C	1358	~1250
11	Fe-31Ni-19Cr-1.77Nb-0.57Si-0.004C	Not Detected	~1250
11.5	Fe-31Ni-19Cr-1.84Nb-0.67Si-0.116C	1348	~1250
12	Fe-31Ni-19Cr-1.93Nb-0.61Si-0.079C	1348	~1250
13	Fe-31Ni-19Cr-4.42Nb-0.02Si-0.015C	1333	1250
14	Fe-31Ni-19Cr-4.51Nb-0.08Si-0.210C	1361	1243
15	Fe-31Ni-19Cr-4.88Nb-0.66Si-0.010C	1290	1256
16	Fe-31Ni-19Cr-4.77Nb-0.64Si-0.216C	1355	1248

alloying elements do not vary in a systematic manner. The experimental matrix consists of two sets of alloys (one Ni-base and one Fe-base), and each set has factorial variations in Nb, Si, and C.

The total volume percentages of eutectic-type constituents ( $\gamma$ /NbC +  $\gamma$ /Laves) and individual volume percentages of each eutectic-type constituent for these experimental alloys are summarized in Figures 4.24 and 4.25.

For total volume percentage measurements, Fe- and Ni-base alloys with similar levels of Nb, Si, and C are matched for comparison. The results from individual constituent measurements, where such distinctions were possible, are aligned to make similar comparisons. There are several important effects of Fe, Nb, Si, and C displayed in these figures. First, at similar levels of minor alloy additions (Nb, Si, and C), the Fe-base alloys generally form higher levels of total eutectic-type constituents.

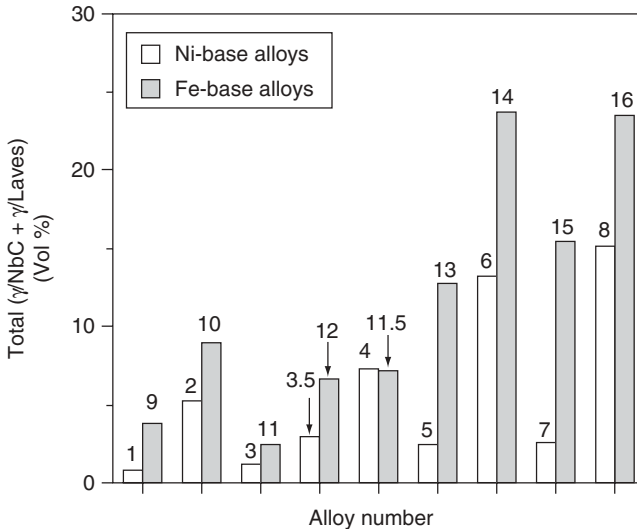


**Figure 4.24** Summary of total ( $\gamma/\text{NbC}$  and  $\gamma/\text{Laves}$ ) constituents measured in experimental Nb-bearing alloys. (From DuPont *et al.* [14,16,20])

Measurements of the individual eutectic-type constituents (Figure 4.25) indicate that this response can be attributed primarily to the formation of higher amounts of  $\gamma/\text{Laves}$  in the Fe-base alloys. It is worth noting that no Laves phase exists in the simple Ni-Nb binary phase diagram while the Fe-Nb system forms the Laves phase over a composition range of 38-to-50wt% Nb and a broad temperature range of 600-to-1400°C (1110-to-2550°F).<sup>(29)</sup> The Ni-Nb system forms  $\text{Ni}_3\text{Nb}$  over the composition range of approximately 33-to-38wt% Nb (at 1200°C). The addition of Fe to Ni-Nb alloys is well known to promote Laves phase at the expense of the  $\text{Ni}_3\text{Nb}$  phase.<sup>(23,25)</sup> Thus, Fe additions to the austenite matrix, at the expense of Ni, can be expected to promote the formation of more  $\gamma/\text{Laves}$ .

The addition of Si has a similar effect, as the amount of  $\gamma/\text{Laves}$  always increases with increasing Si within a given matrix composition (see Table 4.5 for alloy numbers, and compare Alloy 5 to 7, 6 to 8, 13 to 15, and 14 to 16). The Laves promoting tendency of Si has been documented in commercial superalloys as well.<sup>(23,25)</sup> Nb additions promote higher volume fractions of total eutectic. This is to be expected, since each of the secondary phases that forms in the eutectic-type structures (NbC and Laves) are both highly enriched in Nb. At high C levels, Nb additions generally promote more  $\gamma/\text{NbC}$  (compare Alloy 2 to 6, 4 to 8, 10 to 14, 11.5 to 16 in Table 4.6). When the C and Fe levels are both high, Nb additions will increase the amount of both the  $\gamma/\text{NbC}$  and  $\gamma/\text{Laves}$  constituents (compare Alloys 10 to 14 and 11.5 to 16). Alloys with high C levels (even-numbered alloys) form large amounts of the  $\gamma/\text{NbC}$  eutectic-type constituent.

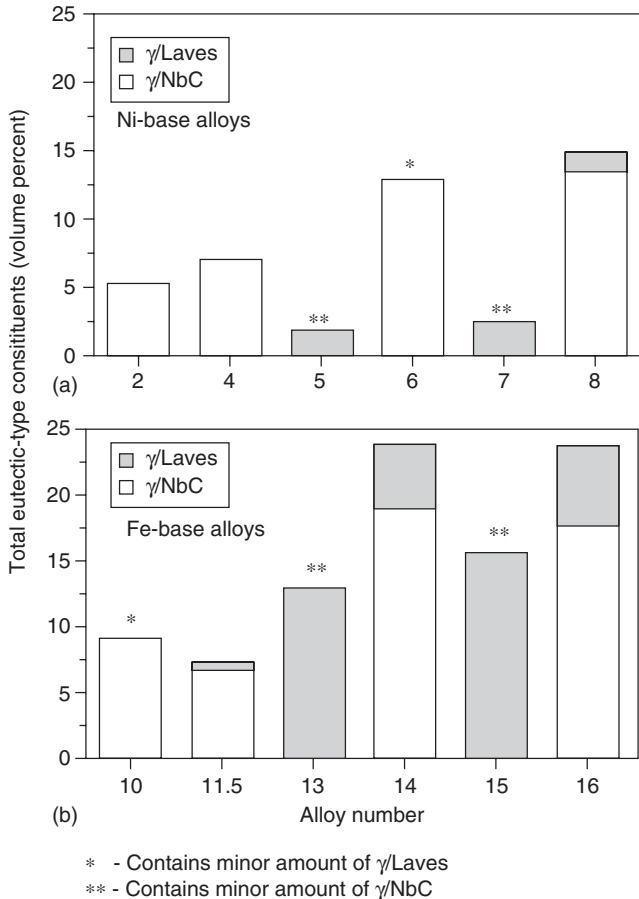


**Figure 4.25** Summary of individual  $\gamma/\text{NbC}$  and  $\gamma/\text{Laves}$  constituents measured in experimental Nb-bearing alloys. (From DuPont *et al.* [14,16,20])

The data in Table 4.6 also show that, at similar levels of solute elements, the solidification reaction temperatures in the Fe-base alloys are consistently higher than those in the corresponding Ni-base alloys. Microprobe measurements have shown that the Fe contents of the eutectic-type constituents in the Fe-base alloys are considerably higher than those in the Ni-base alloys.(14,20,22) Considering that the melting temperature of Fe is higher than that of Ni, the higher reaction temperatures for the Fe-base alloys are to be expected. The Fe content also exerts a strong influence by affecting the segregation potential of Nb. Figure 4.26 shows the variation in  $k_{\text{Nb}}$  as a function of nominal Fe content.

This data was obtained from a number of experimental and commercial alloys and shows that Fe increases the segregation potential of Nb (i.e., lower the value of  $k$ ). This increased segregation tendency of Nb has a significant effect in terms of secondary phase formation, since both of the secondary

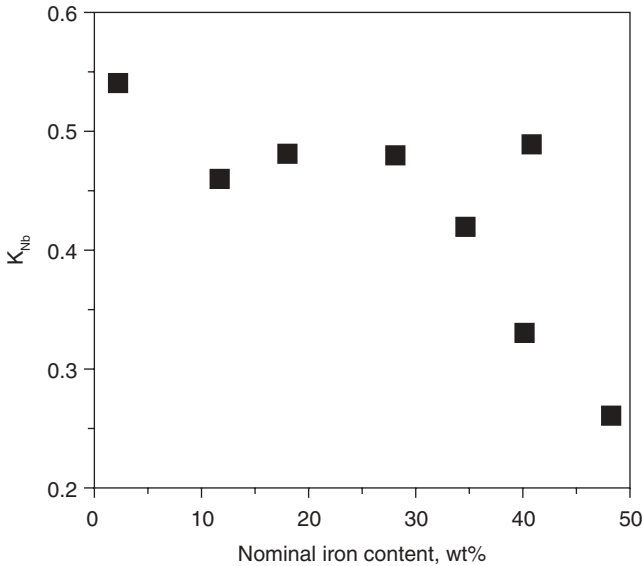


**Figure 4.26** Equilibrium distribution coefficient for Nb as a function of nominal Fe content for Nb bearing superalloys. (From DuPont *et al.* [14,16,20])

phases which form during solidification (NbC and Laves) are Nb rich. This effect has been attributed to the influence Fe has on the solubility of Nb in the austenitic matrix and was briefly described in Chapter 2. The maximum solid solubility of Nb in  $\gamma$ -Ni is 18.2 wt% Nb [at 1286 °C (2347 °F)], while  $\gamma$ -Fe can only dissolve a maximum of 1.5 wt% Nb at a comparable temperature of 1210 °C (2210 °F). Thus, iron additions decrease the solubility of Nb in the  $\gamma$ -(Fe,Ni,Cr) matrix and lead to a concomitant reduction in  $k_{Nb}$ .

The reaction sequence observed in Nb-bearing superalloys is similar to that expected in the ternary Ni-Nb-C system. The liquidus projection for the Ni-Nb-C system was estimated by Stadelmaier and Fiedler (30), and the Ni-rich corner of this diagram is redrawn in Figure 4.27. The liquidus projection exhibits three primary phase fields of interest:  $\gamma$ , NbC, and  $Ni_3Nb$ . A primary C (graphite) phase field exists at high C contents, but is not of interest. As previously noted, additions of Fe, Cr, and Si to the Ni-Nb system are well known to promote Laves at the expense of  $Ni_3Nb$ . Thus, by replacing  $Ni_3Nb$  with Laves, the Ni-Nb-C liquidus projection can be utilized as a guide in developing a qualitative description of the solidification reaction sequences in Nb-bearing superalloys. (14,15,20,22) Solidification begins with formation of primary  $\gamma$  dendrites which, upon forming, reject Nb and C to the liquid. As solidification proceeds, the liquid composition moves away from the Ni-rich corner (dotted line in Figure 4.27), becoming progressively richer in Nb and C until it reaches the monovariant eutectic line between  $\gamma$  and NbC. At this point,  $\gamma$  and NbC form simultaneously from the liquid by a eutectic-type reaction as the liquid composition travels down the eutectic line.

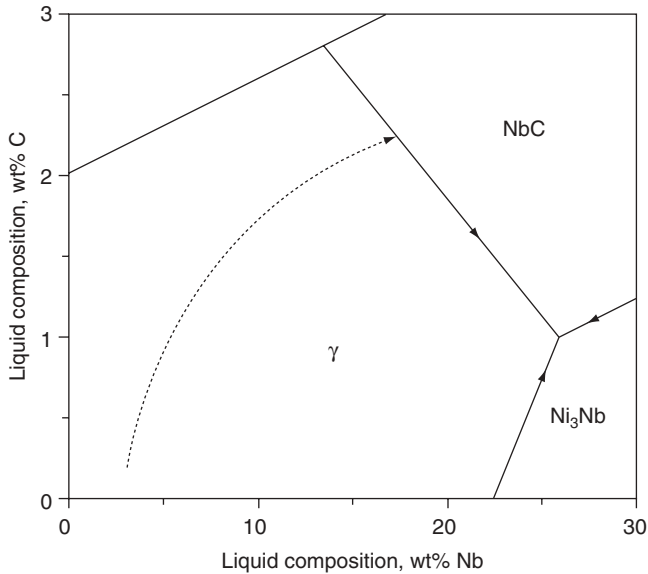


**Figure 4.27** Ni-Nb-C liquidus projection. (Redrawn from Stadelmaier and Fiedler [30])

Due to the high C content of NbC (~9.5 wt%), its formation depletes the liquid of C while the Nb content of the liquid continues to increase. If the C content of the alloy is high enough and the Nb content low enough, then solidification can be completed along  $\gamma$ /NbC eutectic line and no Laves phase will form.(16) For most alloys however, this does not occur and the liquid composition continues to be enriched until the Laves phase forms. According to the simple ternary Ni-Nb-C liquidus projection, solidification should terminate with the ternary  $L \rightarrow (\gamma + \text{NbC} + \text{Laves})$  ternary eutectic reaction where the liquidus surface is at an apparent minimum. Under this condition, the  $\gamma$ , NbC, and Laves phases should be intermixed. However, this type of structure is not observed in alloys that form both the NbC and Laves phases (e.g., Figure 4.21). Instead, the  $\gamma$ /NbC and  $\gamma$ /Laves eutectic-type constituents are always distinctly separated. This indicates that the actual liquidus projection for multi-component alloys is more properly represented by a Class II reaction in which the local minimum on the liquidus surface occurs where the  $\gamma$ /Laves eutectic line intersects the “Ni-Nb binary” side of the diagram.(21) This accounts for the spatially separate  $\gamma$ /NbC and  $\gamma$ /Laves eutectic-type constituents that are observed experimentally.

Solute redistribution modeling was recently applied to develop quantitative relations between composition and resultant fusion zone microstructures of Nb bearing alloys.(16) Based on the similarity to the simple Ni-Nb-C, the multi-component alloys were modeled as a ternary system by grouping the matrix (Fe,Ni,Cr) elements together as the “solvent” to form the  $\gamma$  component

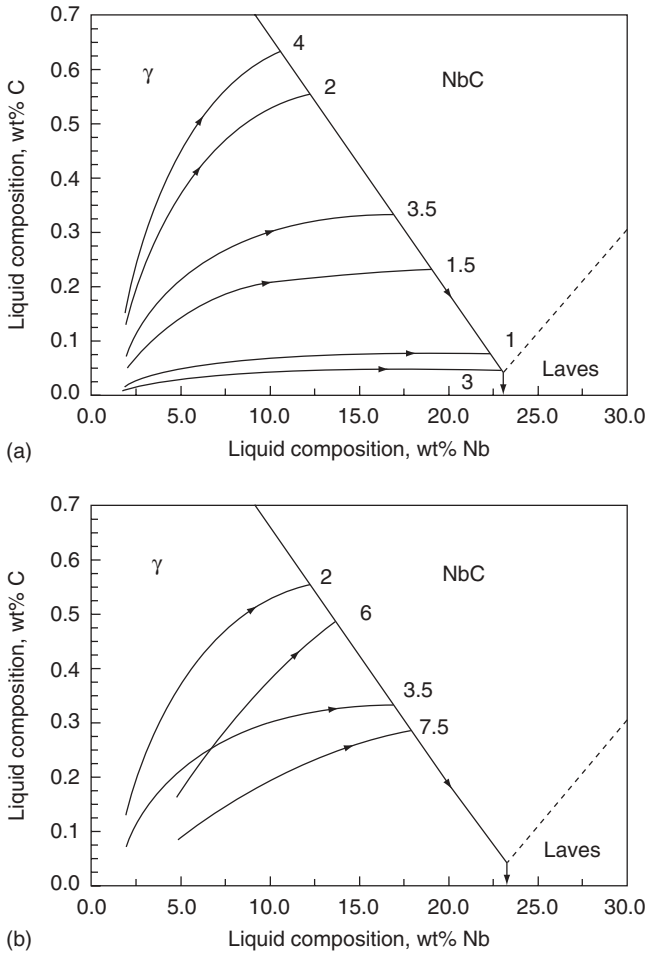


**Figure 4.28** Solute redistribution modeling results for experimental Ni base Nb bearing alloys. a) Alloys with similar Nb levels and increasing C content. b) Alloys with systematic variations in Nb and C content. (From DuPont *et al.* [14,20])

of the  $\gamma$ -Nb-C pseudo-ternary solidification diagram. Figure 4.28 shows typical modeling results for alloys with similar Nb levels and increasing C content (Figure 4.28a) and alloys with systematic variations in Nb and C contents (Figure 4.28b). The liquidus projections were determined experimentally by quantitative metallography and microprobe measurements.(14,20)

It is readily apparent that the point of intersection between the primary solidification path and line of two-fold saturation is a strong function of C content. Although C additions are intuitively expected to promote the  $\gamma$ /NbC eutectic type constituent, this analysis provides a quantitative rationale for the observed behavior. The intersection point occurs at higher C contents as the

nominal C content of the alloy increases. As a result, the liquid composition must “travel” a long distance down the  $L \rightarrow (\gamma + \text{NbC})$  line of two fold saturation, forming  $\gamma/\text{NbC}$  as it travels, before the  $\gamma/\text{Laves}$  constituent can possibly form. This explains why C additions often eliminate formation of the  $\gamma/\text{Laves}$  constituent—the solute rich liquid can be completely consumed along the  $\gamma/\text{NbC}$  eutectic line when the C content is high. The relative temperature at which the  $L \rightarrow (\gamma + \text{NbC})$  reaction starts is also readily assessed, where high nominal C contents drive the start of the reaction to higher temperatures. This is experimentally revealed in the reaction temperature data (Tables 4.5 and 4.6).

The increase in reaction temperature with increasing C content is not initially intuitive, particularly when one considers that the liquidus slope for C is negative.(23,25) This, at first, suggests that any increase in carbon in the liquid should drive the reaction to lower temperatures. The true effect can be understood by considering the relation between Nb and C along the  $\gamma/\text{NbC}$  eutectic line. The slope of this line is  $-0.047 \text{ wt}\% \text{C}/\text{wt}\% \text{Nb}$  for the Ni-base alloys. Thus, for every 0.047 wt% increase in C content, there is a corresponding decrease of 1 wt% Nb in the liquid. Assuming the liquidus slope for each element is constant and equal to the values determined by Cieslak *et al.*(25), where:  $m_{1,C} = -108.6^\circ\text{C}/\text{wt}\% \text{C}$  and  $m_{1,\text{Nb}} = -11.1^\circ\text{C}/\text{wt}\% \text{Nb}$ , then there is a drop in the reaction temperature of  $\approx 5.1^\circ\text{C}$  for every increase of 0.047 wt% C and a simultaneous increase in the reaction temperature of  $11.1^\circ\text{C}$  for the corresponding decrease in 1 wt% Nb content. Thus, a net increase of  $6^\circ\text{C}$  in reaction temperature is expected with every 0.047 wt% increase in C content (1 wt% decrease in Nb content). This effect causes the reaction start temperature to increase with increasing nominal carbon content.

The effect of nominal Nb concentration is revealed by comparing Alloy 2 to 6 and Alloy 3.5 to 7.5 in Table 4.6 and Figure 4.28b. When Nb is low, the C content in the liquid increases relatively quickly during the early stage of primary solidification. The rate of C enrichment continuously decreases as the line of two fold saturation is approached. Overall, the reaction start temperature will increase with decreasing Nb (i.e., increasing C/Nb ratio). Again, this trend is consistent with the experimental results. Since the length of the primary solidification paths for the high Nb alloys are shorter, these alloys will exhibit more liquid at the intersection point (i.e., more total eutectic-type constituent). Good agreement was observed between model calculations and experimentally measured values of the amount of total and individual  $\gamma/\text{NbC}$  and  $\gamma/\text{Laves}$  constituents using this approach.

The results described above illustrate the strong influence that minor variations in alloy composition have on the solidification behavior and resultant fusion zone microstructure of these alloys. As discussed in more detail below, these minor variations also have a strong effect on the resultant weldability. An example for Alloy 718 is shown in Table 4.7, which lists the chemical composition of five different heats of Alloy 718 that contain variations in Nb and C concentrations and the measured start temperature of the  $L \rightarrow \gamma + \text{NbC}$

**TABLE 4.7 Compositions (in Weight Percent) Along with Measured and Calculated  $L \rightarrow \gamma + \text{NbC}$  Temperatures for Five Different Heats of Alloy 718.**

Element	Heat 1	Heat 2	Heat 3	Heat 4	Heat 5
Ni	Bal.	Bal.	Bal.	Bal.	Bal.
Al	0.46	0.41	0.28	0.46	0.42
Cr	17.65	17.15	17.68	17.32	17.19
Fe	19.36	20.56	19.47	19.49	19.19
Mo	2.90	2.92	2.87	2.88	2.86
Nb	5.17	5.02	2.97	6.38	5.07
Ti	0.90	0.87	0.84	0.88	0.90
C	0.04	0.02	0.05	0.06	0.09
Measured $L \rightarrow \gamma + \text{NbC}$ Temperature, °C	1260 ±12	Not Detected	1290 ±9	1283 ±9	1296 ±9
Calculated $L \rightarrow \gamma + \text{NbC}$ Temperature, °C	1260	1237	1297	1264	1294

reaction for each alloy. Note that a seemingly small change in C content from 0.04 to 0.09 wt% increases the  $L \rightarrow \gamma + \text{NbC}$  start temperature by an average of  $\sim 36^\circ\text{C}$ . The experimentally determined pseudo binary diagram for Alloy 718 (Figure 4.23) cannot account for higher C alloys in which the  $\gamma/\text{NbC}$  constituent accounts for a large fraction of the total eutectic-type constituent in the final microstructure. In this case, calculated phase diagrams can be combined with solute redistribution calculations to quantitatively account for these variations.

Figure 4.29 shows calculated solidification paths of five different heats of Alloy 718 plotted on the calculated liquidus projection for this alloy.(31) The liquidus projection was computed by determining the position of the monovariant eutectic lines that separate the  $\gamma$ , NbC, and Laves primary phase fields. Although the diagram is displayed as a ternary projection, it accounts for the presence of eight elements (Ni, Fe, Cr, Mo, Al, Ti, Nb, and C) by approximating the matrix  $\gamma$  as a single elemental constituent. The liquid composition at which the  $L \rightarrow \gamma + \text{NbC}$  reaction is replaced by  $L \rightarrow \gamma + \text{Laves}$  is calculated at 19.1 wt% Nb and 0.03 wt% C. These values are in excellent agreement with those previously reported as 19.1 wt% Nb and 0.04 wt% C.(14,20) Superimposed on the diagram are the primary solidification paths, which were computed with a ternary solute redistribution model.(16) The intersection of the primary solidification path with the  $\gamma/\text{NbC}$  eutectic line provides a predicted value for the start temperature of the  $L \rightarrow \gamma + \text{NbC}$  reaction. These predicted values are noted in Figure 4.29 and summarized in Table 4.7, and good agreement is observed between the calculated and measured reaction temperatures. This example highlights the usefulness of calculated phase diagrams for assessing the effect of minor composition variations on the fusion zone solidification behavior and resultant microstructure.

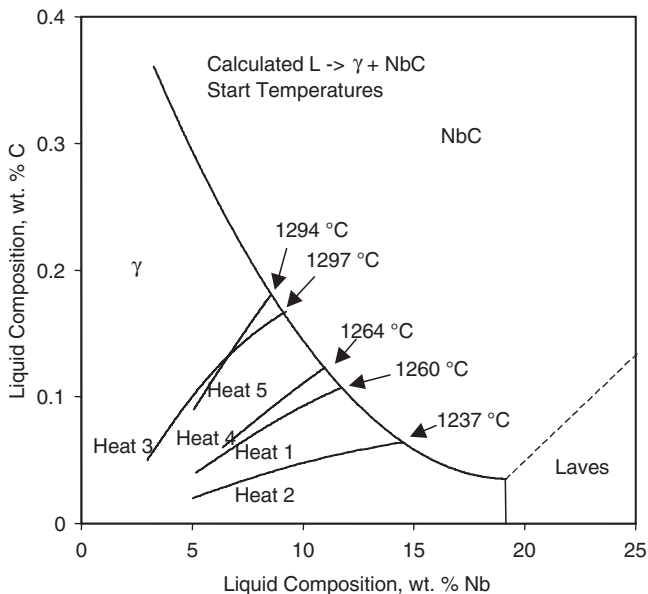


**Figure 4.29** Calculated solidification paths of five different heats of Alloy 718 plotted on the calculated liquidus projection. (From DuPont *et al.* [31])

#### 4.3.1.6 Fusion Zone Microstructure Predictions using New PHACOMP

The New PHACOMP procedure described in Chapter 2 can often be used to predict phase formation in the fusion zone when more complicated thermodynamic calculation routines or pertinent thermodynamic data are not available. The connection between the use of phase diagrams and the New PHACOMP procedure lies within the relation between the eutectic composition in the liquid and the maximum solubility in the solid. This is most easily understood with the aid of the simple binary phase diagram shown in Figure 4.30. Assuming dendrite tip undercooling is negligible, the first solid will form at a composition  $kC_0$  from liquid which is at the nominal composition  $C_0$ . As solidification proceeds, the solid and liquid interfacial compositions follow the solidus and liquidus lines of the phase diagram, respectively. This process continues until the maximum solubility of solute is locally met in the solid at the solid/liquid interface, at which point a secondary phase begins to form by a eutectic reaction. Thus, the eutectic transformation coincides with the condition at which the maximum solubility in the solid is met.

The process is similar in multi-component alloys, except that the planar phase field regions of the simple binary diagram evolve into more complicated volumes and more than one reaction can occur over a range of temperatures. The phase diagram approach monitors the *liquid* composition in order to assess the phases that will form at the end of solidification, while the New PHACOMP routine is used to predict phase formation by monitoring the

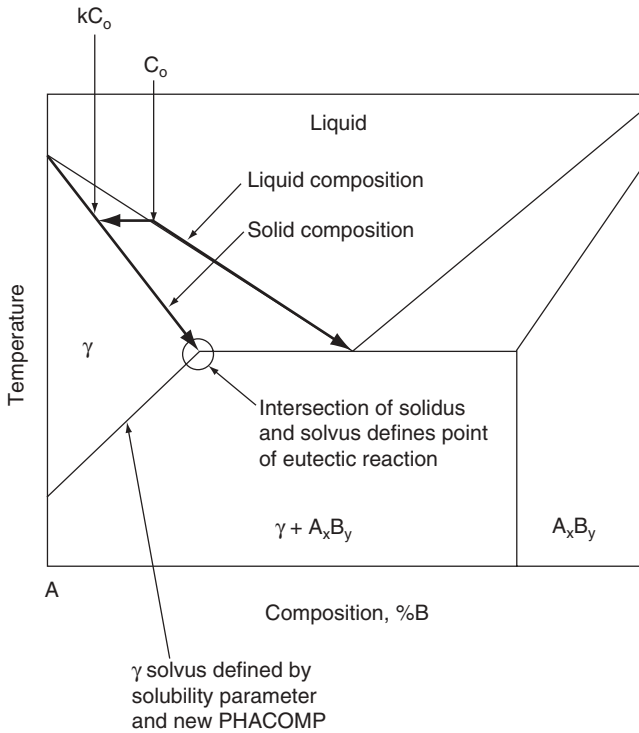


**Figure 4.30** Binary phase diagram showing coincidence of solidus and solvus intersection point to the eutectic temperature.

solubility limit of the *solid*. However, from Figure 4.30 it is clear that these two approaches “converge” and provide similar information at the terminal stages of solidification where a eutectic type reaction is induced because the solubility limit of the solid is met.

With these concepts in mind, the formation of topologically closed packed (TCP) phases (such as P,  $\sigma$ , and Laves) in the fusion zone of Ni-base alloys can be understood by considering how the average *d*-electron energy above the Fermi level,  $M_d$ , varies across the cellular substructure due to microsegregation. As discussed in Chapter 2, the value of  $M_d$  is given by:

$$M_d = \sum (x_i)(m_d) \quad (\text{Eqn. 4.3})$$

where  $x_i$  is atomic fraction of element *i* in the nickel matrix and  $m_d$  is the metal *d*-level of element *i*. Values of  $m_d$  for various elements are summarized in Table 2.3. The value of  $M_d$  is a minimum at the cell core and increases as the cell boundary is approached due to microsegregation. When the actual  $M_d$  level reaches the critical temperature dependent value of  $M_{d,\text{crit}}$  (Eqn. 4.4),

then the solid solubility will be met and a eutectic type reaction will occur involving a TCP phase:

$$M_{d,crit} = 6.25 \times 10^{-5}(T) + 0.834 \quad (\text{Eqn. 4.4})$$

An example of this is shown in Figure 4.31, which shows the  $M_d$  profiles across the cellular substructure of several commercial alloys along with the  $M_{d,crit}$  values for each alloy (horizontal dotted line).<sup>(32)</sup> (Both solid solution and precipitation strengthened alloys are analyzed in Figure 4.31 since, as noted previously, the segregation tendency of various elements in these alloys is independent of their intended purpose.) The variation in  $M_d$  was determined through microprobe data and Eqn. 4.3. The  $M_d$  level exceeds the  $M_{d,crit}$  level for alloys C-22, C-276, 625, and 718, thus correctly predicting the occurrence of TCP phases in the interdendritic regions in these alloys. The Laves phase forms in Alloys 625 and 718. Alloy C-22 forms both the P and  $\sigma$  phases, while Alloy C-276 only forms P phase during solidification. Alloy C-4 does not form any TCP phase in the fusion zone during solidification, and the results shown in Figure 4.31 accurately reflect this.

More recently this approach has been improved by including the formation of carbides and providing a method for quantitative estimates of the reaction temperatures.<sup>(33)</sup> This is accomplished by using simple solute redistribution equations to calculate the variation in solid composition as a function of temperature and then comparing these results to the temperature dependent composition values needed in the solid to form either the carbide or TCP phase. The critical value of alloying element needed in the primary  $\gamma$  to form carbides is calculated through solubility product relations while the critical value needed to form TCP phases is determined through the New PHACOMP calculation routine.

For the alloying elements except C, the Scheil equation is used to determine the relation between the interfacial solid composition,  $C_{s,i}^*$ , and temperature via:

$$C_{s,i}^* = k_i C_{o,i} \left[ \frac{T_o - T}{T_o - T_l} \right] \quad (\text{Eqn. 4.5})$$

where  $C_{s,i}^*$  is the concentration of element  $i$  in the solid at the solid/liquid interface,  $k_i$  is the distribution coefficient for element  $i$  between liquid and primary solid,  $C_{o,i}$  is the nominal alloy content of element  $i$ ,  $T_o$  is the melting point of the pure solvent,  $T_l$  is the liquidus temperature of the alloy, and  $T$  is actual temperature. For C, the equilibrium lever law is applied to relate the C concentration in the solid to temperature.<sup>(14,34)</sup>

$$C_{s,C} = \frac{k_C C_{o,C}}{1 - \frac{T_l - T}{T_o - T}} \quad (\text{Eqn. 4.6})$$

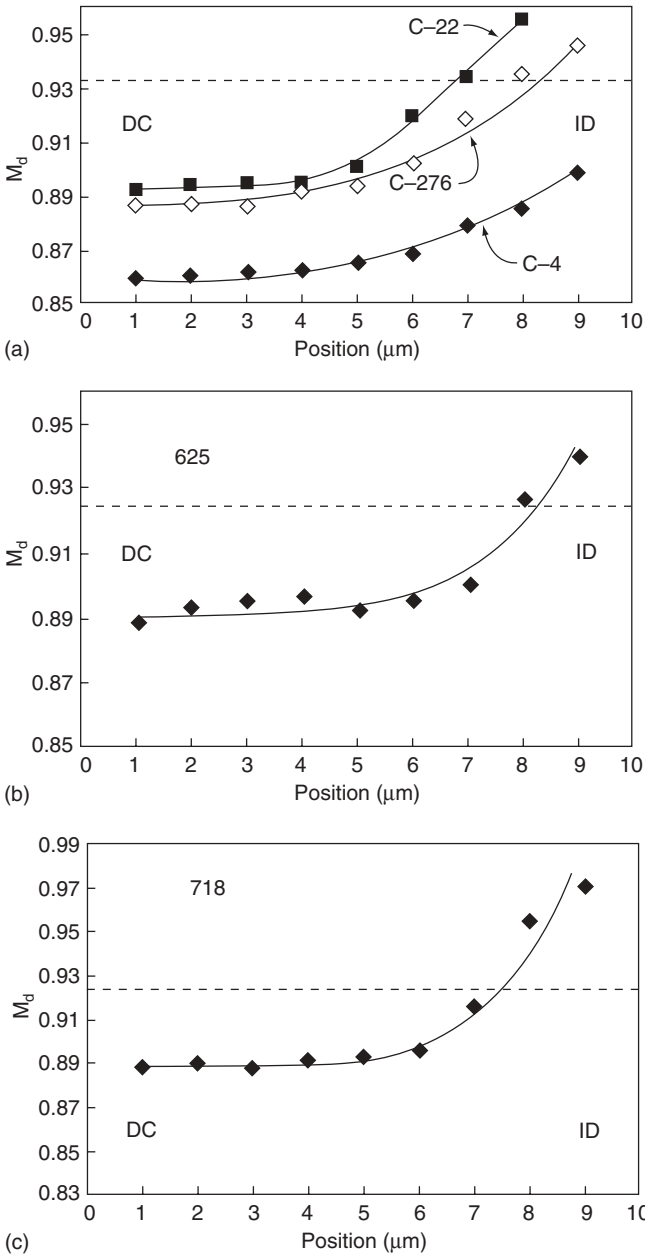


**Figure 4.31**  $M_d$  profiles across the cellular substructure of several commercial alloys (data) along with the  $M_{d,crit}$  values for each alloy (horizontal dotted line). (From Cieslak *et al.* [32])

The concentration of matrix elements (i.e., Fe,Ni,Cr) in the primary solid at the solid/liquid interface is estimated to vary with temperature in the same ratio as their nominal alloy content.

Carbide phases will precipitate during solidification when the maximum solid solubility of the metallic carbide forming element and C has been locally exceeded in the solid at the solid/liquid interface. The solubility product for this reaction can be expressed as a function of temperature in the general form:

$$\ln(MC) = A - \frac{B}{T} \quad (\text{Eqn. 4.7})$$

Where A and B are material constants and T is absolute temperature. The temperature dependent  $\gamma$ /TCP solvus is given by Eqn. 4.4.

These relations can be utilized to estimate temperatures reactions involving both carbides and TCP phases in the following manner. The variation in primary  $\gamma$  composition with temperature is first established with the solute redistribution Eqns. 4.5 and 4.6. From this, the variation in  $M_d$  and  $\ln(MC)$  with temperature is calculated. The temperature dependant values of  $\ln(MC)$  are then compared with the corresponding temperature dependant values of  $A-B/T$  to estimate when the composition of the primary  $\gamma$  dendrites meets conditions for formation of carbides. In a similar manner, the temperature dependent values of  $M_d$  are compared with the corresponding temperature dependant values of  $M_{d,crit}$  to determine when TCP phases will form.

An example calculation is shown graphically in Figure 4.32 for an alloy that exhibits the  $L \rightarrow (\gamma + NbC)$  and  $L \rightarrow (\gamma + \text{Laves})$  transformations. The figure shows the temperature dependant values of  $\ln(NbC^{0.81})$  and  $M_d$ . Superimposed on each plot is the temperature dependent values of  $A-B/T$  and  $M_{d,crit}$ . The intersection point of the  $\ln(NbC^{0.81})$  curve with the  $A-B/T$  curve signifies the initiation temperature of the  $L \rightarrow (\gamma + NbC)$  reaction. Similarly, the  $L \rightarrow (\gamma + \text{Laves})$  transformation is predicted to initiate at the temperature where the  $M_d$  and  $M_{d,crit}$  curves intersect. The results correctly predict occurrence of the  $L \rightarrow (\gamma + NbC)$  reaction prior to the  $L \rightarrow (\gamma + \text{Laves})$  transformation. The predicted reaction temperatures of 1355 °C (2470 °F) for the  $L \rightarrow (\gamma + NbC)$  reaction and 1190 °C (2175 °F) for the  $L \rightarrow (\gamma + \text{Laves})$  reaction are in reasonable agreement with the measured values of 1328 °C (2420 °F) and 1190 °C, respectively. The results also capture variations in reaction temperature associated with nominal alloy compositions. For example, the value of  $A-B/T$  depends only on temperature and the position of this curve therefore does not change with variations in nominal alloy content. As the C content increases, the  $\ln(NbC^{0.81})$  curve shifts upwards. The upward shift in the  $\ln(NbC^{0.81})$  curve indicates the maximum solid solubility of Nb and C in the primary austenite will be met at higher temperatures as the nominal C content in the alloy is increased. As a result, the  $L \rightarrow (\gamma + NbC)$  reaction is predicted to occur at higher temperatures during solidification as the C content is increased, a trend which has been verified experimentally.(23,25)

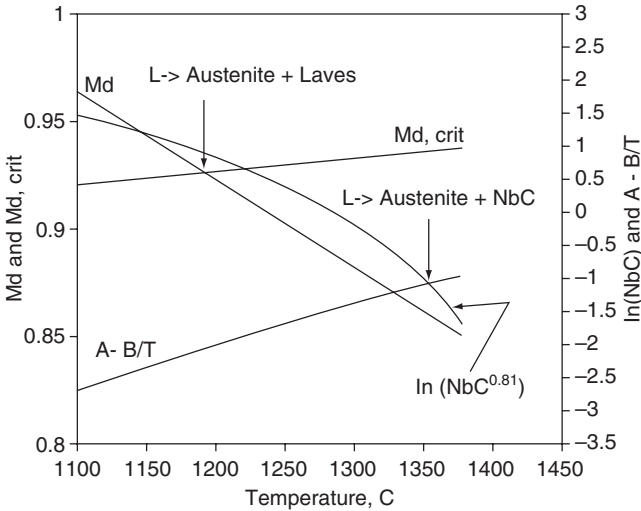


**Figure 4.32** Graphical representation of combined solubility product/New PHACOMP calculations for a nickel alloy.

### 4.3.2 Heat-Affected Zone

The heat affected zone (HAZ) that develops in the precipitation-strengthened Ni-base alloys is dependent on the microstructure of the base metal. These alloys can be welded in either the solution annealed or precipitation-hardened conditions. Welding when the base metal is in the solution annealed condition is often specified when cracking in the fusion zone or partially-melted zone (PMZ) of the HAZ is a concern. When the base metal is in the precipitation-hardened condition the intrinsic restraint in the HAZ and weld metal will be considerably higher than when the base metal is in the “softened” condition. When welding with the base metal in the solution annealed condition, the entire structure must be heat treated following welding to restore the strength of the base metal and weldment. In situations in which postweld heat treatment is not possible, these alloys are welded in the precipitation-hardened condition. Both situations are described in this section.

When the base metal is in the solution annealed (or partially solution annealed) condition, microstructural evolution in the HAZ is similar to that described in Section 3.3.2. Metallurgical reactions include grain growth, grain boundary segregation, grain boundary liquation, constitutional liquation, and on-cooling precipitate formation. The degree of grain growth is determined by the starting base metal grain size and the thermal history experienced by the HAZ. This is dictated by the weld heat input and the heat flow conditions surrounding the weld. Since many Ni-base superalloys are supplied in the fine-grained condition to provide good high-cycle fatigue resistance, grain growth in the HAZ is often undesirable.

Grain boundary segregation was described in Section 3.3.2 and the basic principles are the same for the precipitation-strengthened alloys. Since some of the Ni-base superalloys contain B for improved elevated temperature creep resistance, segregation of this element to HAZ grain boundaries can be a problem since it may lead to grain boundary liquation. Under sufficient restraint this can lead to cracking in the PMZ. This is discussed in more detail in Section 4.5.2.2. Segregation of other alloy and impurity elements to the HAZ grain boundaries is also possible. These elements include Al, Ti, Si, Nb, S, and P. Sulfur and phosphorus segregation can be problematic, but in most superalloys the level of these elements is usually sufficiently low (less than 100 ppm) that segregation of these impurities is inconsequential.

Constitutional liquation was first proposed in 1966 by Pepe and Savage (35) based on work with steels, but was soon associated with HAZ liquation in Ni-base alloys by Duvall and Owzarski at Pratt&Whitney.(36,37) The basis of this mechanism requires the reaction between a “constituent” particle and the surrounding matrix such that local melting occurs at the constituent/matrix interface, hence the term “constitutional” liquation. Under the conditions of constitutional liquation, the constituent particle itself does not melt. Most of the particles that undergo constitutional liquation (such as NbC and TiC) have melting temperatures far exceeding that of the base metal. Rather, it is the intermediate composition in the reaction zone between the particle and the matrix that melts. In order for this mechanism to be operative:

- 1) the particle must react with the matrix to create a composition gradient around the particle, and
- 2) the reaction zone composition must undergo melting below the melting temperature of the surrounding matrix.

A simple binary phase diagram that exhibits a eutectic reaction between a particle phase,  $A_xB_y$ , and the matrix phase,  $\alpha$ , can be used to describe constitutional liquation, as shown in Figure 4.33. When an alloy of composition  $C_A$  is heated, a reaction between the matrix and particle will occur. The nature of that reaction at temperatures  $T_1$ ,  $T_2$ ,  $T_e$ , and  $T_3$  in Figure 4.33 is shown schematically in Figure 4.34.

At room temperature, the particle of composition  $A_xB_y$  resides in a matrix of composition  $C_0$ , as shown in Figure 4.34A. If this microstructure were heated slowly, the particle would dissolve when the temperature exceeded the solvus temperature at approximately  $T_2$  in Figure 4.33. Under the rapid heating conditions experienced in the HAZ, the particle does not totally dissolve. Rather, as the microstructure is rapidly heated to  $T_2$ , the particle starts to react with the surrounding matrix. Since equilibrium is generally maintained at the particle matrix interface, the particle of composition  $A_xB_y$  is in contact with a matrix composition indicated by the point “b” on the solvus line. A composition gradient resulting from the partial particle dissolution now exists in the

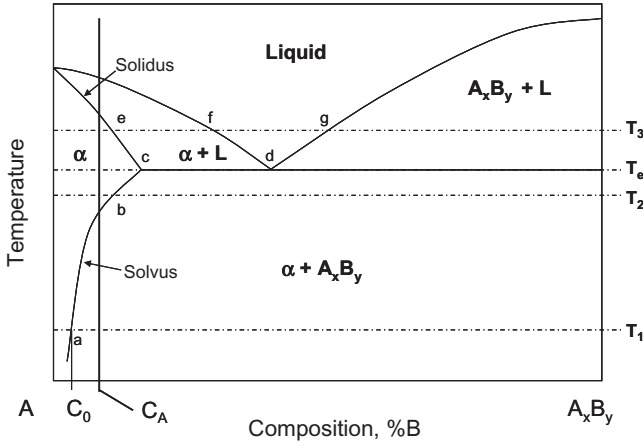


Figure 4.33 Binary phase diagram used to describe constitutional liquation.

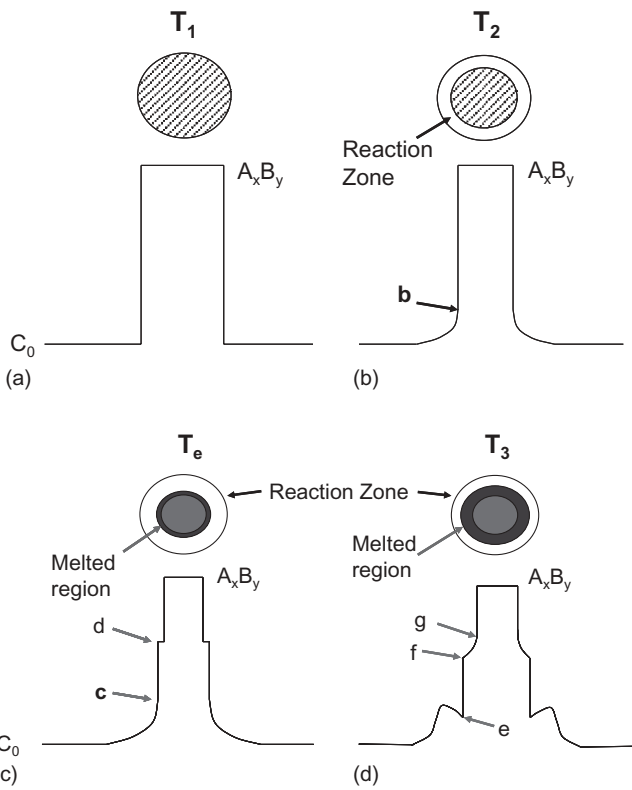


Figure 4.34 Schematic illustration of the constitutional liquation mechanism.

matrix. This occurs in a reaction zone surrounding the particle where B atoms are diffusing into the surrounding matrix.

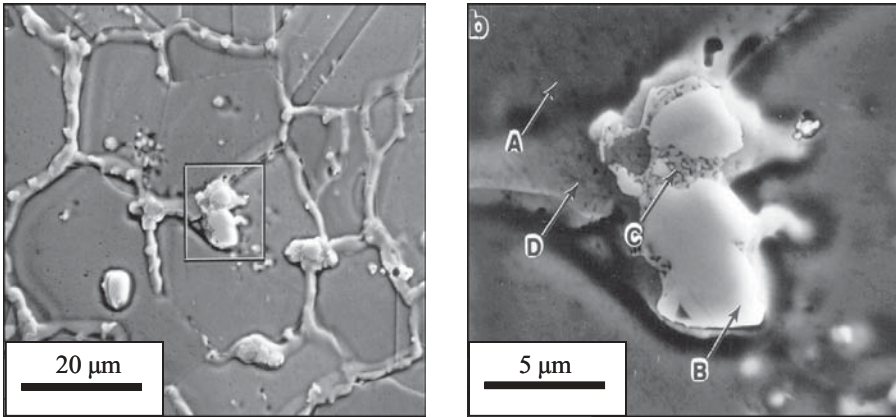
As the alloy is heated from  $T_2$  to  $T_e$ , the interface composition continues along the solvus line of the phase diagram. As shown in Figure 4.34C, when this composition reaches point “c” at the eutectic temperature, equilibrium dictates that a liquid of composition “d” must be in contact with the solid. As a result, liquid of eutectic composition is formed in the system within the reaction zone. This liquid completely surrounds the particle and represents the onset of “constitutional liquation.”

As the microstructure continues to be heated to  $T_3$ , additional liquid forms in the system. The composition of this liquid ranges from “g” at the particle interface to “f” at the matrix interface, as shown in Figures 4.33 and 4.34D. The composition of the matrix in contact with the liquid is now represented by point “e” on the solidus line. Again, all interface compositions must obey microscopic equilibrium as dictated by the phase diagram. Note that a solute “hump” is predicted in the solid matrix within the reaction zone. This occurs because the solid composition achieved at  $T_e$  (point “c”) has now decreased to “e” since the solid composition must lie along the solidus line. Above  $T_3$  additional constitutional liquation will occur around the particle until the alloy exceeds the solidus temperature and bulk melting of the matrix begins.

For constitutional liquation to occur, the particle must partially, but not completely, dissolve upon heating to the eutectic temperature. If complete dissolution occurs, such as during slow heating, no constitutional liquation can occur. Under extremely rapid heating conditions, constitutional liquation can be suppressed if no particle dissolution occurs. Thus, the welding thermal cycle, especially for arc welding processes, provides a unique situation under which constitutional liquation can occur. An example of a NbC particle that has undergone constitutional liquation in a weld HAZ is shown in Figure 4.35. The implications of constitutional liquation on HAZ liquation cracking is described in Section 4.5.2.

### 4.3.3 Postweld Heat Treatment

The postweld heat treatment (PWHT) response of precipitation hardened nickel alloys was discussed in general terms in Section 4.3.1.2. Table 4.8 summarizes typical PWHT cycles that are used on several precipitation-strengthened Ni-base alloys. These treatments are generally designed to restore strength in the weld by precipitation and can also provide relief of residual stresses. It is important to note that multiple PWHT cycles can be used to accent various properties within a given alloy, so it is difficult to make generalizations about PWHT schedules for a wide range of alloys. For example, when Alloy 718 selected for fatigue-limited service, it is typically heat treated using a low-temperature anneal in the range from 955–1010 °C (1750–1850 °F) to ensure a fine grain size. The low temperature anneal is followed by a rapid cool and precipitation treatment that occurs from lower temperature.



Location	Structure	Composition (wt%)					
		Fe	Ni	Co	Nb	Ti	Si
A	Gamma matrix	Bal	37.0	11.8	5.8	1.5	0.7
B	Nb-rich carbide	Bal	0.2	-	85.3	13.4	0.3
C	Laves phase	Bal	33.4	10.9	25.9	3.3	1.0
D	Grain boundary gamma	Bal	38.5	11.3	10.2	2.6	0.9

**Figure 4.35** Constitutional liquation of a NbC particle.

**TABLE 4.8** Typical Recommended Post Weld Heat Treatments for Several Precipitation Strengthened Ni-base Alloys.

Base Metal/Filler Metal	UNS	Recommended Postweld Heat Treatment Procedures
K500/FM64	N05500	1100°F/16 hr, furnace cool (15°F/h) to 900°F, air cool.
750/FM69	N07750	1300°F/20 hr, air cool.
718/FM718	N07718	1325°F/8 hr, furnace cool to 1150°F, Held at 1150°F for 8 hours, air cool.
725/FM725	N07725	1900°F/1 hr plus 1350°F/8 hr, furnace cool to 1150°F, held at 1150°F for 8 hours, air cool.
80A/FM80A	N07080	1700°F/1 hr, air cool to 1380°F, held at 1382°F for 4 hours, air cool.
90/FM90	N07090	1700°F/1 hr, air cool to 1380°F, held at 1382°F for 4 hours, air cool.
263/FM263	N07263	1472°F/8 hr, air cool.
909/FM909	N19909	1325°F/8 hr, furnace cool at 100°F/1 h to 1150°F, held at 1150°F for 8 hours, air cool.

For creep-limited service, a higher temperature anneal in the range from 1010–1065 °C (1850–1950 °F) is chosen to produce coarse grains in the base metal, followed by a precipitation heat treatment. If impact strength is to be enhanced, a high temperature anneal of 1065 °C (1950 °F) is chosen and the precipitation treatment is conducted at 760 °C (1400 °F) for ten hours followed by a furnace cool and a hold at 650 °C (1200 °F) for 20 hours. These treatments are all variations to the PWHT recommendations listed in Table 4.8.

Most of the precipitation-strengthened Ni-base alloys should be cooled rapidly from their annealing temperature prior to the aging treatment. The rapid cool is required to avoid precipitate overaging. Some of the earlier alloys were occasionally welded in the overaged condition to help improve weldability when thick sections were joined. Originally, strain-age cracking (discussed in more detail below) was often encountered when thick sections of the rapid-aging alloys such as K-500 or X-750 were welded without intermediate anneals. Once welding was completed, the entire fabricated part could be solution annealed, cooled quickly, and then aged to avoid strain-age cracking. In many cases, the PWHT can compromise the weldability in the event the need for repair or alteration arises. For example, for optimum creep resistance for high temperature service, the precipitation-strengthened alloys are normally given an elevated temperature anneal to increase the grain size prior to the aging heat treatment. Once the grain size has been coarsened, the material can become more susceptible to heat affected zone liquation cracking, as discussed in Section 4.5.2.

PWHT schedules can also be required for dissimilar weld combinations, and Ni-base welding consumables can be chosen for their combination of good corrosion resistance and PWHT compatibility with steels. For example, some of the hardenable steels such as AISI 4340 and 8620 can be overlaid with Filler Metal 725, and the PWHT required by the steel can benefit the nickel alloy weld deposit. An abbreviated aging treatment for the weld overlay (i.e., without the use of the normal post weld solution anneal) can provide overlay strength that slightly overmatches that of the steel. Such a treatment also provides tempering for the steel substrate. For example, a direct aging treatment for this substrate/overlay combination of 1200 °F/eight hours or 1150 °F/ten hours results in a yield strength of 97 ksi (670 MPa) for the overlay, while a 1200 °F/24 hours treatment increases the yield strength to 114 ksi (785 MPa). Any of these treatments will preserve the original properties of the 4340 or 8620; provide a tempering treatment for the martensite formed in the HAZ of the steel by the weld overlay; and strengthen the FM 725 weld overlay. In addition, the good corrosion resistance of the alloy 725 weld overlay is generally still maintained after the aging heat treatment.

#### 4.4 MECHANICAL PROPERTIES OF WELDMENTS

Typical mechanical property ranges of weldments in several precipitation-strengthened nickel alloys are given in Table 4.9. In each case, the tensile

**TABLE 4.9 Mechanical Properties of Filler Metals for Precipitation-Strengthened Ni-base Alloys.**

Type	UNS	Tensile	Yield	Elongation, %	Reduction in Area, %	Hardness, R <sub>C</sub>
		Strength, ksi	Strength, ksi			
FM64	N05500	100–150	80–110	30–15	45–28	28–35
FM69	N07750	120–170	80–120	35–15	48–20	30–40
FM718	N07718	160–220	140–180	28–10	30–12	35–50
FM725	N07725	120–175	70–130	35–15	35–20	25–40
FM80A	N07080	160–180	110–120	30–35	15–20	
FM90	N07090	130–160	100–115	20–10		
FM263	N07263	120–140	75–80	35–40		
FM909	N19909	150–190	130–150	14–18	20–32	
625 PLUS	N07716	160–190	100–140	20–40	40–60	
Thermo-Span		150–180	90–130	10–20	25–35	

properties are approximately the same values as the base metals in the annealed condition. For maximum tensile values, a postweld solution anneal is typically used followed by a custom-designed heat treatment that precipitates the pertinent strengthening phase. Slightly higher temperature and longer aging times generally provide for better impact properties.

#### 4.5 WELDABILITY

Potential weldability issues for precipitation-strengthened Ni-base alloys include fusion zone solidification cracking, HAZ liquation cracking, strain-age cracking, and ductility dip cracking. Some of the concepts used to understand susceptibility of these alloys to weld solidification cracking are similar to those of the solid-solution strengthened alloys described in Chapter 3, although the addition of alloying elements to improve elevated temperature properties can provide additional challenges. HAZ liquation cracking can occur due to both grain boundary segregation and constitutional liquation mechanisms. In particular, alloys strengthened by the addition of Nb can be particularly susceptible to HAZ liquation cracking due to the constitutional liquation of NbC. Strain-age cracking is a solid-state phenomenon that is unique to this class of alloys. The alloys that are strengthened by additions of Al and Ti through the precipitation of  $\gamma'$  are most susceptible to strain-age cracking. As discussed in more detail in Section 4.5.3, the cracking sensitivity is strongly dependent on the Al and Ti content and concomitant kinetics of precipitation. The severe strain-age cracking susceptibility of alloys with high Al and Ti contents has been directly linked to the rapid aging response of these alloys. One of the driving forces for the development of Alloy 718 and subsequent Nb-bearing alloys was the slow aging response of  $\gamma''$ -Ni<sub>3</sub>Nb that make these alloys

essentially immune to strain-age cracking. Although these alloys are potentially susceptible to ductility dip cracking (DDC), there have been only limited reports of DDC in precipitation-strengthened superalloys. This may be due to the nature of the weld microstructure or that the precipitation-strengthened alloys are not used in thick-section applications and weld restraint is not sufficient to promote DDC.

The following sections will review the weld solidification, HAZ liquation, and strain age cracking susceptibility of the precipitation-strengthened alloys. Particular emphasis is given to the elemental effects on cracking susceptibility and how composition and/or microstructure can be altered to reduce or eliminate cracking in these alloys.

#### 4.5.1 Solidification Cracking

The general factors that control solidification cracking susceptibility of Ni-base alloys were briefly reviewed in Section 3.5.1. The solidification cracking response of  $\gamma'$  strengthened alloys is strongly affected by the level of minor elements such as P, S, B, C, and Zr. The impurity elements P and S should be held as low as possible for improved cracking resistance since they generally provide no benefit to alloy performance.

**4.5.1.1 Effect of Minor Element Additions—B and Zr** The elements B, C, and Zr are often added for grain boundary strengthening where good creep strength is required, so their level must be controlled to achieve a balance of high temperature strength and weldability. The role of B on weldability is well established and this element has a strong, deleterious effect on solidification and liquation cracking susceptibility. An example of this for Alloy 214 is shown in Figure 4.36 which shows the total crack length from Varestraint tests for two heats of Alloy 214 with different B concentrations (0.0002 and 0.003 wt%).(38) The cracking resistance of the low B heat is excellent, while the high B heat is very susceptible to cracking. The high B alloy also had a slightly higher Zr level (<0.02 wt% vs. 0.07 wt%), which may also have affected the results. The effect of B is similar to that shown in Chapter 3 for the B-containing C-4 alloys. The detrimental influence of B can be attributed to its strong segregation tendency and formation of a  $M_3B_2$  type phase that forms at the relatively low temperature of  $\sim 1200^\circ\text{C}$  ( $2190^\circ\text{F}$ ). The addition of B also appears to lower the solid/liquid surface energy, which exacerbates cracking by promoting extensive wetting of the solidification grain boundaries and interdendritic regions by the terminal solute rich liquid.

The low temperature phase that forms during the terminal stage of solidification depends on the presence and amount of the minor alloying elements. For example, in Alloy 80A, the combined presence of Zr and S leads to formation of ZrS in the grain boundary and interdendritic regions.(39) An intermetallic phase based on Ni and Zr also forms, which appears similar to that which forms in Alloy 738.(18,19) Upon removal of Zr from Alloy 80A, a TiS

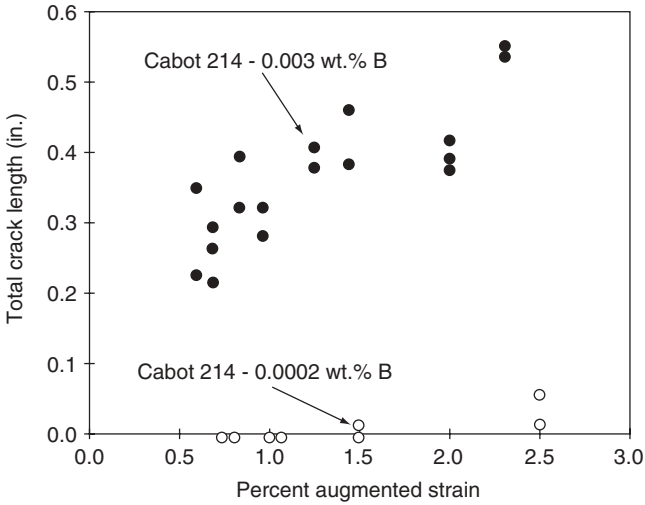


**Figure 4.36** Vareststraint solidification cracking results for Alloy 214 with 0.0002 wt% B and 0.003 wt% B. (From Cieslak *et al.* [38])

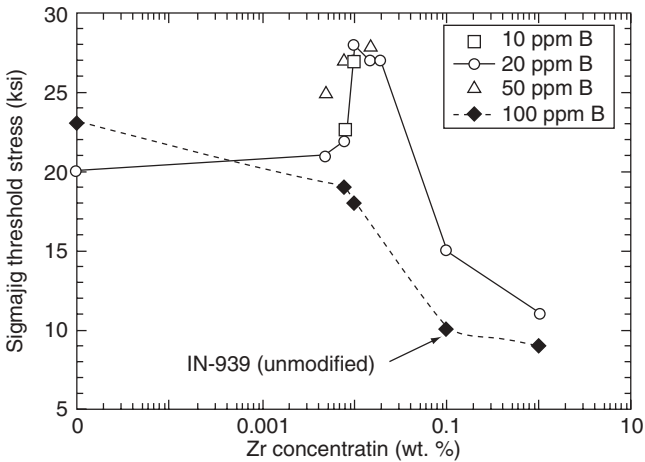


**Figure 4.37** Influence of Zr and B on the solidification cracking susceptibility of Alloy 939. (From George *et al.* [40])

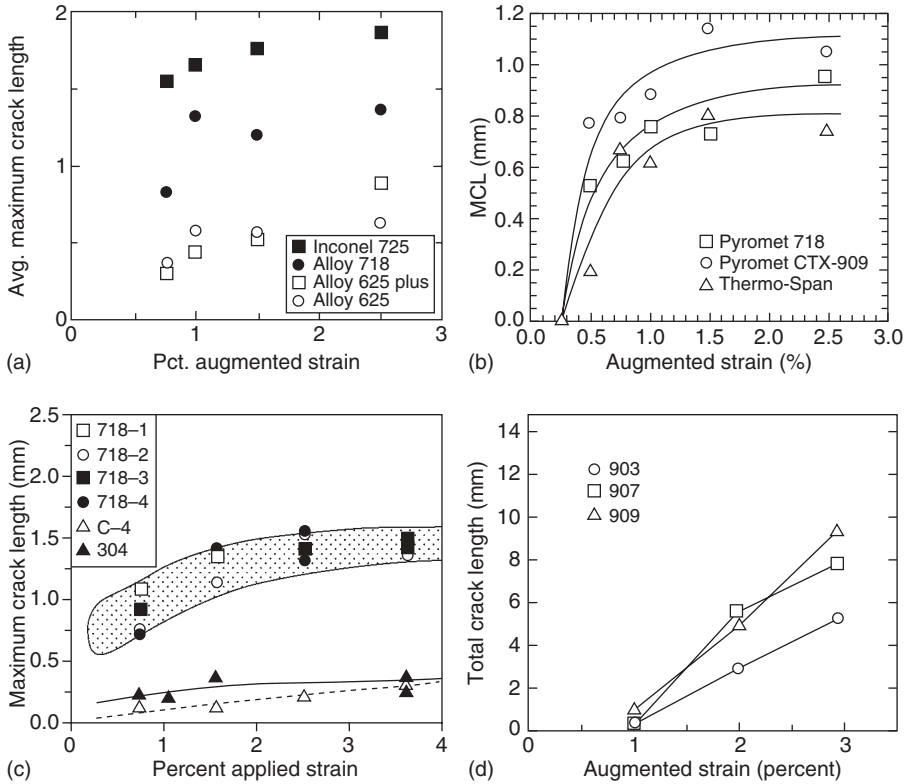
compound forms instead of ZrS. The formation temperature of the ZrS and TiS phases are each ~1170°C (2140°F) and therefore would be expected to have similar effects on weldability.

Figure 4.37 shows the combined influence of Zr and B on the solidification cracking susceptibility of Alloy 939. (40) These results were obtained from the Sigmajig test in which the magnitude of the transverse stress required to induce complete separation of the sample via solidification cracking is determined. Thus, a higher threshold stress implies greater cracking resistance. The

nominal Zr and B levels for commercial Alloy 939 are 0.1 wt% and 0.01 wt%, respectively. Although Zr additions are generally viewed as having a deleterious effect on cracking resistance in these types of alloys, these results show that Zr additions up to ~0.04 wt% can be tolerated with no adverse effect on cracking susceptibility when the B level is held to 10–50 ppm (0.001 to 0.005 wt%). The results even suggest that Zr additions in the 0.01–0.04 wt% range provide a favorable effect when the B level is low, although the reasons for this are currently not clear. At the 100 ppm B level, any addition of Zr has a detrimental influence on cracking susceptibility. The results shown in Figure 4.37 were obtained on alloys that had sulfur levels in the 20–40 ppm range. A reduction in the S concentration down to <1 ppm showed that higher amounts of B and Zr can be tolerated. For example, at the 0.1 wt% Zr/100 ppm B level, an alloy with <1 ppm S exhibited twice the threshold stress in the SigmaJig test (21 ksi) compared to an alloy that had 20–40 ppm S (10 ksi). These results clearly demonstrate the beneficial effect of maintaining low S levels for accommodating higher amounts of minor elements that are detrimental from a cracking standpoint, but beneficial from a grain boundary strengthening perspective.

**4.5.1.2 Effect of Nb Additions** The fusion zone solidification cracking susceptibility of Nb-bearing alloys strengthened by  $\gamma''$  is primarily controlled by the formation temperature of the  $\gamma$ /Laves eutectic type constituent and the relative amount and morphology of the  $\gamma$ /NbC and  $\gamma$ /Laves constituents. Figure 4.38 shows Vareststraint weldability results for a number of commercial Nb-bearing Ni base alloys.(27,41,42) (Results for both precipitation- and solid-solution strengthened alloys are provided in this figure since, as previously explained, the solidification response and resultant solidification cracking behavior are generally independent of the purpose of the alloy addition.) The 900 series and Thermo-span alloys are low thermal expansion solid-solution strengthened alloys used in high temperature applications where dimensional tolerance control is required over a wide range of temperatures.

These weldability results are useful from a practical perspective for developing a ranking of cracking susceptibility among commercial alloys. The composition of each alloy is summarized in Table 4.10 along with the liquidus and  $L \rightarrow \gamma + \text{Laves}$  temperatures and solidification temperature ranges. The results presented in Figure 4.38 a, b, and c are particularly useful because they were produced under essentially identical conditions from the same laboratory and can therefore be directly compared. This comparison is summarized in Figure 4.39, where the maximum crack length (MCL) of each alloy at the highest applied strain is used as an indicator of cracking susceptibility. The results for 304 stainless steel and Alloy C-4 are also shown as a basis for comparison, since these are Nb-free alloys. Note that the cracking susceptibility of the Nb-bearing alloys is considerably higher than that of 304 stainless steel and the C-4 alloy. This increased susceptibility is attributed to formation of the low temperature  $\gamma$ /Laves constituent that widens the solidification temperature range. The results shown in Figure 4.38d indicate that the cracking susceptibil-



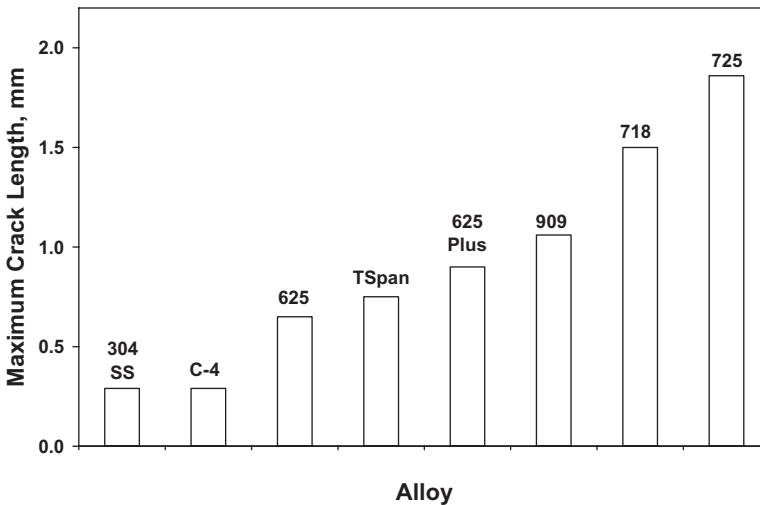
**Figure 4.38** Summary of Vareststraint weldability results for a number of commercial Nb-bearing superalloys. (From Maguire and Michael [27], Cieslak *et al.* [41], and Robino *et al.* [42])

ity of Alloys 907 and 909 are similar, while Alloy 903 exhibits slightly lower cracking susceptibility.

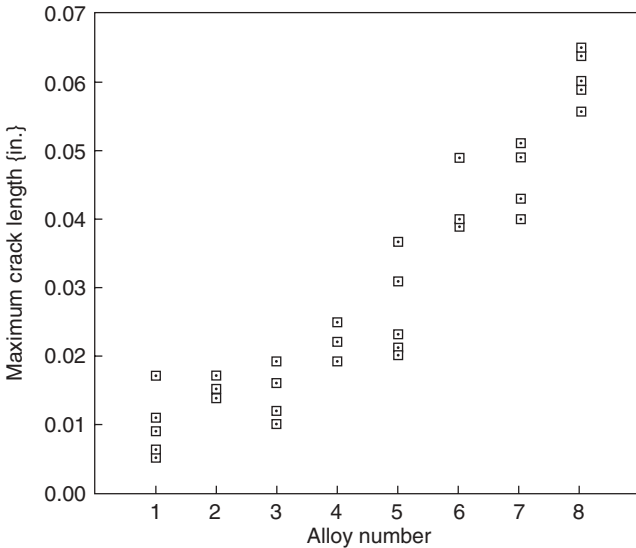
It is difficult, however, to develop general correlations between alloy composition, solidification behavior, and resultant weldability among the commercial Nb-bearing alloys. The high cracking susceptibility of Alloy 725 can probably be attributed to its low  $\gamma$ /Laves formation temperature (Table 4.10). However, Alloy 625 PLUS exhibits a similar  $L \rightarrow \gamma + \text{Laves}$  temperature to Alloy 725, but its cracking susceptibility is significantly lower. As mentioned previously, the cracking susceptibility of engineering alloys can often be correlated to the solidification temperature range. The solidification temperature range of fusion welds is best represented by the separation between the liquidus temperature and terminal solidus temperature (in this case the  $L \rightarrow \gamma + \text{Laves}$  temperature) because solidification initiates epitaxially at the fusion line without the need for undercooling. (43) Review of the data in Table 4.10 and Figure 4.39 indicates there is no direct relation between the solidification temperature range and cracking susceptibility for these alloys.

**TABLE 4.10 Summary of Alloy Compositions (wt%), Liquidus Temperatures, L →  $\gamma$  + Laves Transformation Temperatures, and Solidification Temperature Ranges ( $\Delta T$ ) For a Number of Commercial Nb-bearing Ni-base Alloys.**

Element	625	625 Plus	ThermoSpan	909	718	725
Ni	Bal.	Bal.	24.42	37.3	Bal.	Bal.
Fe	2.54	5.18	Bal.	Bal.	18.10	8.72
Cr	22.14	21.03	5.45	0.48	18.18	20.84
Co	—	—	28.84	14.25	—	—
Nb	3.86	3.39	4.92	5.00	5.25	3.62
Mo	8.79	7.96	0.02	0.10	3.12	7.57
Ti	0.26	1.31	0.86	1.62	0.95	1.64
Al	0.18	0.18	0.49	0.05	0.56	0.24
C	0.039	0.009	0.005	0.02	0.040	0.010
Si	0.10	0.03	0.24	0.40	0.21	0.92
Liquidus, °C	1357	1356	1413	1395	1362	1335
L → $\gamma$ + Laves Temp., °C	1150	1126	1226	1187	1198	1118
$\Delta T$ , °C	207	230	187	208	164	217
Reference	27	27	42	42	27	27

**Figure 4.39** Ranking of solidification cracking susceptibility of commercial alloys based on Varestraint results.

Cieslak (23,25) observed a similar phenomenon on eight different heats of Alloy 625 that had factorial variations in Nb, Si, and C. The Varestraint results of these alloys are summarized in Figure 4.40. The total alloy content generally increases with increasing alloy number, and these results demonstrate that Nb, Si, and C all have a detrimental effect within the range considered. The low



Alloy compositions (all values in weight percent).

Alloy	Nb	Si	C
1	0.01	0.03	0.006
2	0.01	0.03	0.031
3	0.02	0.35	0.006
4	0.02	0.39	0.036
5	3.61	0.03	0.009
6	3.60	0.03	0.038
7	3.57	0.38	0.008
8	3.53	0.46	0.035

**Figure 4.40** Varestraint weldability results of eight different heats of Alloy 625 with variations in Nb, Si, and C. (From Cieslak *et al.* [23,25])

Nb alloys solidified as single phase austenite, thus demonstrating that Nb is required to form the Laves phase in these alloys. The detrimental effect of Nb and Si is generally attributed to their tendency to promote the  $\gamma$ /Laves constituent. It will be shown later that C additions at higher levels are beneficial to cracking resistance in these types of alloys. As with the commercial alloys, no direct correlation between cracking susceptibility and solidification temperature range was observed.

More recent weldability results acquired from the large set of experimental alloys listed in Table 4.6 have shed light on this phenomenon. Figure 4.41 shows the MCL of each experimental alloy. Within the Ni-base alloys, there is a clear separation in weldability among the low C alloys ( $\leq 0.017$  wt% C) with relatively poor weldability, and the high C alloys ( $\geq 0.052$  wt% C), which

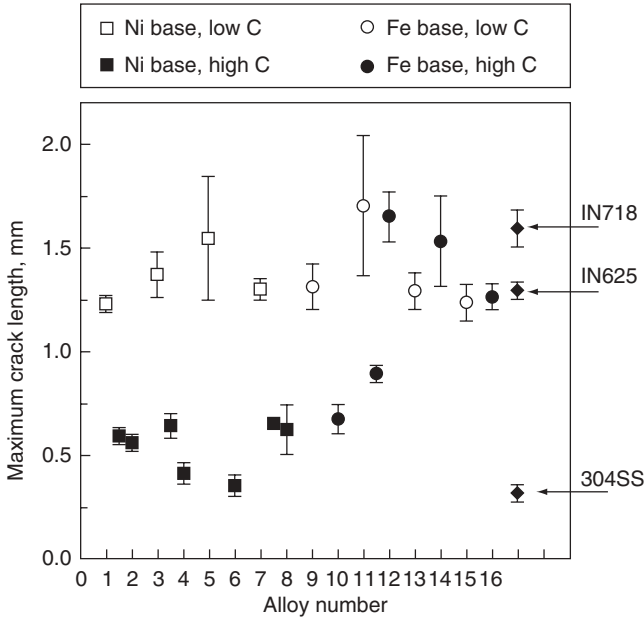


**Figure 4.41** Maximum crack length for experimental Nb bearing alloys along with data for commercial alloys 625, 718, and 304 SS.

show very good resistance to solidification cracking. Within the Fe-base alloys, the addition of C is only beneficial when the Nb content is low ( $\leq 1.93$  wt%), and the C level must be above  $\sim 0.10$  wt% to provide the advantageous effect. Within the Fe-base alloys with high Nb, C has no beneficial effect even at the 0.21 wt% level. MCL values for Alloys 718 and 625 are shown for comparison, and they fall within the range of the experimental alloys. Type 304 stainless steel represents an alloy that is very resistant to solidification cracking.

The high C, Ni-base alloys show cracking resistance which is comparable to Type 304 stainless steel. This is a significant improvement over the experimental and commercial alloys with low to moderate C contents. As discussed in Section 4.3.1, C content has a significant effect on the primary solidification path and resultant solidification temperature range of these alloys. As the C content is increased, the primary solidification path is driven far into the C-rich side of the solidification surface and intersects the  $\gamma/\text{NbC}$  eutectic line at relatively high temperatures near the end of solidification (see Figures 4.27–4.29). Thus, C additions decrease the solidification temperature range of the primary  $L \rightarrow \gamma$  reaction. Figure 4.42 shows the MCL as a function of the actual solidification temperature range and, as with the commercial alloys, no direct correlation is observed.

More detailed characterization has shown that cracking resistance in these alloys is determined by the relative amount and morphology of  $\gamma/\text{NbC}$  and  $\gamma/\text{Laves}$  constituents that form in the crack susceptible mushy zone. All of the

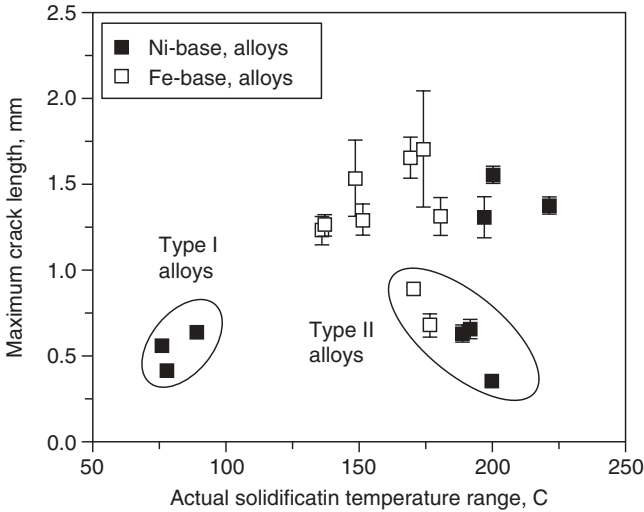


**Figure 4.42** Maximum crack length as a function of actual solidification temperature range for experimental Nb bearing superalloys.

alloys fell into one of four microstructural morphologies shown in Figure 4.43. At the bottom of each figure, the formation of two neighboring solidification cells within a grain is depicted growing into the trailing edge of the weld pool. The relation between temperature and phase stability in the mushy zone is shown by the temperature gradient diagram in the middle of the figure, where the dendrite tips are at the liquidus temperature (assuming negligible undercooling). This point represents the boundary between the liquid weld pool and solid + liquid mushy zone. The distance at which the actual temperature in the mushy zone reaches the terminal solidus temperature defines the boundary between the mushy zone and fully solidified weld metal. The relation between temperature, distance, phase stability, and the solidification path is given by combining the  $\gamma$ -Nb-C liquidus surface with the other two figures.

Type I microstructures are found in the Ni-base alloys with low Nb and high C that exhibit only the  $L \rightarrow (\gamma + \text{NbC})$  reaction. Due to the high C/Nb ratio of these alloys, the interdendritic liquid becomes highly enriched in C as the solidification path progresses towards the eutectic line between  $\gamma$  and NbC. The primary solidification path intersects the eutectic line at a relatively high temperature. As a result, the  $\gamma/\text{NbC}$  starts forming a short distance from the dendrite tips. Because of the nature of solute redistribution (particularly carbon) in these alloys, the remaining liquid is completely consumed along the  $\gamma/\text{NbC}$  eutectic line, so the  $\gamma/\text{Laves}$  constituent does not form.<sup>(16)</sup> As a result, the mushy zone in these alloys is relatively small and the distance available for crack propagation is relatively short. This leads to the good resistance to solidification cracking observed for these alloys.

Type II microstructures were observed in the high Nb/high C Ni-base alloys and low Nb/high C Fe-base alloys. The solidification process is similar

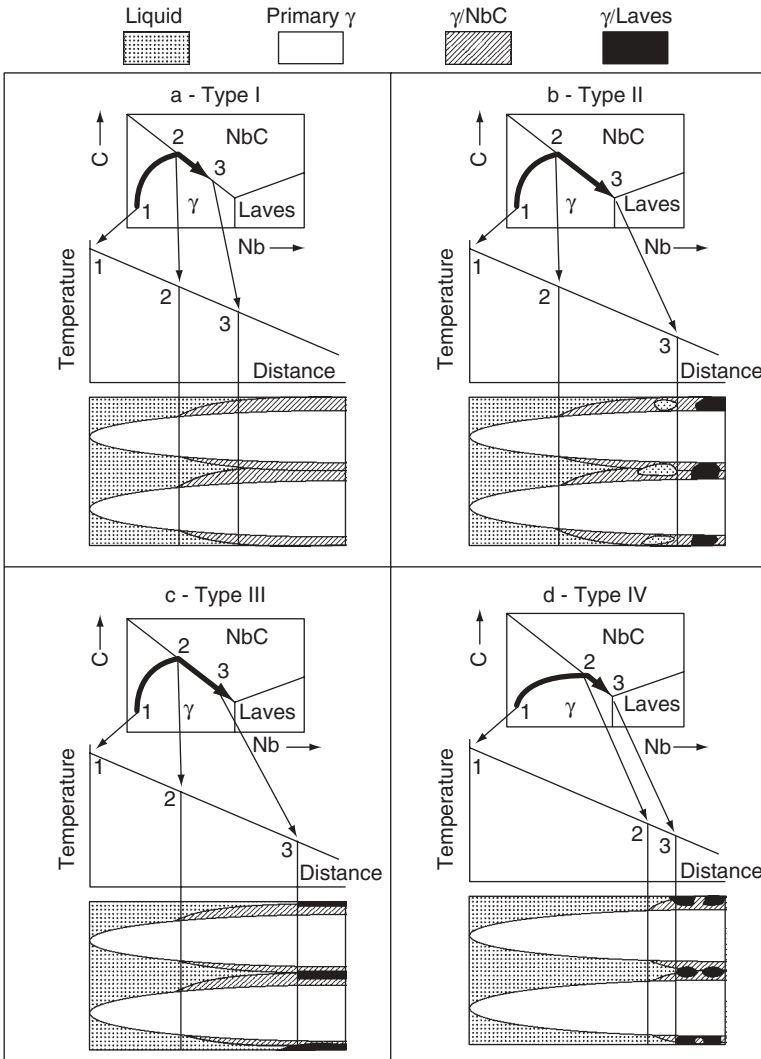


**Figure 4.43** Schematic illustration showing development of four distinct microstructural morphologies in Nb bearing superalloys.

to Type I, except that a larger amount of liquid is generally present when the primary solidification path intersects the  $\gamma/\text{NbC}$  eutectic line, and the liquid is not completely consumed during the  $L \rightarrow (\gamma + \text{NbC})$  reaction. As a result, the  $\gamma/\text{Laves}$  constituent forms. The  $L \rightarrow (\gamma + \text{Laves})$  reaction occurs at very low temperatures and thus extends the mushy zone out to larger distances. This has the potential of increasing the maximum crack length. However, the amount of  $\gamma/\text{Laves}$  constituent which forms in these alloys is below  $\sim 2$  volume percent. At this level, the  $\gamma/\text{NbC}$  always envelops the  $\gamma/\text{Laves}$  and keeps it

isolated. This suggests that the last residual liquid, from which the  $\gamma$ /Laves forms, is also isolated within the mushy zone during crack advancement. With this type of morphology, the isolated liquid pockets should have little or no deleterious effect and crack propagation through the entire mushy zone is therefore unlikely. The Varestraint data tend to support this. The MCL values for these alloys are in the range of 0.35 to 0.89 mm, which is similar to the range of 0.41 to 0.64 mm observed in the Type I alloys which form no  $\gamma$ /Laves and have excellent weldability. These results suggest that the effective solidification temperature range for these alloys is more appropriately defined as the separation between the liquidus temperature and the  $L \rightarrow \gamma + \text{NbC}$  reaction temperature.

The main difference between the Type II and Type III morphologies lies with the amount and distribution of the  $\gamma$ /Laves constituent, where the Type III alloys form  $\gamma$ /Laves in quantities greater than two volume percent. As a result, the  $\gamma$ /Laves is observed in a continuous network. The actual size of the mushy zone in the Type III alloys is expected to be similar to that for Type II since each type terminates solidification with the  $L \rightarrow (\gamma + \text{Laves})$  reaction. However, with the residual liquid existing in a continuous network, crack propagation through most of the low temperature region of the mushy zone is more favorable for alloys that possess the Type III microstructure. Thus, the solidification temperature range governing crack propagation in these alloys should be given by the separation between the liquidus and  $L \rightarrow \gamma + \text{Laves}$  reaction.

The Type IV microstructures are generally produced by low C alloys that exhibit a primary solidification path which travels very close to the  $\gamma$ -Nb "binary" side of the solidification surface. The primary path just barely intersects the eutectic line between  $\gamma$  and NbC before solidification terminates with the  $L \rightarrow (\gamma + \text{Laves})$  reaction. The eutectic type reactions in this region of the solidification surface occur at low temperatures. Thus, with this solidification path, the mushy zone is relatively large and consists mainly of liquid and primary  $\gamma$  with small amounts of  $\gamma$ /NbC and  $\gamma$ /Laves. The MCL values of all these alloys are high (1.23 to 1.70 mm), suggesting that crack propagation through all or most of the mushy zone is likely.

Based on these considerations, the terminal solidus temperatures affecting solidification cracking for Type III and Type IV microstructures should be appropriately given by the temperature of the terminal  $L \rightarrow (\gamma + \text{Laves})$  reaction. However, the temperature range affecting solidification cracking for the Type II alloys is more realistically represented by using the temperature of the  $L \rightarrow (\gamma + \text{NbC})$  reaction as the terminal solidus point because the volume fraction of  $(\gamma + \text{Laves})$  that forms at the end of solidification is quite small. Using this approach, the MCL and effective solidification temperature data are re-plotted in Figure 4.44 and the correlation between cracking susceptibility and the solidification temperature range is now readily apparent. The data are grouped into two distinct regions of the plot which separate the low and high C alloys. This improved correlation, although somewhat qualitative,

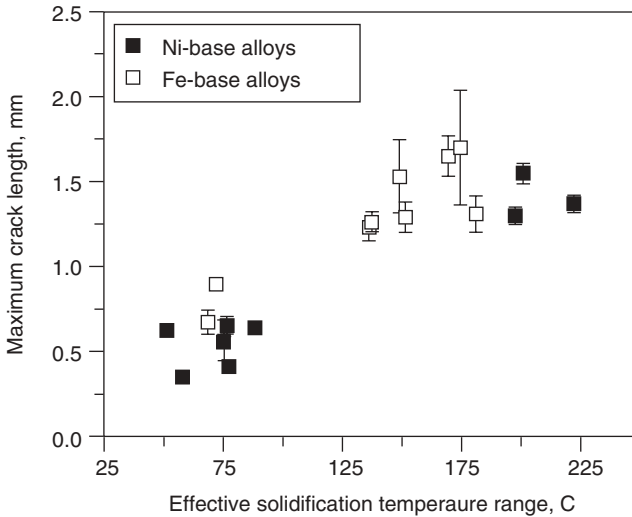


**Figure 4.44** Maximum crack length as a function of effective solidification temperature range for experimental Nb bearing superalloys.

serves to support the proposed mechanisms of crack propagation through the various types of microstructures. Thus, cracking susceptibility can be interpreted by knowledge of the solidification temperature range and type/amount of constituent which forms at the terminal stages of solidification.

It should be noted, however, that this correlation does not take into the account the effect of crack backfilling on solidification cracking susceptibility. It is generally recognized that the backfilling of solidification cracks by the terminal eutectic liquid can reduce or eliminate solidification cracking, particularly at low restraint levels. This effect is difficult to quantify using the Varestraint test (see Chapter 8), since the relatively high strains used to induce cracking tend to overwhelm the backfilling effect.

Nevertheless, the Varestraint solidification cracking results demonstrate that alloy composition can be manipulated to control the relative amount of the  $\gamma/\text{NbC}$  and  $\gamma/\text{Laves}$  constituents for optimal weldability. In view of this, Figure 4.45 provides solute redistribution modeling results showing the amounts of total eutectic ( $\gamma/\text{NbC} + \gamma/\text{Laves}$ ) and individual  $\gamma/\text{NbC}$  and  $\gamma/\text{Laves}$  eutectic constituents that form as a function of nominal Nb and C content. The results are separated for Fe-base and Ni-base alloys due to the variations in  $\gamma/\text{Laves}$  eutectic composition ( $C_e$ ) and  $k_{\text{Nb}}$  values ( $k_{\text{Nb}} = 0.45$  for Ni-base alloys vs.  $k_{\text{Nb}} = 0.25$  for Fe-base alloys,  $C_e = 23.1$  wt% Nb for Ni-base alloys vs.  $C_e = 20.4$  wt% Nb for Fe-base alloys). The combined ( $\gamma/\text{NbC} + \gamma/\text{Laves}$ ) content increases with increasing Nb and C in the alloy. The total eutectic-type constituent is simply equivalent to the amount of liquid which exists when the primary  $L \rightarrow \gamma$  solidification path intersects the eutectic line separating the  $\gamma$  and NbC phases. As the alloy is enriched in Nb and C, the nominal alloy

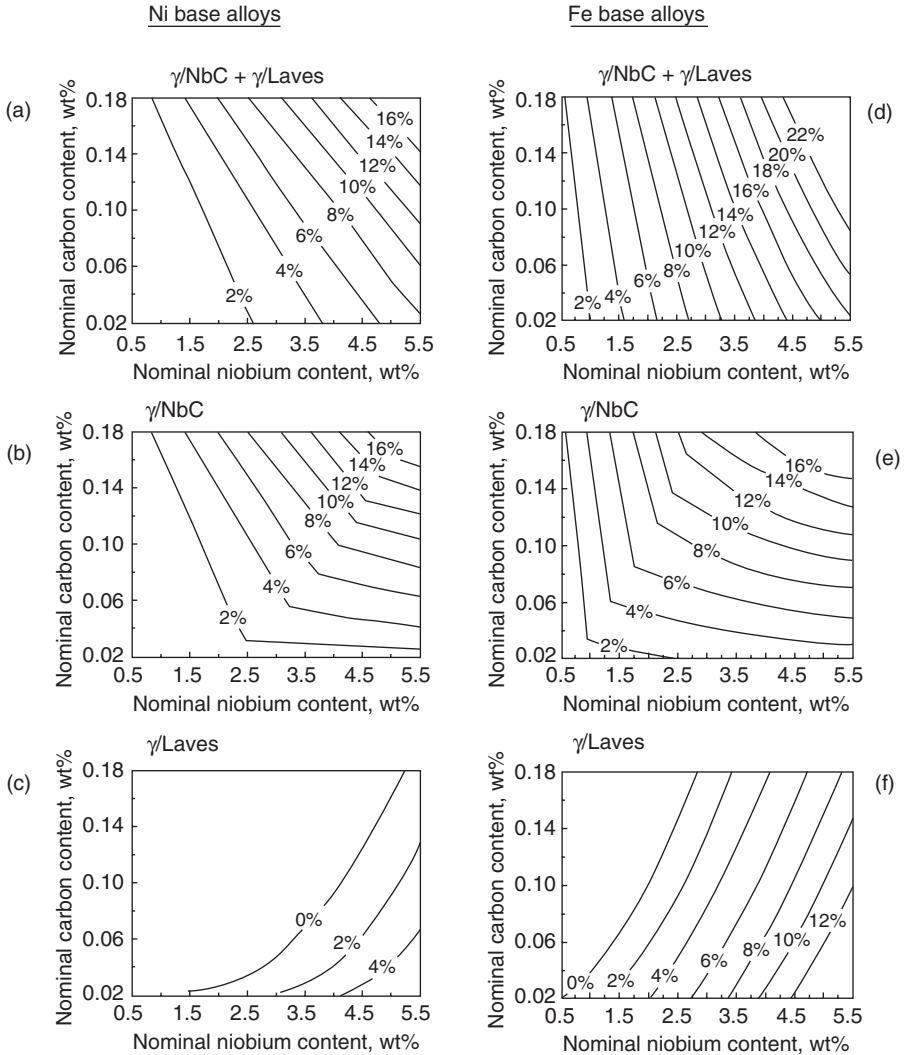


**Figure 4.45** Solute redistribution modeling results showing amounts of total eutectic ( $\gamma/\text{NbC} + \gamma/\text{Laves}$ ) and individual  $\gamma/\text{NbC}$  and  $\gamma/\text{Laves}$  eutectic constituents that form in experimental Fe base and Ni base alloys.

composition moves closer to the eutectic composition and, as a result, more of the eutectic constituents form.

At any given nominal alloy composition, the Fe-base alloys always form more total and individual amounts of the eutectic constituents. This occurs because the Fe-base alloys have lower values of  $k_{\text{Nb}}$  and  $C_e$ . However, the iso-weight percentage curves for each constituent move in different directions; the  $\gamma/\text{NbC}$  constituent is favored by additions of both Nb and C while the

$\gamma$ /Laves constituent is promoted by alloys with low C and high Nb. Thus, although there is a wide range of alloy compositions which can lead to formation of identical amounts of the  $\gamma$ /NbC constituent, the amount of  $\gamma$ /Laves will be much different. These correlations should be helpful for future alloy design strategies and interpretation of weldability data from newer Nb-bearing superalloys. From a practical standpoint, manipulation of alloy composition to eliminate formation of the low temperature  $\gamma$ /Laves constituent is the simplest and most direct route for improving resistance to weld solidification cracking. The results shown in Figure 4.45c and 4.45f are particularly useful for this purpose, as nominal Nb and C contents located to the left of the 0%  $\gamma$ /Laves curves will not form this constituent.

**4.5.1.3 Cast Pin Tear Test Results** The cast pin tear (CPT) test has also been used to determine susceptibility of Ni-base superalloys to weld solidification cracking.(44) This test technique, described in Chapter 8, allows alloys that are highly susceptible to solidification cracking to be evaluated since the strains leading to cracking are much lower than those applied in the Vareststraint test. Strain during solidification is controlled by altering the length of the cast pin, with longer pins producing more shrinkage strain during solidification. Pins of different lengths are cast and the cracking around the circumference of the pin is measured under a binocular microscope. Using the CPT test, the cracking susceptibility for René alloys 77, 80, 125 and 142, Alloy 718, and Waspaloy was determined. Alloy 600, a solid solution strengthened alloy with good resistance to solidification cracking, was included as a reference material.

The CPT results for these alloys are shown in Figure 4.46. Alloys that exhibit 100% circumferential cracking at the shortest pin lengths (lowest shrinkage strains) are the most susceptible to solidification cracking. René

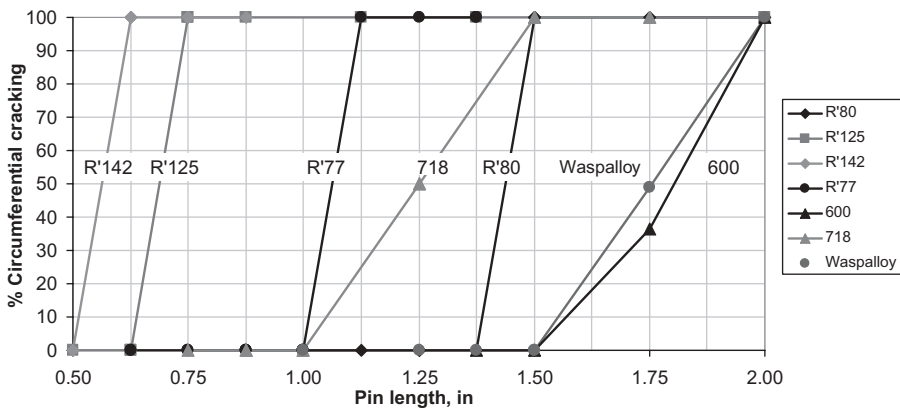


**Figure 4.46** Cast pin tear test results for several Ni-base superalloys and Alloy 600. (From Alexandrov *et al.* [44])

alloys 125 and 142 are known to be extremely susceptible to solidification cracking in practice and, thus, the CPT test appears to provide a good order ranking for these materials. Alloy 600, which is known to be resistant, requires the longest pin lengths to induce cracking.

Metallurgical examination of the pins revealed that the cracking is characteristic of weld solidification cracking that occurs in actual welds. Metallographic sections of the cracks in a number of these alloys are shown in Figure 4.47. Note that both René 125 and 142 show evidence of liquid films along the

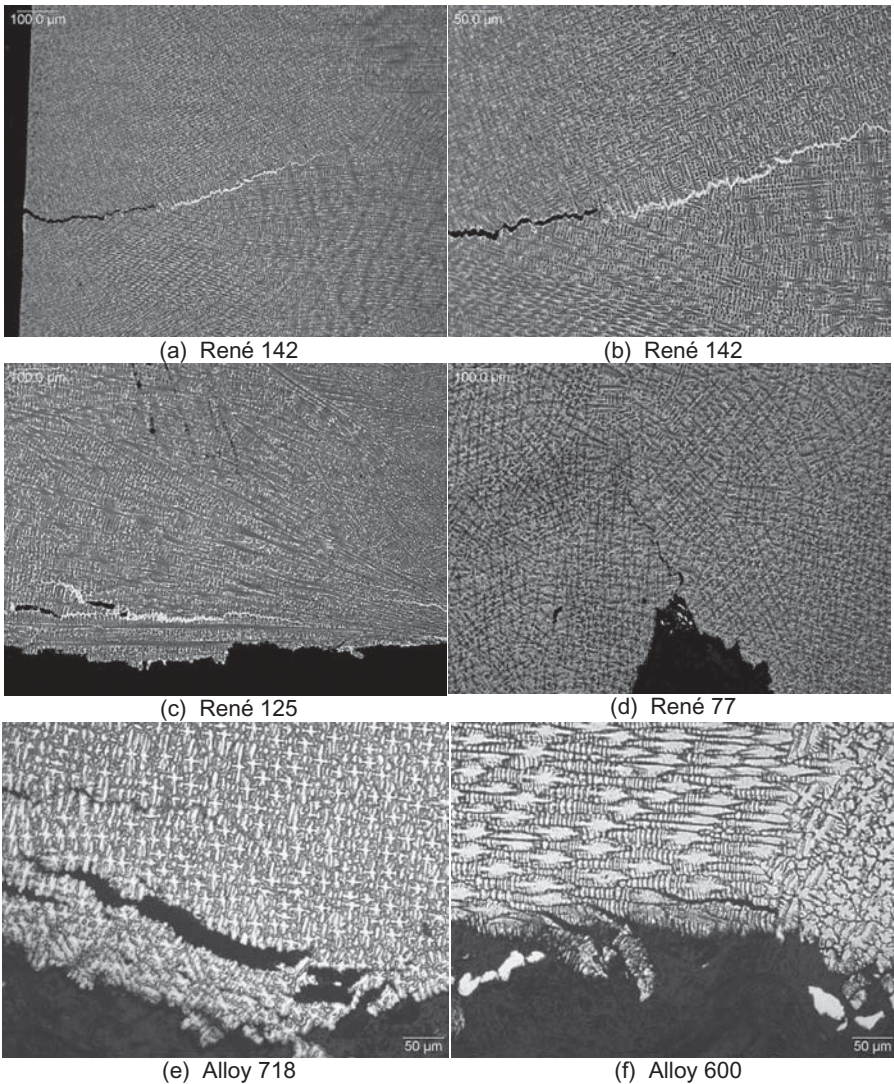


**Figure 4.47** Solidification cracking in cast pin tear test samples from Figure 4.46.

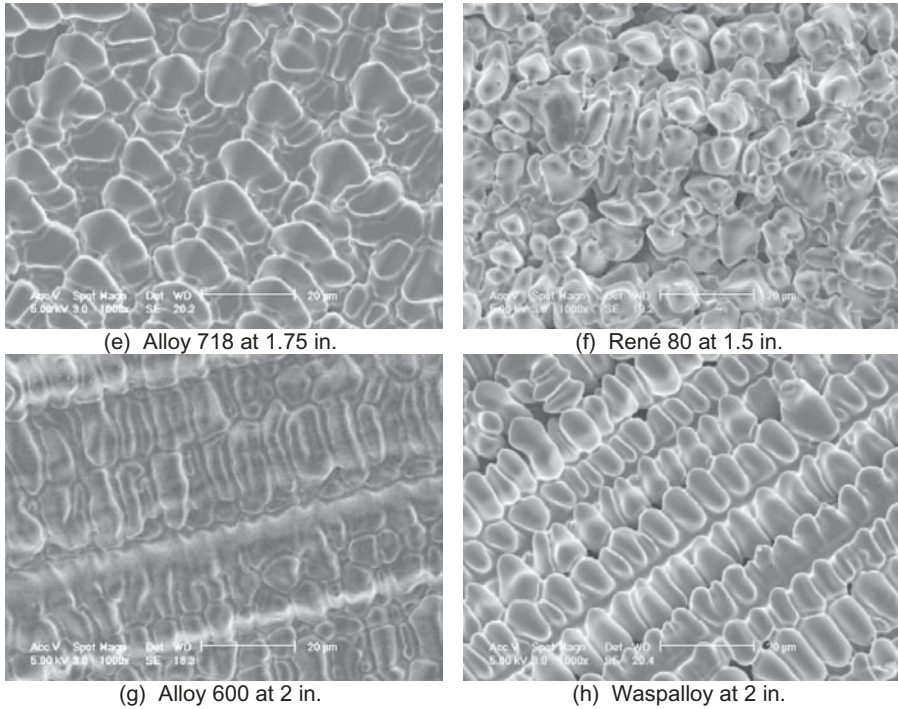


**Figure 4.48** Solidification crack fracture morphology from the cast pin tear test samples.

solidification crack paths. Examination of the crack surfaces in the SEM, as shown in Figure 4.48, revealed the classic dendritic fracture morphology that is characteristic of weld solidification cracking.

**4.5.1.4 Summary of Solidification Cracking** Weld solidification cracking in the precipitation-strengthened Ni-base alloys is a function of both minor element additions, such as B and Zr, and Nb, which is added as a strengthening agent to some of these alloys. Both B and Zr segregate strongly during solidification and result in the formation of low-melting eutectic constituents that can promote solidification cracking. The cracking susceptibility of the Nb-bearing superalloys has been studied extensively and the effect of Nb additions is well understood. Segregation of Nb during solidification leads to the formation of both  $\gamma/\text{NbC}$  and  $\gamma/\text{Laves}$  constituents via eutectic reactions that expand the solidification temperature range and promote cracking. Preventing solidification cracking in these alloys can be difficult, since Nb, B, and Zr are all intentional additions. The presence of S and P can also exacerbate solidification cracking, but these impurities are usually maintained at very low levels in these alloys and filler metals.

## 4.5.2 HAZ Liquection Cracking

HAZ liquation cracking in precipitation strengthened Ni-base superalloys is associated with the formation of liquid films along grain boundaries in the partially melted zone (PMZ) of the HAZ. As discussed previously in Sections 3.5.2 and 4.3.2, this liquation can occur by a segregation mechanism, constitutional liquation, or melting of eutectic constituents. Many of the superalloys are susceptible to HAZ liquation cracking and a number of investigators have studied the problem.

In the early study of HAZ cracking in the wrought alloys Udimet 700 and Waspaloy, Owczarski *et al.* (36) found that constitutional liquation was initiated in the vicinity of MC-type carbides and/or borides. They postulated that the abrupt decomposition of these particles occurred during rapid heating leading to constitutional liquation, grain boundary wetting, and subsequent cracking. In a later study on wrought Hastelloy X and Alloy 718 (37), they again found that a PMZ formed in these alloys by constitutional liquation reactions involving MC-type and  $M_6C$ -type carbide particles that decomposed during rapid heating.

Since the early weld HAZ simulation studies of Owczarski and Duvall (36,37), resulting in the proposed mechanism of constitutional liquation of MC-type carbides, investigators have concentrated on the origin of the grain boundary liquid, i.e., the liquation mechanism. Several investigators have suggested the operation of additional mechanisms of HAZ grain boundary liquation.

E.G. Thompson (45), in his early studies of HAZ liquation cracking in Alloy 718, indicated that the formation of the intergranular films in Alloy 718 was related to Laves phase, although a possible carbide or silicide origin was also considered. However, R.G. Thompson and coworkers (46,47) showed later that cracking was associated with the constitutional liquation of niobium carbides resulting in a drastic reduction in elevated temperature ductility. The liquation mechanism they proposed is shown schematically in Figure 4.49. Laves phase, which was found by E.G. Thompson along the liquated grain boundaries, was proposed to be a product of the solidification process and not directly related to the increase in hot cracking susceptibility. Radhakrishnan and Thompson (48) have also suggested that localized melting in wrought Alloy 718 may result from the complete dissolution of fine Nb-rich carbides during rapid heating and liquation of the Nb-enriched matrix at peak temperatures.

The HAZ liquation cracking susceptibility of cast Alloy 718 was studied by Baeslack and Nelson. (49) They concluded melting of Laves phase in the interdendritic regions of the casting promoted the HAZ liquation cracking. This Laves phase forms during the terminal solidification of the casting and is simply remelted in the HAZ of the weld. Compared with the Nb-rich MC-type carbides which promote constitutional liquation in wrought Alloy 718, the Laves phase does not depend on a dissolution reaction to form liquid and

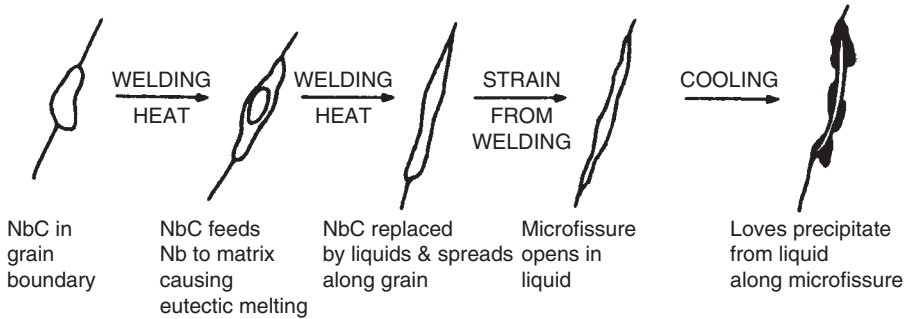


**Figure 4.49** HAZ liquation cracking mechanism for Alloy 718. (From Thompson *et al.* [46]. Courtesy the American Welding Society)

readily melts upon reheating. Because a high volume fraction of Laves phase is present in cast Alloy 718, HAZ liquation can be extensive resulting in increased cracking sensitivity relative to the wrought alloy. Further studies by Baeslack *et al.*(50) demonstrated that the substitution of Nb with Ta in cast Alloy 718 results in the formation of TaC and Ta-containing Laves phases that raised the HAZ liquation temperature. These Ta-modified alloys exhibited a marked reduction in liquation cracking susceptibility relative to the Nb-containing alloys. Similarly, substitution of Co for Fe in René 220C was found to eliminate or reduce the Laves phase and provide improved HAZ cracking resistance relative to cast Alloy 718.(51)

In general, the HAZ cracking susceptibility of cast Alloy 718 is greater than that of its wrought counterpart. It is clear that constitutional liquation of Nb-rich MC carbides promotes HAZ liquation cracking in the wrought condition and that the degree of liquation is a strong function of carbide distribution and grain size. In cast Alloy 718, both Nb-rich carbides and Laves phase form during the final stages of solidification but HAZ liquation cracking is dominated by the melting of the Laves phase rather than constitutional liquation of the carbide, since Laves phase melting occurs at a lower temperature.(52)

**4.5.2.1 Composition Effects** The effect of alloy and impurity elements on the weldability of Ni-base superalloys has received considerable attention. Alloying elements can influence HAZ liquation cracking in a number of ways, including:

- 1) the liquation mechanism (formation and composition of the liquating species),
- 2) the degree of liquation (amount of liquid that forms),
- 3) the temperature range over which the liquid is present, and
- 4) the distribution of the liquid (wetting characteristics)

The elements that have been studied to the greatest degree include intentional alloying elements such as niobium, carbon, boron, and zirconium, and impurity elements including sulfur, phosphorus, and lead.

The effects of magnesium, silicon and manganese on HAZ liquation cracking of Alloy 718 were investigated by Morrison *et al.*(53) They found that HAZ liquation cracking susceptibility was reduced when the magnesium, manganese and silicon levels were kept above a minimum level. It is believed that manganese is beneficial because it tends to tie up sulfur, which would otherwise have a detrimental effect if it segregated to grain boundaries. The beneficial effect of magnesium and silicon is not clear, but it is possible that the high affinity of Mg for sulfur also limits sulfur segregation. In contrast, Lucas and Jackson (54) showed that Alloy 718 is most susceptible to HAZ liquation cracking when the combined levels of Mn and Si are high. Studies by Savage *et al.*(55) with Alloy 600 demonstrated that both Mn and Si reduced the detrimental effect of sulfur (which they found had a highly detrimental effect). However, when these elements were present together, they were not very effective due to a significant silicon-manganese interaction. They also found that titanium and aluminum have beneficial effects on the cracking susceptibility. The beneficial effect of Ti, Al, Mn, and Si was postulated to result from (in addition to the mechanism discussed above for Mn and Si) the excellent deoxidizing influence of these four elements. Since oxygen has been observed to lower the surface free energy of sulfides, it was suggested that these elements could increase the surface free energy by the reduction of dissolved oxygen, thereby decreasing cracking tendencies. Although these conclusions were based on the behavior of Alloy 600, it is presumed that similar effects would occur in the Ni-base superalloys.

The detrimental effects of minor elements Pb, S, P, Zr, and B on both HAZ liquation and weld metal solidification cracking were first pointed out by Pease.(56) In studying Alloy 800, Canonico *et al.*(57) showed that S, B, P, and to a lesser extent C and Si were harmful to the weldability. The synergistic detrimental effect of C and B on HAZ liquation was described by Owczarski (58) in several superalloys, including Alloy 718. Sometimes the effect of a single element is not very clear because of interactive effects with other elements. For example, Yeniscavich and Fox (59) showed that in Hastelloy X the summation of the detrimental effects of P, B, C, and S resulted in cracking. A small change in each element separately had no effect on the cracking susceptibility.

Impurity elements, especially S and P, were found by Vincent (60) to segregate to grain boundaries during the aging heat treatment, which promoted grain boundary wetting and resulted in differences in the liquation cracking susceptibility between solutionized (927°C/1hr/AC) and solutionized and aged (650°C/10hr/AC) wrought Alloy 718. Boron has been shown by Kelly (52,61) to have the most detrimental effect on HAZ liquation cracking in cast Alloy 718 because it promotes grain boundary wetting. This was also verified by other investigators.(62)

The effect of niobium on liquation cracking susceptibility has been studied extensively, particularly in Alloy 718 where it is added to promote strengthening by gamma double-prime precipitation. However, because it also forms NbC and Laves phase, it has been found to promote HAZ liquation cracking via constitutional liquation of NbC in wrought alloys and melting of Nb-rich Laves phase in cast material.(63) The partial substitution of Nb with Ta was shown to reduce cracking susceptibility in cast Alloy 718 (50) and René 220C.(51,52) Unfortunately, complete substitution of Nb is not possible since it is needed to precipitation strengthen the material.

In summary, the influence of the different alloying and impurity elements on HAZ liquation cracking susceptibility is dependent on the overall composition. Clearly, the reduction of S and P to very low levels is beneficial and does not alter the performance of the alloy. It is also clear that B is a detrimental element with respect to HAZ liquation cracking, but this must be balanced against the improvement in creep properties that is gained by additions of B. The individual influence of the many elements added to Ni-base superalloys is unclear and is complicated by interactive effects with other elements. In general, the use of weldability testing is warranted to determine susceptibility of individual alloys.

**4.5.2.2 Effect of Grain Size** Many investigators have demonstrated that materials with fine grain size tend to be resistant to HAZ liquation cracking relative to coarse grain versions of the same material.(45,46,64,65) This grain size effect is generally attributed to one or more of the following factors:

- (1) As grain size decreases, grain boundary area increases allowing strain to be more readily accommodated, thereby reducing the unit strain for a given grain boundary.(47,66) This in turn reduces the potential for grain boundary sliding and crack initiation.
- (2) The large grain boundary area associated with materials with fine grain size results in reduced stress concentration applied to grain boundary triple points in which crack initiation is most likely to occur.(67)
- (3) The grain size determines the liquid film concentration along grain boundaries (i.e., the thickness of the liquid layer) and the rate at which the liquid solidifies. Large grain size (less grain boundary area) promotes an increase in liquid continuity at grain boundaries and thus reduces the extent of solid–solid grain boundary interfacial area. This results in a reduction in the strength across the partly melted zone (PMZ). The thicker liquid layer associated with a large grain size also requires relatively longer time to resolidify on cooling, allowing for more strain accumulation in the PMZ and a greater possibility for crack formation.(47)

It is clear that the large grain size associated with castings results in higher cracking susceptibility relative to wrought versions of the same alloy. Also,

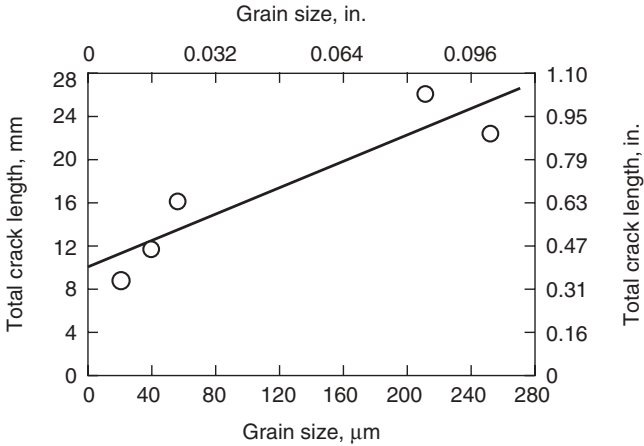


**Figure 4.50** Effect of grain size on HAZ liquation cracking in Alloy 718 using the spot Varestraint test. (From Radhakrishnan and Thompson [48])

Thompson (63) indicated that the intergranular liquid in castings is more stable during cooling since it is surrounded by a solute-rich, interdendritic region that reduces the concentration gradient. Both phenomena contribute to the increased cracking susceptibility in castings.

While grain size control in casting is difficult, wrought material can be thermo-mechanically processed to produce extremely fine grains. Fine grained superalloys are often desirable for improved fatigue resistance at elevated temperature. This finer grain size will also provide improved HAZ liquation cracking resistance for the reasons listed above. Control of base metal grain size is particularly effective in low heat input welds where grain growth in the PMZ is inhibited by rapid heating and cooling rates to peak temperatures.

Radhakrishnan and Thompson (68) and Guo *et al.* (69) both demonstrated the effect of grain size on HAZ liquation cracking susceptibility. Using the spot Varestraint test, cracking in the HAZ of wrought Alloy 718 doubled as the grain size increased from an average diameter of 40 μm to over 200 μm, as shown in Figure 4.50. Guo *et al.* performed electron beam welds on wrought Alloy 718 at average grain diameters of 50, 100, and 200 μm and two boron levels. Their results are shown in Figure 4.51. Increasing grain size clearly increases susceptibility to HAZ liquation cracking, although the effect of boron segregation to the grain boundaries has an equally damaging effect. In the case where boron and impurity content (P and S) can be kept low, the use of fine-grained base metals may help to reduce or eliminate HAZ liquation cracking in many alloys.

HAZ liquation cracking during electron beam welding can often be eliminated by the use of fine grained base metals. In high heat input welds, the use of fine grain base metals is less effective since grain growth will be more pro-

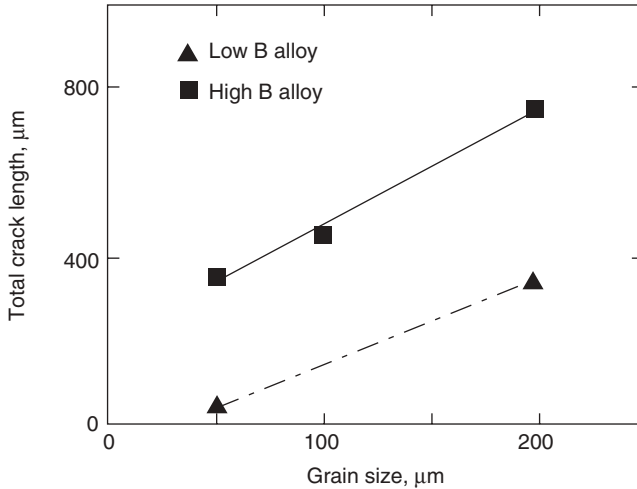


**Figure 4.51** Effect of grain size and boron content on HAZ liquation cracking in Alloy 718 electron beam welds. (From Guo *et al.* [69])

nounced and metallurgical reactions that lead to grain boundary melting (impurity segregation, constitutional liquation, etc.) are more likely.

**4.5.2.3 Effect of Heat Treatment** A number of investigators have evaluated the effect of preweld base metal heat treatment or “conditioning” treatments as a means to control HAZ liquation cracking susceptibility. The results of these studies have been contradictory. Schwenk (70) showed that if welded in the solution-treated condition, René 41 was less susceptible to HAZ cracking than when it was welded in fully aged condition. However, Owczarski *et al.* (37) showed that solution treated Udimet 700 base metal has lower ductility at welding temperatures compared with the fully aged alloy, suggesting that solution annealing prior to welding is not appropriate for this alloy.

Some investigators have shown that solution annealing reduces HAZ liquation cracking susceptibility in Alloy 718, while age-hardening increases it. (36,45,46) Duvall and Owczarski (36) were among the earliest who observed the difference in HAZ liquation cracking susceptibility between the solution annealed and age-hardened conditions. However, they did not provide an explanation in their study as to why solution annealing the base metal resulted in a marked improvement.

Gordine (71) found that the solution treatment temperature before welding has an important influence upon HAZ liquation cracking susceptibility in Alloy 718. The use of high temperature solution heat treatments before welding resulted in higher susceptibility to HAZ liquation cracking. Solution treatments at 927°, 1038° and 1149°C (1700°, 1900° and 2100°F, respectively) all resulted in grain boundary melting in the PMZ of the subsequent weld.

However, only the specimen solution treated at 1149°C (2100°F) showed evidence of cracking. Although no explanation was provided, his results revealed that HAZ liquation cracking is not a direct result of grain boundary melting alone because this occurred in all three solution heat treatment conditions.

Boucher (64) suggested that by “tempering” prior to welding, a solute blocking effect can be achieved to reduce cracking susceptibility in Alloy 718. A tempering treatment above 850°C (1560°F) can precipitate  $\delta$  phase ( $\text{Ni}_3\text{Nb}$ ) to stabilize Nb, appreciably reducing the amount of diffusible Nb which is responsible for HAZ liquation cracking. Tempering treatments at 900° and 955°C (1650° and 1750°F) were found to be most effective. It was postulated that because  $\delta$  phase only dissolves at temperatures above 1010°C (1850°F), the release of Nb is restricted to a narrow region very close to the fusion boundary (that region heated above 1010°C) and is only present for a short period of time. Thus, grain boundary liquation resulting from Nb diffusion is restricted to a very narrow region of the HAZ and is dependent on the rate at which the  $\delta$  phase dissolves. This “solute blocking” method was found effective in reducing cracking susceptibility in Alloy 718 over a large range of base metal grain sizes.

Conversely, Vincent (60), in his early work on Alloy 718, suggested that the precipitation of  $\delta$  phase during solution annealing increased HAZ liquation cracking resistance. Later, by comparing the results of solutionizing (927°C (1700°F)/one hour/AC) and of solutionizing plus aging heat treatment (650°C (1200°F)/10 hour/AC), he suggested that the increased liquation cracking susceptibility resulting from the solutionizing plus aging heat treatment was due to the segregation of impurity elements to grain boundaries during the aging heat treatment that promoted grain boundary liquation during welding.

Thompson and Genculu (46) in their early study of Alloy 718 found that the constitutional liquation of NbC is a prerequisite for the on-cooling ductility loss observed using the Gleeble hot ductility test. In agreement with Duvall and Owczarski (36,37), they found that HAZ liquation cracking was initiated by the constitutional liquation of niobium-rich carbides. Intergranular liquid in simulated HAZ samples produced by this reaction was found in both the solution annealed and the age-hardened conditions. At the same time, they observed that heat treatments significantly altered the HAZ liquation cracking susceptibility of Alloy 718. It was postulated that the role of heat treatment in determining the magnitude of the on-cooling hot ductility loss was related to its effect on the amount and distribution of Nb available to the liquated grain boundaries. Their experimental results were not able to either confirm or refute this hypothesis, but certain circumstantial evidence was presented in its support. It was argued that as-received material, which had been annealed at 2000°F (1093°C), had more “free Nb” available to accumulate at the grain boundaries than did the solution annealed material that contained significant  $\delta$  phase precipitated throughout the matrix. The higher free Nb content would

render the material more susceptible to liquation cracking, since Nb could simply diffuse to the grain boundary. In the material with heavy  $\delta$  phase precipitation,  $\delta$  phase dissolution would be required before free Nb was available to segregate to the grain boundary. Following this argument, the solution annealed plus age-hardened material would also take free Nb out of the solution by the formation of the  $\gamma''$ -Ni<sub>3</sub>Nb precipitate. However, their hot ductility results showed the solution annealed plus age-hardened material to be more crack-sensitive than the material solution annealed condition at 2000 °F. To explain this result, it was then argued that during age-hardening impurity segregation to the grain boundaries dominated the effect of tying up Nb. This is similar to the argument made by Vincent.(60)

In a subsequent study, Thompson *et al.*(72) again showed the beneficial effect of solution annealing and the detrimental effect of age-hardening on the HAZ liquation cracking susceptibility of Alloy 718. In this case, phase changes during heat treatment, including the precipitation of  $\delta$  phase (Ni<sub>3</sub>Nb) during solution annealing and the precipitation of  $\gamma'$  plus  $\gamma''$  during age-hardening, did not correlate with the observed changes in HAZ liquation cracking susceptibility. Grain growth during heat treatment was not a significant factor in altering HAZ liquation cracking since the material with the largest starting grain size exhibited the largest change in HAZ liquation cracking susceptibility but showed no significant change in grain size in the HAZ. However, the rate of equilibrium grain boundary segregation was found to correlate closely with the changes in HAZ liquation cracking susceptibility during heat treatment. They attributed the differences in HAZ liquation cracking susceptibility between solution annealing and solution annealing plus age-hardening to the changes in grain boundary composition due to segregation during heat treatment.

The homogenization treatments of cast Alloy 718 have been shown by Huang *et al.*(62) to have different effects on HAZ liquation cracking susceptibility. Over the homogenization temperature range of 1037-to-1163 °C (1900-to-2025 °F), the TCL (total crack length obtained during the Varestraint test) initially decreased and then increased with the homogenization temperature. No correlation was found between the TCL and the volume fraction of secondary phases, i.e. Laves and MC-type carbide phases. It was postulated that boron segregation to the grain boundary resulting from both equilibrium and non-equilibrium segregation during heat treatment resulted in the variation in HAZ liquation cracking susceptibility.

Lu (73) studied the HAZ liquation cracking susceptibility of wrought and cast Alloy 718 from actual gas turbine engine hardware that had experienced multiple repair and postweld heat treatment cycles. Following weld repair, a low temperature solution annealing heat treatment is applied in the temperature range from 925-to-1010 °C (1700-to-1850 °F), following by an aging treatment. As can be seen in the time-temperature-transformation diagram for Alloy 718 in Figure 4.12 (74), this can result in the formation of  $\delta$  phase after multiple PWHT cycles are applied. Both the wrought and cast microstructures

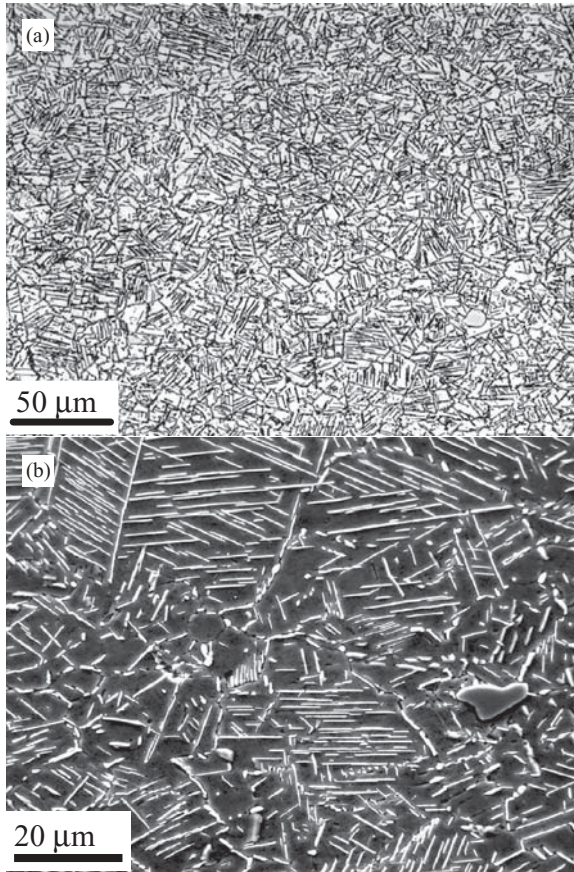


**Figure 4.52** Wrought Alloy 718 microstructure after multiple PWHT cycles in the temperature range from 925 to 1010°C (1700 to 1850°F). The needle-like constituent is  $\delta$  phase. a) Optical, b) SEM. (From Lu [73])

contained considerable  $\delta$  phase at levels of approximately 30 and 12 vol%, respectively, as shown by the light optical and SEM photomicrographs in Figures 4.52 and 4.53.

Note that the  $\delta$  phase forms uniformly within the wrought structure, but is concentrated in the interdendritic regions of the cast structure due to Nb segregation. A small amount of Laves phase that formed during the original solidification of the casting is also present. The on-heating and on-cooling hot ductility behavior of wrought and cast materials are shown in Figures 4.54 and 4.55, respectively. Susceptibility to HAZ liquation cracking can be estimated by the difference between the nil strength temperature (NST) and the ductility recovery temperature (DRT) on cooling. For the cast material this value is 280°C while for the wrought material it is approximately 230°C, thus

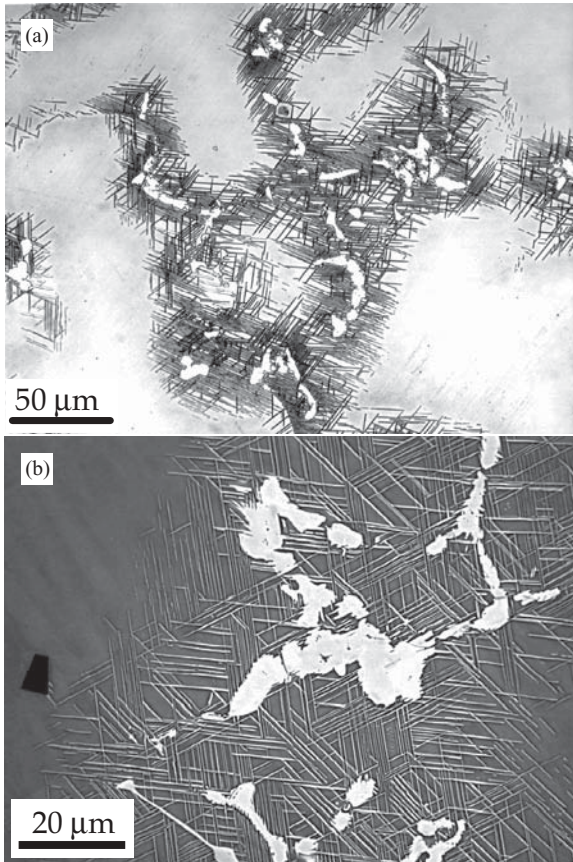


**Figure 4.53** Cast Alloy 718 microstructure after multiple PWHT cycles in the temperature range from 925 to 1010°C (1700 to 1850°F). Both  $\delta$  and Laves phase form along the interdendritic boundaries. a) Optical, b) SEM. (From Lu [73])

predicting higher HAZ liquation cracking susceptibility for the cast material. In fact, both of these values are quite high and both the wrought and cast material would be expected to be susceptible to HAZ liquation cracking. Based on the hot ductility data of Qian and Lippold (75), the NST-DRT value for wrought Alloy 718 that is free of  $\delta$  phase is on the order of only 100°C. The effect of high levels of  $\delta$  phase on the repair weldability of Alloy 718 turbine engines components is described in more detail in Chapter 6.

The effect of prior base metal heat treatment on HAZ liquation cracking susceptibility is, at best, unclear. Most of the reported work has dealt with Alloy 718 and has investigated the effects of heat treatment on grain size, precipitation ( $\delta$  phase or  $\gamma''$ ), and grain boundary segregation. While, in general, welding with the base metal in the solution annealed condition appears to provide better resistance to HAZ liquation cracking than when the

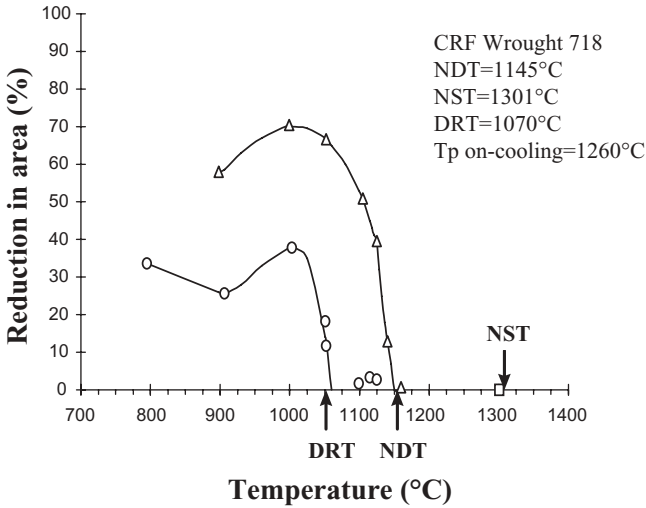


**Figure 4.54** Hot ductility behavior of wrought Alloy 718 containing nominally 30 vol%  $\delta$  phase. (From Lu [73])

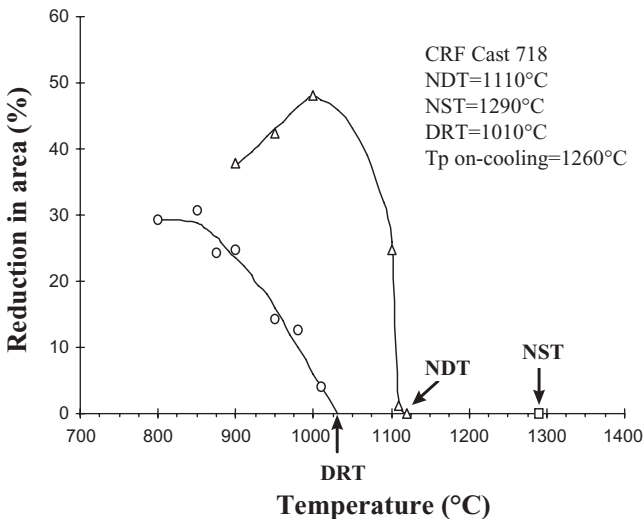


**Figure 4.55** Hot ductility behavior of cast Alloy 718 containing nominally 12 vol%  $\delta$  phase and 3 vol% Laves phase. (From Lu [73])

base metal is in the fully-aged condition, this approach does not assure freedom from cracking. The thermal cycle imposed on the HAZ greatly influences the degree of constitutional liquation, precipitate dissolution, and grain boundary segregation that can occur. All of these factors impact the amount of liquid that forms along the PMZ grain boundaries.

**4.5.2.4 Effect of Thermal Stress/Strain** The heat of welding results in thermal expansion followed by contraction in the HAZ surrounding the weld. In general, lower heat input reduces the volume of weld metal that undergoes shrinkage during cooling and results in less overall contraction in the HAZ during cooling. This, in turn, should lower the local thermal strain in the HAZ and reduce cracking susceptibility. It is well known that minimizing weld heat input can be an effective method for eliminating or minimizing HAZ liquation cracking. Unfortunately, this approach is not always appropriate and has a negative effective on productivity (more welding time required).

Electron-beam welding (EBW) can be used to achieve very low heat inputs and has been used successfully to produce defect-free welds in Nimonic 80A.(76) This was not the case with Alloy 718 as shown by Gordine (71) who observed HAZ cracks in EB welds. Boucher *et al.*(64,77) showed that weld pool morphology determines the level of tensile stresses in the penetration direction which, in turn, influences the number of microcracks that form in the HAZ in Alloy 718 and Waspaloy. The number of fissures decreases with the increase in the ratio of width to depth (W/D ratio) due to lower stresses which develop locally at the edges of the solid areas. Values for the W/D ratio of about two for GTA welding make the fissuring disappear (Figure 4.56), while EB welding with W/D ratio values far below one lead to cracking. Welding speed and weld pool morphology are correlated. Changing the welding speed or material thickness without changing the weld pool morphology does not decrease the number of cracks.

Koren *et al.* (78) suggested that thermal stresses are generated in welding as a result of steep temperature gradients associated with rapid heating and solidification. Weld HAZ cracking of Alloy 713C can be minimized by optimizing welding current and speed as well as energy input. The tendency for cracking was found to decrease with increasing energy input and decreasing

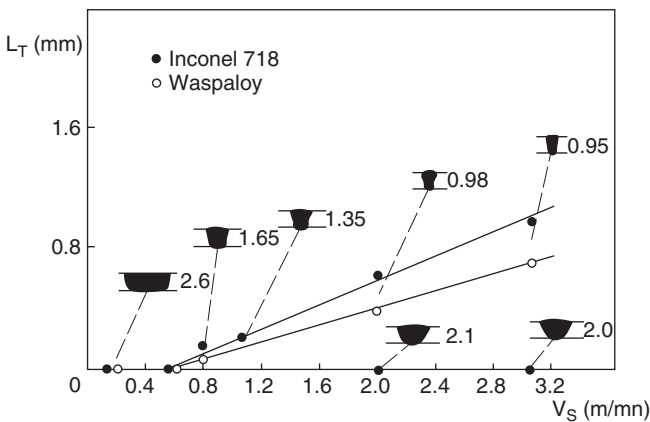


**Figure 4.56** Influence of welding speed ( $V_s$ ) and width/depth ratio on crack length ( $L_T$ ) for gas tungsten arc welds in Alloy 718 and Waspaloy. (From Boucher *et al.* [77])

welding speed due to the reduction of the rate of straining imposed on the solidifying weld.

**4.5.2.5 Summary of HAZ Liquation Cracking** HAZ liquation cracking in Ni-base superalloys has been a persistent problem and has been studied extensively in Alloy 718. Both the constitutional liquation of NbC and the segregation of boron to the HAZ grain boundaries contribute to the high cracking susceptibility of this alloy. In other alloys, segregation of boron, sulfur and phosphorus to the grain boundaries has been shown to promote cracking, while additions of manganese and magnesium may reduce cracking. The effect of Mn and Mg may be due, in part, to their ability to tie up sulfur.

The effect of the starting base metal microstructure on cracking susceptibility has also been studied by many investigators, often with conflicting results. In general, base metals that have a refined grain size and are in the solution annealed condition have a reduced susceptibility to cracking. It is thought that solution annealing prevents strain concentration in the HAZ since no strength gradient will be present, as in the aged condition. A fine grain size creates more grain boundary area, reducing the unit strain per grain boundary and requiring more liquid to wet the boundaries. It should be noted, however, that use of a fine grained material for avoiding liquation cracking may not always be possible as it may have an adverse effect on applications at high operating temperatures where creep resistance is important. In Alloy 718, the presence of a high fraction of  $\delta$  phase has been shown to increase cracking susceptibility. This is presumably due to the dissolution of the  $\delta$  phase in the HAZ and the subsequent segregation of Nb to the grain boundaries where it promotes liquid film formation.

Clearly, there is no single definitive mechanism to describe HAZ liquation cracking in precipitation-strengthened Ni-base alloys and the source of grain boundary liquid that leads to cracking varies among the different alloys. The use of weldability testing, particularly the hot ductility test, can be useful in determining the relative susceptibility of these alloys to cracking. Often, however, cracking in highly susceptible alloys can only be avoided by control of welding processes and procedures to minimize the restraint during welding.

### 4.5.3 Strain-Age Cracking

Strain-age cracking (SAC) is a form of reheat, or postweld heat treatment, cracking that is specific to the precipitation strengthened Ni-base alloys. It is a solid-state cracking phenomenon that is most often observed in the HAZ just adjacent to the fusion boundary, although it is possible for SAC to occur in the weld metal of these alloys. In most cases, it occurs during postweld heat treatment, but is also possible (although unlikely) during reheating in multi-pass welds. This form of cracking is most prevalent with the  $\gamma'$ ,  $\text{Ni}_3(\text{Al,Ti})$ , strengthened alloys and many of these alloys are considered “unweldable” because of this cracking mechanism.

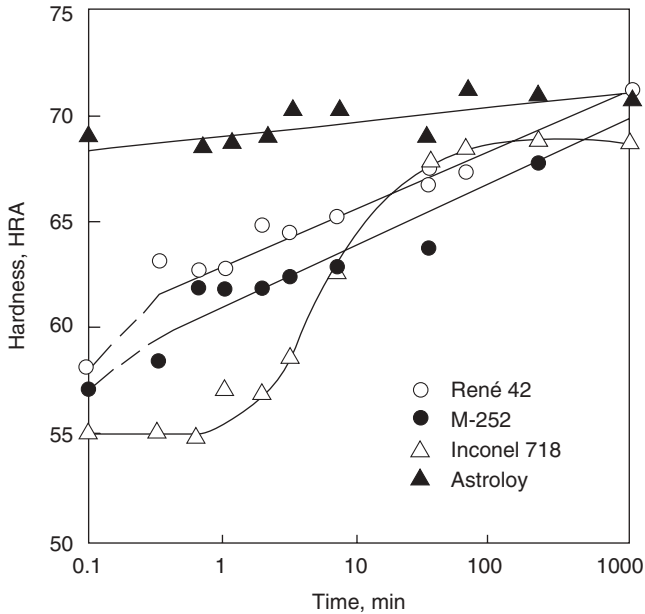


**Figure 4.57** Hardening rate as a result of precipitation for several Ni-base superalloys. (From Wilson and Burchfield [79]. Courtesy the American Welding Society)

The rate of  $\gamma'$  precipitation is influenced both by composition (Ti + Al content) and base metal condition. For example, even small amounts of cold work in the base metal will accelerate precipitation. Figure 4.57 from Wilson and Burchfield (79) shows the rate of hardening due to precipitation in three  $\gamma'$  strengthened alloys (René 42, M-252, and Astroloy). Note that hardening of these alloys occurs extremely rapidly after solutionizing and holding at the aging temperature. In contrast, Alloy 718, which is strengthened by  $\gamma''$ , hardens initially at a much slower rate. It will be seen that the rate of precipitation (hardening) is a key factor in controlling susceptibility to strain-age cracking.

A schematic illustration of a representative thermal history for welded and postweld heat treated Ni-base superalloys is shown in Figure 4.58.(80) During the weld thermal cycle, strengthening precipitates (and other constituents) that are present in the base metal dissolve in the austenite matrix and some grain growth will occur, depending on weld heat input. Since the as-welded fusion zone and HAZ are effectively solutionized, significant softening occurs. A postweld heat treatment consisting of solution annealing and aging must be applied to strengthen the weldment and base metal to the original base metal strength level. The solution heat treatment also serves to relax residual stresses resulting from the welding process. Ideally, the weldment is heated to an appropriate solution annealing temperature where alloying additions go back in solution and residual stresses relax, and then cooled to an aging tempera-

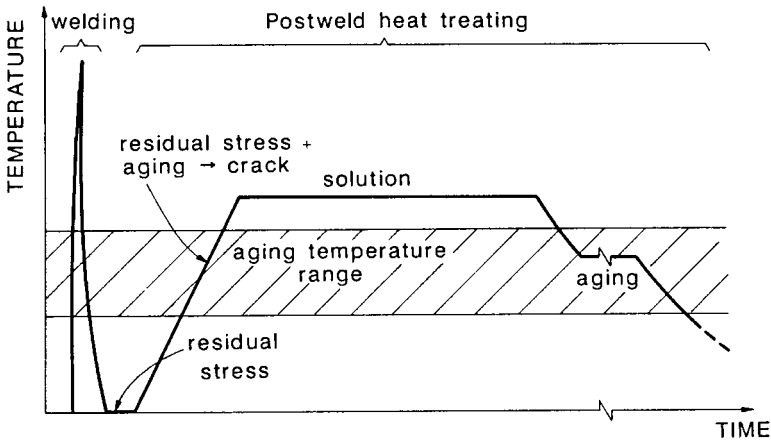


**Figure 4.58** Schematic of the thermal history during welding and postweld heat treatment of Ni-base superalloys. (From Kou [80])

ture where precipitation is controlled such that the required mechanical properties are achieved.

In practice, it may be difficult (or impossible) to prevent the precipitation of  $\gamma'$  during heating to the solution annealing temperature. This is a function of the alloy composition and the differences in hardening rates, as illustrated in Figure 4.57. The relationship between the heating cycle and precipitation is illustrated in Figure 4.59.(81) Strengthening precipitates, such as  $\gamma'$  and  $\gamma''$ , exhibit a distinct “C-curve” temperature-time regime in which precipitation is possible. If the weldment can be heated rapidly enough to avoid intersecting the C-curve, then precipitation will not occur and solution annealing of the weldment can be achieved. If the weldment cannot be heated rapidly enough (or if the C-curve is shifted to the left in Figure 4.59), precipitation will occur and the alloy will begin to harden. The precipitation during heating tends to occur in the same temperature range where significant stress relaxation occurs and this can lead to locally high strains at the grain boundaries. If these strains are sufficiently high, grain boundary failure will occur and a strain-age crack will form. Thus, strain-age cracking takes its name from the simultaneous presence of both strain and a strong aging reaction. The mechanism for SAC is described in the following section.

**4.5.3.1 Mechanism for Strain-Age Cracking** As described above, the term strain-age cracking (SAC) is derived from the fact that both local strain and aging must occur nearly simultaneously. The term should not be confused with the metallurgical phenomenon of “strain aging” observed in carbon steels. SAC in welds has been studied extensively in various Ni-base superalloys and the severity of this problem has led to the development of SAC resistant alloys, such as Alloys 718 and 706.

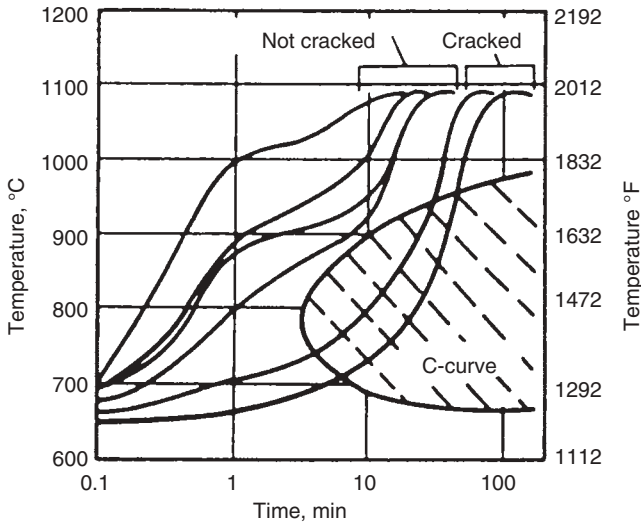


**Figure 4.59** Schematic illustration of the effect of heating rate and precipitation behavior on susceptibility to strain-age cracking. (From Berry and Hughes [81], Courtesy the American Welding Society)

It is generally agreed that SAC in Ni-base superalloys results from low ductility in the HAZ accompanied by high strain accumulation in the same region.(82–85) Such reduction of ductility is associated with the development of grain “stiffening” and/or grain boundary weakening during PWHT. Most investigators attribute this to intragranular precipitation hardening combined with precipitation-free zones at grain boundaries, or intergranular carbide precipitation.(84) If the decrease in ductility during PWHT occurs before or at a faster rate than stress relief, the “embrittled” region in the HAZ may crack due to its inability to accommodate the redistribution of strain associated with the stress-relieving process.

The following general observations have been made regarding SAC:

- It is always intergranular.
- It is most prevalent in the HAZ adjacent to the fusion line and in some cases is associated with the partially-melted zone (PMZ).
- It occurs during postweld heating to the solution annealing temperature due to simultaneous precipitation and local strain accumulation at grain boundaries.

The stresses which cause cracking may have three origins:

- 1) weld residual stress,
- 2) thermally-induced stresses arising from the difference in the coefficient of thermal expansion between the base material and weld metal, and
- 3) stresses from dimensional changes caused by precipitation.

In general, the precipitates have a different lattice parameter than the matrix and their formation will lead to a local grain boundary stress.

Based on the published literature the metallurgical contributors to SAC are the following:

- The rate of hardening (strengthening). Materials which harden more slowly allow better accommodation of the stresses (for example, Alloy 718 as shown in Figure 4.57).
- Intragranular precipitation resulting in hardening of the grain interior leading to stress concentration at the grain boundaries. This mechanism was originally proposed by Prager and Shira (86) based on the work of Younger *et al.* (87) on austenitic steels.
- “Transient embrittlement” of the HAZ due to the precipitation of *intergranular* carbides. According to this theory (88–90) the embrittling reaction is thought to result from solution of carbides during weld thermal cycle and subsequent re-precipitation in continuous “films” of  $M_{23}C_6$ -type carbides along grain boundaries during heat treatment. These carbides “films” are not capable of resisting the stresses caused by the precipitation of  $\gamma'$ , and presumably failure occurs at the carbide/matrix interface at the grain boundary.
- Partial melting along grain boundaries adjacent to the fusion line. This may be due to impurity segregation or constitutional liquation.

The mechanism for strain-age cracking in Ni-base alloys is still not well defined, although it is clear that both compositional and restraint factors play a role. It is well known, for instance, that certain alloys are more resistant to strain age cracking than others. This resistance is generally attributed to the rate and nature of the precipitation reaction(s) that promotes strengthening. The  $\gamma'$  strengthened alloys are the most susceptible and the influence of Ti and Al content has been well documented. The relationship of Ti and Al content to SAC was originally proposed by Prager and Shira (86) and a diagram based on their work which includes additional modern alloys is shown in Figure 4.60. The band running from approximately 3wt% Al to 6wt% Ti separates alloys that are resistant (below) from those that are susceptible (above). The higher Al + Ti contents promote a stronger and more rapid precipitation of  $\gamma'$ . This, in effect, shifts the nose of the precipitation curve to much shorter times making it difficult to suppress precipitation during postweld heating to the solution annealing temperature range. This is shown schematically in Figure 4.61 as a function of (Ti + Al) content for several heating rates.

Duvall and Owzarski (91) demonstrated the effect of (Ti + Al) content in a study of the postweld heat treatment cracking susceptibility of Waspaloy and Alloy 718. They showed that HAZ cracking obeyed a C-curve behavior, as shown in Figure 4.62, and that the C-curve for Alloy 718 was displaced to longer times. The C-curve for Waspaloy (containing 3 wt% Ti and 1.4 wt% Al)

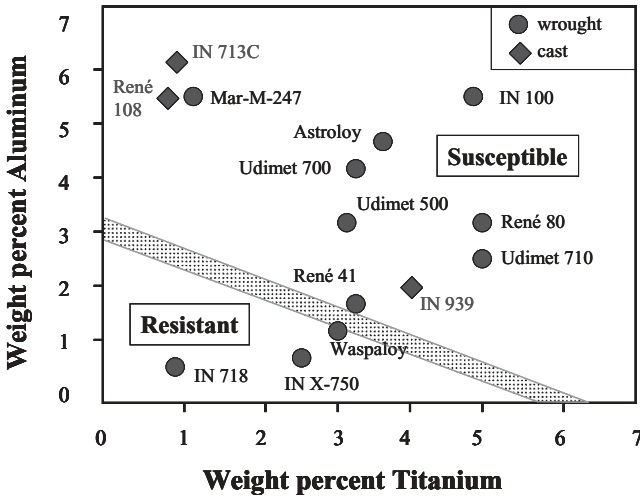


**Figure 4.60** Effect of Al and Ti content on susceptibility to strain-age cracking in Ni-base superalloys. (Modified from Prager and Shira [86])

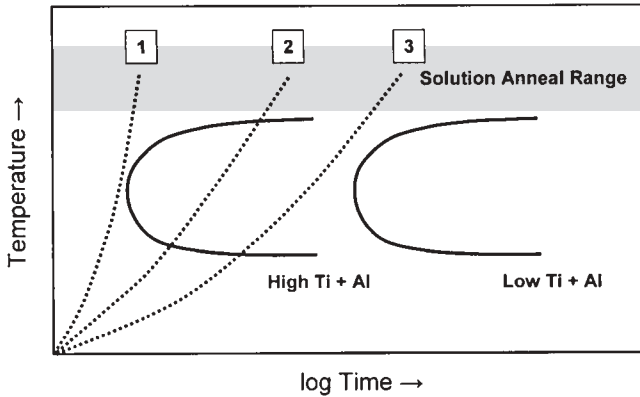


**Figure 4.61** Schematic illustration of the effect of (Ti + Al) content and heating rate to the solution annealing temperature.

represents the  $\gamma'$  precipitation regime while the Alloy 718 (containing 0.9 wt% Ti, 0.5 wt% Al, and 5 wt% Nb) C-curve represents the precipitation regime for  $\gamma''$ . These results again demonstrate the beneficial effect of the sluggish precipitation reaction of  $\gamma''$  in avoiding SAC during postweld heat treatment of Ni-base superalloys. In this same study, they found no indication of the “transient embrittlement” phenomenon. Instead, the ductility was kept at a moderately low level during aging in the cracking temperature range by a combination of microstructural interactions produced during welding and heat treatment. Changes in cracking susceptibility between different heats of

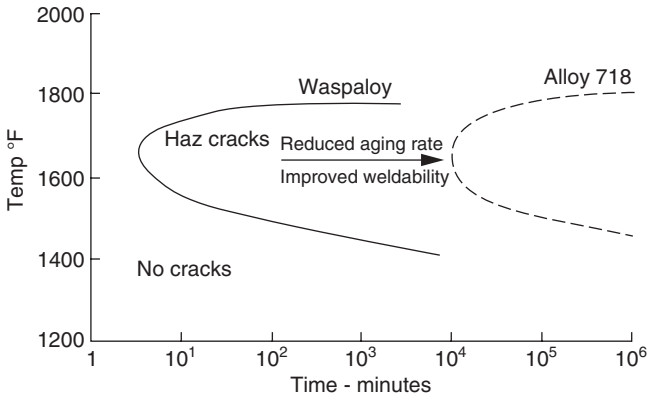


**Figure 4.62** C-curve strain age cracking behavior for Waspaloy and Alloy 718 showing much greater tolerance for PWHT cracking for Alloy 718 due to slower aging rate. (From Duval and Owzarski [36]. Courtesy the American Welding Society)

Waspaloy resulted from changes in ductility, which were caused by  $\gamma'$  precipitation and intergranular carbide precipitation. Within groups of susceptible and non-susceptible microstructures, wide differences in the amount and morphology of carbides were observed.

Norton and Lippold (92) used a Gleeble-based test to study the SAC susceptibility of Waspaloy and Alloy 718. In this test, samples are initially subjected to a HAZ thermal cycle and then cooled to room temperature under restraint, so that considerable room temperature residual stress was present. The sample was then immediately heated into the aging temperature range where the stresses were allowed to relax and precipitation of  $\gamma'$  (Waspaloy) or  $\gamma''$  (Alloy 718) occurred with hold time. Since the sample was fixed, precipitation resulted in increased stress in the sample, as shown in Figure 4.63. After a predetermined time (up to four hours) the samples were then pulled to failure and their ductility measured. These tests resulted in the development of three-dimensional C-curves based on test temperature, time, and strength/ductility. This data could then be used to generate two-dimensional, ductility C-curves for specific time-temperature conditions. An example of this for both alloys after three hours of PWHT is shown in Figure 4.64. This data again shows the beneficial effect of  $\gamma''$  versus or  $\gamma'$  precipitation with respect to SAC.

Analysis of these samples also clearly reveals the nature of SAC in Ni-base superalloys. The photomicrograph in Figure 4.65 shows the region near the fracture in a Waspaloy sample. Cracks are intergranular and tend to initiate at grain boundary triple points. Higher magnification examination of the grain boundaries in the SEM revealed no evidence of carbides or continuous carbide precipitation, suggesting that the “transient embrittlement” phenomenon is not occurring in Waspaloy. This is in agreement with the conclusion of Duval

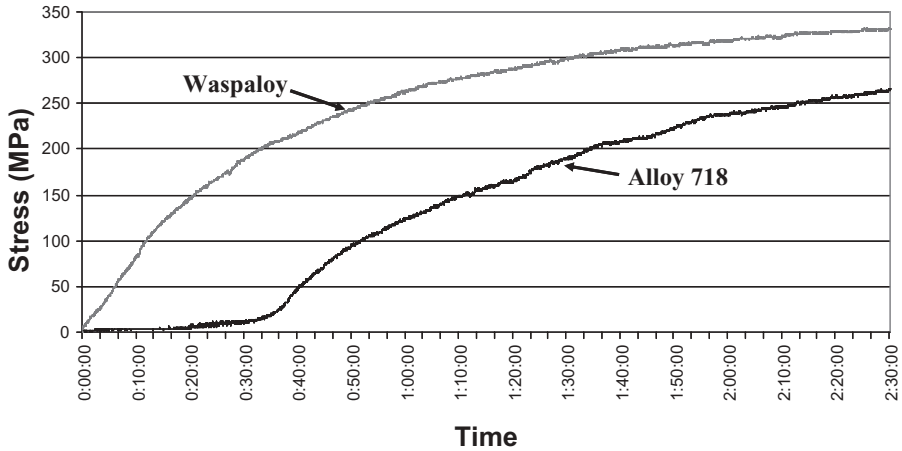


**Figure 4.63** Effect of postweld aging time on stress in the simulated HAZ of Waspaloy and Alloy 718. (From Norton and Lippold [92]).

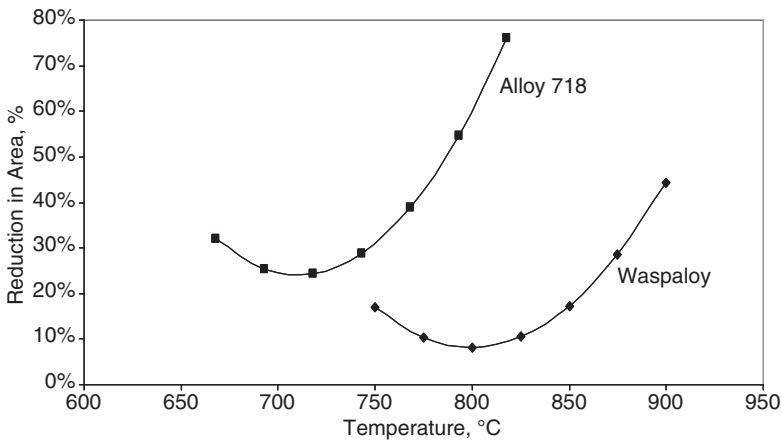


**Figure 4.64** Postweld heat treatment ductility curves for Waspaloy, and Alloy 718 after three hours of aging following a simulated HAZ thermal cycle. (From Norton and Lippold [92]).

and Owzarski.(93) Examination of the fracture surfaces of Waspaloy and Alloy 718 samples indicated that the fracture morphology is either smooth or ductile intergranular. An example of both of these fracture morphologies can be seen in Figure 4.66.

**4.5.3.2 Effect of Residual, Thermal and Aging Stresses, and Joint Restraint** It is widely believed that PWHT cracking is the result of stresses developed during post weld heat treatment that are relaxed preferentially in the HAZ at the same time that the ductility of the HAZ is reduce by metal-

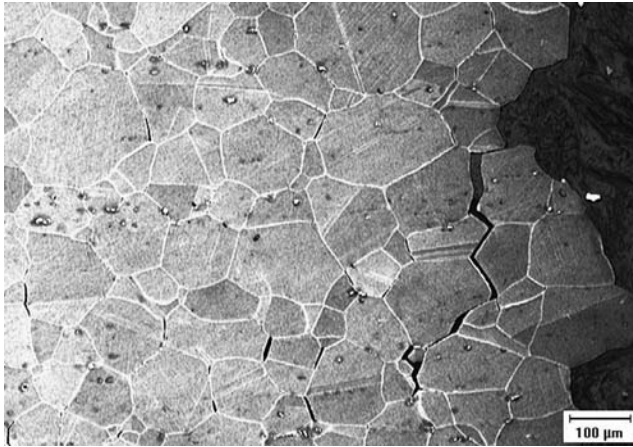


**Figure 4.65** Intergranular strain-age cracking in the simulated HAZ of Waspaloy. (From Norton and Lippold [92])

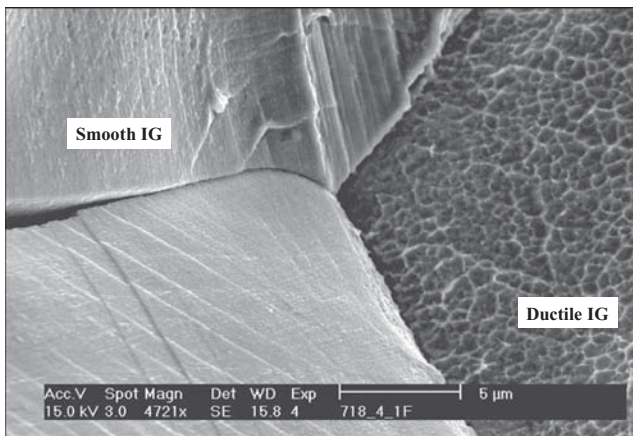


**Figure 4.66** Fracture morphology of strain-age cracking in Alloy 718. (From Norton and Lippold [92])

lurgical reactions. The stresses contributing to cracking have been suggested to include residual welding stresses, stresses due to localized thermal expansion, and aging contraction stresses.(90,93)

The level of weld residual stresses developed would depend upon heat input, component geometry, mechanical properties of the material, and elastic stiffness of the restraining elements. As with other materials, the residual stresses in heavily restrained superalloy weldments are considered to be of the order of the yield strength of these materials. In the HAZ, this would correspond to the yield strength of the alloy in the solutionized condition. The thermal stresses in complex assemblies are likely to be strongly influenced by

component geometry and uniformity of heating. High thermal stresses can be generated by relatively small temperature difference in cases where the material is fully restrained against expansion. Since welds in turbine engine components are often severely restrained, the magnitude of thermal stresses created during post weld heat treatment is likely to be of considerable significance.

Aging contraction results from the precipitation of  $\gamma'$ , which tends to increase with the volume fraction of  $\gamma'$  precipitation. (See Section 4.2.) Such contraction can lead to the development of significantly high stresses. Although the overall contraction of the component is important, the difference in aging contraction between the HAZ and the base metal may be of particular concern. This difference may lead to excessive localized straining in the HAZ and aggravate the tendency for PWHT cracking, particularly in the case where the base metal is in the fully aged condition. The stresses that accumulate by aging in the HAZ can be clearly seen from the work of Norton and Lippold (92) who showed stresses on the order of 250–350 MPa (35–50 ksi) in simulated HAZs in Alloy 718 and Waspaloy that aged for over two hours (Figure 4.63). Fawley and Prager (94) showed that for René 41, PWHT cracking could be avoided when the aging stresses were reduced by a more sluggish precipitation of  $\gamma'$ .

The propensity for SAC in a given alloy increases with the degree of weldment restraint. Even highly crack-resistant materials such as Alloy 718 can be susceptible to cracking during PWHT if the restraint level produces exceedingly large residual stresses. (86,89) These residual stresses are then relaxed during PWHT, leading to cracking. The data of Norton and Lippold (92) showed that Alloy 718 exhibits a ductility minimum similar to Waspaloy (Figure 4.64), but the minimum level for Waspaloy is much lower (~10% vs. 25%) resulting in higher susceptibility. If the ductility of Alloy 718 can be exhausted by high strains resulting from stress relaxation in the HAZ, cracking of this alloy is also possible. Thus, control of residual stresses during welding can be a good antidote for SAC in superalloys that have moderate SAC susceptibility.

**4.5.3.3 Composition Effects** As previously discussed and illustrated in Figure 4.60, the tendency of superalloys for SAC is a strong function of the total amount of hardener content of the alloy itself. Those alloys with higher total Al + Ti (>6 wt.%) content are more susceptible to SAC than those which are lower in hardener content. This is related to the fact that as the hardener content increases:

- 1) aging occurs more rapidly during PWHT (Figure 4.61),
- 2) the volume fraction of strengthening precipitate increases, and
- 3) aging contraction stresses increase.

An increasing volume fraction of  $\gamma'$  in the superalloys has the net effect of reducing ductility and increasing the local stresses by aging. This, in turn, lowers the ductility of the alloy and increases the tendency to cracking. By

using niobium as the primary strengthening element, alloys such as Alloy 718 are effectively resistant to SAC due to the sluggish aging response of  $\gamma''$  precipitation (Figure 4.62), although they may not be totally immune, as noted in the previous section.

The effect of other elements on SAC is not so clear. Hughes and Berry (90) showed that heats of René 41 with reduced levels of carbon are more resistant to SAC, while Koren *et al.* (78) found that low carbon content is detrimental to SAC resistance in Alloy 713C. It is proposed that the lower carbon content results in fewer carbides to pin the grain boundaries and prevent boundary migration in the HAZ. Thus, the lower carbon alloys would be more prone to grain coarsening.

Boron is added to many superalloys to improve stress-rupture (creep) properties. Thamburaj *et al.* (95) found that higher levels of boron were related to the improved resistance of René 41 to SAC. Carlton and Prager (96) found that the presence of oxygen was a prerequisite for SAC in René 41 and stated that oxygen segregation to grain boundaries will reduce grain boundary strength. They indicated that oxygen will have a similar effect with Alloy 718 and Waspaloy. There have been virtually no studies on the effect of the impurities sulfur and phosphorus on SAC in these alloys. While it is presumed that these impurities will have a negative effect, in practice, the low levels of (S + P) in most superalloys make the effect negligible.

**4.5.3.4 Grain Size** Fine-grained materials increase the amount of grain boundary area and have been found to be more resistant to SAC than those that are coarse grained. (90,96) Presumably, the increased grain boundary area in fine grained alloys provides greater opportunity for stress relaxation by grain-boundary sliding. In addition, embrittling phases that may form at the grain boundaries are spread over a wider area forming a layer that is either thinner or discontinuous. It can also be argued that the fine grain size reduces the unit strain per grain boundary and thus stresses resulting from relaxation and/or aging are better accommodated in the structure, minimizing the strain localization at individual boundaries. These arguments are similar to those used to explain the beneficial effect of fine grain size on susceptibility to HAZ liquation cracking in Section 4.5.2.2. As also mentioned in that section, use of a fine-grained material for avoiding cracking may not always be possible as it can have an adverse effect on applications at high operating temperatures where creep resistance is important.

**4.5.3.5 Preweld Condition of the Base Metal** Many investigations have shown that the base metal should be soft to allow the stresses developed during welding and during postweld heat treatment to be relaxed. Welds made on solution-annealed base metal have been shown (86) to have considerably more resistance to SAC than those made on mill-annealed or fully aged metal. Superior resistance to PWHT cracking in René 41 was obtained through slow cooling from the solution-annealing temperature, which led to coarse, over-

aged  $\gamma'$  precipitation and resulted in a softer base metal.(95) A two-step overaging treatment (solutionizing 1170°C (2140°F)/four hour/forced air cool and aging 1080°C (1975°F)/16 hour/furnace cool to 1010°C (1850°F)/four hour/Ac) resulted in excellent resistance to PWHT cracking in Udimet 700.(93) Again, the overaging of the  $\gamma'$  precipitates leads to an overall softening of the base metal and stabilizes these precipitates during reheating to the solution annealing temperature during PWHT. The net effect is to reduce the local stresses that concentrate in the HAZ during PWHT.

**4.5.3.6 Effect of Welding Procedure** Residual stresses can be reduced and metallurgical damages can be minimized by reducing the weld heat input. Wu and Herfert (88) showed that low weld heat input inhibits the precipitation of deleterious carbide films along the grain boundaries in René 41. Low heat input welding techniques may generally be useful as part of a solution to SAC, but it is unlikely that a total solution can be obtained by simply “tweaking” welding parameters. Very low heat input can be obtained by using EB welding. But certain alloys develop HAZ liquation cracks as a result of EB welding, which may aggravate the degree of PWHT cracking during subsequent post-weld heat treatment.

Preheating has been shown to be useful in reducing SAC, but the preheat temperatures may be extremely high. For example, in a study by Duvall and Doyle (97), Alloy 713C vanes were preheated to 538°C (1000°F) and held at this temperature while repair welds were made. Preheating and welding were carried out in an inert atmosphere. This procedure was found to substantially decrease the degree of both hot cracking (solidification and HAZ liquation cracking) and SAC. King *et al.*(98) found that high preheat temperatures, 705°–955°C (1300°–1750°F), successfully avoided cracking during welding and PWHT in high strength, cast superalloy vanes. In the turbine engine industry, this technique is often referred to as “SWET” welding (superalloy welding at elevated temperature).(99)

The weld joint geometry can also be an important factor influencing SAC, since it can influence the restraint level in the weldment. Various studies (54,100,101) indicate that changes in weld-bead contour influence the tendency for HAZ liquation cracking. Liquation cracks in EB welds are known to occur preferentially in the “nail-head” area of the weld and below (86) These liquation cracks can then become initiation sites for SAC during subsequent heat treatment.

The use of lower strength, more ductile filler metals such as Alloy 625 (a solution-strengthened Ni-base alloy) was found to make the repair welds in Alloy 713C vanes resistant to SAC.(86) However, it should be recognized that the Alloy 625 weld metal cannot be strengthened during PWHT.

**4.5.3.7 Effect of Postweld Heat Treatment** Most nickel-base superalloys require a full solution anneal and aging treatment following welding in order to restore mechanical properties. Simply aging after welding is usually not

appropriate since the weld metal and HAZ cannot be restored to full strength and there is the possibility of overaging the base metal (if welding is performed on fully aged material). In addition, the aging temperature is not high enough to allow sufficient stress relief and severe cracking may occur.

As shown in Figure 4.59, rapid heating to the solution temperature may be effective in preventing SAC. This is possible since a sufficient temperature is reached in which stress relaxation occurs prior to the onset of precipitation. For small components or alloys with low or moderate (Ti + Al) content, such an approach may be possible. In such cases, both the weld residual stresses and stresses associated with precipitation are eliminated or avoided. In large components, such rapid heating approaches are usually not possible and can even be more damaging, since temperature gradients within the component can create large thermal stresses.

A stepped-heating technique may be effective in some situations, particularly where weld residual stresses are not excessive. This technique involves slowing heating the component to about 500 °C (930 °F) and soaking at this temperature to reduce thermal gradients throughout the component and relieve some of the residual stress. The component is then rapidly heated through the crack-sensitive temperature range to the solution temperature. The success of such a technique is dependent on the original level of residual stress, the amount of residual stress that can be relieved during the low temperature soak, and the rapidity at which the component can be heated through the precipitation range.

It has also been reported that a protective atmosphere during heat treatment is beneficial.(78) PWHT cracking was eliminated in high-purity dry argon, argon containing 0.5% oxygen, and vacuum atmospheres. The detrimental effect of an oxygen-rich atmosphere is thought to be due to the rapid diffusion of oxygen along grain boundaries and the consequent formation of oxides which are not able to resist plastic deformation during stress relaxation.(96) It is clear that oxygen is at best contributory, and that the exclusion of oxygen from the heat-treatment environment cannot eliminate SAC in most cases. For example, D'Annessa and Owens (102) indicated that PWHT in a vacuum may eliminate cracking only in materials which have marginal susceptibility to SAC (such as Waspaloy and René 41), but is not effective in highly susceptible alloys.

Localized solution treatment at 1065 °C (1950 °F) for five minutes of repair welds in René 41 was found to prevent failure during subsequent aging.(103) The effects of the localized solution treatment were to:

- 1) homogenize the weld metal,
- 2) cause the aging precipitates to be more uniformly and finely distributed, and
- 3) prevent the precipitation of carbides since fast cooling rates are associated with such treatments.

However, the role of the various influences observed was not explained. In addition, care must be taken to avoid producing sufficiently high thermal stresses to leave high residual stresses on cooling.

**4.5.3.8 Summary of Strain-Age Cracking** Strain-age cracking in the precipitation-strengthened Ni-base alloys occurs due to the local accumulation of strain and the concomitant hardening of the microstructure due to precipitation. Local strains develop due to both the relaxation of weld residual stresses and precipitation-induced stresses. Non-uniform heating during postweld heat treatment may also contribute some thermally-induced stresses. The combination of straining and hardening due to precipitate aging can lead to “strain-age” cracking. This form of cracking is most often observed in the HAZ.

The most effective method to avoid SAC is through alloy selection. Alloys that are strengthened by the  $\gamma'$ ,  $\text{Ni}_3(\text{Ti},\text{Al})$ , precipitate are the most prone to SAC. As shown in Figure 4.60, as Ti and Al content of the alloy increases, susceptibility to SAC increases. By reducing (Ti + Al) content or strengthening the alloy by precipitation of  $\gamma''$  ( $\text{Ni}_3\text{Nb}$ ), susceptibility to SAC can be reduced or eliminated. Alloy 718, which is strengthened by  $\gamma''$ , was developed as a SAC-resistant superalloy and is widely (and successfully) used in welded applications.

Many of the high-strength superalloys (those with high Ti + Al content) are effectively “unweldable” due to SAC. The high levels of (Ti + Al) result in a high volume fraction of  $\gamma'$ , providing high strength at elevated temperatures, but also exacerbating SAC during PWHT. Welding in the solution annealed or overaged condition may provide some relief from SAC in these high-strength superalloys. The use of low-heat input welding processes and fine-grained base metal will also improve resistance to SAC, but avoiding cracking in highly-constrained structures can be challenging.

## REFERENCES

1. Decker, R. F. 2006. “The Evolution of Wrought Age-Hardenable Superalloys,” *JOM*, Sept. 2006, pp. 33–39.
2. Decker, R. F. and Mihalisin, J. R. 1969. Coherency strains in gamma prime hardened nickel alloys, *Transactions of ASM Quarterly*, 62: 481–489.
3. Thornton, P. H., Davies, P. H., and Johnston, T. L. 1970. Temperature dependence of the flow stress of the gamma prime phase based upon  $\text{Ni}_3\text{Al}$ , *Metallurgical Transactions A*, 1: 207–218.
4. Biss, V. and Sponseller, D. L. 1973. Effect of molybdenum on gamma prime coarsening and on elevated-temperature hardness in some experimental Ni-base superalloys, *Metallurgical Transactions A*, 4: 1953–1960.
5. Gaurd, R. W. and Westbrook, J. H. 1959. *Transactions of the Metallurgical Society of AIME*, 215: 807–816.
6. Beardmore, P, Davies, R. G., and Johnston, T. L. 1969. Temperature dependence of the flow stress of nickel-base alloys, *Transactions of AIME*, 245: 1537–1545.

7. Decker, R. F. 1969. Strengthening mechanisms in nickel base superalloys, Steel Strengthening Mechanisms Symposium, Climax Molybdenum Company, Zurich, Switzerland, pp. 1–24.
8. Gibbons, T. B. and Hopkins, B. E. 1971. Influence of grain size and certain precipitate parameters on the creep properties of Ni-Cr base alloys, *Metal Science Journal*, 5: 233–240.
9. Brooks, C. R. 1982. *Nickel base alloys, in Heat treatment, structure, and properties of nonferrous alloys*, ASM International, Materials Park, OH.
10. Lifshitz, I. M. and Sloyozov, V. V. 1961. The kinetics of precipitation from supersaturated solid solutions, *Journal of Physical Chemistry of Solids*, 19: 35–50.
11. Brooks, J. W. and Bridges, P. J. 1988. *Metallurgical Stability of INCONEL Alloy 718, Superalloys*, ASM International, Materials Park, OH, pp. 33–42.
12. Barker, J. F., Ross, E. W., and Radavich, J. F. 1970. Long time stability of Inconel 718, *Journal of Metals*, 22: 31–41.
13. Radavich, J. F. 1989. *The physical metallurgy of cast and wrought alloy 718, Superalloy 718*, ASM International, Materials Park, OH, pp. 229–240.
14. DuPont, J. N., Robino, C. V., and Marder, A. R. 1998. Solidification of Nb-Bearing Superalloys: Part II. Pseudo Ternary Solidification Surfaces, *Metallurgical and Material Transactions A*, 29A: 2797–2806.
15. DuPont, J. N., Robino, C. V., and Marder, A. R. 1988. “Solidification and weldability of Nb-bearing superalloys,” *Welding Journal*, 77: 417s–431s.
16. DuPont, J. N., Robino, C. V., and Marder, A. R. 1988. Modeling solute redistribution and microstructural development in fusion welds of Nb bearing superalloys, *Acta Metallurgica*, 46: 4781–4790.
17. Babu, S. S., Miller, M. K., Vitek, J. M., and David, S. A. 2001. Characterization of the microstructure evolution in a nickel base superalloy during continuous cooling conditions, *Acta Materialia*, 49: 4149–4160.
18. Rosenthal, R. and West, D. R. F. 1999. Continuous gamma-prime precipitation in directionally solidified IN 738 LC alloy, *Materials Science and Technology*, 15: 1387–1394.
19. Ojo, O. A., Richards, N. L., and Chaturvedi, M. C. 2006. Study of the fusion zone and heat affected zone microstructures in tungsten inert gas welded INCONEL 738LC superalloy, *Metallurgical and Material Transactions*, 37A: 421–433.
20. DuPont, J. N., Robino, C. V., Marder, A. R., Notis, M. R., and Michael, J. R. 1988. “Solidification of Nb-Bearing Superalloys: Part I. Reaction Sequences”, *Metallurgical and Material Transactions A*, 29A: 2785–2796.
21. Rhines, F. N. Phase diagrams in metallurgy, McGraw Hill, New York, N.Y., pp. 175–185.
22. Banovic, S. W. and DuPont, J. N. 2003. Dilution and microsegregation in dissimilar metal welds between super austenitic stainless steels and Ni base alloys, *Science and Technology of Welding and Joining*, 6: 274–383.
23. Cieslak, M. J. 1991. The welding and solidification metallurgy of Alloy 625, *Welding Journal*, 70: 49s–56s.
24. Cieslak, M. J., Headley, T. J., Knorovsky, G. A., Romig, A. D., and Kollie, T. 1990. A comparison of the solidification behavior on incoloy 909 and inconel 718, *Metallurgical Transactions A*, 21A: 479–488.

25. Cieslak, M. J., Headley, T. J., Kollie, T., and Romig, A. D. 1988. A melting and solidification study of Alloy 625, *Metallurgical Transactions A*, 19A: 2319–2331.
26. Knorovsky, G. A., Cieslak, M. J., Headley, T. J., Romig, A. D., and Hammeter, W. F. 1989. *Inconel 718: A solidification diagram*, *Metallurgical Transactions A*, 20A: 2149–2158.
27. Maguire, M. C. and Michael, J. R. 1994. “Weldability of alloys 718, 625, and variants”, *Superalloys 718, 625, 706 and Various Derivatives*, TMS, Warrendale, PA, pp. 881–892.
28. Eiselstein, H. L. 1965. “Advances in technology of stainless steels”, *ASTM STP* 369, pp. 62–79.
29. Baker, H. Ed., *Alloy phase diagrams*, ASM International, Materials Park, OH.
30. Stadelmaier, H. H. and Fiedler, M. 1975. The ternary system nickel-niobium-carbon, *Z. Metallkde*, 9: 224–225.
31. DuPont, J. N. Newbury, B. D. Robino, C. V., and Knorovsky, G. A. 1999. The Use of Computerized Thermodynamic Databases for Solidification Modeling of Fusion Welds In Multi-Component Alloys, 9th International Conference on Computer Technology in Welding, National Institute of Standards and Technology, Detroit, MI, pp. 133–142.
32. Cieslak, M. J., Knorovsky, G. A., Headley, T. J., and Romig, A. D. 1986. “The use of New PHACOMP in understanding the solidification microstructure of nickel base alloy weld metal,” *Metallurgical Transactions A*, 17A: 2107–2116.
33. DuPont, J. N. 1998. “A Combined Solubility Product/New PHACOMP Approach for Estimating Temperatures of Secondary Solidification Reactions in Superalloy Weld Metals”, *Metallurgical and Material Transactions*, 29A: 1449–1456.
34. Clyne, T. W. and Kurz, W. 1981. “Solute redistribution during solidification with rapid solid-state diffusion,” *Metallurgical Transactions A*, 12A: 965–971.
35. Pepe, J. J. and Savage, W. F. 1967. “Effects of constitutional liquation in 18-Ni maraging steel weldments,” *Welding Journal*, 46: 411s–422s.
36. Duvall, D. S. and Owczarski, W. A. 1967. “Further heat affected zone studies in heat resistant nickel alloys,” *Welding Journal*, 46: 423s–432s.
37. Owczarski, W. A., Duvall, D. S., and Sullivan, C. P. 1966. “A model for heat affected zone cracking in nickel base superalloys,” *Welding Journal*, 45: 145s–155s.
38. Cieslak, M. J., Stephens, J. J., and Carr, M. J. 1988. A study of the weldability and weld-related microstructure of Cabot Alloy 214, *Metallurgical Transactions A*, 19A: 657–667.
39. Gozlan, E., Bamberger, M., and Dirnfeld, S. F. 1992. Role of Zr in the phase formation at the interdendritic zone in nickel-based superalloys, *Journal of Materials Science*, 27: 3869–3875.
40. George, E. P., Babu, S. S., David, S. A., and Seth, B. B. 2001. IN939 based superalloys with improved weldability, Condition and Life Management for Power Plants, Porvoo, Finland, pp. 139–148.
41. Cieslak, M. J., Headley, T. J., and Romig, A. D. 1986. “The welding metallurgy of Hastelloy alloys C-4, C-22, and C-276,” *Metallurgical Transactions A*, 17A: 2035–2047.

42. Robino, C. V., Michael, J. R., and Cieslak, M. J. 1997. "Solidification and welding metallurgy of thermo-span alloy," *Science and Technology of Welding and Joining*, 2: 220–230.
43. David, S. A. and Vitek, J. M. 1989. Correlation between solidification parameters and weld microstructures, *International Materials Reviews*, 1989, pp. 213–245.
44. Alexandrov, B. T., Nissley, N. E., and Lippold, J. C. 2008. Evaluation of weld solidification cracking in Ni-base superalloys using the cast pin tear test, *Hot Cracking Phenomena in Welds II*, Springer, ISBN 978-3-540-78627-6, pp. 193–214.
45. Thompson, E. G. 1969. Hot cracking studies of Alloy 718 weld heat-affected zones, *Welding Journal*, 48: 70s–79s.
46. Thompson, R. G. and Genculu, S. 1983. "Microstructural evolution in the HAZ of Inconel 718 and correlation with the hot ductility test," *Welding Journal*, 62: 337s–346s.
47. Thompson, R. G., Cassimus, J. J., Mayo, D. E., and Dobbs, J. R. 1985. "The relationship between grain size and microfissuring in Alloy 718," *Welding Journal*, 64: 91s–96s.
48. Radhakrishnan, B. and Thompson, R. G. 1991. "A phase diagram approach to study liquation cracking in Alloy 718," *Metallurgical Transactions*, 22A: 887–902.
49. Baeslack, W. A. III and Nelson, D. E. 1986. "Morphology of weld heat-affected zone liquation in cast Alloy 718," *Metallography*, 19: 371–379.
50. Baeslack, W. A. III, West, S. L., and Kelly, T. J. 1988. "Weld cracking in Ta-modified cast Inconel 718," *Scripta Metallurgica*, 22: 729–734.
51. Kelly, T. J. 1990. "Rene 220C- The new, weldable, investment cast superalloy," *Welding Journal*, 69: 422s–430s.
52. Kelly, T. J. 1986. "Investigation of elemental effects on the weldability of cast nickel-based superalloys," *Advances in Welding Science and Technology*, David, S. A. editor, Metals Park, OH, ASM International, 623–627.
53. Morrison, T. J., Shira, C. S., and Weisenberg, L. A. 1969. The influence of minor elements on Alloy 718 weld microfissuring. *The Welding Research Council Bulletin*, pp. 47–67.
54. Lucas, M. J. and Jackson, C. E. 1970. "The welded heat-affected zone in nickel-base Alloy 718," *Welding Journal*, 49: 46s–54s.
55. Savage, W. F., Nippes, E. F., and Goodwin, G. M. 1977. "Effect of minor elements on hot-cracking tendencies of Inconel 600," *Welding Journal*, 56: 245s–253s.
56. Pease, G. R. 1957. "The practical welding metallurgy of nickel and high nickel alloys," *Welding Journal*, 36: 330s–334s.
57. Canonico, D. A., Savage, W. F., Werner, W. J., and Goodwin, G. M. 1969. "Effects of minor additions on the weldability of Incoloy 800," Proceedings of conference on "Effects of Minor Elements on the Weldability of High-Nickel Alloys," Welding Research Council, New York, 68–92.
58. Owczarski, W. A. 1969. "Some minor element effects on weldability of heat resistant nickel-base superalloys," Proceedings of conference on "Effects of Minor Elements on the Weldability of High-Nickel Alloys," Welding Research Council, New York, 6–23.

59. Yeniscavich, W. and Fox, C. W. 1969. "Effects of minor elements on the weldability of Hastelloy Alloy X," Proceedings of conference on "Effects of Minor Elements on the Weldability of High-Nickel Alloys," Welding Research Council, New York, 24–35.
60. Vincent, R. 1985. "Precipitation around welds in the nickel-base superalloy Inconel 718," *Acta Metallurgica*, 33: 1205–1216.
61. Kelly, T. J. 1989. "Elemental effects on cast 718 weldability," *Welding Journal*, 68: 44s–51s.
62. Huang, X., Richards, N. L., and Chaturverdi, M. C. 1992. "An investigation of HAZ microfissuring mechanisms in Cast Alloy 718," Proceedings of 3rd International SAMPE Metals Conference, SAMPE, CA.
63. Thompson, R. G. 1988. "Microfissuring of Alloy 718 in the weld heat-affected zone," *Journal of Metals*, 40: 44–48.
64. Boucher, C., Varela, D., Dadian, M., and Granjon, H. 1976. Hot cracking and recent progress in the weldability of the nickel alloys Inconel 718 and Waspaloy, *Revue de Metallurgie*, 73: 817–831.
65. Bologna, D. J. 1969. "Metallurgical factors influencing the microfissuring of Alloy 718 weldments," *Metals Engineering Quarterly*, 9: 37–43.
66. Fletcher, M. J. 1970. "Electron-beam welding of Nimonic 80A," *Welding and Metal Fabrication*, 38: 113–115.
67. Williams, J. A. and Singer, A. R. E. 1968. "A review of hot shot cracking," *The Journal of the Australian Institute of Metals*, 11: 2.
68. Radhakrishnan, B. and Thompson, R. G. 1991. Modeling of Microstructure Evolution in the Weld HAZ, *Metal Science of Joining*, M. J. Cieslak *et al.* eds., TMS/AIME, pp. 31–40.
69. Guo, H. Chaturvedi, M., and Richards, N. L. 1999. Effect of nature of grain boundaries on intergranular liquation during weld thermal cycling of a Ni-base alloy, *Science and Technology of Welding and Joining*, Vol. 3: 257–259.
70. Schwenk, W. and Trabold, A. F. 1963. "Weldability of René 41," *Welding Journal*, 42: 460s–465s.
71. Gordine, J. 1971. "Some problems in welding Inconel 718," *Welding Journal*, 50: 480s–484s.
72. Thompson, R. G., Dobbs, J. R., and Mayo, D. E. 1986. "The effect of heat treatment on microfissuring in Alloy 718," *Welding Journal*, 65: 299s–304s.
73. Lu, Q. 1999. PhD Dissertation, HAZ Microstructural Evolution in Alloy 718 after Multiple Repair and PWHT Cycles, The Ohio State University.
74. Sims, C. T., Stoloff, N. S., and Hagel, W. C. 1987. *Superalloys II*, John Wiley and Sons, New York, pp. 3–4, 27–188, 495–515.
75. Qian, M. and Lippold, J. C. 2003. Liquation phenomena in the simulated heat-affected zone of Alloy 718 after multiple postweld heat treatment cycles, *Welding Journal*, 82(6): 145s–150s.
76. Kelly, T. J. 1986. "Investigation of elemental effects on the weldability of cast nickel-based superalloys," *Advances in Welding Science and Technology*, David, S. A. editor, Metals Park, OH, ASM International, 623–627.
77. Boucher, C., Dadian, M., and Granjon, H. 1977. "Final report COST 50," Institute de Soudure, Paris.

78. Koren, A., Roman, M., Weisshaus, I., and Kaufman, A. 1982. "Improving the weldability of Ni-base superalloy 713C," *Welding Journal*, 61: 348s–351s.
79. Wilson, R. M. and Burchfield, L. W. G. 1956. *Welding Journal*, Vol. 35, p. 32s.
80. Kou, S. 1969. *Welding Metallurgy*, 1<sup>st</sup> Edition, published by Wiley Interscience, Inc.
81. Berry, T. F. and Hughes, W. P., *Welding Journal*, Vol. 46, p. 505s.
82. Baker, R. G. and Newman, R. P. 1969. "Cracking in Welds," *Metal Construction and Br. Weld. J.*, Vol. 1, Feb. pp. 1–4.
83. Franklin, J. G. and Savage, W. F. 1974. "Stress Relaxation and Strain-Age Cracking in René 41 Weldments," *Welding Journal*, 53, pp. 380s.
84. McKeown, D. 1971. "Re-Heat Cracking in High Nickel Alloy Heat-Affected Zone," *Welding Journal*, 50, pp. 201s–206s.
85. Nakao, Y. 1988. "Study on Reheat Cracking on Ni-base superalloy, Waspaloy," *Transactions of the Japan Welding Society*, Vol. 19, No.1, April pp. 66–74.
86. Prager, M. and Shira, C. S. 1968. "Welding of precipitation-hardening nickel-base alloys," *Welding Research Council Bulletin* 128.
87. Younger, R. N. and Barker, R. G. 1961. Heat-affected zone cracking in welded austenitic steels during heat treatment, *Brit. Weld. Jour.* 8(12): 579–587.
88. Wu, K. C. and Herfert, R. E. 1967. Microstructural studies of René 41 simulated weld heat-affected zones, *Welding Journal*, 46: 32s–38s.
89. Weiss, S., Hughes, W. P., and Macke, H. J. 1962. Welding evaluation of high temperature sheet materials by restraint patch testing, *Welding Journal*, 41: 17s–22s.
90. Hughes, W. P. and Berry, T. F. 1967. A study of the strain-age cracking characteristics in welded Rene 41-Phase I, *Welding Journal*, 46: 361s–370s.
91. Duvall, D. S. and Owczarski, W. A. 1969. Studies of postweld heat-treatment cracking in nickel-base alloys, *Welding Journal*, 48: 10s–22s.
92. Norton S. J. and Lippold, J. C. 2003. Development of a Gleeble-based Test for Postweld Heat Treatment Cracking Susceptibility, Trends in Welding Research, Proc. of the 6th International Conference, ASM International, pp. 609–614.
93. Duvall, D. S. and Owczarski, W. A. 1971. Heat treatments for improving the weldability and formability of Udimet 700, *Welding Journal*, 50: 401s–409s.
94. Fawley, R. W. and Prager, M. 1970. Evaluating the resistance of René 41 to strain-age cracking, *Welding Research Council Bulletin* 150: 1–12.
95. Thamburaj, R., Goldak, J. A., and Wallace, W. 1979. The influence of chemical composition on post-weld heat treatment cracking in René 41, *SAMPE Quarterly*, 10: 6–12.
96. Carlton, J. B. and Prager, M. 1970. Variables influencing the strain-age cracking and mechanical properties of René 41 and related alloys, *Welding Research Council Bulletin* 150: 13–23.
97. Duvall, D. S. and Doyle, J. R. 1973. Repair of turbine blades and vanes, ASME publication 73-GT-44.
98. King, R. W., Hatala, R. W., and Hauser, H. A. 1970. Welding of superalloy turbine hardware, *Metals Engineering Quarterly*, 10: 55–58.

99. Flowers, G., Kelley, E., Grossklaus, W., Barber, J., Grubbs, G., Williams, L. 2000. U.S. Patent Number 6,084,196, issued July 4.
100. Adam, P. 1978. *Welding of high-strength gas turbine alloys*, *High Temperature Alloys for Gas Turbines*, London Applied Science Publishes, 737–768.
101. Arata, Y. *et al.* 1978. Fundamental studies on electron beam welding of heat-resistant superalloys for nuclear plants (Report 4), *Transaction of the Japan Welding Research Institute*, 7: 41–48.
102. D’Annessa, A. T. and Owens, J. S. 1973. Effects of furnace atmosphere on heat treatment cracking of René 41 weldments, *Welding Journal*, 52: 568s–575s.
103. Lepkowski, W. J., Monroe, R. E., and Rieppel, P. J. 1960. Studies on repair welding age-hardenable nickel-base alloys, *Welding Journal*, 39: 392s–400s.

# Oxide Dispersion Strengthened Alloys and Nickel Aluminides

The oxide dispersion strengthened alloys and nickel aluminides represent two specialty groups of Ni-base alloy that have been developed for demanding service environments, normally requiring good corrosion and creep resistance at elevated temperature. The oxide dispersion strengthened alloys are produced using a mechanical alloying process that uses a ball mill to mechanically mix the metal and oxide species. This mixture is then formed and heat-treated to develop the necessary mechanical properties. Nickel aluminides are based on either the NiAl or the Ni<sub>3</sub>Al intermetallic system. Both these intermetallic alloys are quite strong and considerably lighter than conventional Ni-base superalloys because of the high volume fraction of aluminum, but they have negligible ductility and toughness. Because of the desirable strength-to-weight ratio, both the ODS and nickel aluminide alloys are of great interest to the aerospace turbine engine industry. Not surprisingly, these alloys have some unique weldability issues as described in this chapter.

## 5.1 OXIDE DISPERSION STRENGTHENED ALLOYS

### 5.1.1 Physical and Mechanical Metallurgy

Ni-base oxide dispersion strengthened (ODS) alloys utilize a fine dispersion of insoluble oxide particles as their primary strengthening agent. Because the oxide particles are insoluble, these materials must be prepared with mechanical alloying techniques using a powder metallurgy route. The first step is to mix individual powders in a ball mill that consist of an oxide powder (typically yttria—Y<sub>2</sub>O<sub>3</sub>) along with powders of Ni, Cr, and a master alloy that contains additional elements. The oxide particles exhibit very fine particle diameters on the order of 25–50 nm (0.025–0.050 μm). During mixing within the grinding balls, repeated deformation, fracture, and cold welding occurs to produce

composite of metal and oxide powder particles with an oxide interparticle spacing on the order of  $\sim 0.5 \mu\text{m}$ . This first step of powder production is unique to the preparation of ODS alloys.

After the powders are produced, they can then be consolidated into various product forms using standard powder metallurgy techniques. A typical post-powder processing route consists of a hot isostatic pressure (HIP) operation for powder consolidation, followed by hot working into the final product shape. The final step includes a high temperature anneal that is intended to produce recrystallization and grain growth. The large grain size is preferred for high temperature creep resistance, and the grains usually form with a high aspect ratio aligned in the hot working direction. The optimal grain orientation is one in which the grains are oriented parallel to the maximum applied stress for the best high temperature strength.

The chemical compositions of several commercially available ODS alloys are provided in Table 5.1. The “MA” in the alloy designation indicates that these materials are “mechanically alloyed.” Although Alloy MA956 is a Fe based alloy, it is included in this discussion since the basic physical metallurgy principles and challenges associated with joining are similar to those of the Ni-base alloys. Alloy MA754 was the first ODS alloy produced on a commercial basis. Alloy MA758 is similar to MA754 except for higher Cr concentration for improved resistance to oxidation. The mechanical properties of these two alloys are similar. Several ODS alloys have been developed that exploit strengthening by solid solution hardening in addition to the presence of oxide particles and the  $\gamma'$  phase. Examples of this are included in Table 5.1 with the MA760 and MA6000 alloys that have Al and Ti in order to form the  $\gamma'$ - $\text{Ni}_3(\text{Al,Ti})$  precipitate and additions of W and Mo for solid-solution strengthening.

A representative microstructure of a Ni base ODS alloy is shown in Figure 5.1.(1) The light optical photomicrographs reveal the elongated grain structure that forms in the rolling direction, while the TEM photomicrograph shows the very fine dispersion of  $\text{Y}_2\text{O}_3$  particles. (The coarser particles with a diameter of  $\sim 0.25 \mu\text{m}$  are titanium carbo-nitrides.) The ODS alloys achieve strength levels at elevated temperatures that exceed those of the  $\gamma'$  and  $\gamma''$  strengthened Ni base superalloys.

The 1000 hour rupture strengths of two ODS Alloys (MA 754 and MA 6000) are compared to a wide range of Ni-base superalloys in Figure 5.2.(2)

**TABLE 5.1 Composition of Several Oxide Dispersion Strengthened Alloys (wt%).**

Alloy	Ni	Fe	Cr	Al	Ti	W	Mo	Ta	$\text{Y}_2\text{O}_3$	C	B	Zr
MA754	Bal	—	20	0.3	0.5	—	—	—	0.6	0.05	—	—
MA758	Bal	—	30	0.3	0.5	—	—	—	0.6	0.05	—	—
MA760	Bal	—	20	6.0	—	3.5	2.0	—	0.95	0.05	0.01	0.15
MA6000	Bal	—	15	4.5	2.5	4.0	2.0	2.0	1.1	0.05	0.01	0.15
MA956	—	Bal	20	4.5	0.5	—	—	—	0.5	0.05	—	—

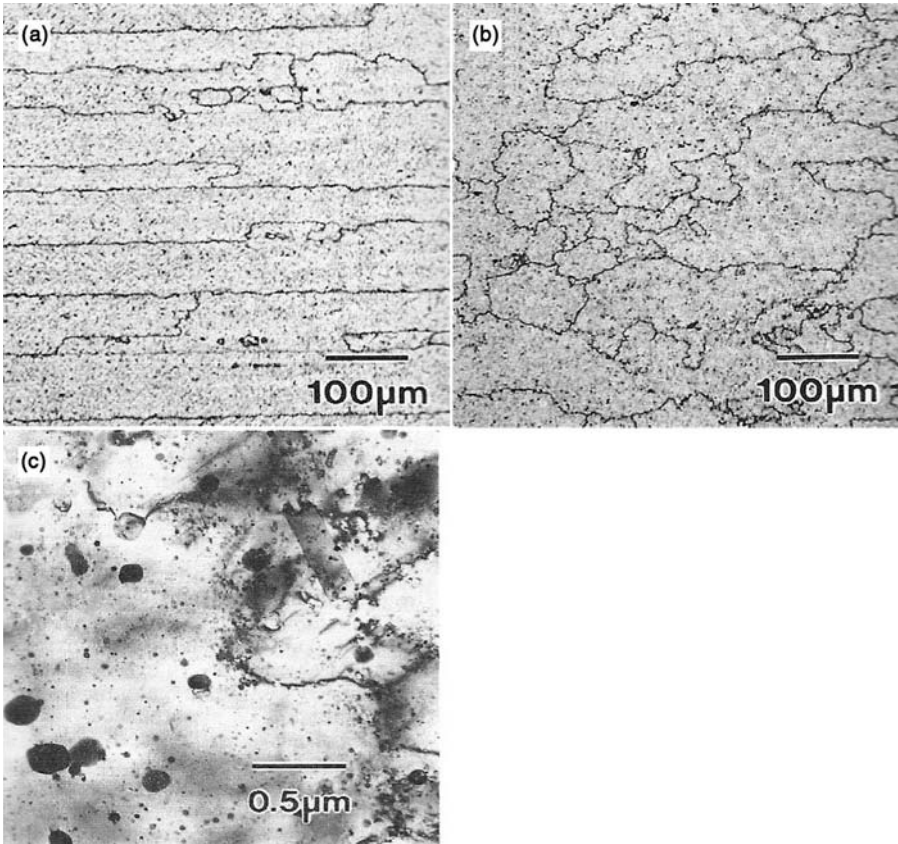


**Figure 5.1** Photomicrographs of an ODS alloy (MA754). a) Light optical photomicrograph taken along the rolling direction. b) Light optical photomicrograph taken transverse to the rolling direction. c) Transmission electron microscopy photomicrograph showing fine dispersion of  $Y_2O_3$  particles. (From deBarbadillo *et al.* [1]. Courtesy ASM International)

At lower operating temperatures, the Ni-base superalloys provide higher strength levels due to the presence of the  $\gamma'$  or  $\gamma''$  precipitate. However, as the temperature is increased, the  $\gamma'$  or  $\gamma''$  precipitates first begin to coarsen and, at higher temperatures, will eventually dissolve and result in a severe loss of strength. The insoluble oxides in the ODS alloys are essentially immune to coarsening and dissolution. The resistance to particle coarsening can be understood by recalling that the particle coarsening rate ( $dr/dt$ , Eqn. 4.2) is directly proportional to the solubility ( $C_o$ ) in the matrix. In a physical sense, this reflects the need for the solute element of interest to first be dissolved within the matrix before it is capable of diffusing through the matrix to cause coarsening. Since the oxide particles are insoluble in Ni, the coarsening process is effectively eliminated.

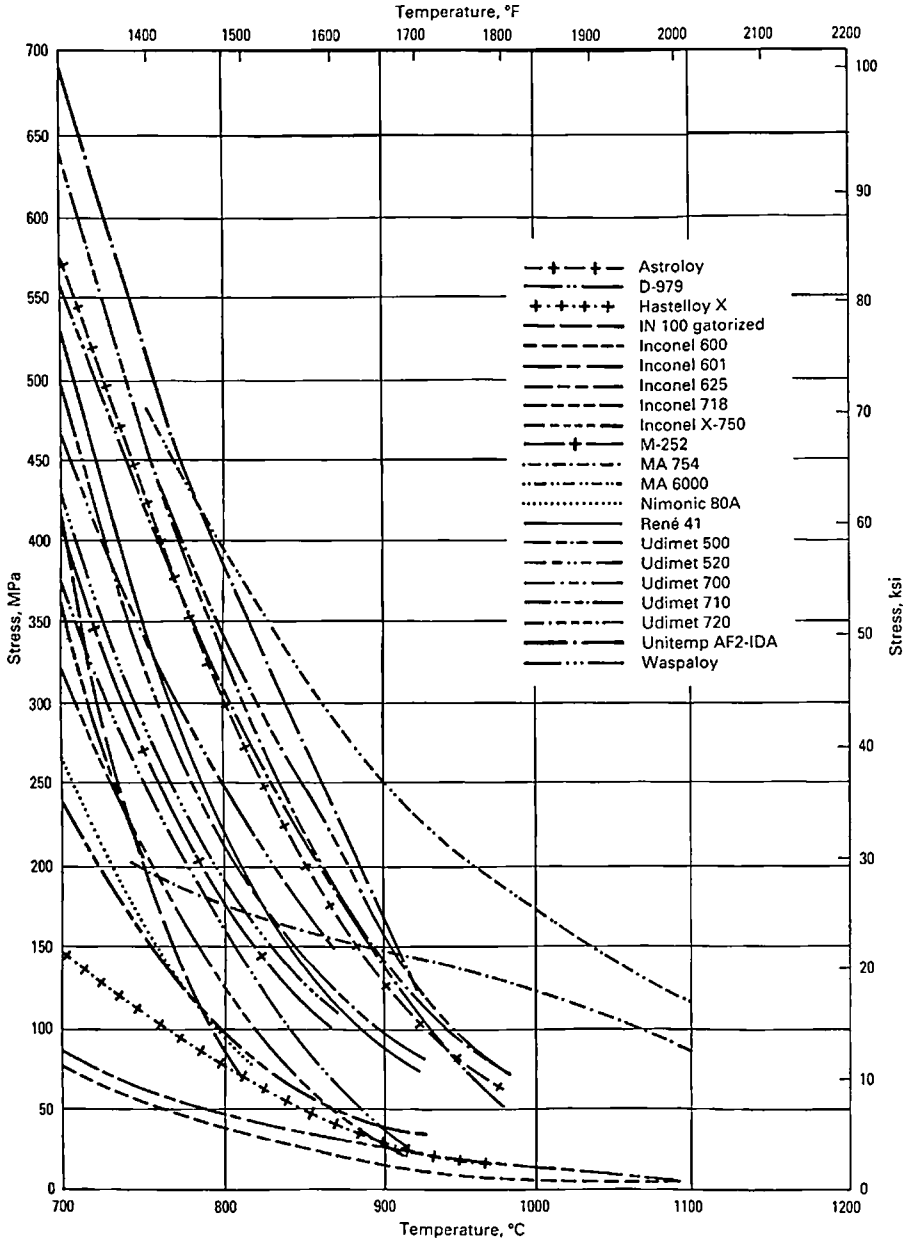


**Figure 5.2** Comparison of the 1,000 hour rupture strengths of ODS Alloys MA6000 and MA754 to other Ni-base superalloys. (From Stoloff [2]. Courtesy ASM International.)

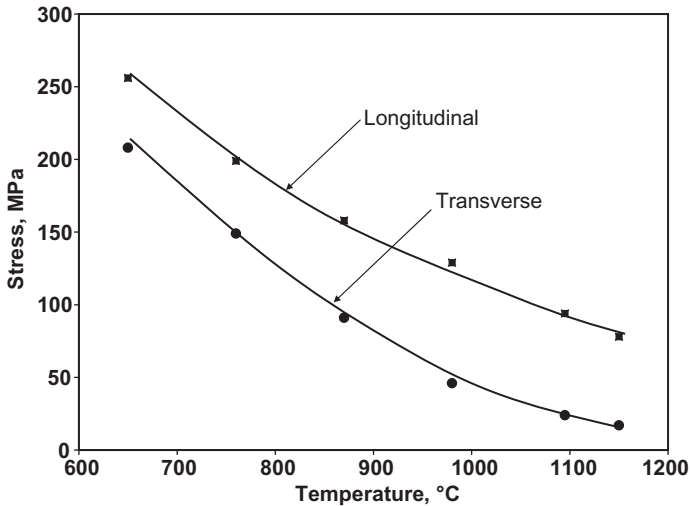


**Figure 5.3** 1000-hr stress-rupture data for Alloy MA754 in both the longitudinal and transverse direction. Microstructure in these orientations is shown in Figure 5.1. (From deBarbadillo *et al.* [1]. Courtesy ASM International)

These alloys exhibit excellent strength over the entire high temperature range as exhibited by the data for alloy MA6000 in Figure 5.2. The anisotropic nature of the grain structure needs to be accounted for when designing with ODS alloys, since the transverse properties are inferior to those in the rolling direction. An example of this is provided in Figure 5.3, which shows the stress required to cause rupture in 1000 hours in the longitudinal and transverse directions for Alloy MA754.(1)

### 5.1.2 Welding Metallurgy

It is virtually impossible to retain the creep properties in fusion welds of ODS alloys because the favorably oriented columnar grain morphology and fine oxide dispersion are lost in the fusion zone during melting and solidification. The oxide particles will agglomerate and typically float to the surface of the weld pool, while the fusion zone is liquid. As a result, both the number density and volume fraction of the particles decrease significantly, while the particle size increases. In this condition, the particles lose most of their ability to improve high temperature strength. Any strengthening component due to the favorably-oriented columnar grains is also severely impacted because the weld metal grains will grow essentially perpendicular to the fusion boundary during solidification. Equiaxed grains can also form near the centerline of the weld where the level of constitutional supercooling is the highest and impart additional reductions in strength. As a result of these microstructural changes,

fusion welds in ODS alloys can exhibit creep properties that are typically only 10 to 50% of the base metal properties.(3,4)

There are several steps that can be taken to provide modest improvements in performance when fusion welding must be used to join ODS alloys.(4) A postweld recrystallization and grain growth treatment can be conducted to increase the grain size in the fusion zone, but this is typically only effective if a cold working step is used after welding and before postweld heat treating. This approach is most effective when the base metal is welded in the unrecrystallized condition. Lap joints that are produced by resistance welding can provide a more favorable grain orientation relative to the maximum applied stress. If possible, the fusion zone in arc welds should be placed in lower stress and temperature regions.

High energy density processes such as electron and laser beam welding typically provide better weld properties than the arc processes.(4,5) With the high energy density processes, the time spent in the solidification temperature range is reduced while the solidification rate is increased. As a result, the detrimental impact on oxide dispersion is not as severe compared to the arc processes. An example of this is shown in Figure 5.4, which compares the oxide sizes of GTA and laser welds made on Alloy MA754.(5) The reduced heat input in the laser weld leads to a finer grain size and reduced coalescence of the oxide particles. For the laser weld shown, the  $Y_2O_3$  oxide particles were on the order of 0.1 to 0.4 $\mu m$  in diameter. While this is still larger than those in the unaffected base metal ( $\sim 0.05\mu m$ ), it is smaller than those observed in the GTA weld, which were  $\sim 3\mu m$  in diameter. The volume fraction of oxides in the laser weld was also higher than in the GTA weld, which can be attributed to reduced agglomeration and subsequent flotation of the oxides to the surface associated with a shorter solidification time.

Table 5.2 compares the room temperature, short term mechanical properties of the base metal, GTA weld, and laser weld. The laser weld exhibits only a mild reduction in mechanical properties (e.g., 95% of the base metal yield strength), while the strength and hardness of the GTA weld are significantly reduced (55% of base metal yield strength). These differences are attributed to the smaller grains and higher fraction of oxide particles in the laser weld. Similar retention of the short term room temperature properties has been observed in electron beam welds of Alloy MA956, in which ultimate strength values  $\sim 90\%$  of the base metal were observed.(3) It should be noted, however, that similar performance would generally not be expected under conditions where stress rupture properties are important. Under these conditions, the fine fusion zone grain size is detrimental to performance, and the coarsened oxides would induce a more significant loss in strength. As a result, the high temperature properties of laser and electron beam welds are typically only on the order of  $\sim 50\%$  of the base metal properties.(3,4) Slight improvements may be possible in butt welds by using inclined beam angles to produce welds in which their centerline is not perpendicular to the surface of the plate.(6) This can help to reduce the applied stress acting on the fusion boundary.

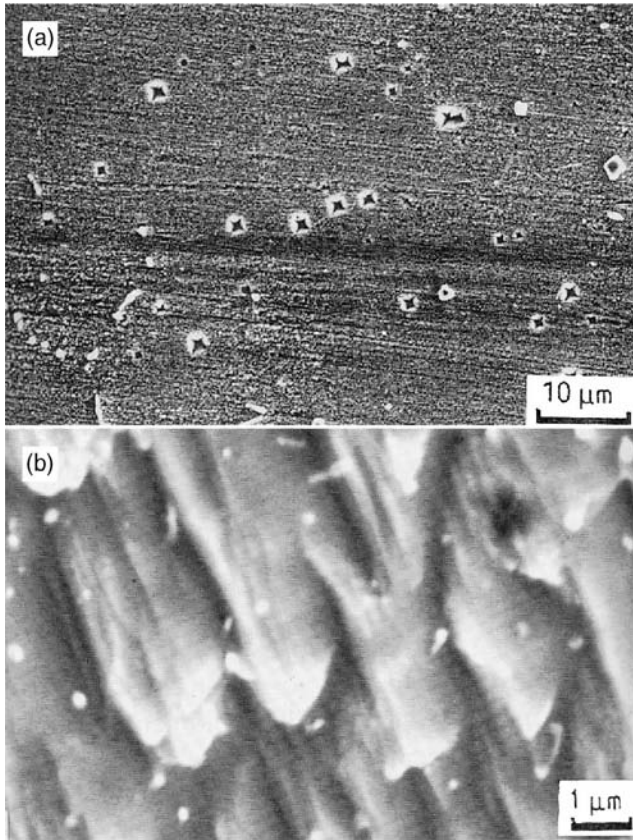


**Figure 5.4** Comparison of GTA weld (a) and laser weld (b) in Alloy MA754. Light optical photomicrograph (a), SEM photomicrograph (b). (From Molian *et al.* [5])

**TABLE 5.2 Mechanical Properties of Base Metal, GTA Weld, and Laser Weld in Alloy MA754. (From Molian *et al.* [5])**

	Base Metal	Laser Weld	GTA Weld
Yield Strength, MPa (ksi)	656 (95)	620 (90)	360 (52)
Ultimate Strength, MPa (ksi)	825 (120)	815 (118)	540 (78)
Hardness, DPH	335	300	185
Elongation, %	19	22	19
Reduction in Area, %	16	18	16

Brazing can be used to join ODS alloys with some success. The braze microstructure will not exhibit the grain morphology and oxide dispersion responsible for the base metal properties. Thus, the strength of the joint must be obtained through careful selection of the brazing alloy.

Kelly investigated brazing of Alloy MA754 using three commercial brazing alloys: AM788, TD6, and B93.(7) B93 and TD6 are Ni-base braze alloys, while the AM788 is a Co-base alloy. The B93 and AM788 alloys contain B as a melting point depressant. The braze microstructures were found to consist of an austenitic matrix with various amounts of an unidentified second phase. Joints made with the boron-containing alloys contained some dispersoids in the braze joint and was attributed to diffusion of B into the ODS alloy that promoted liquation and subsequent release of oxide particles from the base metal into the braze alloy. The B-free TD6 alloy required a relatively high brazing temperature of 1315°C (2400°F). This was thought to be responsible for porosity observed in both the base metal near the joint as well as the braze joint, although the mechanism associated with this was not discussed.

The high brazing temperature required for this alloy may also present a challenge since it is above the limit of many commercial furnaces. Results from stress rupture tests indicated that joints made with the B93 and AM788 alloys exhibited a 1000 hour rupture strength of 97 MPa (14 ksi) at 980°C (1800°F). Joints made with the AM788 alloy exhibited a 1000 hour rupture strength of 35 MPa (5 ksi) at 1093°C (2000°F). These values are between the rupture strengths established for the base metal in the transverse and longitudinal directions (see Figure 5.3). Extended tests are probably required to confirm that this behavior is maintained at the longer exposure times representative of actual service conditions.

Transient liquid phase (TLP) bonding has also been evaluated as a joining process for ODS alloys. TLP is essentially a brazing process where the molten braze material reacts with the base material to form a solid joint. Research conducted to date has shown that the final grain morphology of the joint will depend on the bonding time, interlayer composition, and starting microstructure (i.e., recrystallized versus unrecrystallized).(8,9) Although no bulk melting occurs with this process, melting is required within the interlayer alloy and locally within the base metal at the base metal/interlayer interface. The localized melting of the base metal occurs when it dissolves the interlayer that contains melting point depressants. This base metal dissolution leads to agglomeration of the oxide particles and a concomitant loss of joint strength.(8) Stress rupture testing of Alloys MA956 and MA754 joined with the TLP process have shown that the joint properties can not match that of the base metal in the transverse direction.(10,11)

Solid-state joining processes have also been investigated for potential improvements in the weld properties of ODS alloys. Kang *et al.*(12) and Shinozaki *et al.*(13) investigated the microstructure and mechanical properties of friction welds produced in Alloy MA956. As shown in Figures 5.5 and 5.6, the weld exhibited three microstructural regions. Region III was the unaffected

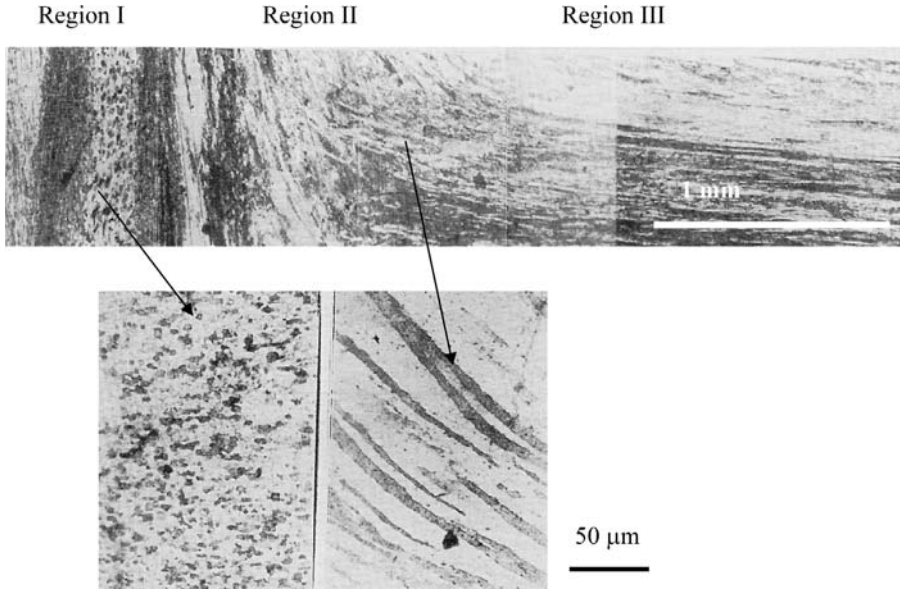


**Figure 5.5** Light optical photomicrographs of friction welded Alloy MA956 showing three different microstructural regions of the weld. (From Shinozaki *et al.* [13]. Courtesy the American Welding Society)

base metal that exhibited a fine oxide dispersion and grains with a high aspect ratio that were elongated in the rolling direction. The grains in Region II were plastically deformed during the welding cycle and, as a result, became increasingly reoriented parallel to the plane of the joint as the weld interface was approached. Region I exists at the weld interface and consists of equiaxed grains due to the dynamic recrystallization that occurs with severe plastic deformation at elevated temperature. The oxide particles in Regions I and II are irregularly shaped and have coarsened relative to the base metal (Figure 5.6). This coarsening has been attributed to a mechanism in which the smaller  $Y_2O_3$  particles agglomerate with the larger alumina ( $Al_2O_3$ ) and titanium carbonitride ( $Ti(C,N)$ ) particles under the influence of combined heat and plastic deformation. Short term tensile tests conducted at room temperature and  $650^\circ C$  ( $1200^\circ F$ ) showed that the weld properties were very similar to that of the base metal, and fracture generally occurred away from the weld interface.

The creep-rupture properties of friction welds in Alloy MA956 made at two different forging pressures are compared to the base metal properties in the longitudinal and transverse directions in Figure 5.7. The creep rupture properties of the welds are only about 10% of the base metal properties. Depending on the forging pressure, fracture occurred in Region I, II, or at the boundary between these two regions. Premature fracture at these locations was associated with the corresponding microstructural changes shown in Figure 5.5 and 5.6. In Region I, premature failure occurs due to the fine recrystallized grains

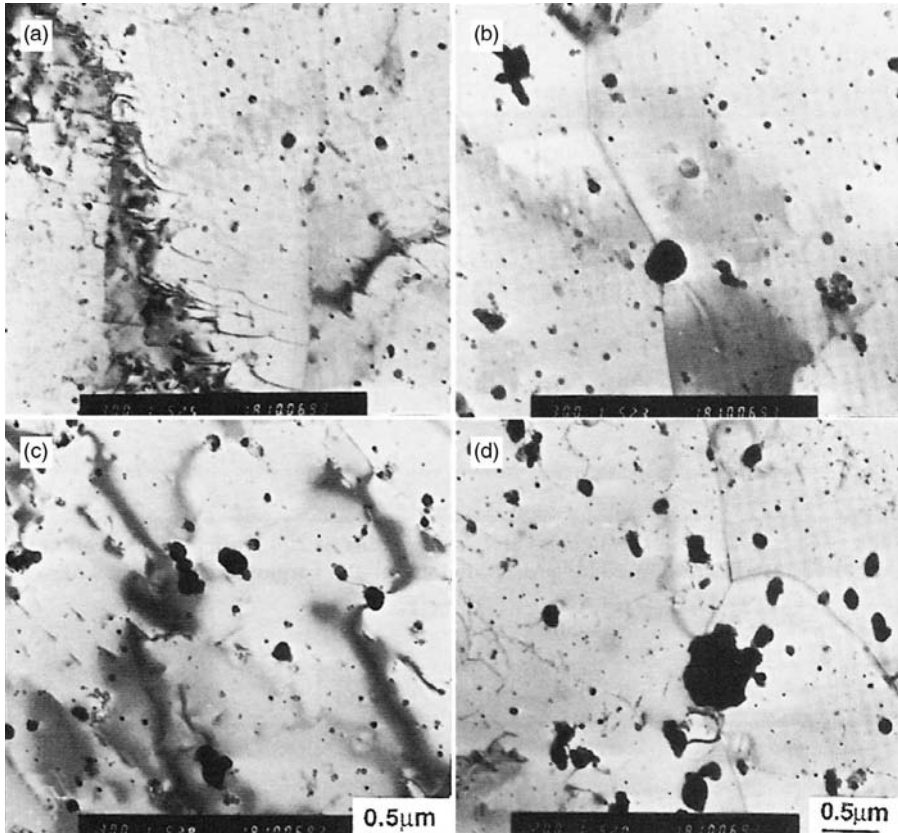


**Figure 5.6** TEM photomicrographs of three regions observed in friction welded Alloy MA956. a) Region III, b) Region II, c) Region I at joint centerline, d) Region I at the boundary between Regions I and II. (From Shinozaki *et al.* [13]. Courtesy the American Welding Society)

and large agglomerated particles. The reduced properties in Region II are associated with the large oxide particles and unfavorable grain orientation in which many of the grain boundaries are aligned at  $45^\circ$  to the tensile axis where the resolved shear stress is a maximum. This orientation can accelerate grain boundary sliding during high temperature deformation. It is worth noting that Moore *et al.* (14) observed that the creep rupture strengths of friction welds in Alloy TD-Ni were also less than 10% of the base metal properties.

Moore and Glasgow investigated the potential for diffusion welding of Alloy MA6000. (15) Samples were diffusion bonded for 1.25 hours at temperatures in the range from 1000-to-1200°C (1830-to-2190°F), and the influence of the initial base metal condition (recrystallized or unrecrystallized) was examined. Postweld heat treatments were conducted with the following stepped treatment schedule: 1250°C/one hour, followed by 955°C/two hours,

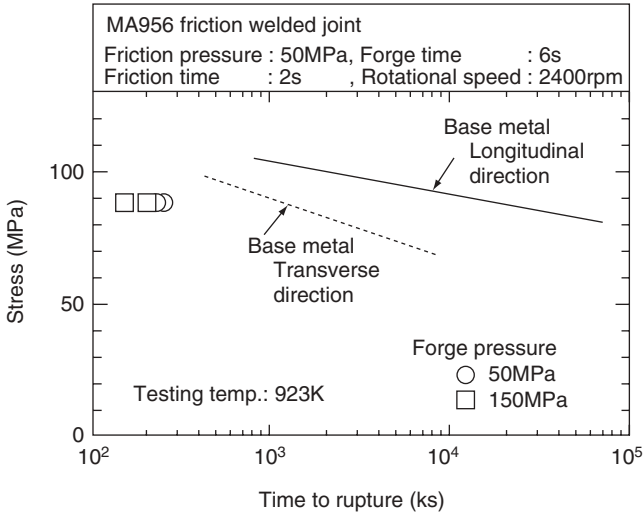


**Figure 5.7** Creep-rupture properties of welds made at two different forging pressures compared to base metal properties in the longitudinal and transverse directions for Alloy MA956. (From Shinozaki *et al.* [13]. Courtesy the American Welding Society)

followed by 845°C/twenty-four hours. Air cooling was conducted between each step. Attempts to produce welds in which one or both of the base metals on either side of the weld were in the recrystallized condition were generally unsuccessful. In the recrystallized condition, the high base metal strength at the elevated diffusion bonding temperature (due to the large grain size) prevented the proper deformation needed at the weld interface for bonding. An attempt was made to use higher compressive stresses during welding in order to produce deformation at the interface, but this was not successful because it caused cracking in the base metal.

Adequate deformation during diffusion welding was possible and successful welds could be made when both members were in the unrecrystallized condition. Stress rupture properties for these welds at 1000°C (1830°F) are shown in Figure 5.8. Results for the base metal at 982° and 1038°C (1800° and 1900°F) are also shown for reference. Joints welded with one base metal in the unrecrystallized condition were inferior to those in which both base metals were unrecrystallized. However, even these welds exhibit properties that are well below those of the base metal. Premature failure was generally attributed to some small grains that existed in the weld interface region due to inadequate grain growth during the post weld heat treatment. Possible changes in the oxide morphology and their potential impact on properties were not considered. Nevertheless, these results indicate that further improvements may be possible with optimized postweld heat treatment schedules that produce a more favorable grain morphology near the weld interface. Investigations on the effect of the oxide dispersion near the interface are also warranted, since

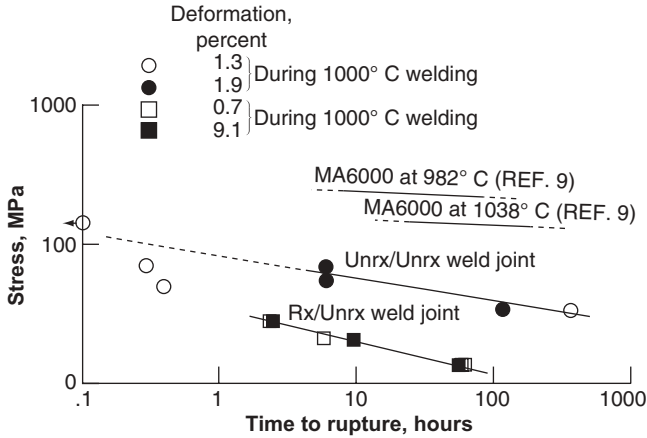


**Figure 5.8** Stress rupture properties at 1000°C (1830°F) for diffusion welds produced in Alloy MA6000. Results for the base metal at 982 and 1038°C (1800 and 1900°F) are also shown for reference. (From Moore and Glasgow [15]. Courtesy the American Welding Society)

an improvement in this dispersion would undoubtedly improve stress-rupture properties.

More recently, Nishimoto *et al.* (16) investigated the use of the pulsed electric current sintering (PECS) technique for joining of ODS Alloys MA754 and MA956. With this process, ODS powders that match the base metal composition are placed between the mating surfaces and supported by a carbon die. The joint is then heated in a vacuum under pressure while a pulsed direct current is applied. The pulsed current creates a spark discharge between the powders that removes surface oxides that may otherwise hinder diffusion. Heating of the powders occurs by both resistive heating from the applied current and heat conduction through the die. The addition of current increases the powder consolidation rate and permits densification at lower temperatures and shorter times.

Welds were produced with the PECS process under various temperatures, pressures, hold times, and powder sizes. The densification rate of powders within the bond increased significantly with increasing pressure and temperature and, to a lesser extent, with decreasing particles size. Under the optimum combination of temperature and pressure, fully dense welds could be produced in six minutes or less. The time required for complete densification was longer in Alloy MA754 (Ni base) compared to MA956 (Fe based). Although the reasons for this were not discussed, this is probably associated with the different diffusion rates between the alloys, since substitutional diffusion rates in ferrous alloys are typically about two orders of magnitude higher than those in Ni-base alloys. Analysis of the densification kinetics showed that consolida-

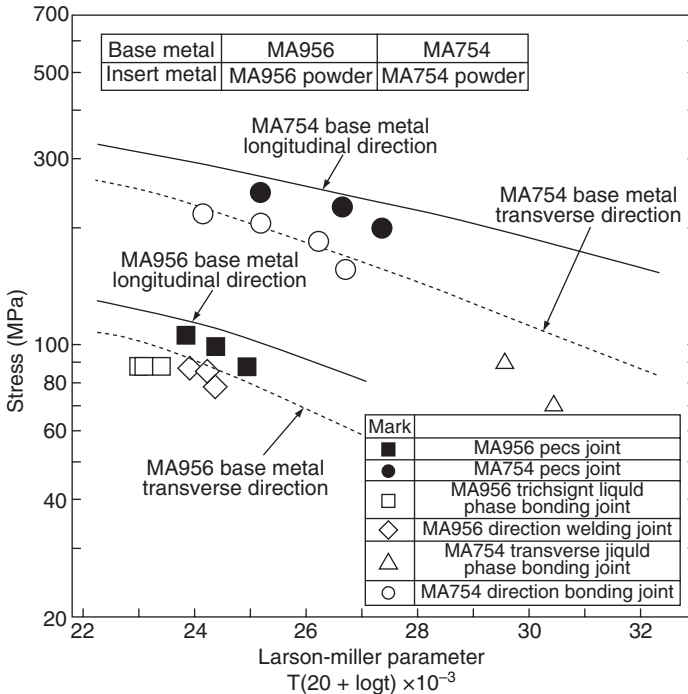


**Figure 5.9** Creep rupture strength of welds on Alloys MA754 and MA956 produced with the pulsed electric current sintering (PECS) process compared to welds made on the same alloys with other joining processes. Rupture strengths of the base metals are also shown. (From Nishimoto *et al.* [16])

tion to ~95-to-99% relative density is controlled by plastic flow of the particles, while the remaining stages of consolidation are controlled by volume diffusion.

The creep rupture strength of welds produced with the PECS process relative to those produced with other processes such as transient liquid phase bonding, friction welding, and diffusion bonding is shown in Figure 5.9. The rupture strengths for the base metals in the longitudinal and transverse directions are also shown. The rupture strengths of the PECS welds are markedly improved over the other processes and are close to the base metal properties in the longitudinal direction. Microstructural analysis of the welds demonstrated that the size and interparticle spacing of the oxide particles in the welds were similar to that of the base metal. This confirmed that particle agglomeration did not occur during welding and led to the good stress-rupture properties. This process appears to be quite promising for joining of ODS alloys in which joint efficiency is critical.

### 5.1.3 Summary of the Weldability of ODS Alloys

Joining of ODS alloys presents a significant challenge due to the difficulty in maintaining the favorable oxide distribution and high aspect ratio of the grains. Fusion welding processes are particularly detrimental to weld metal properties due to oxide agglomeration/flotation and loss of the favorable grain morphology. High energy density fusion welding processes (such as electron beam welding) can provide some improvement due to the shorter residence time in the weld pool, but the weld properties are still below those of the base metal. Similarly, various solid-state and brazing processes have been shown to provide only limited improvements relative to fusion welding. Of the processes considered to date, the PECS process appears to provide the best opportunity for preserving the weld metal properties, and further efforts are needed in this area to make this process commercially viable.

## 5.2 NICKEL ALUMINIDE ALLOYS

Nickel aluminides have been the topic of considerable interest since the 1970s due to their unusual elevated temperature properties, including both high strength and good corrosion resistance. Considerable research has been conducted in an effort to improve the ductility and toughness of these alloys by a combination of composition and microstructure optimization. The processing of these materials is critical to achieving acceptable mechanical properties and, not surprisingly, the weldability of these alloys is a challenging issue.

### 5.2.1 Physical and Mechanical Metallurgy

The nickel aluminum phase diagram is shown in Figure 5.10.(17) Ni-aluminide alloys are designed around either the  $\text{Ni}_3\text{Al}$  or NiAl intermetallic system.  $\text{Ni}_3\text{Al}$  represents the  $\gamma'$  strengthening precipitate that was discussed in Chapter 4. As shown in Figure 5.10, this phase forms over a relatively narrow composition range and has a melting temperature of  $1395^\circ\text{C}$  ( $2540^\circ\text{F}$ ). This alloy exhibits the unusual property of increasing strength versus temperature from room temperature to  $700^\circ\text{C}$  ( $1290^\circ\text{F}$  or  $973\text{K}$ ), as shown in Figure 5.11.(18) The polycrystalline form of  $\text{Ni}_3\text{Al}$  has been found to be inherently brittle, suffering intergranular fracture with low ductility. Considerable work has focused on the addition of “ductilizing” elements that oppose grain boundary fracture. These elements include boron, zirconium, iron, and chromium. It has been proposed that grain boundary embrittlement is associated with oxygen segregation and the presence of moisture has a significant negative effect on the ductility of the  $\text{Ni}_3\text{Al}$  alloys.(19) Alloying additions that tie up oxygen or processing conditions that preclude moisture have been shown to reduce the tendency for grain boundary fracture.

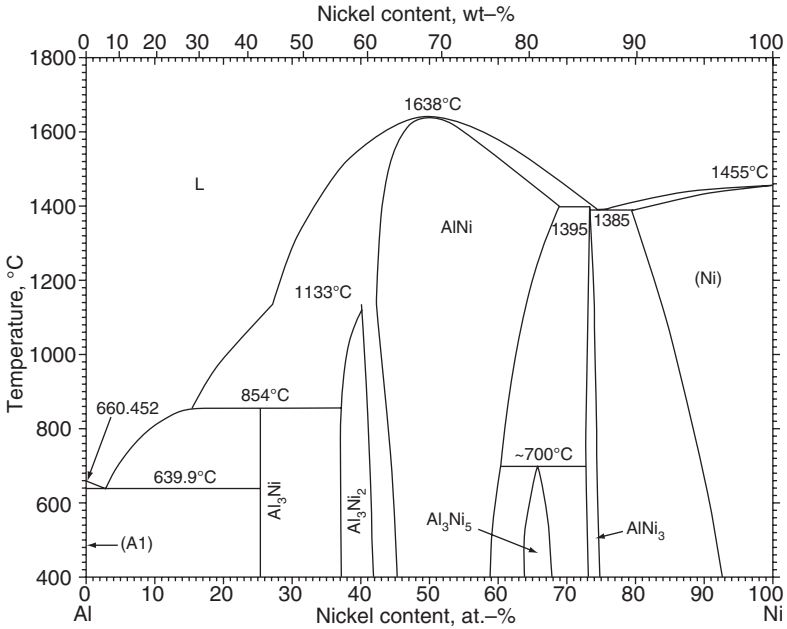


Figure 5.10 Ni-Al phase diagram. (From [17], Courtesy ASM International)

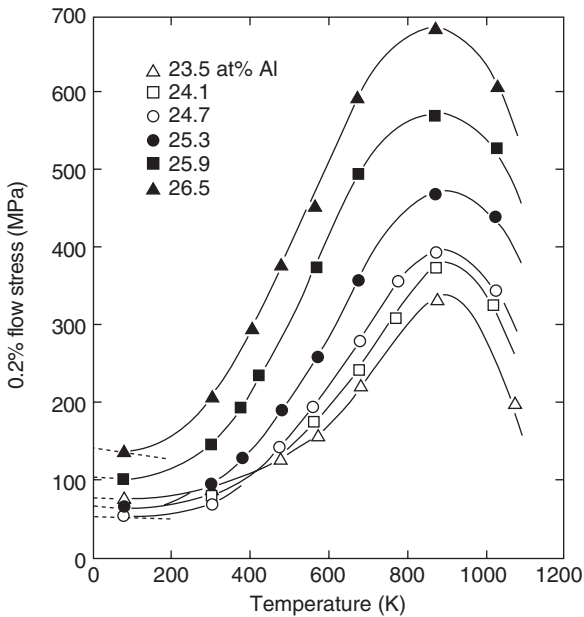


Figure 5.11 Effect of Al content on the flow stress of Ni<sub>3</sub>Al alloys as a function of temperature. (From Noguchi *et al.* [18])

**TABLE 5.3 Nominal Composition (wt%) of Several Ni<sub>3</sub>Al Alloys.**

Alloy	Al	Fe	Cr	Mn	Zr	Ti	Mo	B
Designation								
IC14	10	10	—	1.0	—	0.5	—	0.05
IC25	10	10	—	0.5	—	0.5	—	0.05
IC103	10	10	—	0.5	—	0.5	—	0.02
IC50	10	—	—	—	0.5	—	—	0.02
IC218	8	—	8	—	0.8	—	—	0.02
IC221	8	—	8	—	1.7	—	1.5	0.02
IC396(306)	8	—	8	—	0.8	—	3.0	0.01

**TABLE 5.4 Function of Alloying Elements Added to Ni<sub>3</sub>Al Alloys. (From Deevi *et al.* [21])**

Element	Function
Cr	Reduces oxygen embrittlement at elevated temperature
Zr	Provides high temperature strength Reduces casting porosity by formation of Ni <sub>5</sub> Zr eutectic phase
Hf	Provides high temperature strength Possible oxygen “getter”
Mo	Provides strength at high and low temperature
B	Improves grain boundary cohesive strength

The nominal compositions of a number of Ni<sub>3</sub>Al alloys whose welding behavior have been reported in the literature are provided in Table 5.3. Most of the alloys reported here were developed at the Oak Ridge National Laboratory and their development history has been reported in several review papers.(20–22) The effect of alloying additions on the properties or performance of the Ni<sub>3</sub>Al intermetallics was summarized by Deevi *et al.*(21) and is provided in Table 5.4. The yield strength, ultimate tensile strength, and elongation of a number of these alloys as a function of temperature are shown in Figure 5.12. Note that all these alloys start to lose appreciable strength above 800 °C (1470 °F) and show a ductility minimum between 600° and 800 °C.

The NiAl alloys exist over a much wider range of composition (see Figure 5.10) and exhibit the highest melting temperature (1638 °C) in the nickel-aluminum system. NiAl has lower density, higher elastic modulus, and higher thermal conductivity than Ni<sub>3</sub>Al, and also possesses excellent oxidation resistance. Thus, NiAl would appear to be an even more attractive alternative than Ni<sub>3</sub>Al to replace conventional Ni-base superalloys. Unfortunately, these alloys have extremely poor ductility and creep resistance and are extremely difficult to process. This is demonstrated by the relationship between tensile ductility and grain size at 400 °C (750 °F), as shown in Figure 5.13.(23) Because of these limitations, the use of alloys based on the NiAl system is severely restricted,

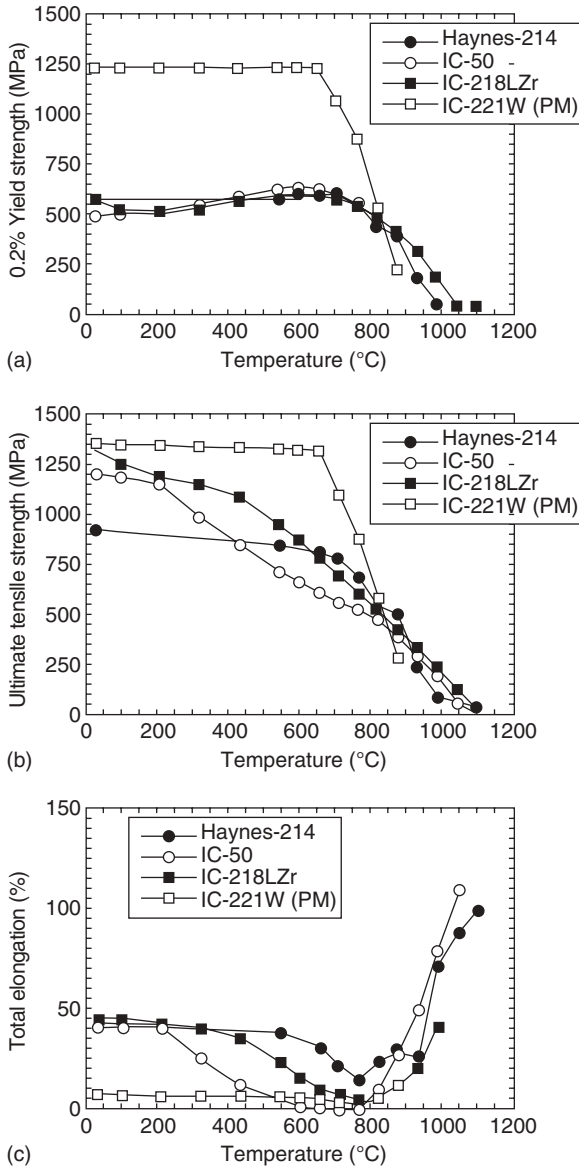


**Figure 5.12** A comparison of a) yield strength, b) tensile strength, and c) elongation as a function of temperature for wrought alloys IC50 and IC218Zr and powder metallurgy (PM) alloy IC221W. The Co-base alloy Haynes 214 is provided for comparison. (From Deevi *et al.* [21])

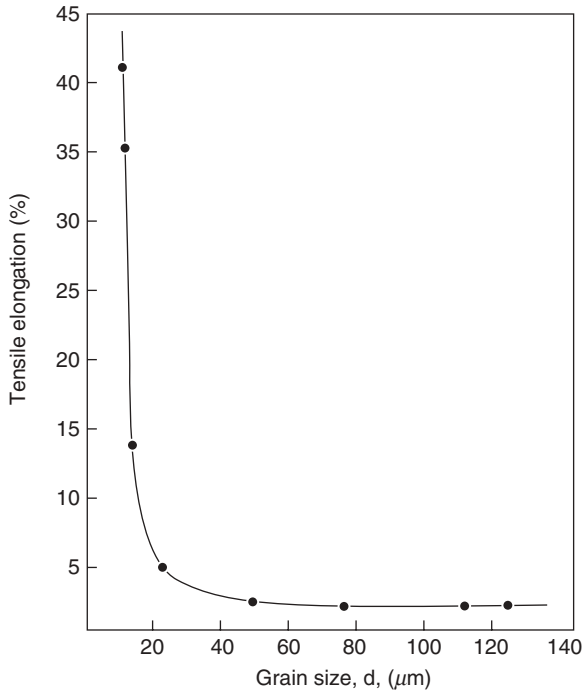


**Figure 5.13** Influence of grain size on the tensile ductility of NiAl at 400°C. (From Schulson and Barker [23])

particularly where thermo-mechanical processing is required for fabrication. A number of excellent reviews of the physical and mechanical metallurgy of the nickel-aluminides are available in the literature.(24–26)

## 5.2.2 Weldability of the Ni-Aluminides

**5.2.2.1 Elevated Temperature Cracking** A major challenge in the implementation of Ni-aluminide alloys has been their weldability. Because of their limited ductility, the thermal stresses associated with fusion welding can lead to cracking in and around the weld. In addition, these alloys are susceptible to weld solidification cracking and HAZ liquation cracking. David *et al.* (27) reported severe cracking in the fusion zone and HAZ of the boron-containing IC-14 and IC-25 alloys during autogenous gas tungsten arc (GTA) welding. They did not determine whether this was “hot” cracking in which grain boundary liquid films lead to failure, or a form of elevated temperature, solid-state grain boundary cracking. Crack-free welds in these alloys were produced using electron beam (EB) welding over a narrow range of travel speeds and electron beam focus conditions, as shown in Figure 5.14. In order to determine the effect of boron on cracking susceptibility, a series of EB welds were made on

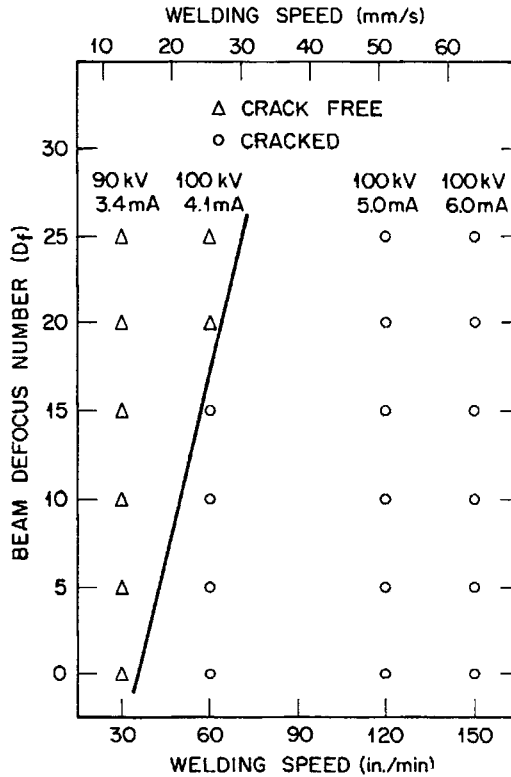


**Figure 5.14** Cracking in electron beam welds in alloy IC25 as a function of welding speed and beam defocus conditions. (From David *et al.* [27]. Courtesy the American Welding Society)

a Ni-12.7Al alloy that had boron levels ranging from 0 to 1000 ppm. The results of these experiments (Figure 5.15) revealed that the boron-free alloy was very crack susceptible, but that susceptibility dropped as boron increased to 250 ppm. Cracking then increased as the boron level was increased to 500 and 1000 ppm. Although the authors do not speculate on the mechanism, it would appear from the cracking behavior that additions of boron up to 250 ppm helps suppress solid-state, grain boundary fracture, but at higher levels boron can promote grain boundary liquation. Since the alloys investigated were simple Ni-Al-B ternaries, the effect of other alloying additions on the boron effect was not determined.

Schulson (28) and Chen (29) related cracking in the HAZ to both grain size and boron content. Reducing the base metal grain size reduces the stress concentration at individual grain boundaries while boron increases grain boundary strength. For example, maintaining grain size below about 20  $\mu\text{m}$  was

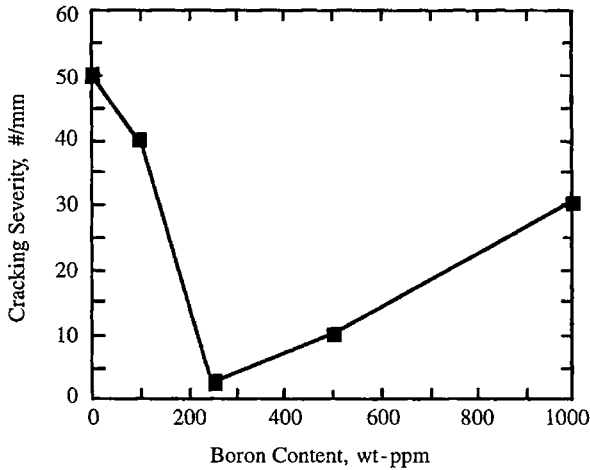


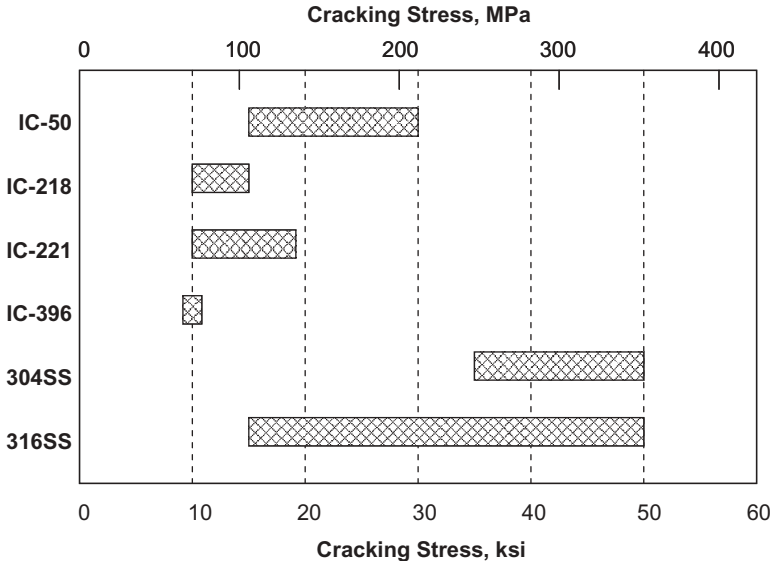
**Figure 5.15** Effect of B content on cracking of electron beam welds in  $\text{Ni}_3\text{Al}$  alloys. (From David *et al.* [27]. Courtesy the American Welding Society)

found to result in crack-free laser welds in alloys containing 200–500 ppm boron.

Goodwin and David (30) used the Sigmajig test to study the weld solidification cracking susceptibility of a number of  $\text{Ni}_3\text{Al}$  alloys containing additions of Cr, Zr, Mo, and B. The Sigmajig test determines the applied stress required to promote solidification cracking in the material, where lower stress to initiate cracking is associated with higher cracking susceptibility. Their results are shown in Figure 5.16 and compared to cracking susceptibility of two austenitic stainless steels.

In general, the solidification cracking resistance of these alloys is quite low. The addition of the “ductilizing” elements Cr and Zr (added to improve thermo-mechanical processing of the base metal) appears to increase weld solidification cracking susceptibility. Santella and Feng (31) showed that the addition of Zr promotes the formation of the  $\text{Ni-Ni}_5\text{Zr}$  eutectic constituent and that additions of 5 wt% Zr results in over 20 vol% of the eutectic constituent. According to Santella and Sikka (32) the threshold stress for cracking in the Sigmajig test increases with additions of Zr up to about 4.5 wt% (see Figure 5.17) but they were unable to explain this beneficial effect or the fact that further Zr additions above 4.5 wt% resulted in higher cracking susceptibility. This is contradictory to the “eutectic healing” phenomenon that is common in other alloy systems.

**5.2.2.2 Hot Ductility Behavior** Because weld cracking in  $\text{Ni}_3\text{Al}$  alloys often occurs in the HAZ, the hot ductility behavior of these alloys has been evaluated to determine the relationship between ductility and temperature. (33,34) Santella and David (33) studied the hot ductility behavior of the IC-25 alloy with 500 ppm boron and the IC-103 alloy with 200 ppm boron, as



Alloy	Ni	Al	Cr	Zr	Mo	B
IC-50	Bal	11.3	-	0.6	-	0.02
IC-218	Bal	8.5	7.8	0.8	-	0.02
IC-221	Bal	8.5	7.8	1.7	-	0.02
IC-396	Bal	8.0	7.8	0.8	3.0	0.01

**Figure 5.16** Weld solidification cracking susceptibility of a number of Ni<sub>3</sub>Al alloys containing additions of Cr, Zr, Mo, and B using the Sigmajig test. (From Goodwin and David [30])

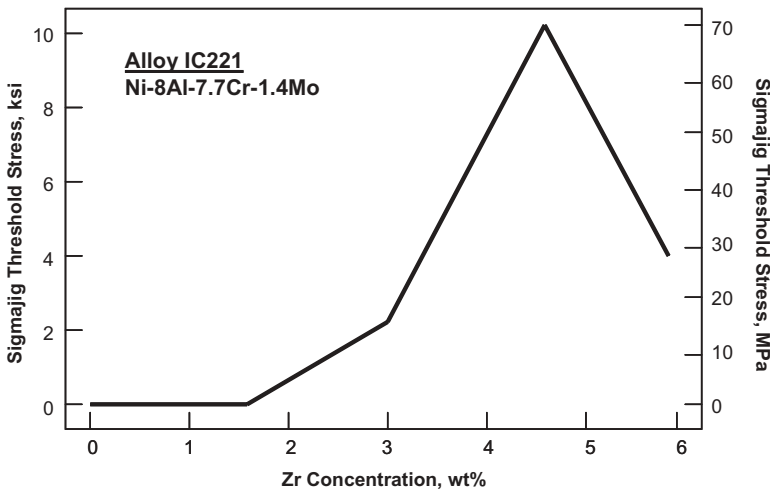


**Figure 5.17** Effect of Zr concentration on the solidification cracking susceptibility of a Ni-8Al-7.7Cr-1.4Mo alloy. (From Santella and Sikka [32]. Courtesy the American Welding Society)

shown in Figure 5.18. The on-heating hot ductility for both alloys showed a drop in ductility above 700°C. The lower boron alloy showed a recovery in on-heating ductility above 1100°C (2010°F). When the materials were heated to a peak temperature of 1325°C (2415°F) and then tested on-cooling, the elevated temperature ductility peak disappeared for the IC-103 alloy and both exhibited very low ductility until cooled below 800°C. This low on-cooling ductility correlates with the high susceptibility for HAZ cracking in the IC-25 alloy, but does not explain why the IC-103 alloy shows better resistance to HAZ cracking during EB welding.

The hot ductility behavior of the Ni<sub>3</sub>Al alloys was also found to be influenced by grain size. Edwards *et al.*(33) found that reducing the grain size of a powder metallurgy version of IC-50 resulted in an increase in hot ductility above 1000°C (1830°F), as shown in Figure 5.19. These were on-heating hot ductility tests that simulated the heating portion of the HAZ of an electron beam weld. This improvement in hot ductility was associated with a reduction of slip path length and the introduction of antiphase domain (APD) structure. Introduction of high fractions of APD structure by heat treatment were found to provide significant improvement in the hot ductility of this alloy.

**5.2.2.3 Brazing** Because of the severe cracking problems associated with fusion welding of the nickel-aluminide alloys, a number of studies have investigated the use of brazing to join these materials. In particular, the NiAl alloys have been the target of many of these studies because of their low ductility and toughness which makes fusion welding of these alloys virtually impossible. Gale *et al.*(35,36) and Orel *et al.*(37) have used transient liquid phase (TLP) bonding (also known as diffusion brazing) to join NiAl to itself and other Ni-base alloys. Using this process, the brazing alloy melts and then undergoes isothermal solidification due to diffusion of the substrate material into the braze joint. In one study, they used a pure copper braze material to join NiAl to a Ni-base superalloy (MM-247).(31) With this combination, diffusion of Ni into the molten copper at the brazing temperature (1150°C/12 hours) resulted in isothermal solidification within 20 minutes. These bonds had good mechanical properties as evidenced by shear testing that resulted in failure in the NiAl. Ni-Si-B braze alloys have also been used to join NiAl.(32) Brazing was conducted at both 1065°C (1950°F) and 1150°C (2100°F) with a Ni-4.5Si-3.2B braze alloy (AWS BNi-3). Again, holding at these temperatures resulted in isothermal solidification of the braze joint primarily due to boron diffusion into the NiAl substrate. Diffusion of Al into the braze joint resulted in the formation of Ni<sub>3</sub>Al and boride formation is possible (Ni<sub>3</sub>B and M<sub>23</sub>B<sub>6</sub>). No mechanical properties were reported for these joints.

### 5.2.3 Summary of the Weldability of Nickel Aluminide Alloys

Ni-aluminide alloys are extremely difficult to weld under almost all circumstances. Fusion welding of the NiAl alloys is virtually impossible due to their

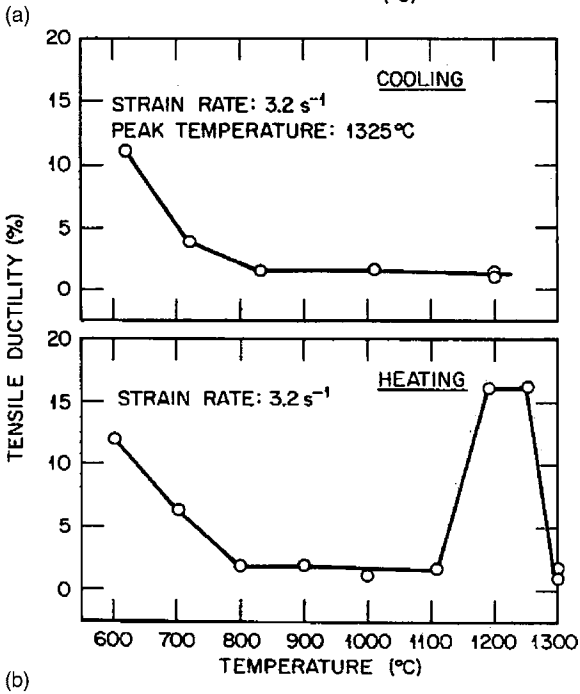
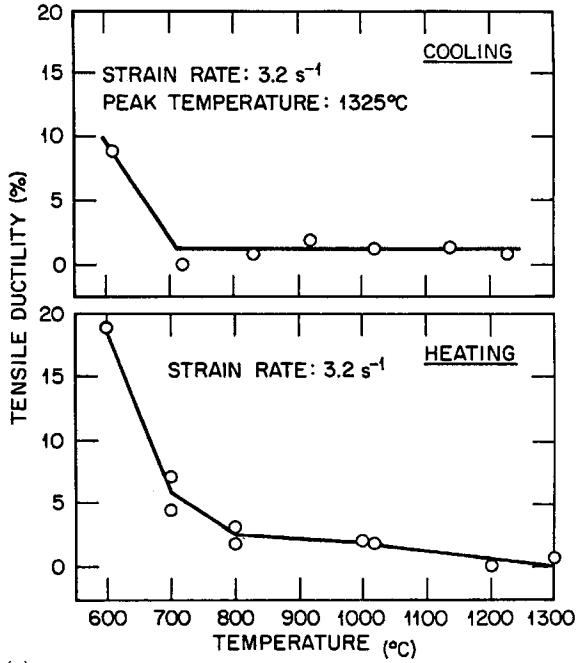


**Figure 5.18** Hot ductility behavior of a) Alloy IC25 (500ppm B) and b) IC103 (200ppm B). (From Santella and David [33]. Courtesy the American Welding Society)

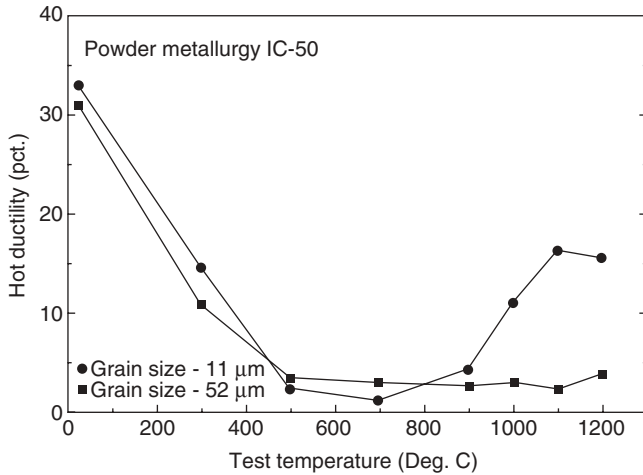


**Figure 5.19** On-heating hot ductility of powder metallurgy processed IC50 with average grain diameter of 11 and 50 μm. (From Edwards *et al.* [34])

low ductility and toughness. Fusion welding of the Ni<sub>3</sub>Al alloys has been demonstrated using GTA, laser, and electron beam welding, although cracking in the fusion zone and HAZ is frequently encountered. Electron beam welding at low travel speeds and under proper beam focus conditions has produced crack-free welds, but the range of conditions is quite narrow. Additions of boron at the level of 250 ppm also appears to reduce cracking, but levels both above and below this amount result in an increase in cracking. The addition of hafnium has also been shown to improve HAZ cracking resistance. The mechanism for cracking in the Ni<sub>3</sub>Al alloys has not been clearly defined and it appears to be a combination of solidification, liquation, and solid-state cracking. Many of these alloys show a stronger tendency to crack in the HAZ than in the fusion zone.

Brazing has been shown to be a viable method for joining both the NiAl and Ni<sub>3</sub>Al alloys. Although the high brazing temperatures (950–1150 °C) can result in the alteration of the base metal microstructure, it has been demonstrated that defect-free joints can be made with these alloys and with dissimilar combinations.

## REFERENCES

1. deBarbadillo, J. J. and Fischer, J. J. 1990. Dispersion strengthened nickel base and iron base alloys, in *ASM Handbook, Vol.2*, ASM International, Materials Park, OH, pp. 943–949.
2. Stoloff, N. S. 1990. Wrought and P/M superalloys, in *ASM Handbook, Volume 1*, ASM International, Materials Park, OH, pp. 950–980.

3. Kelly, T. J. 1982. *The development of a weldable Fe-Cr-Al ODS alloy (ASM Paper 8201-075)*, ASM International, Materials Park, OH, pp. 1–30.
4. O'Donnell, D. 1993. Joining of oxide dispersion strengthened materials, in *ASM Handbook, Vol. 6*, ASM International, Materials Park, OH, pp. 1037–1040.
5. Molian, P. A., Yang, Y. M., and Patnaik, P. C. 1992. Laser welding of oxide dispersion strengthened alloy MA 754., *Journal of Materials Science*, 27: 2687–2694.
6. Kelly, T. J. 1983. Joining mechanical alloys for fabrication, *Frontiers of High Temperature Materials II*, Proceedings, Conference, London, Session III. [Paper 1.]; 22–25 May 1983, Suffern, NY 10901, USA.
7. Kelly, T. J. 1982. Brazing of Inconel alloy MA 754 for high temperature applications, *Welding Journal*, 61(10): 317s–319s.
8. Ekrami, A. and Khan, T. I. 1999. Transient liquid phase diffusion bonding of oxide dispersion strengthened nickel alloy MA 758, *Materials Science and Technology*, 15:946–950.
9. Saha, R. K. and Khan, T. I. 2006. Effect of bonding temperature on transient liquid phase bonding behavior of a Ni based oxide dispersion strengthened superalloy, *Journal of Materials Engineering and Performance*, 15(6): 722–728.
10. Morimoto, S. and Hirane, T. 1986. Report on the 123rd committee on heat resisting metals and alloys, *Japan Society for the Promotion of Science*, 27(2): 255–264.
11. Nakao, Y. and Shinozaki, K. 1991. Report on the 123rd committee on heat resisting metals and alloys, *Japan Society for the Promotion of Science*, 32(2): 209–221.
12. Kang, C. Y., North, T. H., and Perovic, D. D. 1996. Microstructural features of friction welded MA 956 superalloy material, *Metallurgical and Material Transactions A*, 27A: 4019–4029.
13. Shinozaki, K., Kang, C. Y., Kim, Y. C., Aritoshi, M., North, T. H., and Nakao, Y. 1997. The metallurgical and mechanical properties of ODS Alloy MA 956 friction welds, *Welding Journal*, 76(8): 289s–299s.
14. Moore, T. J. 1968. Friction welding Udimet 700, *Welding Journal*, 47(4): 253–261.
15. Moore, T. J. and Glasgow, T. K. 1985. Diffusion welding of MA 6000 and a conventional nickel base superalloy, *Welding Journal*, 64(8): 219s–226s.
16. Nishimoto, K., Saida, K., and Tsuduki, R. 2004. In situ sintering bonding of oxide dispersion strengthened superalloys using pulsed electric current sintering technique, *Science and Technology of Welding and Joining*, 9(6): 493–500.
17. Baker, H. Ed. 1992, *Alloy phase diagrams*, ASM International, Materials Park, OH.
18. Noguchi, O., Oya, A., and Suzuki, T. 1981. *Met Trans*, 12A: 1647–1653.
19. George, E. P., Liu, C. T., and Pope, D. P. 1996. *Acta Mater.*, 44(5): 1757–1763.
20. Darolia, R., Lewandowski, J. J., Liu, C. T., Martin, P. L., Miracle, D. B., and Nathal, M. V. (Eds.), *Structural Intermetallics*, TMS, Warrendale, PA, 1993.
21. Deevi, S. C., Sikka, V. K., and Liu, C. T. 1997. Processing, properties and applications of nickel and iron aluminides, *Progress in Materials Science*, 42: 177–192.
22. Whang, S. H., Liu, C. T., Pope, D. P., and Stiegler, J. O. (Eds.), *High Temperature Aluminides and Intermetallics*, Proc. ASM/TMS Symposium, TMS-AIME, Warrendale, PA, 1990.
23. Schulson, S. and Barker, D. R. 1983. *Scripta Metall.*, 17: 519–522.
24. Liu, C. T. and Kumar, K. S. 1993. *Jour. Metall.*: 38–44.

25. Miracle, D. B. 1993. *Acta Metall. Mater.*, 41(3): 649–684.
26. Noebe, R. D., Bowman, R. R., and Nathal, M. V. 1993. *Inter. Mater. Rev.*, 38(4): 193–232.
27. David, S. A., Jemian, W. A., Liu, C. T., and Horton, J. A. 1985. *Welding Journal*, 64(1): 22s–28s.
28. Schulson, E. M. 1966. in *Brittle Fracture and Toughening of Intermetallic Compounds*, eds. N.S. Stoloff and V.K. Sikka, Chapman and Hall, New York.
29. Chen, C. and Chen, G. H. 1988. *Scripta Metall.*, 22: 1857–1861.
30. Goodwin, G. M. and David, S. A. 1990. Weldability of Nickel Aluminides, Proc. IIW Annual Meeting, Montreal, Canada.
31. Santella, M. L. and Feng, Z. 1996. Analysis of weld solidification cracking in cast nickel aluminide alloys, *4th Int. Trends in Welding Research*, ASM International, pp. 609–614.
32. Santella, M. L. and Sikka, V. K. 1994. Certain aspects of the melting, casting and welding of Ni<sub>3</sub>Al alloys. Proc. 2nd Int. Conf on Advanced Joining Technologies for New Materials, Cocoa Beach FL, USA, American Welding Society.
33. Santella, M. L. and David, S. A. 1986. A study of heat-affected zone cracking in Fe-containing Ni<sub>3</sub>Al alloys, *Welding Journal*, 75(5): 129s–137s.
34. Edwards, G. R., Maguire, M. C., and Damkroger, B. K. 1990. Relationships between microstructure and HAZ weld cracking, *Recent Trends in Welding Science and Technology*, (ed. S. A. David and J. M. Vitek), ASM International, Metals Park, OH, pp. 649–654.
35. Gale, W. F. and Guan, Y. 1996. *Metall. Mater. Trans. A*, 27A: 3621.
36. Gale, W. F. and Guan, Y. 1999. Microstructure and mechanical properties of transient liquid phase bonds between NiAl and a Ni-base superalloy, *Jour. Mat. Science*, 34: 1061–1071.
37. Orel, S. V., Parous, L. C., and Gale, W. F. 1995. Diffusion brazing of Ni-aluminides, *Welding Journal*, 74(9): 319s–324s.

## Repair Welding of Ni-base Alloys

Ni-base alloys are often used at elevated temperatures and in corrosive environments that result in gradual degradation in the form of erosion, cracking, or embrittlement. Since Ni-base alloys are expensive, repair is often a more economic choice than replacement. For example, turbine engine components such as frames, buckets, and blades may be repaired multiple times during their service lifetime. Since the microstructure of the original base metal can be altered by elevated temperature exposure, the procedures used for repair welding may vary significantly from those used for original fabrication. In the case of the precipitation-strengthened and single crystal alloys, the filler metals selected for repair may be of different composition than the base metal. In situations in which postweld heat treatment is required to restore mechanical properties, cracking may be a problem, particularly in high performance alloys strengthened by the gamma prime ( $\gamma'$ ) and/or gamma-double prime ( $\gamma''$ ) precipitate.

This chapter describes weldability issues associated with the repair of Ni-base alloys, including problems that are typically encountered during repair and postweld heat treatment and precautions that can be employed to insure successful repair of these alloys.

### 6.1 SOLID-SOLUTION STRENGTHENED ALLOYS

In general, the solid solution strengthened alloys typically provide the least challenge in terms of weld repair, provided appreciable microstructural changes have not occurred during service. As described in Chapters 2 and 3, although these alloys are generally designed to be single phase, many commercial alloys are actually beyond their solubility limit. As a result, secondary phases can often form during long term, elevated temperature service. The

formation of these phases can have a significant effect on both the mechanical properties and weldability.

An example of this is provided in Figure 6.1, which shows the microstructure of the solid solution strengthened Alloy 625 after exposure for 46,000 hours at 1200°F (650°C).<sup>(1)</sup> This alloy has undergone extensive secondary phase formation under these conditions. The small precipitates are  $\gamma'$ , the needle shaped constituent is the brittle  $\delta$  phase, and the grain boundaries are covered primarily with carbides. Table 6.1 shows the tensile properties and impact toughness of the same alloy after aging at temperatures from

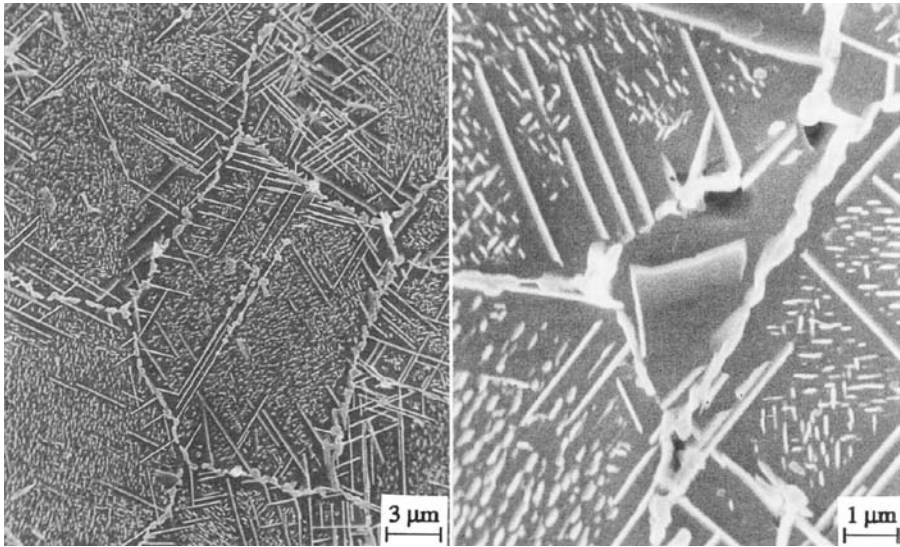


**Figure 6.1** SEM photomicrographs of various phases that form in alloy 625 after exposure at 1200°F for 46,000 hours. The small precipitates are  $\gamma'$ , the needle shaped constituent is the brittle  $\delta$ -phase, and the grain boundaries are covered primarily with carbides. (From Radavich and Fort [1])

**TABLE 6.1 Variations in Mechanical Properties of Alloy 625 that occur with Aging.**

Condition	Yield Strength (ksi)	Ultimate Strength (ksi)	Elongation (%)	Impact Toughness (ft-lbs)
Mill Annealed	66	128	46	81
1200°F/8,000 hrs	118	164	18	5
1400°F/8,000 hrs	97	143	13	5
1600°F/8,000 hrs	64	127	26	15
1200°F/16,000 hrs	119	165	12	4
1400°F/16,000 hrs	96	140	12	4
1600°F/16,000 hrs	63	128	32	14

1200-to-1600°F (650-to-870°C) up to 16,000 hours. Comparison is made to the alloy in the mill annealed condition. Note that the formation of these phases is accompanied by a significant reduction in ductility and toughness. These changes in microstructure and properties can present challenges when attempts are made to weld repair service-exposed material. First, the significant reductions in ductility can often lead to cracking during welding because the alloy may not be able to accommodate the residual stress from welding. Second, the presence of secondary constituents can often promote cracking due to liquation.

When weld repair is required, the mechanical properties and weldability can often be restored by a pre-weld heat treatment that is designed to dissolve the secondary phase(s). In this sense, available TTT diagrams are a useful aid to design effective treatments, and this is discussed in more detail in the next section. Similar concerns are expected in other solid solution alloys that may form other phases during long term exposure such as  $\sigma$ , P, and  $\mu$ . Precipitation strengthened alloys often require similar treatments, and this is discussed in detail in the next section.

## 6.2 PRECIPITATION-STRENGTHENED ALLOYS

Repair welding of Ni-base superalloys is widely used in the turbine engine industry (both aerospace and land-based) in order to extend service life and avoid the costs associated with component replacement. Repair of rotating components is usually associated with turbine blade corrosion/erosion at the tips or edges of the turbine blades and buckets. For these repairs, low heat input overlay techniques employing gas tungsten arc welding, laser beam welding, or brazing are used to build up layers of material to restore the original shape of the component. A postweld heat treatment (PWHT) consisting of a solution anneal and aging treatment is then applied to restore the strength of the component. Ideally, the repair is made with a matching (or near matching) filler metal that will achieve the same strength and corrosion resistance of the base metal. In some cases, solid-solution strengthened filler metals, such as Filler Metal 625, are used for these repairs in order to avoid solidification cracking. The inherent disadvantage of the use of solid-solution strengthened filler metals is that the repair weld cannot be hardened by heat treatment and the elevated temperature properties of the repaired component are compromised.

The static (non-rotating) components of turbine engines are also subject to repair welding, primarily due to fatigue cracking that occurs in service. These components must also be solution annealed and aged following welding to restore the required mechanical properties. Considerable research has been conducted on the repair welding characteristics of Ni-base superalloys, particularly Alloy 718 and Waspaloy which are widely used to construct static components in the hot section of aerospace turbine engines, since they are

resistant to strain-age cracking. Most of these studies are focused on the degradation in weldability that occurs after multiple repair and PWHT cycles. The following sections review the repair weldability issues of these alloys.

### 6.2.1 Alloy 718

Alloy 718 in both the wrought and cast form is widely used in static (non-rotating) components of turbine engines. It can be fabricated into a variety of shapes by casting or forging, exhibits high resistance to strain-age cracking (SAC), and maintains relatively high strength up to 650°C (1200°F). The resistance to SAC results from the substitution of Nb for the strengthening agents Ti and Al and the resultant formation of the  $\gamma''$  ( $\text{Ni}_3\text{Nb}$ ) precipitate, which forms more slowly than  $\gamma'$ . A discussion of strain-age cracking susceptibility can be found in Section 4.5.3.

In most applications, Alloy 718 is repaired using a matching filler metal that allows the repaired component to be fully hardened by a solution annealing and aging treatment following welding. In some cases, a solution annealing heat treatment is applied prior to repair welding to reduce the susceptibility to liquation cracking by reducing the overall restraint. Thus, in a typical repair welding scenario the Alloy 718 base metal may see two solution annealing heat treatments. Experience in the turbine engine industry has shown that repeated solution annealing heat treatments associated with repair welding can lead to considerable  $\delta$ -phase formation in both the wrought and cast microstructure. This accumulation of  $\delta$ -phase appears to result in embrittlement of the base metal, leading to cracking during repair welding after multiple repair/PWHT cycles.

**6.2.1.1 Effect of  $\delta$ -phase Formation.** As shown in Figure 6.2, after extended exposure above 650°C (1200°F) the  $\gamma''$  precipitate will form the stable orthorhombic structure of  $\text{Ni}_3\text{Nb}$  known as  $\delta$ -phase.(2,3) As the volume fraction of  $\delta$ -phase in the microstructure increases, the ductility of both the wrought and cast forms of Alloy 718 decreases and can lead to “ $\delta$ -phase embrittlement”.(4,5) If the service temperature of Alloy 718 is maintained below 650°C, very little  $\delta$ -phase will form in service and embrittlement can be avoided. In turbine engine structural components in which periodic repair is required, PWHT after repair welding can lead to  $\delta$ -phase formation. A typical PWHT for wrought Alloy 718 consists of a 900–950°C (1650–1740°F) solution annealing treatment followed by a dual aging treatment at 720°C (1325°F) for eight hours plus 620°C (1150°F) for eight to ten hours. This heat treatment optimizes both the fatigue strength and creep properties of the component.

As can be seen from Figure 6.2, exposure in the solution annealing temperature range of 900–950°C can lead to the formation of  $\delta$ -phase after less than an hour of exposure time. Thus, after multiple repair and PWHT cycles a considerable volume fraction of  $\delta$ -phase will form in the structure leading to both embrittlement and degradation of weldability. The formation of

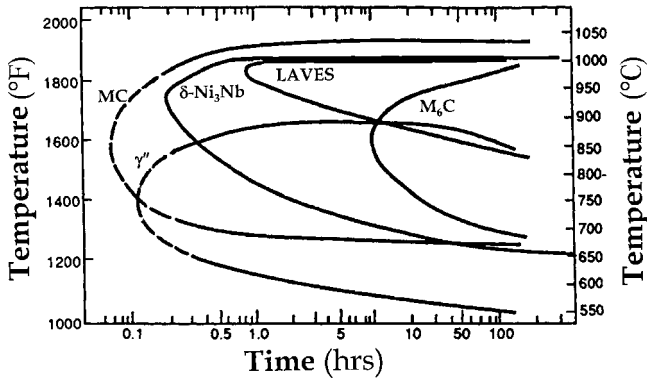


**Figure 6.2** Time-temperature-precipitation (TTP) curve for Alloy 718. (From Sims *et al.* [2])

$\delta$ -phase during PWHT can be avoided by solution annealing above the  $\delta$  solvus [1025–1050°C (1900–1950°F)], but this may not be acceptable in wrought materials in which maintaining a fine grain size is critical to the fatigue strength of the material.

The accumulation of  $\delta$ -phase in the wrought and cast microstructure has been found to affect the repair weldability of Alloy 718. Turbine engine components that have undergone multiple repair/PWHT cycles become highly susceptible to cracking in the HAZ of the wrought or cast base metal that contains a high volume fraction of  $\delta$ -phase. Examples of this cracking in both wrought and cast Alloy 718 from actual turbine engine components (compressor rear frame sections) are shown in Figure 6.3. Although the exact number of repair/PWHT cycles is not known for these components, it is estimated to be as many as 40. The base metal microstructure of these service-exposed components is shown in Figures 6.4 and 6.5. In the wrought component (Figure 6.4), the  $\delta$ -phase is uniformly distributed, forming a continuous grain boundary network with intragranular needlelike precipitates. In the cast component (Figure 6.5), the needlelike  $\delta$ -phase was localized in the interdendritic regions due to the segregation of Nb that occurs during solidification of the casting. This interdendritic region also contains Laves phase which is a byproduct of solidification. (See Chapter 3)

The effect of multiple repair and PWHT on the repair weldability of Alloy 718 has been studied extensively by Lu, (6), Mehl and Lippold (7), Hooijmans *et al.* (8), Bowers *et al.* (9), and Qian and Lippold. (10) These studies evaluated both actual Alloy 718 components that had been removed from service due to poor repair weldability and special compositions of Alloy 718 where multiple repair/PWHT cycles had been simulated in the laboratory.

Mehl and Lippold (7) evaluated the HAZ liquation cracking susceptibility of a wrought Alloy 718 turbine engine component that had been “retired” because of poor repair weldability. Both weld metal and base metal were

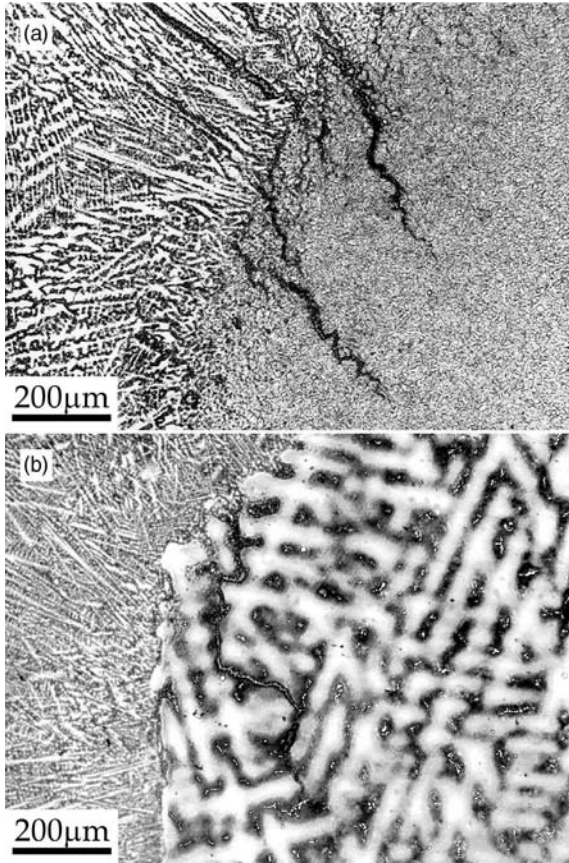


**Figure 6.3** Heat-affected zone liquation cracking in Alloy 718 repair welds in (a) wrought and (b) cast turbine engine components. (From Lu [6])

tested. The base metal and weld metal contained approximately 26% and 30%  $\delta$ -phase, respectively. In addition, base and weld metal samples were subjected to a PWHT consisting of a solution annealing treatment at either 910° or 1040° C (1700° or 1900° F) following by the standard two-stage aging treatment listed above. These samples along with samples from the original component and a reference wrought alloy containing 16%  $\delta$ -phase were evaluated using the hot ductility test. Results of these tests are provided in Table 6.2. Using this test, the liquation cracking temperature range (LCTR) is determined and serves as a measure of liquation cracking susceptibility. (See Chapter 8 for description of this test). As shown in Table 6.2, the effect of heat treatment and  $\delta$ -phase content on the LCTR is minimal. Reducing  $\delta$ -phase content to below 10% using the 1040° C treatment does result in a slight reduction in LCTR, but the improvement is not significant. This study suggested

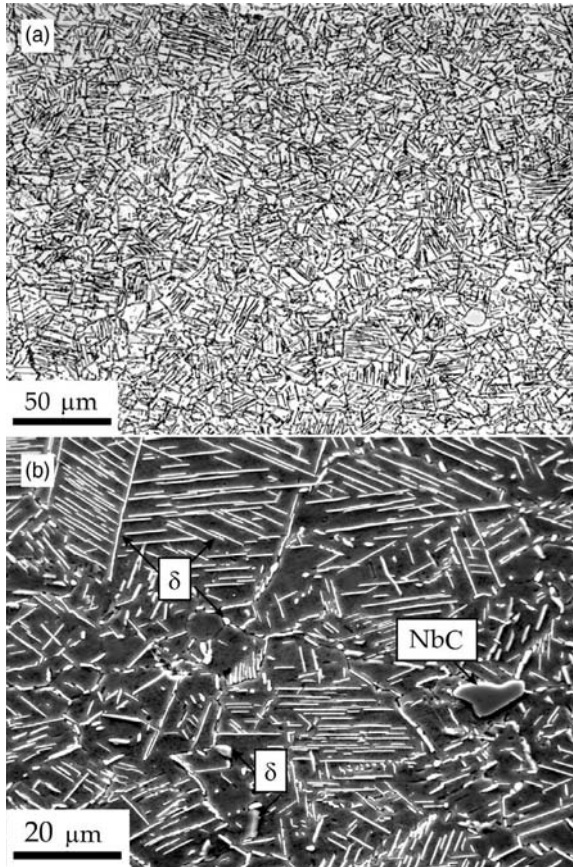


**Figure 6.4** Wrought Alloy 718 microstructure from turbine engine component subjected to multiple repair and PWHT cycles, a) optical micrograph, b) SEM micrograph. (From Lu [6])

that dissolution of the  $\delta$ -phase by solution annealing above the  $\delta$  solvus results in only a minor improvement in liquation cracking resistance.

Hooijmans *et al.*(8) conducted a study of the effect of multiple repair/PWHT cycles on both cast and wrought heats of Alloy 718 containing controlled levels of Nb and B. The composition and heat treatment schedule for these heats are provided in Table 6.3. The selection of a 950 °C (1740 °F) solution annealing temperature was designed to promote  $\delta$ -phase formation (see Figure 6.2) while minimizing grain growth. The materials were subjected to 20 and 40 PWHT cycles and then evaluated for liquation cracking susceptibility using the hot ductility test.  $\delta$ -phase formation in these materials was extensive, particularly in the high Nb heats subjected to 40 PWHT cycles (Figure 6.6).

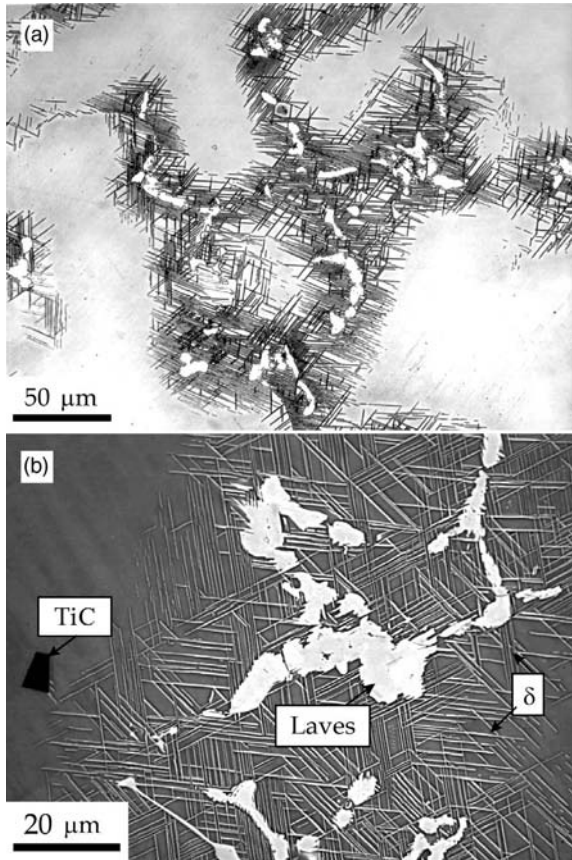


**Figure 6.5** Cast Alloy 718 microstructure from turbine engine component subjected to multiple repair and PWHT cycles, a) optical micrograph, b) SEM micrograph. (From Lu [6])

**TABLE 6.2** Effect of Postweld Heat Treatment and Volume Fraction  $\delta$ -phase on the Liquation Cracking Temperature Range for Wrought Base Metal and Weld Metal from a “Retired” Alloy 718 Turbine Engine Component. (From Mehl and Lippold [7])

Condition (1)	Volume Fraction $\delta$ -phase	Liquation Cracking Temperature Range ( $^{\circ}\text{C}$ )
Reference	16	170
Wrought BM	26	190
BM/925 $^{\circ}\text{C}$	26.9	180
BM/1040 $^{\circ}\text{C}$	8.7	180
Weld Metal	30.5	190
WM/925 $^{\circ}\text{C}$	17.8	190
WM/1040 $^{\circ}\text{C}$	8.1	170

(1) PWHT consisted of solution annealing for 1 hour at either 925 $^{\circ}$  or 1040 $^{\circ}\text{C}$  (1700 $^{\circ}$  or 1900 $^{\circ}\text{F}$ ), followed by aging at 720 $^{\circ}\text{C}$  (1325 $^{\circ}\text{F}$ ) for 8hrs plus 620 $^{\circ}\text{C}$  (1150 $^{\circ}\text{F}$ ) for eight hours.

**TABLE 6.3 Composition of Wrought and Cast Alloy 718 Heats Subjected to Simulated PWHT Cycles. (From Hooijmans *et al.* [8])**

Wrought Designation	Nb	B	Cast Designation	Nb	B
W997	4.4	0.003	C997	4.5	0.004
W995	4.9	0.004	C995	5.1	0.005
W996	5.5	0.005	C996	5.4	0.006

Bulk Composition (wt%): 20.0Cr, 18.0Fe, 2.9Mo, 1.0Ti, 0.5Al, 0.014C, bal Ni.

Heat Treatment: 950 °C (1740 °F)/15 minutes, 775 °C (1425 °F)/five hours plus 665 °C (1230 °F)/one hour.

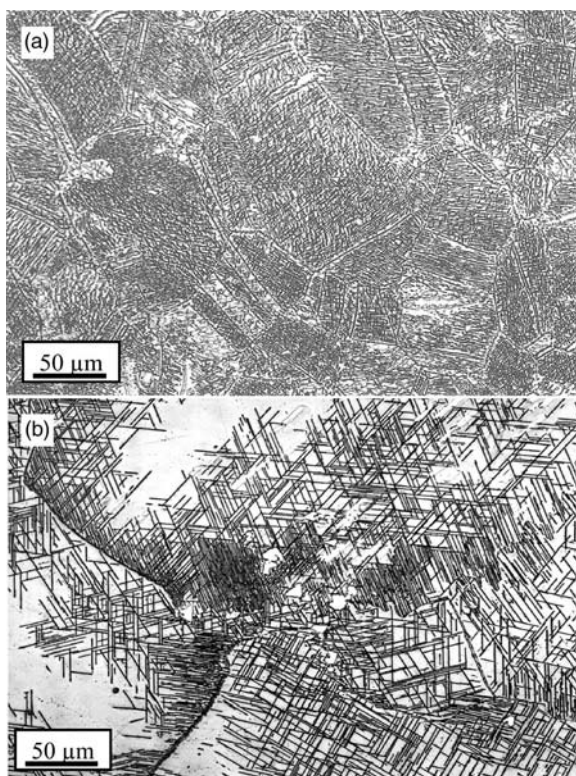


**Figure 6.6** Extensive  $\delta$ -phase formation in high Nb Alloy 718 after 40 PWHT cycles using a solution annealing temperature of 950 °C (1740 °F), a) wrought, and b) cast. (From Hooijmans *et al.* [8])

The results of the hot ductility tests showed no clear relationship between the number of PWHT cycles and the liquation temperature range for either the cast or wrought materials, nor was there an apparent effect of Nb and B content. The wrought material with the lowest Nb and B content (W997) had the best resistance to liquation cracking, while the medium and high Nb and

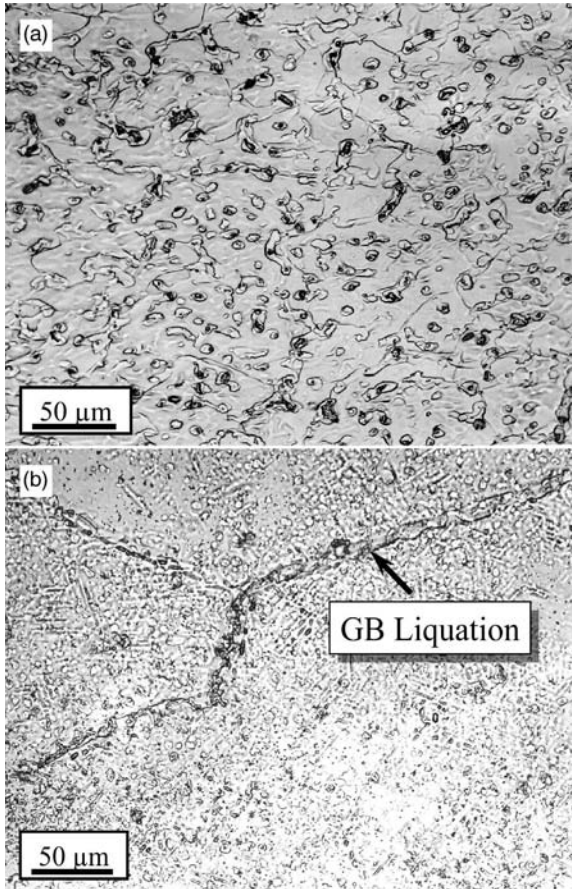


**Figure 6.7** Local melting in wrought (a) and cast (b) Alloy 718 hot ductility samples heated to 1260°C (2300°F). These materials had been subjected to 20 PWHT cycles prior to testing. (From Hooijmans *et al.* [8])

B cast alloys (C995 and C996) have the highest susceptibility. Examination of the hot ductility samples heated to a peak temperature of 1260°C (2300°F) showed evidence of considerable  $\delta$ -phase dissolution and Nb enrichment along the grain boundaries, resulting in local grain boundary melting at this temperature (Figure 6.7). Grain boundary melting is also associated with the melting of Laves phase in the cast alloys, as shown in Figure 6.8 from the work of Lu.(6)

Qian and Lippold (10) evaluated the effect of long term exposure at 954°C (1750°F) on the hot ductility of wrought Alloy 718 containing 5 wt% Nb. Exposure for 40 and 100 hours at this solution annealing temperature was designed to simulate the multiple PWHT cycles that lead to the formation of  $\delta$ -phase. The grain size was also kept constant at approximately 80 $\mu$ m average

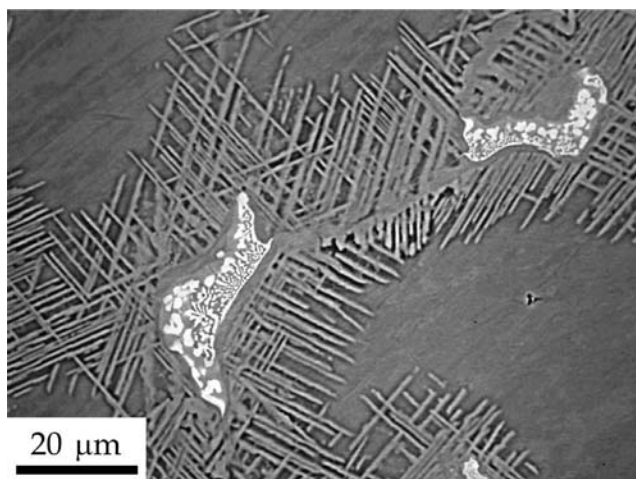


**Figure 6.8** Local melting of Laves phase along the grain boundary of cast Alloy 718 containing  $\delta$ -phase. Sample was heated to a peaking temperature of 1200°C (2190°F). (From Lu [6])

**TABLE 6.4 Results of Hot Ductility Testing of Wrought Alloy 718 after Exposure at 954°C (1750°F) for up to 100 hours. (From Qian and Lippold [10]. Courtesy of the American Welding Society)**

Condition	Nil-ductility Temp., °C	Nil-strength Temp., °C	Ductility Recovery Temp., °C (1)	Liquation Cracking Temp. Range, °C
As-received	1199	1274	1171	103
954°C/40 hrs	1191	1272	1158	114
954°C/100 hrs	1190	1276	1149	127

(1) Determined using peak temperature of 1240°C.

grain diameter in this experiment. The hot ductility test was again used to assess HAZ liquation cracking susceptibility. The hot ductility testing showed a small, but perceptible increase in cracking susceptibility as exposure time at 954°C increased, as shown by the hot ductility data in Table 6.4. The LCTR increased from 103°C to 114°C after 40 hours, and to 127°C after 100 hours. Again the effect of increased  $\delta$ -phase appears to be quite subtle with respect to liquation cracking.

The onset of liquation in both cast and wrought Alloy 718 has been summarized by Lu (6) based on extensive metallographic and fractographic study of the hot ductility behavior of the materials listed in Table 6.3. The on-heating ductility curves for both wrought and cast Alloy 718 representing multiple repair/PWHT cycles are shown in Figure 6.9. For the wrought material, loss in ductility is associated with both the constitutional liquation of Nb-rich MC carbides and the dissolution of  $\delta$ -phase that promotes segregation of Nb to

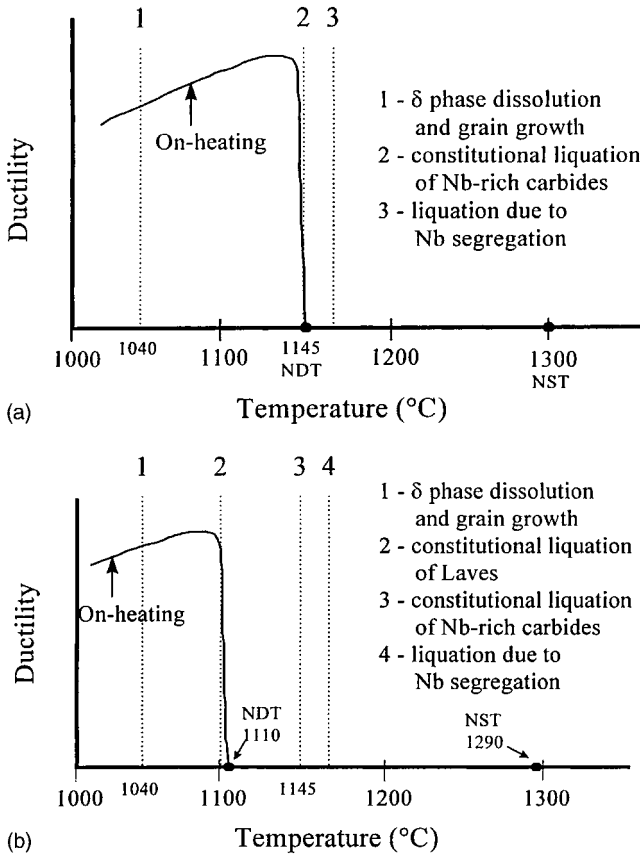


**Figure 6.9** Schematic illustration of the hot ductility behavior of wrought (a) and cast (b) Alloy 718 after multiple repair/PWHT cycles that promote  $\delta$ -phase precipitation. (From Lu [6])

grain boundaries. For cast material, the onset of ductility loss corresponds to the liquation of Laves phase and additional liquation occurs due to constitutional liquation of Nb-rich carbides and  $\delta$ -phase dissolution. In both cases, grain boundary liquation leading to loss in ductility occurs at temperature well below the nil strength temperature of the material.

**6.2.1.2 Rejuvenation Heat Treatments** The embrittling effect of  $\delta$ -phase formation can potentially be reversed by the use of a high temperature “rejuvenation” heat treatment. In order to dissolve the  $\delta$ -phase, the component must be heated above the solvus temperature, approximately 1010°C (1850°F) as shown in Figure 6.2. For wrought components, where control of grain size is critical to maintaining elevated temperature fatigue properties such rejuvenation treatments must be carefully applied so as not to compromise service

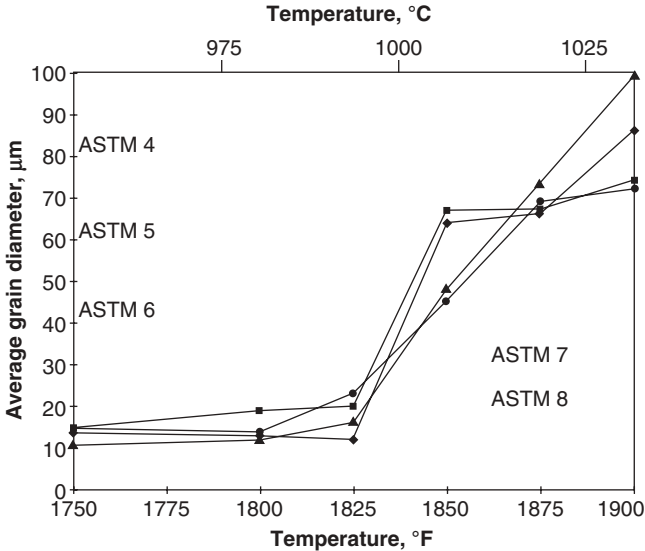


**Figure 6.10** Grain size versus 1 hour heat treatment temperature for service-exposed wrought Alloy 718.

performance. The effect of rejuvenation heat treatment temperature on grain size in actual turbine engine components that contained high levels of  $\delta$ -phase is shown in Figure 6.10. Note that there is virtually no grain growth following one hour exposures at temperatures up to 1825°F (995°C). In the range from 1850-to-1900°F (1010 to 1040°C) grain size increases dramatically, presumably due to the dissolution of the  $\delta$ -phase.

Qian and Lippold (11) studied the effect of rejuvenation heat treatments for two hours in the range from 995-to-1040°C (1825-to-1900°F) on wrought Alloy 718 that had been previously exposed for 100 hours at 954°C (1750°F) to induce extensive  $\delta$ -phase precipitation. Rejuvenation at 995°C removed most of the intragranular  $\delta$ -phase, but a continuous film of  $\delta$ -phase remained along the grain boundaries. The 1040°C heat treatment eliminated essentially all the  $\delta$ -phase, but resulted in significant grain growth relative to the original wrought structure. Rejuvenation at 1010°C was found to be a good compromise between  $\delta$ -phase dissolution and grain growth. Surprisingly, the grain size actually decreased after rejuvenation at 995° and 1010°C. The reason for this is discussed below.

Hot ductility testing was used to determine the effect of rejuvenation at 1010°C on susceptibility to HAZ liquation cracking. A small, but perceptible, reduction in liquation cracking susceptibility was observed in the rejuvenated material relative to the material containing a high volume fraction of  $\delta$ -phase. This improvement in HAZ liquation cracking resistance is presumably due to dissolution of the  $\delta$ -phase, but may also be related to the reduction in grain

size. The elimination of  $\delta$ -phase by rejuvenation at 1010°C reduces the grain boundary enrichment of Nb that occurs in the HAZ during repair welding and, presumably, reduces the temperature range over which cracking occurs. Based on the work of Qian and Lippold (11), it is possible to restore the HAZ liquation cracking resistance of wrought Alloy 718 by the use of rejuvenation heat treatment at temperatures just slightly above the  $\delta$ -phase solvus temperature.

An interesting outcome of rejuvenation heat treatment studies of wrought Alloy 718 was the reduction in grain size and increase in “special” grain boundaries in the rejuvenated microstructure.(12,13) This reduction in grain size relative to the wrought microstructure containing a high volume fraction of  $\delta$ -phase appears to occur by a simple recrystallization mechanism associated with residual warm-working deformation. The elimination of the  $\delta$ -phase allows the recrystallization to proceed by eliminating  $\delta$ -phase pinning of the grain boundaries. The rejuvenated microstructures also exhibited a high fraction of “special” grain boundaries which tend to resist HAZ liquation cracking. These special grain boundaries are described crystallographically by a coincident site lattice (CSL) model which indicates the number of CSL sites in adjacent grains.(14–16) Increasing the fraction of special grain boundaries has been shown to reduce cracking susceptibility in Ni-base alloys due to intergranular stress corrosion cracking and creep.(16,17) These special grain boundaries have been shown to resist HAZ liquation cracking in Alloy 718, where liquation cracking is essentially blunted by special grain boundary segments resulting from the formation of annealing twins.(12) The use of “grain boundary engineering” to develop microstructures resistant to cracking during repair welding may offer a solution to the repair weld cracking problems associated with Alloy 718.

**6.2.1.3 Summary of Repair Weldability of Alloy 718** Repair of Alloy 718 in either the cast or wrought form is usually conducted using a matching filler metal that allows the weldment to be hardened by heat treatment following the repair. The postweld heat treatment consists of solution annealing followed by a two step aging treatment, such as 720°C (1325°F) for eight hours plus 620°C (1150°F) for eight to ten hours. In some cases, solution annealing of the component is also conducted prior to repair welding in order to reduce susceptibility to cracking during repair.

Selection of the solution annealing temperature is dependent on the nature of the component and its intended service use. In wrought components where fatigue behavior is important, maintaining a fine grain size is imperative and solution annealing is usually conducted in the temperature range from 900–950°C (1650–1740°F). As shown in Figure 6.2, prolonged exposure or multiple excursions into this temperature range will result in the formation of  $\delta$ -phase and “ $\delta$ -phase embrittlement” is possible. For cast components where grain size control is not an issue (the grain size is already large), solution annealing can be performed above the  $\delta$ -phase solvus.

Experience in the gas turbine engine industry has shown that Alloy 718 components that are subjected to multiple repair and PWHT cycles become progressively more difficult to weld and exhibit cracking after either repair welding or PWHT following welding. It is presumed that this degradation of weldability is associated with the accumulation of  $\delta$ -phase in the microstructure. The effect of  $\delta$ -phase on the repair weldability of Alloy 718 has been studied in some detail using both laboratory tests and extensive metallurgical characterization. Accumulation of  $\delta$ -phase in both the wrought and cast base metal has been shown to increase susceptibility to HAZ liquation cracking, although this increase is not dramatic. It is likely that the progressive decrease in repair weldability results from both an increase in HAZ liquation cracking susceptibility and inherent embrittlement in the solid-state.

Rejuvenation heat treatments above the  $\delta$ -phase solvus temperature are effective in dissolving the  $\delta$ -phase and restoring some level of weldability. In wrought components where elevated temperature fatigue strength is important, these rejuvenation heat treatments must be carefully controlled to prevent excessive grain growth (see Figure 6.10). Heat treatments at temperatures just above the solvus, in the range from 980-to-1010 °C (1800-to-1850 °F) show potential for dissolving substantial  $\delta$ -phase in wrought Alloy 718 while avoiding significant grain growth. The development of a high fraction of “special” grain boundaries through grain boundary engineering approaches have also been shown to improve resistance to cracking in the wrought material.

### 6.2.2 Waspaloy

Waspaloy is a  $\gamma'$  strengthened superalloy containing nominally 20Cr-14Co-1.5Al-3Ti-4Mo-0.05Zr-0.005B. It has been widely used in the turbine engine industry for both rotating and static components and is considered to be moderately weldable. The relatively low Ti+Al content makes it marginally resistant to strain-age cracking and, thus, it is often used in applications where repair welding can extend the service lifetime of the component.

Waspaloy is normally strengthened by a three-step sequence comprising a solution heat treatment, followed by stabilization and age-hardening. There are two conditions of heat treatment for Waspaloy depending on the application. To achieve good high temperature creep and stress rupture properties, such as required for turbine blades and buckets, the following heat treatment is used:

- Solution heat treat at 1080 °C (1975 °F) for 4 hours and air cool
- Stabilize at 845 °C (1550 °F) for 24 hours and air cool
- Age at 760 °C (1400 °F) for 16 hours and air cool to achieve a hardness of HRC 32–38.

To optimize both room temperature and elevated temperature tensile properties, the following heat treatment is recommended. Discs, shafts and most sheet and strip components are used in this condition.

- Solution heat treat at 995 °C (1825 °F) for four hours and oil quench
- Reheat to 845 °C (1550 °F) for four hours and air cool
- Age for 760 °C (1400 °F) for 16 hours and air cool to achieve a hardness of HRC 32–38.

Note that the primary difference between these heat treatments is the solution heat treatment temperatures, where solution treating at 1080 °C (1975 °F) confers the highest stress-rupture and creep strength, while the lower solution treatment at 995 °C (1825 °F) results in higher tensile and yield strength from room temperature up to about 815 °C (1500 °F). Heat treatment following repair welding would use one of these approaches, depending on the properties that were to be achieved.

Similar to Alloy 718, Waspaloy also exhibits degradation in repair weldability following multiple repair/PWHT cycles. Qian and Lippold (18) studied the effect of simulated repair/PWHT cycles on both a Waspaloy wrought bar in the solution annealed condition and a forged turbine disk in the fully aged condition. In order to simulate the multiple repair and PWHT cycles, both materials were subjected to a 1080 °C/four hours heat treatment for ten cycles and an isothermal hold at 1080 °C for 40 hours. In both cases, the total time at the solution annealing temperature was 40 hours. The grain size and hardness of the wrought and forged materials as a consequence of these heat treatments is provided in Table 6.5. Note that the grain size of both materials increases dramatically with heat treatment. The forged material exhibited a bimodal grain size and had residual warm work as a result of forging. Upon heat treatment the hardness of the forging dropped significantly due to the dissolution of  $\gamma'$  and annealing of the warm-worked material.

Hot ductility testing was again used to determine the HAZ liquation cracking susceptibility of the as-received and heat treated material. As shown in

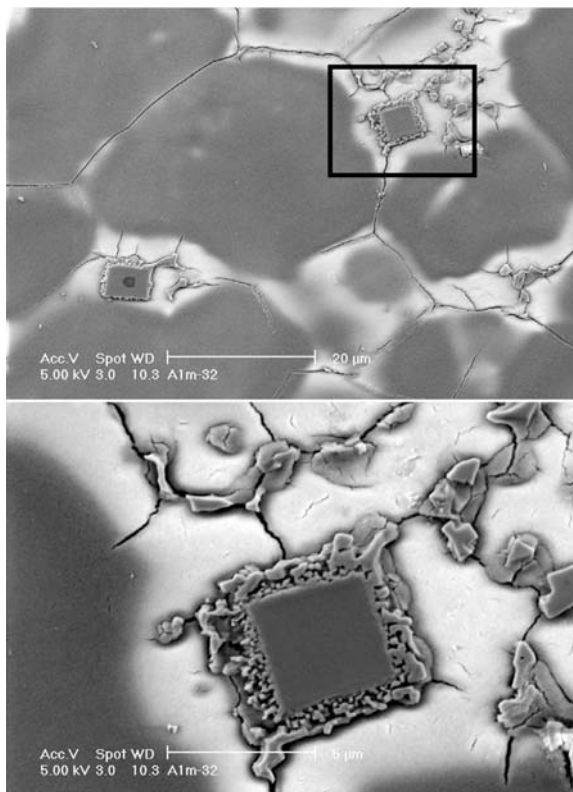
**TABLE 6.5 Microstructure and HAZ Liquation Cracking Susceptibility of Waspaloy in the Wrought and Forged Condition and After Elevated Temperature Exposure. (From Qian and Lippold [18]. Courtesy the American Welding Society)**

Material Form	Condition	Grain Size, $\mu\text{m}$ (1)	Hardness ( $H_v$ )	LCTR, °C
Wrought Bar	As-received	15	297	209
	1080 °C/40 hrs	145	325	237
Forged Disk	As-received (aged)	190/46	398	126
	1080 °C/40 hrs	560/255	277	270
	1080 °C/100 hrs	586/250	270	85

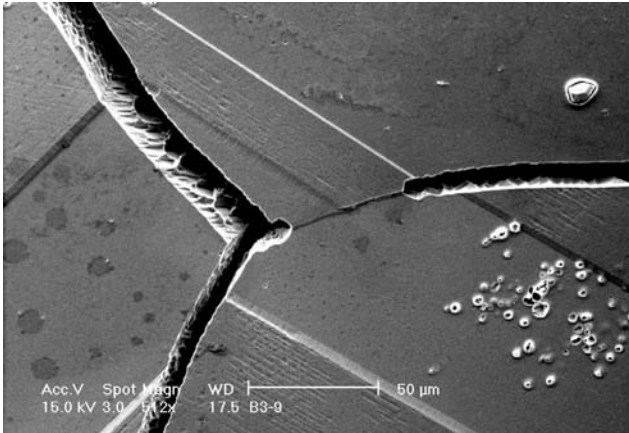
(1) the forged disk material exhibited a bimodal grain size.

Table 6.5, the cracking susceptibility of the wrought material, as determined by the liquation cracking temperature range (LCTR), increased slightly upon heat treatment (209 °C versus 237 °C). The cracking susceptibility of the forged disk increased dramatically with heat treatment (LCTR of 126 °C versus 270 °C).

In both wrought and forged Waspaloy, the increase in HAZ liquation cracking susceptibility with prolonged heat treatment at 1080 °C (1975 °F) is attributed to the increase in grain size. No other significant microstructural changes were observed. The finer grain size of the wrought bar accounts for its higher resistance to cracking. In both materials, the grain boundary liquation mechanism was associated with the constitutional liquation of Ti-rich, MC carbides and segregation of boron to the grain boundaries. The forged disk material had a higher boron content than the wrought bar (0.005 versus 0.002 wt%), which probably also contributed to the higher cracking susceptibility of the disk. An example of constitutional liquation of the MC carbides and grain boundary wetting is shown in Figure 6.11. These SEM micrographs clearly



**Figure 6.11** Constitutional liquation associated with Ti-rich, MC carbides in a Waspaloy hot ductility sample heated to a peak temperature of 1300 °C (2370 °F). (From Qian and Lippold [18]. Courtesy the American Welding Society)



**Figure 6.12** Grain boundary segment in Waspaloy forged disk resistant to HAZ liquation cracking. Material was heat treated at 1080°C for 100 hrs. (From Qian and Lippold [18]. Courtesy the American Welding Society)

show the reaction zone and local melting at the particle/matrix interface that is characteristic of the constitutional liquation mechanism.

It was also found that an increase in the fraction of “special” grain boundaries in the forged Waspaloy disk resulting in an improvement in HAZ liquation cracking resistance. (12,19) When the disk alloy was heat treated for 100 hours at 1080°C (1975 °F) the fraction of special grain boundaries increased dramatically with a resultant dramatic decline in the LCTR (Table 6.5). As with Alloy 718, this improvement in cracking resistance is associated with the generation of grain boundaries that are resistant to wetting by liquid films, thereby improving the hot ductility of the material. An example of this is shown in Figure 6.12, where the intersection of an annealing twin with the grain boundary has altered the grain boundary character such that boundary liquation is unfavorable. This suggests that the use of grain boundary engineering techniques to increase the fraction of special grain boundaries in Waspaloy (and other Ni-base superalloys) may be effective in improving the repair weldability of superalloys.

### 6.3 SINGLE CRYSTAL SUPERALLOYS

Single crystals of Ni-base superalloys are critical high temperature materials to the aerospace and energy industries due to their combination of superior strength, ductility, and fracture resistance at elevated temperatures. There are two distinct advantages in the use of single crystal superalloys. First, both the creep resistance and thermo-mechanical fatigue behavior are enhanced due to the absence of grain boundaries. Second, minor elements that are required

for grain boundary strengthening in the polycrystalline superalloys (including carbon, boron, and zirconium) can be removed. This increases the incipient melting temperature of the single crystal superalloys. However, the cost of single crystal components can be very high due to the complex solidification processing associated with growing single crystals. For example, single crystal gas turbine blades can cost as much as \$30,000 each or equivalently \$3 million per row of blades in a standard turbine engine.(20) Thus, it is imperative that reliable repair strategies for single crystal alloys are available in order to extend their service life and make their use economically viable. Repair of single crystal components by welding is required to eliminate casting defects and to repair wear, blade tip erosion, and thermal fatigue cracking that can occur in service.

Successful repair of Ni-base single crystal alloys requires preservation of the single crystal structure during solidification of the weld pool. In other words, solidification must occur epitaxially from the underlying single crystal substrate without the nucleation of equiaxed grains in the liquid. These equiaxed grains are often referred to as “stray” grains.(21,22) The formation of stray grains within the weld pool is often attributed to the constitutional supercooling mechanism. During welding, solidification initiates epitaxially from the substrate without the need for nucleation.(23) As the solidification progresses, the solid rejects solute into the liquid (for elements in which the equilibrium partition coefficient is less than unity). Depending on the alloy composition, growth velocity of the solid/liquid interface, and the diffusivity of solute in the liquid, the liquid is usually not capable of completely transporting the solute away from the interface by diffusion and/or convection. This leads to a solute gradient in the liquid in which the solute concentration is highest at the solid/liquid interface and decays to the nominal solute concentration outside the solute boundary layer. As shown schematically in Figure 6.13, this variation in concentration causes a variation in the liquidus temperature ahead of the solid/liquid interface. If the actual temperature distribution in the liquid (i.e., the temperature gradient) is below that of the liquidus temperature, then the liquid can be supercooled below its liquidus temperature. In this condition, the planar interface is no longer stable and breaks down into a cellular or dendritic morphology.

Breakdown of the planar interface into cellular or dendritic morphologies *does not* lead to the formation of stray grains. In fact, maintenance of a planar solid/liquid interface during solidification of superalloys is very difficult, and solidification of single crystals typically occurs in a cellular or dendritic mode. The single crystal structure will be maintained as long as growth continues to occur epitaxially, regardless of whether the interface adopts a planar, cellular, or dendritic morphology. Thus, strictly speaking, conventional constitutional supercooling theory only applies to the initial breakdown of the planar solid/liquid interface and cannot fully explain the columnar-to-equiaxed transition without considering nucleation effects. However, it is generally understood (23,24) that the high level of constitutional supercooling that occurs near the

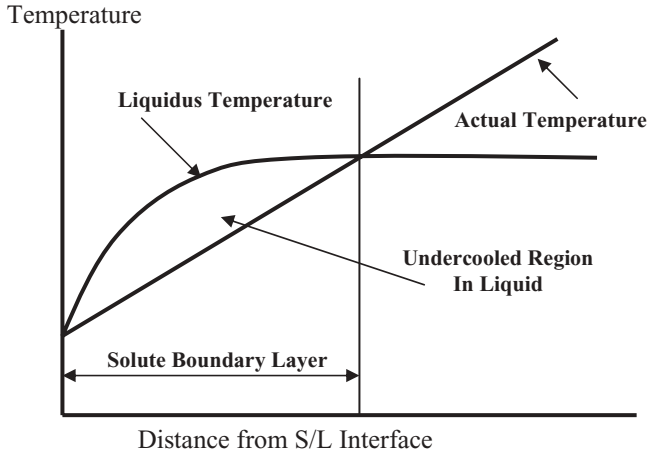


**Figure 6.13** Variation in liquidus temperature (due to presence of solute boundary layer) and actual temperature in the liquid ahead of the solid/liquid interface that causes undercooling in the liquid.

centerline of the weld pool plays an important role in providing the undercooling required for nucleation of stray grains.

The degree of undercooling in the liquid depends on the temperature gradient in the liquid and growth rate of the solid/liquid interface. The role of temperature gradient is easily understood by examination of Figure 6.13. Welding conditions that promote higher temperature gradients will be favorable for minimizing undercooling in the liquid and avoiding the formation of stray grains. Conditions that lead to lower growth velocities are beneficial because they minimize the liquidus temperature gradient (by affecting the solute rejection rate into the liquid). The influence of welding parameters on the temperature gradient, growth rate, and resultant susceptibility to stray grains are described in the next section. The temperature gradient within the weld pool is highest at the fusion boundary and lowest at the centerline. Conversely, the growth rate approaches zero at the fusion boundary and approaches (or even exceeds) the heat source travel speed at the weld centerline.(23,25) Therefore, the degree of constitutional undercooling is generally highest at the centerline, and the high degree of undercooling at this location can provide the undercooling required to nucleate new grains within the liquid. This leads to the columnar-to-equiaxed transition (CET) and formation of stray grains.

Liu and DuPont (26) showed this effect in a weld repair made on a single crystal alloy, CMSX-4, as shown in Figure 6.14. Figure 6.14A shows a cross sectional light optical photomicrograph of a repair weld on CMSX-4 with the accompanying electron backscattered diffraction (EBSD) pattern for the boxed area shown in Figure 6.14B. Note the large difference in dendrite arm spacing between the base metal casting and weld due to differences in cooling

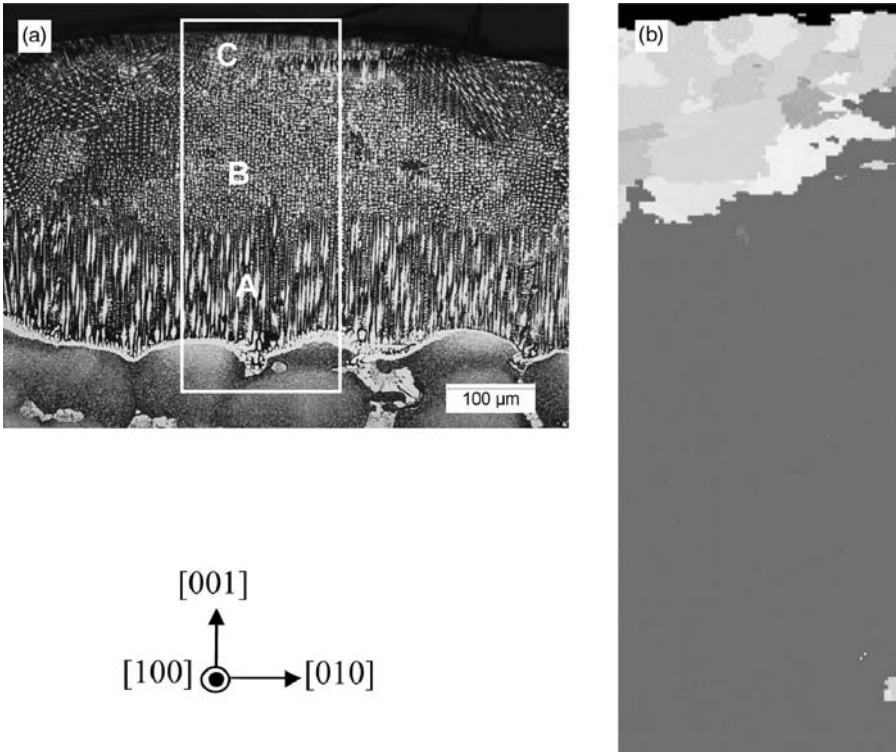


**Figure 6.14** Example of weld repair made on single crystal Alloy CMSX-4. a) light optical photomicrograph, b) EBSD pattern showing regions of single crystal and stray grain regions in the weld. (From Liu and DuPont [26])

rates. The base metal crystallographic directions are noted in the figure. Three different dendrite morphology regions are observed: Region A, in which the columnar dendrites grew epitaxially from the substrate in the  $[001]$  direction; Region B, in which epitaxial dendrite growth occurred in the  $[100]$  direction (the heat source travel direction); and Region C, which consists of stray grains near the top of the weld where the  $G/V$  ratio is low. Note that, although there is an apparent “boundary” between regions A and B, this merely marks the regions of the two orthogonal growth directions, and the single crystal structure is maintained in Regions A and B as revealed by the EBSD pattern.

The constitutional supercooling mechanism has been supported by a wide range of experimental observations in studies conducted on single crystal alloys using a variety of techniques, including laser surface melting (with no filler metal additions) (27–29), laser cladding (30) and electron beam welding. (22–24,31) For example, studies on electron beam and pulsed laser beam welds of a single crystal Ni-base superalloy PWA 1480 by David *et al.* (21,22) showed that it was difficult to maintain the single crystal structure

during welding due to the formation of equiaxed stray grains. In contrast, similar experiments conducted on a relatively “pure” austenitic Fe-15Cr-15Ni stainless steel single-crystal demonstrated nearly perfect retention of the single crystal nature in electron beam welds.(30) The difference in these results can generally be attributed to the solute content of the different alloys. Although Cr and Ni segregate to the liquid during solidification, it is well known that the equilibrium partition coefficients ( $k$ ) for both Cr and Ni are close to unity and do not segregate strongly during solidification.(32) This, combined with the low level of other elements in the Fe-15Cr-15Ni alloy, minimizes the build up of solute in the liquid during solidification. As a result, the liquidus temperature variation is minimized and provides a concomitant reduction in the level of constitutional supercooling in the liquid. Thus, the reduced level of solute segregation makes it easier to avoid the CET. In contrast, commercial single crystals require the addition of substitutional and interstitial alloying elements, many of which partition strongly during solidification. This leads to higher concentration gradients in the liquid and associated enhanced constitutional supercooling.

### 6.3.1 Control of Single Crystal Weld Repairs

The ability to successfully preserve the single crystal structure in the fusion zone during repair welding requires a full understanding of the processing and material parameters that control the onset of the columnar-to-equiaxed transition (CET). Hunt (33) was the first to develop an approximate analytical expression that described the CET. In that work, expressions for the nucleation rate were combined with dendrite growth undercooling equations to establish the condition for the CET. The type of growth that occurred was assumed to depend on the volume fraction of equiaxed grains that formed in the undercooled region when the advancing columnar front met the equiaxed grains. The structure was assumed to be fully columnar, and thus the CET avoided, when the volume fraction of equiaxed grains was less than 0.0066. This led to the following condition for avoiding the CET:

$$G > 0.617(100N_o)^{1/3} \left[ 1 - \frac{(\Delta T_N)^3}{(\Delta T_c)^3} \right] \Delta T_c \quad (\text{Eqn. 6.1})$$

Where  $G$  is the temperature gradient in the liquid,  $N_o$  is the total number of heterogeneous sites available for nucleation per unit volume,  $\Delta T_N$  is the associated undercooling required for nucleation, and  $\Delta T_c$  is the undercooling at the solid/liquid interface, which depends on the temperature gradient and growth rate. The value of  $\Delta T_c$  can be calculated using dendrite growth undercooling models.(34,35) The practical difficulty in the application of Eqn. 6.1 lies in the ability to determine appropriate values of  $\Delta T_N$  and  $N_o$ . Nevertheless, the model is useful because it was shown to correctly capture the observed effects of

various factors on the CET such as growth rate, temperature gradient, and alloy composition.

More recently, Gaumann *et al.* (36) extended the analysis proposed by Hunt. The composition profile in the liquid was calculated directly using the appropriate solution of the diffusion equations for an isolated dendrite with a parabolic tip geometry. This was then used to determine the liquidus temperature profile ( $T_z$ ). The actual local temperature profile in the liquid ( $T_{q,z}$ ) was considered to be controlled by heat extraction through the solid and was determined through knowledge of the temperature gradient and dendrite tip temperature as determined by the KGT model.(35) The actual undercooling ( $\Delta T_z$ ) at any location within the liquid is then given by:

$$\Delta T_z = T_z - T_{q,z} \quad (\text{Eqn. 6.2})$$

Equiaxed grains will nucleate anywhere in this undercooled region where the actual undercooling is more than that required for nucleation,  $\Delta T_z > \Delta T_N$ . The volume fraction of equiaxed dendrites within the undercooled region was then determined by integration of the growth equation, and the critical volume fraction required for a fully equiaxed structure originally proposed by Hunt was used as the critical CET value. Comparison of this improved model to the original one proposed by Hunt showed that differences existed between the two approaches at low and high temperature gradients. These differences were primarily attributed to the improved ability to accurately predict the dendrite tip undercooling.

Figure 6.15 shows an example of a microstructure selection map that was generated for the Ni base single crystal CMSX-4 using the detailed approach described above.(27) The solid, continuous line in the plot represents the transition between values of the solid/liquid interface growth rate ( $V$ ) and

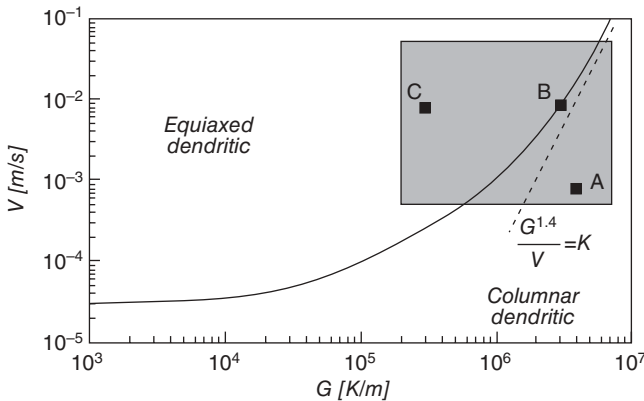


**Figure 6.15** Processing map for Alloy CMSX-4 showing range of V-G conditions that produce columnar dendritic and equiaxed dendritic growth. (From Gauman *et al.* [27])

temperature gradient in the liquid ( $G$ ) that lead to the CET. A  $G$ - $V$  combination below this line will result in columnar, single crystal growth, while combinations above this line lead to equiaxed growth and loss of the single crystal structure. Material parameters required for calculation of the map were determined using a multi-component thermodynamic database. The values of  $N_0$  and  $\Delta T_N$  were assumed to be  $N_0 = 2 \times 10^{15}/\text{m}^3$  and  $\Delta T_N = 2.5^\circ\text{C}$ . An increase in the value of  $N_0$  or a decrease in the value of  $\Delta T_N$  will widen the range where equiaxed growth occurs. This map is useful in a practical sense because it permits identification of the combinations of  $G$  and  $V$  which permit retention of the single crystal structure during weld repair. The use of heat flow equations can then be used to link  $V$  and  $G$  to the weld processing parameters such as heat source power, travel speed, and preheat temperature in order to develop process-microstructure maps for successful weld repair. This is discussed below.

Gaumann *et al.* (27,30) developed a simplified relationship between the temperature gradient, growth velocity, volume fraction of equiaxed grains ( $\phi$ ), and the nuclei density ( $N_0$ ), as:

$$\frac{G^n}{V} = a \cdot \left[ \sqrt[3]{\frac{-4\pi N_0}{3 \ln(1-\phi)}} \cdot \frac{1}{n+1} \right]^n \quad (\text{Eqn. 6.3})$$

where  $a$  and  $n$  are material constants that are determined by fitting calculations of the constitutional dendrite tip undercooling ( $\Delta T$ ) from the KGT model to an equation of the form  $\Delta T = (aV)^{1/n}$ . For CMSX-4, these values are  $a = 1.25 \times 10^6 \text{ K}^{3.4}/\text{ms}$  and  $n = 3.4$ . This relation is valid under high temperature gradient conditions in which the value of  $N_0$  is most important for controlling nucleation and the value of  $\Delta T_N$  can be ignored. Welds can be prepared under various values of  $G$  and  $V$  and the resultant volume fraction of equiaxed grains ( $\phi$ ) can be directly measured on the weld cross-sections. In this case,  $N_0$  is the only unknown in Eqn. 6.3 and can thus be determined experimentally by fitting Eqn. 6.3 to the measured values of  $\phi$ . For CMSX-4, this results in  $N_0 = 2 \times 10^{15}/\text{m}^3$ . When the original condition for a fully columnar microstructure proposed by Hunt is invoked ( $\phi = 0.0066$ ), all values on the right hand side of Eqn. 6.3 are known and lead to the following condition for avoiding the CET:

$$\frac{G^n}{V} > K \quad (\text{Eqn. 6.4})$$

Where  $K$  is a material constant that depends on  $N_0$ ,  $\phi$ ,  $a$  and  $n$ . For CMSX-4,  $K = 2.7 \times 10^{24} \text{ K}^{3.4} \cdot \text{m}^{-4.4} \cdot \text{s}$ . This approximate condition is shown as the dotted line in Figure 6.15 and it can be seen that this approximation is more restrictive than the results obtained by the detailed calculations. However, Eqn. 6.3 is useful because it permits straightforward coupling of  $V$  and  $G$  to the weld processing parameters.

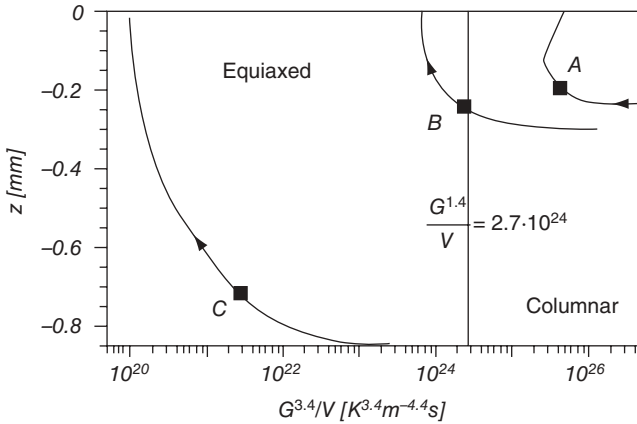


**Figure 6.16** Microstructure selection map for three different welds on Alloy CMSX-4 (labeled A, B, and C) prepared under different processing conditions. (From Gauman *et al.* [27])

Figure 6.16 shows an example of a microstructure selection map for three different welds on Alloy CMSX-4 (labeled A, B, and C) prepared under different processing conditions. This plot shows the variation in the  $G^n/V$  ratio as a function of depth in the weld pool. The values of  $G$  were estimated with the Rosenthal heat flow solution, while the values of the dendrite growth velocity ( $V_{hkl}$ ) along the solid/liquid interface were determined through the dendrite velocity analysis proposed by Rappaz: (31)

$$V_{hkl} = V_b \left( \frac{\cos \theta}{\cos \psi} \right) \quad (\text{Eqn. 6.5})$$

Where  $\theta$  is angle between the solidification front normal and heat source travel direction and  $\psi$  is the angle between the normal to the solidification front and the dendrite growth direction.

As expected, the  $G^n/V$  ratio is highest at the fusion line (bottom of the weld) and decreases as the top of the weld is approached. The critical value for the CET of CMSX-4 is superimposed on the plot. Welds prepared under conditions in which the critical value of  $G^n/V$  remains below this critical value everywhere in the weld are expected to retain the single crystal structure (e.g., weld A), while welds prepared with regions less than this value (e.g., welds B and C) will undergo the CET and lose the single crystal structure. Figure 6.17 shows cross-sectional EBSD maps for conditions A and C in which the misorientation angle between grains is indicated in order to identify individual grains. These results are in good agreement with the predictions of Figure 6.16.

Figure 6.18 shows a process-microstructure map that was proposed to reveal semi-quantitative relations between the important processing parameters of

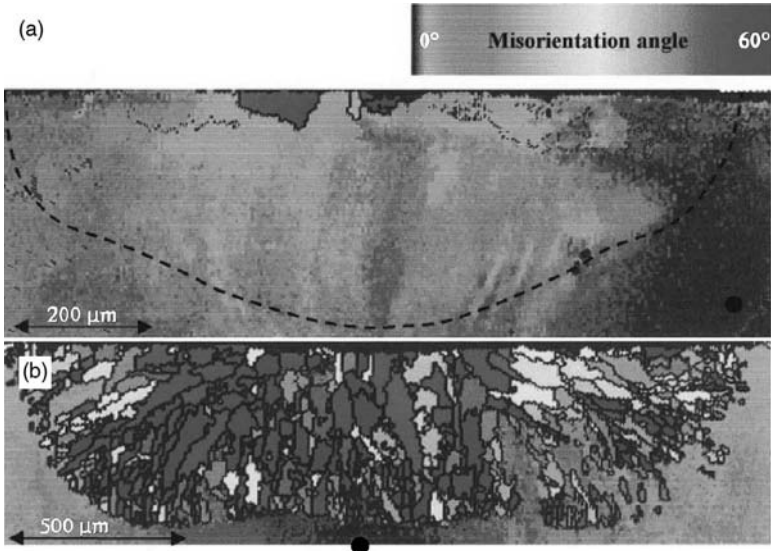


**Figure 6.17** Cross-sectional EBSD maps for conditions A and C shown in Figure 6.15 in which the misorientation angle between grains is indicated in order to identify individual grains. (From Gauman *et al.* [27])

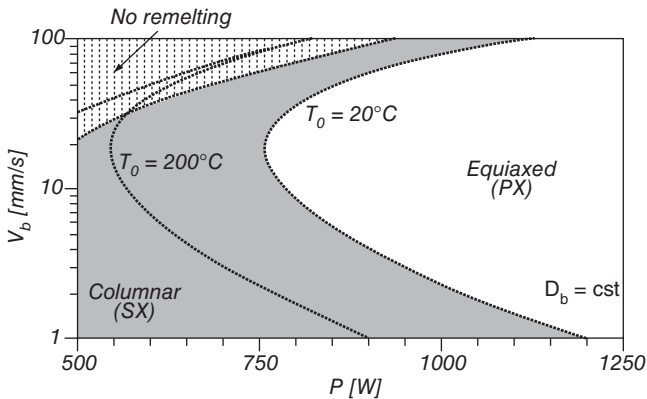


**Figure 6.18** Process-microstructure map for Alloy CMSX-4 that reveals the semi-quantitative relations between heat source travel speed ( $V_b$ ), power ( $P$ ), and preheat temperature ( $T_0$ ) and the type of dendrite growth. (From Gauman *et al.* [27])

heat source travel speed ( $V_b$ ), power ( $P$ ), and preheat temperature ( $T_0$ ). This map was calculated using a single, integrated average of the  $G^n/V$  ratio to represent the variation in  $G$  and  $V$  that occurs with position in the melt pool. The region of high  $V$  and low  $P$  represents very low heat input conditions that are insufficient to cause melting. At any travel speed, a reduction in power is

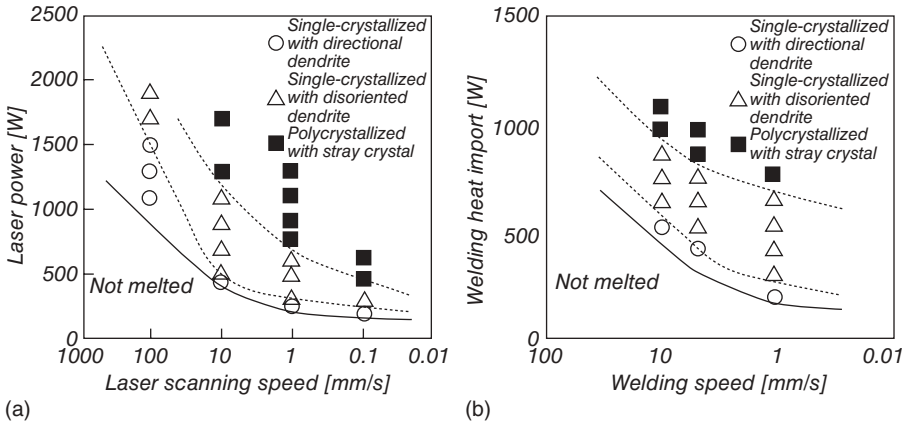


**Figure 6.19** Influence of heat source power and travel speed on stray formation susceptibility of Alloy CMSX-4 for a) laser welds and b) GTA welds. (From Yoshihiro *et al.* [37])

beneficial, and this can be attributed to an increase in the temperature gradient. The results suggest that the effect of heat source travel speed depends on the level of heat source power. At low powers (i.e.,  $< \sim 550$  W), the travel speed has no significant effect. Apparently, at this low power level, the gradient is high enough to avoid reaching the level of undercooling required for nucleation, regardless of the travel speed and resultant growth rate. At higher powers, the calculated results suggest that an increase in travel speed is deleterious to preserving the single crystal columnar zone.

Experimental results generated to date generally confirm the expected influence of power described above, but not travel speed. For example, Yoshihiro *et al.* (37) recently investigated the microstructure of welds on Alloy CMSX-4 prepared over a wide range of powers and travel speeds using both the laser and gas tungsten arc (GTA) heat sources. A summary of their experimental results are shown in Figure 6.19. They identified three types of morphologies: single crystals with directional dendrites that only grow in the [001] direction from the bottom of the weld, single crystal with disoriented dendrites, and welds with stray grains. The single crystal welds with disoriented dendrites simply indicate the presence of dendrites that grew in directions orthogonal to the [001] direction (e.g., as shown previously, for example, as location B in Figure 6.14). These results demonstrate that a reduction in power and increase in travel speed are always beneficial for preserving the single crystal structure *within the range of parameters investigated*. The processing window for the GTA welds is slightly smaller than the laser welds. This is probably associated with the higher intensity heat source of the laser that produces a higher temperature gradient.

Vitek (38) recently improved upon the model developed by Gaumann *et al.* (27) that permitted a more in depth analysis of the effect of travel speed.

In the early model, the  $G^n/V$  ratio was used as an indicator of stray grain formation, and a simple  $G^n/V$  value was calculated at the centerline of the weld and averaged through the thickness. This neglects orientation effects of the solidification front and does not provide an accurate representation of stray grain tendency because the fraction of stray grains does not vary linearly with  $G^n/V$ . With the newer approach of Vitek, the fraction of stray grains was determined directly at discrete positions in the weld pool and used to determine an area weighted average of stray grains as an indicator of stray grain tendency. This improves the accuracy by accounting for the pool shape and variations in  $G$  and  $V$  around the pool.

Figure 6.20 shows the calculated variation in the weighted area fraction of stray grains in the weld ( $\bar{\phi}_c$ ) as a function of welding speed for two three different weld powers. The tendency for stray grain formation decreases ( $\bar{\phi}_c$  decreases) with a decrease in power and an increase in welding speed. Increasing travel speed is particularly advantageous. The only minor exception to this trend is observed at the lowest power and travel speed, where an increase in travel speed causes a small increase in  $\bar{\phi}_c$  initially before  $\bar{\phi}_c$  then decreases with increasing travel speed. These results indicate that, within this regime, the potential beneficial effect of the increase in temperature gradient produced by increasing travel speed is outweighed by the detrimental effect of an increase in growth rate that occurs with increasing travel speed. This can be understood by noting that the formation of strain grains depends on the  $G^n/V$  ratio (where  $n = 3.4$  for CMSX-4, for example). Thus, stray grain forma-

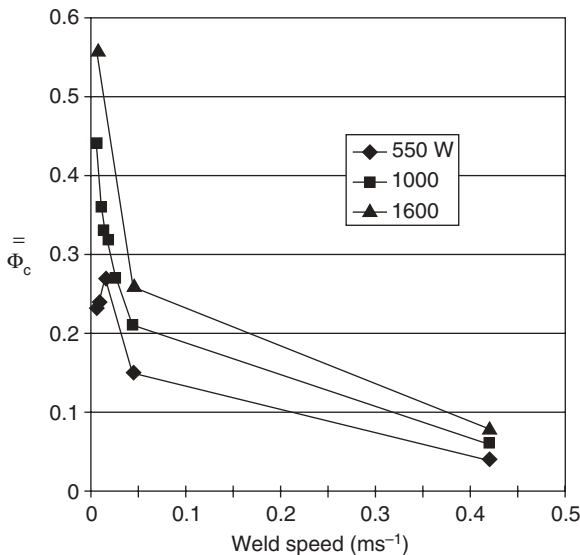


**Figure 6.20** Calculated variation in the weighted area fraction of stray grains in the weld ( $\bar{\phi}_c$ ) as a function of welding speed for two three different weld powers.

tion is more sensitive to  $G$  than  $V$ . The anomalous effect of travel speed at low power has been attributed to changes in weld pool shape. At low powers and travel speeds, the weld pool shape is one in which the area susceptible to stray grain formation is a relatively large fraction of the total weld pool area. However, this trend is quickly diminished with further increases in travel speed.

The substrate orientation relative to the direction of the heat source travel speed can also influence the formation of stray grains. In the results presented thus far, fairly simple orientations were considered in which the direction of the heat source travel was coincident with one of the crystallographic  $\langle 100 \rangle$  easy growth directions. In this case, the dendrite growth velocities across the line of symmetry in the fusion zone are equivalent, and therefore the tendency for stray grain formation is symmetrical about the weld centerline. In real applications, there are likely to be conditions in which welding is required in an asymmetrical direction relative to the easy growth directions. An example of this is shown in Figure 6.21 for the Rene N5 alloy. (24) This photomicrograph is overlaid with the EBSD map and shows extensive stray grain formation only on the right side of the weld.

This effect is caused by differences in the growth angle ( $\psi$  in Eqn. 6.5) across the weld centerline that occurs due to the asymmetric welding condition. On the right side of the weld, the value of  $\psi$  is larger due to the asymmetry. Equation 6.5 indicates that the growth velocity will increase with increasing  $\psi$ . In addition, the temperature gradient in the direction of dendrite growth

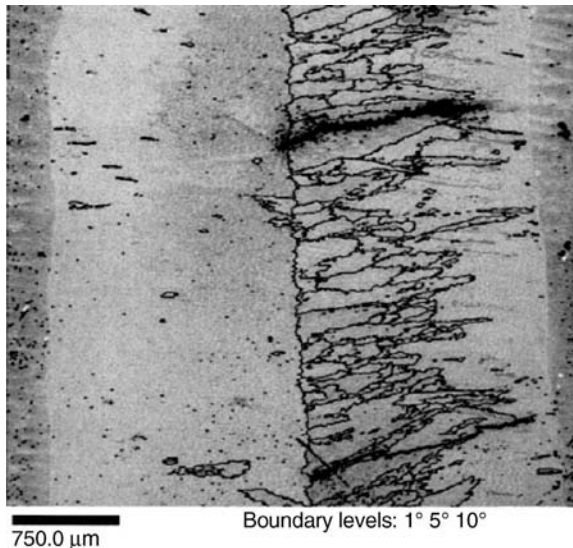


**Figure 6.21** Example of stray grain formation in an asymmetric weld on Alloy Rene 5. (From Park *et al.* [24])

will decrease as  $\psi$  increases.(38) Therefore, the G/V ratio is always lower on the right side of the weld. As a result, the critical G/V ratio required to reach the CET is obtained on the right side of the weld, while the G/V ratio on the left is high enough to generally avoid the CET. This highlights the need for carefully considering the crystal orientation when conducting repairs.

In this same work, Park *et al.*(39) demonstrated that the cooling rate (product of G and V) is symmetrical across the weld centerline. This carries important implications for identifying the mechanism of the CET. It is thought that the CET could also be induced by fragmented dendrites that are pushed into the solidification front by convection. Such dendrites would induce the CET by forming heterogeneous nucleation sites. In this case, convection would become more prevalent as  $G \times V$  decreases, and a decrease in cooling rate would therefore expect to lead to more stray grains. The value of  $G \times V$  was shown to be constant across the fusion line for the weld made in Figure 6.21, but the extent of stray grain formation is not. Therefore, the dendrite fragmentation mechanism is not likely to be operable in fusion welding.

The weld pool shape also has an important effect on maintaining the single crystal structure because it effects the variation in growth velocity with position along the solid/liquid interface and hence the amount of constitutional undercooling. This can be understood by inspection of Eqn. 6.5 and noting that the angles  $\theta$  and  $\psi$  will depend on the pool shape. Rappaz *et al.*(31) used this expression to determine the dendrite growth velocity as a function of position in the weld pool. Equation 6.5 permits direct calculation of the potential  $\langle 100 \rangle$  growth velocities as a function of position for a given solidification front orientation and heat source direction. The active dendrite direction is then chosen by noting that the direction with the lowest growth velocity and concomitant minimum dendrite undercooling will dominate the other possible growth directions. This also coincides with the direction that is most closely aligned to the normal to the solid/liquid interface in which the temperature gradient is the highest and the value of  $\psi$  is the lowest.

Liu and DuPont (25,26,40) recently extended this analysis by combining Eqn. 6.5 with a mathematical model of the melt pool. The 3-D shape of the melt pool was modeled as the segment of an ellipsoid. As shown in Figure 6.22,

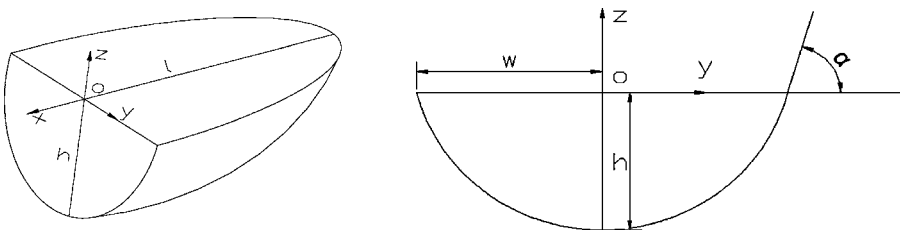


**Figure 6.22** Schematic illustration showing four geometrical parameters ( $w$ ,  $l$ ,  $h$ ,  $\alpha$ ) used to represent the melt pool shape for predicting dendrite growth directions and velocities in single crystals.

four geometrical parameters ( $w, l, h, \alpha$ ) were used to represent the melt pool shape, with  $w$  being half the maximum width,  $l$  being the length between the location of maximum depth (also maximum width) and the trailing point,  $h$  being the maximum depth of the melt pool, and  $\alpha$  being the angle between the substrate surface and the tangent of the melted trace in the transverse cross-section. These melt pool geometrical parameters are controlled by the heat and fluid flow conditions during processing and can be determined either computationally from a heat and fluid flow simulation or experimentally by directly measuring these parameters *in-situ* or after processing.

The melt pool shape corresponding to the solidification front is given by:

$$x = f(y, z) = -A \left[ 1 - \frac{y^2}{B^2} - \frac{(z-D)^2}{(h+D)^2} \right]^{0.5} \quad (\text{Eqn. 6.6})$$

where

$$D = \frac{h^2}{w \tan \alpha - 2h} \quad (\text{Eqn. 6.7})$$

$$A = \frac{l(h+D)}{(2hD+h^2)^{0.5}} \quad (\text{Eqn. 6.8})$$

$$B = \frac{w(h+D)}{(2hD+h^2)^{0.5}} \quad (\text{Eqn. 6.9})$$

The unit vector of the normal to this surface can be represented by the following components:

$$\vec{n} = \frac{1}{\left[ 1 + (\partial f / \partial y)^2 + (\partial f / \partial z)^2 \right]^{0.5}} \begin{vmatrix} 1 \\ -\partial f / \partial y \\ -\partial f / \partial z \end{vmatrix} \quad (\text{Eqn. 6.10})$$

Coupling of this 3-D melt pool model to the dendrite growth analysis represented by Eqn. (6.5) permits detailed investigations of the effects of both melt pool shape and substrate orientation on the dendrite growth directions and velocities. A comparison of experimental and calculated dendrite growth directions are shown in Figure 6.23, and good agreement is observed.

Figure 6.24 compares computational results for two different melt pool shapes. Figures 6.24a and 6.24c show the ratio of dendrite growth velocity to beam velocity as a function of position in the melt pool, and Figures 6.24b and 6.24d show the active dendrite growth directions throughout the weld. The results shown in Figure 6.24a and 6.24b are for a relatively deep weld typical of high power conditions in which the height and width are of equal dimensions. Figures 6.24c and 6.24d show results for a shallower weld typical of lower power conditions in which the depth is only half the width. The results

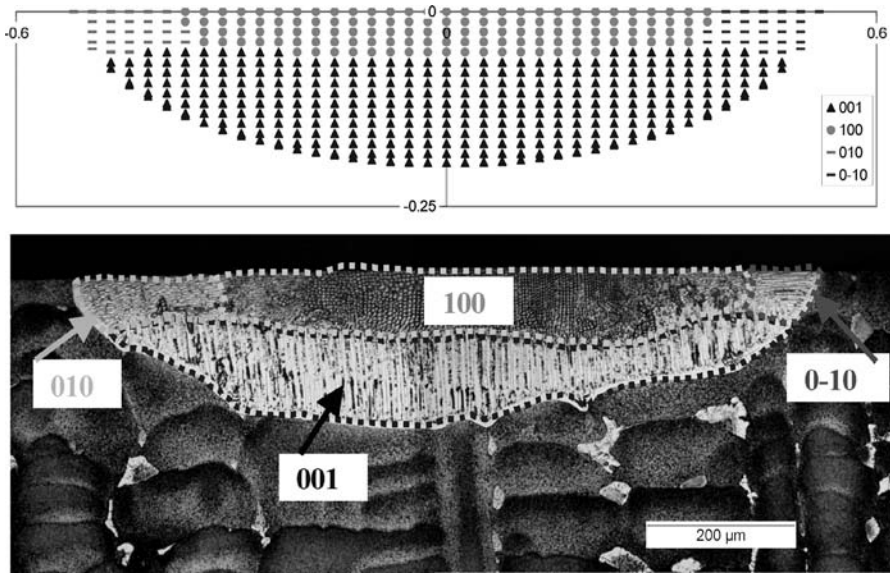


**Figure 6.23** Comparison of experimental and calculated dendrite growth directions for a laser weld made on Alloy CMSX-4. (From Liu and Dupont [25])

represent welds made along the  $[100]$  direction on the  $(100)$  plane. Note that the pool shape has a significant effect on the operable dendrite growth direction and resultant velocity. When the weld is relatively deep, growth is activated in four  $\langle 100 \rangle$  type directions. Dendrites grow from the bottom of the pool in the  $[001]$  direction, from the sides of the pool in the  $[010]$  and  $[0\bar{1}0]$  directions, and from the back of the pool (along the heat source travel direction) in the  $[100]$  direction. The favored growth along the  $[100]$  direction that is coincident with the heat source direction causes the maximum growth velocity to equal that of the heat source velocity in this location, as shown by the velocity results in Figure 6.24a. When the weld is shallow (Figures 6.24c and 6.24d) growth can only occur from the bottom of the pool, and as a result, the maximum growth velocity is only 70% of the heat source velocity. These modeling results explain the experimental data shown in Figure 6.19 on CMSX-4, in which higher powers were observed to promote growth of dendrites from the sides of the weld pool (referred to as “disoriented dendrites”).

The influence of substrate orientation is shown in Figure 6.25 for a weld representative of heat source travel along the  $[01\bar{1}]$  direction on the  $(111)$  plane. This asymmetric orientation causes asymmetry in both the dendrite growth directions and velocities. For example, note that growth from the  $[010]$  direction initiates from the left side of the pool (in the viewing direction shown) and grows well past the weld centerline. Also note that the  $[00\bar{1}]$  growth that is coincident with the heat source direction is skewed off the weld

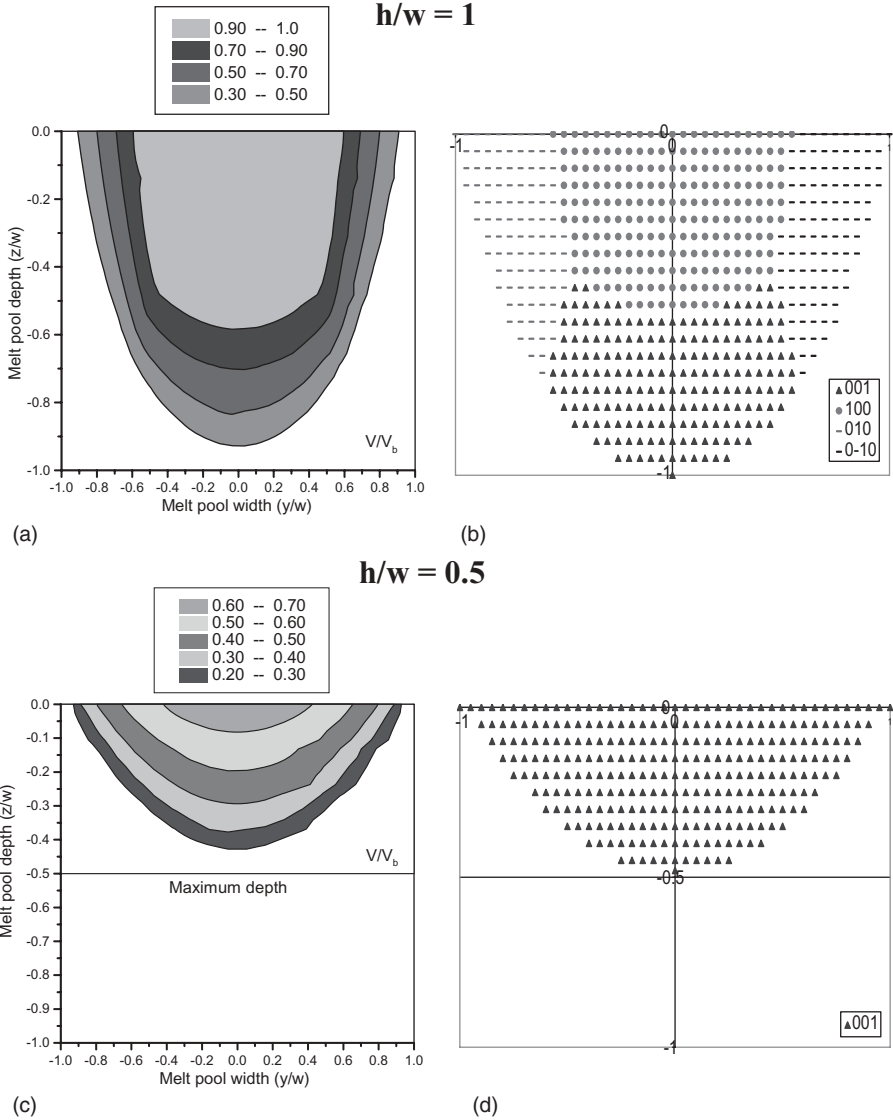


**Figure 6.24** Computational results showing ratio of dendrite growth velocity to beam velocity (a and c) and active dendrite growth directions (b and d) as a function of position in the melt pool for two different melt pool shapes. a and b)  $h/w = 1$ , c and d)  $h/w = 0.5$ .

centerline. As a result of this asymmetry, the dendrite growth velocity can reach values that are 1.4 times that of the heat source velocity near the top of the pool. Such effects account for the asymmetrical stray grain formation previously shown in Figure 6.21.

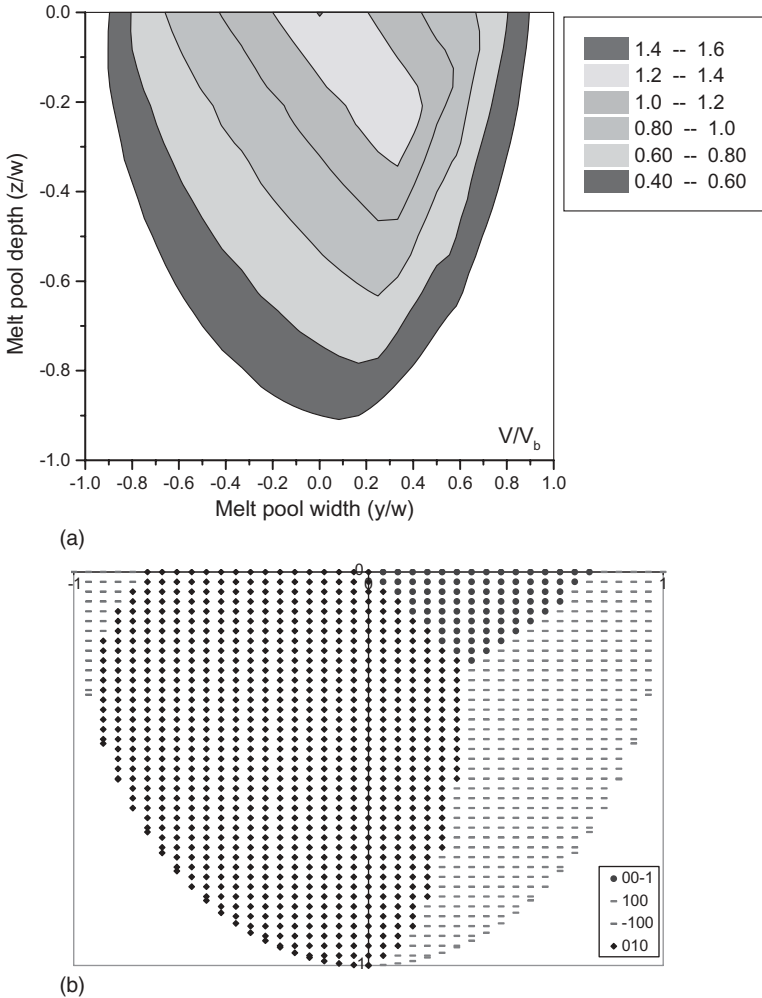


**Figure 6.25** Computational results showing ratio of dendrite growth velocity to beam velocity (a) and active dendrite growth directions (b) as a function of position in the melt pool for a weld representative of heat source travel along the  $[01\bar{1}]$  direction on the  $(111)$  plane.

### 6.3.2 Solidification Cracking

Solidification cracking has also been observed to be a problem in weld repair of single crystals. An example of this can be seen in the previous results shown in Figure 6.21. Note that solidification cracks are only associated with the boundaries from the stray grains that form on the right side of the weld. Solidification cracks, when present, are nearly always observed to occur along the stray grain boundaries. Based on the established mechanisms of solidifica-

tion cracking (described in Chapter 3), this is not surprising since the grain boundaries are the most vulnerable regions of cracking. However, the formation of stray grains does not always lead to cracking, and this suggests that other factors besides the mere presence of stray grains are also important. Previous work (39,41) has shown that the degree of thermo-mechanical stress that develops during solidification and the boundary angle between stray grains also control the cracking susceptibility.

Wang *et al.* (41) recently conducted a set of clever experiments to investigate the influence of grain boundary misorientation on cracking susceptibility on single crystal Alloy MC2. Bi-crystal welds with symmetrical tilt boundaries were prepared as shown in Figure 6.26. Here the tilt boundary ( $\theta$ ) is given by  $\theta = \alpha + \alpha$ , where  $\alpha$  is the angle between the [100] direction of each crystal and the welding direction. For comparison, single crystals were also prepared as shown in Figure 6.26c. The [001] directions were parallel so that  $\theta = \alpha - \alpha = 0$ . This produced a non-zero  $\alpha$  value equivalent to the bi-crystal welds, but led to the production of a single crystal since  $\theta = 0$ . Laser welds were then made on firmly clamped plates at a constant set of weld parameters, but with

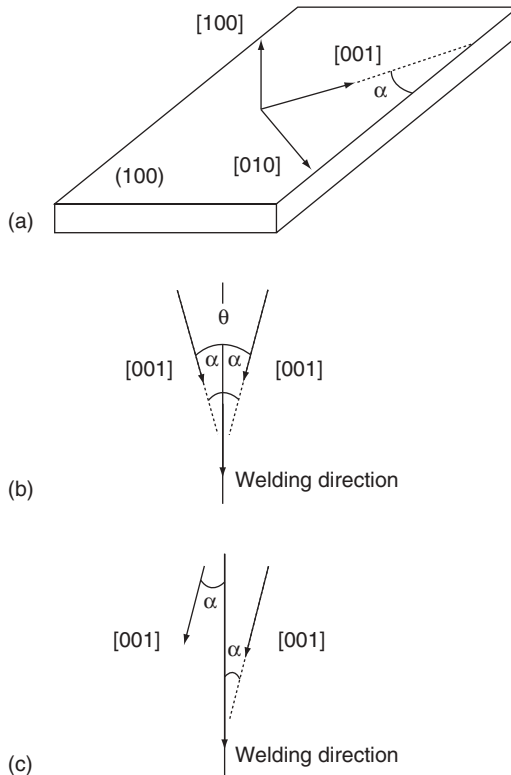


**Figure 6.26** Schematic illustration showing preparation of bi-crystal welds with symmetrical tilt boundaries and preparation of single crystal welds. (From Wang *et al.* [41])

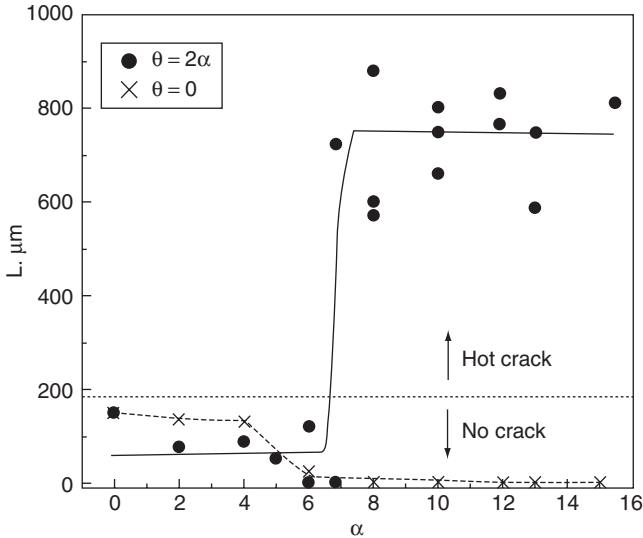


**Figure 6.27** Variation in crack length as a function of angle  $\alpha$  for bi-crystal ( $\theta = 2\alpha$ ) and single crystal ( $\theta = 0$ ) welds on Alloy MC2. (From Wang *et al.* [41])

variations in the  $\alpha$  angle for both the single and bi-crystals. The crack length associated with each weld was then measured. The cracking results are shown in Figure 6.27, which plots the solidification crack length ( $L$ ) as a function of angle  $\alpha$ . Crack lengths below  $\sim 200\mu\text{m}$  (dotted line) were only observed at the start of welding and were caused by the initially unwelded gap between the two plates. These were not solidification cracks. These results show that the single crystals were immune to cracking regardless of the  $\theta$  value, while the bi-crystals exhibited cracking at misorientation angles greater than a critical value of  $\theta \approx 13^\circ\text{C}$ . The cracking severity was essentially independent of  $\theta$  above this critical value.

These results were attributed to the effect of grain boundary misorientation on the grain boundary energy and resultant ability for two grains to bridge and form a solid/solid boundary that resists cracking. When the grain boundary energy ( $\gamma_{\text{gb}}$ ) is less than  $2\gamma_{\text{sl}}$  (the solid/liquid interfacial energy), the liquid that separates dendrites from opposite grains is unstable and the dendrites will bridge to form a solid/solid boundary as soon as they reach an interaction distance  $\delta$ . The value of  $\delta$  represents the thickness of the diffuse interface. For a single crystal,  $\gamma_{\text{gb}} = 0$  and the dendrites within the single crystal grain will thus form a solid coherent network that resists cracking. This is shown schematically in Figure 6.28a for dendrites within a single grain, and the temperature at which the solid network forms is noted as  $T_b^a$ . This position occurs where the solid fraction is on the order of 0.94. In contrast,  $\gamma_{\text{gb}} > 0$  when dendrites from grains with a misorientation angle attempt to bridge to form a solid/solid boundary. The value of  $\gamma_{\text{gb}}$  will increase with increasing misorienta-

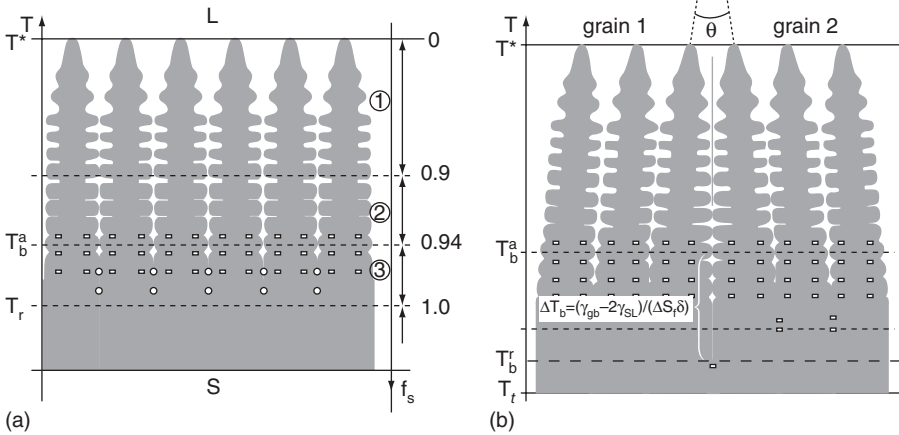


**Figure 6.28** Schematic illustration showing influence of misorientation angle ( $\theta$ ) on stability of intergranular liquid film. a) single crystal in which  $\theta = 0$ , b) bi-crystal for which  $\theta > 0$ .

tion angle up to a maximum value at an angle of  $\theta \approx 15^\circ$ . The value of  $\gamma_{gb}$  remains constant with a further increase in  $\theta$ . Thus, as  $\theta$  increases, a condition will eventually be met in which  $\gamma_{gb} > 2\gamma_{sl}$ . Under this condition, the grain boundary liquid film remains stable until a critical undercooling below  $T_b^a$  is achieved.

The undercooling is given by:

$$\Delta T_b = \frac{\gamma_{gb} - 2\gamma_{sl}}{\Delta S_f \delta} \tag{Eqn. 6.11}$$

Where  $\Delta S_f$  is the entropy of fusion per unit volume and  $\delta$  is the interface thickness. Thus, as  $\theta$  increases, this results in an increase in  $\gamma_{gb}$  and a concomitant increase in  $\Delta T_b$  via Eqn. 6.11. This is shown schematically in Figure 6.28b for the bridging of dendrites across two grains with a misorientation angle. Since the liquid film is stabilized to lower temperatures, the crack susceptible solid + liquid regime is widened and the cracking susceptibility increases as a result. The critical value of  $\theta$  that will cause cracking will obviously depend on the welding parameters and resultant thermo-mechanical stresses that are needed to initiate and propagate a crack. However, the results reveal the important effect of grain boundary misorientation on cracking susceptibility.

### 6.3.3 Optimizing Processing Parameters

The results described above highlight the need for proper control of the welding parameters in order to produce repair welds with the correct shape, growth velocity distribution, and temperature gradient required to produce a

crack-free, single crystal structure. In terms of processing parameters, the weld power, travel speed, and preheat temperature need to be optimized. The single crystal orientation will also play a role. Susceptibility to stray grain formation will be reduced with decreasing power and increasing travel speed. The only possible exception to this trend may occur at low powers and travel speeds, in which an initial increase in travel speed may be detrimental. Increasing the preheat temperature has a detrimental effect because it reduces the temperature gradient. Symmetrical orientations will be least susceptible to stray grain formation, but this has a smaller effect than the welding parameters.(38) Although elimination of stray grain formation will generally reduce solidification cracking problems (because cracks form primarily along stray grain boundaries), this consideration must be balanced with the formation of residual stresses. As discussed above, the reduction of residual stress generally favors conditions that promote stray grain formation—lower travel speeds, higher powers, and the use of preheating. Thus, these two opposing criteria need to be optimized for a given application.

Anderson and DuPont (42) recently conducted an extensive investigation of stray grain formation and solidification cracking susceptibility of Alloy CMSX-4 using the electron beam welding (EBW) and gas tungsten arc welding (GTAW) processes. Figure 6.29 shows the overall stray grain area fraction as a function of beam power and travel speed for the EB welds. Figure 6.29a provides a summary of all the results, and the data is repeated in Figure 6.29b at a reduced range of stray grain area fraction values. The maximum stray grain area fraction is reached at an intermediate travel speed of ~6mm/s. Beyond this value, the stray grain content decreases with increasing travel speed. This variation in stray grain content with travel speed can be explained based on the relative increases in temperature gradient and growth rate with changes in travel speed. When the travel speed is low, initial increases in the speed will cause an increase in the growth rate with only minor changes in the temperature gradient. As a result, the  $G/V$  ratio generally decreases, and the amount of stray grains will therefore increase. Further increases in the travel speed will induce larger increases in the temperature gradient, and, according to Eqn. 6.3,  $G$  has a larger effect on stray grain formation than  $V$  (since  $n = 3.4$ ). Thus, stray grain formation will subsequently decrease with further increases in the travel speed. The negative influence of increasing weld power on stray grain formation can be understood by considering its effect on the temperature gradient. An increase in the power will produce a decrease in the temperature gradient, thus promoting more stray grains to form in the weld.

A limited set of stray grain measurements were performed on the GTA weld structures. Those results are shown in Figure 6.30 along with data from welds conducted using the EB processes at an equivalent absorbed power of 180 watts. Data for several laser welds made at an equivalent absorbed power are also shown for comparison. Note that the GTA welds always exhibit more stray grains than the EB welds, and the laser welds are intermediate to these two cases. It is interesting to note that the trend in stray grain fraction among

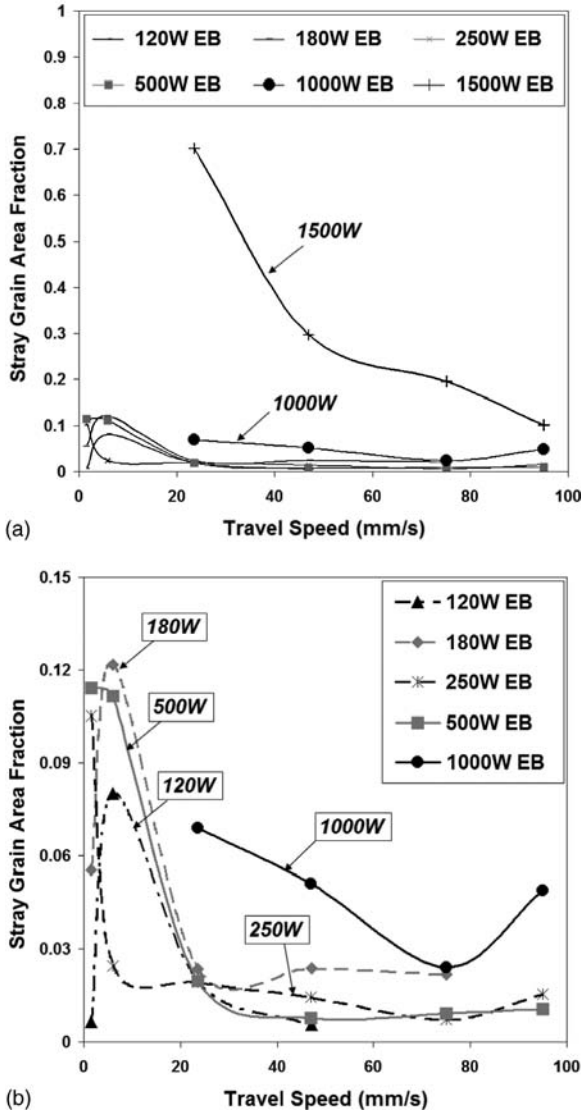


**Figure 6.29** The effect of welding parameters on stray grain area fraction within the electron-beam weld structures for the  $[100] \parallel (001)$  substrate orientation in alloy CMSX-4. (From Anderson and DuPont [42]. Courtesy the American Welding Society.)

the three processes correlates to the differences in energy density. The energy density of the heat source influences the temperature gradient in the weld pool, in which welds produced with higher energy density processes will experience steeper temperature gradients. Thus, welds produced with higher energy density processes are expected to exhibit lower stray grain fractions than welds

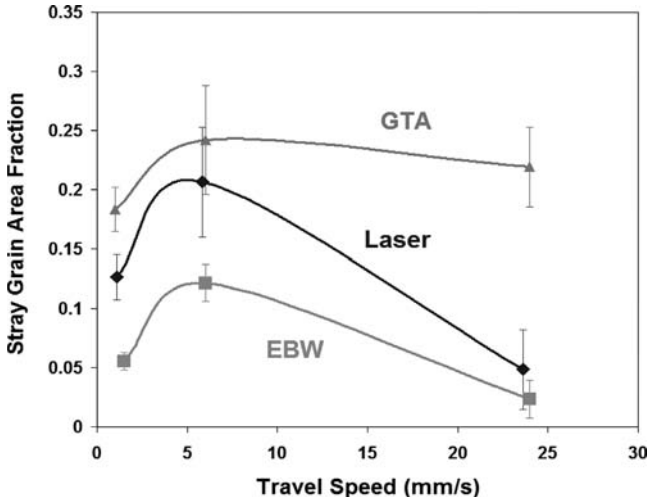


**Figure 6.30** The effect of welding process on stray grain area fraction in alloy CMSX-4 for an equivalent absorbed power over a range of travel speeds. (From Anderson and DuPont [42]. Courtesy the American Welding Society.)

made using lower energy density processes at equivalent levels of input power and travel speed. This accounts for the relatively high stray grain content of the GTA welds.

Figure 6.31 summarizes the cracking susceptibility of all the EB (Figure 6.31a) and GTA (Figure 6.31b) welds as a function of absorbed power and travel speed. These results clearly show that crack-free welds are promoted by low heat inputs (i.e., low power and high travel speed). This result is not surprising, considering the influence of processing parameters on stray grain formation, and the link between stray grain formation and cracking susceptibility. Since stray grains can generally be reduced under low heat input conditions, the cracking susceptibility will also be reduced as the heat input is decreased. The reduced heat input may also be beneficial due its effect on solidification shrinkage and size of the crack-susceptible mushy zone. The smaller welds produced under lower heat input conditions will exhibit reduced strain from solidification shrinkage along with a smaller crack-susceptible mushy zone, and these factors may also contribute to the reduced cracking susceptibility.

Careful examination of Figure 6.31 indicates there is a significant difference in the range of processing parameters between the two processes that can be used to produce crack-free welds. This is shown in Figure 6.32, which compares the position of the crack/crack-free boundary for each process. Although the position of these boundaries are only approximate and apply only to the conditions used in this investigation (42), the results clearly demonstrate the beneficial effect of the EB process over the GTA process. Reference to Figure 6.30 indicates this can likely be attributed to differences in power density and

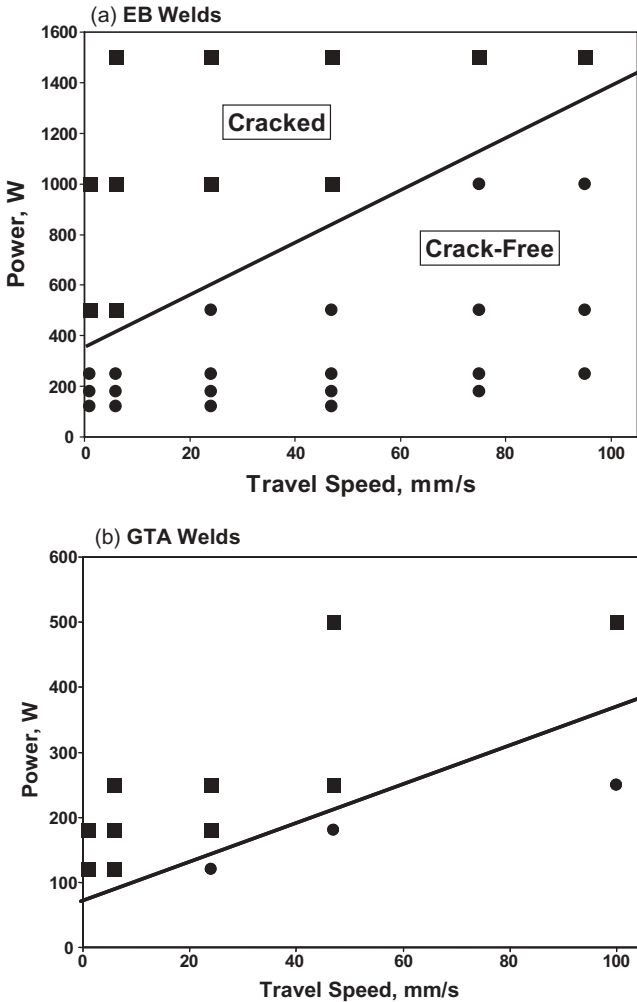


**Figure 6.31** Solidification cracking susceptibility in EB welds (a) and GTAW welds (b) as a function of absorbed power and travel speed for alloy CMSX-4. (From Anderson and DuPont [42]. Courtesy the American Welding Society.)

resultant temperature gradient. The higher power density and concomitant temperature gradient of the EB process reduces the stray grain content and, therefore, helps reduce the incidence of cracking.

As previously mentioned, successful weld repair of single crystal turbine blades requires minimizing both the amount of stray grains and solidification cracks. Fortunately, a reduction of the stray grain content typically leads to crack-free welds, and each defect, in turn, can be minimized by reductions in the heat input. In view of this, Figure 6.33 summarizes the influence of heat input on stray grain area fraction and cracking susceptibility for the EB welds. These results show that, for the current conditions, there is a critical heat input

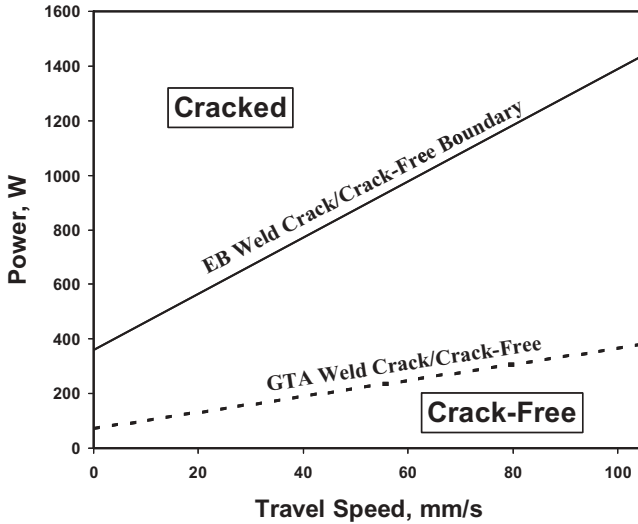


**Figure 6.32** Comparison of Crack/Crack-Free processing regimes for the EB and GTA welds made on single crystal alloy CMSX-4. (From Anderson and DuPont [42]. Courtesy the American Welding Society.)

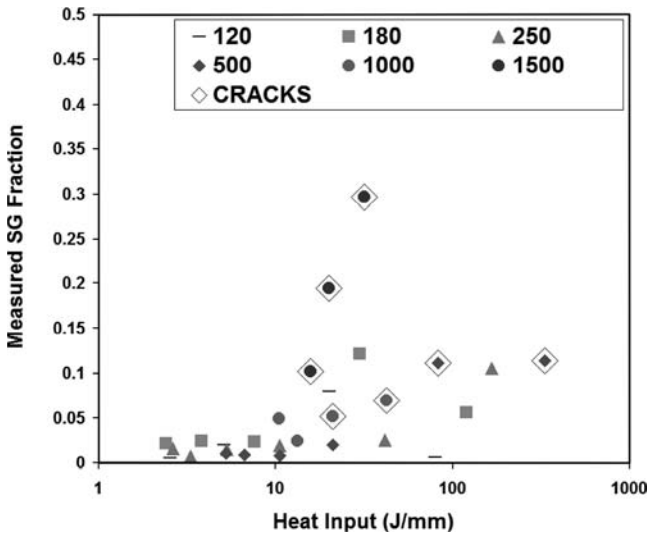


**Figure 6.33** Effect of heat input on the stray grain area fraction and solidification cracking susceptibility in EB welds in single crystal alloy CMSX-4. (From Anderson and DuPont [42]. Courtesy the American Welding Society.)

of  $\sim 13\text{J/mm}$ . Welds made below this heat input level are consistently crack-free with very low stray grain contents ( $<5\%$ ).

It is important to note that effective weld repairs can still be accomplished when small amounts of stray grains form. Stray grain formation (and the potential for associated cracking) typically occurs in the top section of the weld repair in which the undercooling is the highest. This undesirable zone can be re-melted by subsequent layers and replaced with a single crystal zone under the right set of conditions. An example of this is shown in Figure 6.34, which

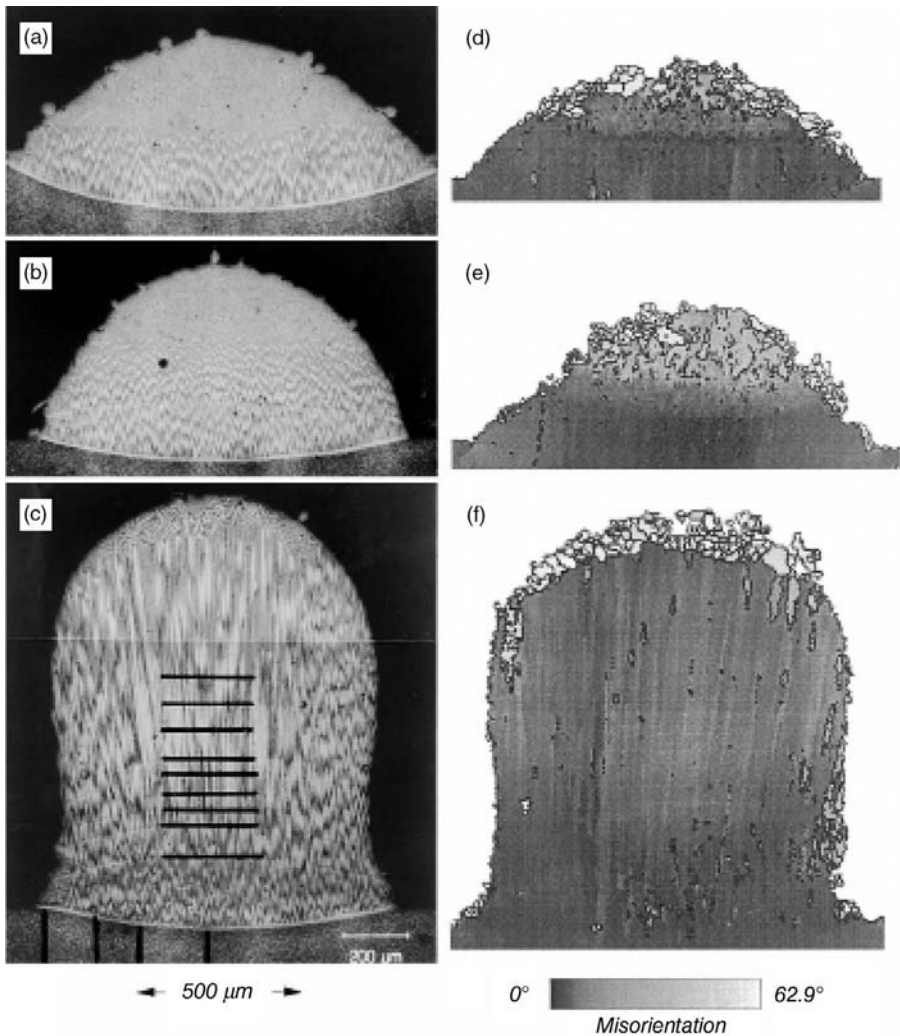


**Figure 6.34** Light optical photomicrographs (left) and EBSD patterns (right) of weld repairs made on Alloy CMSX-4 after one (a and d), two (b and e), and ten (c and f) layers of weld have been deposited. (From Gauman *et al.* [30])

shows weld repairs made on Alloy CMSX-4 after one, two, and ten layers of repair weld have been deposited. (30) The stray grains present after the first and second layer occupy a significant fraction of the total layer thickness. However, most of these areas are re-melted and replaced by single crystal layers by subsequent passes. This approach requires that the depth of melting from the subsequent layer is greater than that of the stray grain depth from the previous layer. Parameters required to achieve this can be estimated through heat and fluid flow simulations.

## REFERENCES

1. Radavich, J. F. and Fort, A. 1994. "Effects of long term exposure in alloy 625 at 1200 F, 1400 F, and 1600 F," *Superalloys 718, 625, 706 and Various Derivatives*, TMS, Warrendale, PA, pp. 635–647.
2. Sims, C. T., Stoloff, N. S., and Hagel, W. C. 1987. *Superalloys II*, John Wiley and Sons, New York, pp. 27–188, 495–515.
3. Brooks, J. W. and Bridges, P. G. 1988. *Metallurgical Stability of Inconel Alloy 718, Superalloys 1988*, ed. S. Reichman, D. N. Duhl, G. Maurer, S. Antolovich, and C. Lund, The Metallurgical Society of AIME, pp. 33–42.
4. Radavich, J. F. and Korth, G. E. 1992. *High Temperature Degradation of Alloy 718 after Longtime Exposures, Superalloys 1992*, ed. S. D. Antolovich, R. W. Stusrud, R. A. MacKay, T. Khan, R. D. Kissinger, and D. L. Klarstrom, The Metallurgical Society of AIME, pp. 497–506.
5. Campo, E., Turco, C., and Catena, V. 1985. The Correlation between Heat Treatment, Structure, and Mechanical Characteristics in Inconel 718, *Metallurgical Science and Technology*, 3, pp. 16–21.
6. Lu, Q. PhD dissertation, 1999. The Ohio State University.
7. Mehl, M. and Lippold, J. C. 1997. *Effect of  $\delta$ -phase precipitation on the repair weldability of Alloy 718. 4th Int. Symposium on 718, 625, 706, and Derivatives*. Edited by E. A. Loria, Pub. By TMS, Warrendale, PA, pp. 731–742.
8. Hooijmans, J. W., Lin, W., and Lippold, J. C. 1997. *Effect of multiple postweld heat treatments on the weldability of Alloy 718. 4th Int. Symposium on 718, 625, 706, and Derivatives*. Edited by E. A. Loria, Pub. By TMS, Warrendale, PA, pp. 721–730.
9. Bowers, R. J., Lippold, J. C., and Hooijmans, J. W. 1997. The Effect of Composition and Heat Treatment Cycles on the Repair Weldability of Alloy 718, *Material Solutions '97*, ASM International, Indianapolis, 14–18 September 1997.
10. Qian, M. and Lippold, J. C. 2003. Liquation Phenomena in the Simulated Heat-affected Zone of Alloy 718 after Multiple Postweld Heat Treatment Cycles, *Welding Journal*, 82(6): 145s–150s.
11. Qian, M. and Lippold, J. C. 2003. The Effect of Rejuvenation Heat Treatments on the Repair Weldability of Wrought Alloy 718, *Materials Science and Engineering A*, 340(1–2): 225–231.
12. Qian, M. and Lippold, J. C. 2003. The Effect of Annealing Twin-Generated Special Grain Boundaries on HAZ Liquation Cracking of Nickel-base Superalloys, *Acta Materialia*, 51(12): 3351–3361.

13. Qian, M. and Lippold, J. C. 2007. Investigation of grain refinement during a rejuvenation heat treatment of wrought alloy 718, *Materials Science and Engineering A*, 456(2007): 147–155.
14. Ranganathan, S. 1966. On the geometry of coincident site lattices, *Acta. Cryst.*, Vol. 21, pp. 197–199.
15. Palumbo, G. and Aust, K. T. 1992. Special properties of sigma grain boundaries, *Material Interfaces*, D. Wolf and S. Yip, eds., Chapman and Hall: London, pp. 190–211.
16. Lehockey, E. M. and Palumbo, G. 1997. On the creep behavior of grain boundary engineered nickel, *Materials Science and Engineering A*, 237, pp. 168–172.
17. Palumbo, G., King, P. G., Aust, K. T., Erb, U., and Lichtenberger, P. C. 1991. Grain boundary design and control for intergranular stress-corrosion resistance, *Scripta Metallurgica et Materialia*, Vol. 25, pp. 1775–1780.
18. Qian, M. and Lippold J. C. 2002. Effect of Multiple Postweld Heat Treatment Cycles on the Weldability of Waspaloy, *Welding Journal*, 81(11): 233s–238s.
19. Qian, M. and Lippold J. C. 2003. The Effect of Grain Boundary Character Distribution on the Repair Weldability of Waspaloy, *Trends in Welding Research VI*, Proc. of the 6th International Conference, ASM International, pp. 603–608.
20. Cullison, A. 2003. Power industry experiences surge in welding research, *Welding Journal*, 82(9): 40–43.
21. David, S. A., Vitek, J. M., Babu, S. S., Boatner, L. A., and Reed, R. W. 1997. Welding of nickel base superalloy single crystals, *Science and Technology of Welding and Joining*, (2): 79–88.
22. Vitek, J. M., David, S. A., and Boatner, L. A. 1997. Microstructure development in single crystal nickel base superalloy welds, *Science and Technology of Welding and Joining*, (2): 109–118.
23. David, S. A. and Vitek, J. M. 1989. Correlation between solidification parameters and weld microstructures, *International Materials Reviews*, (5): 213–245.
24. Park, J. W., Babu, S. S., Vitek, J. M., Kenik, E. A., and David, S. A. 2003. Stray grain formation in single crystal Ni-base superalloy welds, *Journal of Applied Physics*, 94(6): 4203–4209.
25. Liu, W. and DuPont, J. N. 2004. Effects of melt-pool geometry on crystal growth and microstructure development in laser surface-melted superalloy single crystals. Mathematical modeling of single crystal growth in a melt pool (Part I), *Acta Materialia*, (52): 4833–4847.
26. Liu, W. and DuPont, J. N. 2005. Direct laser deposition of a single crystal Ni3Al-based IC221W alloy, *Metallurgical and Material Transactions A*, 36A: 3397–3406.
27. Gauman, M., Bezencon, C., Canalis, P., and Kurz, W. 2001. Single-crystal laser deposition of superalloys: processing-microstructure maps, *Acta Materialia*, 49: 1051–1062.
28. Narasimhan, S. L., Copley, S. M., Van Stryland, E. W., and Bass, M. 1979. Solidification of a laser melted nickel-base superalloy, *Metallurgical and Material Transactions A*, 10A: 654–655.
29. Yang, S., Huang, W., Liu, W., Zhong, M., and Zhou, Y. 2002. Development of microstructures in laser surface remelting of DD2 single crystal, *Acta Materialia*, 50: 315–325.

30. Gauman, M., Henry, S., Cleton, F., Wagniere, J. D., and Kurz, W. 1999. Epitaxial laser metal forming: analysis of microstructure formation, *Materials Science and Engineering A*, 271: 232–241.
31. Rappaz, M., David, S. A., Vitek, J. M., and Boatner, L. A. 1989. Development of microstructures in Fe-15Ni-15Cr single crystal electron beam welds, *Metallurgical and Material Transactions A*, 20A: 1125–1138.
32. Brooks, J. A. and Thompson, A. 1991. Microstructural development and solidification cracking susceptibility of austenitic stainless steel welds, *International Materials Reviews*, 36: 16–44.
33. Hunt, J. D. 1983. Steady state columnar and equiaxed growth of dendrites and eutectic, *Materials Science and Engineering A*, 65: 75–83.
34. Burden, M. H. and Hunt, J. D. 1974. Cellular and dendritic growth. II., *Journal of Crystal Growth*, 22(2): 109–116.
35. Kurz, W., Giovanola, B., and Trivedi, R. 1986. Theory of microstructural development during rapid solidification, *Acta Materialia*, 34(5): 823–830.
36. Gauman, M., Trivedi, R., and Kurz, W. 1997. Nucleation ahead of the advancing interface in directional solidification, *Materials Science and Engineering A*, 226: 763–769.
37. Yoshihiro, F., Saida, K., and Nishimoto, K. 2006. Study of microstructure in surface melted region of Ni base single crystal superalloy CMSX-4, *Materials Science Forum*, 512(5): 313–318.
38. Vitek, J. M. 2005. The effect of welding conditions on stray grain formation in single crystal welds—theoretical analysis, *Acta Materialia*, 53: 53–67.
39. Park, J. W., Vitek, J. M., Babu, S. S., and David, S. A. 2004. Stray grain formation, Thermomechanical stress and solidification cracking in single crystal nickel base superalloy welds, *Science and Technology of Welding and Joining*, 9(6): 472–482.
40. Liu, W. and DuPont, J. N. 2005. Effects of crystallographic orientations on crystal growth and microstructure development in laser surface-melted superalloy single crystals. Mathematical modeling of single crystal growth in a melt pool (Part II), *Acta Materialia*, 53: 1545–1558.
41. Wang, N., Mokadem, S., Rappaz, M., and Kurz, W. 2004. Solidification cracking of superalloy single crystal and bi-crystals, *Acta Materialia*, 52: 3173–3182.
42. Anderson, T. D. and DuPont, J. N. 2009. Stray grain formation and solidification cracking susceptibility of single crystal Ni-base superalloy CMSX-4, submitted for publication to the *Welding Journal*, August, 2008.

# Dissimilar Welding

Ni-base alloys are often welded to dissimilar alloys, particularly steels, and Ni-base filler metals are used to join other dissimilar combinations, such as pressure vessel steels to stainless steels. Proper selection of filler metals for these dissimilar combinations is essential and knowledge of the metallurgical behavior of dissimilar welds is required to prevent problems during fabrication or in service. This chapter describes the welding metallurgy and weldability associated with dissimilar welds that involve Ni-base alloys and filler metals. In particular, the use of Ni-base filler metals for cladding and for transition joints critical to the power generation industry is discussed in detail.

## 7.1 APPLICATION OF DISSIMILAR WELDS

There are a number of situations where dissimilar combinations of Ni-base alloys provide engineering advantages. In general, these applications take advantage of several inherent properties of Ni-base alloy welding materials that make them ideal choices for specific types of applications. Each application in which the Ni-base welding material is used to weld other base metals usually takes advantage of unique characteristics of the as-cast or as-deposited weld metal that allows it to provide equal to or better properties than that of the wrought base metal. In the first case, Ni-base filler metals (normally the solid-solution strengthened alloys) are used to weld overlay structural materials, such as Cr-Mo alloy steel waterwall tubing in power boilers. In another case, Ni-base filler metals are used to join low alloy steels to austenitic stainless steels in power plant applications requiring elevated temperature creep and thermal-fatigue resistance. When austenitic stainless steels are welded directly to carbon steels either by using autogenous “pressure welding” or by using an austenitic stainless steel filler metal, the difference in coefficient of thermal expansion (CTE) can lead to fatigue and creep failures in the HAZ of the carbon steel after extended exposure at elevated temperature.(1) The use of

---

*Welding Metallurgy and Weldability of Nickel-Base Alloys*, by John N. DuPont, John C. Lippold, and Samuel D. Kiser  
Copyright © 2009 John Wiley & Sons, Inc.

a Ni-base alloy filler metal provides a gradation of CTE across the weld joint that better distributes stresses resulting from CTE differences between the carbon steel and stainless steel at elevated temperatures. There are also metallurgical advantages realized by the use of Ni-base filler metals for this dissimilar combination. These are described in more detail in Section 7.3.2.

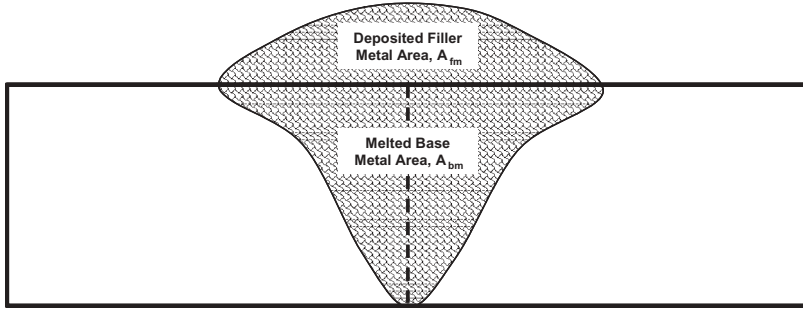
Another type of application takes advantage of the superior corrosion resistance of some Ni-base weld metals in the as-deposited condition when used to weld lower alloy corrosion resistant base metals.(2) This type of application overcomes the well-known pitting and crevice attack of matching weld metals caused by segregation of the cast weld structure by purposely choosing “over-alloyed” weld metals for certain applications. Likewise, in galvanically-active corrosion environments, the over-alloyed weld metals often provide more noble welds so that the resultant corrosion attack is spread over a large area of anodic base metal and thus protects the welds against accelerated corrosion attack.(2) Finally, there are other considerations such as low temperature impact strength in the as-welded condition that lead to the selection of the ERNiCrMo-3 and ERNiCrMo-4 filler metals to be chosen for welding cryogenic steels such as 5% and 9% Ni steels.(3) Another classic case of dissimilar welding is when nickel alloys are chosen to weld a wide variety of cast iron materials.

## 7.2 INFLUENCE OF PROCESS PARAMETERS ON FUSION ZONE COMPOSITION

The weld deposit that develops during fusion welding of dissimilar alloys will achieve a chemical composition intermediate between the two alloys. The chemical composition will, in turn, have a significant influence on the fusion zone microstructure, and its resultant corrosion resistance, mechanical properties, and weldability. Thus, it is useful to consider how variations in processing parameters affect the weld metal composition for dissimilar weld applications. The final fusion zone composition will depend on the individual compositions of the base and filler metals and the degree of dilution of the filler metal by the base metal(s). Note that dilution is defined in terms of the change of filler metal composition by mixing with the base metal. For example, a weld with 20% dilution will consist of 80% filler metal and 20% base metal. Figure 7.1 shows this schematically in the simplest form, where a single pass weld is deposited onto a base metal of a different composition. The degree of mixing for the simple case illustrated is defined by the dilution,  $D$

$$D = \frac{A_{bm}}{A_{bm} + A_{fm}} \quad (\text{Eqn. 7.1})$$

where  $A_{bm}$  is the melted cross-sectional area of the base metal and  $A_{fm}$  is the cross-sectional area of the deposited filler metal. The concentration of any



$$\text{Dilution (\%)} = \frac{A_{bm}}{A_{bm} + A_{fm}} \times 100$$

**Figure 7.1** Simple sketch of weld made with deposited filler metal for dilution calculations.

element *i* in the fusion zone ( $C_{fz}^i$ ) can be determined through knowledge of dilution and concentration of the element in the base metal ( $C_{bm}^i$ ) and filler metal ( $C_{fm}^i$ ) via:

$$C_{fz}^i = DC_{bm}^i + (1 - D)C_{fm}^i \tag{Eqn. 7.2}$$

This assumes sufficient mixing occurs in the liquid state so that macroscopic composition gradients are not formed in the weld deposit. Previous work (4,5) has shown that concentration gradients in dissimilar metal welds typically exist only near the fusion boundary over distances on the order of a few hundred microns.

Equation 7.2 predicts that the fusion zone composition will vary linearly with dilution from the filler metal composition (for  $D = 0$ ) to the base metal composition (for  $D = 1$ ). The dilution level is strongly affected by the welding parameters.(6,7) In simple single pass welds, energy and mass balance considerations can be used to show that the dilution depends on the heat source power ( $VI$ ) and volumetric filler metal feed rate ( $V_{fm}$ ) as (4):

$$D = \frac{1}{1 + \frac{V_{fm}E_{bm}}{\eta_a\eta_m VI - E_{fm}V_{fm}}} \tag{Eqn. 7.3}$$

Where  $\eta_a$  and  $\eta_m$  are the energy transfer and melting efficiencies and  $E_{bm}$  and  $E_{fm}$  are the melting enthalpies of the base metal and filler metal. Values for  $\eta_a$  for various processes have been measured by calorimetric means and are well known (8), while values for  $\eta_m$  can be estimated based on knowledge of the processing parameters.(9) The quantity  $\eta_a\eta_m VI$  represents the melting power,

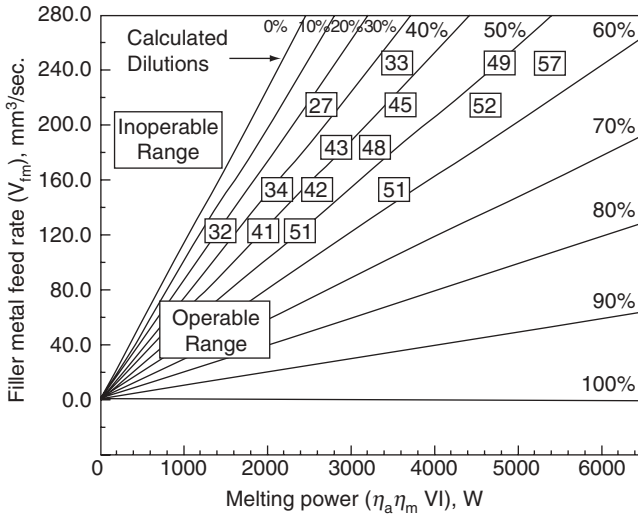


**Figure 7.2** Effect of filler metal feed rate and power on dilution for a stainless steel. (From DuPont and Marder [4])

which is the fraction of heat source power that is actually used for melting the base metal and the filler metal.

Figure 7.2 shows a graphical plot of Equation 7.3 that is useful for illustrating the effects of processing parameters on dilution.(4) The filler metal feed rate ( $V_{fm}$ ) is plotted as a function of the melting power ( $\eta_a \eta_m VI$ ) and the slopes which correspond to various calculated dilution levels are plotted in 10% increments. In this example, Type 308 stainless steel is deposited onto carbon steel. A boundary between an “inoperable range” and “operable range” is also plotted. This line is also denoted as the 0% dilution line, since this represents the condition where no mixing would occur between the base metal and filler metal. Measured data for deposition of Type 308 stainless steel onto carbon steel by the submerged arc welding process are also plotted for validation of the calculations. For a fixed filler metal feed rate, the dilution increases with increasing power. In this case, the extra melting power can not be absorbed by the filler metal if the filler metal feed rate is fixed, so the base metal absorbs the extra melting power which results in an increase in the melting rate of the base metal with an accompanying increase in dilution. A filler metal feed rate of zero corresponds to an autogenous weld which always has 100% dilution, as shown in the diagram. Conversely, for a given power, an increase in the filler metal feed rate results in a decrease in dilution. In this case, dilution decreases because the cross sectional area of deposited filler metal increases. In addition, the filler metal now consumes a larger portion of the total power and less energy is available to melt the base metal. As a result, the base metal volumetric melting rate decreases and dilution is reduced. The behavior exhibited

in Figure 7.2 would be similar for Ni-base filler metals. This is of particular importance in processes such as gas tungsten arc welding (GTAW) and plasma arc welding (PAW) where wire feed rate is independent of welding current. Power ratio and energy density equations have been developed by Gandy *et al.* to describe this behavior.(10)

Although the heat source travel speed does not appear in Equation 7.3, it affects the dilution indirectly by affecting the melting efficiency. Melting efficiency increases with increasing travel speed.(8,9) This increase in melting efficiency produces a concomitant increase in dilution via Equation 7.3. This trend has been observed experimentally.(4,11) The consumable electrode arc processes generally do not permit independent control over the filler metal feed rate and power. For these processes, the filler metal feed rate is set and the electrical characteristics of the power source control the required current (power) level. With the non-consumable electrode processes, the filler metal feed rate and power can be controlled independently, and dilution is generally easier to control with these processes (for example, the gas tungsten arc cold wire feed process). The welding processes type will affect dilution because it controls the energy transfer and melting efficiency values ( $\eta_a$  and  $\eta_m$ ). Thus, welds made with different processes under identical welding parameters will generally produce different dilution levels. Similarly, welds made with different filler metals or base metals under identical processing conditions will also generally produce different dilution levels due to changes in the melting enthalpy values ( $E_{bm}$  and  $E_{fm}$ ). Additional factors will affect the dilution level in multipass welds. For example, an increase in the degree of overlap between adjacent passes will decrease the dilution because less base metal is melted. An increase in the preheat or interpass temperature will increase the dilution because it reduces the amount of energy required for melting the base metal, thus increasing the base metal melting rate. In some cases, such as welding cast iron, it is imperative to use preheat to minimize the formation of martensite but welding parameters must be chosen judiciously to avoid excessive dilution. Such factors need to be considered when fusion zone composition control is important in dissimilar weld applications.

### 7.3 CARBON, LOW ALLOY AND STAINLESS STEELS

Ni-base alloys are often used for dissimilar welds where carbon steels are joined to Ni-base alloys or stainless steels. They are also used for cladding carbon steels in applications in which stainless steel cladding does not provide sufficient corrosion protection. In most cases, the solid-solution strengthened Ni-base alloys are used for these applications since the added strength that would be gained by the use of precipitation strengthened alloys would significantly overmatch the strength of the steel and the postweld heat treatment (PWHT) necessary to achieve this strength is incompatible with most steels. However, in applications in which valves for the oil field applications are

overlaid with Alloy 625 for resistance to hydrogen sulfide ( $H_2S$ ) SCC, some valves such as those made of steel alloy 8630 benefit from being overlaid with precipitation-strengthened filler metals (Alloy 725). These filler metals can be strengthened to a beneficial level by PWHT that is required to temper the martensite that forms in the HAZ of the steel.

The large composition differences between the Ni-base alloys and steels can result in a wide range of weld metal microstructures and properties. In most cases, dilution must be carefully controlled to prevent the formation of intermediate phases that can lead to embrittlement or compromise weldability. In general, the dissimilar weld metals tend to be austenitic due to the strong austenite stabilizing effect of Ni. However, the solidification temperature range of the weld metal is significantly affected from dilution by the Fe-based alloys. Dissimilar welds between Ni-base alloys and steels also exhibit a composition transition region between the diluted weld metal and the base metal. In many cases, this transition region may contain a layer of martensite. The following sections describe microstructure evolution in the weld metal and along the fusion boundary in dissimilar welds where Ni-base alloys are used to join steels.

### 7.3.1 Determining Weld Metal Constitution

The weld metal dilution formula provided in Equation 7.1 can be used to calculate the composition of Ni-base weld metals diluted by steels. In almost all cases (unless dilution by the steel is extremely high), the weld metal will be fully austenitic (fcc-Ni) with the possibility of some fraction of second phase formation due to solidification segregation. For welds made to carbon steels or stainless steels the Schaeffler Diagram (12) can be used to determine the constitution of the weld metal. This diagram was developed to predict the weld metal constitution (phase balance) of stainless steels, but can be applied to dissimilar welds with carbon steels and stainless steels.

The Schaeffler Diagram is shown in Figure 7.3. Although the Ni-equivalent axis does not allow the composition of Ni-base filler metals to be plotted, virtual tie lines can be used to determine the effect of base metal dilution and provide insight into the microstructure that can form in the composition transition zone adjacent to the fusion boundary. Tie lines between a hypothetical Ni-base filler metal and a carbon steel and austenitic stainless steel are superimposed in Figure 7.3. Note that for the dissimilar weld to the austenitic stainless steel, the tie line lies entirely within the austenite phase field and predicts that weld metals of this combination will be fully austenitic under all conditions. For dissimilar welds with carbon steels, all dilution levels below approximately 75% will be fully austenitic. Above 75% dilution (75% carbon steel, 25% Ni-base filler metal) some martensite will form in the weld metal and above 85% the microstructure will be fully martensitic. Dilution levels above 50–60% are difficult to achieve in practice, so the development of a weld metal

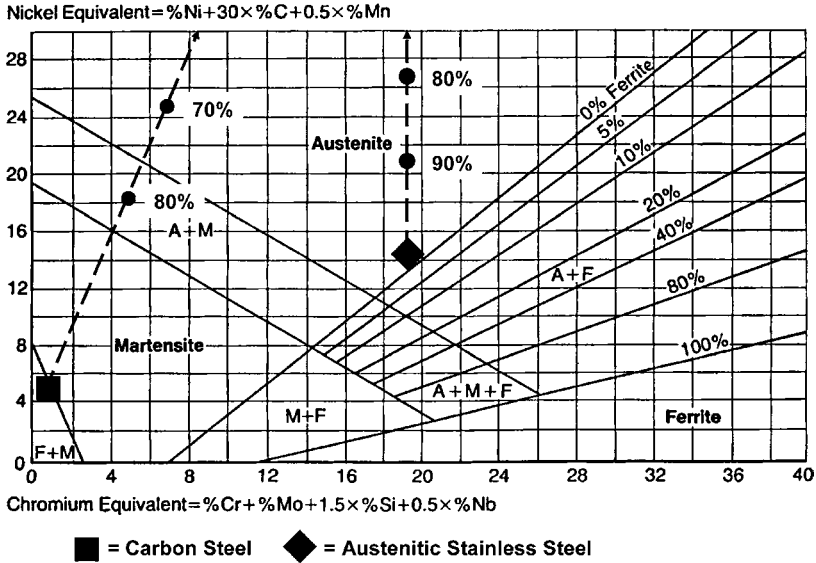


**Figure 7.3** The Schaeffler Diagram with tie lines to a Ni-base alloy superimposed for a carbon steel and austenitic stainless steel. The percentages along the tie lines represent the dilution level.

that contains substantial martensite is unlikely. However, a composition transition zone must exist at the fusion boundary that spans the composition range represented by the Schaeffler diagram and predicts that some martensite must be present at the fusion boundary. This will be described in more detail in the next section.

It should be pointed out that the Schaeffler diagram only predicts formation of three major phases (fcc austenite, bcc ferrite, and bct martensite). Other constituents, including carbides, laves phase, sigma phase, etc., that can potentially form in these dissimilar weld metals are not predicted using the Schaeffler diagram. The formation of carbides can be of particular interest, especially in dissimilar combinations with carbon steels where the composition of the diluted filler metal can introduce high levels of carbon. Unfortunately, there are not simple constitution diagrams available to predict the formation of these secondary constituents. The use of computational techniques (as described in Chapter 2) can be useful in predicting the constitution of dissimilar weld metals between Ni-base alloys and steels. It should be noted, however, that these calculated phase stability diagrams are based on equilibrium thermodynamic conditions and cannot compensate for the rapid cooling rates and solidification segregation associated with the weld metal. For this reason, they should be used as an indicator of potential constituents only, not a predictor of weld metal microstructure.

### 7.3.2 Fusion Boundary Transition Region

Predicting the transition region microstructure can be difficult, since it may change dramatically over a very short distance (~1 mm). In dissimilar combinations of Ni-base filler metals and steel base metals, the microstructure of this region may differ significantly from both the bulk weld metal and HAZ and is subject to local compositional gradients and diffusional effects. For example, if the base metal has a higher carbon content than the weld metal (which is usually the case for carbon steels and most Ni-base filler metals), carbon will diffuse (or “migrate”) from the HAZ to the fusion zone during welding or PWHT.(13) This can potentially result in a narrow martensitic region at the fusion boundary that exhibits high hardness.(14) If the weld metal is high in chromium and the base metal has little or no chromium (as is the case when using Ni-Cr or Ni-Cr-Fe with carbon steels), the tendency for carbon to migrate from the HAZ into the weld metal during PWHT is very great.

Microstructure evolution along the fusion boundary in dissimilar metal welds made with Ni-base filler metals can be quite complex. In situations in which the base metal is ferritic at temperatures near the melting point (as with most carbon and low alloy steels) and the weld metal is austenitic, normal epitaxial growth may be suppressed. This can result in the formation of Type II boundaries that run roughly parallel to the fusion boundary.(15) These are in contrast to the Type I boundaries that result from columnar growth from base metal grains into the weld metal and are oriented roughly perpendicular to the fusion boundary.

A schematic of the weld fusion boundary is shown in Figure 7.4 under “normal” conditions (top) and the situation where the base metal and weld metal have different crystal structures (bcc versus fcc) at the solidification temperature.(16) Note that distinct boundaries are present in the dissimilar weld, the Type I boundaries running roughly perpendicular to the fusion boundary (along the original solidification direction) and the Type II boundaries parallel to the fusion boundary. Type II boundaries do not exist under normal weld solidification conditions where the base and filler metals are of similar composition.

Type II boundaries are of special interest because a number of instances of in-service cracking, sometimes termed “disbonding,” have been associated with them. As shown in Figure 7.4, a Type II boundary is essentially a grain boundary that runs approximately parallel to the fusion boundary, but located a very short distance (a few microns) into the fusion zone. Nelson *et al.* have studied the mechanism of Type II boundary formation in cladding of ferritic steels with austenitic (fcc) filler metals.(16–18) They concluded that such boundaries form when the substrate (mild steel or low alloy steel) exists as delta ferrite at the temperature where the fcc cladding alloy is solidifying. This suppresses normal epitaxial nucleation at the fusion boundary and necessitates heterogeneous nucleation of the fcc weld metal. However, shortly after

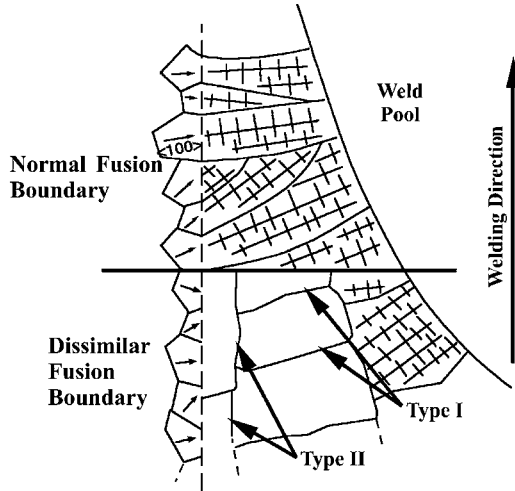


**Figure 7.4** Schematic representation of formation of Type II boundaries when austenitic weld metal solidifies in contact with ferritic base metal. (From Nelson *et al.* [17]. Courtesy the American Welding Society.)

solidification, cooling causes the carbon steel substrate to transform to austenite. Then the fusion boundary, formerly a bcc-to-fcc interface, becomes an fcc-to-fcc interface with considerable orientation mismatch across that interface. The fusion line is then a high energy boundary which is mobile. The boundary migrates into the fcc-Ni cladding a short distance, driven by the temperature gradient, composition gradient and strain energy produced by differences in lattice parameter between the fcc cladding alloy and the fcc substrate. It is then locked in place as the weld metal cools and boundary migration ceases.

A schematic of this mechanism from the work of Nelson *et al.* (17,18) is shown in Figure 7.5. Note that the Type II boundaries form within the temperature range when the carbon steel, or substrate alloy) is in the austenite phase field. Thus the weld heat input and temperature gradient in the HAZ will have some influence over Type II boundary formation, since this dictates the time over which both the weld metal and HAZ are FCC and boundary migration can occur. Nelson *et al.* verified this mechanism by using MONEL<sup>®</sup> filler metal on pure iron and Type 409 ferritic stainless steel. In the former case, Type II boundaries were present as long as there was not sufficient base metal dilution to cause the weld metal to solidify as ferrite. In the latter case, no Type II boundaries form since the Type 409 is fully ferritic from room temperature to melting. Since austenite is never present in the base metal substrate, the mechanism described in Figure 7.5 is inoperable.

An example of Type II boundaries that form in the MONEL/iron system is shown in Figure 7.6.(19) Subsequent to the formation of the Type II boundary, the carbon steel substrate transforms to ferrite or other decomposition

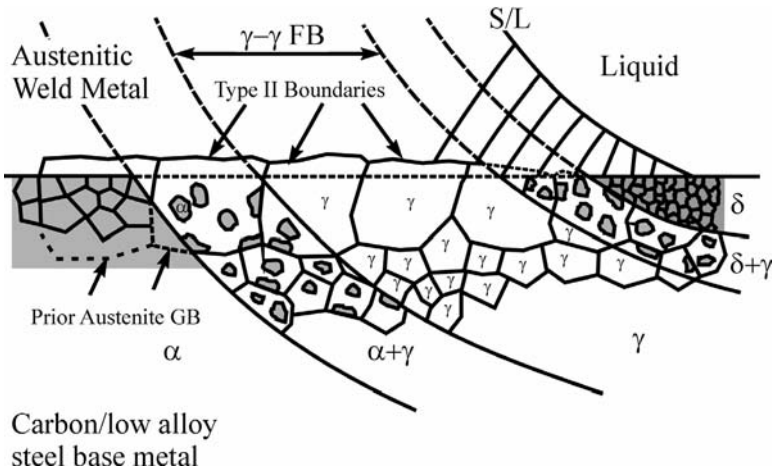


**Figure 7.5** Mechanism for Type II boundary formation during dissimilar welding between an austenitic weld metal and a carbon/low alloy steel. (From Nelson *et al.* [17]. Courtesy the American Welding Society.)

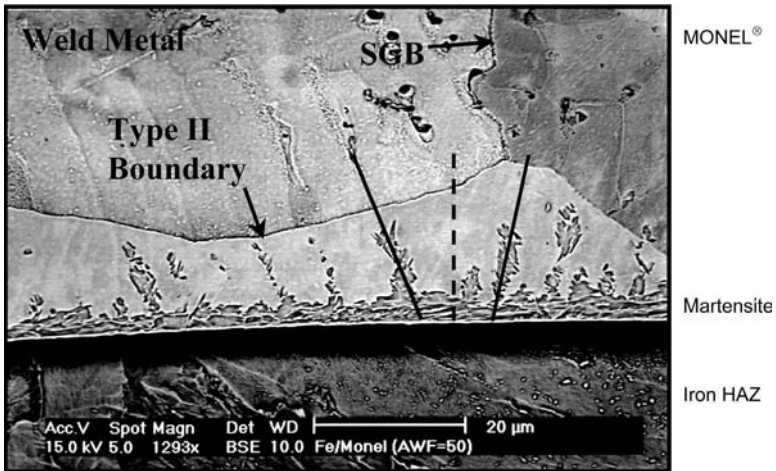


**Figure 7.6** Transition Region of MONEL<sup>®</sup> (70Ni-30Cu) cladding on pure Iron (56% Base Metal Dilution). (From Rowe *et al.* [19]. Courtesy the American Welding Society.)

products, and the compositional transition zone, or a part of it, transforms to martensite. The martensite may extend to the Type II boundary, or may stop short of it. Figure 7.6 shows an example of martensite stopping short of the Type II boundary. There is a mismatch in coefficient of thermal expansion between the bcc or martensite side of the transition region and the fcc-Ni cladding side. Thermal cycling sets up strain in this region, and the Type II

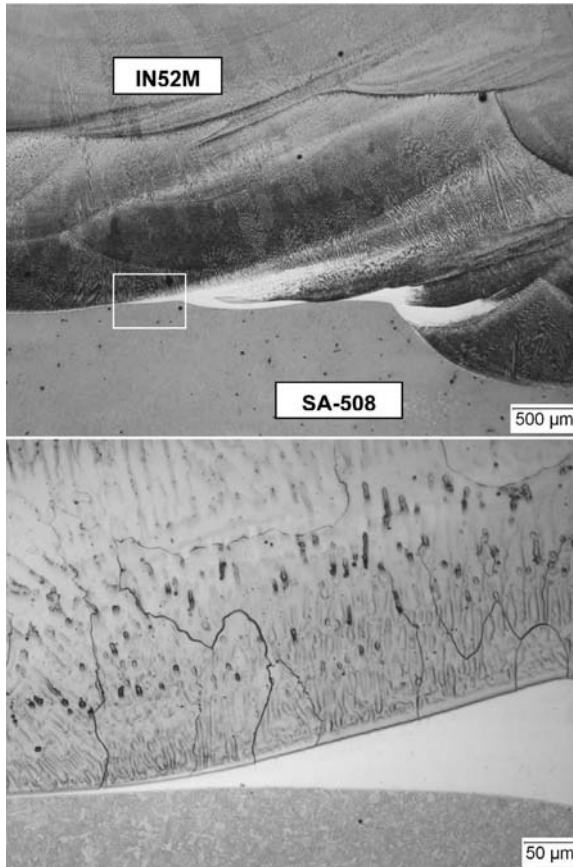


**Figure 7.7** IN52M overlay interface with SA-508, Class 2 nozzle. Top, 25X. Bottom, outlined area in top photo showing higher magnification of the interface, 200X.

boundary is a weak, approximately planar, interface that makes it a preferential cracking site (see Section 7.3.3.2 on Clad Disbonding). In addition, the martensite is a potential location for hydrogen-induced cracking if the service environment produces hydrogen charging.(20)

In certain dissimilar combinations, martensite may be present along the fusion boundary due to the transition in composition between a carbon steel or low alloy steel and a Ni-base filler metal. As previously described, the Schaeffler Diagram can be used to predict the presence of martensite. As shown in Figure 7.3, a layer of martensite would be expected to form at the fusion boundary of dissimilar welds with Ni-base filler metals and carbon steel base metals. An example of this is shown in Figure 7.7, where FM 52M (ERNiCrFe-7A) has been deposited on a carbon steel. This narrow region will exhibit high hardness relative to the adjacent diluted weld metal and the HAZ.

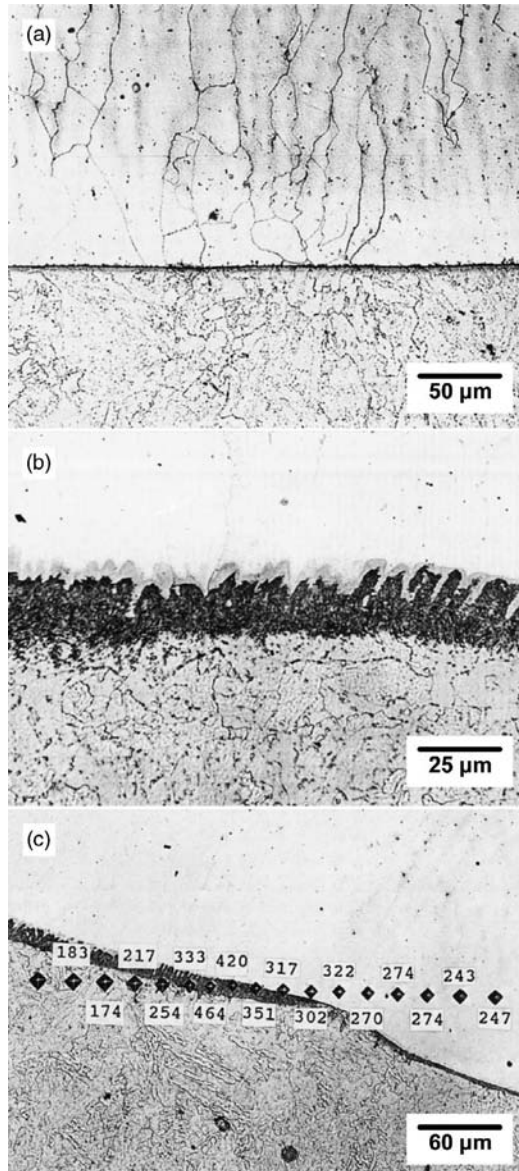
Carbon migration has been observed from carbon steel base metals across the fusion boundary into the transition region.(13,21) This results from the carbon gradient that is present (higher C in the carbon steel base metal) and the affinity of carbon for the higher-Cr weld metal. This migration can result in local microstructural changes in both the HAZ and transition region. An example of this from the work of Gittos and Gooch (21) is shown in Figure 7.8. In this study, they use submerged arc strip cladding to deposit ERNiCr-3 on 2.25Cr-1Mo steel. Note that in the as-welded condition (Figure 7.8A) the weld fusion boundary appears as a sharp interface with no evidence of epitaxial nucleation and growth in the weld metal. The narrow dark etching feature at the interface represents untempered martensite. When this microstructure is tempered (690°C/30 hours), the dark etching region at the interface becomes more prominent (Figure 7.8B). This results from carbon migration from the steel into the weld metal and subsequent tempering of the martensite that is present at the fusion boundary. Even after tempering, this band has relatively high hardness, as shown by the hardness traverse in Figure 7.8C, where hardness values above 450 VHN are measured. The width of the martensite band is generally quite narrow (1–5 μm) as compared to the situation when austenitic stainless steel filler metals are used.

The diffusion of carbon during PWHT can produce a carbon-depleted zone in the HAZ, immediately adjacent to the fusion boundary. This depletion in carbon can result in the formation of soft, low carbon ferrite in a narrow region of the HAZ. This local softened zone has been shown to lead to premature failure in creep during service exposure.(21,22) This failure mechanism will be discussed in Section 7.3.3.3.

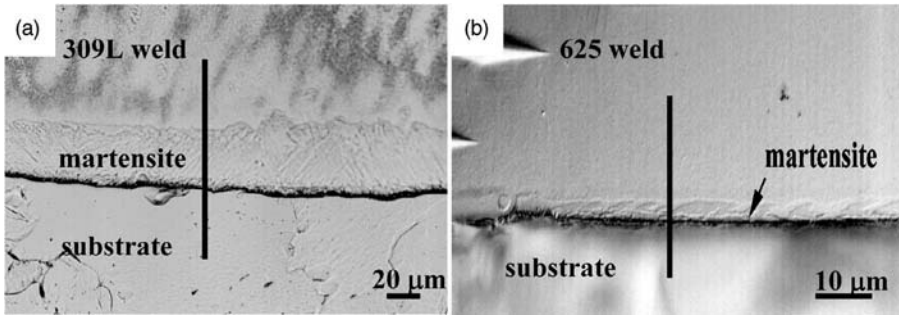
It is generally recognized that the use of Ni-base filler metals will result in the formation of a thin martensite layer at the fusion line, while the martensite layer that results from the use of stainless steel filler metals is relatively thick. The reasons for this have recently been explored by DuPont and Kusko.(5) In this work, FM 625 and 309L stainless steel were deposited onto A285 carbon steel using the electroslag welding process. The composition gradients across the fusion line were measured using electron probe microanalysis (EPMA), and the width of the martensite layer adjacent to the fusion line was measured using image analysis.

Figure 7.9 shows light optical photomicrographs of the martensite layer observed in the welds deposited using 309L (Figure 7.9a) and Alloy 625 (Figure 7.9b) filler metals. The black vertical line in each photomicrograph represents the locations of EPMA traces. The variation in martensite layer widths is readily evident from these figures. The martensite layer in the 309L weld ranged from 30–37 μm in thickness, while that in the Alloy 625 weld was only 1–3 μm in thickness.

The variation in major alloying elements (Fe, Ni, and Cr) across the fusion lines of the welds is shown in Figure 7.10. The composition gradient is steeper for the weld prepared with the Alloy 625 filler metal because of the increase



**Figure 7.8** Fusion boundary between ERNiCr-3 (FM 82) strip clad deposit on 2.25Cr-1Mo steel, a) as-welded, b) after PWHT at 690°C (1275°F) for 30 hours, c) Vickers hardness traverse across interface following PWHT. (From Gittos *et al.* [21]. Courtesy the American Welding Society.)



**Figure 7.9** Light optical micrographs of the martensite layer observed in the composition transition zone in overlays made with a) Type 309L, and b) Alloy 625 filler metals. (From DuPont and Kusko [5]. Courtesy the American Welding Society.)

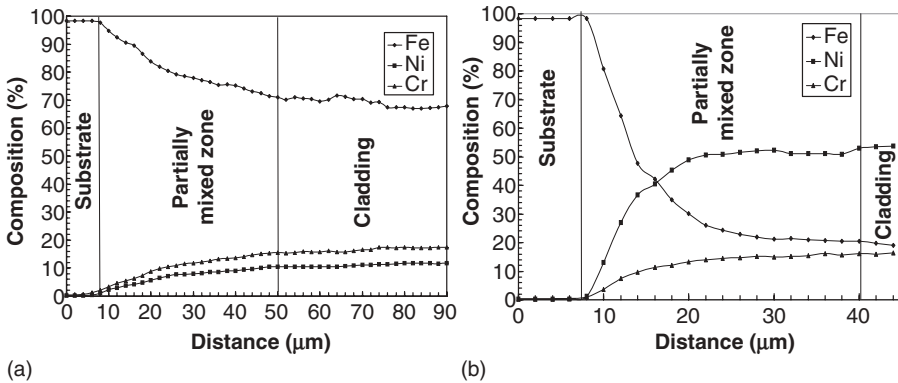


**Figure 7.10** Electron probe microanalysis (EPMA) measurements across the composition transition zone for a) Type 309L and b) Alloy 625 dissimilar welds on carbon steel from the locations shown in Figure 7.9. (From DuPont and Kusko [5]. Courtesy the American Welding Society.)

in nominal Ni content and decrease in nominal Fe content compared to the weld prepared with 309L stainless steel.

The composition gradients produce a variation in the martensite start ( $M_s$ ) temperature across the fusion boundary, and the differences in composition gradients and resultant  $M_s$  gradients between the two welds can be used to explain the observed variation in martensite widths. Using the measured values for Ni, Cr, and Mo along with estimated values of C and Mn, the variation in  $M_s$  temperature across the composition transition zone (or partially mixed zone) was determined, as shown in Figure 7.11. The two curves on each plot represent the highest and lowest possible  $M_s$  temperature based on the range in dilution that was determined. The martensite layer within the transition zone should begin near the start of the composition gradient adjacent to

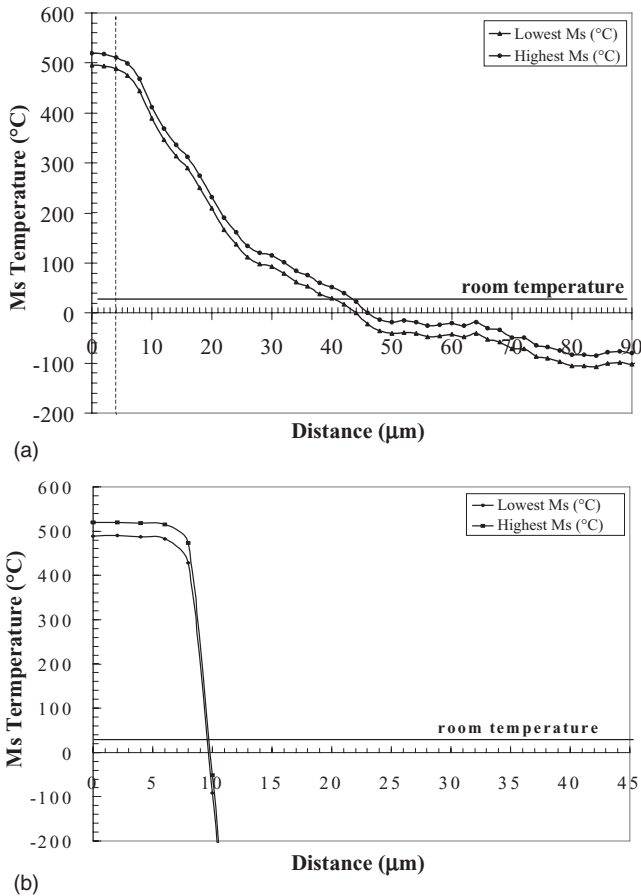


**Figure 7.11** Variation in the martensite start temperature across the fusion boundary for a) Type 309L and b) Alloy 625 based on EPMA composition data. (From DuPont and Kusko [5]. Courtesy the American Welding Society.)

the carbon steel base metal and end at a location where the  $M_s$  temperature intersects room temperature. The exact start and end locations cannot be known with a high degree of certainty since this will depend on the local hardenability (as determined by local composition) and local cooling rate.

However, comparison of the  $M_s$  gradient plots in Figure 7.11 clearly show that a thinner martensite layer is expected in welds prepared with Ni-base filler metals. This can be attributed to the higher concentration gradient within the composition transition zone (due to higher Ni concentration), which, in turn, stabilizes the austenite at a shorter location within the transition zone. According to Figure 7.11, the martensite layer should be approximately 35–39  $\mu\text{m}$  for the weld prepared with 309L filler metal and approximately 2–3  $\mu\text{m}$  in the weld prepared with the Alloy 625 filler metal. These values compare

reasonably well with those measured at the location of the microprobe trace for each weld in Figure 7.9,  $\sim 34\ \mu\text{m}$  for 309L and  $\sim 3\ \mu\text{m}$  for Alloy 625.

It should be noted that the exact width of the martensite layer can vary within a given weld due to local variations in the composition gradient (due to local variations in fluid flow behavior) and local variations in cooling rate. In addition, variations in fluid flow behavior are expected when changes are made to processing parameters. The objective in this work was not to predict the size of the martensite layer within a given weld or with variations in processing parameters, but to demonstrate why differences exist between the widths of martensite layers in welds prepared with Ni-base and stainless steel alloys. These results demonstrated that the reduced width of the martensite layer in Ni-base alloys can be attributed to the steeper gradient in composition and concomitant  $M_s$  temperature within the composition transition zone.

### 7.3.3 Weldability

A number of cracking mechanisms are associated with dissimilar metal welds between carbon steels and stainless steels using Ni-base filler metals, or when cladding carbon steels. These include solidification cracking, clad “disbonding” along Type II grain boundaries in the weld metal, creep failure in the HAZ of the carbon steel, and postweld heat treatment (PWHT) cracking.

**7.3.3.1 Solidification Cracking** Solidification cracking in dissimilar welds joining carbon and stainless steels with Ni-base filler metals, or during cladding of these steels, can potentially be a problem since the weld metals of these combinations will invariably be fully austenitic (fcc-Ni), even under conditions where the Ni-base filler metal is heavily diluted by the steel. Figure 7.12 shows examples of weld solidification cracking that occur in dissimilar welds between Filler Metal 52M (ERNiCrFe-7A) and both carbon steel A36 and stainless steel Type 304L. Note that in both cases the weld metal is fully austenitic as evidenced by the distinct weld metal substructure (cells and dendrites). It has been well documented that weld metals that solidify as austenite and are fully austenitic at room temperature are inherently susceptible to weld solidification cracking due to the segregation that occurs during solidification and the tendency for liquid films to wet the austenite grain boundaries.

Susceptibility to solidification cracking in dissimilar combinations between Ni-base alloys and steels is a strong function of weld metal dilution by the substrate. With many of the Ni-base filler metals that are used for dissimilar welds with steel (FM82, FM52, and Alloy 625), dilution by the steel tends to expand the solidification temperature range. Since the width of the solidification temperature range is roughly proportional to cracking susceptibility, dilution by the steel tends to increase the solidification cracking susceptibility of the dissimilar weld. In the case of the solidification cracking shown in Figure 7.12, cracking occurs due to the dilution of FM52M by the steel substrate. As the Fe content of the deposit increases, the solidification temperature range

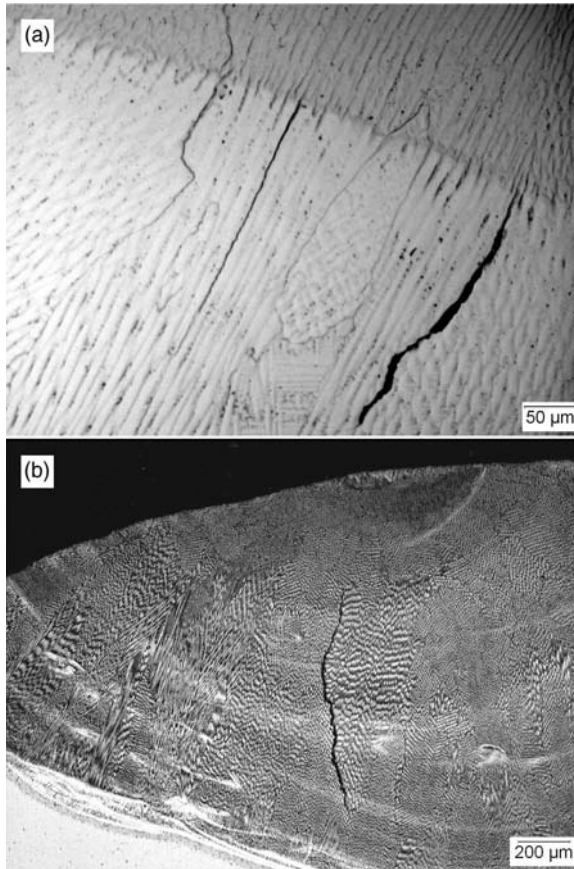


**Figure 7.12** Examples of weld solidification cracking in Filler Metal 52M (ERNiCrFe-7A) dissimilar weld overlays on a) carbon steel A36, and b) stainless steel Type 304L.

increases leading to higher cracking susceptibility. When dilution is low, FM52M has good resistance to solidification cracking.

An example of this is shown in Figure 7.13 for a dissimilar weld between an experimental Ni-7.5Cu filler metal and Type 304L stainless steel.(23) The solidification range was determined by actual measurements using the single sensor differential thermal analysis (SS-DTA) technique (24) and by Scheil-Gulliver simulation. Note that the undiluted filler metal exhibits a solidification temperature range of approximately 100°C, but dilution by 304L expands the range significantly—30% dilution results in a near-doubling of the solidification range.

Limits for Fe, Cr, and Cu have been proposed by Avery and Kiser for nickel and nickel alloys, as shown in Table 7.1.(25,26) Note that limits on Fe and Cr are recommended for the Ni, Ni-Cu, and Ni-Cr-Fe systems and Cu is limited

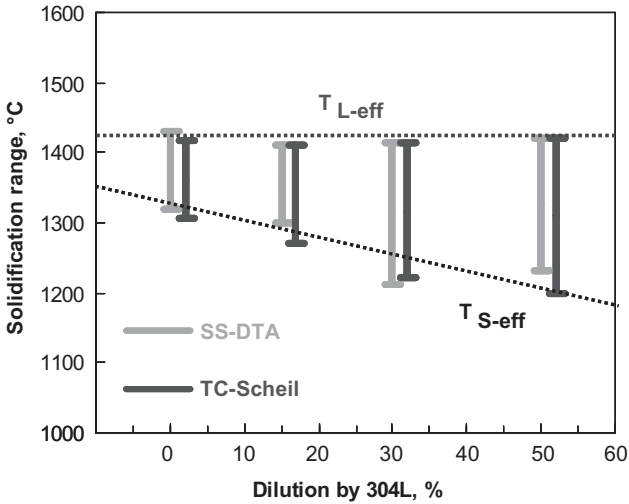


**Figure 7.13** Effect of dilution on the solidification temperature range of a dissimilar weld between a Ni-7.5Cu filler metal and Type 304L stainless steel. (From Sowards *et al.* [23].)

**TABLE 7.1** Approximate Limit of Diluting Elements (in wt%) to Prevent Solidification Cracking in Dissimilar Welds made with Ni-base Filler Metals. (From Avery [25]. Courtesy the Nickel Development Institute.)

Weld Metal	Iron	Diluting Elements		
		Nickel	Chromium	Copper
Nickel	30%	—	30%	Unlimited
Ni-Cu	25% SMAW 15% GMAW	Unlimited	8%	Unlimited
Ni-Cr-Fe (1)	25%	Unlimited	30%	15%

(1) Silicon should be limited to less than 0.75%.

to a maximum of 15 wt% in the Ni-Cr-Fe system. Silicon is also limited to less than 0.75 wt% in this system.

Another factor that can influence the solidification cracking susceptibility is the impurity content of the base metal. If steel base metals have high levels of sulfur and phosphorus, dilution of the filler metal by the base metal can result in impurity segregation during solidification and higher susceptibility to weld solidification cracking. Most Ni-base filler metals contain extremely low levels of sulfur and phosphorus to reduce susceptibility to solidification cracking, so increases in impurity content by dilution will increase susceptibility. Although there are no definitive guidelines with respect to allowable impurity

content, a general rule is that base metals with sulfur levels exceeding 0.010 wt% and phosphorus levels exceeding 0.020 wt% should be treated carefully. At these impurity levels, careful control of heat input, dilution, and weld bead shape may be required to prevent solidification cracking.

**7.3.3.2 Clad Disbonding** Many structural steels are clad with Ni-base or austenitic stainless steel filler metals to provide corrosion resistance, particularly for elevated temperature service. Clad “disbonding” typically occurs along Type II boundaries (see Figures 7.4–7.6) in the clad deposit. This form of cracking is most common in structural steels clad with austenitic stainless steels, but it is also possible when cladding is done with Ni-base alloys. The precise mechanism for this type of failure is not known, but it may involve carbide precipitation, impurity segregation, the orientation of the boundary perpendicular to the direction of principal stress, hydrogen induced cracking in a thin martensite zone in the compositional transition zone, or a combination of these. In all cases, the disbonding occurs along Type II boundaries and represents intergranular fracture.

Disbonding may occur during the actual cladding operation, during subsequent postweld heat treatment, or in service. It is often difficult to know when the actual failure occurs during fabrication, since inspection is usually not carried out until after the PWHT is completed. Unfortunately, there is no way to avoid Type II boundary formation in many of the common dissimilar combinations used in the power generation industry and elsewhere.

**7.3.3.3 Creep Failure in the HAZ of Carbon Steel or Low Alloy Steel** Failure in the steel HAZ adjacent to the fusion boundary has been observed in thick-section structural welds. Carbon migration from the HAZ to the Cr-bearing weld metal during welding, PWHT, or service exposure results in a soft ferritic HAZ microstructure.(13,21,22) Under imposed residual and thermal stresses (CTE mismatch between HAZ and weld metal), creep cracks can occur along the ferrite grain boundaries. An example of creep failure in a dissimilar weld between a 2.25Cr-1Mo structural steel and Type 321 stainless steel made with Filler Metal 82 (ERNiCr-3) is shown in Figure 7.14 from the study by Klueh and King.(22) These failures typically occur after 10-to-15 years of elevated temperature service.

Ni-base filler metals are often used to join stainless steels to carbon steels in order to reduce the elevated temperature stresses associated with differences in coefficient of thermal expansion. The average linear CTE for carbon steel in the temperature range from 70–1110 °F (20–600 °C) is on the order of 7.5–8  $\mu\text{in}/\text{in}/^\circ\text{F}$ , while austenitic stainless steels are on the order of 9.5–10 (same units). This difference in CTE can result in large local stresses when a dissimilar weld is heated to elevated temperature. Because the carbon steel has a lower CTE, it will try to constrain the stainless steel weld from expanding. This results in locally high stresses at the interface. The carbon migration from the HAZ of the carbon steel leads to the formation of a very soft ferritic region

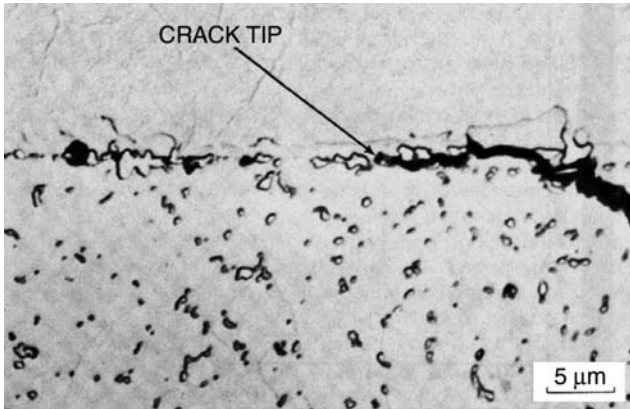


**Figure 7.14** Creep failure in the HAZ of a 2.25Cr-1Mo steel welded to Type 321 stainless steel using ERNiCr-3 (FM82) filler metal. Failure occurred after extended service exposure (From Klueh *et al.* [22]. Courtesy the American Welding Society.)

between the stronger weld metal and base metal, and high local strains will be concentrated in this region. Over time, grain boundary sliding occurs, eventually leading to a creep, or stress rupture, failure in the carbon steel HAZ.

The use of Ni-base filler metals, or inserts, has been effective in reducing the thermally-induced CTE mismatch stresses, thereby avoiding cracking. The use of Ni-base filler metals is generally recommended for service temperatures exceeding 425 °C (800 °F).<sup>(25)</sup> This is helpful because Ni-base alloys have a CTE (on the order of 8  $\mu\text{in}/\text{in}/^\circ\text{F}$ . in the same temperature range as noted above) that is closer to that of the carbon steels than that of the austenitic stainless steels. Thus, the stronger nickel alloy actually protects the weaker ferritic HAZ and shifts most of the stress caused by the CTE mismatch to the austenitic stainless HAZ which is much stronger and more crack resistant. By using this gradation in CTE across the weld joint rather than an abrupt change at the fusion boundary, longer service life is attained. Because Ni-base filler metals are compatible with both carbon steels and austenitic stainless steels the use of filler metals, such as ENiCrFe-2 (Weld A), ENiCrFe-3 (FM 182) or ERNiCr-3 (FM 82), may be useful in avoiding creep failures in service. These weld deposits will be fully austenitic, so precautions against weld solidification cracking should be taken, as discussed in Section 7.3.3.1. Figure 7.15 shows a bar chart composed of data collected and compiled by the Electric Power Research Institute that compares the average life of dissimilar joints in power plants around the world for various weld metals.<sup>(27)</sup>

**7.3.3.4 Postweld Heat Treatment Cracking** Dissimilar welds with carbon steels are often subject to PWHT in order to both temper the martensite that forms in the HAZ of the carbon steel and in the composition transition region at the fusion boundary and relieve residual stresses. For structural steels, these

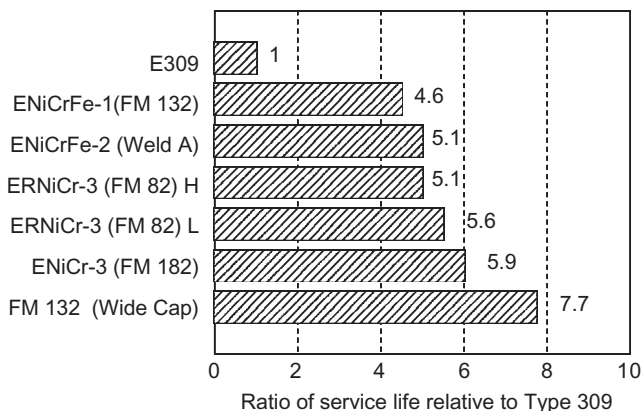


**Figure 7.15** Bar chart comparing the average life of dissimilar joints in power plants around the world for various weld metals. The numbers represent the life ratio relative to standard Type 309 stainless steel. For FM 82, both high (H) and low (L) heat input welds are included. (Courtesy W. Childs [27].)

heat treatments are usually conducted in the range from 650-to-700 °C (1200-to-1290 °F) for up to 24 hours, depending on the steel and section thickness. This can sometimes lead to cracking in either the weld metal or HAZ. In pressure vessel steels that contain Cr, Mo, and V as secondary hardening agents, this cracking often takes the form of “reheat” or postweld stress relief cracking.(28,29) PWHT cracking in dissimilar welds is often exacerbated by stresses resulting from the difference in coefficient of thermal expansion during heating. In some cases, slower heating rates to the PWHT temperature can help relieve these stresses and prevent cracking in thick section or highly restrained weldments.

#### 7.4 POSTWELD HEAT TREATMENT CRACKING IN STAINLESS STEELS WELDED WITH Ni-BASE FILLER METALS

PWHT cracking may also occur when iron-nickel-chromium alloys used for elevated temperature service are welded with Ni-base filler metals. For example, Alloy 800H (UNS N08810) is often welded with Weld A (ENiCrFe-2) filler metal. During postweld stress relief in the temperature range from 885–912 °C (1625–1675 °F), cracking has been observed in both the weld metal and HAZ. An example of weld metal PWHT cracking in Weld A weld metal in a thick section weld in Alloy 800H is shown in Figure 7.16, along with the accompanying fracture morphology. These cracks occur along migrated grain boundaries in the weld metal and are characteristic of reheat cracking. It is postulated that the presence of Nb in this weld metal leads to the formation of NbC

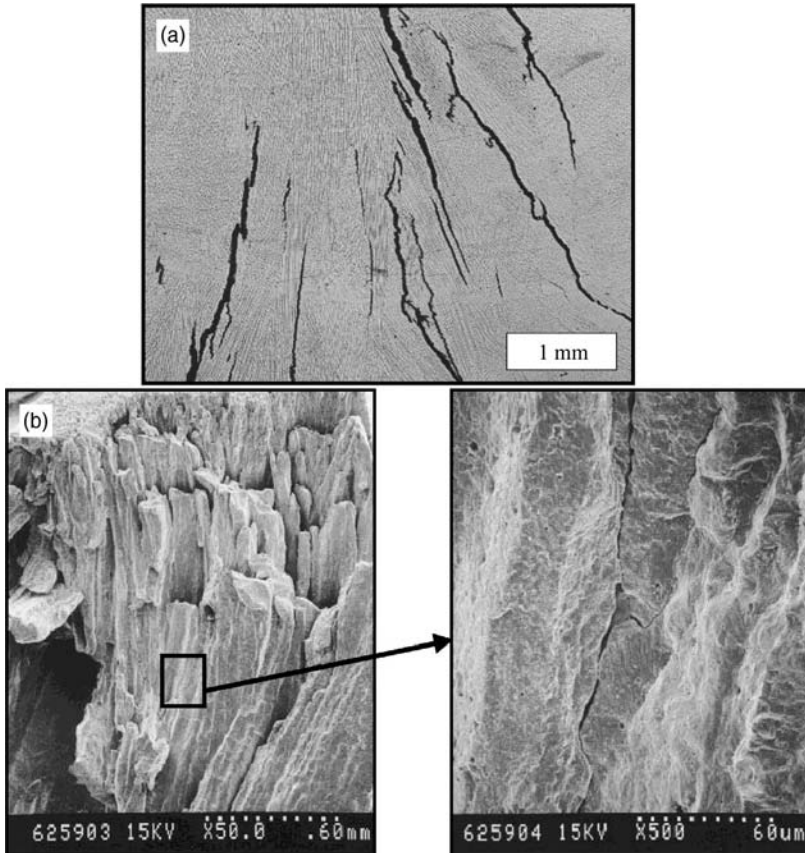


**Figure 7.16** PWHT cracking in ERNiCrFe-2 (Weld A) weld metal after stress relief at 900°C. a) Cracking along weld metal migrated grain boundaries, b) fracture surface morphology.

during PWHT and coupled with stress relaxation, results in grain boundary cracking. (See Section 7.7.2)

A related mechanism that can occur in Alloy 800H and other austenitic stainless steel alloys (304H, 316H) welded with Ni-base filler metals is termed “relaxation cracking.” This form of cracking occurs after service exposure and has been observed in both the HAZ and weld metal. It is related to the formation of carbides at the service temperature and the gradual relaxation of residual stresses that leads to intergranular failure. The mechanism for relaxation cracking is similar to reheat and PWHT cracking and requires the formation of a strengthening precipitate (in this case a carbide) at the service temperature. These carbides locally strengthen the matrix and concentrate stress along grain boundaries as the residual stresses relax. PWHT is the best antidote for avoiding relaxation cracking, but often PWHT cracking may be

the result. For applications in which Alloy 800H or 800HT is used above 540°C (1000°F), PWHT is specified by ASME Section VIII, part UNF-56. According to this specification, PWHT shall consist of a minimum of 885°C (1625°F) for 1.5 hours for thicknesses up to one inch and for 1.5 hours plus one hour per inch of thickness for thicknesses in excess of one inch. This heat treatment precipitates and grows discrete  $M_{23}C_6$  particles in preference to allowing embrittling grain boundary films of  $M_{23}C_6$  to form if the PWHT is not employed.

## 7.5 SUPER AUSTENITIC STAINLESS STEELS

Super austenitic stainless steels are used in applications that require good resistance in aggressive corrosion environments. These relatively high nickel stainless steels contain Mo additions (~6–7.5 wt%) and high N contents (up to ~0.5 wt%) for improved corrosion resistance. The addition of Mo and N promote selective dissolution of iron at the surface and lead to chromium enrichment beneath the passive film, thus increasing corrosion resistance.(30) A nitride layer has also been detected at the film-metal interface along with a ferrous molybdate layer in the outer regions of the passive film. These phases have been proposed to provide secondary kinetic barriers for further enhancement in corrosion performance. However, during solidification of the weld, Mo segregates preferentially to the last-to-solidify region due to the low solubility of Mo in the austenite phase. This results in a depletion of Mo at the cores of the cells and dendrites in the weld metal.(31,32)

In addition, the low diffusion rate of Mo in austenite coupled with the rapid cooling during welding does not allow for Mo to diffuse back towards the dendrite cores to eliminate the concentration gradient. This can lead to low corrosion resistance of the weld metal relative to the base metal. An example of this is provided in Figure 7.17, which shows the critical pitting potential of the base metal and welds for a stainless steel with systematic variations in Mo concentration.(33) Although the beneficial effect of Mo on the pitting resistance of the base metal is clearly evident, fusion welding almost completely negates the beneficial effect. An example of this localized form of corrosion is shown in Figure 7.18 for an autogeneous weld in Alloy AL6XN exposed in a controlled corrosion test.(34) These alloys are also prone to solidification cracking since they solidify as austenite.

High Mo- and W-containing Ni-base filler metals are often utilized during fusion welding of these alloys because W also imparts pitting resistance and does not partition as severely as Mo during solidification.(35) As a result, the dendrite cores provide more uniform resistance to pitting. For these reasons, Ni alloys with overmatching Mo and Cr with W are often chosen instead of the matching filler metal that leads to weld metal corrosion.(31,32) While these filler metals do not eliminate microsegregation of Mo during solidification, the dendrite core compositions contain W and are increased in Mo relative to those in autogenous welds and this helps to minimize preferential attack at

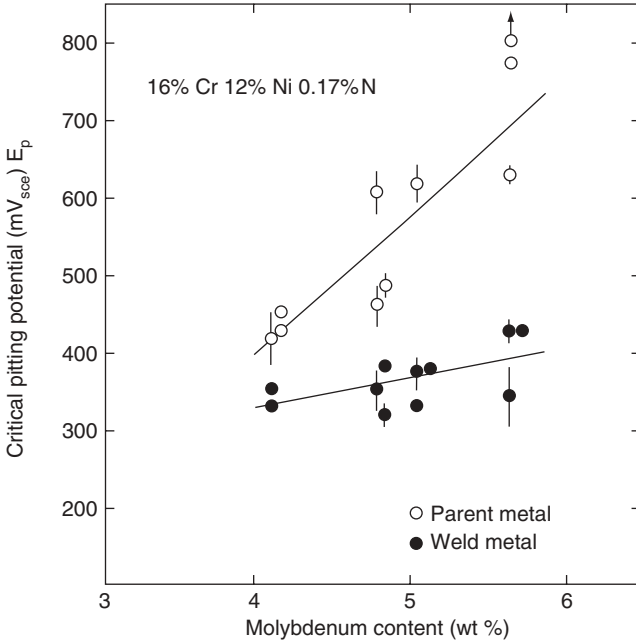


**Figure 7.17** Pitting potential as a function of Mo content. (From Garner [33].)

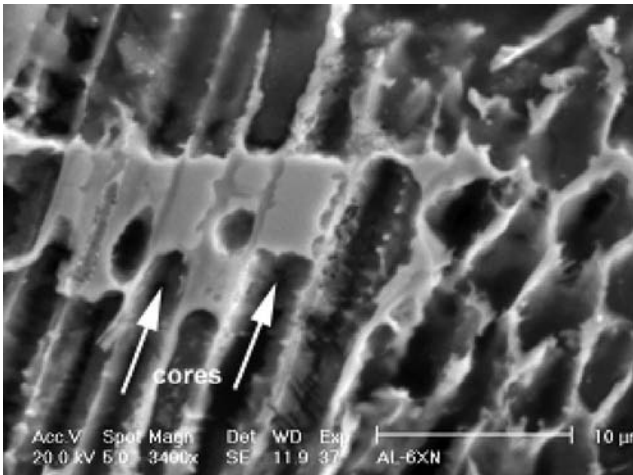


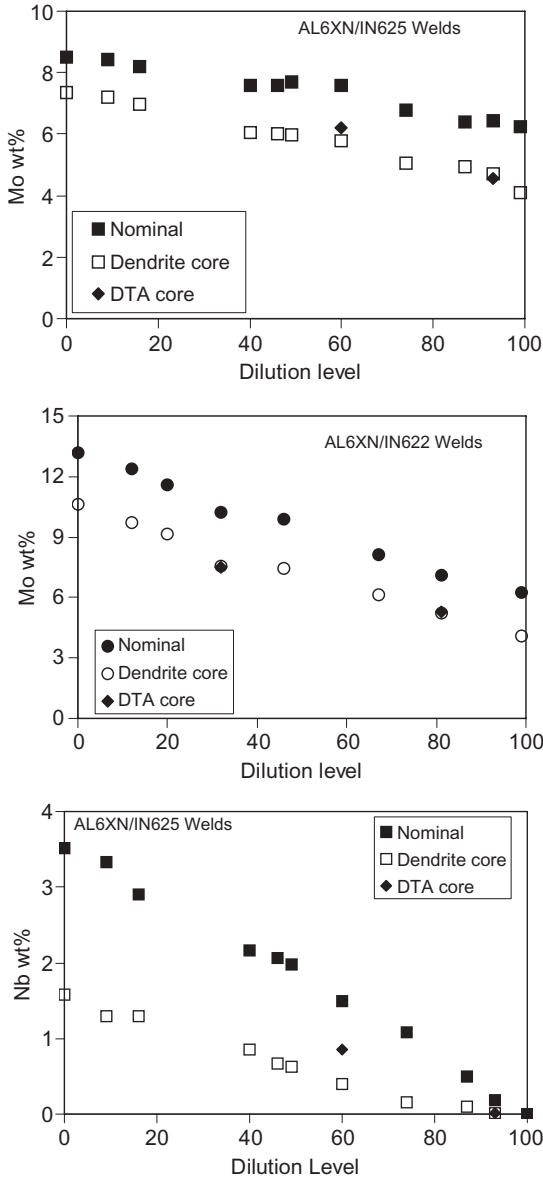
**Figure 7.18** Example of dendrite core corrosion attack in autogenous welds in superaustenitic stainless steel AL6XN. Arrows indicate dendrite core regions. (From DuPont [34].)

the dendrite cores. With this approach, the final distribution of Mo (and other alloying elements) will be controlled by the filler metal composition, welding parameters (which control the dilution and resultant nominal weld metal composition), and the segregation potential of each element. These factors, in turn, will govern the solidification behavior and resultant corrosion resistance and hot cracking susceptibility of the fusion zone. Since potentially wide ranges of weld metal composition are possible in practice, a large variation in fusion zone cracking susceptibility may be encountered.

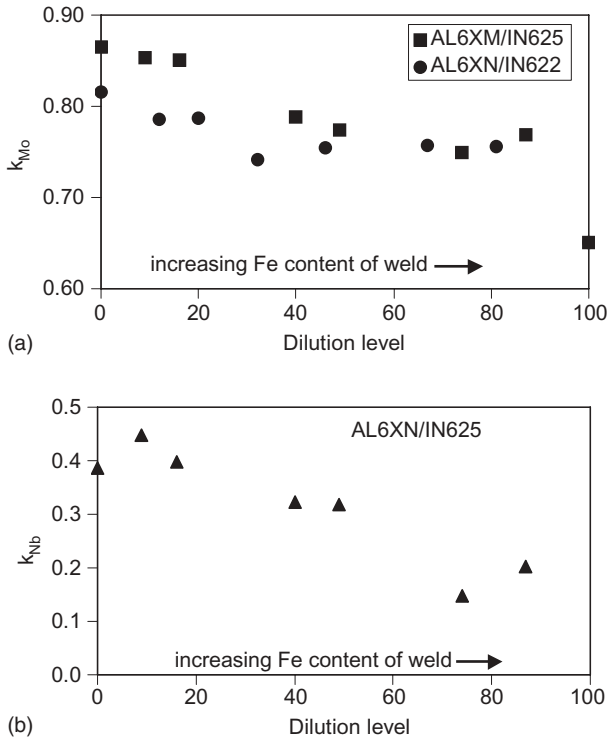
Recent work has established the relations between filler metal composition, welding parameters, welding microstructure and resultant corrosion resistance and solidification cracking susceptibility in alloy AL6XN.(31,32) Fusion welds were prepared with two different filler metals (FM622 and FM625) over the entire dilution range. The welds were characterized by various microscopy techniques, while the corrosion resistance was determined using crevice corrosion tests. Solidification cracking susceptibility was evaluated using differential thermal analysis (DTA) and Vareststraint testing.

Figure 7.19 shows the Mo and Nb nominal and dendrite core compositions for the welds as a function of dilution level. For both sets of data, as the dilution level increased, the amount of Mo and Nb decrease for both the nominal and dendrite core compositions. Also included in Figure 7.19 is the dendrite core compositions from two DTA samples extracted from welds prepared with FM622 that were re-melted and solidified at a rate of 0.3°C/second. These samples were analyzed to assess the potential for back diffusion of Mo toward the dendrite cores during the slower cooling rate imposed by the DTA technique. By comparison, the fusion welds solidified at a rate of ~300°C/sec. Although the DTA samples were solidified at a cooling rate three orders of magnitude slower than the welds, the Mo core compositions are essentially equivalent to those in the welds of identical nominal compositions. Thus, the Mo core concentration is essentially independent of cooling rate within the range of cooling considered. This can be understood by reference to the elemental segregation concepts described in Chapter 3, in which back-diffusion of substitutional alloying elements in austenitic alloys was shown to be very unlikely under most cooling rate conditions.

Figure 7.20 shows the equilibrium partition coefficients for Mo and Nb as a function of dilution. From a corrosion perspective, it is desirable for the partition coefficient,  $k$ , to be as close to unity as possible, since the dendrite core composition is given as  $C_{\text{core}} = kC_o$ , in which  $C_o$  is the nominal composition. The Mo partition coefficient decreases as the iron content in the weld increases (i.e., as the dilution level increases). A similar trend is observed for Nb. These effects are controlled by the influence of Fe on the solubility of Mo and Nb in austenite. The maximum solid solubility of Mo in  $\gamma$ -Ni is 35 wt% (at 1200°C), while a maximum of only 2.9 wt% Mo can be dissolved in  $\gamma$ -Fe (at ~1150°C).(36) A similar trend is observed with Nb, in which the maximum solid solubility of Nb in  $\gamma$ -Ni is 18.2 wt% (at 1286°C), while it is only 1.3 wt% at a similar temperature (1210°C) in  $\gamma$ -Fe. Thus, iron additions to the weld will



**Figure 7.19** Dendrite core compositions of AL6XN welds made with FM625 and FM622 filler metals as a function of dilution, a) Mo concentration in FM625, b) Mo concentration in FM622, and c) Nb concentration in FM625.



**Figure 7.20** Effect of dilution by AL6XN on the partition coefficient,  $k$ . a) Mo in FM 622 and 625, b) Nb in FM625.

decrease the solubility of Mo and Nb in austenite and result in a concomitant decrease in the  $k$ -values for Mo and Nb. This, in turn, increases the partitioning of these elements during solidification. Since the fusion zone composition depends on the arc power and volumetric filler metal feed speed (37), the segregation potential of Mo and Nb will be indirectly affected by the welding parameters.

Increasing the Fe content of Ni-base filler metals increases the solidification temperature range, thereby increasing the potential for weld solidification cracking. Figure 7.21 shows the total crack length as a function of dilution level, as determined using the Varestraint test.(32) Type 316L stainless steel was used as baseline in this study, since it exhibits excellent resistance to weld solidification cracking. As shown in Figure 7.21, the AL6XN alloy and welds prepared with the Ni-base filler metals were more susceptible to cracking compared to the 316L alloy. This is expected because the 316L solidified in a primary ferrite mode, which provides excellent cracking resistance. In contrast, the AL6XN alloy and welds prepared with the Ni-base alloys solidify in an austenitic primary mode, with an expected increase in cracking susceptibility.

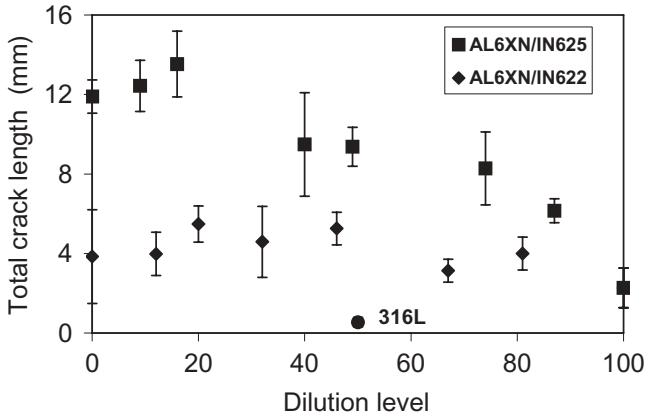


**Figure 7.21** Varestraint test results for FM 622 and 625 filler metals diluted by AL6XN. Stainless steel 316L is included for comparison. (From DuPont *et al.* [32]. Courtesy the American Welding Society.)

**TABLE 7.2 Solidification data for AL6XN, FM 622, and FM 625 determined using DTA.** (From Banovic *et al.* [32]. Courtesy the American Welding Society.)

Alloy/Weld	Liquidus Temp. °C (°F)	Terminal Reaction	Terminal Reaction Temp., °C (°F)	Solidification Temp. Range, °C (°F).
AL6XN	1410 (2570)	$L \rightarrow (\gamma + \sigma)$	1354 (2470)	56 (100)
FM 622	1393 (2540)	$L \rightarrow (\gamma + \sigma)$	1285 (2345)	108 (195)
FM 625	1360 (2480)	$L \rightarrow (\gamma + \text{Laves})$	1152 (2105)	208 (375)
AL6XN/IN622 (46% Dilution)	1383 (2520)	$L \rightarrow (\gamma + \sigma)$	1305 (2380)	78 (140)
AL6XN-IN625 (46% Dilution)	1368 (2495)	$L \rightarrow (\gamma + \text{Laves})$	1172 (2140)	196 (355)

Welds prepared with FM 625 exhibit the poorest resistance to solidification cracking, and the cracking susceptibility increased with decreasing dilution. In contrast, welds prepared with FM 622 were more resistant to solidification cracking, and cracking susceptibility is not particularly sensitive to the dilution level.

Autogenous AL6XN welds and dissimilar welds prepared with FM 622 exhibit a two step solidification reaction sequence represented by  $L \rightarrow \gamma$  followed by  $L \rightarrow (\gamma + \sigma)$ . The welds prepared with FM 625 undergo a three step solidification process:  $L \rightarrow \gamma$ ,  $L \rightarrow (\gamma + \text{NbC})$ , followed by  $L \rightarrow (\gamma + \text{Laves})$ . Table 7.2 summaries the solidification behavior of the base metal and filler metals along with welds prepared with each filler metal at identical dilution levels. The data bounds the possible range of behavior expected for dissimilar

welds with AL6XN for each filler metal. Autogenous welds on the AL6XN base metal solidify over a relatively narrow temperature range of 56 °C. The FM 622 filler metal exhibits a similar reaction sequence and solidifies over a larger temperature range of 108 °C. The weld between AL6XN and FM 622 exhibits the same reaction sequence as the “end members”, and exhibits an intermediate solidification temperature range of 78 °C. This change in solidification temperature range can primarily be attributed to the increase in the  $L \rightarrow (\gamma + \sigma)$  reaction temperature which occurs as the iron content of the weld increases. This influence from iron has also been observed for the  $L \rightarrow (\gamma + \text{Laves})$  reaction in welds prepared with FM 625 and has been documented in other work as well.(38) However, the general solidification behavior of fusion welds made with FM 625 is significantly different. In this case, the addition of Nb leads to the formation of Laves at low temperatures and results in a significant widening of the solidification temperature range. This difference in reaction sequence and solidification temperature range accounts, in part, for the observed differences in weldability between the welds prepared with FM 622 and FM 625.

The data presented in Table 7.2 does not explain, however, the observed dependence of total crack length on dilution displayed in Figure 7.21. The details of this dependence can be understood by considering the relationship between weld metal dilution and secondary phase formation. As described in Chapter 3, increasing amounts of solute enriched liquid (which transforms to a secondary phase) leads to increased solidification cracking susceptibility because it interferes with the formation of solid/solid boundaries, thus preventing accommodation of shrinkage strain across the boundaries. Figure 7.22

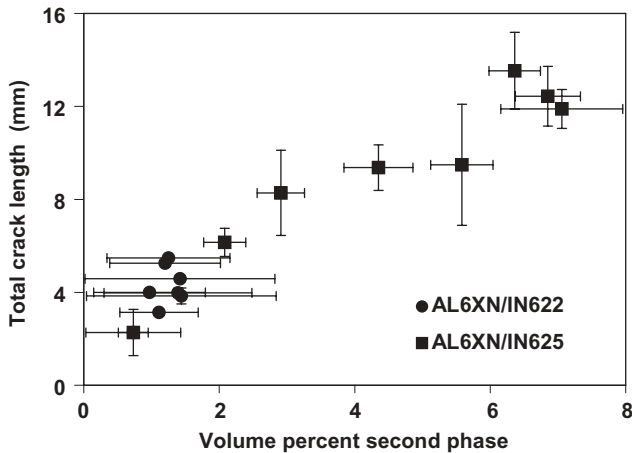


**Figure 7.22** Solidification cracking susceptibility as a function of volume fraction second phase for dissimilar welds between stainless steel AL6XN and Filler Metals 622 and 625. (From DuPont *et al.* [32]. Courtesy the American Welding Society.)

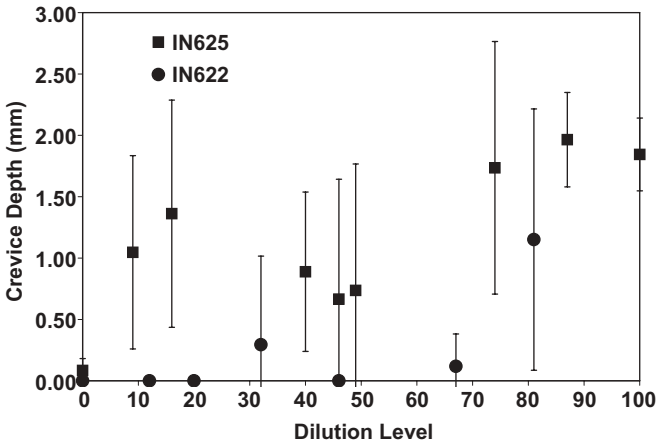


**Figure 7.23** Crevice corrosion as a function of dilution of Filler Metals 622 and 625 by super austenitic stainless steel AL6XN. (From DuPont [34].)

shows the direct relation between crack length and volume percent of secondary phase for all the dilution levels. Note that the data for the welds prepared with FM 622 are grouped at the lower left portion of the plots where low amounts of secondary phase correspond to low crack lengths (good weldability). It is also interesting to note that, although a wide range of weld compositions were investigated, there is a smooth transition between the data represented by the welds prepared with FM 622 and FM 625. Thus, the general superior cracking resistance of welds prepared with FM 622 filler metal is attributed to a reduced solidification temperature range, while the variation in cracking resistance with dilution observed for welds prepared with FM 625 is associated with variations in the secondary phase content.

The effect of dilution of FM 622 and FM 625 by AL6XN on crevice corrosion resistance was also evaluated, as shown in Figure 7.23.(34) The results generally show that the highest degree of attack occurs at the highest dilution levels, which can again be attributed to reduced Mo concentration at the average level in the weld metal and at the minimum level at the dendrite cores. The crevice corrosion resistance of welds made with FM 622 is insensitive to dilution up to ~ 70%, and consistently exhibits better resistance compared to welds made with FM 625. This may be associated with the higher Mo concentration and beneficial effects of 3% W in welds prepared with FM 622 along with the absence of severe microsegregation of Nb that occurs in the welds prepared with FM 625. These results show that welds prepared with FM 622 at low dilution levels provide the best performance in terms of resistance to solidification cracking and corrosion. The dilution can be minimized by depositing welds at the highest filler metal feed rate and lowest arc power that is possible while still maintaining adequate fusion.

## 7.6 DISSIMILAR WELDS IN Ni-BASE ALLOYS—EFFECT ON CORROSION RESISTANCE

Similar to the situation described above for the Mo-bearing super austenitic stainless steels, Ni-base alloys that contain Mo for corrosion resistance are sometimes susceptible to attack when welded with matching filler metals. This is again due to the segregation of Mo during solidification that leads to Mo depletion at the dendrite cores. Table 7.3 lists a number of corrosion resistant Mo-bearing alloys that were welded with matching composition filler metals compared to the same alloys welded with high Mo and W filler metal ERNiCrMo-14 (FM 686 CPT). All welds were exposed to ASTM G-48 (so called “Green Death”) for 72 hours at 103°C (217°F). Note that all the as-welded joints made with ERNiCrMo-14 filler metal that contains 4%W have survived without attack, while welds in these same alloys made with a matching filler metal have been subject to attack. This demonstrates the important contribution of W which resists segregation during solidification and helps maintain the corrosion resistance of the weld metal.

## 7.7 9%Ni STEELS

Steels containing nominally 9wt% nickel and low carbon are widely used for cryogenic applications, particularly for the storage of liquefied natural gas (LNG). These steels have a nominal composition of Fe-9Ni-0.8Mn-0.3Si-0.1C. LNG tanks constructed of 9Ni steels and welded with Ni-base consumables have been in service since the late 1980s with no reported failures.(39) Welding of these tanks is normally conducted using SMAW and SAW.(3,40) The liquefaction temperature of natural gas (methane) is approximately  $-163^{\circ}\text{C}$  ( $-261^{\circ}\text{F}$ ), thus the toughness of welded 9Ni steels is of critical importance for the use of these steels for LNG tanks. Ni-base filler metals exhibit good fracture toughness at these temperatures, their coefficient of thermal expansion (CTE) closely match the 9Ni steels, and tensile strength is comparable. For these reasons, Ni-base filler metals, including the ENiCrMo-3 and -6, ERNiCrMo-3, -4 and -13 classifications and ERNiMo-8 and -9 have all been used to weld these steels, although the ERNiCrMo-3 and -4 types (such as Alloys 625 and C-276) are the most widely used. The room temperature tensile properties and cryogenic Charpy V-notch toughness values for these consumables and 9Ni steel are provided in Table 7.4.

### 7.7.1 Physical Metallurgy of 9%Ni Steels

9%Ni steel is a member of a family of nickel steels that were developed as early as the 1940s.(41) While lower nickel (3.5% and 5%) steels were developed first, it wasn't until 1947 that steels containing approximately 9% Ni were introduced.(42) At that time, the desire to store and process petroleum gases

**TABLE 7.3 Pitting Corrosion Resistance of Several Mo-bearing Alloy Welds made with Matching Filler Metals and Filler Metal 686CPT.**

Base Metal	Matching Filler Metal	ERNiCrMo-14
Alloy C-2000	Severe Attack (3 samples)	No Attack
Alloy 59	Severe Attack (3 samples)	No Attack
Alloy C-276	Severe Attack (3 samples)	No Attack
Alloy 622	Severe Attack (2 samples, 1 sample not attacked)	No Attack
Alloy C-22	Severe Attack (3 samples)	No Attack
Alloy 686	No Attack	No Attack

Note: The samples tested here are gas-tungsten-arc welds in 6mm thick plates. Triplicate tests were conducted in an oxidizing chloride pitting solution of 11.9% H<sub>2</sub>SO<sub>4</sub> + 1.3% HCl + 1% FeCl<sub>3</sub> + 1% CuCl<sub>2</sub> (so called Green Death) for three days at boiling, 103°C (217°F).

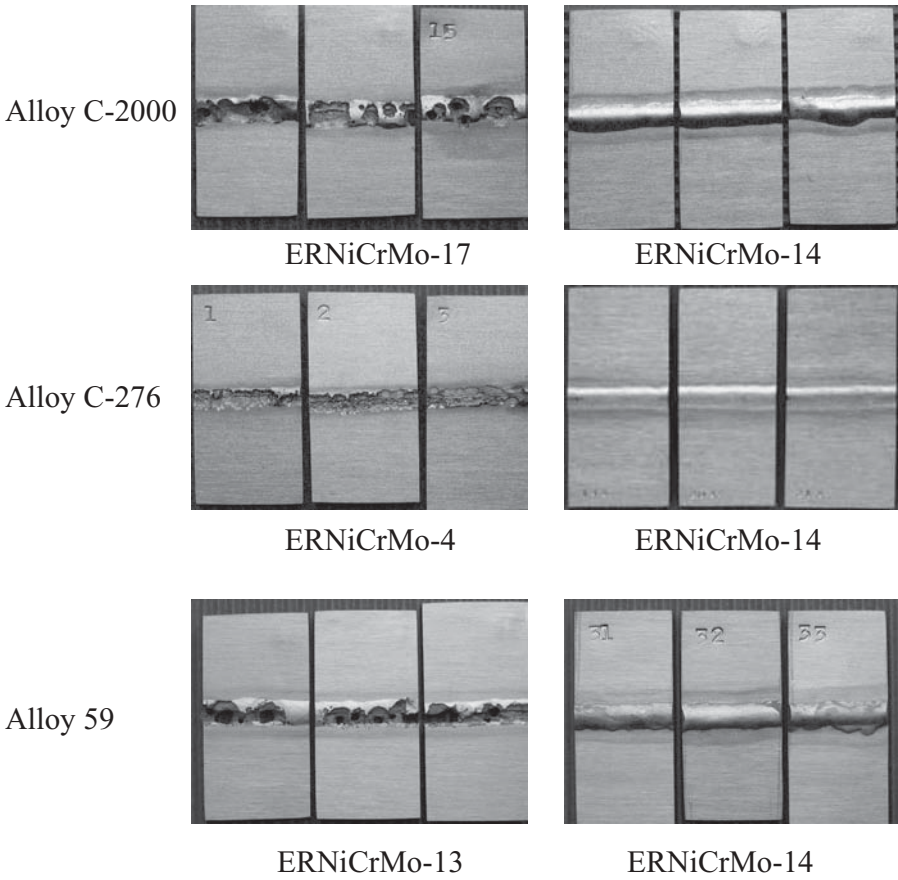


**TABLE 7.4 Room Temperature Tensile Properties and Cryogenic Toughness of 9Ni Steel and Several Ni-Base Filler Metals. (From Karlsson *et al.* [40])**

Material	Specification	Tensile Strength MPa (ksi)	Yield Strength MPa (ksi)	Elongation %	Charpy V-notch Toughness (J) at -196 °C
9Ni steel	ASTM 553/553M-93 (1)	690–825 (100–120)	>515 (75)	>20%	>34
	ASTM 553/553M-95 (2)	690–825 (100–120)	>585 (85)	>20%	>34
Alloy 625	ERNiCrMo-3 (3)	720 (104)	440 (64)	40	90
Alloy C-276	ERNiCrMo-4 (3)	700 (101)	480 (70)	35	75
Alloy 59	ERNiCrMo-13 (3)	675 (98)	470 (68)	45	70

(1) Double normalized and tempered.

(2) Quenched and tempered.

(3) Filler metal data from all weld metal SAW deposits, Courtesy ESAB.

in liquefied form was strong enough to stimulate the development of an economical material with acceptable impact strength at  $-166^{\circ}\text{C}$  ( $-267^{\circ}\text{F}$ ) along with good weldability.

Research conducted at INCO that varied nickel content in low carbon steels revealed that a ductile-to-brittle transition temperature (DBTT) does not exist above 13% nickel. Figure 7.24 shows the effect of nickel content on the Charpy V-notch toughness of low carbon steels containing 0 to 13% Ni from room temperature to  $-200^{\circ}\text{C}$  ( $-328^{\circ}\text{F}$ ).<sup>(42)</sup> The combination of nickel content and heat treatment has been found to provide the optimum toughness in these steels. A double normalizing and reheat treatment just above the  $A_1$  temperature produced a good combination of strength and toughness. (See ASTM A533/553M-93) This consisted of a first normalizing treatment at  $900^{\circ}\text{C}$  ( $1650^{\circ}\text{F}$ ), then a second at  $790^{\circ}\text{C}$  ( $1450^{\circ}\text{F}$ ) for grain refinement, followed by a reheat to  $565^{\circ}\text{C}$  ( $1050^{\circ}\text{F}$ ). The metallographic investigation showed that  $565^{\circ}\text{C}$  was above the  $A_1$  temperature and caused the carbides to transform to islands of nickel- and carbon-enriched austenite which remained stable to  $-195^{\circ}\text{C}$  ( $-320^{\circ}\text{F}$ ). Thus, the “duplex” structure of tempered martensite with dispersed islands of austenite resulted in good tensile strength and excellent impact toughness at relatively low cost. It was later discovered that a quenched and tempered heat treatment (see ASTM A553/A553M-95) also provided excellent properties with yield strength actually slightly higher than the double normalized material, as shown in Table 7.4.

The quench and tempered heat treatment consists of an austenitizing treatment in the range from 800-to- $925^{\circ}\text{C}$  ( $1475$  to  $1700^{\circ}\text{F}$ ), water quenching, and

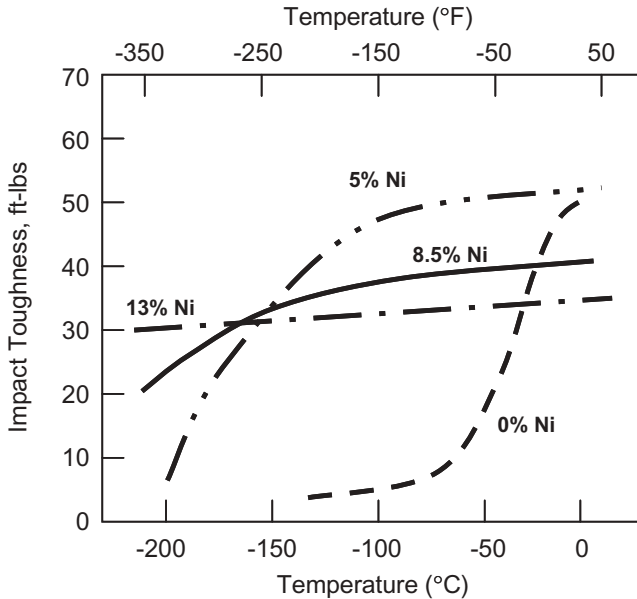


**Figure 7.24** The effect of nickel content on Charpy V-notch impact toughness of normalized low carbon steels. (From Armstrong *et al.* [41].)

then tempering in the range from 565-to-635°C (1050 to 1175°F). Again, this tempering treatment is above the  $A_1$  temperature and results in the formation of stable austenite that improves the cryogenic fracture toughness. It has been proposed that the exceptional cryogenic fracture toughness of these steels is a function of three factors:

- 1) the presence of stable retained austenite (on the order of 10 volume percent),
- 2) the reduction in carbon content of the martensite during tempering, and
- 3) the refined, duplex grain size.

Not unexpectedly, the HAZ microstructure of the 9Ni steels will differ from that of the base metal and will vary from location to location depending on the peak temperature and cooling rate. In general, the coarse grained HAZ adjacent to the fusion boundary would be expected to suffer the greatest degradation in properties, since this region is fully austenitized and will experience the most significant grain growth. Dhooze *et al.* (43) have suggested that the impact toughness in the HAZ can be reduced as much as 50 percent relative to the base metal. They also found that a postweld heat treatment at 600°C (1110°F) followed by rapid cooling can increase the HAZ toughness.

**TABLE 7.5 Effect of HAZ Peak Temperature on the Microstructure and Properties of a 9Ni Steel. (From Nippes *et al.* [44]. Courtesy the American Welding Society.)**

Condition	ASTM Grain Size	Hardness, R <sub>C</sub>	Retained Austenite, %	Impact Energy at -196°C, J (ft-lb)
Base metal, Q&T	9	20	9.4 ± 0.3	112 (82)
HAZ—500°C (930°F)	9	23	3.9 ± 0.6	104 (77)
HAZ—1000°C (1830°F)	11–12	37–38	<1.0	59 (44)
HAZ—1300°C (2370°F)	4–5	36	2.9 ± 0.1	38 (28)

The HAZ of these steels has also been studied by Nippes and Balaguer.(44) They used Gleeble<sup>®</sup> thermal simulation to study the effect of HAZ peak temperature on microstructure and impact toughness. The results of this study are summarized in Table 7.5 and the impact toughness as a function of peak temperature in the HAZ is shown in Figure 7.25. They found that heating to 500°C (930°F) results in a decrease in retained austenite, but little change in impact toughness. Heating to a peak temperature of 1000°C (1830°F), results in a decrease in both grain size and retained austenite but a sharp increase in hardness due to the formation of untempered martensite on cooling. This leads to a sharp drop in impact toughness. When heated to 1300°C (2370°F), a further decrease in impact toughness occurs due to the coarsening of the prior austenite grains. Based on these results, it is clear that a postweld tempering treatment is needed to restore the toughness of the transformed region of the HAZ to that of the base metal. This may also be accomplished during multipass welding by controlled weld heat input such that underlying passes are tempered by subsequent passes. It should be noted, however, that although the cryogenic toughness of the as-welded HAZ of the 9Ni steels is degraded relative to the base metal, the values still exceed the minimum called out in the specification (Table 7.4). For this reason, large field-welded LNG tanks can be safely put into service in the as-welded condition.

### 7.7.2 Hot Cracking of Ni-base Weld Deposits

One problem that has plagued the use of Ni-base filler metals for joining 9Ni steels is weld hot cracking. The Ni-base weld deposit will always solidify as austenite, even when highly diluted by the 9Ni steel, and therefore the potential for hot cracking exists. Karlsson *et al.*(45) have studied the cracking susceptibility of submerged arc welding (SAW) deposits on 9Ni steels using ERNiCrMo-3 (Alloy 625), ERNiCrMo-4 (Alloy C-276), and ERNiCrMo-13 (Alloy 59) consumables. They used both metallographic techniques and

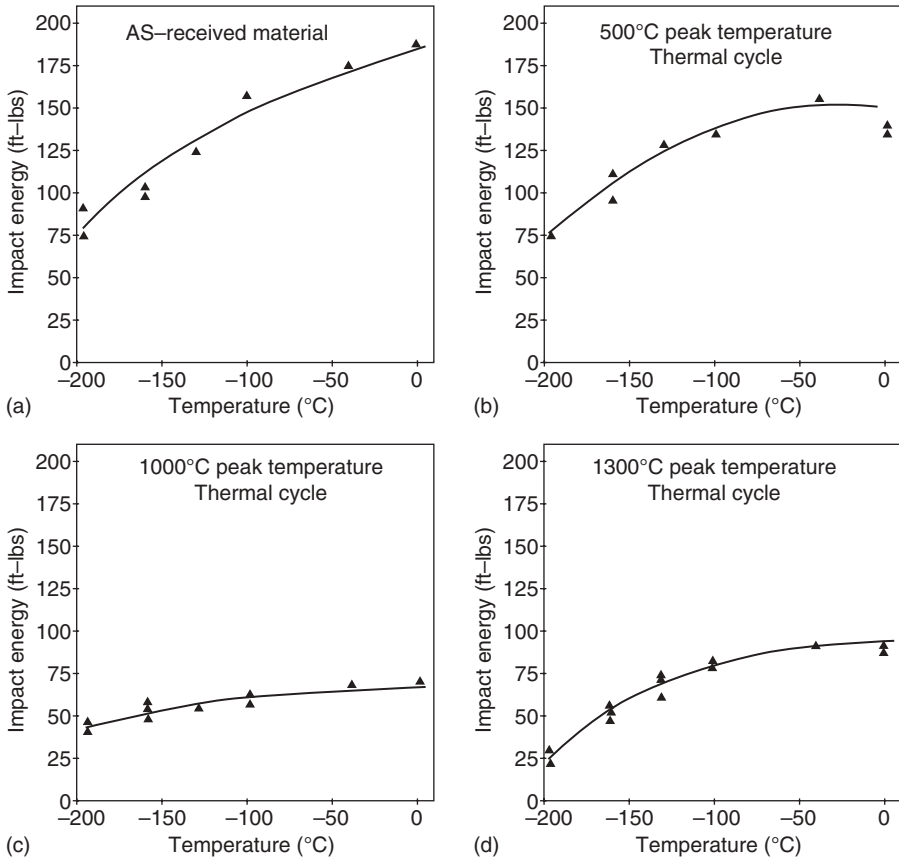


**Figure 7.25** Impact toughness versus temperature for the simulated HAZ in 9Ni steels, a) Q&T base metal, b) 500°C peak, c) 1000°C peak, and d) 1300°C peak. (From Nippes *et al.* [44]. Courtesy of the American Welding Society.)

weldability testing to evaluate susceptibility to hot cracking in multipass SAW deposits made using both high and low weld heat inputs (1.5 and 0.9 kJ/mm, respectively). The results of this evaluation are provided in Table 7.6. Based on these results, the FM 625 deposits appear to be the most resistant based on metallographic and bend test results. (a face bend test was used to open up small cracks). However, the Varestraint test results indicate that FM 625 is the most susceptible with FM 59 the most resistant. This apparent contradiction is associated with the degree of strain that is applied during Varestraint testing, as discussed in Section 3.5.1. Since FM 625 forms considerable liquid of eutectic composition at the termination of solidification, crack “healing” is possible at low restraint levels. When higher “augmented” strains are applied, such as during the Varestraint test, this healing phenomenon is ineffective and cracks may form.

**TABLE 7.6 Hot Cracking Susceptibility of SAW Weld Deposits on 9Ni steels made using Ni-base Filler Metals. A value of 1 is most crack resistant and 6 most susceptible. (From Karlsson *et al.* [45])**

Weld Metal	Heat Input (1)	Metallography and Bend	
		Test Ranking	Varestraint Ranking
FM 59	L	3.2	2.6
	H	3.5	1.3
FM 625	L	1.2	3.9
	H	1.7	4.7
FM C-276	L	5.2	3.6
	H	5.3	4.2

(1) L = 0.9kJ/mm, H = 1.5kJ/mm.

The cracking reported by Karlsson *et al.*(45) is reported as “hot cracking” and consisted of a combination of weld solidification cracking, weld metal liquation cracking, and ductility-dip cracking. In general, these cracks were quite small and reported as “micro-cracks,” but a number of large cracks were observed in the C-276 deposits. Additional testing is warranted to determine the root cause of the cracking in these filler metals and to develop crack-resistant consumable for joining the 9% Ni steels.

## 7.8 SUPER DUPLEX STAINLESS STEELS

Super duplex stainless steels, such as Alloys 2507 (UNS S32750) and DP3 (UNS S31260 are often used in aggressive corrosion environments where service temperatures are below approximately 350 °C (660 °F). These steels contain 24–26 Cr, 5–8 Ni, 3–5 Mo and 0.2–0.3 N and up to 0.5 W (DP3 only). They have good resistance to chloride stress corrosion cracking, pitting and crevice corrosion. The corrosion behavior of the weld metal of these steels is largely controlled by the microstructure balance of ferrite and austenite with an approximate 50–50 balance providing optimum corrosion resistance. Under normal fabrication conditions, this balance can be achieved by a postweld heat treatment (PWHT). For field fabrication, such as the construction of large pipelines, PWHT may not be possible with the potential for the corrosion resistance of the weld metal to be compromised. In these cases, Ni-base filler metals may be used since a PWHT is not needed to improve corrosion resistance of the weld deposit.

An example of the use of ERNiCrMo-14 (INCO-WELD® Filler Metal 686CPT™) for field fabrication of large diameter Alloy 2507 pipe for geothermal brine service has been reported by Furmanski *et al.*(46) A multipass weld procedure was developed and mechanical and corrosion testing was performed on samples in the as-welded condition. The weld metal in this dissimilar combination is fully austenitic. Bend tests revealed that these welds were free of

defects and pitting corrosion testing per ASTM G48, Practice C showed virtually no general corrosion and no pitting at 35°C. Based on these results, it appears that Ni-base filler metals of the ERNiCrMo-14 type are suitable for use with super duplex stainless in aggressive corrosion environments in the as-welded condition. Other Ni-base filler metals would also be compatible with the duplex and super duplex stainless steels, depending on the service environment.

## 7.9 CASE STUDIES

### 7.9.1 Postweld Heat Treatment Cracking of Thick Section Welds in Alloy 800H Made with ENiCrFe-2 Filler Metal

A large, thick-walled “hydrogenation” reactor had experienced Postweld Heat Treatment (PWHT) cracking in the vicinity of nozzle welds in the lower portion of the reactor. This reactor was constructed of Alloy 800H, an austenitic stainless steel with a nominal composition 20Cr-32Ni-0.5Ti-0.5Al-0.1C. The 800H grade is a modified version of Alloy 800, with higher carbon and a larger grain size to improve elevated temperature stress-rupture properties. The 800H base metal was supplied as three-inch thick plate and conformed to ASME SB409. All nozzle welds in the reactor vessel were made using shielded metal arc welding (SMAW) with Weld A (ENiCrFe-2) filler metal. The compositions of the base and filler metal are provided in Table 7.7.

Cracking was initially reported during original vessel fabrication. This cracking was associated with fillet welds in nozzles on the bottom of the

**TABLE 7.7 Chemical Composition (wt%) of Alloy 800H and Weld A Filler Metal.**

Element	Alloy 800H	Weld A
Iron	44.15	8.07
Chromium	20.71	14.43
Nickel	32.99	72.48
Copper	0.36	0.02
Aluminum	0.35	NA
Titanium	0.29	NA
Niobium	<0.01	1.58
Molybdenum	0.02	1.46
Silicon	0.1	0.51
Manganese	0.8	1.36
Carbon	0.08	0.04
Nitrogen	0.02	NA
Sulfur	<0.001	0.005
Phosphorus	0.004	0.007

reactor vessel. These cracks were repaired at the fabrication shop, given a local PWHT, and inspected. The vessel was then hydrotested, and shipped to the erection site. During erection, additional cracks were found in the same nozzle fillet welds. These cracks were ground out and repaired and then the bottom of the vessel was subjected to a PWHT. Inspection following this repair revealed extensive cracking in the welds in the same nozzles and one additional nozzle. A third repair attempt, followed by PWHT, also resulted in cracking in the nozzle fillet welds. At that point, “boat” samples were removed for metallurgical analysis in order to determine the root cause of cracking.

PWHT is recommended for Alloy 800H in applications where the material will be used in prolonged elevated temperature service. Such a PWHT is now mandated by the ASME Code.<sup>(47)</sup> The purpose of the PWHT is to “stabilize” the Alloy 800H heat-affected zone (HAZ) microstructure, such that it will be resistant to relaxation cracking in service. The specifications for the PWHT used for this reactor were as follows:

- Heat from ambient to 425 °C (800 °F) at a controlled rate between 28 and 55 °C/hr (50 and 100 °F/hr)
- Above 425 °C (800 °F) heat at a maximum 110 °C/hr (200 °F/hr)
- Hold at 900 ± 13 °C (1650 ± 25 °F) for 3.5 hours.
- Cool slowly under insulation to 315 °C (600 °F)
- Remove insulation and air cool from 315 °C (600 °F)

During the second repair and PWHT, it was thought that the cooling rate from the soaking temperature may have been too rapid, thereby resulting in cracking due to large temperature differentials between the reactor vessel and nozzles. The cooling rate from the soaking temperature during the PWHT after the third repair was carefully controlled to minimize these differentials below 150 °F. This apparently had little effect on the susceptibility of the welds to cracking.

Some representative surface breaking cracks from the boat sample removed from the reactor nozzle welds after the third repair and PWHT are shown in Figure 7.26.

At higher magnification (Figure 7.27) it can be seen that these cracks form preferentially along the high angle, migrated grain boundaries in the weld metal. Even in regions where boundary cracking was not observed, there was evidence of void formation at the boundary.

Based on metallographic and fractographic evidence (see Figure 7.16), the most likely cause for failure is reheat cracking. The mechanism for reheat cracking is as follows:

- During welding, precipitates dissolve and grain growth occurs. Impurity segregation to grain boundaries is possible.

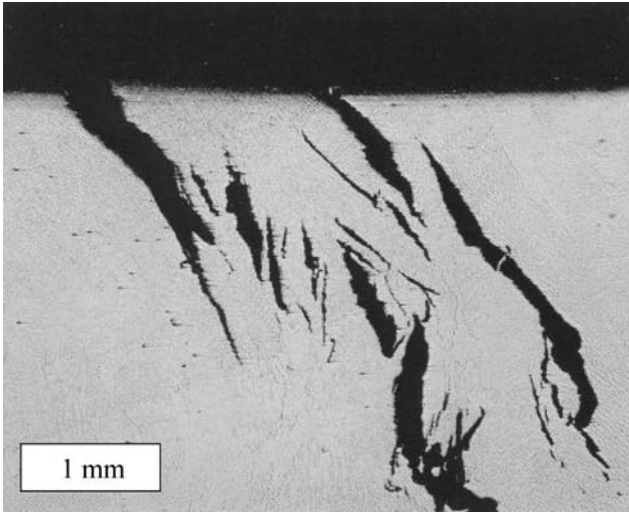


**Figure 7.26** Surface breaking cracks from a boat sample removed from a nozzle fillet weld made with ENiCrFe-2 (Weld A) filler metal.

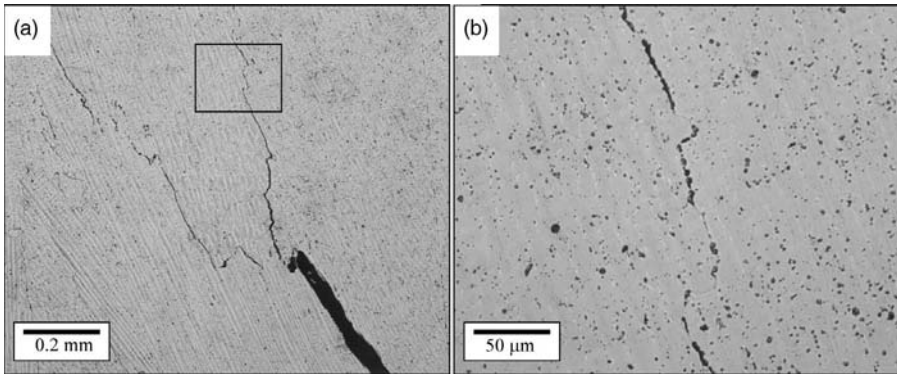


**Figure 7.27** Cracking along weld metal grain boundaries in WELD A deposit, a) Low magnification of multiple cracks, b) inset from (a) showing linking of voids along the grain boundary.

- During cooling from the welding temperature, residual stresses develop in the weldment. The residual stresses may be particularly high in thick section weldments.
- As the weldment is heated to the PWHT temperature, residual stresses begin to relax and precipitation reactions can occur. If the relaxation and precipitation temperature ranges overlap, stress redistribution may occur locally in the microstructure.

- As precipitates form intragranularly and along grain boundaries, a precipitate free zone exists just adjacent (a few microns) to the boundary. Since this is a soft region in the microstructure, straining of these boundaries will occur and grain boundary failure (cracking) is possible if the local strain exceeds the grain boundary ductility. The grain boundary ductility is further reduced by impurity segregation to the boundary. Some theories also propose that the formation of brittle grain boundary films can lead to cracking.

The key ingredients for reheat cracking are, therefore, the formation of strengthening precipitates in the same temperature range where stress relaxation occurs. For reheat cracking, this occurs during the heating portion of the PWHT cycle. Controlling reheat cracking requires the management of one of these phenomena.

Although ENiCrFe-2 (Weld A) deposits are not generally considered to be susceptible to reheat (or stress relief) cracking, it appears that this form of cracking may occur in situations where the weld restraint and associated residual stresses are quite high. It is postulated that the precipitation of NbC during PWHT has contributed to mechanism of reheat cracking in the weld metal. From Table 7.7, it can be seen that the Nb content of the filler metal is 1.58wt% with carbon on the order of 0.04wt%. Such a Nb content could lead to NbC precipitation during heating to the PWHT temperature of 900°C (1650°F).

In an attempt to manage the weld metal stress relaxation, an intermediate PWHT was attempted before the joint was completely welded out. It was hoped that the reduced residual stresses in the partially welded joint would minimize stress relaxation and avoid cracking. Unfortunately, this approach was not successful. Attempts were also made to locally relieve weld residual stresses by hammer peening the welds between passes. This was also unsuccessful, presumably because the peening only affected the surface of the weld and not the underlying weld metal. The nozzle welds were eventually completed by a combination of weld heat input control (to minimize residual stresses) and slower heating rates to the PWHT temperature. This latter approach allows more residual stress to be relaxed prior to the onset of carbide precipitation.

### **7.9.2 Alloy 925 Welded with ERNiCrMo-15 (INCO-WELD 725NDUR) for Manufacturing Vacuum Insulated Oil Patch Tubing**

Vacuum insulated double-walled tubing (VIT) has been employed over the years in the petrochemical industry to prevent the increase in crude oil viscosity due to cool down. This application sometimes requires the VIT to combine high strength with good corrosion resistance for extreme sour (H<sub>2</sub>S) environments. Because of its combination of strength and corrosion resistance, Alloy 925 was chosen as a candidate tubing material for this application.(48) Alloy

**TABLE 7.8 Compositions (wt%) of Alloy 925 and Two Heats of Filler Metal 725.**

Element	Alloy 925	Filler metal 725	
		Filler metal A	Filler metal B
C	0.03 max	0.006	0.003
Cr	19.5–22.5	20.81	20.75
Mo	2.5–3.5	8.04	7.97
Ni	42.0–46.0	58.68	58.60
Fe	22 min	7.17	7.46
Mn	1.0 max	0.06	0.07
Cu	1.5–3.0	1.5	3.0
Ti	1.9–2.4	1.48	1.49
Nb	0.5 max	3.46	3.40
Al	0.1–0.5	0.24	0.22
Si	0.5 max	0.04	0.03
S	0.03 max	0.03 max	0.03 max

925 (UNS N09925) is an age-hardenable nickel-iron-chromium alloy with additions of molybdenum, copper, titanium and aluminum (see Table 7.8) designed to be age-hardenable by precipitation of  $\gamma'$ ,  $\text{Ni}_3(\text{Ti},\text{Al})$ . The nickel content is sufficient for resistance to chloride-ion stress corrosion cracking and nickel, in conjunction with the molybdenum and copper, provides outstanding resistance to reducing chemicals. The molybdenum provides protection against pitting and crevice corrosion, while the chromium provides resistance to oxidizing environments.

Welding of Alloy 925 for the VIT application presented a significant challenge, since the filler metal must ensure good weldability coupled with adequate strength and corrosion resistance in sour environments. The age-hardenable INCO-WELD Filler Metal 725NDUR (ERNiCrMo-15) was recommended for welding Alloy 925 because it provides over-matching strength and corrosion resistance. The composition of ERNiCrMo-15 is also listed in Table 7.8. The root pass was deposited by gas tungsten arc welding (GTAW) using filler metal A and then the joint was completed using manual pulsed gas metal arc welding (P-GMAW) with filler metal B. Postweld heat treatment (PWHT) was performed at 732 °C (1350 °F) for four hours followed by air-cooling.

The application in the petroleum industry required the materials to be resistant to corrosion environments containing  $\text{H}_2\text{S}$ ,  $\text{CO}_2$ , and chlorides, and to exhibit a minimum yield strength of 115 ksi (795 MPa) and a minimum room temperature Charpy impact value of 25 ft-lbs (42 J). The mechanical properties for the welded Alloy 925, as well as Alloy 925 at different conditions, are shown in Table 7.9. It shows that after PWHT the mechanical properties of the weld exceed the properties of aged Alloy 925, and also meet the minimum requirement for petrochemical industry applications.

**TABLE 7.9 Typical Mechanical Properties of Alloy 925 and Welded Alloy 925 using Filler Metal 725 after PWHT at 732°C (1350°F) for 4 hours followed by air-cooling. (From Shademan *et al.* [48])**

Alloy	Condition	Yield Strength ksi (MPa)	Tensile Strength ksi (MPa)	Elongation (%)	Impact Energy @ RT, ft-lbs (J)
Alloy 925	SA/Aged	113 (779)	172 (1214)	26	—
	CW	129 (889)	140 (965)	17	—
Alloy 925	CW/Aged	153 (1055)	176 (1214)	19	—
	Cast/SA/Aged	107 (736)	128 (880)	23	—
Alloy 925/ FM725	PWHT	115 (793)	154 (1062)	16	30(51)

Stress corrosion cracking (SCC) susceptibility of the welded Alloy 925 VIT and base metal 925 was evaluated in a sour environment containing H<sub>2</sub>S, CO<sub>2</sub>, and chlorides. The particular condition for the SCC test is in a deaerated 25% NaCl solution with 3 psig (0.021 MPa) CO<sub>2</sub>, 3 psig (0.021 MPa) H<sub>2</sub>S, 3000 psig (20.7 MPa) total pressure at 200°F (93.3°C) for 30 days.(48) Both the 725 weld metal (three C-ring specimens) and base metal (three C-ring specimens) of Alloy 925 were tested in the sour environment. The C-ring test specimens containing the weldment were taken from a longitudinally welded wall of Alloy 925 tubing with filler metal 725 (heat A) shown in Table 7.8. All the specimens were loaded to 100% of the actual yield strength according to NACE standard TMO 177, method C.

SCC testing showed no cracking and only superficial pits on the surface of both the weld metal and base metal. The C-ring SCC results clearly indicated that both base metal and welded Alloy 925 after PWHT did not crack and performed well in the sour environment. Although some superficial pits were observed, the pitting density was low and the pits were too shallow for any pit depth measurements. To summarize, Alloy 925 welded with filler metal 725 provides the required mechanical properties and corrosion resistance for service in sour environments containing H<sub>2</sub>S, CO<sub>2</sub> and chlorides for severe service VIT applications.

### 7.9.3 Corrosion-Fatigue of Alloy 625 Weld Overlays

Ni-base weld overlay coatings are used extensively for corrosion protection of waterwalls in coal-fired power plants that operate under so-called low NO<sub>x</sub> firing conditions. It has recently been recognized that certain weld overlay coatings are susceptible to cracking while operating in this combustion environment. Recent results have established the mechanism associated with this form of failure.(49) Figure 7.28 shows a photograph of an Alloy 625 weld overlay with extensive cracks oriented circumferentially around the waterwall

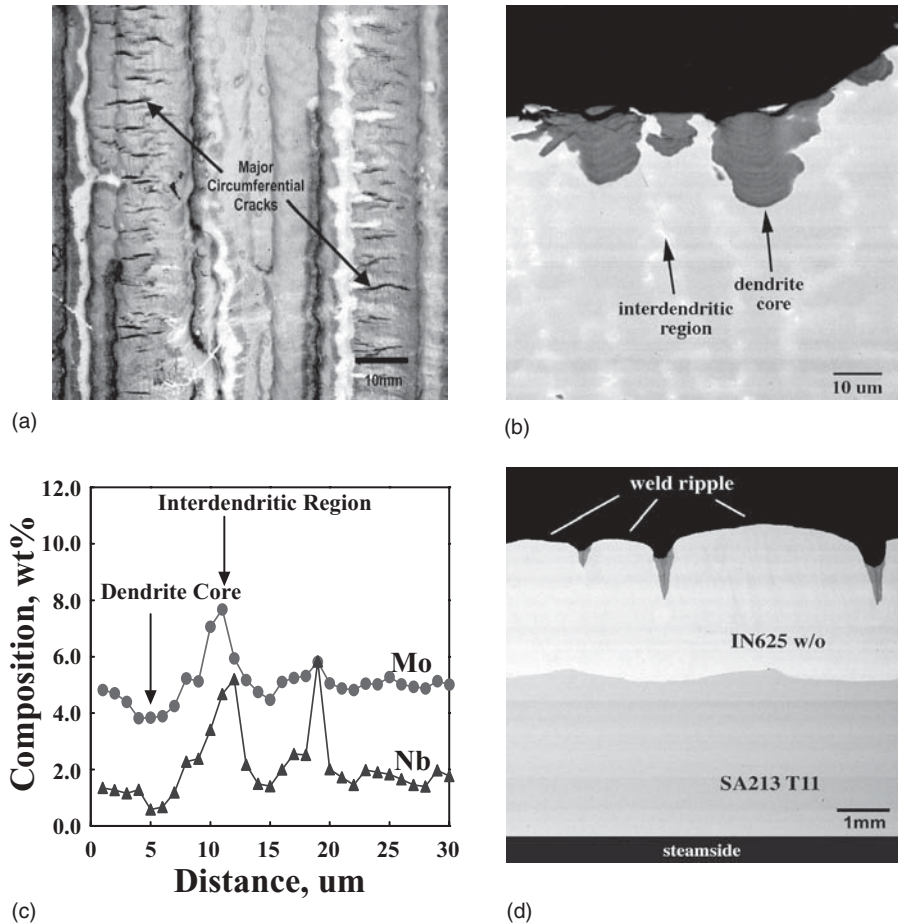


**Figure 7.28** Alloy 625 overlay, a) macrograph showing extensive transverse cracking b) light optical photomicrograph showing oxide penetration and cracking early in the growth stage, c) EPMA data showing distribution of alloying elements across the dendritic substructure of the overlay, and d) low magnification light optical photomicrograph showing crack initiation at locations of weld ripple. (From Luer *et al.* [49].)

tubes. Figure 7.28b shows a cross-sectional light optical photomicrograph of several small cracks that were examined early in the growth stage, and Figure 7.28c shows the distribution of alloying elements across the dendritic substructure of the overlay. The overlay shows the expected concentration gradients in Nb and Mo, where these elements are depleted at the dendrite core regions. As a result, the corrosion rate is accelerated in these regions and localized attack occurs preferentially at the dendrite cores. These localized penetrations form stress concentrations that eventually grow into full size fatigue cracks under the influence of stress from thermal fluctuations during operation. As

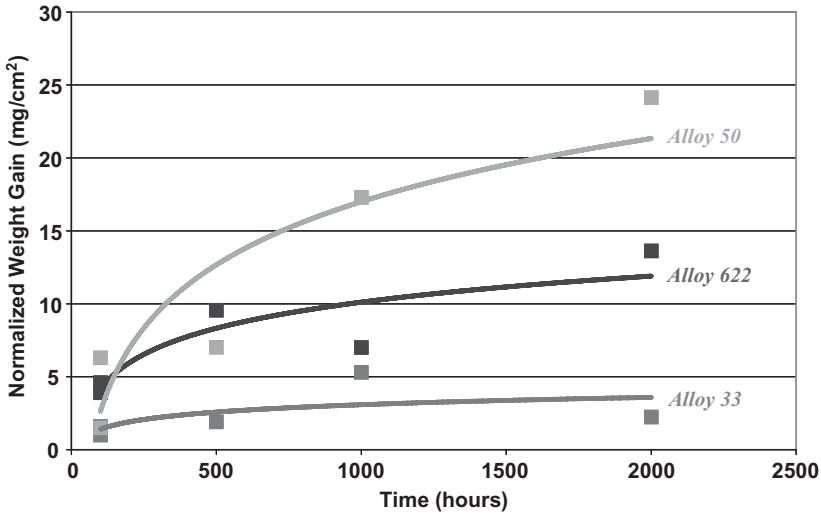


**Figure 7.29** Results from 2000 hour corrosion tests of three different weld overlays that were exposed to a simulated low NO<sub>x</sub> combustion environment (10%CO-5%CO<sub>2</sub>-2%H<sub>2</sub>O-0.12%H<sub>2</sub>S-N<sub>2</sub>, in vol %) at 500 °C. (From Deacon *et al.* [50].)

shown in Figure 7.28d, most cracks initiate at the valleys of weld ripple where an additional stress concentration exists. Thus, this is a form of corrosion-fatigue cracking, where the fatigue cracks are initiated by localized corrosion that occurs in regions where alloy-depleted dendrite cores are aligned under the valleys of surface weld ripples.

As explained in detail in Chapter 3, it is impossible under normal arc welding conditions to avoid microsegregation of Nb and Mo during solidification of Ni-base alloys. Thus, the recent approach to help avoid this problem involves the use of higher Cr alloys that do not contain Mo or Nb. High-Cr alloys are beneficial because Cr helps promote the formation of a protective chromium oxide scale for corrosion protection and Cr does not segregate extensively during solidification. Figure 7.29 shows results from 2,000 hour corrosion tests of three different weld overlays that were exposed to a simulated low NO<sub>x</sub> combustion environment (10%CO-5%CO<sub>2</sub>-2% H<sub>2</sub>O-0.12%H<sub>2</sub>S-N<sub>2</sub>, in vol %) at 500 °C. Alloy 622 is basically a Ni-21Cr-14Mo-4Fe-4W alloy, while Alloy 50 has a nominal composition of Ni-20Cr-14Fe-12Mo-1.6W. In contrast, Alloy 33 has a nominal composition of Ni-33Cr-32Fe-1.5Mo. This alloy was chosen for its high Cr level and low Mo level. With this approach, Mo microsegregation is essentially eliminated, and corrosion protection is provided by the higher Cr content. The Alloy 50 and 622 weld overlays were prepared at a dilution level of 6% and 7%, respectively, while the Alloy 33 overlay was prepared at 12% dilution. Note that the best corrosion resistance is provided by the Alloy 33 weld overlay, even though it was prepared at a slightly higher dilution level.

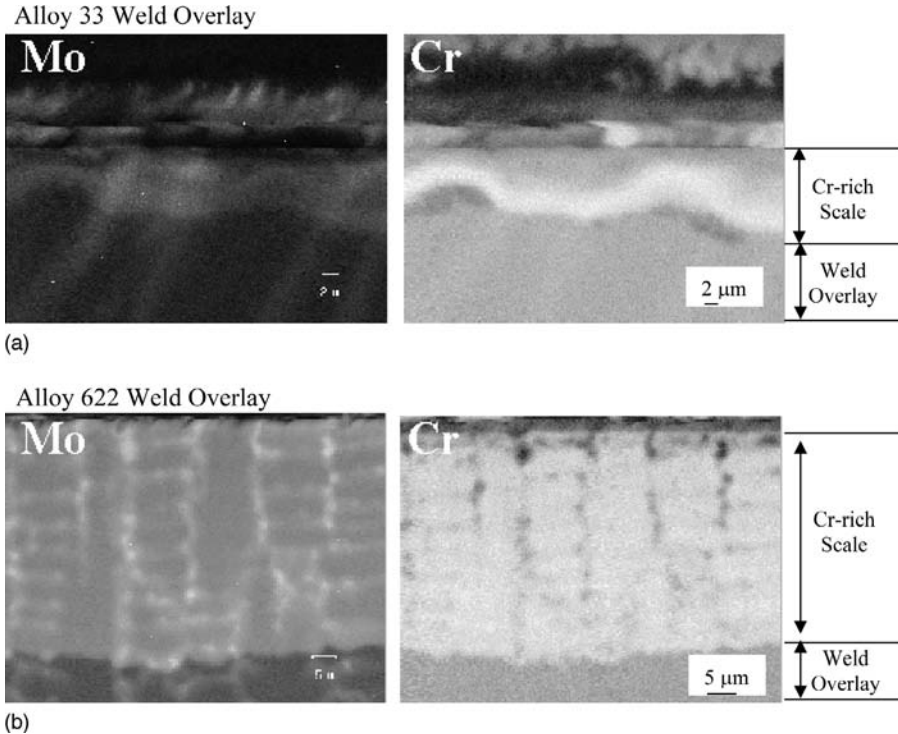


**Figure 7.30** X-ray maps acquired from Alloy 622 and 33 weld overlays after 2000 hour exposure to a simulated low NO<sub>x</sub> environment showing the relative concentrations of Mo and Cr in the overlay and Cr-rich scale that forms on the surface of each overlay. (From Deacon *et al.* [50].)

Figure 7.30 shows SEM X-ray composition maps acquired from the Alloy 622 and 33 overlays after the full 2,000 hours of exposure. These results explain the observed difference in the corrosion performance. The maps show the relative concentrations of Mo and Cr in the overlay and Cr-rich scale that forms on the surface of each overlay. Note that the Mo segregation that exists in the overlay of Alloy 622 persists through the Cr-rich scale. Also note that the Cr concentration is low within the scale in areas where the Mo concentration is high. These Cr-depleted regions within the scale provide avenues for fast diffusion of corrosive gases through scale, where the gas can then react with and corrode the underlying weld overlay. The Alloy 50 weld overlay showed similar features. In contrast, the Mo segregation is minimal in the Alloy 33 overlay because the nominal Mo concentration is very low (~1.5 wt%). As a result, the Cr-rich scale exhibits a uniform Cr concentration and therefore is more protective. Note that the scale is much thinner on the Alloy 33 overlay compared to that on the Alloy 622 weld overlay, which indicates less of the Alloy 33 weld overlay was consumed due to corrosion. This difference accounts

for lower weight gain and improved corrosion resistance of the Alloy 33 weld overlay.

#### 7.9.4 Overlay of “Safe-End” Welds using High-Cr, Ni-base Filler Metals

In the nuclear power industry, attachment of stainless steel pressure piping to large pressure vessels (such as steam generators) is accomplished using what is termed a “safe-end” weld. There are several variations of the safe-end weld, but all rely on the use of a Ni-base filler metal to join the pressure vessel steel nozzle to the austenitic stainless steel piping. For many applications, Filler Metal 82 or 182 (ERNiCr-3 or ENiCrFe-3) has been the consumable of choice for this application. The use of the Ni-base “buffer” between the pressure vessel steel nozzle and the austenitic stainless steel piping (normally Type 304L or 316L) prevents the onset of creep cracking, as described in Section 7.3.3.3. Unfortunately, the use of these lower chromium (18–22 wt%) filler metals has led to a corrosion cracking problem known as primary water stress corrosion cracking (PWSCC) in many power plants. Since the replacement of these welds would be both extremely expensive and result in considerable down time, an overlay procedure has been developed that can be applied over the existing safe-end welds. Such an overlay provides additional structural support in the event that PWSCC occurs and also generates compressive stresses in the underlying weld metal that can retard the progression of PWSCC in the FM 82/182 deposit.

Since chromium levels exceeding 25 wt% are believed to mitigate PWSCC, Filler Metals 52 and 52M (ERNiCrFe-7 and ERNiCrFe-7A) have been used extensively in the US for these overlay applications. The thickness of the overlay is controlled such that it maintains the “pressure boundary,” i.e., it has sufficient strength to insure safe operation even if PWSCC penetrates entirely through the FM 82/182 weld. Since the safe-end weld joins a pressure vessel steel to austenitic stainless steel piping (often with an intermediary stainless steel casting) the Ni-base filler metal will be diluted by both carbon steel and stainless steel.

There have been a number of instances where the initial overlay pass on the stainless steel has encountered cracking in the weld metal. An example of this is shown in Figure 7.31, where ERNiCrFe-7A was applied to Type 316L piping.<sup>(51)</sup> The root cause of the cracking was determined to be weld solidification cracking arising from both the dilution of the filler metal by Fe from the stainless steel and the abnormally high sulfur content (~0.015 wt%) of the Type 316L pipe that was being overlaid. Subsequent studies showed that solidification cracking can occur even in low sulfur stainless steels if dilution of the Ni-base filler metal by the stainless steel is above approximately 40%, as shown in Figure 7.32 for welds made using GTAW with cold wire feed.<sup>(52)</sup>

In order to avoid this type of cracking, a Type 308L “buffer layer” was first applied over the stainless steel pipe section of the safe-end. Because the Type

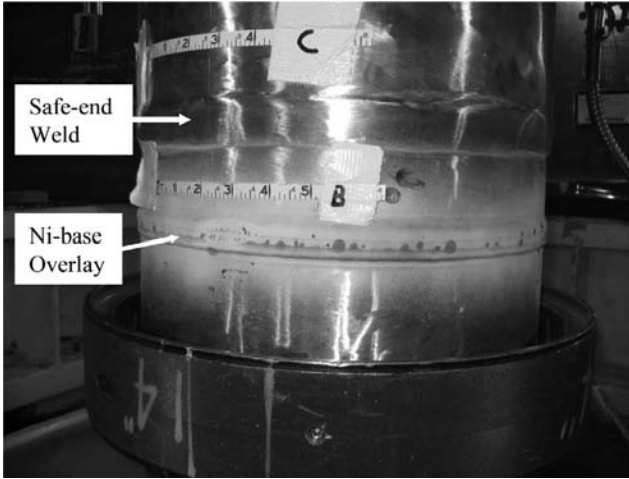
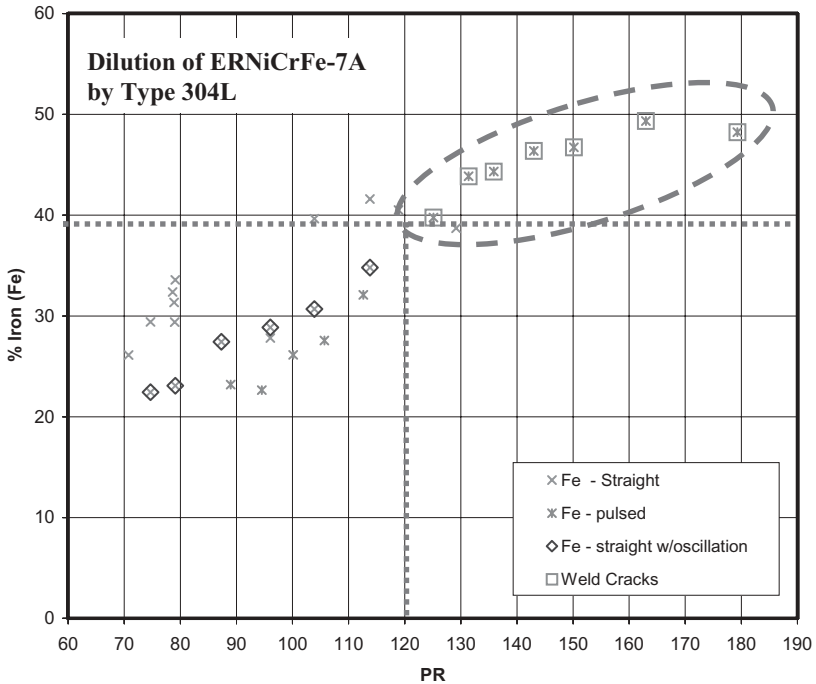


**Figure 7.31** Dye penetrant indications in Filler Metal 52M overlay on Type 316L stainless steel. (From Smith [51])



$$\text{Power Ratio} = \frac{I \times V}{(WFS/TS) \times A_{\text{wire}}}$$

**Figure 7.32** Effect of Fe content on the solidification cracking susceptibility of Filler Metal 52M diluted by Type 304L stainless steel. Cracking is observed in welds made at power ratios exceeding 120 and Fe content over 40wt%. (From Frederick [52])

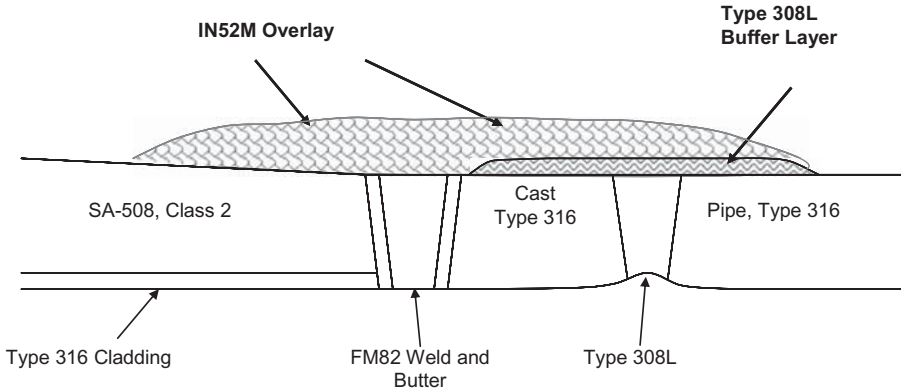


**Figure 7.33** Schematic of weld overlay configuration for a safe-end weld incorporating a Type 308L buffer layer over the stainless steel.

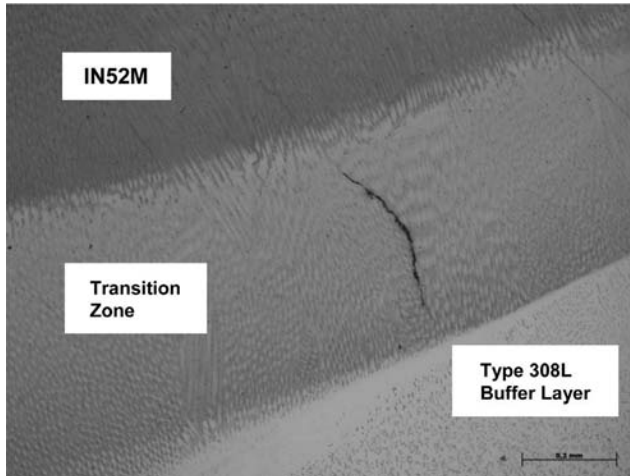


**Figure 7.34** Solidification cracking in the composition transition zone between the Filler Metal 52M overlay and the Type 308L buffer layer.

308L weld metal solidifies as ferrite, its solidification cracking resistance is much higher and it is immune to dilution effects by the underlying substrate.<sup>(1)</sup> The overlay configuration to avoid solidification cracking in the deposit on the stainless steel is shown in the schematic in Figure 7.33. This configuration has proved to be quite successful in the field, although it is likely that some small cracks may form in the composition transition zone between the Type 308L and the Ni-base filler metal, as shown in Figure 7.34. These cracks are quite small and limited by the thickness of the transition zone (typically one mm or less), and do not compromise the integrity of the overlay. It does indicate, however, that dilution of Ni-base filler metals by Fe can

potentially lead to solidification cracking if dilution is not controlled below some critical level.

## REFERENCES

1. Lippold, J. C. and Kotecki, D. J. 2005. *Welding Metallurgy and Weldability of Stainless Steels*, John Wiley and Sons, Inc. Hoboken, N.J., ISBN 0-47147379-0.
2. Kiser, S. 1990. Nickel-alloy consumable selection for severe service conditions, *Welding Journal*, 69(11): 30–35.
3. Hilkes, J., Neessen, F., and Caballero, S. 2004. Electrodes for Welding 9% nickel Steel, *Welding Journal*, 83(1): 30–37.
4. DuPont, J. N. and Marder, A. R. 1996. Dilution in Single Pass Arc Welds, *Metallurgical and Material Transactions B*, 27B: 481–489.
5. DuPont, J. N. and Kusko, C. S. 2007. Martensite Formation in Austenitic/Ferritic Dissimilar Alloy Welds, *Welding Journal*, 86(2): 51s–54s.
6. Chandel, R. S. 1987. Prediction of Weld Metal Dilution from SAW Parameters, *Welding Review*, 6(1): 45–46.
7. Oh, Y. K., Deletion, J. H., and Chen, V. S. 1990. Low-Dilution Electroslag Cladding for Shipbuilding, *Welding Journal*, 69(8): 37–44.
8. Fuerschbach, P. W. and Knorovsky, G. A. 1991. A Study of Melting Efficiency in Plasma Arc and Gas Tungsten Arc Welding, *Welding Journal*, 70(11): 287s–297s.
9. DuPont, J. N. and Marder, A. R. 1995. Thermal Efficiency of Arc Welding Processes, *Welding Journal*, 74(12): 406s–416s.
10. Gandy, D. W., Findlan, S. J., Childs, W. J., and Smith, R. E. 1992. A better way to control GTA weld dilution, *Welding Design & Fabrication*, August 1992: pp. 40–43.
11. Forsberg, S. G. 1985. Resistance Electroslag (RES) Surfacing, *Welding Journal*, 64 (8): 41–48.
12. Schaeffler, A. L. 1949. Constitution diagram for stainless steel weld metal, *Metal Progress*, 56(11): 680–680B.
13. Lundin, C. D. 1982. Dissimilar Metal Welds—Transition Joints Literature Review, *Welding Journal*, 61(2): 58-s–63-s.
14. Pan, C., Wang, R., and Gui, J. 1990. Direct TEM Observation of Microstructures of the Austenitic/Carbon Steels Welded Joint, *Journal of Materials Science*, 25: 3281–3285.
15. Matsuda, F. and Nakagawa, H. 1984. Simulation test of disbonding between 2.25%Cr-1%Mo steel and overlaid austenitic stainless steel by electrolytic hydrogen charging technique, *Transactions of JWRI*, 13(1): 159–161.
16. Nelson, T. W., Lippold, J. C., and Mills, M. J. 1999. Nature and Evolution of the Fusion Boundary in Ferritic-Austenitic Dissimilar Metal Welds—Part 1: Nucleation and Growth, *Welding Journal*, 78(10): 329s–337s.
17. Nelson, T. W., Lippold, J. C., and Mills, M. J. 2000. Nature and Evolution of the Fusion Boundary in Ferritic-Austenitic Dissimilar Metal Welds—Part 2: On-Cooling Transformations, *Welding Journal*, 79(10): 267-s–277-s.

18. Nelson, T. W., Lippold, J. C., and Mills, M. J. 1998. Investigation of boundaries and structures in dissimilar metal welds, *Sci. and Tech. of Weld. and Joining*, 3(5): 249.
19. Rowe, M. D., Nelson, T. W., and Lippold, J. C. 1999. Hydrogen-Induced Cracking along the Fusion Boundary of Dissimilar Metal Welds, *Welding Journal*, 78(2): 31s–37s.
20. Sakai, T., Asami, K., Katsumata, M., Takada, H., and Tanaka, O. 1982. Hydrogen induced disbonding of weld overlay in pressure vessels and its prevention *Current Solutions to Hydrogen Problems in Steels*. Proceedings, 1st International Conference, Washington, DC, 1–5 Nov. 1982. Eds: C.G. Interrante and G.M.P. Publ: Metals Park, OH 44073, USA; American Society for Metals; ISBN 0-87170-148-0. pp. 340–348.
21. Gittos, M. F. and Gooch, T. G. 1992. The interface below stainless steel and nickel-alloy claddings, *Welding Journal*, 71(12): 461s–472s.
22. Klueh, R. L. and King, J. F. 1982. Austenitic stainless steel-ferritic steel weld joint failures, *Welding Journal*, 61(9): 302s–311s.
23. Sowards, J. W., Alexandrov, B. T., Lippold, J. C., Liang, D., and Frankel, G. S. 2007. Development of a Ni-Cu for welding stainless steels, *Proc. of Stainless Steel World 2007*, KCI Publishing (on CD).
24. Alexandrov, B. T. and Lippold, J. C. 2007. Single Sensor Differential Thermal Analysis of Phase Transformations and Structural Changes during Welding and Postweld Heat Treatment, *Welding in the World*, 51(11/12): 48–59.
25. Avery, R. E. 1991. Pay attention to dissimilar metal welds—guidelines for welding dissimilar metals, *Chemical Engineering Progress* (May 1991) and *Nickel Development Institute Series No. 14-018*.
26. Kiser, S. D. 1980. Dissimilar welding with nickel alloys, *Welder & Fabrication Magazine*, January 1980.
27. Unpublished research from W. Childs, Electric Power Research Institute, Palo Alto, CA.
28. Threadgill, P. L. 1985. Avoiding HAZ Defects in Welded Structures, *Metals and Materials*, July 1985, pp. 422–430.
29. Dhooge, A. and Vinckier, A. 1992. Reheat Cracking—Review of Recent Studies (1984–1990), *Welding in the World*, 30(3/4): 44–71.
30. Halada, G. P., Clayton, C. R., Kim, D., and Kearns, J. R. 1995. Electrochemical and surface analytical studies of the interaction of nitrogen with key alloying elements in stainless steels, Paper no. 531, *Corrosion 95*, March 26–31, NACE, Orlando, FL.
31. Banovic, S. W., DuPont, J. N., and Marder, A. R. 2003. Dilution and microsegregation in dissimilar metal welds between super austenitic stainless steels and Ni Base alloys, 2003, *Sci. & Tech. of Welding and Joining*, 6(6): 374–383.
32. DuPont, J. N., Banovic, S. W., and Marder, A. R. 2003. Microstructural Evolution and Weldability of Dissimilar Welds between a Super Austenitic Stainless Steel and Nickel Base Alloys, *Welding Journal*, 82(6): 125s–135s.
33. Garner A. 1985. How stainless steel welds corrode, *Metal Progress*, 127(5): 31–36.
34. DuPont, J. N. 2004. Unpublished research on corrosion of Mo bearing stainless steel welds, Lehigh University.
35. Cieslak, M. J., Headley, T. J., and Romig, A. D. 1986. The welding metallurgy of Hastelloy alloys C-4, C-22, and C-276, *Metallurgical Transactions A*, 17A: 2035–2047.

36. Baker, H., 1992. *Alloy phase diagrams*, ASM International, Materials Park, OH.
37. Banovic, S. W., DuPont, J. N., and Marder, A. R. 2001. Dilution Control in GTA Welds Involving Super Austenitic Stainless Steels and Nickel Base Alloys, *Metallurgical and Materials Transactions B*, 32B: 1171–1176.
38. DuPont, J. N., Robino, C. V., Marder, A. R., Notis, M. R., and Michael, J. R. 1998. Solidification of Nb-Bearing Superalloys: Part I. Reaction Sequences, *Metallurgical and Material Transactions A*, 29A: 2785–2796.
39. Gulati, K. C. 2005. A new full containment LNG storage system, *LNG Journal*, May/June, pp. 1–6.
40. Karlsson, L., Rigdal, S., Stridh, L. E., and Thalberg, N. 2005, Efficient welding of 9% Ni steel for LNG applications, *Stainless Steel World 2005*, KCI Publishing, ISBN 0-907-3-16800-7, pp. 412–420.
41. Armstrong, T. N. and Gagnebin, A. P. 1940. Impact properties of some low alloy nickel steels at temperatures down to  $-200^{\circ}\text{F}$ , *Trans. ASM.*, Vol. 28.
42. Armstrong, T. N. and Brophy, G. R. 1947. Some properties of low carbon 8.5% nickel steel, *Proc. of Petroleum Mechanical Engineering*, ASME, Houston, TX, October 1947.
43. Dhooge, A., Provost, W., and Vinckier, A. 1982. Weldability and fracture toughness of 9% nickel steel, part 1—weld simulation testing, part 2—wide plate testing, *Welding Research Council Bulletin No. 279*.
44. Nippes, E. F. and Balaguer, J. P. 1986. A study of the weld heat-affected zone toughness of 9% nickel steel, *Welding Journal*, 65(9): 237s–243s.
45. Karlsson, L., Bergquist, E. L., Rigdal, S., and Thalberg, N. 2008. Evaluating hot cracking in Ni-base SAW consumables for Welding of 9%Ni steel, *Hot Cracking Phenomena in Welds II*, publ. by Springer, ISBN 0-978-3-540-78627-6, pp. 329–348.
46. Furmanski, G., Kiser, S. D., and Shoemaker, L. E. 2008. A NiCrMo product provides optimum weldments in superduplex pipeline for geothermal power service, NACE Corrosion Conference 2008, Paper No. 08177.
47. ASME Code 1998, Section VIII, Division 1, UNF-56, p. 205.
48. Shademan, S. S. and Kim, D. S., 2005. Mechanical and corrosion performance of welded alloy 925 VIT in sour environment, *Corrosion/2005*, paper No. 05104, NACE International, Houston, TX, USA, pp. 1–20.
49. Luer, K. R., DuPont, J. N., Marder, A. R., and Skelonis, C. K. 2001. Corrosion Fatigue of Alloy 625 Weld Claddings Exposed to Combustion Environments, *Materials at High Temperatures*, 18: 11–19.
50. Deacon, R. M., DuPont, J. N., and Marder, A. R. 2007. High Temperature Corrosion Resistance of Candidate Nickel Based Weld Overlay Alloys in a Low NOx Environment, *Materials Science & Engineering A*, 460: 392–402.
51. Courtesy R. E. Smith, Structural Integrity Associates, May 2007.
52. Courtesy G. Frederick, Electric Power Research Institute, Charlotte, NC, May 2008.

# Weldability Testing

## 8.1 INTRODUCTION

The definition of the term “weldability” varies widely and is often used to describe a material’s ability to be readily fabricated, to perform in service, or both. The AWS definition represents a global approach to the term weldability which includes aspects of both fabrication and service.

### **Definition of Weldability** (American Welding Society)

The capacity of a material to be welded under fabrication conditions imposed into a specific, suitably designed structure and to perform satisfactorily in the intended service.

Weldability is most often used to define a material’s resistance to cracking during fabrication. Thus, a material that has “good weldability” would be resistant to various forms of cracking during welding, requiring essentially no rework or repair. This chapter will review the concepts of material weldability from the standpoint of weld cracking, concentrating primarily on cracking that occurs during welding or due to postweld processing. A number of weldability tests will then be described that allow quantification of a material’s weldability. This is not meant to be a comprehensive review of weldability testing techniques. There are literally hundreds of tests that have been developed to evaluate materials’ weldability. This chapter describes several weldability tests that have been referred to in this text and with which the authors have personal experience.

Fabrication-related defects include cracking phenomena that are associated with the metallurgical nature of the weldment, and process- and/or procedure-related defects. A number of different cracking mechanisms have been identified in Ni-base alloys and have been described in the chapters dealing with the particular types of alloys. These can be broadly grouped by the temperature range in which they occur.

**Hot cracking** includes those cracking phenomena associated with the presence of liquid in the system and is localized in the fusion zone and PMZ region of the HAZ. **Warm cracking** occurs at elevated temperature in the solid-state, i.e., no liquid is present in the system. These defects may occur in both the fusion zone and HAZ. **Cold cracking** occurs at or near room temperature and is usually synonymous with hydrogen-induced cracking.

### 8.1.1 Weldability Testing Approaches

Because the concept of weldability is so broad, there are a wide variety of test techniques that can be used to assess or quantify weldability. These tests can address issues associated with the process and/or welding procedures, cracking during welding and postweld processing, and service performance and structural integrity.

Mechanical testing is commonly required by specification to qualify welding procedures to meet strength, ductility, and toughness requirements. Other tests including fatigue, fracture toughness, and corrosion tests are often used to insure the performance of welded structures. Almost all of these test procedures have been standardized and can be found in publications of the American Welding Society (AWS), American Society for Testing Materials (ASTM), and other professional societies and authorized bodies.

In addition, many specialized tests have been developed to address fabrication issues, especially cracking. Few of these tests have been standardized and poor correlation among tests designed to evaluate or quantify the same phenomenon is common.

### 8.1.2 Types of Weldability Test Techniques

Weldability test techniques can be broadly grouped into four categories: mechanical, non-destructive, service performance, and specialty. With the exception of the inspection (non-destructive) techniques, these tests are destructive in nature, requiring sectioning of welds and special sample preparation. The destructive evaluation techniques are obviously not applicable in a manufacturing or quality control environment, but should be implemented at the material selection and procedure qualification stage.

Specialty tests to evaluate susceptibility to various metallurgically-related defects, such as solidification cracking or hydrogen cracking, should be conducted in the alloy development or selection stage. Failure to address issues related to susceptibility to cracking during fabrication can result in considerable cost and development time penalties.

Tests for evaluating the susceptibility to “hot” cracking can be separated into three categories. Representative, or “self-restraint,” tests use the inherent restraint of the test assembly to cause cracking. They are termed “representative” because they can be used to represent the actual joint configurations and restraint levels of the parts to be welded. The drawback of these tests is that

there is usually little quantification of cracking susceptibility, the specimen either cracks or does not. As a result, no specific data such as cracking temperature range or stress/strain to cause cracking is obtained, making it difficult to compare different materials. Numerous examples exist of good resistance to cracking in representative tests, or mockups, which did not translate to resistance under actual fabrication conditions.

Simulative tests usually involve the use of tension or bending to simulate high restraint levels in welds. These tests operate under strain control, strain rate control, or stress control. Most are capable of providing some measure of cracking susceptibility that can be used to compare different materials and that may provide metallurgical information.

Hot ductility tests simply measure the strength and ductility of materials at elevated temperatures. Since weld cracking is associated with insufficient ductility relative to the imposed strain, an understanding of the material's hot ductility will often provide insight into the potential for cracking.

## 8.2 THE VARESTRAINT TEST

The Variable Restraint, or Varestraint, test was developed in the 1960s by Savage and Lundin at Rensselaer Polytechnic Institute.(1) It was devised as a simple, augmented strain type test that would isolate the metallurgical variables that cause hot cracking. Since its introduction, numerous modifications have been made to the original test and a number of variants are used worldwide. The test itself has never been fully standardized and a variety of test techniques are in use today. In the 1990s, Lin and Lippold at Ohio State University developed test techniques that allow the magnitude of the crack susceptible region (CSR) to be determined using Varestraint testing.(2)

There are three basic types of Varestraint tests, as shown in Figure 8.1. The original test was a longitudinal type, whereby bending is applied along the length of the weld. This type of test produces cracking in both the fusion zone and adjacent HAZ. Since in some cases it is desirable to separate HAZ liquation cracking from solidification cracking, the spot and transverse tests were developed. The transverse test applies bending strain across the weld and generally restricts cracking to the fusion zone (there is little or no strain applied to the HAZ). The spot Varestraint test uses a small spot weld to develop a susceptible HAZ microstructure. The sample is then bent when the weld is still molten in order to isolate cracking in the HAZ.

The gas tungsten arc welding process is most commonly used for these tests, although other fusion welding processes can also be used. Welds are usually autogenous, although filler metal deposits can be tested using special samples. Bending is normally very rapid, but some slow bending versions of the test have been developed.

The augmented strain is controlled by the use of interchangeable die blocks, in which the strain ( $\epsilon$ ) in the outer fibers of sample is given by:

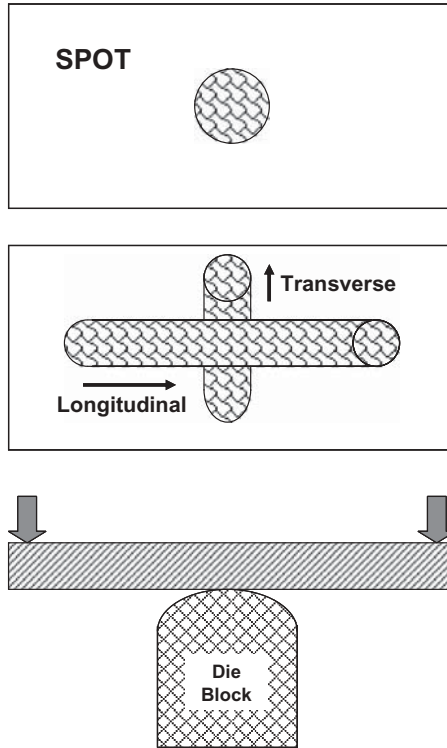


**Figure 8.1** Different types of Varestraint tests.

$$\varepsilon = t/(2R + t) \quad (8.1)$$

where  $t$  is the sample thickness and  $R$  is the radius of the die block.

A number of metrics have been developed to quantify cracking susceptibility using the Varestraint test. Most of these require the measurement of crack lengths on the surface of the as-tested sample using a low power (20–50X) microscope. Total crack length is the summation of all crack lengths, while maximum crack length is simply the length of the longest crack observed on the sample surface. More recently, the concept of maximum crack distance (MCD) has been adopted to allow more accurate determination of the cracking temperature range.

The strain to initiate cracking, the so-called threshold strain, has also been used to quantify cracking susceptibility. The saturated strain represents the level of strain above which MCD does not change. It is important to test at saturated strain when determining the maximum extent of the crack susceptible region, as described in the following sections.

### 8.2.1 Technique for Quantifying Weld Solidification Cracking

This section describes a technique developed by Lin and Lippold (2) for quantifying weld solidification cracking susceptibility using the Transvarestraint test. A schematic illustration of the test is shown in Figure 8.2. Above a critical strain level, designated the saturated strain, the MCD does not increase with increasing strain. This indicates that the solidification crack has propagated the full length of the crack susceptible region. Typical cracking as it appears at the trailing edge of the weld pool is shown in Figure 8.3 for an austenitic stainless steel sample tested at 5% strain. By testing over a range of augmented strain, an MCD versus strain plot such as that shown in Figure 8.4 can be generated. In this manner, the threshold strain for cracking to occur and the saturated strain above which the MCD does not increase can be identified. The typical strain range over which samples are tested is 0.5–7%.

Most stainless steels and Ni-base alloys exhibit saturated strain levels between 3% and 7%. Threshold strain levels are generally in the range from 0.5-to-2.0%, depending on the alloy and its solidification behavior. Although the threshold strain may, in fact, be an important criterion for judging susceptibility to weld solidification cracking, the MCD above saturated strain is much easier to determine and provides a measure of the solidification cracking temperature range (SCTR).

In order to determine SCTR, the cooling rate through the solidification temperature range is measured by plunging a thermocouple into the weld

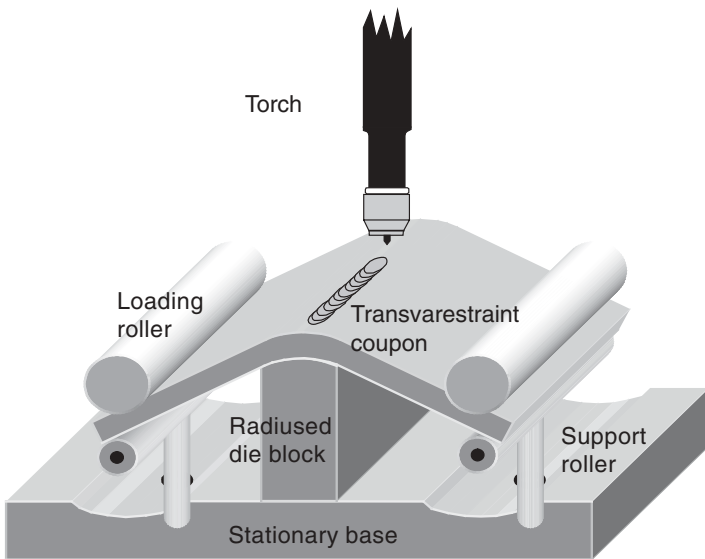


**Figure 8.2** Schematic of the Transvarestraint test for evaluating weld solidification cracking susceptibility. (From Finton [3].)

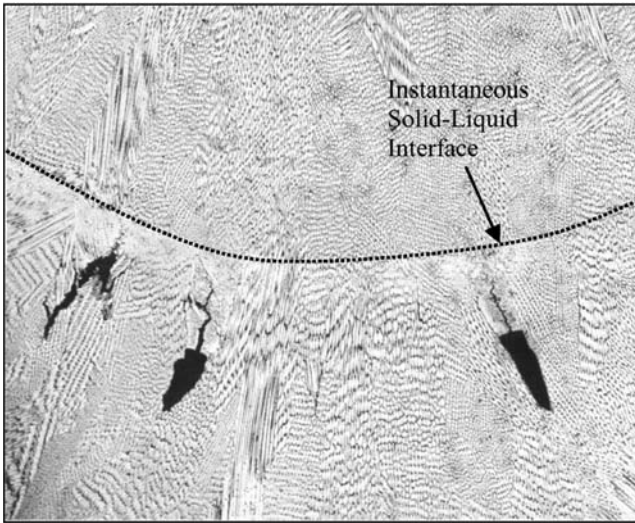


**Figure 8.3** Weld solidification cracking in a Type 316 stainless steel Transvarestraint specimen. View is looking down on the surface of the sample. (From Finton [3].)

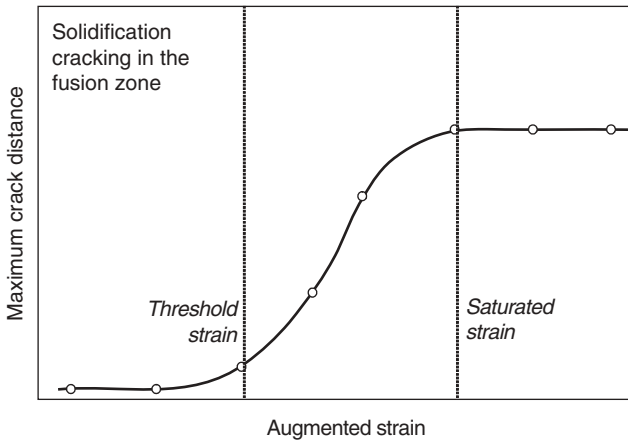


**Figure 8.4** Maximum crack distance in the fusion zone versus applied strain during Transvarestraint testing.

pool. The time over which cracking occurs is approximated by the MCD above saturated strain divided by the solidification velocity. Using this approach, SCTR can be calculated using the following relationship, where  $V$  represents the welding velocity:

$$SCTR = [Cooling Rate] \times [MCD/V] \tag{8.2}$$

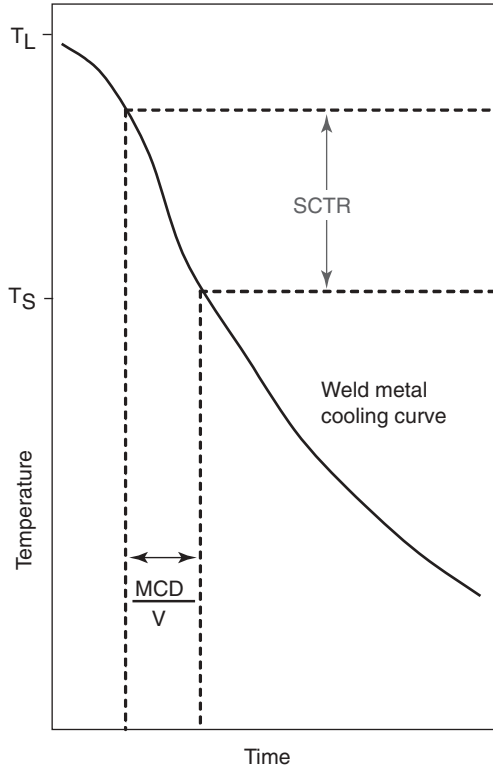


**Figure 8.5** Method for determining the solidification cracking temperature range (SCTR) using the cooling rate through the solidification temperature range and maximum crack distance (MCD) at saturated strain.

The concept for determining SCTR using this approach is shown in Figure 8.5. By using a temperature rather than a crack length as a measure of cracking susceptibility, the influence of welding variables (heat input, travel speed, etc.) can be eliminated. SCTR then represents a metallurgically significant, material-specific measure of weld solidification cracking susceptibility.

SCTR values for a number of austenitic stainless steels and Ni-base alloys are provided in Table 8.1. Alloys that solidify as primary ferrite (such as the Types 304 and 316L stainless steels) have low SCTR values, typically less than 50 °C. Ni-base alloys exhibit SCTR values from 50 °C to over 200 °C. The SCTR data allows a straightforward comparison of cracking susceptibility. These values may also allow alloy selection based on restraint conditions. For example, in high restraint situations, SCTR values below 100 °C may be required to prevent cracking, while for low restraint weldments 150–200 °C may be sufficient.

Recently, Finton and Lippold (3) used a statistical approach to evaluate the variables associated with transverse Varestraint testing. This study used both

**TABLE 8.1 Solidification cracking temperature range (SCTR) values for several stainless steels and Ni-base alloys obtained using the Transvarestraint test.**

Alloy	Primary Solidification Mode	SCTR (°C)
Austenitic SS, Type 304L	BCC—ferrite	31
Austenitic SS, Type 316L	BCC—ferrite	49
Alloy C-22	FCC—austenite	50
Alloy 617	FCC—austenite	58
Alloy 230W	FCC—austenite	95
Austenitic SS, Type 310	FCC—austenite	139
Alloy Hast W	FCC—austenite	145
Alloy Hast X	FCC—austenite	190
Austenitic PH, A-286	FCC—austenite	418

**TABLE 8.2 Variables and variable ranges for Transverse Varestraint testing of stainless steels and Ni-base alloys.**

Variable	Range
Arc Length Range:	0.05–0.15 in. (1.25–3.8 mm)
Maximum Voltage Changes:	±1–1.5 volts
Minimum Specimen Length:	3.5 in. (89 mm)
Minimum Specimen Width (parallel to welding direction)	3.0 in. (76 mm)
Current Range:	160–190 amps
Travel Speed Range:	4–6 in./min (1.7–2.5 mm/sec)
Augmented Strain Range:	3–7%
Ram Travel Speed Range:	6–10 in./sec (152–254 mm/sec)

austenitic stainless steels (Type 304 and 310) and Ni-base alloys (Alloys 625 and 690) to determine the statistical importance of different variables and to establish variable ranges in which testing should be conducted to give reproducible results. Based on this study, they recommended the variable ranges in Table 8.2 for use with stainless steels and Ni-base alloys.

### 8.2.2 Technique for Quantifying HAZ Liquation Cracking

Susceptibility to HAZ liquation cracking can be quantified using both the Varestraint test and the hot ductility test, as described by Lin *et al.*(4) The Varestraint test technique for HAZ liquation cracking differs from that described previously for weld solidification cracking, since it uses a stationary spot weld to generate a stable HAZ thermal gradient and microstructure. The technique developed by Lin *et al.* used both an “on-heating” and “on-cooling” approach to quantify HAZ liquation cracking. A schematic of the test is shown in Figure 8.6.

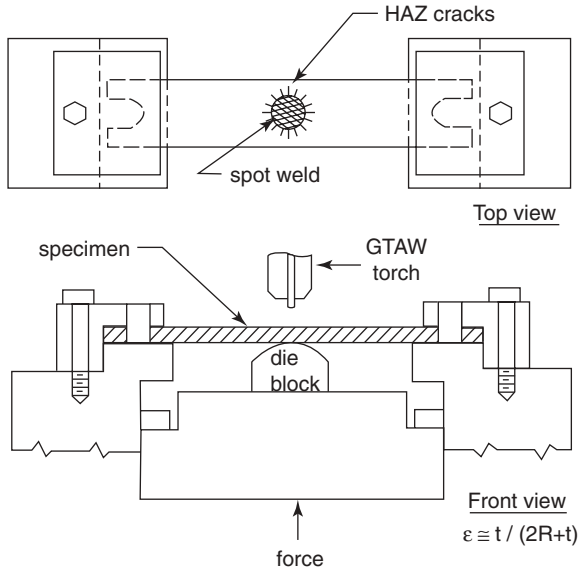


**Figure 8.6** Schematic illustration of the spot Varestraint test. (From Lin *et al.* [4]. Courtesy American Welding Society.)

The on-heating test is conducted by initiating the GTA spot weld, ramping to the desired current level, and then maintaining this current level until the weld pool size stabilizes and the desired temperature gradient in the HAZ is achieved. For the austenitic stainless steels evaluated by Lin *et al.* (4) a spot weld surface diameter of approximately 12 mm was achieved after a weld time of 35 seconds. The arc is then extinguished and the load immediately applied to force the sample to conform to the die block. By using no delay time between extinction of the arc and application of load, HAZ liquation cracks initiate at the fusion boundary and propagate back into the HAZ along liquated grain boundaries (Figure 8.7).

By plotting maximum crack length (MCL) versus strain, a “saturated strain” can be determined that defines the strain above which the maximum crack length does not change. Examples of on-heating MCL versus strain plots for Type 310 and A-286 stainless steels are shown in Figure 8.8A. Note that a threshold strain for cracking cannot be identified for A-286 and that both materials achieve saturated strain at 3%.

For the on-cooling test, the same procedure as described above is used, but after the arc is extinguished there is a delay before the sample is bent. By controlling the delay, or cooling, time, the weld is allowed to solidify and the temperature in the PMZ drops until eventually the liquid films along grain boundaries are completely solidified. By plotting MCL versus cooling time, the time required for liquid films in the PMZ to solidify can be determined. This is shown in Figure 8.8B. Note that more than four seconds are required

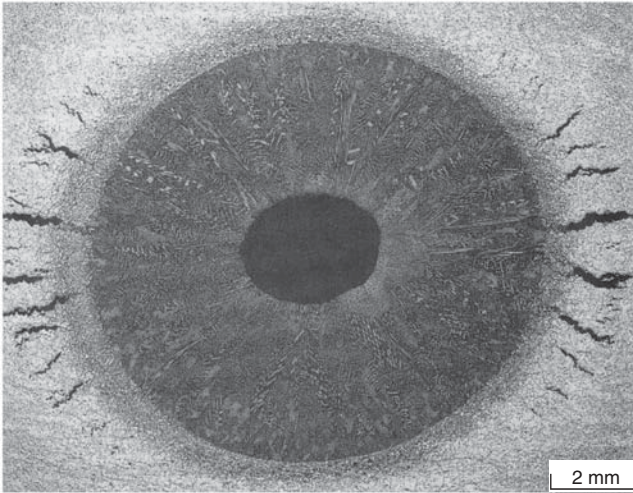


**Figure 8.7** Spot Varestraint test sample (plan view) of A-286 stainless steel tested at 5% strain.

before cracking disappears in A-286, indicating that the grain boundary liquid films persist to quite low temperatures.

By measuring the temperature gradient in the HAZ using implanted thermocouples, it is possible to determine the thermal crack susceptible region (CSR) surrounding the weld within which HAZ liquation cracking is possible. As described by Lin *et al.*(4) this is done by converting the MCL at saturated strain for both on-heating and on-cooling spot Varestraint tests to a temperature by multiplying the MCL by the temperature gradient in the HAZ. Using this approach, it is possible to describe the region around a moving weld pool that is susceptible to HAZ liquation cracking.

Plots of the thermal CSR for A-286 and Type 310 are shown in Figure 8.9. Note that the width of the CSR at the periphery of the weld is 222 °C for A-286 and only 61 °C for Type 310. It is also interesting that, based on the on-cooling data, the PMZ in A-286 does not fully solidify until the temperature reaches 1035 °C (1895 °F) while for Type 310 it is 1296 °C (2365 °F). This technique provides a quantifiable method to determine the precise temperature ranges within which cracking occurs and allows differences in HAZ liquation cracking susceptibility among materials to be readily measured. Although this procedure was developed using austenitic stainless steels, it works equally well with Ni-base alloys.

### 8.3 MODIFIED CAST PIN TEAR TEST

The cast pin tear (CPT) test was originally developed by Hull (5) to evaluate the solidification cracking susceptibility of a wide range of stainless steel com-

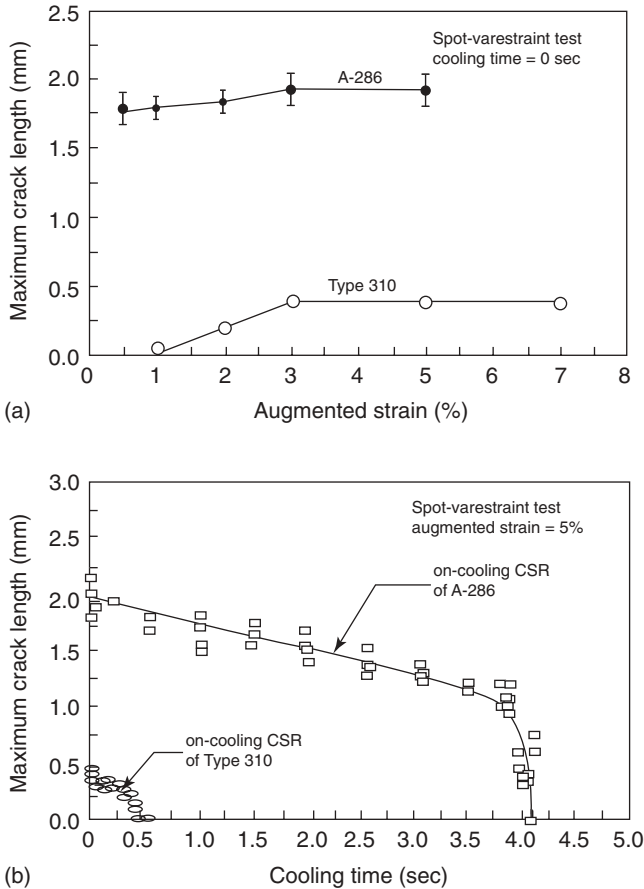


**Figure 8.8** On-heating (a) and on-cooling (b) HAZ liquation cracking in Type 310 and A-286 as measured by the spot Varestraint test. (From Lin *et al.* [4]. Courtesy American Welding Society.)

positions and allowed the development of equivalency relationships for predicting ferrite content and solidification cracking susceptibility of these steels. Small samples of the desired composition were levitation melted and then poured into molds and allowed to solidify. By controlling the length and width of the molds, the restraint in the solidified “pins” could be varied and a relationship between pin length and onset of cracking was used to determine cracking susceptibility. A modified version of the CPT test was recently developed at The Ohio State University and has been used to evaluate the weld solidification cracking susceptibility of a number of Ni-base alloys. The motivation for the development of the modified CPT test was to allow the evaluation of alloys that are extremely susceptible to weld solidification cracking and to facilitate alloy development, allowing the cracking susceptibility of experimental alloys to be readily determined using only small amounts of material.

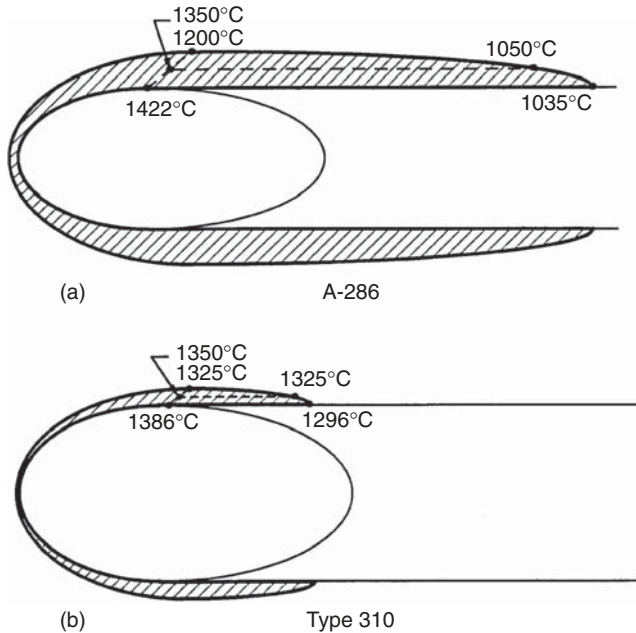


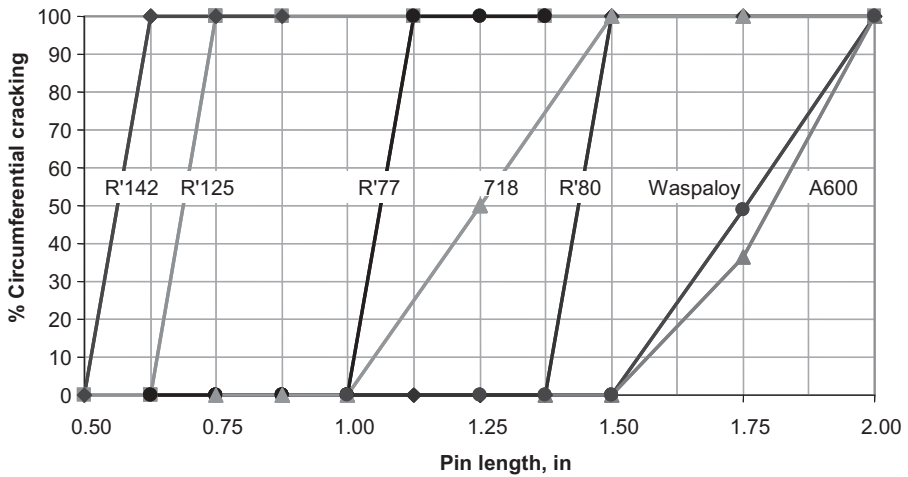
**Figure 8.9** The thermal crack susceptible region (CSR) as determined from the spot Varestraint test for a) A-286, and b) Type 310. (From Lin *et al.* [4]. Courtesy American Welding Society.)

The CPT test developed at OSU uses a water cooled copper hearth and an arc welding torch to melt and contain small charges of material. These molten charges are then dropped into copper molds ranging in length from 0.5-to-2.0 inches (12.5-to-50 mm). The mold contains a “foot” feature at the bottom which anchors the pin and solidification proceeds upward to the head of the pin. When solidification restraint becomes high enough small circumferential cracks form on the outside surface of the pin and with increased pin length complete separation due to solidification cracking can occur.

A typical set of cast pins is shown in Figure 8.10. Standard sample diameter is 0.375 in. (9.5 mm) between the foot and head of the pin. Since the pin solidifies from the bottom up, solidification cracks tend to form just below the head of the pin, as indicated by the arrows in Figure 8.10. Cracking data from this test is plotted as percent circumferential cracking versus pin length. The cracking behavior of a number of Ni-base alloys tested using the modified CPT test is shown in Figure 8.11.(6) Materials that transition to 100% circumferential cracking at the shortest pin lengths are most susceptible to solidification cracking. Thus, based on the results shown in Figure 8.11, René Alloys 142 and 125 would be the most susceptible to solidification cracking while Waspaloy and Alloy 600 would be the most resistant. These results are consistent with actual practice.



**Figure 8.10** Example of cast pins from modified cast pin tear test. The samples are 0.375 in. (9.5 mm) in diameter and have a bottom foot feature. Arrows indicate the location where solidification cracks are normally observed.



Alloy	Solidification Range (°C)
600	133
Waspaloy	164
718	189
René 125	190
René 142	185

**Figure 8.11** Cast pin tear test results for several Ni-base alloys. (From Alexandrov *et al.* [6].)

A major advantage of the modified CPT test is that very little material is required to determine cracking susceptibility. The cast pins range in weight from approximately 10 grams (0.5 in. pin) to approximately 16 grams (2.0 in. pin). Because of this, an entire evaluation program can be conducted with less than 500 grams of material. This is a tremendous advantage over such tests as the Varestraint and Sigmajig tests which require experimental materials to be processed to plate or sheet form in order to be tested. The CPT apparatus can also be used to determine the phase transformation behavior using the patented single sensor differential thermal analysis (SS-DTA) technique.(7) Using this technique, a thermocouple implanted through the hearth of the melting apparatus measures the thermal cycle upon cooling to room temperature and determines the solidification temperature range. In Figure 8.11, the solidification temperature range is listed for a number of the alloys tested. Note that there is relatively good correlation between this temperature range and cracking susceptibility with the more susceptible alloys exhibiting a wider solidification range.

#### 8.4 THE SIGMAJIG TEST

The Sigmajig test was developed by Goodwin (8) in order to evaluate the solidification and liquation cracking susceptibility of thin sheet materials. Small samples (typically 50 mm × 50 mm) are clamped in a fixture and a stress applied across the sample using a strain-gaged bolt loading arrangement. An autogenous weld is then made transverse to the applied load (stress) under conditions that insure full penetration, usually at high travel speeds. Samples are run at increasing stress levels until through-thickness cracking is observed in the sample, normally in the fusion zone. This stress level is then designated the threshold stress for cracking. As the stress is incremented to higher levels, cracking will occur along the entire length of the sample (100% of the sample length), as illustrated in Figure 8.12.

This test is very useful for testing sheet materials (thicknesses less than 3 mm), since the Varestraint test is not appropriate for materials thicknesses less than about 3 mm due to buckling of the sample during bending. Autogenous welding is normally conducted using the gas tungsten arc welding (GTAW) process, although the use of laser and electron beam welding is also possible. Control of the welding conditions is critical, and typically high travel speeds that create an elongated, teardrop-shaped weld pool provide the best results. This allows stresses to concentrate at the weld centerline giving rise to centerline solidification cracking. In some materials, it may be possible to induce HAZ liquation cracking, but in general the Sigmajig test is most useful for assessing weld solidification cracking.

Typical test results are reported as threshold cracking stress, or the minimum stress to promote observable cracking in the sample. The relative values of the threshold stress for cracking are then used to compare cracking susceptibility.

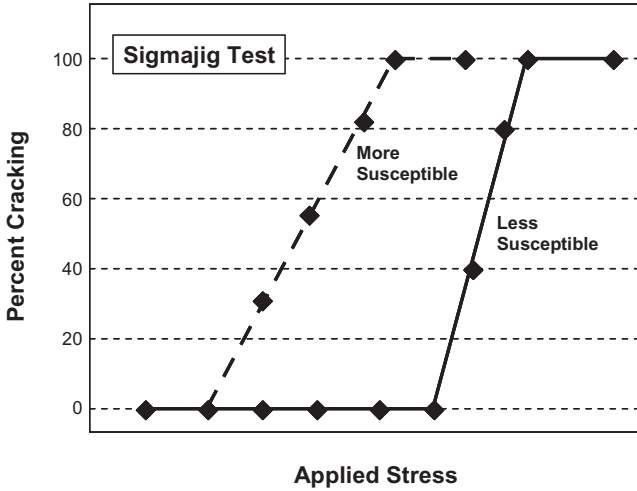


Figure 8.12 Testing and evaluation procedure for the Sigmajig test.

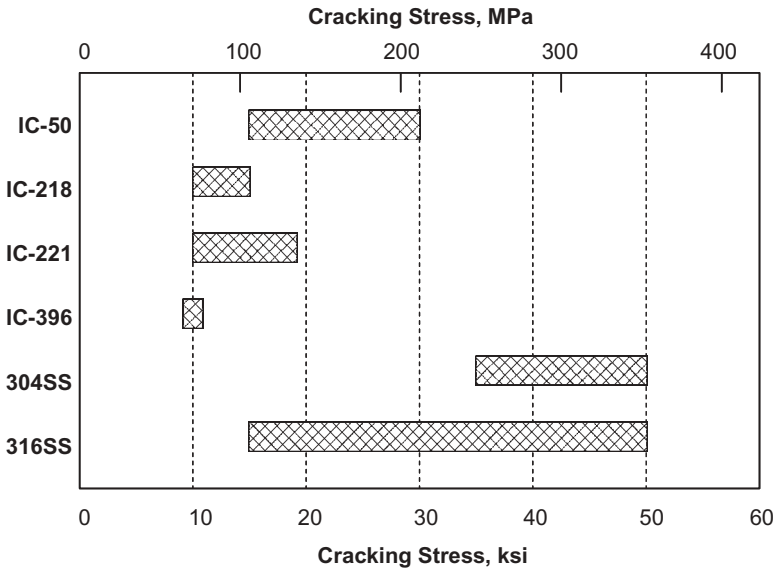


Figure 8.13 Example of Sigmajig test results for Ni-aluminides and two austenitic stainless steels. (see Figure 5.14)

An example of such results for some Ni-aluminide alloys was shown previously in Figure 5.14 and is reproduced here in Figure 8.13. The ranges of cracking stress in Figure 8.13 represent the variation of multiple compositions within the alloy system, rather than variability within a single material. For example, Tye316SS may undergo either primary ferrite or primary austenite solidification resulting in large variation in cracking susceptibility.

## 8.5 THE HOT DUCTILITY TEST

Elevated temperature ductility can provide some indication of a material's weldability, since cracking is usually associated with an exhaustion of available ductility. Most hot ductility testing involves both heating (or "on heating") and cooling (or "on cooling") tests. In order to properly simulate the heating and cooling rates associated with welding, special equipment has been developed to rapidly heat and cool small laboratory samples. The most widely used test machine for accomplishing this was developed by Savage and Ferguson at Rensselaer Polytechnic Institute (RPI) in the 1950s.(9) The inventors called this machine the "Gleeble," a namesake that is a closely-guarded secret of RPI graduates. The machine is now produced commercially by DSI, Inc. in Poestenkill, NY.(10)

The Gleeble uses resistance heating ( $I^2R$ ) to heat small samples under precise temperature control, and cools them by conduction through water-cooled copper grips. Quench systems are also available for accelerated cooling. Heating rates up to 10,000°C/second are possible. The Gleeble also is capable of mechanically testing samples at any point along the programmed thermal cycle.

Hot ductility testing will allow a ductility "signature" to be developed for a material. This signature will exhibit several distinct features, as shown schematically in Figure 8.14. When ductility is measured on heating, most materials will exhibit an increase in ductility with increasing temperature followed by a

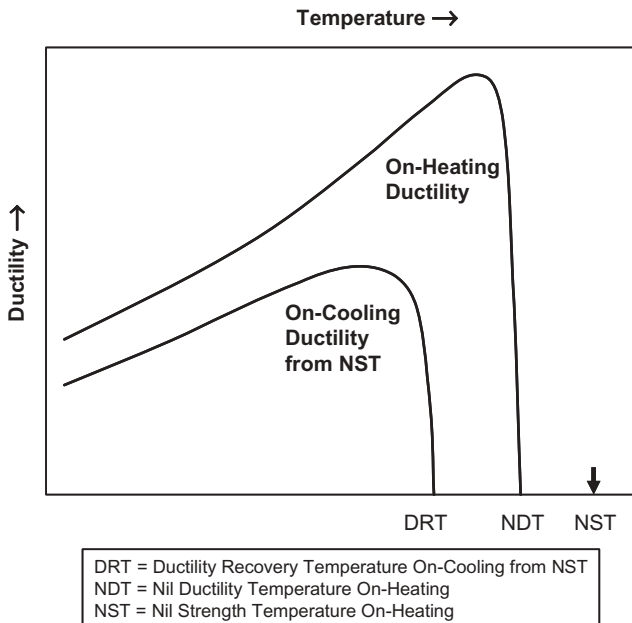


**Figure 8.14** Schematic illustration of a hot ductility signature showing on-heating and on-cooling ductility curves and the location of the nil ductility temperature (NDT), nil strength temperature (NST), and ductility recovery temperature (DRT).

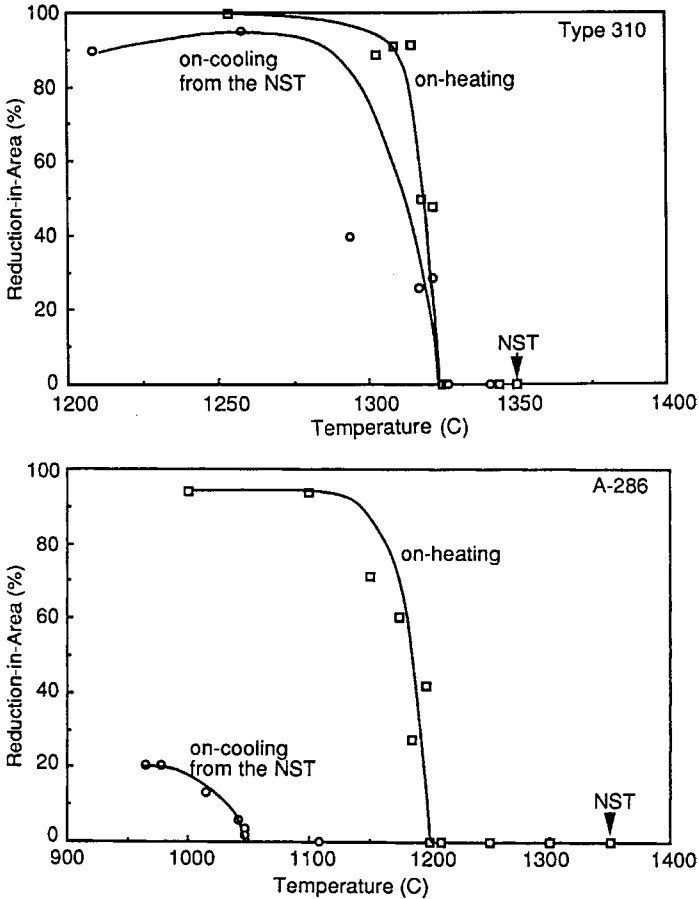


**Figure 8.15** Hot ductility test results for Type 310 and A-286 austenitic stainless steels. (From Lin *et al.* [4]. Courtesy American Welding Society.)

fairly abrupt drop. This drop is associated with the onset of melting. The temperature at which ductility drops to zero is termed the nil ductility temperature (NDT). At the NDT, the material still has measurable strength. Additional tests are conducted to determine the point at which the strength is zero, termed the nil strength temperature (NST).

To determine the on-cooling ductility curve, samples are heated to the NST (or a temperature between NDT and NST), cooled to a pre-programmed temperature, and tested. The point at which measurable ductility is observed is termed the ductility recovery temperature (DRT). At the DRT, liquid formed upon heating to the NST has solidified to the point that the sample exhibits measurable ductility when pulled in tension.

Examples of hot ductility test results for stainless steels alloys Type 310 and A-286 from the work of Lin *et al.* (4) are shown in Figure 8.15. These are the

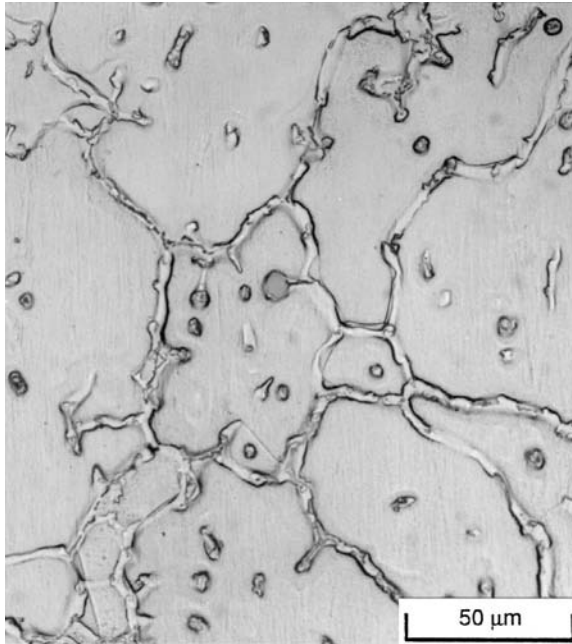


**Figure 8.16** A-286 after heating to the nil strength temperature (1350°C). (From Lin [13].)

same materials that were described previously for the spot Varestraint Test. Note that the on-heating and on-cooling ductility curves for Type 310 are nearly identical and that the NDT and DRT are essentially equivalent. The NST is only 25°C above the NDT. This indicates that grain boundary liquid films that form between the NDT and NST on-heating solidify on cooling at 1325°C. Because of the narrow temperature range over which liquid films are present in the HAZ/PMZ, this material would have good resistance to HAZ liquation cracking. In contrast, the on-heating and on-cooling ductility curves are quite different for A-286. The NDT for A-286 is approximately 1200°C, while the NST is 1350°C. After heating to the NST, on-cooling ductility does not recover until approximately 1050°C. Thus, grain boundary liquid films are present over a 300°C temperature range below the NST. This produces a very wide HAZ/PMZ region and renders the material susceptible to HAZ liquation cracking. A photomicrograph of an A-286 sample heated to the NST temperature is shown in Figure 8.16. Note the complete coverage of the grain boundaries by liquid films.

The hot ductility behavior can be determined for Ni-base alloys using the technique described above, as shown in Figure 8.17 for Alloys 625 and 690.(11,12) Note that the hot ductility behavior of the two alloys is quite dif-

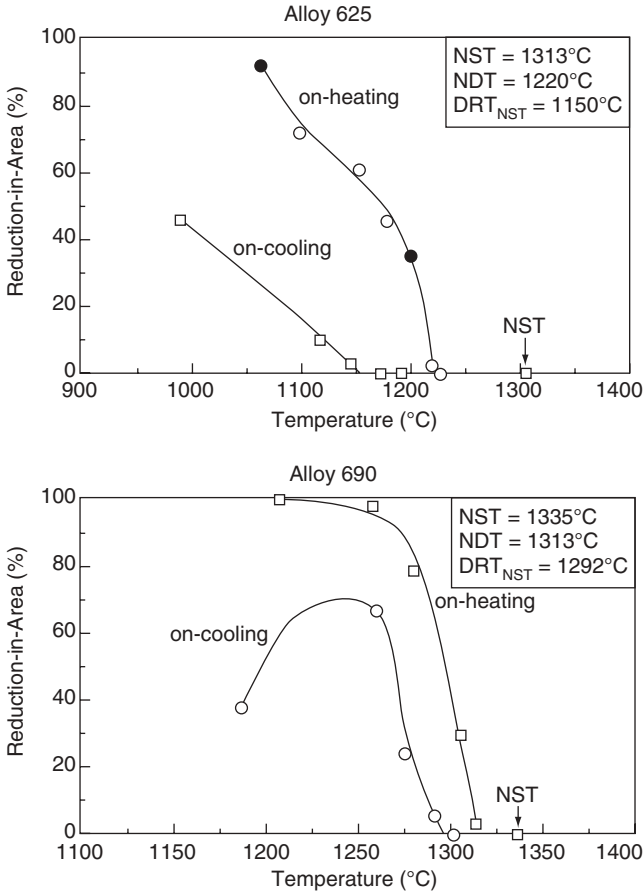


**Figure 8.17** Hot ductility results for Alloys 625 and 690. (From Lin *et al.* [11] and Lippold *et al.* [12].)

ferent. The NDT and DRT temperatures for Alloy 625 are well below those for Alloy 690.

Similar to the spot Vareststraint test, the hot ductility results (NDT, NST, and DRT from the hot ductility curves) can be used to define the crack susceptible region (CSR) in the HAZ. In advance of the weld, liquation will begin when the material is heated above the NDT. The difference between the NDT and the liquidus temperature at the fusion boundary then defines the width of the on-heating liquation temperature range. For convenience, the NST is used to approximate the liquidus temperature.

In the cooling portion of the HAZ, liquid films in regions heated between NDT and NST will solidify. The value of DRT varies as a function of the peak temperature and is the lowest at the point closest to the fusion

boundary. The difference between NST and DRT will then represent the maximum temperature range over which liquid films are present in the HAZ. This value can then be used to define the liquation cracking temperature range (LCTR). The LCTR represents a measure of liquation cracking susceptibility, similar to SCTR for the weld metal. From Figures 8.15 and 8.17 the following LCTR values can be determined: Type 310 = 25 °C, Alloy 690 = 43 °C, Alloy 625 = 163 °C, and A-286 = 300 °C, and. Based on these values, Type 310 would be the most resistant to HAZ liquation cracking, A-286 the most susceptible, and Alloys 625 and 690 intermediately susceptible.

Unfortunately, there is no standardized procedure for generating hot ductility curves. The following summarizes the procedure used by Lin (13) to generate the data shown in Figures 8.15 and 8.17:

1. Specimens were 0.25 inches. (6.35 mm) in diameter and 4.0 inches. (100 mm) long with threaded ends.
2. Specimen free span (Gleeble jaw spacing) was 1.0 inch (25 mm). All tests run in argon.
3. NST was determined by heating at linear rate of 200 °F/second (111 °C/second) under a static load of 10 kg until sample failure.
4. On-heating tests were conducted by heating to the desired peak temperature at a rate of 200 °F/second (111 °C/second) and then pulling the samples to failure at a rate of 2 inches/second (50 mm/second).
5. On-cooling tests were performed after heating the sample to the NST at 200 °F/second (111 °C/second) and then cooling to the desired temperature at 50 °C/sec. On-cooling samples were also pulled to failure at a rate of 2 inches/second.

It should be noted that Step 5 may need to be altered when testing Ni-base alloys, since many of these alloys undergo extensive liquation at the NST. This is a particular problem with many of the precipitation strengthened alloys. In these cases, a peak temperature midway between the NST and NDT should be selected. Peak temperatures for on-cooling tests that are at or below NDT are not appropriate because insufficient grain boundary liquation occurs and the microstructure will not be representative of the partially-melted zone that forms in many Ni-base alloys.

Other investigators have used different testing conditions, particularly heating and cooling rates and stroke rate during testing. Again, there is no standardized procedure for hot ductility testing and the effects of the testing variables have not been comprehensively evaluated. The procedures recommended here represent “best practices” determined in the Welding Metallurgy Laboratory at The Ohio State University.

## 8.6 THE STRAIN-TO-FRACTURE TEST

As discussed in Chapter 3, ductility dip cracking (DDC) is a solid-state, intergranular cracking phenomenon that occurs in both weld metals and HAZs of Ni-base alloys. Although DDC can occur during Varestraint testing, it is difficult to identify and quantify since it occurs just below the temperature range in which solidification and liquation cracking occurs. The hot ductility test can also be used to detect susceptibility to DDC, but its sensitivity to the onset of DDC can be relatively low.

In order to better quantify susceptibility to DDC, the strain-to-fracture (STF) test was developed in 2002 by Nissley and Lippold at The Ohio State University.(14,15) The STF test employs a “dogbone” tensile sample with a GTA spot weld applied in the center of the gage section. The spot weld is made under controlled solidification conditions using welding current downslope control. This results in an essentially radial array of grain boundaries within the spot weld. A schematic illustration of a STF sample is shown in Figure 8.18.

Samples are then tested in a Gleeble™ thermo-mechanical simulator at different temperatures and strains. For stainless steels and Ni-base alloys, temperature and strain ranges are typically from 650-to-1200 °C (1200-to-2190 °F) and zero-to-twenty percent, respectively. After testing at a specific temperature-strain combination, the sample is examined under a binocular microscope at 30X to determine if cracking has occurred and any cracks observed at this magnification are simply counted.

Using this data, a temperature versus strain envelope is developed that defines the regime within which DDC may occur. Both a threshold strain for cracking ( $\epsilon_{\min}$ ) and ductility-dip temperature range (DTR) can be extracted

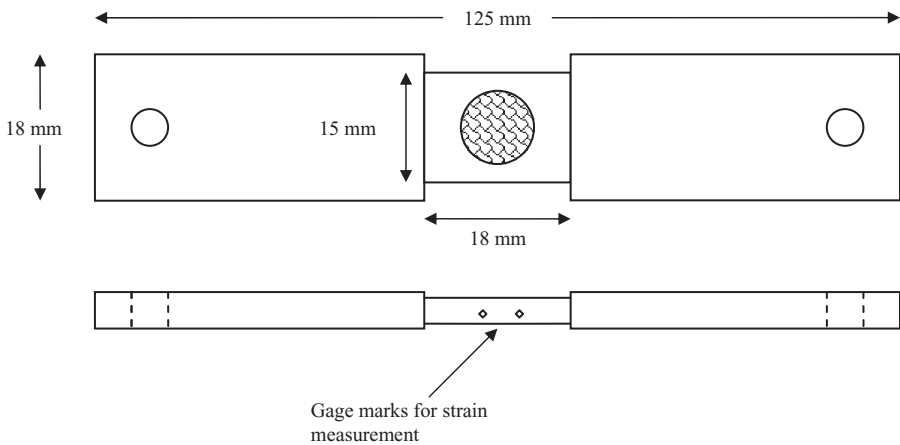


**Figure 8.18** Schematic of the Strain-to Fracture test sample with GTA spot weld in the gage section.

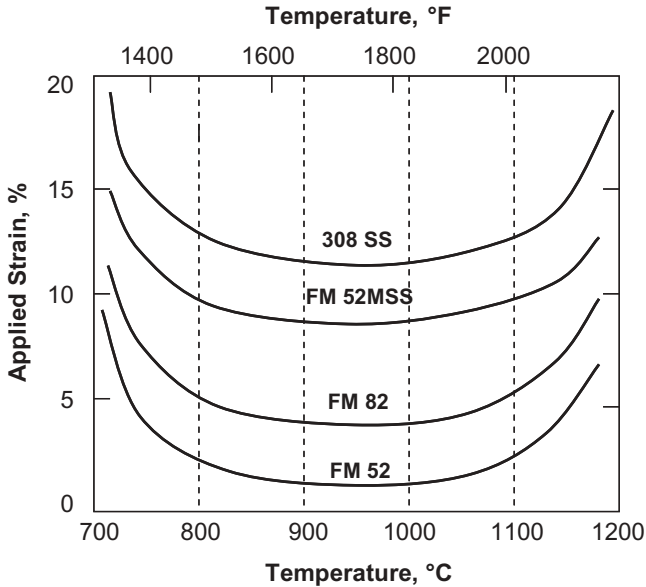


**Figure 8.19** Applied strain vs. temperature strain-to-fracture test results for three Ni-base filler metals and an austenitic stainless steel filler metal (Type 308).

from these curves. Temperature-strain curves are shown in Figure 8.19 for three Ni-base filler metals: FM82, FM52, and FM52MSS, and an austenitic stainless steel filler metal (Type 308) that is known to be very resistant to DDC. Based on these curves, FM52 would be the most susceptible to DDC and FM52MSS the most resistant. These results are consistent with DDC susceptibility in highly restrained weldments.

Since the introduction of this test in 2002, the method for assessing susceptibility to DDC has evolved in order to better differentiate materials. Many of the Ni-base alloys exhibit  $\epsilon_{\min}$  values in the range from two-to-four percent and have similar DTRs—normally in the range from 700-to-1150°C. However, when evaluating the increase in the number of cracks as a function of increasing strain above the threshold strain, a significant difference in behavior has been observed, particularly in Ni-base filler metals. It has also been noted that the minimum in the strain versus temperature curve for most materials occurs at approximately 950°C (1740°F). For this reason, a new measure for assessing susceptibility to DDC using the STF test has been adopted, as shown in Figure 8.20.(16) In this figure (similar to Figure 3.50), STF data at 950°C for a number of Ni-base filler metals is presented, including those in the filler metal classes ERNiCr-3 (FM82), ERNiCrFe-7 (FM52 and FM68HP), and ERNiCrFe-7A (FM52M and FM69HP). There are also two experimental alloys containing higher levels of Nb and Mo (FM52X-D,H). Note that all the ERNiCrFe-7/7A filler metals exhibit similar  $\epsilon_{\min}$  values, but the number of cracks that form at strains above  $\epsilon_{\min}$  varies widely. For example, the  $\epsilon_{\min}$  values for FM52M-B and

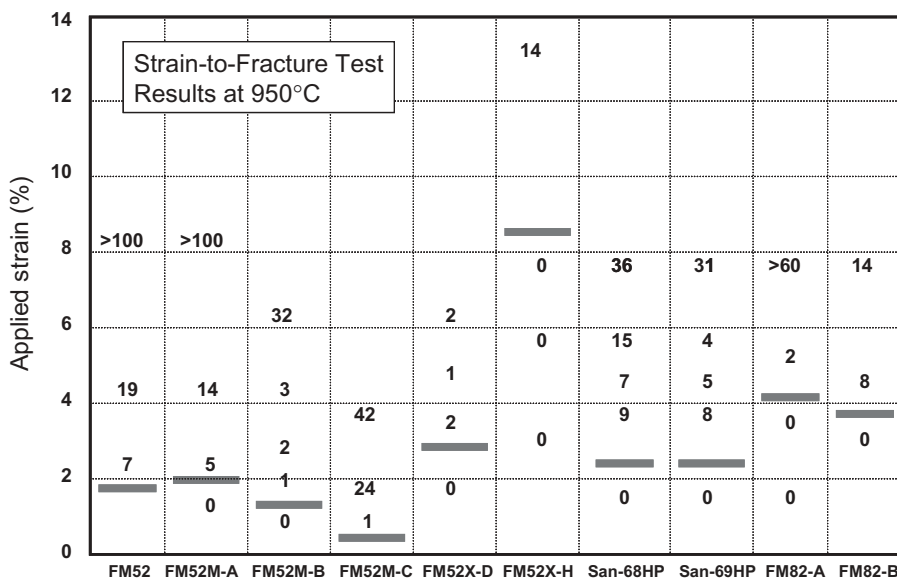


**Figure 8.20** Comparison of strain-to-fracture behavior of Ni-base filler metals at 950°C.

FM52M-C are similar, but the transition to “gross” cracking occurs at much lower strain in the FM52M-B filler metal. This filler metal would be expected to have much better resistance to DDC than the other FM52/52M filler metals. This test continues to be optimized as an effective technique for assessing susceptibility to DDC.

## 8.7 OTHER WELDABILITY TESTS

There are numerous other weldability tests applicable to Ni-base alloys. Many of these are of the self-restraint type and do not easily lend themselves to producing quantitative results, as the tests described above do. For example, circular patch tests and highly restrained narrow groove weld mockups have been used to study DDC and have shown some promise for screening filler metals, but do not provide the type of quantitative results that are achievable with Gleeble-based tests. Attempts to correlate measures of weldability among test methods have not been very successful, however. Reasons for this failure to develop satisfactory correlations are not entirely clear. A round robin of hot cracking tests was conducted within the International Institute of Welding, and the results are summarized by Wilken (17) along with attempts to account for the variations observed. Weldability testing will continue to be an important method for assessing the performance of Ni-base alloys, but more emphasis needs to be placed on optimizing and standardizing existing test techniques rather than developing new techniques.

## REFERENCES

1. Savage, W.F. and Lundin, C.D. 1965. The Varestraint test, *Welding Journal*, 44(10): 433s–442s.
2. Lippold, J.C. and Lin, W. Weldability of commercial Al-Cu-Li alloys, *Proc. of ICAA5, Aluminum Alloys—Their Physical and Mechanical Properties*, eds. J.H. Driver *et al.*, Transtec Publications, 1996, pp. 1685–1690.
3. Finton, T. 2003. *Standardization of the Transvarestraint test*. M.S. Thesis, The Ohio State University.
4. Lin, W. Lippold, J.C. and Baeslack, W.A. 1993. An investigation of heat-affected zone liquation cracking, part 1—a methodology for quantification. *Welding Journal*, 71(4): 135s–153s.
5. Hull, F. C., Cast-Pin Tear Test for Susceptibility to Hot Cracking, *Welding Journal*, 38(4): 1959, pp. 176s–181s.
6. Alexandrov, B.T. Nissley, N.E. and Lippold, J.C. 2008. Evaluation of weld solidification cracking in Ni-base superalloys using the cast pin tear test, 2nd International Workshop on Hot Cracking, Berlin, July 2008, Springer-Verlag.
7. Alexandrov, B.T. and Lippold, J.C. 2006. In-situ weld metal continuous cooling transformation diagrams, *Welding in the World*, 50(9/10): 65–74.
8. Goodwin, G. M. 1987. Development of a New Hot-Cracking Test—The Sigmajig, *Welding Journal*, 66(2): 33-s–38-s.
9. Nippes, E.F. and Savage, W.F. 1955. An investigation of the hot ductility of high-temperature alloys, *Welding Journal*, 34(4): 183s–196s.
10. Dynamic Systems, Inc., Poestenkill, NY 12140, www.bleeble.com.
11. Lin, W. Nelson, T.W. Lippold J.C. and Baeslack, W.A. 1993. A study of the HAZ crack-susceptible region in Alloy 625. *International Trends in Welding Science and Technology*, Eds. S.A. David and J.M. Vitek, ASM International, Materials Park, OH, pp. 695–702.
12. Lippold, J.C. Nelson, T.W. and Lin, W. 1992. Weldability testing of Alloy 625 and INCONEL® Alloy 690, Proc. Eighth North American Welding Research Conference, Edison Welding Institute, Columbus, OH, October 19–21, 1992.
13. Wangen Lin. 1991. PhD dissertation, *A methodology for quantifying HAZ liquation cracking susceptibility*. The Ohio State University.
14. N.E. Nissley and J.C. Lippold, 2003. Ductility-Dip Cracking Susceptibility of Austenitic Alloys, Trends in Welding Research, Proc. of the 6th International Conference, ASM International, Materials Park, OH, pp. 64–69.
15. Nissley, N.E. and Lippold, J.C. 2003. Development of the strain-to-fracture test for evaluating ductility-dip cracking in austenitic alloys, *Welding Journal*, 82(12): 355s–364s.
16. Lippold, J.C. and Nissley, N.E. 2007. Ductility dip cracking in high-Cr Ni-base filler metals, 2nd International Workshop on Hot Cracking, Berlin, July 2008, Springer-Verlag.
17. Wilken, K. 1999. Investigation to Compare Hot Cracking Tests—Externally Loaded Specimen, *IIW Document IX-1945-99*, International Institute of Welding, Paris.

## Composition of Wrought and Cast Nickel-Base Alloys (weight per cent)<sup>A</sup>

Alloy	UNS No.	C	Cr	Fe	Mn	Ni	Mo	Ti	Al	Si	Other
<i>Nickel</i>											
200	N02200	0.15	—	0.40	0.35	99.0 min	—	—	—	0.35	Cu 0.25
201	N02201	0.02	—	0.40	0.35	99.0 min	—	—	—	0.35	Cu 0.25
CZ100	N02100	1.00	—	3.00	1.50	Bal.	—	—	—	2.00	Cu 1.25
205	N02205	0.15	—	0.20	0.35	99.0 min	—	—	—	0.15	Cu 0.15
211	N02211	0.20	—	0.75	4.25–5.25	93.7 min	—	—	—	0.15	Cu 0.25
233	N02233	0.15	—	0.10	0.30	99.0 min	—	—	—	0.10	Cu 0.10
253	N02253	0.02	—	0.05	0.003	99.9 min	—	—	—	0.005	Cu 0.10
270	N02270	0.02	—	0.005	0.001	99.97 min	—	—	—	0.001	Cu 0.001
<i>Nickel-Copper Alloys</i>											
M25S	N04019	0.25	—	2.50	1.50	60.0 min	—	—	—	3.5–4.5	Cu 27.0–31.0
M35-2	N04020	0.35	—	2.50	1.50	Bal.	—	0.5	—	2.00	Cu 26.0–33.0
400	N04400	0.30	—	2.50	2.00	63.0–70.0	—	—	—	0.50	Bal. Cu
401	N04401	0.10	—	0.75	2.25	40.0–45.0	—	—	—	0.25	Bal. Cu
404	N04404	0.15	—	0.50	0.10	52.0–57.0	—	—	0.05	0.10	Bal. Cu
405	N04405	0.30	—	2.50	2.00	63.0–70.0	—	—	—	0.50	Bal. Cu
<i>Nickel-Chromium, Nickel-Chromium-Iron, and Nickel-Chromium-Molybdenum Alloys</i>											
600	N06600	0.15	14–17	6–10	1.0	72.0 min	—	—	—	—	—
601	N06601	0.1	21–25	Bal.	1.0	58–63	—	—	1,–1.7	0.5	—
617	N06617	0.15	20–24	3.0	1.0	Bal.	8–10	—	.8–1.5	0.5	Co 10–15
625	N06625	0.10	20–23.	5.0	0.5	Bal.	8–10	—	0.40	1.0	Nb 3.15–4.15
690	N06690	0.05	27–31	7–11	0.5	58.0 min	—	—	—	0.5	—
693	N06693	0.15	27–31	2.5–6.0	1.0	Bal.	—	1.0	2.5–4	0.5	Nb 0.5–2.5
C-4	N06455	0.015	14–18	3.0	1.0	Bal.	14–17	—	—	0.5	—

C-22	N06022	0.01	20-24	3.0	0.5	Bal.	12-14	—	0.08	Co 2.5, W 3.0
C-276	N10276	0.02	14.5-16.5	4-7	1.0	Bal.	15-17	—	0.08	Co 2.5
C-2000	N06200	0.1	22-24	3.0	0.5	Bal.	15-17	0.5	0.08	—
59	N06059	0.10	22-24	1.5	0.50	Bal.	15-16.5	0.4	0.08	—
230	N06230	0.05-0.15	20-24	3.0	0.30-1.0	Bal.	1-3.	.2-.5	0.1	—
RA333	N06333	0.08	24-27	Bal.	2.0	44-47	2.5-4	—	—	—
G3	N06985	0.015	21.0-23.5	18-21	1.0	Bal.	6-8	—	0.25-0.75	Cu 1.5-2.5
HX	N06006	0.05-0.15	20.5-23.0	17-20	1.0	Bal.	8-10	—	0.75-1.5	W 0.2-1.0
S	N06635	0.02	14.5-17	3.0	0.30-1.0	Bal.	14-16.5	0.1-0.5	.2-.75	—
W	N10004	0.12	5.0	6.0	1.0	63.0	24.0	—	—	—
X	N06002	0.05-0.15	20.5-23.0	17-20	1.0	Bal.	8-10	—	0.5	Co 0.5-2.5, W 0.2-1.0
686	N06686	0.01	19-23	2.0	0.75	Bal.	15-17	—	—	W 3.0-4.4

*Iron-Nickel-Chromium Alloys*

HP	N08705	0.35-0.75	19-23	Bal.	2.00	35-37	—	—	2.5	—
800	N08800	0.10	19-23	Bal.	1.5	30-35	—	.15-.6	1.0	—
801	N08801	0.10	19-22	Bal.	1.5	30-34	—	1.0	1.0	—
802	N08802	0.2-0.5	19-23	Bal.	1.50	30-35	—	.15-1.	0.75	—
800H	N08810	0.05-0.1	19-23	Bal.	1.50	30-35	—	.15-.6	1.0	—
800HT	N08811	0.06-0.1	19-23	39.5 min	1.50	30-35	—	.25-.6	1.0	—
825	N08825	0.05	19.5-23.5	Bal.	1.00	38-46	2.5-3.5	0.6-1.2	0.5	Cu 1.5-3.0

*Nickel-Iron Alloys*

52	N14052	0.05	0.25	Bal.	0.6	50.5 nom	—	0.1	0.3	—
Ni-Fe	N14076	0.05	2-3	Bal.	1.5	75-78	0.5	—	0.5	—
Ni-Fe	N14080	0.05	0.3	Bal.	0.8	79-82	3.5-6	—	0.5	—

Alloy	UNS No.	C	Cr	Fe	Mn	Ni	Mo	Ti	Al	Si	Other
<i>Nickel-Molybdenum Alloys</i>											
B	N10001	0.12	1.0	6	1.0	Bal.	26-33	—	—	1.0	—
B-2	N10665	0.01	1.0	2.0	1.0	69	26-30	—	0.5	0.1	—
B-3	N10675	0.01	1-3	1-3	3.0	65 min	27-32	—	0.5	0.1	—
B-10	N10624	0.01	6-10	5.0-8.0	1.0	Bal.	21-25	—	0.5	0.1	—
NiMo	N30007	0.07	1.0	3.0	1.0	Bal.	30-33	—	0.2	1.0	—
NiMo	N30012	0.12	1.0	4-6	1.0	Bal.	26-30	—	0.15	1.0	—
<i>Iron-Nickel Low Expansion Alloys</i>											
36(INVAR)	K93601	0.10	0.5	Bal.	0.6	34-38	0.5	—	0.1	0.35	—
42	K94100	0.05	0.5	Bal	0.8	42.0 nom	0.5	—	0.15	0.3	—
48	K94800	0.05	0.25	Bal.	0.8	48.0 nom	—	—	0.1	0.05	—
902	N09902	0.06	4.9-5.75	Bal.	0.8	41-43.5	—	2.2-2.75	0.3-0.8	1.0	—
903	N19903	—	—	42.0	—	38.0	—	1.4	0.9	—	Co 15.0, Nb 3.0
907	N19907	—	—	42.0	—	38.0	—	1.5	0.03	0.15	Co 13.0, Nb 4.7
KOVAR	K94610	0.04	0.2	53 nom	0.5	29.0	0.2	—	0.1	0.2	Co 17.0
<i>Precipitation-Strengthened Alloys</i>											
K500	N05500	0.25	—	2.00	1.50	63.0-70.0	—	0.35-0.85	2.3-3.15	.50	Cu Bal.
300	N03300	0.40	—	0.60	0.50	97.0 min	—	0.20-0.60	—	.35	Mg 0.2-0.5
301	N03301	0.30	—	0.60	0.50	93.0 min	—	0.25-1.0	4.0-4.75	1.0	—

80A	N07080	0.10	18.0-21.0	3.0	1.0	Bal.	—	1.8-2.7	1.0-1.8	1.0	Co 2.0
X-750	N07750	0.08	14.0-17.0	5.0-9.0	1.0	70.0min	—	2.25-2.75	0.4-1.0	0.50	Nb 0.70-1.2
90	N07090	0.13	18.0-21.0	3.0	1.0	Bal.	—	1.8-3.	0.8-2.0	1.0	Co 15.0-21.0
263	N07263	0.04-0.08	19.0-21.0	0.7	0.60	Bal.	5.6-6.1	1.9-2.4	0.3-0.6	0.40	Co 19.0-21.0
713	N07713	0.08-0.20	12.0-14.0	2.50	0.25	Bal.	3.8-5.2	0.5-1.0	5.5-6.5	—	Nb 1.8-2.8
718	N07718	0.08	17.0-21.0	Bal.	0.35	50.0-55.0	2.8-3.3	0.65-1.15	0.2-0.8	0.35	Nb 4.75-5.50
Waspaloy	N07001	0.03-0.10	18.0-21.0	2.00	1.00	Bal.	3.5-5.0	2.75-3.25	1.2-1.6	—	Co 12-15
Rene 41	N07041	0.12	18.0-22.0	5.00	0.10	Bal.	9.0-10.5	3.0-3.3	1.4-1.8	—	Co 10.0-12.0
214	N07214	0.05	15.0-17.0	2.0-4.0	0.5	Bal.	0.5	0.5	4.0-5.0	—	Co 2.0
U520	N07520	0.06	18.0-20.0	—	—	Bal.	5.0-7.0	2.8-3.2	1.8-2.2	—	Co 12.0-14.0, W 0.8-1.2
702	N07702	0.10	14.0-17.0	2.0	1.0	Bal.	—	0.25-1.00	2.75-3.75	—	Cu 0.5
U720	N07720	0.03	15.0-17.0	—	—	Bal.	2.5-3.5	4.5-5.5	2.0-3.0	—	Co 14.0-16.0
725	N07725	0.03	19.0-22.5	Bal.	0.35	55.0-59.0	7.0-9.5	1.0-1.7	0.35	0.20	Nb 2.75-4.0
751	N07751	0.10	14.0-17.0	5.0-9.0	1.0	70.0min	—	2.0-2.6	0.9-1.5	0.50	Nb 0.70-1.2
706	N09706	0.06	14.5-17.5	Bal.	0.35	39.0-44.0	—	1.5-2.0	0.40	0.35	Nb 2.5-3.3
925	N09925	0.03	19.5-23.5	22.0Min	1.00	38.0-46.0	2.5-3.5	1.9-2.4	0.1-0.5	0.50	Cu 1.5-3.00
945	N09945	0.04	19.5-23.0	Bal.	1.0	45.0-55.0	3.0-4.0	0.5-2.5	0.01-0.7	0.50	Nb 2.5-4.5
909	N19909	0.06	—	Bal.	—	35.0-40.0	—	1.3-1.8	0.15	0.25-0.50	Cu 1.5-3.0 Co 12.0-16.0 Nb 4.3-5.2

<sup>A</sup> single value is a maximum.



# Composition of Nickel and Nickel Alloy Consumables (weight per cent)<sup>A</sup>

AWS Class	Alloy	UNS No.	C	Cr	Fe	Mn	Ni	Mo	Si	Other
<i>Coated Electrodes</i>										
ENi-1	WE141	W82141	0.10	—	0.75	0.75	92.0min	—	1.25	Ti 1.0-4.0
ENi-CI	WE99	W82001	2.00	—	8.00	2.50	85.0min	—	4.00	Cu 2.5
ENiCu-7	WE190	W84190	0.15	—	2.50	4.00	62.0-69.0	—	1.50	Cu Bal., Al 1.75, Ti 1.0
ENiCrFe-1	WE132	W86132	0.08	13-17	11.0	3.50	62.0min	—	0.75	Nb 1.5-4.0
ENiCrFe-2	Weld A	W86133	0.10	13-17	12.0	1.00-3.5	62.0min	0.5-2.5	0.75	Nb 0.5-3.0
ENiCrFe-3	WE182	W86182	0.10	13-17	10.0	5.00-9.5	59.0min	—	1.0	Nb 1-2.5, Ti 1.0
ENiCrFe-7	WE152	W86152	0.05	28.0-31.5	7-12	5.00	Bal.	—	0.75	Nb 1-2.5
ENiMo-7	B-2	W80665	0.02	1.0	2.25	1.75	Bal.	26-30	0.2	W 1.0
ENiCrMo-3	WE112	W86112	0.10	20-23	7.0	1.0	55.0min	8-10	0.75	Nb 3.15-4.15
ENiCrMo-4	WE C-276	W80276	0.02	14.5-16.5	4.0-7.0	1.0	Bal.	15-17	0.2	W 3.0-4.5
ENiCrMo-10	WE C-22	W86022	0.02	20-22.5	2.0-6.0	1.0	Bal.	12.4-14.5	0.2	W 2.5-3.5, Co 2.5
ENiCrMo-14	WE 686	W86686	0.02	19-23	5.0	1.0	Bal.	15-17	0.25	W 3.0-4.4
ENiCrCoMo-1	WE 117	W86117	0.05-0.15	21-26	5.0	0.3-2.5	Bal.	8-10	0.75	Co 9.0-15.0, Nb 1.0
<i>Bare Welding Electrodes and Rods</i>										
ERNi-1	FM61	N02061	0.15	—	1.00	1.00	93.0min	—	0.75	Cu .25, Ti 2.5-3.5, Al 1.5
ERNi-CI	FM99	N02215	1.00	—	4.00	2.50	90.0min	—	0.75	Cu 4.0
ERNiFeMn-CI	FM44	N02216	0.50	—	Bal.	10.0-14.0	35.0-45.0	—	1.0	Cu 2.5
ERNiCu-7	FM60	N04060	0.15	—	2.50	4.00	62.0-69.0	—	1.25	Cu Bal., Ti 1.5-3.0, Al 1.25

ERNiCu-8	FM64	N05504	0.25	—	2.0	1.5	63.0–70.0	—	—	Cu Bal., Ti 0.35–0.85, Al 2.3–3.15
ERNiCr-3	FM82	N06082	0.10	18.0–22.0	3.0	2.50–3.50	67.0 min.	—	—	Nb 2.0–3.0
ERNiCr-4	FM72	N06072	0.01–0.10	42.0–46.0	0.50	0.20	Bal.	—	—	Ti 0.3–1.0
ERNiCrFe-5	FM62	N06062	0.08	14.0–17.0	6.00–10.0	1.00	70.0 min.	—	0.35	Nb 1.5–3.0
ERNiCrFe-6	FM92	N07092	0.08	14.0–17.0	8.00	2.00–2.70	67.0 min	—	0.35	Ti 2.5–3.5
ERNiCrFe-7	FM52	N06052	0.04	28.0–31.5	7.00–11.0	1.00	Bal.	—	0.50	Al 1.10, Ti 1.0
ERNiCrFe-7A	FM52M	N06054	0.04	28.0–31.5	7.00–11.0	1.00	Bal.	—	—	Al 1.10, Ti 1.0, Nb 0.5–1.0
ERNiCrFe-8	FM69	N07069	0.08	14.0–17.0	5.0–9.0	1.0	70.0 min	—	—	Ti 2.25–2.75, Al 0.4–1.0
ERNiFeCr-1	FM65	N08065	0.05	19.5–23.5	22.0 min	1.00	38.0–46.0	2.5–3.5	0.5	Nb 0.70–1.2 Cu, 1.50–3.0, Al 0.20, Ti 0.6–1.2
ERNiFeCr-2	FM718	N07718	0.08	17.0–21.0	Bal.	0.35	50.0–55.0	2.8–3.3	—	Ti 0.65–1.15, Al 0.2–0.8
ERNiMo-3	W	N10004	0.12	4.0–6.0	4.0–7.0	1.0	Bal.	23–26	1.0	Nb 4.75–5.50
ERNiCrMo-3	625	N06625	0.10	20–23	5.0	.50	58.0 min.	8–10	0.5	W 1.0, Co 2.5 Nb 3.15–4.15, Al 0.40, Ti 0.4
ERNiCrMo-7	C-4	N06455	0.015	14–18	3.0	1.0	Bal.	14–18	0.08	W 0.50, Ti 0.70
ERNiCrMo-10	C-22	N06022	0.015	20–22.5	2–6	0.50	Bal.	12.5–14.5	0.08	W 2.5–3.5, Co 2.5
ERNiCrMo-13	59	N06059	0.01	22–24	1.5	0.5	Bal.	15–16.5	0.1	Al 0.1–0.4
ERNiCrMo-14	FM686	N06686	0.01	19–23.	5.0	1.0	Bal.	15–17	0.08	W 3.0–4.4, Al 0.5, Ti 0.25

AWS Class	Alloy	UNS No.	C	Cr	Fe	Mn	Ni	Mo	Si	Other
ERNiCrMo-15	FM725	N07725	0.03	19.0–22.5	Bal.	0.35	55.0–59.0	7.0–9.5	0.20	Ti 1.0–1.7, Al 0.35, Nb 2.75–4.0
ERNiCrMo-17	C-2000	N06200	0.01	22–24	3.0	0.5	Bal.	15–17	0.08	Al 0.5, Cu 1.3–1.9, Co 2.0
ERNiCrWMo-1	230-W	N06231	0.05–.15	20–24	3.0	0.3–1.0	Bal.	1–3	0.25–0.75	Al 0.2–0.5, Co 5.0, W 13–15
ERNiCrCoMo-1	617	N06617	0.05–.15	20–24	3.0	1.0	Bal.	8–10	0.5	Co 10–15, Al 0.8–1.5
<i>Other Classifications</i>										
ASTM B637	FM80A	N07080	0.10	18.0–21.0	3.0	1.0	Bal.	—	1.0	Ti 1.8–2.7, Al 1.0–1.8, Co 2.0
AMS 5829	FM90	N07090	0.13	18.0–21.0	3.0	1.0	Bal.	—	1.0	Ti 1.8–3.0, Al 0.8–2.0, Co 15.0–21.0
AMS 5966A	FM263	N07263	0.04–0.08	19.0–21.0	0.7	0.60	Bal.	5.6–6.1	0.40	Ti 1.9–2.4, Al 0.3–0.6, Co 19.0–21.0
AMS 5884	FM909	N19909	0.06	1.0	Bal.	1.0	35.0–40.0	—	0.25–0.50	Ti 1.3–1.8, Al 0.15, Co 12.0–16.0, Nb 4.3–5.2

^ Single value is a maximum.

AWS Classification	Major Uses
E/ERNi-1	Joining Alloys 200 and 201
E/ERNiCu-7	Dissimilar combinations of steels and Ni alloys
ERNiCr-3	Joining Alloys 400, 405, and K-500
	Joining of Alloys 600 and 601
	Alloys 800, 800H and 800HT for service temperatures to 850 °C (1560 °F)
E/ERNiCrFe-7/7A	Dissimilar combinations of steels and Ni alloys
E/ERNiCrMo-2	Joining high-Cr alloys, such as Alloy 690
E/ERNiCrMo-3	Joining Alloy HX
	Joining Alloy 625
	Joining of 9% Ni steels for cryogenic service
	Dissimilar combinations of steels and Ni alloys
E/ERNiCrMo-4	Joining Alloy C-276 and other pitting resistant alloys
E/ERNiCrCoMo-1	Joining Alloy 617
	Joining Alloy 800HT for service temperatures above 760 °C (1400 °F) to 1150 °C (2100 °F)
ERNiFeCr-1	Joining Alloy 825
E/ERNi-CI	Joining/repair of cast irons, especially in thin sections
ENiFe-CI	Joining/repair of cast irons, especially thick sections and high phosphorus



## Corrosion Acceptance Testing Methods

Corrosion resistance is an important characteristic of Ni-base alloys and weldments. There are many acceptance tests specified in ASTM handbooks and other literature to evaluate the corrosion resistance of alloys for use in different environments. These tests are often misused, since in many cases an acceptance test is specified that is either inappropriate or not representative of an application. For example, in an environment in which an intergranular corrosion test is required, a localized corrosion test will not properly evaluate the material applicability. Table C3.1 presents several commonly used acceptance tests for Ni-base alloys. The ASTM handbook should be consulted for more information regarding test procedures and analysis.

### C.1 ASTM A262 C—HUEY TEST

The A262 method C, also referred to as the Huey test, calls for the test material to be immersed in boiling 65% nitric acid for 240 hours. The acid should be refreshed every 48 hours. The method is designed to sensitize the material and to find grain boundary segregation and precipitation. The typical sensitization treatment is 650–700°C (1200–1290°F) for 30–120 minutes with air cooling. In this temperature range, the precipitation of a secondary phase or carbide on grain boundaries is accelerated. This results in the depletion of the adjacent grain boundary area of chromium with  $M_{23}C_6$  precipitation, or molybdenum in the case of sigma or mu phase precipitation. Because of the depletion, the grain boundary area is susceptible to attack while the bulk of the material is immune. A subsequent annealing heat treatment usually restores corrosion resistance. The anneal must be at a sufficiently high temperature to dissolve the secondary phase, and the material must be cooled rapidly enough to avoid sensitization of the grain boundaries during cool down. Niobium or

**TABLE C3.1 Summary of Corrosion Tests for Ni-base Alloys.**

Astm Test	Reagent	Temp.	Time	Purpose	Problems	Results
A262C Huey Test	65% Nitric Acid	Boiling	240hrs	IGA (Sensitization)	Affected by Heat Treat Time, Temperature, and Rate (1200–1300 °F/30 to 120 minutes)	Corrosion rate in mpy or mm/y
A262 B/ G28 A Streicher Test	H <sub>2</sub> SO <sub>4</sub> /Fe <sub>2</sub> (SO <sub>4</sub> ) <sub>3</sub>	Boiling	24–120hrs	IGA and General Corr.	Stabilize Heat Treat conditions Gen Corrosion may mask IGA	Corrosion rate in mpy or mm/y
G28 B	H <sub>2</sub> SO <sub>4</sub> + HCL + FeCl <sub>3</sub> + CuCl	Boiling	24 hrs	IGA + Mu phase	Stabilize Heat Treat conditions	Corrosion rate in mpy or mm/y Insensitive to Mo variation
G48 A	FeCl <sub>3</sub>	22 to 50 °C	72 hrs	Pitting Corr. General Corr.	Weight Loss Measurement and Pit Density	Pitting—yes or no*
G48 B	FeCl <sub>3</sub>	22 to 50 °C	72 hrs	Crevice Corr. General Corr.	Weight Loss Measurement and Pit Density	Crevice corrosion—yes or no*
G48 C,E	Acidified FeCl <sub>3</sub>	0 to 85 °C	72 hrs	Critical Pitting Temperature	Weight Loss Measurement and Pit Density	Pitting—yes or no*
G48 D,F	Acidified FeCl <sub>3</sub>	0 to 85 °C	2 hrs	Critical Crevice Temperature	Test 5 °C below CPT Weight Loss Measurement and Pit Density	Crevice corrosion—yes or no*
SEP 1877 Method II	H <sub>2</sub> SO <sub>4</sub> /Fe <sub>2</sub> (SO <sub>4</sub> ) <sub>3</sub>	Boiling	24–120hrs	IG Cracking by Bend Test	Requires Crevice Assembly Test 5 °C below CPT Not suitable for >20% Cr alloys Cracks from IGA could open Similar to Streicher Test	Cracking—yes or no

\* At test temperature specified.

titanium is sometimes used as stabilizers to tie up carbon and thus minimize the formation of  $M_{23}C_6$  at the grain boundary. With some alloys, a “stabilization” heat treatment is used instead of the final solution anneal. This heat treatment is conducted in the sensitization temperature range for a sufficient time to allow the Cr-depleted regions at the grain boundaries to “heal” by diffusion of chromium from the surrounding matrix.

Because the Huey test is performed in nitric acid, higher chromium alloys exhibit better corrosion resistance than lower chromium alloys. The corrosion rate for an alloy is dependent upon its chemical composition. Therefore, this test indicates how well the alloy will perform in a strongly oxidizing medium, or the effectiveness of a stabilization heat treatment or final anneal.

### **C.2 ASTM G28 A/A262 B—STREICHER TEST**

The ASTM G28 method A test, identical to the ASTM A262 method B test, is also designed to detect grain boundary segregation and sensitization, but with a much shorter test duration. Unlike the Huey test, the Streicher test is relatively insensitive to molybdenum variations and was developed only to determine the degree of intergranular sensitization. Thus, the Streicher test must not be used to compare alloys for service because it does not predict service life. To properly evaluate an alloy in this test, it is necessary to know a benchmark rate that the alloy should reach. An alloy would be considered acceptable if the corrosion rate is less than its benchmark.

Besides the final heat treatment, there are several factors that influence the corrosion rate of an alloy in the Streicher test. The chemical composition is the largest influence on the corrosion rate of an alloy. Changes in Cr, C, Mo, W, and Fe will influence the corrosion rate. Alloys with higher chromium generally exhibit lower corrosion rates.

### **C.3 ASTM G28 B**

Unlike the G28 A test, the G28B test is essentially a bimodal test for any alloy. The G28B test was designed to find molybdenum-rich precipitates such as mu phase at the grain boundaries. The solution is similar to the “Green Death” solution and can only be used on Ni-Cr-Mo alloys.

### **C.4 ASTM G48 A AND B**

Although both the G48 A and B tests are performed in ferric chloride ( $FeCl_3$ ) solution, the A test is designed to evaluate pitting resistance while the B test measures crevice corrosion resistance. The procedure for both tests requires a weight loss measurement and a suggested testing temperature, because each

alloy has a critical crevice temperature (CCT) and a critical pitting temperature (CPT). Testing at or above this critical temperature will lead to attack. Therefore, testing should be performed below the critical temperatures for acceptance, but testing at insufficiently low temperatures would yield no useful data.

### **C.5 ASTM G48 C AND D (ALSO E AND F)**

Instead of a simple  $\text{FeCl}_3$  solution, tests C and D use hydrochloric acid (HCl) additions to stabilize the solution and provide better repeatability. The standard crevice device and crevice temperature will not vary with the sample size, thus decreasing variability. These tests have a built-in pass/fail interpretation of attack or no attack, or a maximum allowable depth of attack. Therefore, the test results are easily interpreted. These tests, and to an even greater extent, the G48 E and F tests are not often specified as acceptance tests for Ni-base alloys.

## Etching Techniques for Ni-base Alloys and Welds

The microstructure of Ni-base welds can be revealed using a variety of etching techniques. Weld metal, the partially melted zone around the weld, and sometimes the HAZ, are not homogeneous, so they tend to etch differently than base metals. A Ni-base weldment may involve two different alloys, or even joints of a Ni-base alloy to a ferrous material. Various etchants and etching techniques have been found to provide results of interest to the investigator.

The etching techniques described here can be divided into chemical methods or electrolytic methods. In general, chemical methods are simpler to apply and require less equipment, so they tend to be favored by the non-specialist. Electrolytic methods tend to be favored by those who specialize in the examination of corrosion-resistant alloys.

The following tables (D4.1–D4.3) include etching techniques that the authors have found useful in examining the microstructure of Ni-base alloy welds. This is not meant to be an exhaustive list, but merely what the authors commonly use for the materials listed. More extensive listings of etchants and etching methods can be found in the *ASM Metals Handbook* (1), the *CRC Handbook of Metal Etchants* (2), and *Metallography of Superalloys* (3).

**TABLE D4.1 Macro Etchants.**

Etchant	Composition/Use	Notes
Lepito's	a) 15 g (NH <sub>4</sub> ) <sub>2</sub> S <sub>2</sub> O <sub>8</sub> (ammonium persulfate) and 75 ml water, b) 250 g FeCl <sub>3</sub> and 100 ml HCl, c) 30 mL HNO <sub>3</sub> . Mix a and b, then add c, immerse for 30–120 sec at room temperature	Macroetch for general structure of base metals and welds. Good for determining weld penetration and measuring grain size. Not effective at revealing solidification structure.
Mixed acids	Equal parts HCL, HNO <sub>3</sub> , and acetic acids. Use fresh. Swab at room temperature.	A general attack etch that reveals both macro and microstructure. This etchant must be used within a few minutes of mixing and then discarded when it turns orange in color.
HCL and peroxide	Equal parts HCL and H <sub>2</sub> O <sub>2</sub> . Immerse or swab at room temperature.	Reveals general structure.

**TABLE D4.2 Micro Etchants (Swab or Immerse).**

Etchant	Composition/Use	Notes
Mixed acids	Equal parts HCL, HNO <sub>3</sub> , and acetic acids. Use fresh. Swab at room temperature.	A general attack etch will reveal segregation patterns, precipitates, and grain boundaries. This etchant must be used within a few minutes of mixing and then discarded when it turns orange in color.
Glyceregia	15 ml glycerol, 10 ml HCl, and 5 ml HNO <sub>3</sub> . Use fresh. Immerse or swab at room temperature.	Can also use 15/25/5 and 20/10/5 ratios. A general purpose etch similar to Mixed Acids, but not so aggressive. It outlines ferrite and austenite, attacks martensite and sigma phase, and reveals carbides and grain boundaries. Good for NiCrFe and NiFeCr alloys. It should also be used fresh, and discarded when it becomes orange in color.
Nitric-Acetic	10 ml HNO <sub>3</sub> and 90 ml acetic acid. Immerse or swab at room temperature.	Use for Ni and NiCu alloys.

**TABLE D4.2** *Continued*

Etchant	Composition/Use	Notes
Nitric-Hydrofluoric	20ml HNO <sub>3</sub> and 3ml hydrofluoric acid (HF). Immerse or swab at room temperature.	General microstructure etchant. Can also use 30/3 and 50/3 ratios.
HCL/Bromine	Immerse in concentrated HCL for 3 seconds, then rinse in alcohol. Immerse in mixture of 1 part bromine and 99 parts methanol for 10–20 seconds.	Use for NiCrMo and NiFeCrMo alloys to reveal grain boundaries. <b>Caution: do not breathe bromine fumes.</b>
Nital	5ml HNO <sub>3</sub> and 95ml methanol. Swab or immerse at room temperature.	Etches carbon and low alloy steels. Use for dissimilar welds with these steels. See Table D4.3—may also be used as an electrolytic etchant

**TABLE D4.3** **Micro Etchants (Electrolytic).**

Etchant	Composition/Use	Notes
10% Chromic	10g CrO <sub>3</sub> (chromic acid) and 90mL water. Use at room temperature. Etch at 3–6 volts for 5–60 seconds.	A good general etchant for revealing the microstructure of base metals and welds. Reveals segregation behavior and grain boundaries in weld metals. May be used for dissimilar welds with carbon steels if the carbon steel is previously immersion etched with nital.
Phosphoric	80mL H <sub>3</sub> PO <sub>4</sub> and 10mL water. Use at room temperature. Etch at 3 volts for 5–10 seconds.	50/50 and 20/80 ratios may also be used. Reveals grain boundaries in NiFeCo and NiCrFe alloys. Tends to pit the sample if overetched.
Hydrofluoric and Glycerol	5ml HF, 10ml glycerol, 85ml ethanol. Use at room temperature. Etch at 6–12 volts.	Reveals gamma prime precipitation in Ni-base superalloys.
Nital	5ml HNO <sub>3</sub> and 95ml methanol.	Reveals grain boundaries in NiCr, NiFeCr, and NiCrFe alloys.

## REFERENCES

1. *Metals Handbook* Ninth Edition, Volume 9, pp. 305–309. ASM International, Materials Park, OH. 1985
2. *CRC Handbook of Metal Etchants*, Walker, P. and Tarn, W. H., editors. CRC Press, Boca Raton, FL. Pages 1188–1199. 1991.
3. *Metallography of Superalloys*, G.F. Vander Voort, Buehler Ltd., October 2003.

## AUTHOR INDEX

---

### A

- Adam, P. 254  
Alexandrov, B. T. and Lippold, J. C. 153, 377  
Alexandrov, B. T., Nissley, N. E., and Lippold, J. C. 251  
Alexandrov, B. T. and Lippold, J. C. 402  
Alexandrov, B. T., Nissley, N. E. and Lippold, J. C. 402  
Anderson, T. D. and DuPont, J. N. 326  
Arata, Y. 254  
Armstrong, T. N. and Brophy, G. R. 378  
Armstrong, T. N. and Gagnebin, A. P. 378

### B

- Babu, S. S., Miller, M. K., Vitek, J. M., and David, S. A. 249  
Baeslack 225, 226, 251  
Baeslack and Nelson 225  
Baeslack, W. A. III and Nelson, D. E. 251  
Baeslack, W. A. III, West, S. L., and Kelly, T. J. 251  
Baker, H. 44, 152, 250, 279, 378  
Baker, H. Ed. 44, 152, 250, 279  
Baker, R. G. and Newman, R. P. 253  
Banovic, S. W. and DuPont, J. N. 151, 249  
Banovic, S. W., DuPont, J. N., and Marder, A. R. 377, 378  
Banovic, S. W. 44  
Barker, J. F., Ross, E. W., and Radavich, J. F. 249  
Beardmore, P., Davies, R. G., and Johnston, T. L. 248

- Bengough 130, 155  
Bengough, G. D. 155  
Berry, T. F. and Hughes, W. P. 253  
Betteridge, W. and Heslop, J. 44  
Biss, V. and Sponseller, D. L. 248  
Bologna, D. J. 252  
Bose, S. K. and Grabke, H. J. 63  
Boucher 231, 234, 252  
Boucher, C., Dadian, M., and Granjon, H. 252  
Boucher, C., Varela, D., Dadian, M., and Granjon, H. 252  
Bowers, R. J., Lippold, J. C., and Hooijmans, J. W. 324  
Brody, H. D. and Flemings, M. C. 150  
Brooks, C. R. 249  
Brooks, J. A. and Thompson, A. 326  
Brooks, J. W. and Bridges, P. G. 324  
Brooks, J. W. and Bridges, P. J. 43, 249  
Brooks, R. B. 43  
Brown 98, 99, 153  
Brown and Mills 98, 99  
Brown, C. M. and Mills, W. J. 153  
Burden, M. H. and Hunt, J. D. 326

### C

- Campo, E., Turco, C., and Catena, V. 324  
Canonico 227, 251  
Canonico, D. A., Savage, W. F., Werner, W. J., and Goodwin, G. M. 251  
Carlton, J. B. and Prager, M. 253  
Chakrabarti, D. J., Laughlin, D. E., Chen, S. W., and Chang, Y. A. 44  
Chandel, R. S. 376  
Chen, C. and Chen, G. H. 280

- Choi, I. D., Matlock, D. K., and Olson, D. L. 152
- Cieslak 37, 44, 45, 73, 74, 105, 106, 123, 150, 151, 153, 195, 201, 214, 215, 216, 249, 250, 252, 377
- Cieslak, M. J. 44, 45, 150, 151, 153, 249, 250, 377
- Cieslak, M. J., Headley, T. J., and Romig, A. D. 44, 150, 250, 377
- Cieslak, M. J., Headley, T. J., Knorovsky, G. A., Romig, A. D., and Kollie, T. 150, 249
- Cieslak, M. J., Headley, T. J., Kollie, T., and Romig, A. D. 150, 250
- Cieslak, M. J., Knorovsky, G. A., Headley, T. J., and Romig, A. D. 45, 151, 250
- Cieslak, M. J., Stephens, J. J., and Carr, M. J. 153, 250
- Clyne, T. W. and Kurz, W. 151, 153, 250
- Collins 131, 140, 142, 155, 156
- Collins, M. G. and Lippold, J. C. 155
- Collins, M. G., Ramirez, A., and Lippold, J. C. 156
- Cortial 93, 94, 95, 147, 153
- Cortial, F., Corrieu, J. M., and Vernot-Loier, C. 153
- Cullison, A. 325
- D**
- Darolia, R., Lewandowski, J. J., Liu, C. T., Martin, P. L., Miracle, D. B., and Nathal, M. V. 279
- David, S. A. and Vitek, J. M. 251, 325
- David, S. A., Jemian, W. A., Liu, C. T., and Horton, J. A. 280
- David, S. A., Vitek, J. M., Babu, S. S., Boatner, L. A., and Reed, R. W. 325
- Deacon, R. M., DuPont, J. N., and Marder, A. R. 378
- deBarbadillo, J. J. and Fischer, J. J. 278
- Decker, R. F. 14, 248, 249
- Decker, R. F. and Mihalisin, J. R. 248
- Deevi, S. C., Sikka, V. K., and Liu, C. T. 279
- Dhooge, A. and Vinckier, A. 377
- Dhooge, A., Provost, W., and Vinckier, A. 378
- Diehl, M. J. and Messler, R. W. 152
- DuPont 15, 36, 38, 39, 43, 44, 45, 47, 64, 65, 66, 69, 73, 75, 78, 89, 90, 107, 111, 112, 125, 151, 152, 154, 155, 157, 182, 185, 190, 191, 192, 194, 198, 249, 250, 255, 281, 300, 301, 310, 318, 319, 320, 321, 322, 327, 330, 338, 340, 341, 350, 354, 355, 356, 376, 377, 378, 379, 409, 415, 419
- DuPont, J. N. 43, 44, 45, 107, 151, 152, 154, 155, 249, 250, 376, 377, 378
- DuPont, J. N. and Kusko, C. S. 376
- DuPont, J. N. and Marder, A. R. 376
- DuPont, J. N. and Robino, C. V. 154
- DuPont, J. N., Newbury, B. D., Robino, C. V., and Knorovsky, G. A. 250
- DuPont, J. N., Banovic, S. W., and Marder, A. R. 377
- DuPont, J. N., Michael, J. R., and Newbury, B. D. 107, 151
- DuPont, J. N., Newbury, B. D., Robino, C. V., and Knorovsky, G. A. 45
- DuPont, J. N., Robino, C. V., and Marder, A. R. 44, 151, 152, 249
- DuPont, J. N., Robino, C. V., Marder, A. R., Notis, M. R., and Michael, J. R. 43, 151, 249, 378
- DuPont, J. N., Robino, C. V., Mizia, R. E., and Williams, D. B. 152
- Duvall 154, 204, 225, 230, 231, 239, 246, 250, 253
- Duvall and Owzarski 204, 239
- Duvall, D. S. and Doyle, J. R. 253
- Duvall, D. S. and Owczarski, W. A. 154, 250, 253
- Dynamic Systems, Inc. 402
- E**
- E. G. Thompson 225
- Edgecumbe 96, 97, 148, 153
- Edgecumbe-Summers 96, 148, 153
- Edgecumbe-Summers, T. S., Rebak, R. B., and Seeley, R. R. 153
- Edwards, G. R., Maguire, M. C., and Damkroger, B. K. 280
- Eiselstein, H. L. 250
- Ekrami, A. and Khan, T. I. 279
- El-Dasher, B. S., Edgecumbe, T. S., and Torres, S. G. 152
- Ernst, S. C. 152

**F**

- Fawley, R. W. and Prager, M. 253  
 Finton, T. 402  
 Fletcher, M. J. 252  
 Flowers, G., Kelley, E., Grossklaus, W.,  
 Barber, J., Grubbs, G., Williams, L.  
 254  
 Forsberg, S. G. 376  
 Franklin, J. G. and Savage, W. F. 253  
 Fuerschbach, P. W. and Knorovsky, G. A.  
 376  
 Furmanski, G., Kiser, S. D., and  
 Shoemaker, L. E. 378

**G**

- G. F. Vander Voort 422  
 Gale, W. F. and Guan, Y. 280  
 Gallagher, M. 107, 154  
 Gandy, D. W., Findlan, S. J., Childs, W. J.,  
 and Smith, R. E. 376  
 Garner A. 377  
 Garud, Y. S. and Gerber, T. L. 153  
 Gauman, M., Bezencon, C., Canalis, P.,  
 and Kurz, W. 325  
 Gauman, M., Henry, S., Cleton, F.,  
 Wagniere, J. D., and Kurz, W. 326  
 Gauman, M., Trivedi, R., and Kurz, W.  
 326  
 Gaurd, R. W. and Westbrook, J. H. 44,  
 248  
 George, E. P., Babu, S. S., David, S. A.,  
 and Seth, B. B. 250  
 George, E. P., Liu, C. T., and Pope, D. P.  
 279  
 Gibbons, T. B. and Hopkins, B. E.  
 249  
 Giggins, C. S. and Pettit, F. S. 44  
 Gittos, M. F. and Gooch, T. G. 377  
 Goodwin, G. M. 280, 402  
 Goodwin, G. M. and David, S. A. 280  
 Gordine, J. 252  
 Gozlan, E., Bamberger, M., and Dirnfeld,  
 S. F. 250  
 Gulati, K. C. 378  
 Guo 155, 229, 230, 252  
 Guo, H. Chaturvedi, M., and Richards,  
 N. L. 252  
 Guo, Z., Chaturvedi, M. C., and  
 Richards, N. L. 155

**H**

- Hadrill 129, 155  
 Hadrill and Baker 129  
 Hadrill, D. M. and Baker, R. G. 155  
 Halada, G. P., Clayton, C. R., Kim, D.,  
 and Kearns, J. R. 377  
 Headley 106  
 Heckel, R. W., Ricketts, J. H., and  
 Buchwald, J. 44  
 Heijwegen, C. P. and Rieck, G. D. 63  
 Hemsworth 129, 130, 155  
 Hemsworth, B., Boniszewski, T., and  
 Eaton, N. F. 155  
 Heubner, U., Kohler, M., and Prinz, B.  
 151  
 Hilkes, J., Neessen, F., and Caballero, S.  
 376  
 Hirano, K., Agarwala, R. P. 63  
 Hirata, H. 155  
 Hodge, F. G. 14  
 Hondors, E. and Seah, M. P. 154  
 Hooijmans, J. W., Lin, W., and Lippold,  
 J. C. 324  
 Howard-White, F. B. 14  
 Huang 232, 252  
 Huang, X., Richards, N. L., and  
 Chaturverdi, M. C. 252  
 Hughes, W. P. and Berry, T. F. 253  
 Hull, F. C. 402  
 Hunt, J. D. 326

**J**

- Jena, A. K., Rajendraprasad, S. B., and  
 Gupta, K. P. 45  
 Joo, H. and Takeuchi, H. 151  
 Jung, S. B., Yamane, T., Minamino, Y.,  
 Hirao, K., Araki, H., and Saji, S. 63

**K**

- Kain, V., Sengupta, P., De, P. K., and  
 Banerjee, S. 156  
 Kang, C. Y., North, T. H., and Perovic,  
 D. D. 279  
 Karlsson, L., Bergquist, E. L., Rigdal, S.,  
 and Thalberg, N. 378  
 Kattamis, T. Z. and Flemings, M. C. 152  
 Kelly, T. J. 153, 154, 251, 252, 279  
 Kikel 134, 156  
 Kikel and Parker 134

Kikel, J. M. and Parker, D. M. 156  
 King, R. W., Hatala, R. W., and Hauser, H. A. 253  
 Kiser, S. 156, 376, 377  
 Kiser, S. D. 377  
 Klueh, R. L. and King, J. F. 377  
 Knorovsky 44, 151, 187, 250  
 Knorovsky, G. A., Cieslak, M. J., Headley, T. J., Romig, A. D., and Hammeter, W. F. 44, 151, 250  
 Kohler, M. 153  
 Koren, A., Roman, M., Weissshaus, I., and Kaufman, A. 253  
 Kou, S. 253  
 Kurokawa, S., Ruzzante, J. E., Hey, A. M., Dymont, F. 63  
 Kurz, W., Giovanola, B., and Trivedi, R. 326

**L**

Lacombe, P. 63  
 Lee, H. T. and Kuo, T. Y. 156  
 Lehecky, E. M. and Palumbo, G. 325  
 Lienert 106, 151  
 Lienert, T. J., Robino, C. V., Hills, C. R., and Cieslak, M. J. 151  
 Lifshitz, I. M. and Slovozov, V. V. 249  
 Lifshitz, I. M. and Slovozov, V. V. 43  
 Lin, W., Lippold, J. C., and Baeslack, W. A. 402  
 Lin, W., Nelson, T. W., Lippold J. C., and Baeslack, W. A. 402  
 Lin, W., Nelson, T. W., Lippold, J. C., and Baeslack, W. A. 154  
 Lingenfelter 104, 116, 153  
 Lingenfelter, A. C. 153  
 Lippold, J. C. 15, 47, 58, 102, 107, 108, 134, 135, 136, 137, 139, 142, 150, 152, 153, 154, 156, 157, 233, 241, 242, 243, 244, 255, 281, 285, 288, 290, 291, 293, 294, 296, 297, 298, 325, 327, 376, 379, 381, 383, 385, 397, 399, 402, 409, 415, 419  
 Lippold, J. C. and Kotecki, D. J. 154, 376  
 Lippold, J. C. and Lin, W. 156  
 Lippold, J. C. and Nissley, N. E. 156  
 Lippold, J. C., Baeslack, W. A., and Varol, I. 154

Lippold, J. C., Clark, W. A. T., and Tumuluru, M. 150  
 Lippold, J. C., Sowards, J., Alexandrov, B. T., Murray, G. and Ramirez, A. J. 153  
 Lippold, J. C., Sowards, J., Alexandrov, B. T., Murray, G., and Ramirez, A. J. 107  
 Lippold, J. C. and Lin, W. 402  
 Lippold, J. C. and Nissley, N. E. 402  
 Lippold, J. C. Nelson, T. W. and Lin, W. 402  
 Liu, C. T. and Kumar, K. S. 279  
 Liu, C. T., Stiegler, J. O., and Froes, F. H. 43  
 Liu, W. and DuPont, J. N. 325, 326  
 Lu, Q. 252, 324  
 Lucas 227, 251  
 Lucas and Jackson 227  
 Lucas, M. J. and Jackson, C. E. 251  
 Luer, K. R., DuPont, J. N., Marder, A. R., and Skelonis, C. K. 156, 378  
 Lundin, C. D. 154, 376  
 Lundin, C. D., Qiao, C. Y. P., and Swindeman, R. W. 154

**M**

Maguire 106, 153, 186, 214, 250  
 Maguire and Headley 106  
 Maguire, M. C. and Headley, T. J. 153  
 Maguire, M. C. and Michael, J. R. 250  
 Markiv, V. Y. and Gladyshevskiy, E. I. 152  
 Matsuda 131, 153, 155, 376  
 Matsuda, F. 153, 155, 376  
 Matsuda, F. and Nakagawa, H. 376  
 Matsuda, F., Nakagawa, H., Katayama, S., and Arata, Y. 153  
 McKeown, D. 253  
 Mehl, M. and Lippold, J. C. 324  
 Merica, P. 14  
 Messler 85, 86  
 Miracle, D. B. 279  
 Molian, P. A., Yang, Y. M., and Patnaik, P. C. 279  
 Moore, T. J. 279  
 Moore, T. J. and Glasgow, T. K. 279  
 Morimoto, S. and Hirane, T. 279  
 Morinaga, N., Yukawa, N., Adachi, H., and Ezaki, H. 45

Morrison, T. J., Shira, C. S., and Weisenberg, L. A. 251

## N

N. E. Nissley and J. C. Lippold 402  
 Nakao, Y. 253, 279  
 Nakao, Y. and Shinozaki, K. 279  
 Narasimhan, S. L., Copley, S. M., Van Stryland, E. W., and Bass, M. 325  
 Nash, P. 44  
 Nelson 334, 335, 336, 376, 377  
 Nelson, T. W., Lippold, J. C., and Mills, M. J. 376, 377  
 Nippes, E. F. and Balaguer, J. P. 378  
 Nippes, E. F. and Savage, W. F. 402  
 Nishimoto 131, 142, 155, 266, 267, 279  
 Nishimoto, K., Mori, H., and Hongoh, S. 155  
 Nishimoto, K., Saida, K., and Tsuduki, R. 279  
 Nissley, N. 155, 156, 402  
 Nissley, N. E. and Lippold, J. C. 156  
 Nissley, N. E., Collins, M. G., Guaytima, G., and Lippold, J. C. 155  
 Nissley, N. E. and Lippold, J. C. 402  
 Noebe, R. D., Bowman, R. R., and Nathal, M. V. 280  
 Noecker 130, 140, 155  
 Noecker and DuPont 130, 140  
 Noecker, F. F. and DuPont, J. N. 155  
 Noguchi, O., Oya, A., and Suzuki, T. 279  
 Norton S. J. and Lippold, J. C. 253

## O

Oh, Y. K., Devletian, J. H., and Chen, V. S. 376  
 Ojo, O. A., Richards, N. L., and Chaturvedi, M. C. 249  
 Owczarski 154, 225, 227, 230, 231, 250, 251  
 Owczarski, W. A. 154, 250, 251  
 Owczarski, W. A., Duvall, D. S., and Sullivan, C. P. 154, 250

## P

Palumbo, G. and Aust, K. T. 325  
 Palumbo, G., King, P. G., Aust, K. T., Erb, U., and Lichtenberger, P. C. 325  
 Pan, C., Wang, R., and Gui, J. 376

Park, J. W., Babu, S. S., Vitek, J. M., Kenik, E. A., and David, S. A. 325  
 Park, J. W., Vitek, J. M., Babu, S. S., and David, S. A. 326

Patel, S. J. 14

Pauling, L. 43

Pease 227, 251

Pease, G. R. 251

Pepe 154, 204, 250

Pepe and Savage 204

Pepe, J. J. and Savage, W. F. 154, 250

Perricone, M. J. 44, 45, 151, 152

Perricone, M. J. and DuPont, J. N. 44, 152

Perricone, M. J., DuPont, J. N., and Cieslak, M. J. 45, 151

Prager, M. and Shira, C. S. 253

## Q

Qian, M. and Lippold, J. C. 252, 324, 325

## R

R. E. Smith 378

Radavich, J. F. 249, 324

Radavich, J. F. and Fort, A. 324

Radavich, J. F. and Korth, G. E. 324

Radhakrishnan 225, 229, 251, 252

Radhakrishnan and Thompson 225, 229

Radhakrishnan, B. and Thompson, R. G. 251, 252

Ramirez 130, 131, 138, 141, 152, 155

Ramirez and Lippold 130, 131, 138, 141

Ramirez, A. J. and Lippold, J. C. 152, 155

Ranganathan, S. 325

Rappaz, M., David, S. A., Vitek, J. M., and Boatner, L. A. 326

Rhines 130, 155, 249

Rhines and Wray 130

Rhines, F. N. 155, 249

Rhines, F. N. and Wray, P. J. 155

Richards, N. L. and Chaturvedi, M. C. 154

Robino, C. V., Michael, J. R., and Cieslak, M. J. 151, 251

Rosenthal, R. and West, D. R. F. 249

Ross, E. W. and Sims, C. T. 44

Rowe 105, 106, 107, 116, 151, 154, 336, 377

Rowe, M. D., Crook, P., and Hoback, G. L. 107, 151

Rowe, M. D., Ishwar, V. R., and Klarstrom, D. L. 107  
 Rowe, M. D., Nelson, T. W., and Lippold, J. C. 377  
 Rowe, M. D., Ishwar, V. R., and Klarstrom, D. L. 154

**S**

Saha, R. K. and Khan, T. I. 279  
 Sakai, T., Asami, K., Katsumata, M., Takada, H., and Tanaka, O. 377  
 Santella, M. L. and David, S. A. 280  
 Santella, M. L. and Feng, Z. 280  
 Santella, M. L. and Sikka, V. K. 280  
 Saunders, N. 44, 45  
 Saunders, N., Guo, Z., Li, X., Miodownik, A. P., and Schille, J. P. 45  
 Savage 153, 154, 227, 251, 381, 394, 402  
 Savage, W. F. and Krantz, B. M. 154  
 Savage, W. F., Nippes, E. F., and Goodwin, G. M. 153, 251  
 Savage, W. F. and Lundin, C. D. 402  
 Schaeffler, A. L. 376  
 Scheil, E. 150, 153  
 Schulson, E. M. 280  
 Schulson, S. and Barker, D. R. 279  
 Schwenk 230, 252  
 Schwenk, W. and Trabold, A. F. 252  
 Shademan, S. S. and Kim, D. S. 378  
 Shinozaki, K., Kang, C. Y., Kim, Y. C., Aritoshi, M., North, T. H., and Nakao, Y. 279  
 Sims, C. T. 44, 252, 324  
 Sims, C. T., Stoloff, N. S., and Hagel, W. C. 252, 324  
 Singleton, M. F. and Nash, P. 44  
 Sowards, J. W., Alexandrov, B. T., Lippold, J. C., Liang, D., and Frankel, G. S. 377  
 Sponaugle, C. 14  
 Stadelmaier 32, 44, 192, 193, 250  
 Stadelmaier and Fiedler 32, 192, 193  
 Stadelmaier, H. H. and Fiedler, M. 44, 250  
 Stoloff, N. S. 43, 278  
 Sundararaman, M. and Mukhopadhyay, P. 43

Sundman, B. 44  
 Susan, D. F., Robino, C. V., Minicozzi, M. J., and DuPont, J. N. 151  
 Swalin, R. A., Martin, A. 63

**T**

Taylor, A. and Floyd, R. W. 44  
 Thamburaj, R., Goldak, J. A., and Wallace, W. 253  
 Thompson 14, 154, 155, 225, 226, 228, 231, 232, 251, 252  
 Thompson and Beasley 14  
 Thompson and Genculu 231  
 Thompson, E. G. 251  
 Thompson, J. and Beasley 14  
 Thompson, R. G. 154, 155, 251, 252  
 Thompson, R. G. and Genculu, S. 154, 251  
 Thompson, R. G., Cassimus, J. J., Mayo, D. E., and Dobbs, J. R. 155, 251  
 Thompson, R. G., Dobbs, J. R., and Mayo, D. E. 252  
 Thornton, P. H., Davies, P. H., and Johnston, T. L. 43, 248  
 Threadgill, P. L. 377  
 Tuma, H., Vyklicky, M., and Loebl, K. 152  
 Turchi P. A., Kaufman, L., and Liu, Z. 45

**V**

Vincent 154, 227, 231, 232, 252  
 Vincent, R. 154, 252  
 Vitek, J. M. 325, 326  
 Vitek, J. M., David, S. A., and Boatner, L. A. 325

**W**

Walker, P. and Tarn, W. H. 422  
 Wang, N., Mokadem, S., Rappaz, M., and Kurz, W. 326  
 Wangen Lin 402  
 Was, G. S. 152  
 Webb, G. L. and Burke, M. G. 153  
 Weiss, S., Hughes, W. P., and Macke, H. J. 253  
 Whang, S. H., Liu, C. T., Pope, D. P., and Stiegler, J. O. 279  
 Williams, J. A. and Singer, A. R. E. 252  
 Williams, K. J. 152

Wilson, R. M. and Burchfield, L. W. G.  
253

Wray 130

Wu, K. C. and Herfert, R. E. 253

## Y

Yamaguchi 130, 131, 155

Yamaguchi, S. 155

Yang, S., Huang, W., Liu, W., Zhong, M.,  
and Zhou, Y. 325

Yeniscavich 227, 252

Yeniscavich and Fox 227

Yeniscavich, W. and Fox, C. W. 252

Yoshihiro, F., Saida, K., and Nishimoto,  
K. 326

Young 93, 130, 141, 152, 156

Young, G. A., Battige, C. K., Lewis, N.,  
Penik, M. A., Kikel, J., Silvia, A. J., and  
McDonald, C. K. 152

Young, G. A., Capobianco, T. E., Penik,  
M. A., Morris, B. W., and McGee, J. J.  
156

Younger, R. N. and Barker, R. G. 253

## Z

Zhang, J. S., Hu, Z. Q., Murata, Y.,  
Morinaga, N., and Yukawa, N. 45

Zhang, Y. C., Nakagawa, H., and  
Matsuda, F. 155



## SUBJECT INDEX

---

### A

- activation energy term (Q) 63
- age-harden(ed, ing, able) 4, 14, 174, 228, 229, 230, 231, 232, 254, 295, 368
- aging contraction 243, 244
- air induction melting (AIM) 12
- AISI 4340 208
- AL6XN 72, 148, 349, 350, 351, 352, 353, 354, 355, 356
- Alloy 200 56, 85, 145
- Alloy 22 base metal 148
- Alloy 400 6, 9, 10, 56, 85, 144, 149, 150
- Alloy 401 145
- Alloy 404 145
- Alloy 405 145
- Alloy 59 146, 358, 359, 361
- Alloy 600 2, 9, 11, 56, 85, 98, 99, 144, 145, 153, 222, 223, 227, 390
- Alloy 686 9, 144, 358
- Alloy 690 9, 54, 55, 56, 81, 82, 98, 99, 131, 134, 143, 153, 156, 397, 398, 402, 413
- Alloy 693 9, 145
- Alloy 706 9, 40, 161, 174
- Alloy 713 62, 158, 174, 234, 245, 246
- Alloy 718 4, 38, 39, 40, 43, 110, 111, 119, 155, 158, 171, 172, 174, 187, 195, 196, 198, 206, 210, 222, 225, 226, 227, 228, 229, 230, 231, 232, 233, 234, 235, 236, 239, 240, 241, 242, 243, 244, 245, 248, 249, 251, 252, 283, 284, 285, 286, 287, 288, 289, 290, 291, 292, 293, 294, 295, 296, 298, 324
- Alloy 751 9, 161
- Alloy 800 9, 48, 54, 55, 56, 72, 85, 152, 154, 227, 347, 348, 349, 364, 365, 413
- Alloy 825 9, 54, 55, 56, 146, 148, 413
- Alloy 909 9, 161, 174
- Alloy CM247DS 177, 179
- Alloy CMSX-4 301, 303, 305, 306, 307, 312, 318, 319, 320, 321, 323, 324
- Alloy IN738 181
- Alloy MA754 256, 259, 260, 261, 262, 266
- Alloy MA758 256
- Alloy Thermo-Span 120
- Alloy X-750 4, 9, 10, 158
- Alloy 622 15
- Alloys 622 and 625 15
- Alloy 625 54, 81, 107, 117, 148, 200, 216, 357, 386, 396, 397, 398
- Alloys 725, 925 and 945 161
- Alloys HP, 800 and 800H 146
- aluminide(s) 2, 5, 255, 268, 272, 276, 279, 280, 393
- aluminum 2, 4, 9, 10, 12, 130, 158, 227, 255, 268, 270, 364, 368, 402
- Ambrose Monell 6, 7
- anisotropic 99, 259
- Annabergite 5
- anneal(s, ing, ed) 4, 7, 13, 51, 81, 98, 161, 206, 208, 209, 230, 232, 236, 237, 245, 246, 256, 282, 283, 284, 294, 296, 298, 324, 415, 417
- antiphase boundary (APB) 162, 167
- antiphase domain (APD) 276
- APB 162
- aqueous 1, 11, 14, 15, 48, 144, 146
- argon-oxygen-decarburization (AOD) 12

- atomic radii mismatch 16
- austenite 1, 4, 10, 20, 22, 25, 26, 32, 35, 36, 41, 42, 43, 47, 51, 57, 58, 60, 63, 71, 72, 73, 74, 76, 77, 79, 80, 100, 103, 104, 109, 121, 161, 165, 167, 171, 190, 202, 216, 236, 332, 333, 335, 341, 342, 349, 351, 353, 359, 360, 361, 363, 386, 393, 420
- austenitic 1, 10, 11, 44, 47, 48, 55, 57, 59, 71, 82, 88, 111, 128, 130, 131, 133, 136, 151, 152, 153, 154, 155, 156, 192, 239, 249, 253, 262, 274, 302, 326, 327, 332, 333, 334, 335, 336, 338, 342, 345, 346, 348, 349, 351, 353, 356, 357, 363, 364, 373, 376, 377, 378, 383, 385, 386, 387, 388, 393, 395, 400, 402
- autogenous 125, 131, 272, 327, 330, 349, 350, 354, 355, 381, 392
- B**
- back-diffusion 61, 63, 175, 351
- backfill(ed, ing) 110, 113, 114, 220
- billets 13
- boilers 146, 327
- bottom-pouring 13
- braze, brazing, brazeability 145, 262, 268, 276, 278, 279, 280, 283
- brittle 2, 15, 20, 24, 35, 38, 72, 73, 95, 98, 167, 268, 282, 367
- Brody-Flemings 60
- buffer 373, 375
- buffer layer 373, 375
- C**
- C-22 2, 9, 36, 37, 38, 39, 44, 49, 52, 53, 56, 67, 70, 72, 73, 74, 75, 76, 92, 96, 97, 105, 106, 107, 109, 114, 116, 144, 146, 150, 153, 200, 250, 358, 377, 386, 405, 410, 411
- carbide films 84, 246
- carbide(s) 6, 17, 19, 32, 41, 51, 55, 56, 70, 71, 73, 76, 81, 83, 84, 93, 98, 99, 103, 105, 106, 118, 119, 120, 130, 138, 139, 140, 141, 175, 182, 200, 202, 225, 226, 231, 232, 238, 239, 241, 245, 246, 247, 282, 291, 292, 297, 333, 345, 348, 359, 367, 415, 420
- carbon steel(s) 1, 237, 327, 328, 330, 331, 332, 333, 334, 335, 337, 338, 340, 341, 342, 343, 345, 346, 359, 360, 373, 376, 421
- carbon-depleted zone 338
- carbonitride(s) 19, 263
- cast iron(s) 1, 54, 328, 331, 413
- cast pin tear (CPT) 222, 223, 224, 251, 388, 391, 402
- casting(s) 4, 13, 43, 87, 88, 90, 122, 145, 151, 152, 153, 158, 225, 228, 229, 233, 270, 280, 284, 285, 299, 300, 373
- caustic(s) 2, 11, 145
- CCT diagrams 40
- C-curve(s) 237, 239, 240, 241
- Charpy impact energy 96
- Charpy impact toughness 97
- Charpy V-notch impact toughness 360
- Charpy V-notch toughness 357, 359
- chloride ion 11, 146, 368
- chloride stress corrosion 363
- circular patch tests 401
- cladding(s) 156, 327, 331, 334, 335, 336, 338, 342, 345, 376, 377, 378
- class II reaction 184, 193
- classification(s) 2, 3, 51, 54, 114, 116, 117, 122, 155, 357, 412, 413
- Clyne-Kurz model 63, 64
- coarsening 18, 19, 128, 162, 164, 169, 170, 171, 178, 181, 182, 245, 248, 257, 263, 361
- coefficient of thermal expansion (CTE) 1, 238, 327, 336, 345, 347, 357
- coefficient(s) 1, 3, 60, 63, 67, 69, 79, 103, 175, 183, 192, 200, 238, 299, 327, 336, 345, 347, 351, 353, 357
- coherency 19, 248
- cold cracking 380
- cold working 13, 260
- columnar-to-equiaxed transition (CET) 299, 300, 302
- composition(al) transition zone 332, 333, 336, 340, 341, 342, 345, 375
- composition(s, al) 2, 3, 5, 6, 9, 15, 19, 21, 22, 24, 26, 27, 29, 30, 38, 41, 42, 44, 47, 48, 49, 50, 51, 52, 57, 58, 59, 60, 61, 62, 65, 66, 71, 72, 73, 74, 75, 76, 77, 79, 80, 88, 91, 101, 103, 105, 111, 117, 118, 122, 123, 128, 143, 149, 152, 153, 155, 158, 159, 160, 161, 167, 170, 171, 175, 176, 177, 178, 183, 185, 186, 187, 188, 190,

192, 193, 195, 196, 197, 198, 200, 202, 204, 206, 211, 213, 214, 215, 220, 221, 222, 226, 228, 232, 236, 237, 239, 244, 253, 256, 262, 266, 268, 270, 281, 285, 287, 289, 299, 303, 324, 328, 329, 331, 332, 333, 334, 335, 336, 337, 338, 340, 341, 342, 345, 346, 349, 351, 352, 353, 356, 357, 362, 364, 368, 371, 375, 388, 389, 393, 403, 409, 417, 420, 421

computational thermodynamics 16

concentration gradient(s) 60, 61, 64, 69, 87, 88, 89, 146, 170, 175, 178, 180, 228, 302, 329, 341, 349, 370

constitutional liquation 81, 82, 118, 119, 121, 154, 203, 204, 205, 206, 207, 209, 225, 226, 228, 230, 231, 233, 235, 239, 250, 291, 292, 297, 298

corrosion 2, 3, 4, 5, 10, 11, 12, 14, 15, 20, 21, 22, 24, 43, 45, 47, 48, 55, 59, 69, 72, 77, 81, 82, 83, 87, 88, 96, 107, 143, 144, 145, 146, 147, 148, 149, 150, 151, 152, 153, 156, 157, 158, 161, 208, 255, 268, 283, 325, 328, 331, 345, 349, 350, 351, 356, 357, 358, 363, 364, 367, 368, 369, 370, 371, 372, 373, 377, 378, 380, 415, 416, 417, 419

corrosion test(s) 349, 363, 364, 371, 380, 415

critical pitting temperature (CPT) 222, 223, 357, 388, 389, 390, 392, 416, 418

crack susceptible region (CSR) 125, 381, 382, 383, 397

cracking 2, 3, 4, 5, 9, 11, 20, 58, 72, 82, 87, 98, 99, 100, 101, 102, 103, 104, 105, 106, 107, 108, 109, 110, 111, 113, 114, 115, 116, 117, 118, 119, 120, 122, 123, 124, 125, 126, 127, 128, 129, 130, 131, 133, 134, 135, 136, 138, 141, 143, 145, 146, 148, 152, 153, 154, 155, 157, 158, 161, 203, 204, 206, 208, 209, 211, 212, 213, 214, 215, 216, 217, 219, 220, 222, 223, 224, 225, 226, 227, 228, 229, 230, 231, 232, 233, 234, 235, 237, 238, 239, 240, 241, 242, 243, 244, 245, 246, 247, 248, 250, 251, 252, 253, 254, 265, 272, 273, 274, 275, 276, 278, 280, 281, 283, 284, 285, 286, 287, 289, 291, 293, 294, 295, 296, 297, 298, 299, 314, 315, 316, 317,

318, 320, 321, 322, 323, 324, 326, 334, 337, 342, 343, 344, 345, 346, 347, 348, 349, 351, 353, 354, 355, 356, 361, 363, 364, 365, 366, 367, 369, 370, 371, 373, 374, 375, 376, 377, 378, 379, 380, 381, 382, 383, 384, 385, 386, 387, 388, 389, 390, 392, 393, 394, 396, 398, 399, 401, 402, 416

creep strength 5, 12, 15, 17, 19, 48, 146, 161, 167, 171, 211, 296

crevice corrosion 12, 13, 146, 148, 351, 356, 363, 368, 416, 417

cryogenic 1, 47, 48, 54, 57, 328, 357, 359, 360, 361, 413

crystallographic 18, 19, 26, 57, 59, 133, 177, 294, 301, 309, 326

cuboidal morphology 164

## D

decarburizing 13

delta ferrite 22, 111, 334

delta phase formation 84

dendrite tip undercooling 61, 64, 101, 103, 198, 303, 304

dendrite(s) 57, 59, 60, 61, 62, 64, 69, 71, 74, 77, 87, 88, 101, 103, 146, 147, 177, 178, 192, 198, 202, 217, 300, 301, 302, 303, 305, 306, 307, 309, 310, 311, 312, 313, 314, 316, 317, 326, 342, 349, 350, 351, 352, 356, 357, 370, 371

densification 266

depth-to-width (D/W) ratio 126

diffusion bonding 265, 267, 279

dimensional stability 82, 85

disbonding 334, 337, 342, 345, 376, 377

disoriented dendrites 307, 312

dispersoid(s) 5, 262

dissimilar 2, 44, 54, 69, 110, 151, 208, 249, 278, 327, 328, 329, 331, 332, 333, 334, 336, 337, 340, 342, 343, 344, 345, 346, 347, 354, 355, 357, 363, 376, 377, 413, 421

dissimilar alloy(s) 327, 328, 376

double-spot Vrestraint test 134

drill collars 10, 158

ductility recovery temperature (DRT) 233, 394, 395, 396, 397, 398

ductile microvoid coalescence 98

ductile-to-brittle transition temperature (DBTT) 359  
 ductility 1, 7, 55, 72, 84, 95, 96, 98, 99, 147, 158, 167, 255, 268, 276, 278, 283, 357, 359, 360, 361, 378, 380  
 ductility dip cracking (DDC) 3, 59, 100, 109, 128, 129, 130, 131, 132, 133, 155, 156, 209, 211, 363, 399, 402  
 Duranickel 301 158

**E**

easy growth directions 57, 309  
 electric arc furnace (EAF) melting 12  
 electrical 1, 2, 3, 145, 331  
 electron backscattered diffraction (EBSD) 139, 142, 300, 301, 305, 306, 309, 323  
 electron configuration 15  
 electron probe microanalysis (EPMA) 65, 338, 340  
 electron-beam welding (EBW) 229, 234, 252, 254, 268, 278, 301, 318, 392  
 electronegativity 20  
 electronic compounds 41  
 electropositive character 41  
 electroslog remelting 12, 161  
 embrittlement 19, 22, 84, 85, 93, 96, 100, 130, 152, 156, 268, 270, 281, 284, 294, 295, 332  
 entropy 317  
 epitaxial dendrite growth 301  
 equiaxed grains 259, 263, 299, 302, 303, 304  
 equilibrium conditions 33  
 erosion 5, 281, 283, 299  
 eutectic 7, 19, 21, 22, 27, 32, 43, 71, 72, 76, 77, 78, 79, 100, 101, 102, 105, 108, 111, 113, 114, 117, 118, 119, 122, 123, 124, 127, 134, 143, 157, 176, 177, 178, 182, 183, 184, 187, 188, 189, 190, 191, 192, 193, 194, 195, 196, 197, 198, 199, 200, 204, 206, 213, 216, 217, 218, 219, 220, 221, 224, 225, 270, 274, 326, 362  
 eutectic healing 274  
 eutectic-like 17, 72  
 exothermic reaction 158  
 extrusion 13, 81

**F**

fabrication 55, 57, 100, 105, 117, 135, 148, 252, 272, 279, 281, 327, 345, 363, 364, 365, 376, 377, 379, 380, 381  
 fatigue 4, 12, 156, 161, 203, 206, 229, 283, 284, 285, 292, 294, 295, 298, 299, 327, 369, 370, 371, 378, 380  
 Fermi level 42, 199  
 ferrite solidification 22  
 ferritic 334, 335, 345, 346, 376, 377  
 Filler Metal 52M 9, 139, 140, 342, 343, 374, 375  
 Filler Metal 625 283  
 Filler Metal 69 158  
 Filler Metal 725 208, 368, 369  
 Filler Metal 82 93, 98, 99, 131, 133, 135, 136, 137, 138, 140, 142, 345, 373  
 Filler Metals 52 and 52M 373  
 FM 622 353, 354, 355, 356  
 FM 625 92, 144, 338, 354, 355, 356, 362, 363  
 fractographic study 291  
 fracture toughness (JIC) 98, 99, 357, 360, 378, 380  
 free energy 33, 170, 227  
 friction welding 267, 279  
 fusion weld(s, ing) 5, 21, 36, 43, 45, 62, 64, 70, 71, 72, 73, 74, 76, 77, 79, 81, 152, 175, 187, 214, 249, 250, 259, 260, 268, 272, 276, 278, 310, 328, 349, 351, 355, 381  
 fusion zone solidification cracking 25, 100, 122, 126, 209, 213  
 fusion zone(s) 5, 16, 25, 32, 33, 35, 40, 57, 59, 61, 65, 66, 71, 72, 73, 78, 79, 82, 85, 87, 91, 98, 100, 114, 115, 118, 122, 126, 146, 157, 158, 173, 175, 177, 184, 185, 187, 193, 195, 197, 198, 199, 200, 203, 209, 213, 236, 249, 259, 260, 272, 278, 302, 309, 328, 329, 331, 334, 351, 353, 380, 381, 384, 392

**G**

galvanic corrosion 149  
 gamma double prime 4, 161, 184, 281  
 gamma prime 4, 10, 43, 248, 281, 421  
 Gleeble hot ductility 120, 121, 122, 123, 140, 231

globular morphology 55, 104  
 gas metal arc welding (GMAW) 9, 118, 344  
 gas tungsten arc welding (GTAW) 9, 149, 318, 321, 331, 368, 373, 392  
 grain boundary engineering 294, 295, 298  
 grain boundary liquation 81, 118, 119, 203, 204, 225, 231, 273, 292, 297, 398  
 grain boundary segregation 81, 118, 203, 204, 209, 232, 233, 415, 417  
 grain growth 59, 81, 84, 91, 96, 98, 118, 119, 126, 203, 229, 232, 236, 256, 260, 265, 287, 293, 295, 360, 365  
 graphite 2, 145, 192  
 graphitized 2

**H**

hardness 2, 5, 7, 20, 56, 92, 158, 165, 166, 169, 174, 209, 248, 260, 261, 295, 296, 334, 337, 338, 339, 361  
 Hastelloy 2, 7, 9, 10, 22, 35, 36, 44, 45, 73, 108, 119, 150, 151, 154, 225, 227, 250, 252, 377  
 Hastelloy B family 22  
 Hastelloy X 9, 108, 119, 154, 225, 227  
 HAZ 40, 55, 81, 82, 83, 87, 91, 100, 118, 119, 120, 122, 124, 125, 127, 128, 129, 130, 154, 157, 158, 203, 204, 206, 208, 209, 211, 225, 226, 227, 228, 229, 230, 231, 232, 233, 234, 235, 236, 238, 239, 241, 242, 243, 244, 245, 246, 247, 248, 251, 252, 272, 273, 274, 276, 278, 280, 285, 291, 293, 294, 295, 296, 297, 298, 324, 327, 332, 334, 335, 337, 338, 342, 345, 346, 347, 348, 360, 361, 362, 365, 377, 380, 381, 386, 387, 388, 389, 392, 396, 397, 398, 402, 419  
 heat affected zone 5, 16, 33, 38, 81, 154, 203, 208, 249, 250, 251, 252, 253, 280, 286, 365, 378, 402  
 Heliarc 9  
 heterogeneous nucleation sites 310  
 hexagonal closed packed 26  
 high thermal conductivity 11, 158  
 highly restrained narrow groove weld mockups 401

homogenization 13, 82, 87, 88, 90, 147, 148, 152, 180, 232  
 hot cracking 107, 129, 145, 153, 154, 155, 156, 161, 225, 246, 251, 252, 351, 361, 362, 363, 378, 380, 381, 401, 402  
 hot ductility test(s, ing) 134, 154, 235, 251, 276, 286, 287, 289, 291, 293, 296, 381, 386, 394, 395, 398, 399  
 hot isostatic pressure (HIP) 256  
 hot-working 13, 81, 98, 256

**I**

impact toughness 1, 95, 282, 359, 360, 361, 362  
 impurities 4, 122, 124, 131, 204, 224, 245  
 IN713C 4  
 INCO 6, 7, 8, 9, 10, 91, 359, 363, 367, 368  
 ingots 13  
 interdendritic 19, 25, 65, 66, 71, 72, 74, 76, 77, 78, 79, 85, 87, 88, 93, 96, 99, 100, 103, 111, 146, 147, 177, 178, 183, 200, 211, 217, 225, 228, 233, 250, 285  
 interfacial terminal liquid 101  
 intergranular attack (IGA) 55, 83, 416  
 intermediate temperature ductility 155, 157  
 intermetallic(s) 25, 32, 34, 35, 43, 72, 93, 95, 103, 105, 118, 127, 161, 167, 184, 185, 211, 255, 268, 270, 279, 280  
 interpass temperature 331  
 interstitial elements 36, 59, 175  
 INVAR 3, 50, 131, 406  
 INVAR (Fe-36Ni) 131  
 isomorphous 3, 20, 71  
 isothermal 22, 24, 25, 26, 27, 29, 33, 34, 35, 74, 276, 296  
 isothermally 183  
 iso-weight 221

**J**

Johnson-Mehl-Avrami model 38

**K**

k (partition coefficient) 65  
 kinetic barriers 349  
 kinetic models 33  
 K-MONEL 10  
 kupfer nicell 6

**L**

laser cladding 301  
 laser surface melting 301  
 Laves 16, 17, 19, 32, 41, 66, 70, 76, 105, 107, 109, 110, 111, 117, 119, 120, 182, 184, 185, 186, 187, 188, 190, 191, 192, 193, 195, 197, 199, 200, 202, 213, 214, 215, 216, 217, 218, 219, 220, 221, 222, 224, 225, 226, 228, 232, 233, 285, 290, 291, 292, 354, 355  
 lever law 63, 64, 200  
 light optical microscope 57  
 liquation cracking temperature range (LCTR) 286, 288, 297, 398  
 liquidus projection(s) 22, 24, 25, 26, 29, 32, 35, 36, 37, 38, 71, 73, 75, 76, 175, 182, 183, 184, 192, 193, 194, 196, 198  
 liquidus slope 195  
 liquified natural gas (LNG) 357  
 localized thermal expansion 243

**M**

M2S 48, 145, 404  
 MA6000 5, 256, 258, 259, 264, 266  
 MA754 256, 257, 258, 262, 266, 267  
 MA956 256, 260, 262, 263, 264, 265, 266, 267  
 machining 1  
 magnetostrictive 2  
 manual pulsed gas metal arc welding (P-GMAW) 368  
 marine 10, 12, 145, 158  
 martensite 208, 331, 332, 333, 336, 337, 338, 340, 341, 342, 345, 346, 359, 360, 361, 376, 420  
 matrix 1, 2, 4, 10, 18, 19, 20, 24, 26, 41, 51, 55, 72, 79, 82, 118, 121, 131, 138, 145, 158, 161, 164, 165, 167, 169, 170, 171, 187, 188, 190, 192, 193, 197, 199, 202, 204, 206, 225, 231, 236, 239, 257, 262, 298, 348, 417  
 maximum crack distance (MCD) 107, 108, 110, 113, 382, 384, 385  
 maximum crack length (MCL) 107, 213, 216, 219, 387, 388  
 mechanical properties 2, 24, 47, 51, 55, 56, 59, 76, 90, 91, 92, 93, 95, 96, 97, 122, 127, 138, 147, 148, 153, 156, 157, 161, 162, 164, 173, 174, 175, 208, 209, 237,

243, 246, 253, 255, 256, 260, 261, 262, 268, 272, 276, 279, 280, 281, 282, 283, 298, 315, 317, 324, 328, 363, 368, 369, 378, 380, 399, 402  
 mechanically alloyed 5, 256  
 melting enthalpy values 331  
 metastable 19, 26, 171  
 microfissuring 129, 155, 251, 252  
 microprobe 65, 66, 74, 79, 191, 194, 200, 342  
 microstructural evolution 32, 40, 57, 66, 68, 76, 154, 173, 175, 177, 182, 184, 187, 203, 251, 252, 377  
 microstructure evolution 16, 57, 70, 72, 77, 249, 252, 332, 334  
 microstructure(s) 15, 16, 26, 33, 45, 47, 55, 56, 57, 59, 60, 61, 70, 71, 72, 76, 77, 78, 79, 81, 82, 85, 87, 88, 93, 94, 98, 102, 113, 118, 122, 123, 127, 133, 134, 143, 146, 147, 151, 153, 156, 161, 177, 178, 183, 184, 187, 193, 195, 196, 197, 198, 203, 204, 206, 211, 217, 219, 220, 232, 233, 235, 241, 248, 249, 250, 251, 252, 256, 259, 262, 268, 278, 280, 281, 282, 283, 284, 285, 287, 288, 294, 295, 296, 303, 304, 305, 306, 307, 325, 326, 328, 332, 333, 334, 338, 345, 351, 360, 361, 363, 365, 366, 367, 376, 381, 386, 398, 419, 420, 421  
 microvoid(s) 96, 130  
 migrate(s, ed) 59, 122, 131, 132, 133, 134, 138, 139, 140, 142, 334, 335, 347, 348, 365  
 Monel 400 44, 67, 70, 116  
 MONELL metal 8  
 monovariant 176, 183, 184, 192, 197  
 morphology 20, 77, 93, 100, 102, 127, 130, 164, 172, 181, 213, 216, 219, 224, 234, 241, 242, 243, 259, 262, 265, 268, 299, 301, 347, 348  
 multipass 16, 59, 83, 93, 97, 117, 122, 124, 127, 131, 132, 135, 143, 155, 235, 331, 361, 362, 363  
 mushy zone 101, 102, 104, 113, 125, 126, 216, 217, 218, 219, 320  
**N**  
 NbC 32, 66, 70, 76, 82, 105, 109, 110, 119, 120, 121, 133, 138, 140, 143, 182, 184,

- 185, 186, 187, 188, 190, 191, 192, 193,  
194, 195, 196, 197, 202, 204, 206, 207,  
209, 213, 216, 217, 218, 219, 220, 221,  
222, 224, 228, 231, 235, 347, 354, 367
- neutron absorption 79
- New PHACOMP 16, 41, 42, 45, 151, 198,  
200, 203, 250
- NICKEL 6
- nickel alloy 200 11
- nickel alloy 300 11
- nickel carbonyl 11
- Ni-Cu alloy K-500 158
- Ni-Cu alloys K-500 and K-501 12
- nil ductility temperature (NDT) 394, 395
- nil strength temperature (NST) 120, 233,  
292, 394, 395, 396
- NIMONIC 10, 158
- Nimonic 263 161
- Nimonic 80A 158, 234, 252
- Ni-Nb binary 30, 31, 190, 193
- nitride(s) 3, 13, 148, 256, 349
- Ni-X binary systems 66, 77
- non-destructive 380
- non-equilibrium conditions 33
- NOx 369, 371, 372, 378
- nuclear 11, 55, 98, 153, 156, 254, 373
- nucleation 24, 96, 98, 169, 170, 177, 178,  
299, 300, 302, 303, 304, 307, 326, 334,  
338, 376
- O**
- ODS alloys 2, 5, 255, 256, 257, 258, 259,  
260, 262, 266, 267, 268, 279
- on-cooling 203, 231, 233, 276, 376, 386,  
387, 388, 389, 394, 395, 396, 398
- on-heating 233, 276, 278, 291, 386, 387,  
388, 389, 394, 396, 397, 398
- ordered 15, 18, 22, 26, 43, 96, 162, 163,  
167, 280
- orthogonal growth 301
- orthorhombic structure 284
- over-alloyed 328
- oxidation 4, 5, 12, 15, 44, 48, 145, 157,  
161, 256, 270
- P**
- partially melted zone (PMZ) 118, 127,  
204, 225, 228, 229, 230, 233, 380, 387,  
388, 396
- particle/matrix decohesion 98
- partitioning 70, 71, 74, 157, 169, 173, 175,  
353
- passive film 69, 349
- Permanickel 9, 158
- Permanickel 300 158
- petrochemical 1, 15, 47, 367, 368
- PHACOMP 16, 40, 41, 198
- phase diagram(s) 15, 16, 20, 21, 22, 23,  
26, 28, 30, 31, 33, 40, 41, 44, 45, 71,  
79, 80, 152, 190, 196, 197, 198, 199,  
204, 205, 206, 250, 251, 268, 269, 279,  
378
- phase transformation(s) 16, 33, 70, 153,  
175, 182, 184, 377, 392
- pickling 13, 145
- pitting 12, 13, 48, 54, 146, 147, 148, 149,  
150, 328, 349, 350, 358, 363, 364, 368,  
369, 413, 416, 417, 418
- planar interface 299
- planar phase field 198
- plasma arc welding (PAW) 331
- plastic deformation 81, 83, 87, 96, 247,  
263
- platelets 27
- polycrystalline superalloys 299
- polygonization 129
- porosity 2, 3, 9, 262, 270
- post weld heat treatment (PWHT) 82,  
83, 84, 85, 87, 88, 90, 93, 100, 146, 147,  
148, 206, 208, 232, 233, 238, 241, 242,  
244, 245, 246, 247, 248, 252, 284, 285,  
286, 287, 288, 289, 290, 291, 292, 295,  
296, 332, 334, 338, 339, 345, 346, 347,  
348, 349, 363, 364, 365, 366, 367, 368,  
369
- postweld stress relief cracking 347
- precipitate cutting 162, 164
- precipitation 2, 4, 5, 10, 11, 12, 15, 16, 17,  
21, 22, 24, 25, 26, 33, 37, 38, 43, 55, 65,  
71, 76, 77, 81, 84, 85, 91, 93, 94, 107,  
110, 114, 118, 119, 120, 121, 122, 130,  
131, 138, 140, 141, 153, 157, 158, 161,  
162, 169, 173, 175, 177, 200, 203, 204,  
206, 208, 209, 211, 213, 224, 225, 228,  
231, 232, 233, 235, 236, 237, 238, 239,  
240, 241, 244, 245, 246, 247, 248, 249,  
253, 281, 285, 292, 293, 324, 331, 332,  
345, 366, 367, 368, 398, 415, 421

- precipitation-strengthened 2, 4, 16, 22, 65, 91, 118, 119, 120, 122, 157, 158, 161, 173, 175, 203, 204, 206, 208, 209, 211, 224, 235, 248, 281, 332
- preferential attack 69, 349
- preheat(s, ed, ing) 13, 246, 304, 306, 318, 331
- premature void nucleation 98
- pressurized electroslag remelting 12, 13
- primary dendrite arm spacing (PDAS) 88
- primary water stress corrosion cracking (PWSCC) 373
- propagation 99, 100, 217, 219, 220
- pulsed electric current sintering (PECS) 266, 267, 279
- R**
- recrystallization 13, 55, 81, 82, 91, 97, 98, 130, 131, 132, 133, 256, 260, 263, 294
- reheat cracking 129, 130, 155, 253, 347, 365, 367, 377
- relaxation cracking 55, 87, 348, 365
- René 41 158, 174, 230, 244, 245, 246, 247, 252, 253, 254
- René alloys 222
- residual stress(es) 5, 82, 83, 84, 85, 87, 93, 96, 98, 127, 146, 147, 206, 236, 241, 243, 244, 247, 248, 283, 318, 346, 348, 366, 367
- Rosenthal equation 125
- Rosenthal heat flow solution(s) 126, 305
- S**
- saturated strain 110, 382, 383, 384, 385, 387, 388
- SAW deposits 138, 359, 362
- Scheil equation 60, 61, 63, 64, 76, 113, 187, 200
- Scheil partitioning 57
- Scheil-Gulliver approximation 108
- scrubbers 146
- seawater 3, 12, 143, 144, 149, 150
- segregation cracking 129
- service performance 380
- Sigmajig test(s) 212, 213, 274, 275, 392, 393
- signature 394
- simulative tests 381
- single crystal alloy(s) 5, 281, 299, 300, 301, 322
- Single Sensor Differential Thermal Analysis (SS-DTA) 107, 343, 377, 392
- solidification 3, 16, 17, 19, 22, 25, 26, 27, 32, 35, 36, 37, 38, 43, 44, 45, 57, 58, 59, 60, 61, 62, 63, 64, 65, 68, 69, 70, 71, 72, 73, 75, 76, 77, 79, 80, 85, 88, 91, 93, 96, 100, 101, 102, 103, 104, 105, 107, 108, 109, 110, 111, 112, 113, 114, 116, 117, 118, 122, 123, 125, 126, 127, 128, 133, 134, 138, 139, 140, 141, 143, 146, 150, 151, 152, 153, 154, 155, 157, 173, 175, 176, 177, 178, 180, 182, 183, 184, 185, 187, 191, 192, 193, 194, 195, 196, 198, 199, 200, 202, 211, 212, 213, 214, 215, 216, 217, 218, 219, 220, 222, 223, 224, 225, 226, 227, 233, 234, 246, 249, 250, 251, 259, 260, 274, 275, 276, 278, 283, 285, 299, 302, 305, 308, 310, 311, 314, 315, 316, 318, 320, 321, 322, 325, 326, 332, 333, 334, 335, 342, 343, 344, 345, 349, 351, 353, 354, 355, 356, 357, 362, 371, 373, 374, 375, 376, 380, 381, 383, 384, 385, 388, 389, 390, 391, 392, 393, 399, 420
- solidification cracking temperature range (SCTR) 108, 109, 383, 385, 386
- solidification subgrain boundary (SSGB) 57
- solid-solution 2, 3, 4, 12, 14, 16, 17, 19, 20, 21, 22, 24, 29, 47, 51, 55, 56, 57, 65, 70, 72, 76, 81, 82, 84, 85, 87, 91, 93, 100, 103, 105, 108, 110, 118, 119, 120, 121, 129, 130, 143, 146, 161, 162, 165, 166, 173, 175, 187, 209, 213, 256, 281, 283, 327, 331
- solid-solution strengthened 2, 3, 4, 12, 24, 47, 51, 55, 56, 57, 70, 72, 81, 82, 84, 85, 87, 91, 93, 100, 103, 105, 108, 118, 119, 120, 121, 129, 130, 143, 146, 161, 173, 209, 213, 281, 283, 327, 331
- solid-solution strengthener(s) 17, 76, 110
- solid-state diffusion 36, 61, 62, 63, 64, 151, 175, 250
- solidus 1, 60, 101, 105, 118, 128, 129, 141, 187, 198, 199, 206, 214, 217, 219

- solubility 2, 3, 15, 16, 17, 21, 22, 24, 25,  
 26, 28, 29, 32, 35, 41, 42, 43, 45, 51, 66,  
 69, 71, 77, 79, 80, 87, 93, 103, 119, 145,  
 151, 152, 165, 166, 170, 175, 177, 179,  
 187, 192, 198, 199, 200, 202, 203, 250,  
 257, 281, 349, 351, 353  
 solute 17, 57, 58, 59, 60, 61, 63, 64, 72, 77,  
 81, 83, 85, 101, 118, 146, 150, 151, 152,  
 170, 175, 178, 179, 187, 191, 193, 194,  
 195, 196, 197, 198, 200, 202, 206, 211,  
 217, 220, 221, 228, 231, 249, 250, 257,  
 299, 300, 302, 355  
 solute redistribution 57, 58, 59, 61, 63,  
 64, 101, 146, 150, 151, 152, 175, 193,  
 194, 196, 197, 200, 202, 217, 220, 221,  
 249, 250  
 solution annealing 51, 55, 128, 152, 161,  
 230, 231, 232, 235, 236, 237, 238, 239,  
 240, 246, 284, 285, 286, 287, 288, 289,  
 290, 294, 296  
 solvent 11, 187, 193, 200  
 solvus 4, 43, 146, 177, 178, 179, 180, 181,  
 199, 202, 204, 206, 285, 287, 292, 294,  
 295  
 speciality 5, 13, 47, 48, 77, 255, 380  
 spent nuclear fuel 33, 79, 152  
 spheroidal graphite particles 11  
 spinodal decomposition 21  
 stoichiometric 19, 26, 77  
 strain-age cracking (SAC) 4, 130, 141,  
 157, 208, 209, 211, 235, 236, 237, 238,  
 239, 240, 241, 243, 248, 253, 284, 295  
 strain-to-fracture test 131, 134, 135, 136,  
 137, 138, 156, 400, 402  
 stray grain(s) 5, 299, 300, 301, 302, 307,  
 308, 309, 310, 313, 314, 315, 318, 319,  
 320, 321, 322, 323, 324, 325, 326  
 stress corrosion cracking (SCC) 55, 83,  
 98, 128, 144, 146, 153, 294, 332, 368, 369  
 stress relaxation process 83  
 stress relaxation technique(s) 85, 87,  
 147  
 stress-corrosion cracking 11  
 sulfidation 12, 15  
 super lattice dislocations 19, 162, 164  
 superalloy welding at elevated  
 temperature (SWET) 246  
 superalloy(s) 4, 5, 12, 14, 15, 17, 19, 26,  
 30, 32, 40, 41, 43, 44, 45, 64, 66, 68, 103,  
 141, 151, 152, 153, 154, 155, 157, 158,  
 162, 164, 177, 182, 184, 185, 186, 187,  
 188, 190, 192, 203, 204, 211, 214, 217,  
 218, 220, 222, 224, 225, 226, 227, 228,  
 229, 235, 236, 237, 238, 240, 241, 243,  
 244, 245, 246, 248, 249, 250, 251, 252,  
 253, 254, 255, 256, 257, 258, 270, 276,  
 278, 279, 280, 283, 295, 298, 299, 301,  
 324, 325, 326, 378, 402, 419, 421, 422  
 superaustenitic stainless steel(s) 48, 151,  
 350  
 superduplex 48, 378  
 superlattice dislocations 162
- T**
- TCP 7, 19, 40, 41, 43, 72, 73, 74, 75, 96,  
 97, 105, 106, 118, 149, 199, 200, 202  
 TCP phase(s) 40, 41, 43, 72, 73, 74, 75,  
 96, 97, 105, 118, 149, 200, 202  
 terminal liquid 100, 101, 102, 103, 105,  
 110, 111, 113  
 ternary analog 76  
 ternary system(s) 22, 26, 32, 44, 77, 193,  
 250  
 tetragonal 19, 72, 171  
 thermal crack susceptible region 388,  
 390  
 thermal cycling 155, 252, 336  
 thermal expansion 51, 161, 213, 234  
 thermo-mechanical processing 40, 272,  
 274  
 threshold strain(s) 110, 134, 135, 136,  
 138, 382, 383, 387, 399, 400  
 time-temperature-transformation (TTT)  
 37, 38, 39, 171, 172, 283  
 topologically closed packed (TCP) 19,  
 72, 199  
 torsional 10, 12, 158  
 tortuosity 130, 131, 139, 141  
 toughness 1, 3, 5, 19, 55, 59, 72, 84, 91, 93,  
 95, 96, 100, 109, 120, 121, 122, 128, 129,  
 130, 131, 133, 134, 155, 156, 161, 167,  
 171, 209, 211, 225, 230, 231, 232, 233,  
 238, 240, 241, 242, 244, 255, 268, 270,  
 272, 274, 276, 277, 278, 283, 284, 290,  
 291, 292, 297, 298, 363, 367, 380, 381,  
 394, 395, 396, 397, 398, 399, 402  
 transient embrittlement 239, 240,  
 241

- transient liquid phase (TLP) 262, 267, 276, 279, 280  
 transient liquid phase bonding 267, 279  
 transition joints 327, 376  
 transmission electron microscopy 257  
 transmission electron microscopy (TEM) 93  
 Transvarestraint 383, 384, 386, 402  
 triple melt 12, 161  
 triple melt(ed, ing) 12, 161  
 TTT diagram 38, 39, 172, 283  
 Type 304L 109, 136, 137, 138, 342, 343, 344, 373, 386  
 Type 308L 373, 375  
 Type 310 111, 384, 386, 387, 388, 389, 390, 395, 396, 398  
 Type I boundaries 334  
 Type II boundaries 334, 335, 345
- U**  
 Udimet 520 161  
 Udimet 700 225, 230, 246, 253, 279
- V**  
 vacuum arc remelting (VAR) 12, 161  
 vacuum induction melt(ed, ing) (VIM) 12, 161  
 vacuum insulated double-walled tubing (VIT) 367  
 valence 20  
 Varestraint 104, 105, 106, 107, 108, 109, 110, 111, 112, 113, 116, 117, 125, 134, 153, 211, 213, 214, 215, 216, 219, 220, 222, 229, 232, 351, 353, 354, 362, 363, 381, 382, 385, 386, 387, 388, 389, 390, 392, 396, 397, 399, 402  
 VIM/VAR 12, 13
- W**  
 warm cracking 380  
 warm-working deformation 294  
 Waspaloy 107, 119, 159, 174, 222, 225, 234, 239, 241, 242, 243, 244, 245, 247, 252, 253, 283, 295, 296, 297, 298, 325, 390, 407  
 waterwall(s) 327, 369  
 weld hot cracking 361  
 weld metal liquation cracking 100, 122, 129, 134, 363  
 weld repair(s) 2, 5, 232, 281, 283, 300, 301, 302, 304, 314, 321, 323, 324  
 weld residual stress(es) 238, 243, 247, 248, 367  
 weld solidification cracking 58, 100, 101, 103, 105, 107, 109, 110, 117, 126, 128, 129, 143, 153, 209, 222, 223, 224, 251, 272, 274, 275, 280, 342, 343, 344, 346, 353, 363, 373, 383, 384, 385, 386, 389, 392, 402  
 weldability 1, 2, 3, 4, 11, 15, 19, 43, 47, 59, 72, 76, 77, 81, 100, 103, 104, 105, 106, 107, 109, 110, 111, 114, 116, 117, 122, 125, 128, 131, 136, 143, 145, 151, 152, 153, 154, 155, 157, 158, 161, 162, 172, 184, 187, 195, 208, 209, 211, 212, 213, 214, 216, 219, 220, 222, 226, 228, 233, 235, 249, 250, 251, 252, 253, 255, 268, 272, 276, 280, 281, 282, 283, 284, 285, 294, 295, 296, 298, 324, 325, 327, 328, 332, 342, 355, 356, 359, 362, 368, 376, 377, 378, 379, 380, 394, 401, 402, 409, 415, 419  
 welding metallurgy 1, 2, 15, 44, 47, 57, 107, 150, 151, 152, 154, 157, 173, 250, 251, 253, 255, 259, 281, 327, 376, 377, 379, 398, 409, 415, 419
- X**  
 X-750 4, 158, 159, 161, 174, 208, 407
- Y**  
 yttria (Y<sub>2</sub>O<sub>3</sub>) 5
- Z**  
 zero ductility range (ZDR) 120